



# JOURNAL OF THE ELECTROCHEMICAL SOCIETY

ELECTROCHEMICAL  
SCIENCE AND TECHNOLOGY

SOLID-STATE  
SCIENCE AND TECHNOLOGY

REVIEWS AND NEWS



VOL. 123, NO. 1

JANUARY 1976

JESOAN 123 (1) 1-148, 1C-16C



# FUTURE MEETINGS

## Of The Electrochemical Society



WASHINGTON, D.C.—MAY 2, 3, 4, 5, 6 & 7, 1976

### Headquarters at the Sheraton Park Hotel

Planned symposia for the Washington Meeting include the following Divisions and subjects:

**Battery and Electronics**—Materials for Batteries and Fuel Cells; **Corrosion**—General Session; **Corrosion and Industrial Electrolytic**—Electrochemistry and Corrosion Processes in Caustic Solutions; **Dielectrics and Insulation**—General Session; **Dielectrics and Insulation and Electronics**—Etching; **Dielectrics and Insulation, Electronics, and Electrothermics and Metallurgy**—Control and Utilization of Defects in Nonmetallic Solids; **Electronics**—Semiconductors General Session, Surface Properties of Phosphors and Photoconductors, Luminescence General Sessions, General Materials and Processes General Session; **Electronics and Electrothermics and Metallurgy**—International Symposium on Solar Energy, Seventh International Conference on Electron and Ion Beam Science and Technology; **Industrial Electrolytic**—Engineering Analysis and Scale-Up of Electrochemical Systems; **Industrial Electrolytic and Organic and Biological Electrochemistry**—Industrial Electro-Organic Processes; **Organic and Biological Electrochemistry**—Electrochemical Oxidations, General Session; **Physical Electrochemistry**—Spectroscopic Methods in Electrochemical Studies, General Session; **New Technology Subcommittee, Corrosion, Electrothermics and Metallurgy, and Industrial Electrolytic**—International Symposium on Molten Salts; **New Technology Subcommittee, Dielectrics and Insulation, and Electronics**—Inorganic Dielectric Materials for Display and Storage Devices.

---

LAS VEGAS, NEVADA—OCTOBER 17, 18, 19, 20, 21 & 22, 1976

### Headquarters at Caesar's Palace

Planned symposia for the Las Vegas Meeting include the following Divisions and subjects:

**Battery**—Low-Maintenance and Maintenance-Free Lead Acid Batteries, Porous Electrodes: Theory and Practice, General Session; **Battery, Electrodeposition, and Industrial Electrolytic**—High Current Density Electrode Processes; **Corrosion**—Corrosion in Scrubbing Systems, General Session; **Corrosion and Electrothermics and Metallurgy**—Corrosion Encountered in Energy Extraction from Geothermal Brines and Steams, Properties of High Temperature Alloys; **Dielectrics and Insulation and Electronics**—Dielectric Isolation and Semiconductors on Insulating Substrates and Silicon on Sapphire, Materials, Devices and Fabrication Techniques for Image Storage and Display, Materials and Structures for Integrated Optics; **Dielectrics and Insulation, Electronics, and Electrothermics and Metallurgy**—The Chemistry and Crystallography of Electronic Materials Formed by Chemical Vapor Deposition; **Electrodeposition**—Selective Plating, General Session; **Electronics**—LED's and Injection Lasers: Process Technology and Degradation Mechanisms, Lithographic Techniques for Device Processing, Semiconductors General Sessions, General Materials and Processes General Session; **Electrothermics and Metallurgy**—General Session.

---

PHILADELPHIA, PENNSYLVANIA—MAY 8, 9, 10, 11, 12 & 13, 1977

### Headquarters at the Philadelphia Sheraton

Planned symposia for the Philadelphia Meeting include the following Divisions and subjects:

**Corrosion**—General Session; **Corrosion and Electronics**—Deterioration of Electronic Devices; **Corrosion and Electrothermics and Metallurgy**—Corrosion Problems Involving Volatile Corrosion Products; **Dielectrics and Insulation**—Failure Mechanisms in Dielectric Materials, Formation and Storage of Microwave Acoustic Holograph, General Session; **Dielectrics and Insulation and Electronics**—Packaging; **Dielectrics and Insulation and Electrothermics and Metallurgy**—Aluminum in Electrical and Electronics Industry, Metal Substrate Interactions; **Electrodeposition and Physical Electrochemistry**—Mechanisms of Electrocrystallization; **Electronics**—Semiconductors General Session, Effects of Structure and Symmetry on Phosphor Brightness and Color, X-Ray Phosphors and Radiography, Luminescence General Session, General Materials and Processes General Session; **Electronics and Electrothermics and Metallurgy**—Thermodynamics of Metal and Electronic Materials, Third International Symposium on Silicon Materials Science and Technology; **Electrothermics and Metallurgy**—Advanced Techniques for Materials Removal Purposes; **Industrial Electrolytic**—Electrodialysis and Membrane Processes, General Session; **Organic and Biological Electrochemistry**—Biological Redox Processes, Organometallic Transition Metal Complex Electrochemistry, Stereochemical Aspects of Organic Electrode Processes, General Session; **Physical Electrochemistry**—General Session; **New Technology Subcommittee, Battery, and Electronics**—Materials and Processes for Conventional and Electric Vehicles; **Diamond Jubilee Committee (Ad Hoc)**—History of Electrochemistry; **New Technology Subcommittee**—Future of Electrochemistry.



After thorough discussion the Publication Committee and Board of Directors have voted to use SI units in the JOURNAL and other publications of the Society. The units will be phased into the JOURNAL until January 1, 1977 at which time they will become mandatory. While the tendency to unify anything, units included, is sometimes very difficult (as will be evident when the United States converts to the metric system), the benefits appear to outweigh the costs.

A report explaining the use of the units is printed below. Another source of information is the Manual of Symbols and Terminology for Physicochemical Quantities and Units: Appendix III: Electrochemical Nomenclature, Pure and Applied Chemistry, 37, 499-516 (1974) available in reprint from the IUPAC Secretariat, Bank Court Chambers, 2-3, Pound Way, Cowley Centre, Oxford OX4 3YF, England, by surface mail, \$1.20; by airmail, \$1.80. Norman Hackerman Editor

## SI—The International System of Units

SI, the international designation for *Système International d'Unités*, will become mandatory in all publications of The Electrochemical Society on January 1, 1977. Equivalents in English or other common units may also be given in parentheses until the end of 1980 for the benefit of a particular audience. Beginning with 1981 the SI units will be used exclusively in all Society publications. The advantages and practicality of SI are such that it is being adopted throughout the world for all scientific, technical, and practical purposes, and thus its universal and exclusive application is clearly ordained.

SI is essentially an extension and refinement of the metric system. There are seven base units and, currently, some 15 derived units with special names. These, with a set of multiplicative prefixes and a set of rules for their application, form the entire system, but it has been recognized that there are certain other units whose use is so widespread that they must be retained. These are not ordinarily needed in a technical context.

The following tables provide a summary of SI. Its application is straightforward; more detailed discussions and conversion factors are available elsewhere (1, 2).

### References

1. E. A. Mechty, "The International System of Units," Second Revision, 1973, NASA SP-7012, U.S. Government Printing Office, Washington, D.C., 20402, \$0.50.
2. "Metric Practice Guide," ASTM E 380-72<sup>E</sup>, June 1972.

### SI Base Units

Physical quantity	Name	Symbol
length	meter	m
mass	kilogram	kg
time	second	s
electric current	ampere	A
thermodynamic temperature	kelvin	K
luminous intensity	candela	cd
amount of substance	mole	mol

### Other Units in Use with SI

Name	Symbol	Definition
minute	min	60 sec
hour	h	60 min
day	d	24 h
degree	°	( $\pi/180$ ) rad
minute	'	(1/60) <sup>o</sup>
second	"	(1/60) <sup>2</sup>
liter	l	10 <sup>-3</sup> m <sup>3</sup>
tonne	t	10 <sup>3</sup> kg
degree celsius	°C	K-273.15

### Other Selected SI Units

Physical quantity	Units
dynamic viscosity	m <sup>-1</sup> ·kg·s <sup>-1</sup> = Pa·s
electric charge density	m <sup>-3</sup> ·s·A = C/m <sup>3</sup>
electric field strength	m·kg <sup>-1</sup> ·s <sup>-3</sup> ·A <sup>-1</sup> = V/m
electric flux density	m <sup>-2</sup> ·s·A = C/m <sup>2</sup>
energy density	m <sup>-1</sup> ·kg·s <sup>-2</sup> = J/m <sup>3</sup>
energy flux density, irradiance	kg·s <sup>-3</sup> = W/m <sup>2</sup>
entropy, heat capacity	m <sup>2</sup> ·kg·s <sup>-2</sup> ·K <sup>-1</sup> = J/K
magnetic field strength	A/m
molar energy	m <sup>2</sup> ·kg·s <sup>-2</sup> ·mol <sup>-1</sup> = J/mol
moment of force	m <sup>2</sup> ·kg·s <sup>-2</sup> = N·m
permeability	m·kg <sup>-1</sup> ·s <sup>-2</sup> ·A <sup>-2</sup> = H/m
permittivity	m <sup>-3</sup> ·kg <sup>-1</sup> ·s <sup>4</sup> ·A <sup>2</sup> = F/m
specific energy	m <sup>2</sup> ·s <sup>-2</sup> = J/kg
surface tension	kg·s <sup>-2</sup> = N/m
thermal conductivity	m·kg <sup>-1</sup> ·s <sup>-3</sup> ·K <sup>-1</sup> = W/(m·K)

### Derived Units with Special Names

Physical quantity	Name	Symbol	Definition
quantity of electricity	coulomb	C	s·A
capacitance	farad	F	m <sup>-2</sup> ·kg <sup>-1</sup> ·s <sup>4</sup> ·A <sup>2</sup> = C/V
inductance	henry	H	m <sup>2</sup> ·kg <sup>-1</sup> ·s <sup>-2</sup> ·A <sup>-2</sup> = Wb/A
frequency	hertz	Hz	s <sup>-1</sup>
energy, work, quantity of heat	joule	J	m <sup>2</sup> ·kg·s <sup>-2</sup> = N·m
luminous flux	lumen	lm	cd·sr <sup>a</sup>
illuminance	lux	lx	m <sup>-2</sup> ·cd·sr <sup>a</sup>
force	newton	N	m·kg·s <sup>-2</sup>
electric resistance	ohm	$\Omega$	m <sup>2</sup> ·kg·s <sup>-3</sup> ·A <sup>-2</sup> = V/A
pressure	pascal	Pa <sup>b</sup>	m <sup>-1</sup> ·kg·s <sup>-2</sup> = N/m <sup>2</sup>
conductance	siemens	S	m <sup>-2</sup> ·kg <sup>-1</sup> ·s <sup>3</sup> ·A <sup>2</sup> = A/V
magnetic flux density	tesla	T	kg·s <sup>-2</sup> ·A <sup>-1</sup> = Wb/m <sup>2</sup>
potential difference, emf	volt	V	m <sup>2</sup> ·kg·s <sup>-3</sup> ·A <sup>-1</sup> = W/A
power, radiant flux	watt	W	m <sup>2</sup> ·kg·s <sup>-3</sup> = J/s
magnetic flux	weber	Wb	m <sup>2</sup> ·kg·s <sup>-2</sup> ·A <sup>-1</sup> = V·s

<sup>a</sup> sr = steradian.

<sup>b</sup> 1 Pa = 7.50064 × 10<sup>-3</sup> Torr, 1 Torr = 133.322 Pa.

### SI Prefixes and Rules

Prefix	Symbol	Multiplier
tera	T	10 <sup>12</sup>
giga	G	10 <sup>9</sup>
mega	M	10 <sup>6</sup>
kilo	k	10 <sup>3</sup>
(hecto)	(h)	(10 <sup>2</sup> )
(deka)	(da)	(10)
(deci)	(d)	(10 <sup>-1</sup> )
(centi)	(c)	(10 <sup>-2</sup> )
milli	m	10 <sup>-3</sup>
micro	$\mu$	10 <sup>-6</sup>
nano	n	10 <sup>-9</sup>
pico	p	10 <sup>-12</sup>
femto	f	10 <sup>-15</sup>
atto	a	10 <sup>-18</sup>

1. The parenthesized prefixes should be avoided where possible.
2. Compound prefixes should not be used. In the case of mass, the gram, g, is acceptable as a unit with a prefix in place of the kilogram.
3. Prefixes should be limited to the numerators of expressions where possible.

JANUARY 1976

## EDITOR

Norman Hackerman

## DIVISIONAL EDITORS

### BATTERY

R. J. Brodd  
Elton J. Cairns  
F. P. Malaspina

G. F. Nordblom  
Boone B. Owens  
J. L. Weininger

### CORROSION

Theodore R. Beck  
J. W. Faust, Jr.  
Z. A. Foroulls  
R. P. Frankenthal

Jerome Kruger  
Ken Nobe  
Earl S. Snavelly, Jr.  
J. Bruce Wagner

### DIELECTRICS AND INSULATION

Robert S. Alwitt  
Newton Schwartz  
Donald M. Smyth

John Szedon  
Lawrence Young

### ELECTRODEPOSITION

Ugo Bertocci  
Nathan Feldstein

Seymour Senderoff

### ELECTRONICS

Ephraim Banks  
George R. Cronin  
Glenn W. Cullen  
Murray Gershenzon  
James S. Harris  
Simon Larach

I. Arnold Lesk  
Ernest Paskell  
Jerome Prener  
Bertram Schwartz  
P. Wang  
J. M. Woodall

### ELECTROTHERMICS AND METALLURGY

William A. Adams  
Joan B. Berkowitz  
Daniel Cubicciotti  
W. E. Kuhn

F. S. Pettit  
W. W. Smeltzer  
Gene F. Wakefield  
Jack H. Westbrook

### INDUSTRIAL ELECTROLYTIC

Richard C. Alkire

Scott Lynn

### ORGANIC AND BIOLOGICAL ELECTROCHEMISTRY

Manuel M. Balzer  
Arthur A. Pilla

Stanley Wawzonek

### PHYSICAL ELECTROCHEMISTRY

Allen J. Bard  
A. J. de Bethune  
Larry R. Faulkner  
R. M. Hurd  
George J. Janz

Barry Miller  
David K. Roe  
C. W. Tobias  
F. G. Will

## EDITORIAL STAFF

Nancy S. Walters, Assistant to the Editor  
Jack H. Westbrook, News Editor  
Julius Klerer, Book Review Editor

## PUBLICATION STAFF

Sarah A. Kilfoyle, Publication Editor  
Rachel B. Cochran, Assistant Publication Editor

## PUBLICATION COMMITTEE

Newton Schwartz, Chairman  
Bruce E. Deal  
Robert T. Foley  
Norman Hackerman  
Jerome Kruger  
Paul C. Milner  
Jerome S. Prener  
Jack H. Westbrook

## ADVERTISING OFFICE

P.O. Box 2071  
Princeton, N.J. 08540

## EDITORIAL

N. Hackerman  
... 1C

# ELECTROCHEMICAL SCIENCE AND TECHNOLOGY

## TECHNICAL PAPERS

H. A. Frank  
W. L. Long  
A. A. Uchiyama  
... 1

Impedance of Silver Oxide-Zinc Cells

J. H. Kennedy  
J. C. Hunter  
... 10

Thin-Film Galvanic Cell Pb/PbF<sub>2</sub>/PbF<sub>2</sub>, CuF<sub>2</sub>/Cu

E. Peled  
E. Gileadi  
... 15

The Electrodeposition of Aluminum from Aromatic Hydrocarbon  
I. Composition of Baths and the Effect of Additives

## TECHNICAL NOTES

K. Niki  
I. Uchida  
H. A. Laitinen  
... 20

The Electrode Potential of the Chromate (VI)-Lithium Chromate (V) System in Molten Lithium Chloride-Potassium Chloride Eutectic

E. Korowa-Eisner  
E. Gileadi  
... 22

The Rotating Cone Electrode

## BRIEF COMMUNICATION

J. O'M. Bockris  
M. A. Habib  
... 24

A Calculation of the Entropy Maximum for the Double Layer in Terms of the Water Molecule Structure

# SOLID-STATE SCIENCE AND TECHNOLOGY

## TECHNICAL PAPERS

J. Rużyłło  
I. Shiota  
N. Miyamoto  
J.-I. Nishizawa  
... 26

Low Temperature Oxidation of Silicon Studied by Photosensitive ESR and Auger Electron Spectroscopy

H.-U. Schreiber  
E. Frösche  
... 30

High Quality RF-Sputtered Silicon Dioxide Layers

G. C. Schwartz  
V. Platter  
... 34

Anodic Processing for Multilevel LSI

J. A. Borders  
... 37

Ion Backscattering Study of Cu<sub>2</sub>S Formation on Single Crystal CdS





- R. A. Gdula**  
... 42  
The Effects of Processing on Hot Electron Trapping in SiO<sub>2</sub>
- J. H. Kennedy**  
**R. C. Miles**  
... 47  
Ionic Conductivity of Doped Beta-Lead Fluoride
- H. M. Manasevit**  
**F. M. Erdmann**  
**A. C. Thorsen**  
... 52  
The Preparation and Properties of (111)Si Films Grown on Sapphire by the SiH<sub>4</sub>-H<sub>2</sub> Process
- P. J. Tsang**  
**R. M. Anderson**  
**S. Cvikevich**  
... 57  
Amorphous CVD Al<sub>2</sub>O<sub>3</sub> Films by Ta-Doping and Their Physicochemical Properties
- R. Falckenberg**  
... 63  
Flame Fusion Growth of Spinel and Sapphire Crystals for ESFI SOS Technology
- A. K. Sinha**  
... 65  
MOS (Si-Gate) Compatibility of RF Diode and Triode Sputtering Processes
- W. L. Baun**  
**T. J. Wild**  
**J. S. Solomon**  
... 72  
Characterization of Thin Anodized Films on Aluminum with Soft X-Ray Spectroscopy
- M. Koskenlinna**  
**M. Leskelä**  
**L. Niinistö**  
... 75  
Synthesis and Luminescence Properties of Europium-Activated Yttrium Oxysulfide Phosphors
- G. T. Bauer**  
... 79  
On the Kinetics of the X-Ray Irradiation-Caused Degradation of Photoluminescence of Some Phosphors
- J. Kramer**  
... 85  
Low Energy Ion-Electron Luminescence: A New Technique for the Excitation of Inorganic Phosphors
- T. Mitsuyu**  
**K. Wasa**  
**S. Hayakawa**  
... 94  
Structures and Optical Properties of RF-Sputtered Bi<sub>12</sub>GeO<sub>20</sub> Films
- Ch. Kühl**  
**H. Schlötterer**  
**F. Schwidofsky**  
... 97  
An Optically Effective Intermediate Layer Between Epitaxial Silicon and Spinel or Sapphire
- W. R. Fahrner**  
**C. P. Schneider**  
... 100  
A New Fast Technique for Large-Scale Measurements of Generation Lifetime in Semiconductors
- T. L. Chu**  
**H. C. Mollenkopf**  
**S. S. C. Chu**  
... 106  
Deposition and Properties of Silicon on Graphite Substrates
- A. K. Gaid**  
**G. K. Ackermann**  
**V. J. Lucarini**  
**R. L. Bratter**  
... 111  
Preparation and Properties of SiO<sub>2</sub> Films from SiH<sub>4</sub>-CO<sub>2</sub>-H<sub>2</sub>

## DIVISION OFFICERS

### Battery Division

Bernard Agruss, Chairman  
Howard R. Karas, Vice-Chairman  
John P. Wondowski, Secretary-Treasurer  
General Battery Corp.  
P.O. Box 1262  
Reading, Pa. 19603

### Corrosion Division

Roger Staehle, Chairman  
Jerome Kruger, Vice-Chairman  
Ken Nobe, Secretary-Treasurer  
University of California  
Dept. of Engineering  
Los Angeles, Ca. 90024

### Dielectrics and Insulation Division

Benjamin H. Vroman, Chairman  
Laurence D. Locker, Vice-Chairman  
Kim Ritchie, Treasurer  
Rudolf G. Friesser, Secretary  
IBM Corp.  
Computer Division  
Bldg. 330-145, Dept. 365  
East Fishkill Facility  
Hopewell Junction, N.Y. 12533

### Electrodeposition Division

John L. Griffin, Chairman  
Vladimir Hospodaruk, Vice-Chairman  
Nathan Feldstein, Secretary-Treasurer  
Surface Technology, Inc.  
P.O. Box 2027  
Princeton, N.J. 08540

### Electronics Division

Bertram Schwartz, Chairman  
Glenn Cullen, Vice-Chairman (Semiconductors)  
Melvin Tecotzky, Vice-Chairman (Luminescence)  
Mort Panish, Vice-Chairman (General)  
Michael Kestigian, Treasurer  
Thomas Sedgwick, Secretary  
IBM Corp.  
Thomas J. Watson Research Center  
P.O. Box 218  
Yorktown Heights, N.Y. 10598

### Electrothermics and Metallurgy Division

Robert Bakish, Chairman  
John M. Blocher, Jr., Vice-Chairman  
Stephen H. Spacil, Junior Vice-Chairman  
J. Bruce Wagner, Jr., Secretary-Treasurer  
Northwestern University  
Dept. of Materials Science  
Evanston, Ill. 60201

### Industrial Electrolytic Division

D. N. Goens, Chairman  
Thomas C. Jeffery, Vice-Chairman  
Richard C. Alkire, Secretary-Treasurer  
University of Illinois at Urbana-Champaign  
School of Chemical Sciences  
Dept. of Chemical Engineering  
297 Roger Adams Laboratory  
Urbana, Ill. 61801

### Organic and Biological Electrochemistry Division

Manuel M. Baizer, Chairman  
Arthur A. Pilla, Vice-Chairman  
Larry Miller, Secretary-Treasurer  
Colorado State University  
Dept. of Chemistry  
Fort Collins, Colo. 80521

### Physical Electrochemistry Division

James D. E. McIntyre, Chairman  
Stanley Bruckenstein, Vice-Chairman  
Fritz G. Will, Secretary-Treasurer  
General Electric Co.  
Research and Development Center  
Schenectady, N.Y. 12301

## SOCIETY OFFICERS AND STAFF

**Theodore R. Beck, President**  
Electrochemical Technology Corp.  
3935 Leary Way, NW  
Seattle, Wash. 98107

**Michael J. Pryor, Vice-President**  
Metals Research Laboratories  
Olin Corporation  
91 Shelton Ave.  
New Haven, Conn. 06504

**Douglas N. Bennion, Vice-President**  
5532 Boelter Hall  
University of California  
School of Engineering and Applied Science  
Los Angeles, Calif. 90024

**Dennis R. Turner, Vice-President**  
Bell Laboratories  
Room 7F-506  
Murray Hill, N.J. 07974

**Paul C. Milner, Secretary**  
Bell Laboratories  
Room 1D-259  
Murray Hill, N.J. 07974

**Frederick J. Strieter, Treasurer**  
78-14 Fallmeadow Lane  
Dallas, Tex. 75240

**V. H. Branneky, Executive Secretary**  
The Electrochemical Society, Inc.  
P.O. Box 2071  
Princeton, N.J. 08540

**Ernest G. Enck, Executive Secretary Emeritus**  
The Electrochemical Society, Inc.  
P.O. Box 2071  
Princeton, N.J. 08540

**Marie Falloon, Financial Secretary**  
The Electrochemical Society, Inc.  
P.O. Box 2071  
Princeton, N.J. 08540

Manuscripts submitted to the Journal should be sent, in triplicate, to the Editorial Office at P.O. Box 2071, Princeton, N.J. 08540. They should conform to the revised "Instructions to Authors" available from Society Headquarters. Manuscripts so submitted, as well as papers presented before a Society technical meeting, become the property of the Society and may not be published elsewhere in whole or in part without written permission of the Society. Address such requests to the Editor.

The Electrochemical Society does not maintain a supply of reprints of papers appearing in its Journal. A photoprint copy of any particular paper may be obtained from University Microfilms, Inc., 300 N. Zeeb St., Ann Arbor, Mich. 48106.

Inquiries regarding positive microfilm copies of volumes should be addressed to University Microfilms, Inc., 300 N. Zeeb St., Ann Arbor, Mich. 48106.

Walter J. Johnson, Inc., 355 Chestnut St., Norwood, N.J. 07648, have reprint rights to out-of-print volumes of the Journal, and also have available for sale back volumes and single issues, with the exception of the current calendar year. Anyone interested in securing back copies should correspond directly with them.

Published monthly by The Electrochemical Society, Inc., at 215 Canal St., Manchester, N.H.; Executive Offices, Editorial Office and Circulation Dept., and Advertising Office at P.O. Box 2071, Princeton, N.J. 08540, combining the JOURNAL and TRANSACTIONS OF THE ELECTROCHEMICAL SOCIETY. Statements and Opinions given in articles and papers in the JOURNAL OF THE ELECTROCHEMICAL SOCIETY are those of the contributors, and The Electrochemical Society assumes no responsibility for them.

Claims for missing numbers will not be allowed if received more than 60 days from date of mailing plus time normally required for postal delivery of JOURNAL and claim. No claims allowed because of failure to notify the Circulation Dept., The Electrochemical Society, P.O. Box 2071, Princeton, N.J. 08540, of a change of address, or because copy is "missing from files." Subscription to members as part of membership service; subscription to non-members \$50.00 plus \$5.00 for postage outside U.S. and Canada. Single copies \$3.25 to members, \$5.00 to nonmembers. © Copyright 1976 by The Electrochemical Society, Inc. Second Class Postage Paid at Princeton, New Jersey, and at additional mailing offices. Printed in U.S.A.

## SOLID-STATE SCIENCE (Cont.)

**A. P. Turley**  
**R. M. McLouski**  
**P. R. Reid**  
**D. H. McCann**  
... 117

Fabrication of P-Channel Silicon Gate LSI Devices with  $\text{Si}_3\text{N}_4/\text{SiO}_2$  Gate Dielectric

**J. M. Harris**  
**S. S. Lau**  
**M.-A. Nicolet**  
**R. S. Nowicki**  
... 120

Studies of the Ti-W Metallization System on Si

**P. Ostoja**  
**D. Nobili**  
**A. Armigliato**  
**R. Angelucci**  
... 124

Isochronal Annealing of Silicon-Phosphorus Solid Solutions

**T. Takahashi**  
**N. Wakabayashi**  
**O. Yamamoto**  
... 129

Solid-State Ionics—High-Conductivity Solid Copper Ion Conductors  
Organic Ammonium Halide-Copper (I) Halide Double Salts

**V. Geiss**  
**E. Fröschle**  
... 133

Mass Spectrometric Investigation of the Reaction Velocities of  $\text{BCl}_3$  and  $\text{BBr}_3$  with Oxygen and Water Vapor in a Diffusion Furnace

**M. Ducarriour**  
**C. Bernard**  
... 136

Thermodynamic Domains of the Various Solid Deposits in the B-C-H-Cl Vapor System

## TECHNICAL NOTES

**L. M. Foster**  
**J. E. Scardfield**  
... 141

Flux Growth of the Gallium Analog of Beta- $\text{Al}_2\text{O}_3$

**E. P. G. T. van de Ven**  
**H. Koelmans**  
... 143

The Cathodic Corrosion of Aluminum

**W. Bardsley**  
**D. T. J. Hurler**  
... 145

Impurity Striations during Faceted Crystal Growth

## BRIEF COMMUNICATIONS

**W. A. Porter**  
**D. L. Parker**  
**L. G. Reed**  
... 146

The Effect of a Prior Sirtl Etch on Subsequent Thermally Induced Processing Damage in Silicon Wafers

**K.-H. Bachem**  
**M. Heyen**  
... 147

Vapor-Phase Growth of Thin GaAs Multilayer Structures

## REVIEWS AND NEWS

**J. S. Foster, Jr.**  
... 5C

ECS Lecture—Energy—The Short and Long of It

## NEWS

... 9C



## Impedance of Silver Oxide-Zinc Cells

H. A. Frank,\* W. L. Long, and A. A. Uchiyama\*

*Jet Propulsion Laboratory, Pasadena, California 91103*

### ABSTRACT

Over 100 sealed AgO-Zn cells were subjected to prolonged periods of storage over a range of temperatures and storage modes including open circuit, trickle charge, and float charge. Impedances of these cells were monitored throughout and to the end of the storage period at which point their transient voltage characteristics were observed at the onset of discharge. Results revealed that the impedances of these cells tended to increase with time on stand and that the magnitude of the impedance rise was dependent primarily on temperature and to a lesser degree on storage mode. Typical values for 50 A-hr cells were usually less than 100 mohm at time zero (immediately after activation) and from 1 to 30 ohm after 6-10 months of storage. Transient voltages of these cells were noted to drop sharply during the first msec of discharge and then to rise and reach a stabilized value during the following few seconds. Magnitude of the initial drop as well as the stabilized voltage values were found to be related to impedance but not in a linear manner. Magnitude and duration of the low transient voltages may be unacceptable in some applications of these cells. Cause for the impedance variations is attributed to changes that occur at the positive electrode. Results provide new and useful information for designers and users of AgO-Zn-based power systems.

During the course of test and evaluation of AgO-Zn cells and batteries for Mariner spacecraft (1), it was deemed advisable to measure, among other characteristics, internal cell impedance in that these impedance measurements were known to be nondestructive and to provide additional back-up data along with weight, voltage, capacity, etc., to insure uniformity and functionality of the flight cells.

Periodic review of the tabulated data revealed what was believed to be a trend towards increased impedance with increased time on stand. This observation was deemed significant for two reasons. First, the trend had not heretofore been reported in the literature. There was in fact found to be a relative scarcity of information on impedances of AgO-Zn cells (2). Secondly, the trend could conceivably cause voltage regulation problems on the Mariner power system or any other AgO-Zn-based power system which was to be subjected to long periods of stand before use.

As a result of these considerations, it was deemed advisable to initiate a separate and detailed study on the impedance characteristics of AgO-Zn cells. First, it was desired to obtain data on the impedance variations of these cells during the course of stand over a range of temperatures and storage modes including open circuit, trickle charge, and float charge. Next, it was desired to examine the transient voltage characteristics of these cells at the onset of discharge after the stand period. Finally, as a supplemental objective, it was desired to examine any possible correlation between impedance and state of charge of AgO-Zn cells.

### Experimental

The cells which were employed in this study were the same as those which were flown on the Mariner VI and VII spacecraft. These were manufactured by the Electric Storage Battery Company and were designated as Model 257. The cells were packaged in plastic (ABS) cases as three-cell monoblocks as shown in Fig. 1. Rated capacity of each was 50 A-hr. Each cell contained 12 positive and 13 negative plates and its electrolyte consisted of 153g of 45% KOH. Each of the 12 positive plates contained 13.8g of active material with width, height, and thickness of 6.45 cm, 7.82 cm, and 0.65 cm, respectively. Eleven of the 13 negative plates were located in the center of the cell stack.

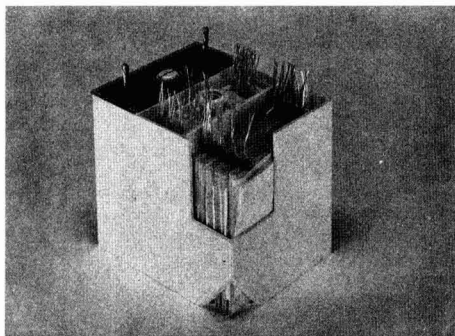


Fig. 1. AgO-Zn monoblock (3 cells, 50 A-hr each)

\* Electrochemical Society Active Member.  
Key words: AgO-Zn cells, impedance of electrochemical cells, storage modes, transient discharge voltages.



These were identical and each contained 11.7g of active material, had the same width and height as above, and thickness of 0.11 cm. The other two negative plates were the end plates in the stack. These contained 5.7g of active material, the same width and height as above, and thickness of 0.07 cm. Absorber material on the positive plates consisted of one turn of polypropylene with thickness of 0.015 cm. Retainer material on the negative plates consisted of one fold of a cellulose material (Viscon Type RD.35) with thickness of 0.008-0.013 cm. Separation consisted of six turns of 0.025 cm cellophane on each positive plate. The positive plates were prepared by first milling sheets of silver powder dispersed in a plastic pore former which was later burned off in a sintering process. Two sheets were then pressed on either side of a silver grid and the assembly was then sintered to form a plate. The negative plates were prepared by pressing a mixture of ZnO, HgO, and Teflon on both sides of a silver grid. The cell was assembled by installing the unformed plates (Ag and ZnO), adding electrolyte, and then forming the plates by charging at 1.85A. Excess electrolyte was then drained from the cell and the cell was finally sealed and ready for use. Over-all cell weight was 660g.

All impedance measurements were made with a commercial milliohmmeter (Keithley Instruments Model 503) modified by placing a 12,000 mF electrolytic capacitor in series with its constant current leads and voltage sensing leads. The instrument operated by delivering 40 Hz square wave current (0.033-0.0001A rms) in the current leads and measuring voltage drop across the voltage sensing leads with a synchronous vacuum tube voltmeter. The meter contained several ranges from 1 mohm to 100 ohm. Calibration checks with precision shunts were performed periodically and accuracy of all ranges was always found to be within  $\pm 2\%$  of full scale.

Test procedures, unless otherwise noted, were the same for each cell and consisted of the following. First, the impedance and open circuit voltage of the cells were measured in the "as-received" condition from the manufacturer. Next, the cells were given a "top-off" charge to insure that they were fully charged at the beginning of the test period. This "top-off" charge was carried out at constant current of 0.6A to a cutoff voltage of 1.97V. At this point, the cells were divided into several groups, each of which was placed on a different mode of stand. One group was left in the open circuit, fully charged condition and placed in an environmental chamber at 4°C. Two other groups were similarly left in the open circuit, fully charged condition and placed in other environmental chambers at temperatures of 21° and 38°C. One group was discharged 50% and then placed on open circuit stand at room temperature, 21°C. Another group was discharged 100% and then placed on open circuit stand again at room temperature. Three other groups were placed on stand under the condition of constant current trickle charge at room temperature and at currents of 2, 5, and 10 mA. Finally, one group was placed on stand under the condition of constant potential "float" charge at 1.87 V/cell and at room temperature. Voltages and impedances of all cells were measured periodically at intervals of at least once per week.

The transient discharge voltage measurements were carried out on three-cell monoblocks rather than on single cells. The monoblocks were wired with heavy duty cable across 4.5 ohm loads (to give a nominal current of 10A) and discharge was triggered with a heavy duty mercury switch. Monoblock voltages were measured with both an oscilloscope (Tektronix, Model 535 A, equipped with a Polaroid camera) and an oscillograph (Sanborn, Model 297).

## Results

Impedance and voltage variations of the cells during the various modes of stand are given in Fig. 2 through 10. In each of these figures the shaded areas cover the

range in values of impedance and voltage for the indicated number of cells. Figures 2, 3, and 4 give the characteristics of cells on stand in the open circuit and fully charged condition at temperatures of 4°, 21°, and 38°C, respectively. Figure 5 gives the characteristics of cells on stand in the open circuit and 50% discharged condition at 21°C. Figure 6 gives the characteristics of cells on stand in the open circuit and 100% discharged condition at 21°C. Figures 7, 8, and 9 give the characteristics of cells on stand at 21°C, with application of constant current trickle charge currents of 2 mA, 5 mA, and 10 mA, respectively. Figure 10 gives the characteristics of cells on stand at 21°C with application of a constant potential "float" charge of 1.87 V/cell.

Figures 11 and 12 give typical variations in impedance and voltage of these cells during the course of charge and discharge.

Table I gives the impedance values of a cell before and 1.0 sec after a discharge period at 10A.

Figures 13, 14, and 15 give the voltage characteristics of three typical monoblocks during the onset of discharge. Table II summarizes the pertinent data from these figures and also gives additional monoblocks and cell data. The first two columns in Table II designate the monoblock numbers and their respective cell numbers. The next two columns give the individual cell and monoblock open circuit voltages, respectively, after they had equilibrated at room temperature and before discharge. The next two columns give the individual cell and monoblock impedances before the discharge period. The next column gives the minimum monoblock voltage during the first millisecond of discharge as per the oscilloscope trace. The last column gives the "stabilized" monoblock voltage after the first few seconds of discharge as per the oscillograph trace.

Figures 16 and 17 give the relationship between a cell's impedance and its transient voltages at the onset of discharge. These curves were obtained by normalizing the data in Table II.

Figures 18 through 21 give the impedance and voltage histories of cells which exhibited short circuit failure modes. Finally, Fig. 21 gives the effect of ambient temperature on the impedance of three typical cells, and Table III gives the resistivity of silver and its oxides.

## Discussion

Falk and Salkind state that the impedance of sealed silver batteries is usually quite low and that typical values for partially discharged cells range from 0.07/C to 0.40/C ohm, where C is the cell capacity in A-hr (3). On this basis, the impedances of the 50 A-hr cells employed herein would be expected to range from 1.4 to 8 mohm. Inspection of Fig. 5 and Table I reveals that the initial impedances of partially discharged 50 A-hr cells ranged from 5 to 11 mohm. Therefore, there appears to be good agreement between the observed and literature values of Ag-Zn cell impedance.

Examination of Fig. 2, 3, and 4 reveals a gradual increase in impedance with time for cells on open circuit stand in the fully charged condition. The change in impedance with time was noted to increase somewhat with ambient temperature. For example, the impedances of cells stored for 8 months were noted to be in the range of 1.3 to 3.3 ohm at 4°C, 2.5 to 3.5 ohm at 21°C, and 9.0 to 16.0 ohm at 38°C. Open circuit voltages of the cells stored at 4° and 21°C were noted to remain relatively constant near 1.86V throughout the entire test period. Open circuit voltages of the cells stored at 38°C were however, noted to decline slightly during this period with a

Table I. Impedance values of cell No. 766 before and 1.0 sec after discharge at 10A. Cell voltage was 1.845V before discharge and 1.390V near end of discharge period.

Impedance before discharge	3.400 ohm
Impedance after 1.0 sec discharge at 10A	0.015 ohm

Table II. Impedances and transient voltages of monoblocks at the onset of a 10A discharge

Monoblock No.	Cell No.	Cell OCV (V)	Monoblock OCV (V)	Cell impedance (ohm)	Monoblock impedance (ohm)	Minimum transient monoblock voltage (V)*	Stabilized monoblock voltage (V)**
1	1639	1.86	5.58	0.080	0.24	4.73	4.80
	1640	1.86		0.075			
	1641	1.86		0.082			
2	1642	1.86	5.58	0.085	0.27	4.6	4.75
	1643	1.86		0.106			
	1644	1.86		0.082			
3	1726	1.86	5.58	0.082	0.21	4.83	4.85
	1727	1.86		0.074			
	1728	1.86		0.071			
4	1741	1.86	5.58	0.071	0.30	4.63	4.75
	1742	1.86		0.146			
	1743	1.86		0.080			
5	1645	1.86	5.58	0.420	1.31	3.63	4.40
	1646	1.86		0.440			
	1647	1.86		0.450			
6	1648	1.86	5.58	0.360	1.18	3.73	4.40
	1649	1.86		0.410			
	1650	1.86		0.410			
7	1729	1.86	5.58	0.330	1.19	3.78	4.50
	1730	1.86		0.400			
	1731	1.86		0.460			
8	1744	1.86	5.58	0.290	1.01	3.88	4.56
	1745	1.86		0.360			
	1746	1.86		0.360			
9	1651	1.85	5.55	2.330	11.73	3.00	4.36
	1652	1.85		5.200			
	1653	1.85		4.200			
10	1654	1.85	5.55	5.700	12.10	2.95	4.30
	1655	1.85		4.200			
	1656	1.85		2.200			
11	1732	1.85	5.55	3.100	10.80	3.00	4.38
	1733	1.85		4.000			
	1734	1.85		3.700			
12	1747	1.85	5.55	3.600	11.40	3.00	4.44
	1748	1.85		4.200			
	1749	1.85		3.600			

\* From oscilloscope trace during first msec.

\*\* From oscillograph trace during first 10 sec.

minimum value of 1.847V for one cell. Examination of Fig. 5 reveals a somewhat lower rate of increase in impedance with time for cells which were stored in the 50% discharged condition. Impedances of a few such cells given in Fig. 5 were found to remain in the range of 0 to 10 mohm throughout the entire test period. Open circuit voltages of these cells remained in the range of 1.59 to 1.62V throughout the test. Examination of Fig. 6 reveals that cells which were stored in the fully (100%) discharged condition exhibit a constant and low impedance in the range of 2 to 3 mohm throughout the entire test. Open circuit voltages of these cells remained in the range of 1.58 to 1.60V during this time.

Examination of Fig. 7, 8, and 9 reveals an unusual but yet consistent shape of the impedance-time curves for cells which were stored with application of a constant current trickle charge. Impedance is noted to first pass through a maximum, then a minimum, and finally to continue a gradual increase with increase in stand time. A rigorous explanation of the shape of these curves is not available at the present time. It is noted, however, that the transition from the maximum to the minimum in the impedance curves occurs at a point in time when the cell voltages rise from the 1.9V level to the 2.0V level. Since gassing ( $O_2$  evolution) is known to occur at the higher voltages, it is quite likely then that the unique shape of the impedance-time curves is associated with gassing and pressure rise. Aside from this point, however, there is noted to be good correspondence, at least in the early stages of stand, between the shape and slope of the impedance vs. time curves for cells stored in this mode and those stored on open circuit. In addition, it

is noted that those cells which were stored at the higher current levels of 5 and 10 mA (not necessarily recommended by the manufacturer) developed leaks after periods of 6 to 2 months, respectively. These current levels are therefore excessive for long-term

Table III. Resistivity of silver and its oxides (10)

Component	Resistivity (ohm-cm)
Ag	$1.6 \times 10^{-6}$
Ag <sub>2</sub> O	$10^8$
AgO	10

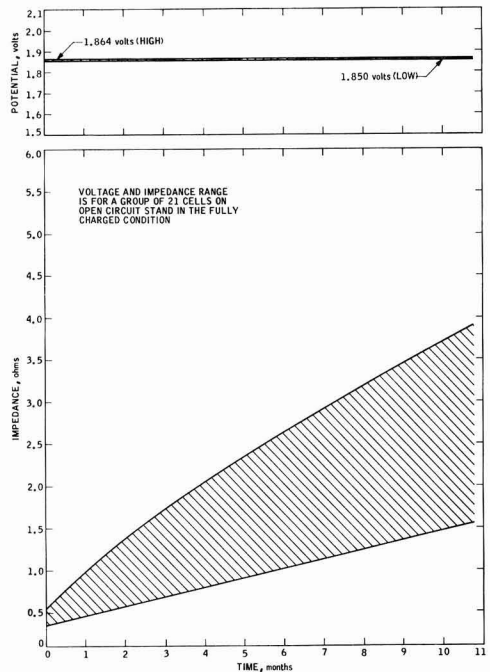


Fig. 2. Voltage and impedance of cells on open circuit stand in the fully charged condition at 4°C.

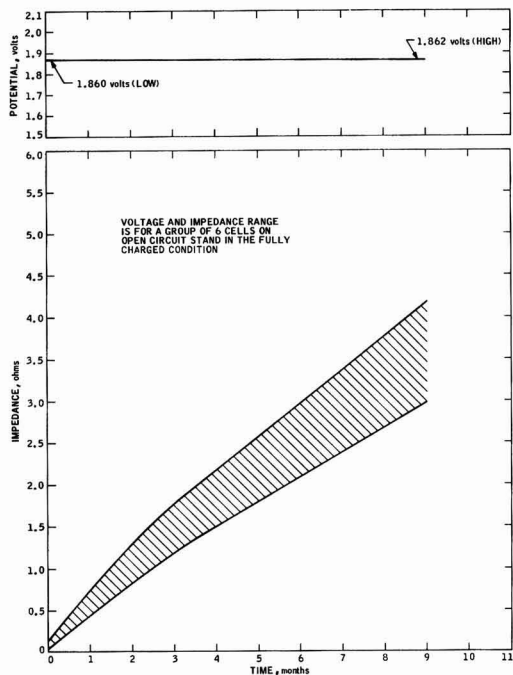


Fig. 3. Voltage and impedance of cells on open circuit stand in the fully charged condition at 21°C.

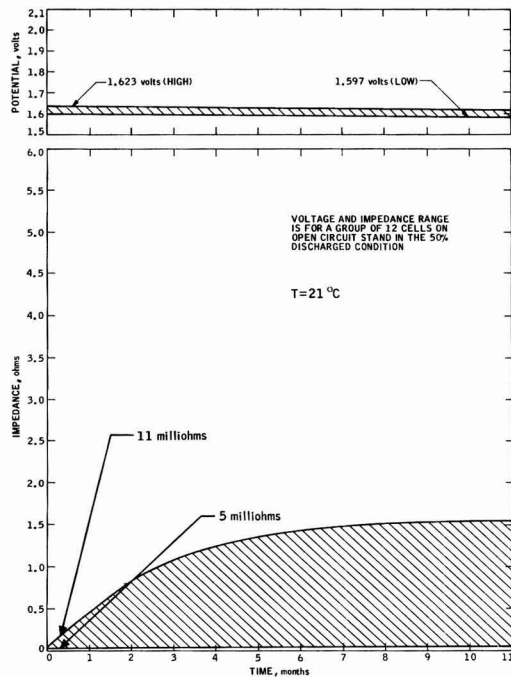


Fig. 5. Voltage and impedance of cells on open circuit stand in the 50% discharged condition at 21°C.

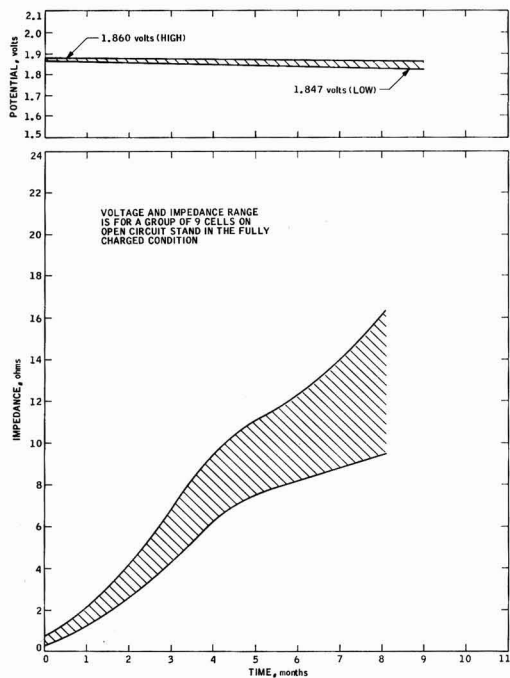


Fig. 4. Voltage and impedance of cells on open circuit stand in the fully charged condition at 38°C.

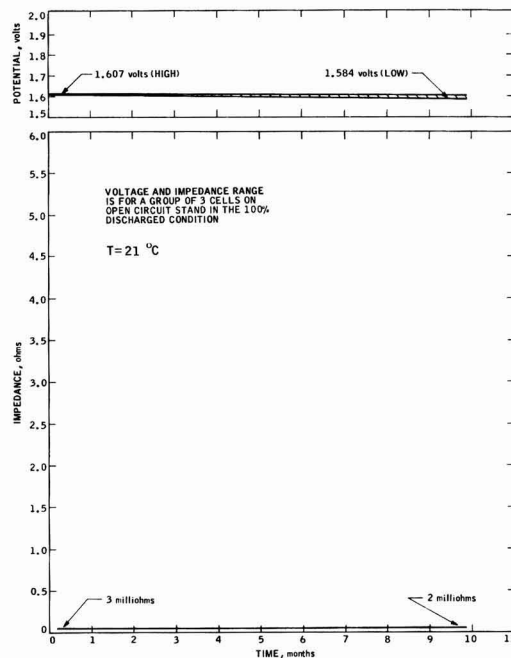


Fig. 6. Voltage and impedance of cells on open circuit stand in the 100% discharged condition at 21°C.

storage of this size cell and the maximum level for safe storage is estimated to be near 2 mA.

The variation of cell impedance with time on stand is attributed to chemical changes that occur within the positive silver electrodes. At any given time the species

which are present in this electrode are the higher oxide, AgO, the lower oxide, Ag<sub>2</sub>O, and silver metal, Ag. In a freshly and fully charged cell, the predominant species is the higher oxide AgO which, as indicated in Table III, has a relatively low resistivity. Hence, the impedance of a freshly charged cell should



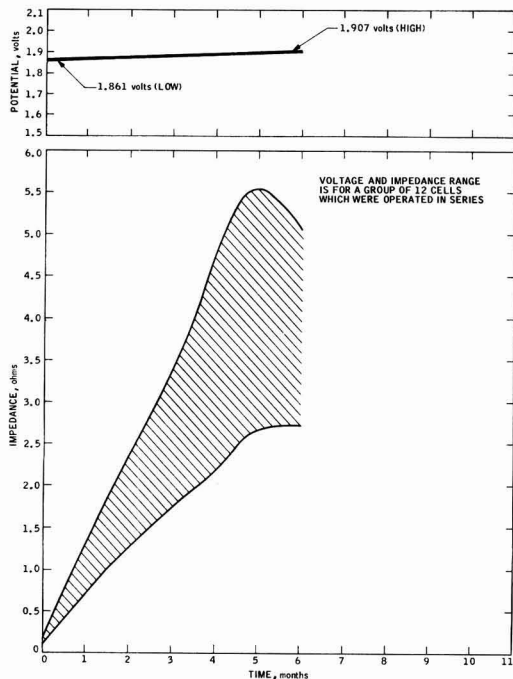


Fig. 7. Voltage and impedance of cells on 2.0 mA constant current trickle charge at 21°C.

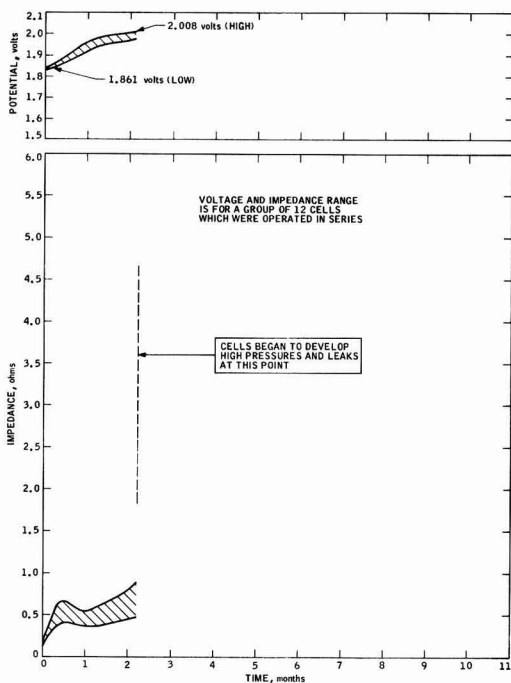


Fig. 9. Voltage and impedance of cells on 10.0 mA constant current trickle charge at 21°C.

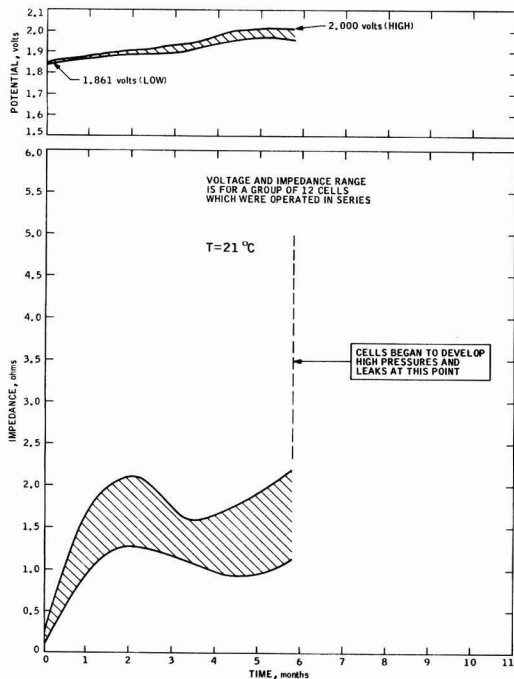


Fig. 8. Voltage and impedance of cells on 5.0 mA constant current trickle charge at 21°C.

and has been found to exhibit relatively low impedance as evidenced by the above results. During the course of extended periods of stand, the higher oxide, AgO, is slowly converted to the lower oxide, Ag<sub>2</sub>O, via two possible chemical reactions. The first of these

involves decomposition of the higher oxide to form the lower oxide and oxygen ( $2AgO \rightarrow Ag_2O + \frac{1}{2}O_2$ ) (4). The second involves reaction of the higher oxide with metallic silver particles and the silver grid to form the lower oxide ( $Ag + AgO \rightarrow Ag_2O$ ) (5). The net result of these reactions is believed to be the formation of a layer of Ag<sub>2</sub>O which completely surrounds the electrode. As noted in Table III, the resistivity of the Ag<sub>2</sub>O material is exceptionally high so that the growth of the layer of this material is the most likely explanation of the observed trend towards increased impedance with time on stand. Support for this explanation is given in a prior study of Ag electrodes by Cahan *et al.* (6). The observed trend toward increased rate of change of impedance at elevated temperatures is compatible with the above in that the above reactions proceed faster at the elevated temperatures and proceed to form the layer at a faster rate. The fact that the partially and completely discharged cells did not exhibit as large a rise in impedance as the fully charged cells is also compatible with the above in that these cells contain appreciable amounts of highly conductive silver particles (see Table III) that provide low resistance electrical paths. The fact that the cells on both constant current and float charge (Fig. 7-10) also exhibited increased impedance with time on stand would at first glance appear to be contradictory to the above explanation regarding a buildup of a layer of Ag<sub>2</sub>O. The basis for this contradiction would be that the application of a charge current would tend to reconvert the high resistance layer of Ag<sub>2</sub>O back to the lower resistance AgO material. The only explanation for the observed results in these cases is, then, that the rate of formation of the Ag<sub>2</sub>O layer (by the above reactions) is greater than the rate of conversion of the Ag<sub>2</sub>O layer to AgO material (by electrochemical reaction). Some basis for this explanation can be established by comparing known rates of formation of Ag<sub>2</sub>O via decomposition of AgO with the rates at which Ag<sub>2</sub>O would be electrochemically reconverted to AgO by the currents employed in these tests. Ruetschi, for example, shows that at 45°C the decomposition rate of AgO in

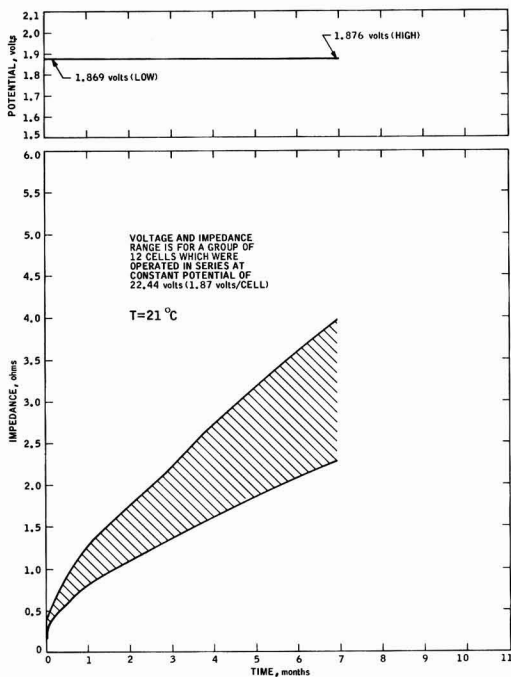


Fig. 10. Voltage and impedance of cells on constant potential float charge at 1.87 V/cell at 21°C.

45% KOH is, in terms of the reaction product, equivalent to approximately  $0.1 \text{ cm}^3 \text{ O}_2/\text{hr-g AgO}$  (7). Since these cells contained 166g of active positive material, the maximum rate, assuming all the material is  $\text{AgO}$ , would be  $16.6 \text{ cm}^3 \text{ O}_2 \text{ hr}$ . Under these conditions, then, the cell would be forming  $\text{Ag}_2\text{O}$  at a current equivalent rate near 80 mA. The current equivalent rate at which  $\text{Ag}_2\text{O}$  is simultaneously being reconverted to  $\text{AgO}$  is equal to the charge currents which varied from 2 to 10 mA for the constant current tests and near 2 mA for the constant potential tests. Comparison of these currents, therefore, reveals that the rates of formation of  $\text{Ag}_2\text{O}$  are, at least in these examples, appreciably greater than the rates at which this material is reconverted to  $\text{AgO}$ . Therefore, there is some basis to believe that high resistance layer of  $\text{Ag}_2\text{O}$  can be formed for the condition of stand with application of small currents by constant current or constant potential charge.

Inspection of Fig. 11 reveals a sharp maximum or peak in voltage during the early portion of a constant

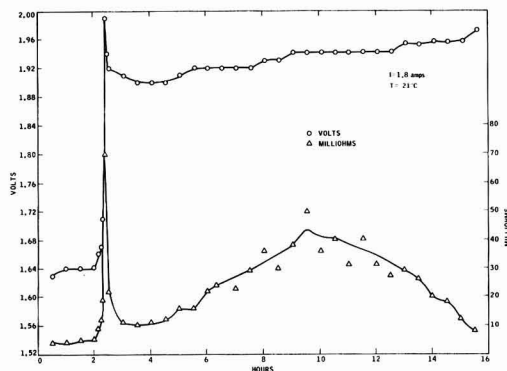


Fig. 11. Voltage and impedance during charge

current charge of this type cell. Cell impedance was also noted to exhibit a maximum or peak during this same time period. This phenomena has been previously reported in the literature (8, 9), and may again be associated with the formation of a high resistance layer of  $\text{Ag}_2\text{O}$  which completely surrounds the electrode. The sharp rise would correspond to the time during charge when the layer of high resistance  $\text{Ag}_2\text{O}$  is completely formed and decline would correspond to the onset of production of lower resistance  $\text{AgO}$  material.

Inspection of Fig. 12 reveals that cell impedance is quite low and in the range of 0 to 10 mohm during discharge. The gradual decline in impedance and slight rise in voltage during discharge is attributed to the formation of increasing amounts of highly conductive metallic silver particles. The frequency of performing measurements during this test was quite long (approximately once each 15 min), so that it was not possible to examine the initial transient voltage and impedance characteristics during the early (0-10 sec) portion of discharge. These characteristics were, however, observed in subsequent tests as described below.

Typical voltage traces of three monoblocks during the onset of discharge at 10A are given in Fig. 13, 14, and 15. The upper curve in each case gives the high-

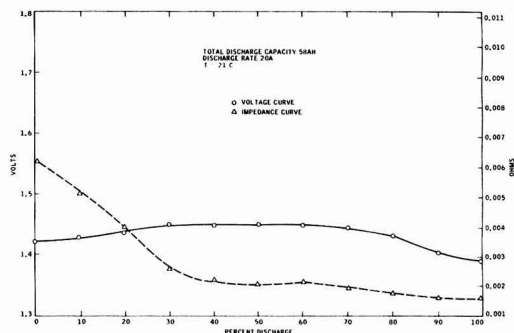


Fig. 12. Voltage and impedance during discharge

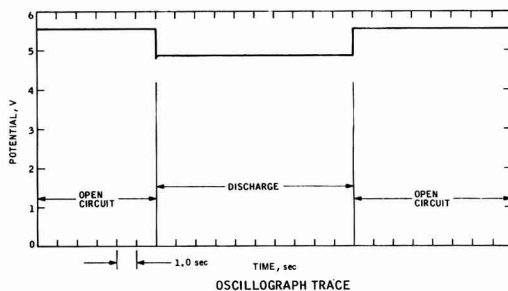
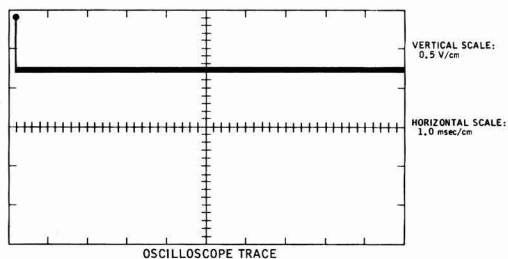


Fig. 13. Transient voltage characteristics of a monoblock with relatively low impedance at the onset of discharge at 10A at 21°C (monoblock No. 3).

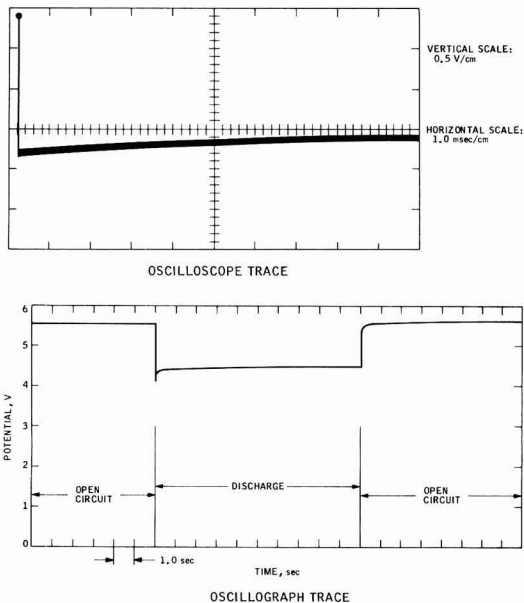


Fig. 14. Transient voltage characteristics of a monoblock with relatively high impedance at the onset of discharge at 10A at 21°C (monoblock No. 8).

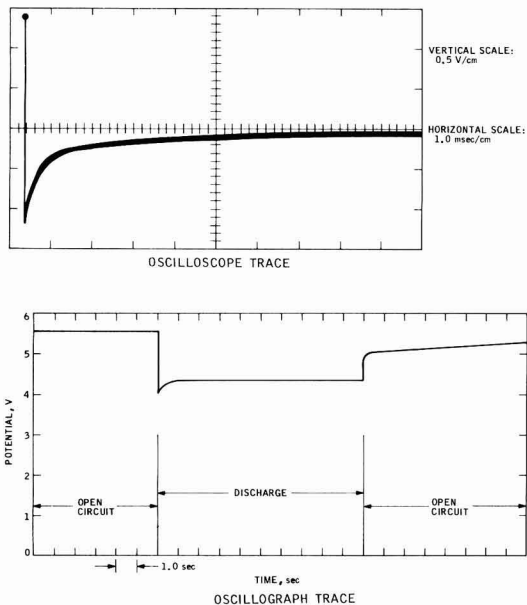


Fig. 15. Transient voltage characteristics of a monoblock with very high impedance at the onset of discharge at 10A at 21°C (monoblock No. 10).

speed oscilloscope trace and the lower curve gives the somewhat lower speed oscillograph trace. Table II summarizes the pertinent data from the traces of these and nine other monoblocks and also gives additional monoblock and unit cell data. Monoblocks 1 through 4 may be classified as "low resistance" units in that their over-all impedances range from 0.21 to 0.30 ohm (0.07-0.10 ohm/cell). These exhibit minimum voltages of 4.60-4.83V (1.52-1.61 V/cell) during the first msec of discharge and stabilized voltages of 4.75-4.85V (1.57-1.61 V/cell) almost immedi-

ately thereafter. Monoblocks 5 through 8 may be classified as medium resistance units in that their over-all impedances range from 1.01 to 1.31 ohm (0.34-0.44 ohm/cell). These exhibit minimum voltages of 3.63-3.88V (1.21-1.29 V/cell) during the first msec of discharge and stabilized voltages of 4.40-4.56V (1.47-1.52 V/cell) within a few seconds thereafter. Monoblocks 9 through 12 may be classified as high resistance units in that their over-all impedances range from 10.80 to 12.10 ohm (3.60-4.03 ohm/cell). These exhibit minimum voltages of 2.95 to 3.00V (0.98-1.00 V/cell) during the first msec of discharge and stabilized voltages of 4.30-4.44V (1.43-1.48 V/cell) within several seconds thereafter. These results indicate a trend of increased time for cell voltage to reach a stabilized value at the beginning of discharge with increased cell impedance. The results also indicate a trend of lower cell voltages with increased cell impedance as discussed in detail below.

The above monoblock data were normalized on a unit cell basis and are given in Fig. 16 and 17 in terms of unit cell voltage vs. corresponding unit cell impedance. Figure 16 pertains to the minimum voltages which were consistently attained during the first msec of discharge at 10A. Figure 17 pertains to the stabilized voltages which were consistently attained after several seconds of discharge at 10A. Also included in these figures, for design purposes, is the

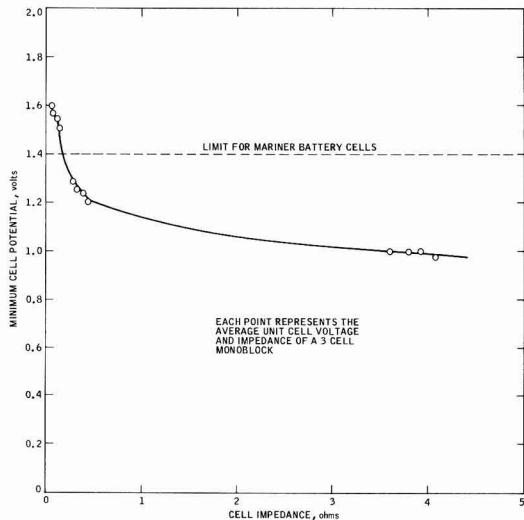


Fig. 16. Minimum cell voltage during first msec of discharge at 10A and at 21°C.

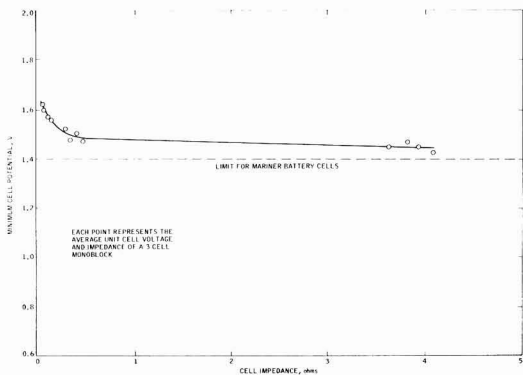


Fig. 17. Stabilized voltages after first few seconds of discharge at 10A and at 21°C.



minimum voltage specification limit for the Mariner cells. From a simplified "Ohm's law" point of view (where voltage is a linear function of impedance at constant current), one might at first predict that these curves should be approximately linear and have a slope of 10 V/ohm. This prediction would at least be thought to be applicable to the curve in Fig. 16 wherein the voltage measurements should not be influenced to any large degree by polarization phenomena in that the measurements were taken at very short periods of time after the start of discharge. Detailed examination of Fig. 16 reveals that only a portion of the curve is in accord with the above relation. This portion is for cells with impedances less than about 0.3 ohm. The curve reveals appreciably higher voltages than would be predicted from the Ohm's law relation for cell with impedances in excess of 0.3 ohm. Detailed examination of Fig. 17 reveals that essentially the whole curve is in disagreement with the above relation. In this case the discrepancy is even larger than the above, i.e., voltages are even higher than in Fig. 16 for corresponding impedance values.

Explanation for the above phenomena is twofold in nature. First, it is quite likely that polarization effects are present and that these effects account for a portion of the above-noted discrepancies. Secondly it is quite likely that there is a decline in cell impedance shortly after the start of discharge. Evidence to this effect was obtained in a special test wherein the impedance of one cell was measured before and 1.0 sec after a discharge at 10.0A. Results given in Table I revealed that the impedance dropped sharply during this period from 3.400 to 0.015 ohm. Based on results of the oscilloscope and oscillograph tracers, it appears that most of this decline in impedance occurs within the first msec of discharge. Although a rigorous explanation for this phenomena cannot be offered at the present time, it is quite likely that it is associated with the electrochemical reduction of the highly resistive layer of  $Ag_2O$ . Regardless of the explanation, however, the result establishes a very practical and significant point in that it suggests a method for avoiding the large transient voltage drops of high impedance cells, i.e., by merely subjecting them to a short "conditioning" discharge before employing them for their primary discharge application. The "conditioning" discharge may be carried out at the C/5 rate for 1.0 sec.

During the course of this investigation there were noted to be several cells, especially those at elevated temperatures, which exhibited sudden voltage declines and subsequent failure. Since logs had been maintained on the voltages and impedances of these cells, it was decided to examine these data in detail in order to establish if these cells exhibited any unusual variations in impedance. In this manner it might be possible to employ the impedance measurement as a means of identifying faulty or deteriorated cells. Figures 18 through 21 give plots of the voltages and impedances of four such cells. Examination of these plots reveals

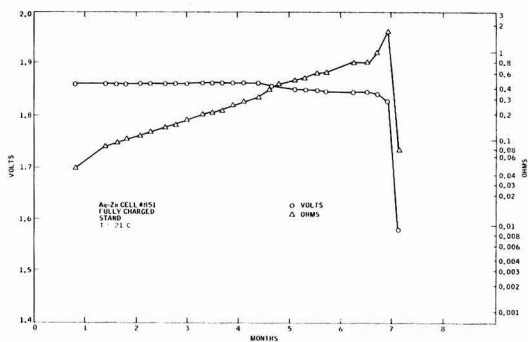


Fig. 19. Deterioration of AgZn cell No. 1069

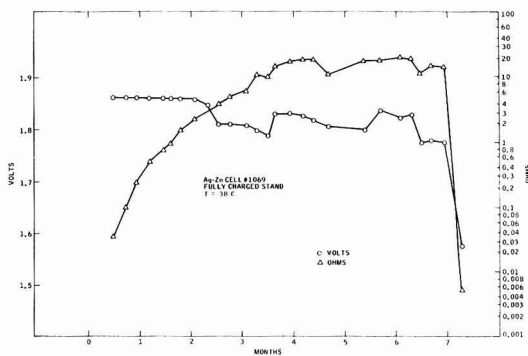


Fig. 20. Deterioration of AgZn cell No. 1071

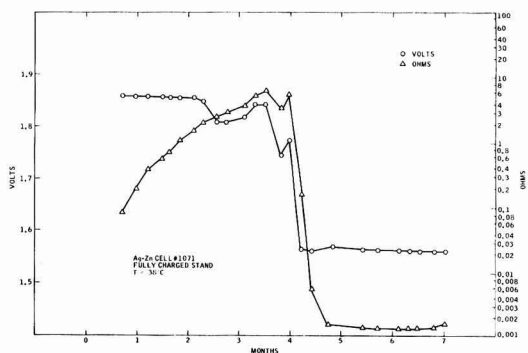


Fig. 21. Deterioration of AgZn cell No. 851

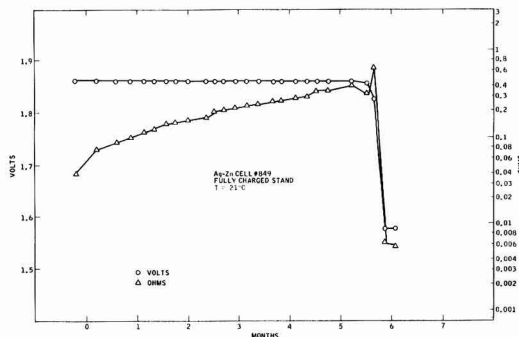


Fig. 18. Deterioration of AgZn cell No. 849

no unusual variations in the impedances of these particular cells up to the point of failure. During this time these cells exhibit a gradual rise in impedance in a similar manner to other cells which did not exhibit failure. At the time of failure, however, these cells exhibit a sharp decline in impedance and also cell voltage. On this basis, then, there does not appear to be any convincing evidence that these impedance measurements may be used to predict the condition or state of charge of Ag-Zn cells in their early stages of life. The feasibility of employing impedance measurements for this purpose cannot, however, be ruled out altogether with the information obtained to date.

The effect of temperature on impedance of these cells is given in Fig. 22. The upper curves give the variation for two typically high resistance cells which had been in storage for almost three years in the fully charged condition at 4°C. The lower curve gives the variation for a typically low resistance cell which had

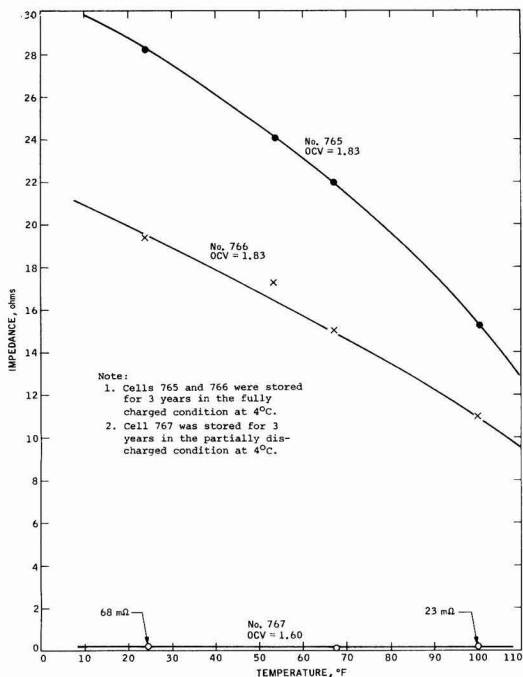


Fig. 22. Effect of temperature on impedance of AgZn cells

been in storage under the same conditions as above but had been partially (about 10%) discharged at room temperature before these impedance measurements. Results indicate that the impedances of all of these cells decline with temperature and in an essentially linear manner in the range of 4° to 38°C.

Finally, it is well to mention that there is some, but not conclusive, experimental data to confirm the belief that the positive electrode, and in particular the Ag<sub>2</sub>O film, is responsible for all the above-observed variations in impedance and voltage. It is conceivable that changes in the negative electrode, the separator, and electrolyte may also occur and may account for some of the observed phenomena. Additional and more fundamental studies involving the use of reference electrodes and microscopic examinations would be required to resolve this issue. Such studies have been outlined and will be carried out at a later date. Results obtained to date do, however, stand by themselves in that they provide the designers of AgO-Zn-based power systems with a great deal of practical and heretofore unpublicized data on the impedance characteristics of these cells.

### Conclusions

Significant findings of this study are summarized below.

1. Impedances of AgZn cells have been found to increase during prolonged periods of storage. The rate of change of impedance with time has been found to increase at elevated temperatures and to be influenced to some degree by the mode of storage.

2. In accordance with prior literature, there has been found to be a peak in the voltage-time curve of Ag-Zn cells during the early portion of constant current charge

3. Impedances of Ag-Zn cells decrease appreciably and rapidly within the first msec of discharge.

4. The instantaneous voltage drop during the first msec of discharge has been found to increase with initial cell impedance, but not in a linear manner.

5. Cell voltages exhibit a partial recovery after the instantaneous voltage drop. The level of recovery and recovery times vary with initial cell impedance. Recovery times for the cells employed here were in the range of essentially zero to several seconds.

6. In order to satisfy demanding voltage regulation requirements, it would be well to subject aged cells to a short preliminary discharge prior to subjecting them to their primary discharge.

### Acknowledgments

This paper presents the results of one phase of research carried out at the Jet Propulsion Laboratory, California Institute of Technology under Contract No. NAS 71000, sponsored by the National Aeronautics and Space Administration.

Manuscript submitted April 25, 1975; revised manuscript received Sept. 8, 1975.

Any discussion of this paper will appear in a Discussion Section to be published in the December 1976 JOURNAL. All discussions for the December 1976 Discussion Section should be submitted by Aug. 1, 1975.

Publication costs of this article were partially assisted by the Jet Propulsion Laboratory.

### REFERENCES

1. "Mariner Mars 1969 Final Project Report," JPL Technical Report 321460 Vol. 1, Development, Design, and Test, pp. 85-89, (Nov. 1, 1970).
2. P. Bauer, "Batteries For Space Power Systems," NASA SP-172, p. 174, National Aeronautics and Space Administration, Washington, D.C. (1968).
3. S. U. Falk and A. J. Salkind, "Alkaline Storage Batteries," p. 424, John Wiley & Sons, Inc., New York (1969).
4. A. Fleischer and J. Lander, "Zinc-Silver Oxide Batteries," p. 123, John Wiley & Sons, Inc., New York (1971).
5. *Ibid.*, p. 149.
6. B. D. Cahan, J. B. Ockerman, R. F. Amlie, and P. Rüttschi, *This Journal*, **107**, 725 (1960).
7. A. Fleischer and J. Lander, "Zinc-Silver Oxide Batteries," p. 125, John Wiley & Sons, Inc., New York (1971).
8. *Ibid.*, p. 134.
9. E. A. Butler, "Studies of Reaction Geometry in Oxidation and Reduction of The Alkaline Silver Electrode," Final Report, JPL Contract 951157, Brigham Young University, Provo, Utah (April 1966).
10. A. Tvarusko, *This Journal*, **115**, 1106 (1968).

# Thin-Film Galvanic Cell Pb/PbF<sub>2</sub>/PbF<sub>2</sub>,CuF<sub>2</sub>/Cu

John H. Kennedy\* and James C. Hunter\*\*

Department of Chemistry, University of California, Santa Barbara, California 93106

## ABSTRACT

Thin-film solid-state galvanic cells were fabricated using Pb metal as anode, PbF<sub>2</sub> as electrolyte, and CuF<sub>2</sub> as cathode. Because of the high resistivity of CuF<sub>2</sub>, it was codeposited with PbF<sub>2</sub> to form a more conductive mixed cathode layer. Such cells developed open-circuit voltages from 0.61 to 0.70V, compared to 0.70V theoretical. Cells were discharged at room temperature with current densities of >10 μA/cm<sup>2</sup>. At elevated temperatures the current densities attainable were considerably higher. Cells discharged under constant load exhibited relatively constant voltage during discharge and a sudden drop-off at the end of discharge. Cathode utilization for the cathode-limited cells was typically 30-40%. Attempts to recharge these cells were unsuccessful.

Thin-film solid-state galvanic cells have been a subject of considerable recent interest. The combination of solid electrolyte materials with thin-film techniques holds promise of yielding miniaturized batteries with high energy density, wide operating temperature range, and long shelf life. Such batteries could complement other miniaturized electronic devices, such as integrated circuits, thin-film resistors, and thin-film capacitors.

Masters, Vouros, and Clune (1, 2) have developed vacuum-evaporated thin-film galvanic cells using silver as anode; silver chloride, bromide, or iodide as electrolyte; and platinum as cathode. This was a concentration cell with rather low power. Goldberg (3) patented improved methods of forming the electrolyte layer in this cell.

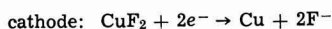
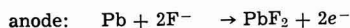
Ervin (4) patented a sprayed-in-place cell using a silver anode, silver rubidium iodide electrolyte, and tellurium tetraiodide cathode.

Sator and Perrot (5, 6) constructed thin-film cells of the type Pb/PbCl<sub>2</sub>/AgCl/Ag. These were developed further by Moulton *et al.* (7), and by Swindells and Lanier (8). Swindells and Lanier also developed an improved cell of the type Mg/MgCl<sub>2</sub>, LiCl/AgCl/Ag. In this cell the MgCl<sub>2</sub> electrolyte was doped with up to 50% LiCl by weight to increase its conductivity.

Liang, Epstein, and Boyle (9) constructed thin-film cells of the type Li/LiI/AgI/Ag. These cells developed over 2V, and could provide current densities of over 100 μA/cm<sup>2</sup>.

In a previous paper we reported the solid electrolyte properties of PbF<sub>2</sub> (10). For thin films,  $\sigma$  values of  $>1 \times 10^{-6}$  (ohm-cm)<sup>-1</sup> were obtained. This conductivity is sufficient that PbF<sub>2</sub> might be of use as electrolyte in thin-film galvanic cells.

CuF<sub>2</sub> is a possible choice for a cathode material. The following reaction



$$\Delta G = \Delta G_f(\text{PbF}_2) - \Delta G_f(\text{CuF}_2) = -32.1 \text{ kcal/mole}$$

leads to a cell voltage of 0.7V. In fact, CuF<sub>2</sub> has already found use as a cathode material in nonaqueous liquid electrolyte batteries (11, 12).

Several problems had to be overcome in order to use CuF<sub>2</sub> as a cathode material in these liquid electrolyte batteries. CuF<sub>2</sub> is a highly resistive material;  $\rho > 10^{10}$  ohm-cm at 25°C (13). In order to use it as a cathode material it was necessary to increase its conductivity. Mixing the CuF<sub>2</sub> with graphite has been tried with

some success (14). This only increases the electronic conductivity which may be sufficient with a liquid electrolyte. In a solid-state system, however, it would also be helpful to increase the ionic conductivity of the cathode. Recharging of liquid electrolyte cells with CuF<sub>2</sub> cathodes has also proven difficult (15), and there is indication of large overvoltage effects in these cells. The high resistivity of CuF<sub>2</sub> was expected to be a problem in solid-state thin-film cells, but it was not clear whether overvoltage effects would be comparable to those in the liquid electrolyte cells.

The presence of water can have large effects on the performance of CuF<sub>2</sub> cathodes for the liquid electrolyte systems. It is desirable to have completely anhydrous CuF<sub>2</sub>, as even small amounts of water react with the Li anodes used in such cells. Water in the cells also increases the solubility of CuF<sub>2</sub> in the electrolyte, leading to dissolution of the cathode and discharge of the cell. Therefore, high purity anhydrous CuF<sub>2</sub> has been used in these cells. Care must also be taken to insure that CuF<sub>2</sub> remains anhydrous, as it tends to absorb water to form the dihydrate



The presence of water would also be expected to cause problems in the formation of thin-film cells with CuF<sub>2</sub> cathodes. Heating CuF<sub>2</sub> in the presence of water leads to decomposition, with the formation of CuO, HF, and H<sub>2</sub>O (16, 17). Even if only small amounts of water were present, the outgassing and resultant spattering could make deposition of good films impossible. In addition, films of CuF<sub>2</sub> may have to be coated to protect them from being attacked by moisture in the air.

Some other fluoride materials are even less stable than CuF<sub>2</sub> and would yield correspondingly higher voltages. Thus a cell with AgF cathode would have a theoretical OCV of 1.3V, while a PbF<sub>4</sub> cathode would lead to an OCV of 2.56V. However, these latter materials are so unstable that it is questionable whether such materials could be vacuum evaporated.

In addition, electronic conductivity of PbF<sub>2</sub> becomes appreciable above 1.3V (10) and, thus, the use of high voltage cells could lead to self-discharge.

Even CuF<sub>2</sub> would be expected to cause difficulties in conventional vacuum evaporation. Evaporation from the typical evaporation sources such as tungsten, molybdenum, carbon, or aluminum oxide boats is thermodynamically unfavorable. However, whether or not successful evaporations can be carried out from any of these sources will depend on the rates of reaction, and even on the degree of wetting of the source by the CuF<sub>2</sub>. We report here the results of fabricating thin-film galvanic cells with PbF<sub>2</sub> electrolyte and CuF<sub>2</sub> cathodes.

## Experimental

*Thin-film deposition.*—Thin films were prepared by vacuum evaporation in a Fairchild custom evaporator

\* Electrochemical Society Active Member.

\*\* Electrochemical Society Student Member.

Key words: copper fluoride, galvanic cell, lead fluoride, solid electrolyte, thin-film cell.

using resistance sources. A Sloan Omni-IIa deposition control unit with quartz crystal oscillator sensor was used to monitor deposition rate and film thickness.

Cells were made with two different geometries. One type of cell (Fig. 1) had twelve small 0.1 cm<sup>2</sup> area cells, while the other type contained four larger 2 cm<sup>2</sup> cells per slide (Fig. 2). Conductivity cells were made by depositing a bottom layer of metal, followed by a layer of the material being studied, and by an upper metal electrode layer. Galvanic cells were made by depositing a bottom layer of anode metal, a middle layer of electrolyte, and two upper layers containing cathode material and cathode current collector. In some cells a layer of Kodak Microneg Photoresist (an organic polymer sensitive to u.v. light) was applied to protect the underlying films from moisture.

**X-ray diffraction analysis.**—A Philips Electronics x-ray diffraction unit with scintillation counter was used with CuK $\alpha$  x-rays. Powder x-ray spectra were made using the conventional holder. X-ray studies could also be made on thin films by breaking the glass microscope slide substrate in half and inserting the half-substrate in the sample holder. A Philips Electronics x-ray fluorescence instrument was also used, with Mo target and LiF crystal, for elemental analysis.

**Electrical measurements.**—OCV measurements were made using a Keithley Model 610c electrometer, with input impedance greater than 10<sup>14</sup> ohm.

A Keithley Model 260 picoampere source was used for constant-current charge and discharge of cells. A Hewlett-Packard Moseley chart recorder Model 7100b was used to record cell voltages during discharge.

Resistivity measurements (standard two-electrode technique) were made using a GRC 1650A bridge at 1 kHz.

## Results and Discussion

**Selection of deposition source.**—Attempts to deposit CuF<sub>2</sub> were made from tungsten and molybdenum boats without success. The resulting films were reddish in color and smooth initially, but upon contact with air they rapidly crinkled and lost adhesion to the substrate. X-ray studies showed only a few very tiny peaks, and these could not be assigned. The films probably contained some hygroscopic tungsten or molybdenum fluorides caused by reaction of CuF<sub>2</sub> with the boats.

Deposits from alumina-lined molybdenum boats were also unsuccessful. Resulting films were yellow

in color and exhibited very poor adhesion. Decomposition again probably occurred. X-ray studies, hampered by the poor adhesion, showed only some tiny peaks which could not be assigned.

Deposition from a carbon source gave films which were identified by x-ray diffraction as anhydrous CuF<sub>2</sub>. The adhesion of these films depended on the substrate temperature; films deposited on unheated substrates had poor adhesion, while those deposited on substrates at 220°C adhered extremely well. It was also found that films deposited with considerable sputtering had poor adhesion, while films evaporated without sputtering exhibited good adhesion. In all of these cases, even for films with poor adhesion, the CuF<sub>2</sub> structure was seen in x-ray studies. Fresh films showed no peaks for any of the hydrated forms of CuF<sub>2</sub> or for any other materials. However, the films were rather dark in color, while pure CuF<sub>2</sub> powder was white. This dark color could be due to the presence of impurities in the film, possibly from partial decomposition to copper metal, or perhaps to the incorporation of some fluorinated carbon compounds from reaction with the evaporation source. This could actually be beneficial for the cathode layer because it might lead to higher electronic conductivity.

**Film sensitivity to moisture in air.**—CuF<sub>2</sub> films deposited on glass substrates from carbon sources seemed only moderately sensitive to moisture in air. The smoother the film the less sensitive it appeared to be, probably because of the reduced true surface area. A study was made in which both CuF<sub>2</sub> powder and a CuF<sub>2</sub> film were exposed to air, and studied at intervals by x-ray. The fresh CuF<sub>2</sub> powder showed only peaks due to CuF<sub>2</sub>, but after exposure to air (>24 hr) a peak assigned to the dihydrate was seen. Another peak due to CuOHF also appeared after longer exposure (>10 days).

The fresh CuF<sub>2</sub> film showed a tiny broad peak due to the dihydrate and/or the oxyfluoride. After 168 days of exposure to air the film's appearance had hardly changed, and an x-ray study at this time showed almost the same features: only a small peak due to the dihydrate and/or the oxyfluoride of about the same height as for the fresh film. However, such a film would react with excess moisture rapidly; for example, holding the slide in one's hand caused crazing and blistering of the film in seconds. Therefore it was concluded that films of anhydrous CuF<sub>2</sub> could be obtained, and with moderate care they could be kept essentially anhydrous. However, for extended use in cells which might be handled frequently it would be necessary to cover the CuF<sub>2</sub> with a protective coating.

**Conductivity of CuF<sub>2</sub> thin films.**—Conductivity measurements were made on Cu/CuF<sub>2</sub>/Cu cells fabricated using the masking geometry described in a previous paper (10). A conductivity value of 1.6 × 10<sup>-9</sup> (ohm-cm)<sup>-1</sup> was found at 25°C. This is somewhat higher than the values of 10<sup>-10</sup>-10<sup>-11</sup> (ohm-cm)<sup>-1</sup> reported for pure chemically formed thin films (13). This difference in conductivity could be due to the presence of impurities in the film as proposed above, or to some grain boundary effects. It should be noted that the increase in conductivity was comparable to the increase in conductivity of PbF<sub>2</sub> films compared to pressed pellet or single crystal PbF<sub>2</sub> noted in our earlier paper. A temperature study was performed, and an Arrhenius plot resulted in a value for  $\Delta H$  of 0.345 eV, somewhat below  $\Delta H$  values for ionic conduction in fluorides. It was not determined whether the observed conductivity was primarily ionic or electronic, but, in any case, the film conductivity was quite low. It was clear that improved CuF<sub>2</sub> cathode conductivity would be necessary for use in thin-film galvanic cells.

**Deposition of mixed PbF<sub>2</sub>-CuF<sub>2</sub> films.**—PbF<sub>2</sub> and CuF<sub>2</sub> were codeposited from the same boat to achieve mixed films with improved ionic conductivity. This was similar to the practice of mixing cathode and elec-

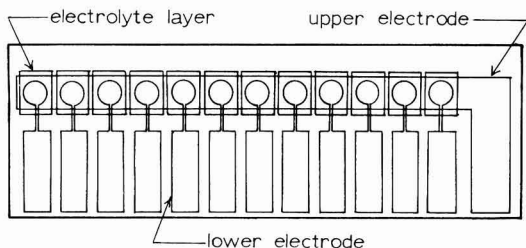


Fig. 1. Thin-film cell configuration of 0.1 cm<sup>2</sup> cells

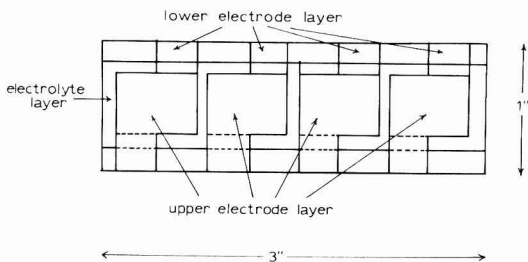


Fig. 2. Thin-film cell configuration of 2 cm<sup>2</sup> cells

trolyte as used in pressed-pellet cells. The  $\text{PbF}_2$  has a lower melting point than  $\text{CuF}_2$  ( $822^\circ\text{C}$  vs.  $950^\circ\text{C}$ ) and was observed to evaporate at lower temperatures. However, it was found that a mixture of the two could be codeposited. One would expect that the initial composition of the evaporant would be relatively rich in  $\text{PbF}_2$  while later in the deposit it would be relatively rich in  $\text{CuF}_2$ . If one deposits a cell in the sequence Pb layer,  $\text{PbF}_2$  layer,  $\text{CuF}_2$ - $\text{PbF}_2$  mixture layer, Cu layer, then one would have the favorable situation of a gradation from  $\text{PbF}_2$ -rich to  $\text{CuF}_2$ -rich through the cathode film, with a very high effective contact area between electrolyte and cathode. The actual composition of the cathode film would depend on the initial composition of the mixture in the evaporation source and to what extent the evaporation proceeded. With initial composition of approximately 70 mole per cent (m/o)  $\text{CuF}_2$ , and evaporating a large part, but not all, of the mixture, one might estimate over-all composition of about 50 m/o  $\text{CuF}_2$ .

X-ray studies were made on the codeposited mixed films. Some structure was seen in early films (Fig. 3a), with peaks attributable to both  $\text{PbF}_2$  and  $\text{CuF}_2$ . However, as care was taken to avoid spattering of the mixture in the boat, and to avoid both the earliest and latest fractions of the deposit by using a shutter in front of the substrate, films were obtained which showed little or no structure under x-ray diffraction (Fig. 3b). Only one very broad peak around  $27^\circ$  could be seen, possibly due to  $\text{CuF}_2$ . Thus it appeared that the mixed films had a very fine-grained or amorphous nature. Studies of such films with scanning electron microscopy showed no visible grains.

**Conductivity of mixed films.**—Conductivity measurements were made on mixed films with copper electrodes. Values for  $\sigma$  were in the range  $10^{-6}$ - $10^{-8}$  ( $\text{ohm-cm}$ ) $^{-1}$ , depending on the extent of the deposit. Longer deposit times with larger amounts of  $\text{CuF}_2$  gave the lower conductivity values. Even so, a marked improvement was achieved compared to the pure  $\text{CuF}_2$  films. Another benefit of the mixed films was the ease of deposition. The  $\text{CuF}_2$ - $\text{PbF}_2$  mixture melted at a lower temperature than the pure  $\text{CuF}_2$ , leading to improved outgassing characteristics and less spattering during deposition. In addition it was found that smooth adherent films could be obtained without substrate heating.

**Galvanic cells.**—Cells of the type  $\text{Pb}/\text{PbF}_2/\text{PbF}_2, \text{CuF}_2/\text{Cu}$  were deposited using the  $0.1 \text{ cm}^2$  area masks.

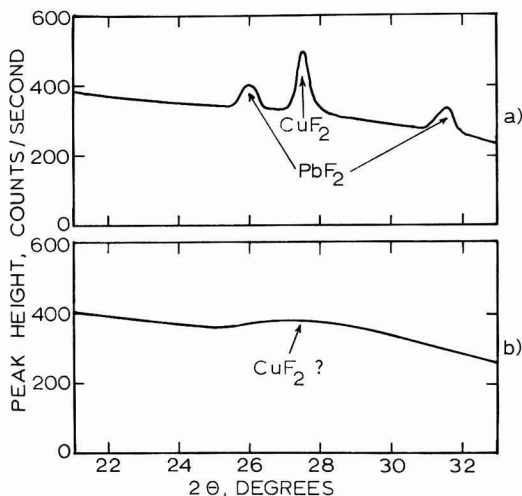
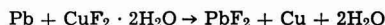


Fig. 3. X-ray spectra of mixed  $\text{PbF}_2/\text{CuF}_2$  films: (a) early film, with  $\text{PbF}_2$  and  $\text{CuF}_2$  peaks, (b) later film, with almost no structure apparent.

In addition, some cells were made with  $2 \text{ cm}^2$  area. The best cells were made without any substrate heating. Substrate heating for the cathode layer led to better adhesion of that layer, but caused the lifting of the underlying layers. Heating the substrate for all the layers led to increased numbers of shorted cells, probably due to increased Pb and  $\text{PbF}_2$  grain size and correspondingly increased numbers of pinholes. The yields of nonshorted  $2 \text{ cm}^2$  cells were smaller than for the  $0.1 \text{ cm}^2$  cells, but with care to avoid spattering of deposits moderate yields of the larger cells could be obtained. Some cells that were found to be initially shorted eventually "healed," but with lower than normal capacity. Finished cells were coated with Kodak Microneg photoresist to protect the  $\text{CuF}_2$  from moisture. Some cells were left uncoated for comparison, and within days these films crazed and blistered. The sealed cells did not show any deterioration after weeks of exposure to air.

The OCV's of cells ranged from 0.56 to 0.70V. However, the lower OCV's were obtained for cells deposited from early fractions of the deposition mixture, and these cells had poor performance. Although no appreciable  $\text{CuF}_2 \cdot 2\text{H}_2\text{O}$  was detected by x-ray, it is interesting to note that the following cell reaction



has a theoretical OCV of 0.57V. This value agrees with the lowest cell values observed and may represent cells which had inadvertently been exposed to water vapor.

The cells with good performance had OCV's of 0.61-0.70V. The occurrence of lower than theoretical OCV in some cells could also indicate the presence of electronic leakage in the cells. However, the electronic conductivity of pure  $\text{PbF}_2$  has been found to be quite low (10), so this was probably not the reason for lower OCV's. Figure 4 shows the OCV of a cell as a function of time. Initial voltage was 0.63V and subsequently rose to 0.66V. Even after several weeks the OCV was the same, and the cell was subsequently discharged with no apparent loss of capacity on storage. Therefore it appeared that the lower OCV's were not due to electronic leakage.

Another possible explanation of OCV lower than theoretical is that a solid solution of  $\text{CuF}_2$  and  $\text{PbF}_2$  was present, and the OCV would then indicate the  $\text{CuF}_2$  activity at the active site. The x-ray data indicated an amorphous phase (Fig. 3b) supporting this possibility.

Cells were discharged under various loads and at different temperatures, and the cell voltages measured vs. time. Figure 5 shows a typical discharge curve for a small  $0.1 \text{ cm}^2$  area cell at  $25^\circ\text{C}$  with a 3.3 megohm load. Upon first application of the load the cell voltage dropped to 0.22V, but as the cell started to discharge, the cell voltage rose gradually to 0.46V. This "activa-

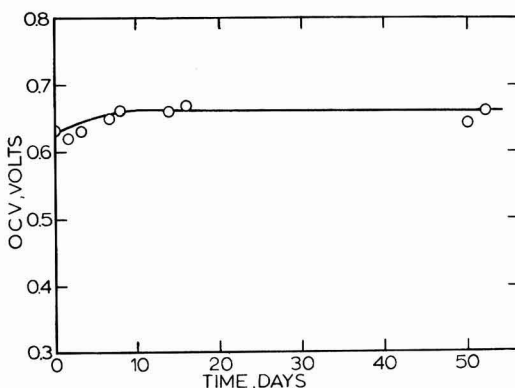


Fig. 4. OCV as a function of time for  $\text{Pb}/\text{PbF}_2/\text{PbF}_2, \text{CuF}_2/\text{Cu}$  cell.



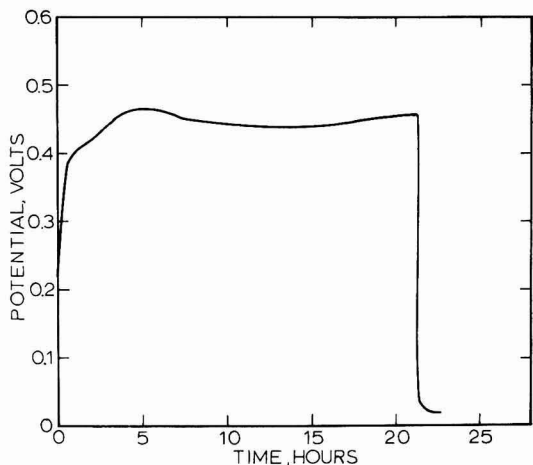


Fig. 5. Discharge curve at 25°C through 3.3 megohm load

tion effect" has been present for other solid-state batteries (18). The voltage then remained nearly constant during the rest of the discharge. Finally, the cell voltage dropped rapidly to 20-50 mV. The open-circuit voltage of such cells measured with an electrometer was still over 0.5V, although it was no longer possible to draw appreciable current from them. This is understandable if we consider the geometry of the cells. With the small 0.1 cm<sup>2</sup> cells, the cathode mixture and the upper copper electrode were deposited in the form of a long strip common to all the cells. But only the CuF<sub>2</sub> located directly above the smaller Pb electrodes could react easily. Once this CuF<sub>2</sub> was consumed there was still sufficient CuF<sub>2</sub> not directly above the Pb electrodes to establish the OCV, but only very low currents could be maintained with the extremely high resistance through the longer electrolyte path.

Figure 6 shows discharge curves for 0.1 cm<sup>2</sup> cells under various constant loads at 25°C, and Fig. 7 shows discharge curves with 300,000 ohm loads at 25°C and at 75°C. From the maximum current densities observed in Fig. 7 and assuming an OCV of 0.7V, one can use an Arrhenius relationship to obtain a  $\Delta H$  value of 0.33 eV. This is quite close to the value obtained from a conductivity cell of pure CuF<sub>2</sub> mentioned earlier, and is smaller than the value of 0.54 eV found for conductivity cells of PbF<sub>2</sub>. This supports the contention that the rate-determining step in the cell reaction involves the CuF<sub>2</sub> cathode material.

Table I summarizes the data for discharge of several cells of both 0.1 and 2 cm<sup>2</sup> area. The actual capacity of the cells is listed, both in terms of coulombs of charge and in terms of equivalents of CuF<sub>2</sub>. These cells were all constructed with an excess of the anode material. Therefore, if the amount of CuF<sub>2</sub> present in the cathode film were known, the actual per cent utilization of cathode material could be calculated. However, the fact

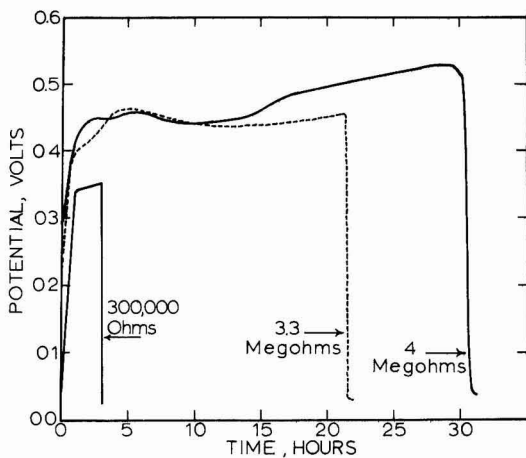


Fig. 6. Discharge curves at 25°C through various loads

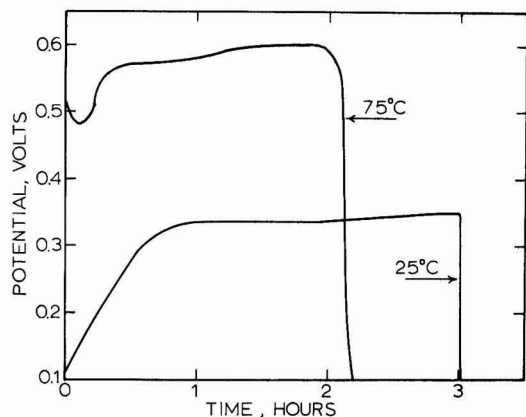


Fig. 7. Discharge curves at 25° and 75°C through 300,000 ohm loads.

that a mixed film was used for the cathode, and that the x-ray diffraction studies gave no peaks prevented calculations based on these methods. The cells were estimated to be about 50 m/o CuF<sub>2</sub> from the evaporation conditions and a check on this assumption was made by studying some of the CuF<sub>2</sub>-PbF<sub>2</sub> films using x-ray fluorescence analysis. Results showed 52-56 m/o CuF<sub>2</sub> in the films. The percentage utilization for the cells listed in Table I was calculated using this information. For the small cells it can be seen that the maximum utilization was 40% with most of the discharges in the range of 30-40%. Therefore, it appears that only a fraction of the available capacity of the cells could be used. A possible explanation is that much

Table I. Performance of Pb/PbF<sub>2</sub>/PbF<sub>2</sub>,CuF<sub>2</sub>/Cu thin-film galvanic cells

Cell	Cell area, cm <sup>2</sup>	Temperature, °C	Load, ohm	Capacity, coulombs*	Capacity, equiv of CuF <sub>2</sub> *	% utilization**
A-78-B4	2.0	25	100,000	$4.9 \times 10^{-2}$	$5.1 \times 10^{-7}$	6.7
A-78-B3	2.0	25	300,000	$1.3 \times 10^{-1}$	$1.4 \times 10^{-6}$	17.9
A-78-S7	0.1	25	300,000	$1.1 \times 10^{-2}$	$1.2 \times 10^{-7}$	30.8
A-78-S10	0.1	25	$3.3 \times 10^6$	$1.0 \times 10^{-2}$	$1.1 \times 10^{-7}$	29.0
A-78-S9	0.1	25	$4 \times 10^6$	$1.3 \times 10^{-2}$	$1.4 \times 10^{-7}$	35.6
A-78-S12	0.1	50	300,000	$0.6 \times 10^{-2}$	$0.6 \times 10^{-7}$	19.3
A-78-S6	0.1	50	$4 \times 10^6$	$1.4 \times 10^{-2}$	$1.4 \times 10^{-7}$	36.8
A-78-S3	0.1	75	300,000	$1.5 \times 10^{-2}$	$1.5 \times 10^{-7}$	40.0
A-78-S8	0.1	75	$4 \times 10^6$	$0.3 \times 10^{-2}$	$0.3 \times 10^{-7}$	8.7

\* Measured capacity from discharge of cells.

\*\* Calculated utilization of cathode, assuming 54 m/o CuF<sub>2</sub> in 10,000Å thick cathode film, or  $3.8 \times 10^{-7}$  equivalent of CuF<sub>2</sub> in each 0.1 cm<sup>2</sup> cell.



of the  $\text{CuF}_2$  was isolated in the  $\text{PbF}_2$ -rich part of the cathode film, without electronic contact to the Cu electrode, or became isolated during discharge. A lack of complete utilization of cell capacity has also been reported by Liang *et al.* (9) for the  $\text{Li/LiI/AgI/Ag}$  system.

The  $\text{Pb/CuF}_2$  cells with high OCV showed no evidence of self-discharge with storage. One particular cell was stored for over six weeks to measure OCV. The cell was subsequently discharged with no loss of capacity. This is in contrast to the thin-film cells of Liang which self-discharged *via* migration of silver ion in the cell (9).

**Recharging of cells.**—Cell A-78-S1 was discharged for one hour at  $1 \mu\text{A}$  current at  $75^\circ\text{C}$ . This was only a partial ( $\sim 33\%$ ) discharge. Figure 8 shows that the cell voltage leveled off at about 0.6V, 0.1V below the theoretical OCV. Then the cell was charged at  $1 \mu\text{A}$ . There appeared to be a slight plateau area around 1.1–1.2V, but the voltage then climbed more steeply again. It is clear from Fig. 8 that the cell reaction was not reversible, and that charging this cell was not feasible at  $75^\circ\text{C}$ .

All attempts to recharge cells after they had been completely discharged met with failure; only extremely low currents would flow through the cells at reasonable charging voltages. Although these currents led to

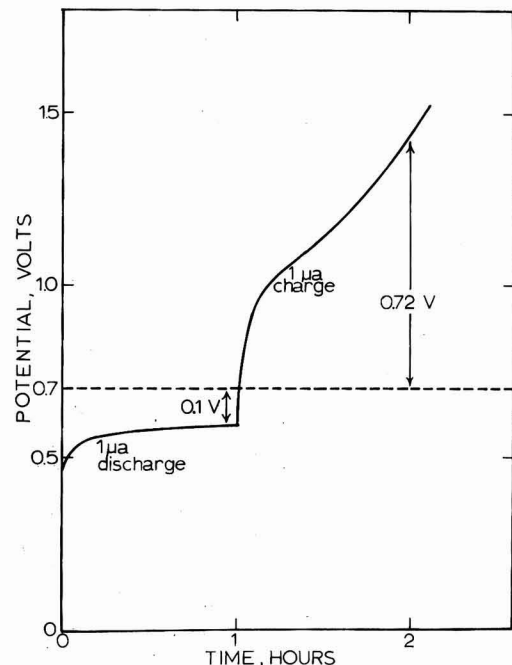


Fig. 8. Attempt to recharge thin-film cell, potential vs. time for  $1 \mu\text{A}$  discharge and  $1 \mu\text{A}$  charge cycles.

the proper QCV, the capacity of recharged cells was small. This discouraging result is consistent with the results of similar recharging attempts for  $\text{CuF}_2$  in non-aqueous liquid electrolyte batteries.

### Summary

Thin-film galvanic cells using  $\text{PbF}_2$  electrolyte, an anion conductor, have been successfully fabricated and discharged electrochemically. It was necessary, however, to codeposit  $\text{PbF}_2$  with the  $\text{CuF}_2$  cathode material to increase its ionic conductivity. The technique of co-deposition is analogous to the conventional technique of mixing electrolyte and electrode material in pressed-powder cells. The  $\text{Pb/PbF}_2/\text{PbF}_2/\text{CuF}_2/\text{Cu}$  cells exhibited discharge characteristics similar to other thin-film cells reported in the literature, but they were not rechargeable.

### Acknowledgments

The authors acknowledge financial support of this project by the National Science Foundation, Grant No. GH-37144. This paper was taken in part from the Ph.D. dissertation of James C. Hunter, University of California, Santa Barbara, 1974.

Manuscript received July 14, 1975; revised manuscript received Aug. 4, 1975.

Any discussion of this paper will appear in a Discussion Section to be published in the December 1976 JOURNAL. All discussions for the December 1976 Discussion Section should be submitted by Aug. 1, 1976.

Publication costs of this article were partially assisted by the University of California, Santa Barbara.

### REFERENCES

1. J. I. Masters, P. Vouros, and J. P. Clune, U.S. Pat. 3,575,715 (1971).
2. J. I. Masters and P. Vouros, *This Journal*, **116**, 880 (1969).
3. G. M. Goldberg, U.S. Pat. 3,554,795 (1971).
4. G. Ervin, U.S. Pat. 3,701,685 (1972).
5. A. Sator, *Compt. Rend.*, **234**, 2283 (1952).
6. M. Perrot and A. Sator, *ibid.*, **234**, 1883 (1952).
7. C. W. Moulton, M. Hacsakaylo, and C. Feldman, Paper 62 presented at the Electrochemical Society Meeting, Toronto, Canada, May 3-7, 1964.
8. F. E. Swindells and W. R. Lanier, U.S. Pat. 3,547,700 (1970).
9. C. C. Liang, J. Epstein, and G. H. Boyle, *This Journal*, **116**, 1322 (1969).
10. J. H. Kennedy, R. Miles, and J. Hunter, *ibid.*, **120**, 1441 (1973).
11. J. J. Auburn, K. W. French, S. I. Lieberman, V. K. Shah, and A. Heller, *ibid.*, **120**, 1613 (1973).
12. K. H. M. Brauer and J. A. Harvey, "Status Report on Organic Electrolyte High Energy Batteries," DA Task 1CO 14501 A 34A-00-01 (1967).
13. S. S. Flaschen and P. D. Garn, *J. Am. Ceram. Soc.*, **42**, 641 (1959).
14. B. Burrows, *This Journal*, **118**, 1130 (1971).
15. P. Bauer, "Batteries for Space Power Systems," p. 199, U.S. Government Printing Office, Washington, D.C. (1968).
16. C. M. Wheeler, Jr. and H. M. Haendler, *J. Am. Ceram. Soc.*, **76**, 263 (1954).
17. L. V. My, G. Perinet, and P. Bianco, *J. Chem. Phys.*, **63**, 719 (1966).
18. C. C. Liang, *Appl. Solid State Sci.*, **4**, 95 (1974).

# The Electrodeposition of Aluminum from Aromatic Hydrocarbon

## I. Composition of Baths and the Effect of Additives

E. Peled\* and E. Gileadi\*

*Institute of Chemistry, Tel-Aviv University, Ramat-Aviv, Israel*

### ABSTRACT

Electroplating of aluminium on copper and steel substrates was conducted at room temperature. The bath consisted basically of  $\text{AlBr}_3$  and an alkali metal bromide such as  $\text{KBr}$  dissolved in a suitable mixture of aromatic hydrocarbons. The bath was operated under conditions resembling industrial operation. Oxygen and humidity were removed by bubbling nitrogen through the bath. The effect of bath composition on the quality of the plated product is discussed in detail. Transference numbers were measured. The aluminium is shown to be present in the form of a negative ion ( $\text{Al}_2\text{Br}_7^-$ ), the transference number of which is larger than that of the solvated positive ion. The reactions taking place during deposition and dissolution of aluminium in this system are discussed in detail.

Aluminium cannot be electrodeposited from aqueous or other protic solvents because decomposition of the solvent, accompanied by copious hydrogen evolution, occurs at the potential required to deposit the metal, and the current efficiency is essentially zero. Attempts to employ aprotic, polar solvents such as acetonitrile, DMF, pyridine, propylene carbonate, etc., failed,<sup>1</sup> probably since the small, highly charged  $\text{Al}^{3+}$  ion is very heavily solvated and decomposition of the solvent requires less energy than desolvation of the ion and electrodeposition of the metal. This is particularly so for the solvent molecules in the inner solvation shell which are highly polarized by the central ion.

Aluminium was successfully electrodeposited by Brenner *et al.* (1) from a bath consisting of  $\text{AlCl}_3$  and  $\text{LiAlH}_4$  dissolved in diethyl ether. This bath has not been adopted on a wide industrial scale because of its hazardous nature and the high cost of the bath components. Two other baths, one based on  $\text{LiAlH}_4$  and  $\text{AlCl}_3$  in tetrahydrofuran (3, 4), the other on molten alkyl aluminium compounds (5), are presently under investigation on pilot plant scale.

Aromatic hydrocarbons represent a unique class of solvents of great interest for electrochemical research and technology. Simple ionic salts, *e.g.*, alkali halides, are insoluble in them because of their low dielectric constant, while covalent salts such as  $\text{AlX}_3$ , where X is a halide ion other than  $\text{F}^-$ , are very soluble. Rigorously dried  $\text{AlBr}_3$  dissolved in an aromatic hydrocarbon yields clear solutions having a pale yellow to orange tint, depending on the hydrocarbon employed. The electrical conductivity is very low (*ca.*  $10^{-9}$  mho  $\text{cm}^{-1}$ ) (6). However, alkali halides can be dissolved in these systems, yielding an electrolytic solution of medium conductivity (up to 6 mmho  $\text{cm}^{-1}$ ) (7-12), which is sufficient both for electrochemical measurements and for electroplating applications. A maximum in conductivity is reached when the molar ratio of, say,  $\text{AlBr}_3$  to  $\text{MBr}$  (where M is an alkali metal or the ammonium ion) is 2:1, indicating that  $\text{Al}_2\text{Br}_7^-$  and  $\text{M}^+$  ions are probably formed. There is evidence in the literature showing that the solvation number of these ions (when  $\text{M} = \text{H}$ ) is different in different hydrocarbons (13). The stability of the solvated  $\text{Al}_2\text{Br}_7^-$  ions (and possibly of some  $\text{AlBr}_4^-$  ions which may also be present when the amount of  $\text{MBr}$  added is increased) depends on the hydrocarbon used. In the presence of  $\text{HBr}$ <sup>2</sup> it is found to increase in the order benzene < toluene < xylene < mesitylene (14). Cryoscopic mea-

surements indicated that in the presence of alkali halides, larger aggregates having the general formula  $(\text{Al}_2\text{Br}_7^- \text{M}^+)_n$ , where *n* may be as large as four, may also be formed (10, 12, 15).

Plotnikov and co-workers studied these systems about forty years ago and showed that it was possible to electrodeposit aluminium on platinum or copper from solutions of  $\text{AlBr}_3/\text{MBr}$  in benzene, toluene, and xylene (7, 16-20). However, the deposits obtained were in most cases of poor quality, the cathodic current efficiencies were low, and the solvents were decomposed in the course of electrolysis (10). Pospekhov, who reviewed the field in 1937, concluded that these systems were not suitable as plating baths for industrial applications (19). Recently, the system of  $\text{AlBr}_3$  dissolved in xylene with  $\text{HBr}$  added was investigated in detail (21, 22). Aluminium was electrodeposited with high current efficiencies of *ca.* 90%. Two side reactions were also observed, *viz.*, reduction of the solvent and hydrogen evolution. Capuano and Davenport published recently a patent (23) and two papers (24, 25) in which the electroplating of aluminium from solutions of  $\text{AlBr}_3$  in mixed aromatic hydrocarbons was reported. The quality of plating was found by these authors to depend on the hydrocarbons used. Thus, for example, benzene mixed with durene gave very poor results, while toluene mixed with ethyl benzene yielded excellent deposits. A main feature of the work of Capuano and Davenport is that all experiments were performed in the presence of small amounts of water (introduced by partial saturation of the hydrocarbon used as solvent with water before addition of  $\text{AlBr}_3$ ), or with  $\text{HBr}$  continuously added (23-25). Water or  $\text{HBr}$  were considered by these authors to be indispensable components of the plating bath, without which aluminium could not be electrodeposited.

In the present work a systematic study of the effect of the composition of the baths on the quality of aluminium electrodeposited on copper or steel substrate, is presented. Special emphasis is placed on the effects of: (i) different aromatic hydrocarbons, (ii) organic and inorganic salts, and (iii) hydrobromic acid on the performance of the plating baths.

### Experimental

Solutions were made up of AR-grade chemicals without further purification. All experiments were performed in airtight cells under an atmosphere of dry nitrogen. The inert gas flow was maintained continuously from the time a solution was made up until it was finally discarded (in many cases this lasted several months). The cell, electrodes, plating procedure, and preparation of metal surfaces were described in an earlier publication (26). Most experiments were

\* Electrochemical Society Active Member.

Key words: aluminium, electrodeposition, nonaqueous plating bath, aromatic hydrocarbons, aluminium bromide.

<sup>1</sup> Reviews of previous work are given in Ref. (1, 2).

<sup>2</sup>  $\text{AlBr}_3$  is very hygroscopic and any moisture absorbed immediately causes the formation of  $\text{HBr}$  and aluminium hydroxide or hydroxybromide.

conducted at cathodic current densities of 5-10 mA · cm<sup>-2</sup>, but in some cases a wider range of 0.5 to 40 mA · cm<sup>-2</sup> was employed. Cathodic and anodic current efficiencies were determined by weighing the samples before and after electrolysis at a constant current. Since the main purpose of the present study was to evaluate the influence of various bath components and additives on the quality of electrodeposits and on the cathodic and anodic current efficiency under conditions resembling industrial operation, the cells were opened for changing samples in the regular laboratory atmosphere and the highly hygroscopic AlBr<sub>3</sub> was used as purchased without further drying.<sup>3</sup> Thus, it may be assumed that varying small amounts of humidity entered the bath and HBr was present in small quantities in all experiments.

The purity of electrodeposited aluminium was determined in the following manner: The sample was rinsed in a warm (60°C) 1M NaOH solution for a few seconds to remove the outermost oxide layer. It was subsequently washed in water, dried in acetone, and weighed. All the aluminium was then dissolved in warm 1M NaOH, the substrate was dried and weighed again. The total amount of aluminium in solution was determined gravimetrically with 8-hydroxy quinoline and this was compared to the weight-loss observed above.

Transference numbers were measured in a conventional Hittorf cell. Copper wires (1 mm diam) were used in the form of a helix for both electrodes. Electrolysis was conducted for 1.5-2 hr at a constant current of 20 mA. The volume of both anode and cathode compartments was 5 cm<sup>3</sup>. The solution, prepared under anhydrous conditions, consisted of 0.7M KBr and 2.0M AlBr<sub>3</sub> in toluene. The concentrations of potassium and aluminium in the anolyte were determined by atomic absorption spectroscopy. Electrolysis time was calculated to give only a small concentration change (ca. 10%). In this way errors due to dissolution of copper and conduction of current by copper ions were minimized. The use of a copper anode insures that changes of concentration of potassium and aluminium in the anolyte are only caused by migration. Use of an aluminium anode would require a knowledge of the current efficiency of anodic dissolution, which has not been measured under the experimental conditions prevailing in this experiment.

## Results

**The basic system.**—The basic system consists of a solution of AlBr<sub>3</sub> in toluene (or benzene) in roughly equal weights. If prepared under rigorously dry conditions, this would have very low conductivity and electrodeposition would not be possible. However, under the conditions maintained in all experiments reported here, some moisture, and hence some HBr, was always present, giving sufficient conductivity to allow electroplating. The basic system and the same system with either an alkali bromide (or iodide) or a Lewis base added were tested.

**Aluminium bromide in toluene or benzene.**—Aluminium bromide is very soluble in aromatic hydrocarbons. Two or three molar solutions of AlBr<sub>3</sub> in benzene or toluene were prepared and tested. A tarlike organic deposit containing little or no aluminium was formed if benzene was the solvent. In toluene a gray to black deposit was produced and the current efficiency for aluminium deposition was less than 50%. Results were generally irreproducible and satisfactory electrodeposits could not be obtained in these systems.

**The effect of addition of hydrocarbons and amines.**—Aromatic hydrocarbons such as ethylbenzene, mesitylene, and naphthalene were added in quantities ranging from 3 to 15 weight per cent (w/o) to the basic system of AlBr<sub>3</sub> in toluene. White gray electrodeposits

having a metallic appearance were observed. A similar improvement in the quality of the electrodeposits resulted from the addition of dimethyl aniline or triethyl amine in comparable concentrations. The cathodic current efficiency was still highly irreproducible and ranged from 20% to nearly 100% in different experiments. Heavy dendrite formation was observed. The conductivity of the solutions varied with time and typically decreased from an initial value of 1-2 mmho · cm<sup>-1</sup> to ca. 0.1 mmho · cm<sup>-1</sup> within a few days.<sup>4</sup>

**The effect of addition of alkali halides.**—Alkali bromides or iodides were added to solutions of AlBr<sub>3</sub> in toluene. The concentrations were about 0.1-1.0M. The conductivity of the baths was increased and stabilized in the range of 0.5-6 mmho · cm<sup>-1</sup>, depending on concentration. Dendrite formation was significantly reduced and the cathodic current efficiency was higher in most experiments. Deposits obtained in freshly prepared solutions were generally poor, but after a few days, and after several samples had been plated, the quality of electrodeposits was greatly improved and was comparable to those described above. Better results were generally observed in the presence of iodides than with bromides.<sup>5</sup> The baths tended to be unstable and were found to deteriorate after a few weeks of operation.

**The complete plating bath.**—The experiments described above have shown that the basic system of AlBr<sub>3</sub> in benzene or toluene with either a Lewis base or an alkali bromide did not yield satisfactory results. A suitable bath should contain both an alkali bromide (or iodide) and a Lewis base such as a large aromatic hydrocarbon or an amine. The effect of the addition of different compounds from these classes is discussed below.

**The effect of alkali halides.**—A solution of AlBr<sub>3</sub> (2-3M) in toluene, with ethylbenzene or naphthalene in concentrations ranging from 3-30 w/o was employed in these experiments. Bromides or iodides of Li<sup>+</sup>, Na<sup>+</sup>, K<sup>+</sup>, and NH<sub>4</sub><sup>+</sup> were added in concentrations of 0.1-1.0M. Excellent electrodeposits were obtained. The current efficiency increased with the concentration of the salt, and the tendency to form dendrites decreased. The purity of the electrodeposited aluminium was 99.5%, equal to the purity of the aluminium anodes used in these experiments.

When the concentration of the alkali salt was higher than 1M, codeposition of the salt and possibly of organic matter occurred. In some cases, when only ca. 70% of the electrodeposit consisted of aluminium, this was immediately apparent upon inspection of the sample. In other cases, when the purity was as high as 95%, apparently smooth and uniform electrodeposits were obtained, but these exhibited very poor corrosion resistance. Codeposition of salt appeared to be more severe in the presence of iodides than with bromides at comparable concentration.

Addition of alkali chlorides caused a decrease in current efficiency and gave rise to electrodeposits of poor quality. In the presence of alkali fluorides a white powder was formed in the bath and the current efficiency for aluminium deposition decreased.

**The effect of cations on bath performance.**—Addition of bromides of Li<sup>+</sup>, Na<sup>+</sup>, K<sup>+</sup>, and NH<sub>4</sub><sup>+</sup> gave indistinguishable results. A few attempts were made to electrodeposit a Mg/Al alloy by adding MgBr<sub>2</sub> in 0.1M concentration. (The solubility of this salt is much lower than that of alkali bromides or iodides.) In these experiments only aluminium was electrodeposited.

Several quaternary ammonium bromides (tetramethyl and tetraethyl ammonium bromide, ethyl pyri-

<sup>4</sup> The initial conductivity depends on the amount of moisture present in the AlBr<sub>3</sub> used or that entering the cell accidentally during preparation of the solution. This may depend on a number of factors such as the temperature and relative humidity, the skill of the experimenter, etc.

<sup>5</sup> It is very likely that part of the AlBr<sub>3</sub> could be replaced by AlI<sub>3</sub> in all plating experiments, yielding similar or even better results. In view of the higher cost and lower stability of AlI<sub>3</sub>, this would be of little industrial interest, however.

<sup>3</sup> Studies in rigorously dried systems are under way and will be reported elsewhere (27, 28).

dinium bromide, and pyridinium hydrobromide) were tested in a bath containing  $\text{AlBr}_3$  in a mixture of, say, toluene and ethylbenzene. These cations caused an apparent improvement in the results. Very smooth deposits were obtained and dendrite formation was completely suppressed. The current efficiency was close to 100% (except in the case of pyridinium hydrobromide where it was only 60-80%). However, the coatings offered poor corrosion protection. Chemical analysis showed that the concentration of aluminium in the electrodeposit was ca. 95% or less, and incorporation of salt took place.

In order to minimize the incorporation of these salts in the electrodeposit and yet make use of their beneficial effects, another series of experiments was conducted. In these, the bath contained an alkali bromide in the usual concentration range (ca. 0.5M) and a small amount (0.01-0.1M) of quaternary ammonium bromide. An improvement in bath performance was observed. Thick and smooth deposits could be formed with few or no dendrites. However, some salt was still incorporated in the electrodeposit; its purity was only 98% and its resistance to corrosion was poor.

The organic cations had a distinct effect on plating from a solution containing only one hydrocarbon. It was already pointed out that a solution of  $\text{AlBr}_3$  and  $\text{MBr}$  in benzene gave tarlike deposits, while in toluene it gave grayish dark aluminium deposits with low cathodic current efficiency. The addition of 0.01 w/o ethyl pyridinium bromide made it possible to electrodeposit aluminium from a solution of  $\text{AlBr}_3$  in benzene at low current efficiencies (although the quality of the electrodeposit was poor). The addition of 0.02 w/o of the same material to the toluene based solution yielded smooth deposits at high current efficiencies, although some salt was still incorporated in the deposited film.

*The effect of Lewis bases.*—Two classes of compounds were tested in these experiments: (i) derivatives of benzene having one or several side chains or naphthalene and its derivatives, and (ii) aromatic and aliphatic amines and some ethers.

In the first group the compounds tested were: ethyl benzene, diethyl benzene, ethyl-methyl benzene, tri-ethyl benzene, mesitylene, durene, hexamethylbenzene, *ter*-butyl benzene, naphthalene and its ethyl and methyl derivatives, and anthracene and its methyl derivatives. These compounds are known to be stronger Lewis bases than toluene or benzene. They were added in concentrations of 0.1M up to several molar to baths consisting of  $\text{AlBr}_3$  (2-3M) and  $\text{MBr}$  (0.1-1M) in toluene. Greatly improved results were observed upon the addition of derivatives of benzene and naphthalene (and of naphthalene itself). The cathodic current efficiency was close to 100% at current densities of 5-10  $\text{mA} \cdot \text{cm}^{-2}$ , and high-quality, pure electrodeposits were obtained.<sup>6</sup> At higher current densities the cathodic current efficiency was found to decrease significantly (at 30  $\text{mA} \cdot \text{cm}^{-2}$  it was down to 40%). The anodic current efficiency was close to 100% when current densities of 1-10  $\text{mA} \cdot \text{cm}^{-2}$  were used for several hours. However, the decrease of weight of anodes after several weeks of operation was higher than that calculated from the total charge passed. This is probably caused by mechanical disintegration of the anodes and to a lesser degree by chemical dissolution which takes place in solutions which have not been rigorously purified and dried (27-29). Addition of anthracene and its derivatives also improved the performance of the baths, but to a lesser extent. These baths tended to deteriorate rather rapidly. In certain baths containing a high concentration of naphthalene (ca. 2M and comparable to the concentration of  $\text{AlBr}_3$ ), codeposition of salt was observed. No such effect was observed when the concentration of naphthalene was below 1M.

In the second group the compounds tested were: pyridine, tri-ethyl-amine, and *N,N* dimethyl aniline.

These compounds are even stronger Lewis bases. Their presence in solution in concentration of a few tenth molar improved the properties of the plating bath in a manner similar to the effect of the hydrocarbons in the first group above. Chemical dissolution of the copper cathodes was observed in freshly prepared solutions containing any one of the above-mentioned amines. Electrolysis of such solutions yielded a highly decorative gold colored deposit of a copper/aluminium alloy which, however, had very poor corrosion resistance. After aging the bath for a few days, chemical dissolution stopped and pure aluminium electrodeposits were obtained.

A higher concentration of *N,N* dimethyl-aniline of ca. 0.7M prevented electrodeposition of aluminium.

In an additional series of experiments, tetrahydrofuran in molar concentration equal to that of  $\text{AlBr}_3$  was added instead of an amine. A tarlike deposit containing some aluminium was formed.

*The effect of HBr.*—A solution of  $\text{AlBr}_3$  and naphthalene in toluene was saturated with HBr. The conductivity of the resulting solution was 13  $\text{mmho} \cdot \text{cm}^{-1}$ . The copper cathode (surface area 10  $\text{cm}^2$ ) dissolved rapidly in this solution (weight loss was 0.08 g/hr) and aluminium could not be electrodeposited. Hydrobromic acid was removed from solution by bubbling dry nitrogen. The decrease in concentration can be followed in this system (where no alkali bromide was added) by the decrease in conductivity. Aluminium could be deposited only when the conductivity was less than 8  $\text{mmho} \cdot \text{cm}^{-1}$ . At 5  $\text{mmho} \cdot \text{cm}^{-1}$  the current efficiency was 35% and at 1  $\text{mmho} \cdot \text{cm}^{-1}$  or less it was close to 100%. In the last solution the rate of corrosion of the copper cathode on open circuit was only 5 mg in 24 hr, more than two orders of magnitude slower than in a solution saturated with HBr.

*The effect of oxygen.*—Oxygen does not react chemically with the components of the bath at a significant rate. Thus, it may be allowed to saturate the bath and can subsequently be removed by bubbling an inert gas without adversely affecting its performance. However, during electroplating oxygen must be absent since its reaction at the electrodes prevents deposition of aluminium and causes rapid deterioration of the bath. In an experiment conducted in a solution saturated with oxygen, the voltage between a copper cathode and an aluminium reference electrode rose within minutes from a few millivolts to many volts. At the end of electrolysis the copper cathode was coated with a black tar which did not contain aluminium.

*The effect of ions of heavy metals.*—Ions of heavy metals, such as copper and iron, interfere with the electrodeposition of aluminium. Alloys of various composition are electrodeposited, the adhesion to the substrate metal is usually poor, and the deposits are gray and have poor corrosion resistance. Heavy ions can be removed by preelectrolyzing on a dummy cathode.

*Transference numbers.*—Preliminary experiments were performed to determine approximately the transference numbers of potassium and aluminium, by the Hittorf method. A solution of 0.7M  $\text{KBr}$  and 2M  $\text{AlBr}_3$  in toluene was employed. Two copper electrodes were used in the cell and chemical analysis of the solution in the anode compartment was carried out. The concentration of potassium was found to decrease while that of aluminium was found to increase. The transference numbers were:  $t_{\text{K}^+} = 0.3 \pm 0.1$  and  $t_{\text{Al}_2\text{Br}_7^-} = 0.7 \pm 0.1$ . If one were to assume that aluminium was present mainly in the form of the smaller ion  $\text{AlBr}_4^-$ , its calculated transference number would be  $t_{\text{AlBr}_4^-} = 1.4 \pm 0.2$  which is clearly unacceptable.

*The solubility of  $\text{AlBr}_3$  and  $\text{KBr}$  in cyclohexane.*—Aluminium bromide was dissolved in 70  $\text{cm}^3$  cyclohexane in an atmosphere of dry nitrogen, giving a clear, colorless solution which was 0.7M in  $\text{AlBr}_3$ . Dry  $\text{KBr}$  (2.1g) was added and the solution was stirred for

<sup>6</sup> Further details on tests of the quality of electrodeposits are given elsewhere (26).



24 hr. Most of the KBr did not dissolve and the concentration of potassium in solution was  $4 \times 10^{-4}M$ . The conductivity was below  $10^{-7}$  mho  $\cdot$  cm $^{-1}$ . No attempt was made to electrodeposit aluminium from this system.

### Discussion

*The structure of the electrolyte.*—Aluminium bromide, which has predominantly covalent bonds, is soluble in aromatic hydrocarbons and in cyclohexane. The resulting solution is nonconducting. Simple ionic salts, such as KBr, are not soluble in hydrocarbons, but are readily soluble in an aromatic hydrocarbon containing  $AlBr_3$ . The solubility of KBr (and other alkali bromides or iodides) is dependent on the concentration of aluminium bromide. In solutions that have not been dried rigorously, it does not exceed the molar ratio of KBr:  $AlBr_3$  (1:2), corresponding to the formation of  $Al_2Br_7^-K^+$ . When a higher proportion of alkali bromide is dissolved, some  $AlBr_4^-K^+$  is probably formed, but the above ratio never exceeds 1:1.

The fact that KBr cannot be dissolved to any significant extent in a solution of  $AlBr_3$  in cyclohexane is rather interesting in view of the fact that the dielectric constants of cyclohexane and, say, toluene are nearly the same. It would appear that the difference is due to the great difference in polarizability of the two types of solvents, which allows stabilization of the ions in the aromatic but not in the alicyclic system. It is interesting to note in this context that the dielectric constant of a solution of toluene containing 50 w/o  $AlBr_3$  was found to be 2.75 (30) while that of pure toluene is 2.28.

The transference numbers reported here, which indicate that aluminium appears in solution as negative ions, are in agreement with the earlier interpretation of Plotnikov *et al.* (7, 10, 11). The fact that  $t_+ < t_-$  indicates that the potassium ion is more heavily solvated.

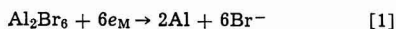
The conductivity observed in these solutions is much lower than for aqueous solutions of comparable concentration. Thus, a solution of 1M  $Al_2Br_7^-K^+$  in toluene has a conductivity of ca. 5 mmho  $\cdot$  cm $^{-1}$ , while the conductivity of an aqueous 1M KCl solution is ca. 100 mmho  $\cdot$  cm $^{-1}$ . This difference can be ascribed to several factors: (i) the viscosity of the organic solution is about four times higher (31), (ii) the radius of the solvated ions is larger, and (iii) partial association of the positive and negative ions may occur.

Double layer capacity measurements, to be reported elsewhere (29), as well as earlier work on solvation, indicate that the solvated radius of ions in this system is larger than in water. This, together with the difference in viscosity, could explain a major part of the difference in conductivity, indicating that ion pair formation is not predominant in this system. This would appear unusual, in view of the low dielectric constant, but can be understood as resulting from the large solvated radii of the ions, which keeps them far apart and reduces the electrostatic attraction forces between them.

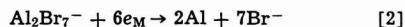
Vapor pressure measurements have shown that in toluene one molecule of the solvent is attached strongly to each  $Al_2Br_6$  molecule forming a  $\pi$  complex (32). When HBr was also present, complexes of the type  $ArH_2^+Al_2Br_7^-$  (14) or  $3Ar \cdot Al_2Br_6 \cdot HBr$  were found (13). The solvation number in this case varies for different aromatic hydrocarbons.

*Reactions at the cathode and the anode.*—The alkali halides added to the solution of  $AlBr_3$  in a mixture of aromatic hydrocarbons serve two purposes: (i) to increase and stabilize the conductivity, and (ii) to convert most of the aluminium present in solution to the negative ion  $Al_2Br_7^-$  (or to  $AlBr_4^-$  in the presence of a high concentration of MBr), as indicated by transference number measurements.

The primary cathode reaction could be either



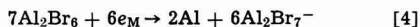
or



When the ratio of molar concentrations of MBr:  $AlBr_3$  is much lower than 0.5, both reactions may occur. As this ratio approaches 0.5, Eq. [2] probably becomes predominant. Since the simple  $Br^-$  ion is apparently not stabilized in this system,<sup>7</sup> Eq. [1] must be followed by a chemical reaction of the type

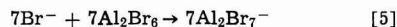


giving the over-all reaction



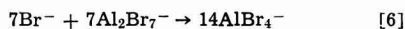
Thus, less than one electron is passed in the over-all reaction for each  $Al_2Br_6$  molecule reaching the surface.<sup>8</sup> This can be put differently by stating that for each molecule of  $Al_2Br_6$  discharged at the electrode, six molecules of  $Al_2Br_6$  are required to complex the free  $Br^-$  ions left behind. Thus, if the current density is too high and/or stirring insufficient, a deficiency of  $Al_2Br_6$  molecules may develop in the diffusion layer causing codeposition of the alkali bromide.

Equation [2] will be followed, for the same reasons, by the chemical step

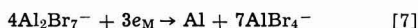


Combining Eq. [2] and [5] gives the same over-all reaction, represented by Eq. [4].

As the ratio of MBr:  $AlBr_3$  approaches or even exceeds 0.5, the primary electrode reaction becomes predominantly that shown in Eq. [2], but this could now be followed by a reaction such as



which leads to the over-all reaction



Here again poor mixing or a high current density could cause a deficiency of  $Al_2Br_7^-$  at the electrode and result in codeposition of the salt. In this situation the number of electrons passed in the over-all reaction per molecule of  $AlBr_3$  (calculated) reaching the surface is  $n = \frac{3}{8}$ .

At the anode the situation is obviously reversed. The over-all reaction given in Eq. [4] is likely to predominate, since this requires only three ions of  $Al_2Br_7^-$  for each atom of aluminium dissolved, while in Eq. [7] one would require seven ions of  $AlBr_4^-$ , the concentration of which is very low in most situations.

If the supply of  $Al_2Br_7^-$  ions to the anode is insufficient due to their low concentration in solution (when the ratio of MBr to  $AlBr_3$  is small compared to 0.5), insufficient stirring, too high current density, or a combination of these factors, anodic dissolution cannot occur at the desired rate, the potential will rise, and side reactions (probably decomposition of the solvent or bromine evolution) will occur which shorten the lifetime of the plating bath.

From the above discussion it may be concluded that the concentration of MBr in solution should be chosen so that it is sufficiently high to provide good conductivity, good throwing power, and efficient anodic dissolution, yet sufficiently low to avoid codeposition of the salt. The importance of proper stirring and of limiting the current density employed becomes evident for both cathodic and anodic reactions.

If oxygen is present in the solution during electrolysis, the anode is covered with an oxide layer and anodic dissolution is diminished. Bromine evolution occurs (10) and this reacts with the solvent to form a

<sup>7</sup> This may be inferred from the fact that MBr is soluble in an aromatic hydrocarbon only in presence of  $AlBr_3$ .

<sup>8</sup> This is an interesting point for the calculation of the diffusion limited current to be expected in, say, a potentiostatic transient. If the concentration of aluminium is expressed formally as the molar concentration of  $AlBr_3$ , the number of electrons passed in the over-all reaction, according to Eq. [4] will be  $n = 3/7$ , rather than 3, as one might be led to assume.

variety of high molecular weight compounds, causing rapid deterioration of the bath. At the cathode oxygen is apparently reduced instead of aluminium and an oxide layer is also formed, as evidenced by the rapid increase in measured voltage drop between the cathode and an aluminium wire reference electrode.

The effect of quaternary ammonium salts in small concentrations is probably due to strong adsorption of the ion at the electrode surface. This also accounts for the tendency of incorporation of salts into the electrodeposits, causing poor corrosion resistance, as described above.

*The effect of HBr and of Lewis bases.*—All the experiments described in this paper were performed under conditions which may resemble industrial operation. Thus, all solutions contained a small amount of HBr, formed as a result of interaction of  $\text{AlBr}_3$  with moisture entering the cell during changing of the samples. It is known (13, 14) that the reaction of HBr with  $\text{AlBr}_3$  and the aromatic hydrocarbon  $\text{ArH}$  gives rise to a complex of the form  $\text{ArH}_2^+ \text{Al}_2\text{Br}_7^-$  which can be reduced at the cathode. The stability of this complex increases in the order benzene < toluene < m-xylene < mesitylene. Reduction of the protonated hydrocarbon competes with electrodeposition of aluminium, and hence the cathodic current efficiency decreases with increasing concentration of HBr until a point is reached where it becomes negligible. This can account for the fact that in the work of Capuano and Davenport (23-25), where moisture or HBr were added on purpose, the cathodic current efficiency was never found to exceed 85%. In the present work, where the level of HBr was kept low, current efficiencies approaching 100% were observed in solutions containing a mixture of hydrocarbons and an alkali halide.

Benzene is a weak Lewis base and hence even a small amount of HBr prevents electrodeposition of aluminium. Toluene is a stronger base and electrodeposition does occur under the same conditions, but at low current efficiencies. When mesitylene is used as the main solvent, or when it is added to toluene in substantial quantities, a higher level of moisture can be tolerated in the system (up to a few tenths per cent  $\text{H}_2\text{O}$ ), still yielding good electrodeposits at high cathodic current efficiencies. The same is true for naphthalene and for derivatives of benzene with highly branched side chains. It would appear that in all these cases the proton is stabilized by the aromatic hydrocarbon, which is a strong Lewis base compared to benzene or toluene, and reduction of the  $\text{ArH}_2^+$  complex occurs at a much slower and often negligible rate. Aliphatic and aromatic amines, which are even stronger Lewis bases, can serve the same purpose.

#### Acknowledgments

The authors wish to thank Mr. Meron, Head, Department of Materials Engineering, Israel Aviation Industries, and Mr. Tillis of the same department for their encouragement in the course of this work. Thanks are also due to Mrs. I. Armel and Mr. Y. Canfi for their technical assistance in performing the experiments described in this paper.

Manuscript submitted June 24, 1975; revised manuscript received Sept. 8, 1975.

Any discussion of this paper will appear in a Discussion Section to be published in the December 1976

JOURNAL. All discussions for the December 1976 Discussion Section should be submitted by Aug. 1, 1976.

#### REFERENCES

1. A. Brenner, in "Advances in Electrochemistry and Electrochemical Engineering," Vol. 5, C. W. Tobias, Editor, p. 217, Interscience, New York (1967); D. I. Couch and A. Brenner, *This Journal*, **99**, 234 (1952).
2. E. J. Smith and L. D. McGraw, in "Modern Electroplating," F. A. Lowenheim, Editor, John Wiley & Sons, New York (1963).
3. M. Yoshio and N. Ishibashi, *J. Appl. Electrochem.*, **3**, 321 (1973).
4. M. Koike and K. Sekimoto, *Kinzoku*, No. 4, 77 (1972).
5. R. Dotzer, *Chem. Ingr. Tech.*, **45**, 653 (1973); G. Iwantschiff and R. Dötzer, *Werkstofftechnik*, **3**, 9/34 U. 10/22 (1972).
6. D. D. Eley and P. J. King, *J. Chem. Soc.*, 1952, 2517.
7. V. A. Plotnikov and S. I. Yakubson, *J. Gen. Chem. USSR*, **6**, 1690 (1936).
8. V. A. Plotnikov and E. Ya. Gorenbein, *ibid.*, **7**, 372 (1937).
9. E. Ya. Gorenbein, *Univ. Etat. Kiev, Bull. Sci. Rec. Chim.*, **1**, 101 (1935).
10. V. A. Plotnikov, I. A. Sheka, and V. A. Yankelevich, *J. Gen. Chem. USSR*, **3**, 481 (1933).
11. V. A. Plotnikov, I. B. Barmashenko, and E. B. Gitman, *Mem. Inst. Chem. Acad. Sci. Ukr. SSR*, **5**, 3 (1938).
12. E. Ya. Gorenbein, *J. Gen. Chem. USSR*, **9**, 2041 (1939).
13. F. Norris and J. N. Ingraham, *J. Am. Chem. Soc.*, **62**, 1298 (1940).
14. H. C. Brown and W. J. Wallace, *ibid.*, **75**, 6268 (1953).
15. V. A. Plotnikov and S. Yakubson, *Z. Physik. Chem.*, **138**, 251 (1928).
16. V. A. Plotnikov and E. Ya. Gorenbein, *Mem. Inst. Chem. Acad. Sci. Ukr. SSR*, **3**, 471 (1936).
17. V. A. Yankelevich and I. A. Sheka, *ibid.*, **5**, 59 (1938).
18. V. A. Plotnikov and S. I. Yakubson, *Z. Physik. Chem. A*, **147**, 227 (1930).
19. D. A. Posphekhov, *Usp. Khim.*, **6**, 515 (1937).
20. V. A. Plotnikov and A. T. Dibrova, *Zapiski Inst. Khim. Acad. Sci. USSR*, **7**, 337 (1940).
21. L. Simanavicius and A. Karpavichyus, *Lietuvos TSR Mokslu Akad. Darbai, Ser. B*, **83**, 1 (1971).
22. L. Simanavicius, A. Karpavichyus, and P. Dobrovolskis, in "Electrodeposition of Metals," Proceedings of the 10th Lithuanian Conference of Electrochemistry, Israel Program for Scientific Translations (1970).
23. G. A. Capuano and W. G. Davenport, *Can. Pat.* 945, 935 (1974), *U.S. Pat.* 3,775,260 (1973).
24. G. A. Capuano and W. G. Davenport, *This Journal*, **118**, 1688 (1971).
25. G. A. Capuano and W. G. Davenport, *Plating*, **60**, 251 (1973).
26. E. Peled and E. Gileadi, *ibid.*, **62**, 342 (1975).
27. E. Peled, A. Meitavski, and E. Gileadi, *Z. Physik. Chem. (N.F.)*, In press.
28. A. Reger, E. Peled, and E. Gileadi, *This Journal*, In press.
29. E. Peled, S. Ziegel, and E. Gileadi, In preparation.
30. J. Timmermans, "Physico Chemical Constants of Binary Systems in Concentrated Solutions," p. 1038, Interscience, New York (1959).
31. I. Gorenbein and G. A. Redlar, *J. Gen. Chem. USSR*, **11**, 1069 (1941).
32. H. C. Brown and W. J. Wallace, *J. Am. Chem. Soc.*, **75**, 6265 (1953).





## The Electrode Potential of the Chromate (VI)-Lithium Chromate (V) System in Molten Lithium Chloride-Potassium Chloride Eutectic

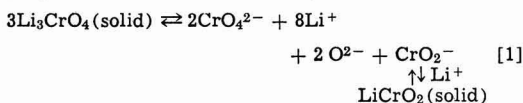
Katsumi Niki\*

Department of Electrochemistry, Yokohama National University, Minami-ku, Yokohama 233, Japan

and Isamu Uchida\* and Herbert A. Laitinen\*

Department of Chemistry, University of Florida, Gainesville, Florida 32611

The electrochemical reduction of chromate ion,  $\text{CrO}_4^{2-}$ , in lithium chloride-potassium chloride eutectic melt (1), and the effect of various divalent metal ions (2-5) and water (6), have been studied extensively. Laitinen and Bankert (1) observed that the reduction of chromate ion was a single, irreversible and diffusion controlled three-electron process, yielding an unstable initial product believed to be  $\text{Li}_5\text{CrO}_4$ . Recently Uchida and Laitinen (6) isolated  $\text{LiCrO}_2$  as the reduction product from moist melts. On the other hand, Niki and Laitinen (7) found that  $\text{Li}_3\text{CrO}_4$ , which is assumed to be one of the intermediate compounds in the reduction of  $\text{CrO}_4^{2-}$  in  $\text{LiCl-KCl}$  melt, is relatively stable in  $\text{LiCl-KCl}$  melt. Because of the limited solubility of  $\text{Li}_3\text{CrO}_4$  there is an equilibrium in the disproportionation reaction; namely



In the present work, the electrode potential of  $\text{CrO}_4^{2-}/\text{Li}_3\text{CrO}_4$  and the equilibrium of the disproportionation reaction of  $\text{Li}_3\text{CrO}_4$  were investigated to correlate these values to the electrochemical behavior of chromate ion.

### Experimental

**Reagent.**— $\text{Li}_2\text{CrO}_4$  was prepared by neutralizing  $\text{CrO}_3$  by  $\text{Li}_2\text{CO}_3$ , and then it was recrystallized and dried at  $200^\circ\text{C}$  under vacuum for about 8 hr. All chemicals used in the present work were either the AR or the primary standard grade. The  $\text{LiCl-KCl}$  eutectic melt was supplied by Anderson Physics Laboratories, Incorporated, Champaign, Illinois.

**$\text{Li}_3\text{CrO}_4$  electrode.**—A mixture of the stoichiometric amount of  $\text{Li}_2\text{CrO}_4$  and  $\text{Li}_2\text{CO}_3$  was maintained at  $450^\circ\text{C}$  in a platinum crucible for 5 hr under vacuum. Then the temperature of the mixture was increased gradually. When a liquid phase formed at about  $550^\circ\text{C}$ , a platinum flag 0.06 mm thick and 6.37 mm in diameter with 36 gauge platinum wire as an electrical lead, was immersed in the melt. After the platinum surface was wetted by the viscous melt, it was pulled out from the melt. Then the temperature of a furnace was increased up to  $750^\circ\text{C}$ . The viscous melt solidified and black crystals covered the surface of the platinum flag. The platinum flags covered by  $\text{Li}_3\text{CrO}_4$  were stored

in a vacuum desiccator and used as indicator electrodes. Fine  $\text{Li}_3\text{CrO}_4$  crystals formed in the crucible were also stored in a vacuum desiccator and used for the disproportionation reaction measurement. The purity of  $\text{Li}_3\text{CrO}_4$  was better than 99% as determined from the close agreement between the observed ratio of  $\text{Cr(VI)}:\text{Cr(III)}$  in a 6N HCl solution with the theoretical ratio of 2:1 and the agreement between the weight of  $\text{Li}_3\text{CrO}_4$  taken and calculated from the total Cr recovered.  $\text{Li}_3\text{CrO}_4$  was handled under nitrogen atmosphere.

**Electrochemical measurement.**—The electrochemical cell assembly has been described in detail (8). A known amount of  $\text{Li}_2\text{CrO}_4$  was added to each compartment containing 3 ml of the melt in the cell, and the exact concentration of chromate ion in the melt was determined by coulometric titration after the potential measurement (2). The electrode potentials of the  $\text{Li}_3\text{CrO}_4$  electrode in the chromate solutions were measured with a Leeds and Northrup Student Type 8687 volt potentiometer against the Pt(II)/Pt electrode. The preparation and construction of Pt(II)/Pt electrode have been described (8-9).

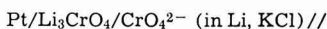
All potentials shown in this work are given with respect to the 1M Pt(II)/Pt electrode, and all experiments were carried out at  $450 \pm 1^\circ\text{C}$ .

**Disproportionation of  $\text{Li}_3\text{CrO}_4$ .**—About 200 mg of  $\text{Li}_3\text{CrO}_4$  was added to each 3 ml compartment in the cell. These compartments were of Pyrex glass with a fritted glass bottom which acted as a salt bridge. The melt was stirred occasionally with a glass rod and maintained for about 30 min. After equilibrium has been attained, the electrode potential of the  $\text{Li}_3\text{CrO}_4$  electrode in these melts was measured and then a sample of the melt containing chromate ion was taken by the sampling tube for the determination of chromium (7).

**Analysis of chromates.**—Analytical procedures for the chromium compounds were the same as in the previous work (7).

### Results and Discussion

**Equilibrium potential of  $\text{CrO}_4^{2-}/\text{Li}_3\text{CrO}_4$  system.**—The electrochemical cell used for the equilibrium potential measurement of the  $\text{CrO}_4^{2-}/\text{Li}_3\text{CrO}_4$  system was

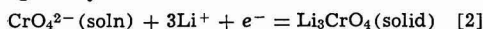


Pt(II) (1.0M in Li, KCl)/Pt

\* Electrochemical Society Active Member.

Key words: chromium (V), lithium chromate (V), electrode potential, molten salt, disproportionation.

The half-cell reaction on the left-hand side of the cell is given by



If the cell reaction is reversible, the equilibrium potential of the  $\text{CrO}_4^{2-}/\text{Li}_3\text{CrO}_4$  system is given by

$$E = E^{\circ'} + \frac{RT}{F} \ln \frac{a_{\text{CrO}_4^{2-}}}{a_{\text{Li}_3\text{CrO}_4}} \quad [3]$$

Since  $\text{Li}_3\text{CrO}_4$  is solid and the activity coefficient of  $\text{CrO}_4^{2-}$  is assumed to be unity, Eq. [3] leads to

$$E = E^{\circ'} + 0.1435 \log C_{\text{CrO}_4^{2-}} \quad (\text{at } 450^\circ\text{C}) \quad [4]$$

The equilibrium potential of the  $\text{Li}_3\text{CrO}_4$  electrode with various concentrations of chromate ion is shown in Fig. 1. The electrode attained an equilibrium potential within 10 min and gave a stable value for more than 1 hr when the concentration of  $\text{CrO}_4^{2-}$  was greater than 0.02M in the melt. At lower concentrations of  $\text{CrO}_4^{2-}$  ( $<0.015\text{M}$ ),  $\text{Li}_3\text{CrO}_4$  on the platinum electrode was probably oxidized to  $\text{CrO}_4^{2-}$  by PtO on the platinum surface and the concentration of chromate ion became higher in the vicinity of the electrode. Accordingly, the electrode potential of the  $\text{Li}_3\text{CrO}_4$  electrode became more positive than that expected from the Nernst equation (4).

The equilibrium potential (V vs. Pt(II), 1M/Pt) of the  $\text{CrO}_4^{2-}/\text{Li}_3\text{CrO}_4$  system at  $450^\circ\text{C}$  is given empirically by

$$E = -(0.761 \pm 0.004) + 0.141 \log C_{\text{CrO}_4^{2-}} \quad [5]$$

The slope of the Nernst equation agreed well with a one-electron process corresponding to Eq. [2].

**Disproportionation of  $\text{Li}_3\text{CrO}_4$  in LiCl-KCl melt.**—In our previous work (7), it was shown that  $\text{Li}_3\text{CrO}_4$  disproportionates to  $\text{CrO}_4^{2-}$  and  $\text{LiCrO}_2$  in the LiCl-KCl melt. If the disproportionation reaction of  $\text{Li}_3\text{CrO}_4$  takes place in the melt according to Eq. [1], when the LiCl-KCl melt is saturated with both  $\text{Li}_3\text{CrO}_4$  and  $\text{LiCrO}_2$ , then the equilibrium constant for this disproportionation reaction is given by

$$K = [\text{CrO}_4^{2-}][\text{O}^{2-}] \quad [6]$$

The concentration of  $\text{CrO}_4^{2-}$  ion in the melt in the

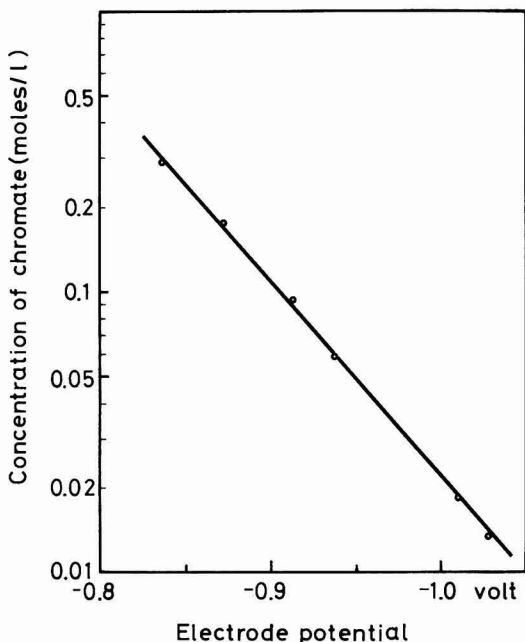


Fig. 1. Equilibrium potential of  $\text{CrO}_4^{2-}/\text{Li}_3\text{CrO}_4$  system in LiCl-KCl eutectic melt at  $450^\circ\text{C}$ .

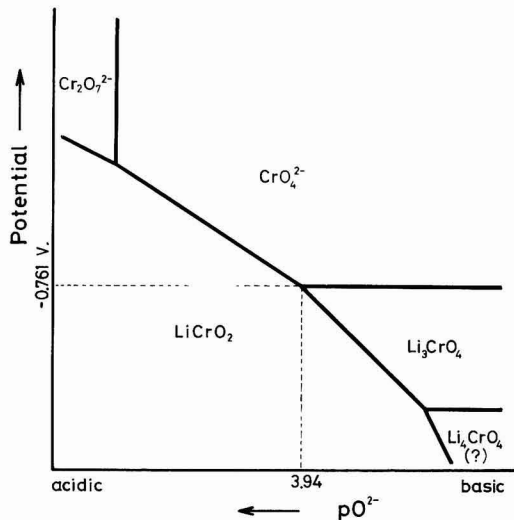


Fig. 2. Potential- $p\text{O}_2^-$  diagram of chromates in LiCl-KCl eutectic melt at  $450^\circ\text{C}$ .

presence of excess amounts of  $\text{Li}_3\text{CrO}_4$  was  $(0.0107 \pm 0.0002)\text{M}$  and the equilibrium constant for the reaction [1] is given by

$$K = [(1.07 \pm 0.002) \times 10^{-2}]^2 \\ = (1.15 \pm 0.04) \times 10^{-4} \text{ mol}^2 \text{ l}^{-2} \quad (\text{at } 450^\circ\text{C})$$

When the concentration of  $\text{CrO}_4^{2-}$  was 1.0M in the melt in the presence of excess amounts of  $\text{Li}_3\text{CrO}_4$ , the electrode potential of the  $\text{CrO}_4^{2-}/\text{Li}_3\text{CrO}_4$  is  $-0.761\text{V}$  (vs. 1.0M Pt(II)/Pt) and the concentration of  $\text{O}^{2-}$  in the melt can be calculated to be  $1.145 \times 10^{-4}\text{M}$ . Figure 2 shows the semiquantitative  $p\text{O}_2^-$ -potential diagram of chromium, which we have described qualitatively in a previous paper (7).

#### Acknowledgment

Part of this research was supported by the Japan Society for the Promotion of Science under the Japan-U.S. Cooperative Science Program, and part by the Army Research Office (Durham) (I. U. and H. A. L.).

Manuscript submitted Feb. 19, 1975; revised manuscript received Sept. 2, 1975.

Any discussion of this paper will appear in a Discussion Section to be published in the December 1976 JOURNAL. All discussions for the December 1976 Discussion Section should be submitted by Aug. 1, 1976.

Publication costs of this article were partially assisted by the University of Florida.

#### REFERENCES

- H. A. Laitinen and R. D. Bankert, *Anal. Chem.*, **39**, 1790 (1967).
- J. H. Propp and H. A. Laitinen, *ibid.*, **41**, 644 (1969).
- B. Popov and H. A. Laitinen, *This Journal*, **117**, 482 (1970).
- K. W. Hanck and H. A. Laitinen, *ibid.*, **118**, 1123 (1971).
- H. A. Laitinen and L. R. Lieto, *Croat. Chem. Acta*, **44**, 275 (1972).
- I. Uchida and H. A. Laitinen, To be published.
- K. Niki and H. A. Laitinen, *J. Inorg. Nucl. Chem.*, In press.
- H. A. Laitinen and C. H. Liu, *J. Am. Chem. Soc.*, **80**, 1015 (1958).
- H. A. Laitinen and J. W. Pankey, *ibid.*, **81**, 1053 (1959).

# The Rotating Cone Electrode

E. Kirowa-Eisner and E. Gileadi\*

*Institute of Chemistry, Tel-Aviv University, Ramat-Aviv, Israel*

The rotating disk electrode and rotating ring-disk electrodes have long become standard tools in the study of electrode reactions. Other configurations such as the rotating hemisphere (1) and rotating ring (2) or ring-ring electrodes (3) have also been tested experimentally and the relevant equations derived. In all these cases, the rate of mass transport, and hence the limiting current density, was always found to be proportional to the square root of the angular velocity,  $\omega$ , as derived by Levich for the rotating disk electrode (4). Recently it was shown (5) that a substantial degree of eccentricity of the rotating disk electrode could be allowed (up to ca. 64% of the radius of the disk) without affecting the limiting current at all.

One of the experimental problems often occurring when a rotating disk electrode is employed is a tendency for a gas bubble to be trapped at the center of the disk where the radial forces are balanced. This occurs particularly when vigorous gas evolution takes place.

Use of a rotating ring instead of a disk has been suggested to overcome this difficulty (2, 3). This may solve the problem partially since, if the bubble trapped at the center of rotation is not too large it will leave the electrode itself unshielded. However, the existence of a bubble at the center of the disk will alter the conditions of flow and, hence, introduce an error in the measurement of the limiting current density.

Recently it has been suggested (6) that a rotating cone electrode could be used instead of a rotating disk. In this configuration, a bubble at the tip of the cone would not be stable, and smooth flow past the electrode surface may be expected even in reactions in which vigorous gas evolution occurs. Preliminary experiments showed that the linear relationship between  $i_L$  and  $\omega^{1/2}$  was maintained for this configuration.

Mass transport to a conical electrode has been considered by several authors (7-10). In all these studies the electrode was stationary and the fluid was forced past it. The boundary layer problem for a rotating cone has been treated by a number of authors (11-13) for heat and mass transport situations not related to electrochemical systems. The equations for a rotating cone electrode have been derived recently by Newman and Mohr (14) in a form commonly used by electrochemists. The result for the local mass transfer rate at the limiting current is

$$j = 0.62C_b\sqrt{\nu\omega \sin \theta} Sc^{-2/3} \quad [1]$$

The over-all mass transfer rate for a conical electrode of base radius  $r$  is

$$J_{tot} = 0.62\pi C_b r^2 \sqrt{\frac{\nu\omega}{\sin \theta}} Sc^{-2/3} \quad [2]$$

where the Schmidt number  $Sc$  is a dimensionless quantity given by  $Sc = \nu/D$ .

These equations may be rewritten in simple form to relate the limiting current density  $i_L$  and the limiting current  $I_L$  on a rotating disk (4) and rotating cone having the same base radius. Thus

$$i_L(\text{cone}) = i_L(\text{disk}) \sin^{1/2} \theta \quad [3]$$

$$I_L(\text{cone}) = I_L(\text{disk}) \sin^{-1/2} \theta \quad [4]$$

## Experimental

The equations given above show that the rotating cone electrode can be a useful tool in electrode kinetic

studies just as the rotating disk, and the very same equations can be used to separate the activation-controlled current from the total current measured under conditions of mixed mass transport and activation control. In this work the validity of the above equations was tested experimentally, care being taken to achieve the highest possible experimental accuracy. Equations [3] and [4] were tested in a solution of 4.00 mM hydroquinone in 2.0M KCl.

*The electrodes, solution, and experimental setup.*—As shown in Fig. 1, a platinum cylinder of 4.80 mm diameter and 11 mm length was press fitted into a Teflon holder (outer diameter 12 mm). The same electrode was machined to different angles ( $\theta = 60^\circ$ - $25^\circ$ ) on an accurate lathe. The electrode assembly was centered carefully to within 0.02 mm to minimize wobble. The accuracy of the angles machined was  $\pm 1/4^\circ$ .

A flat platinum electrode about 2 cm<sup>2</sup> area, situated at a distance of about 2 cm from the rotating electrode served as the counterelectrode. A commercial mercury/mercurous sulfate electrode (Radiometer Type K601) served as the reference.

All chemicals were analytical grade and were used without further purification. Hydroquinone was dried at 80°C. All solutions were prepared in triple-distilled water.

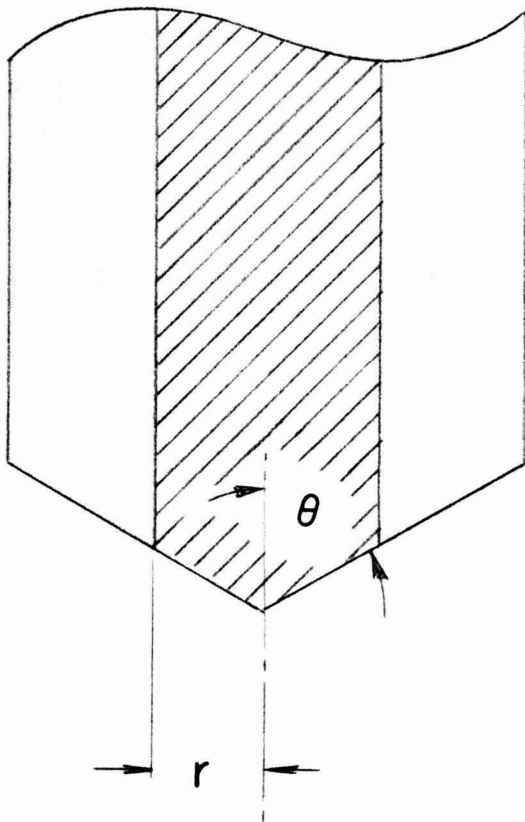


Fig. 1. Structure of cone electrode, defining the cone angle  $\theta$  and radius  $r$ . Shaded area is Teflon holder.

\* Electrochemical Society Active Member.

Key words: rotating electrodes, mass transport.

Measurements were performed potentiostatically, with an Elron Model CHP-1 potentiostat. No IR correction was necessary, since measurements were taken in the limiting current region. A Pine Instrument rotator and a Metrohm Type EA 870-20 thermostated cell were used. Currents were recorded on a Yokogawa Type 3077 X-Y recorder.

**Procedure.**—Each new electrode was degreased with acetone, cleaned in nitric acid (1:1), and washed with triple-distilled water, all in an ultrasonic cleaner. Before each run the electrode was pretreated electrochemically in 0.5M H<sub>2</sub>SO<sub>4</sub> in a procedure similar to that proposed by Gilman (15,16). This consisted of the following sequence of potential (vs. NHE) and time: 1.85V (10 sec); 1.20V (25 sec); 0.10V (25 sec). The sequence was repeated several times, after which a cyclic voltammogram was taken to verify the cleanliness of the surface.

The pretreated electrode was washed with triple-distilled water and transferred to the cell containing about 80 cm<sup>3</sup> of 4.00 mM hydroquinone solution in 2M KCl, which had been deaerated with purified nitrogen. The conical electrode was immersed about 2 cm below solution level. No bubbles were formed even at the highest rotation velocity of 10<sup>4</sup> rpm employed.<sup>1</sup>

The potential was set to a value of 1.02V vs. NHE, in the region of limiting current, and the current was measured. Each measurement was restricted to 5 sec to minimize changes in concentration of hydroquinone during the whole run. At least five runs in freshly prepared solutions were made for each angle of the cone, and the limiting current was measured at nine rotation velocities, between 4 × 10<sup>2</sup> and 1 × 10<sup>4</sup> rpm.

### Results

The dependence of the limiting current  $I_L$  on the square root of the rotation velocity  $\omega$  is shown in Fig. 2 for different values of the angle  $\theta$ . The correlation factor for a single line was very high, in the range of 0.99995-0.99999. The standard deviation of the slope was 0.5% for the rotating cone (based on seven measurements) and 0.2% for the rotating disk (based on six measurements).

In Table I the experimental slopes of  $\partial i_L(\text{cone})/\partial \omega^{1/2}$  are compared with the values calculated according to

<sup>1</sup> In an early experiment, where a thicker Teflon sleeve was employed, bubbles were formed at intermediate rotation velocities.

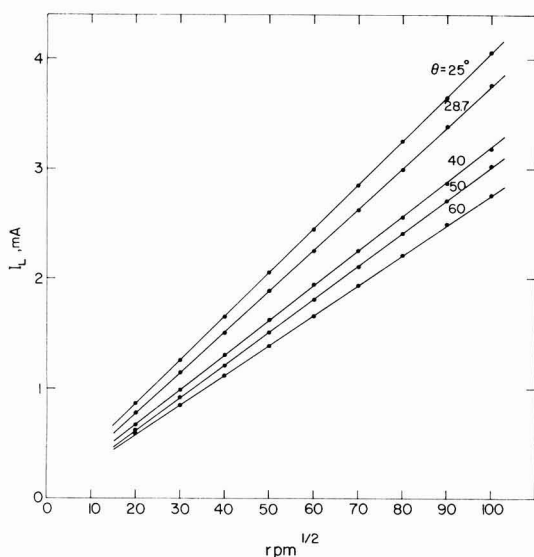


Fig. 2. Limiting current/angular velocity relationship at different cone angles,  $\theta$ . 4 mM hydroquinone, 2M KCl, 25°C. Radius of cone base: 2.4 mm.

Table I. Comparison of experimental and calculated limiting current densities on rotating cone electrode for 4.00 mM hydroquinone in 2M KCl.

Cone angle ( $^{\circ}$ )	$\partial i_L(\text{cone})/\partial \omega^{1/2}$ $\mu\text{A cm}^{-2} \text{rpm}^{-1/2}$		Difference between experimental and calculated values, per cent	
	Experimental for $400 \leq \omega \leq 10^4$ rpm	Calculated after Eq. [3]	For $400 \leq \omega \leq 10^4$ rpm	For $400 \leq \omega \leq 3.6 \times 10^3$ rpm
25	93.0	91.4	+1.8	+1.3
28.7	98.6	97.4	+1.2	+0.5
40	111.2	112.7	-1.3	+0.2
45	118.3	118.2	+0.1	+0.1
50	125.9	123.0	+2.4	+0.2
60	131.4	130.8	+0.5	+0.5

Eq. [3]. A slight positive deviation occurs, which is probably due to imperfections of the surface of the cone electrode causing turbulence, particularly at higher rotation velocities. If the above slopes are recalculated on the basis of the same data but restricted to the range of  $4 \times 10^2 \leq \omega \leq 3.6 \times 10^3$  rpm, agreement between theory and experiment is improved as shown in the last column of Table I. It can be concluded that the current at the rotating cone electrode behaves according to the theoretical equations given above.

### Acknowledgments

The authors wish to acknowledge the help of Professor J. Newman and Dr. C. M. Mohr, Department of Chemical Engineering, University of California at Berkeley, in discussion of the theoretical equations of the rotating cone electrodes.

Thanks are also due to Mrs. G. Costica for technical assistance and Mr. N. Lavie and Mr. Y. Dreilinger for construction of the conical electrodes.

Manuscript submitted June 19, 1975; revised manuscript received Sept. 11, 1975.

Any discussion of this paper will appear in a Discussion Section to be published in the December 1976 JOURNAL. All discussions for the December 1976 Discussion Section should be submitted by Aug. 1, 1976.

Publication costs of this article were partially assisted by Tel-Aviv University.

### LIST OF SYMBOLS

- $C_b$  bulk concentration of active species (mole/cm<sup>3</sup>)  
 $D$  diffusion coefficients (cm<sup>2</sup>/sec)  
 $i_L$  limiting current density (A/cm<sup>2</sup>)  
 $I_L$  limiting current (A)  
 $j$  local mass-transfer rate (mole/cm<sup>2</sup> sec)  
 $J_{\text{tot}}$  total mass-transfer rate (mole/sec)  
 $r$  radius of base of cone electrode\*  
 $\nu$  kinematic viscosity (cm<sup>2</sup>/sec)  
 $\theta$  cone angle (half the opening angle of the cone)\*  
 $\omega$  angular velocity (radian/sec)  
 $Sc$  Schmidt number of solution (dimensionless)

\* See Fig. 1 for definition of  $r$  and  $\theta$ .

### REFERENCES

- D. T. Chin, *This Journal*, **118**, 1434 (1971).
- I. V. Kadja and V. M. Nakic, *J. Electroanal. Chem.*, **34**, 15 (1972).
- I. V. Kadja and V. M. Nakic, *ibid.*, **35**, 177 (1973).
- B. Levich, *Acta Physicochimica U.R.S.S.*, **17**, 257 (1942); B. Levich, "Physicochemical Hydrodynamics," Prentice-Hall, Englewood Cliffs, New Jersey (1962).
- C. M. Mohr, Jr. and J. Newman, *This Journal*, **122**, 928 (1975).
- E. Gileadi, E. Kirowa-Eisner, and J. Penciner, "Interfacial Electrochemistry—An Experimental Approach," Experiment No. 5, Addison-Wesley Publishing Co., Inc., Reading, Massachusetts (1975).
- H. Matsuda, *J. Electroanal. Chem.*, **15**, 109 (1967); *ibid.*, **21**, 433 (1969); *ibid.*, **22**, 413 (1969).
- Khr. Iv. Noninski, *Khim. Ind.*, **44**, 359 (1972); *ibid.*, **45**, 80 (1973).
- J. C. Bazan and C. L. Rosenberg, *Anales Asoc.*

- Quim. Arg., 60, 447 (1972).  
 10. J. Jordan, R. A. Javick, and W. E. Ranz, *J. Am. Chem. Soc.*, 80, 3846 (1958).  
 11. C. S. Wu, *Appl. Sci. Res., Sect. A*, 8, 140 (1959).  
 12. C. L. Tien, *J. Heat Transfer*, 82, 252 (1960).  
 13. C. L. Tien and D. T. Campbell, *J. Fluid Mech.*, 17, 105 (1963).

14. J. Newman and C. M. Mohr, Private communication.  
 15. S. Gilman, *Electrochim. Acta*, 9, 1025 (1964).  
 16. E. Gileadi, E. Kirova-Eisner, and J. Penciner, "Interfacial Electrochemistry—An Experimental Approach," p. 311, Addison-Wesley Publishing Co., Inc., Reading, Massachusetts (1975).

# Brief Communication



## A Calculation of the Entropy Maximum for the Double Layer in Terms of the Water Molecule Structure

J. O'M. Bockris\* and M. A. Habib

School of Physical Sciences, The Flinders University of South Australia, Bedford Park, S. A., 5042, Australia

Oriented dipoles of water at interfaces were first introduced into electrochemical concepts by Lange and Mischenko (1). [See also Bockris and Potter's (2) initial numerical use of the concept.] Recognition of the effects of their presence lacked wide acceptance. Watts-Tobin and Mott (3, 4) and others (5) attributed the anodic capacitance hump to water orientation as a function of potential, thereby signifying that the most random orientation of water dipoles should be at a potential positive to the pzc. This is not consistent with the experimental fact that the dependence of the surface-excess entropy of the electrode-solution interface measured by Hills and Payne (6) and by Harrison *et al.* (7) on electrode charge is near parabolic with a maximum at  $q = -4$  to  $-6 \mu\text{C cm}^{-2}$ . Reeves (8) separated out the contribution to surface-excess entropy by water dipoles. This solvent-excess entropy also shows a maximum at  $q \approx -4 \mu\text{C cm}^{-2}$ . Levine, Bell, and Smith (9) considered the orientation of water molecules in the double layer, but did not calculate the corresponding entropy charge relation. Conway and Gordon (10) considered the entropy change due to water molecule displacement during the adsorption of organic molecules in terms of the original model of water molecule in the double layer due to Bockris, Devanathan, and Müller (11). The conclusion was that the entropy associated with the water molecules would pass through a maximum at the pzc, and this is at variance with the new experimental data (8). Nevertheless, we have found the solvent entropy-electrode charge relation can indeed be quantitatively interpreted in terms of an oriented water layer (3, 4, 11) at the interface.

Let there be  $N$  unassociated solvent dipoles present on the metal surface among which  $N_{\uparrow}$  are with their oxygen end towards the surface (up dipoles) and  $N_{\downarrow}$  are in the reverse position (down dipoles) so that  $N = N_{\uparrow} + N_{\downarrow}$ . The orientational entropy is then given by

$$S = k \ln \frac{N!}{N_{\uparrow}! N_{\downarrow}!} \quad [1]$$

or

$$S = \frac{1}{2} kN [2 \ln 2 - \{(1+R) \ln(1+R) + (1-R) \ln(1-R)\}] \quad [2]$$

where

$$R = (N_{\uparrow} - N_{\downarrow})/N \quad [3]$$

Considering the interaction of a dipole with the double-layer field and the surrounding dipoles,  $N_{\uparrow}$  is given by (22)

$$N_{\uparrow} = N_{\square} \exp \left[ \frac{1}{kT} (-\Delta G_{\uparrow}^c + \bar{\mu}X - U\bar{c}R) \right] \quad [4]$$

where  $N_{\square}$  = number of vacant sites available to unassociated water molecules,  $\bar{\mu}$  = the effective dipole moment of the water molecule adsorbed on the electrode,  $X$  = the double-layer field,  $\bar{c}$  = number of nearest neighbors which interact with the central water,  $U$  = interaction energy of a dipole with its nearest neighbor, and  $\Delta G_{\uparrow}^c$  = the nonelectrostatic part of the chemical term in the free-energy adsorption. Similarly

$$N_{\downarrow} = N_{\square} \exp \left[ \frac{1}{kT} (-\Delta G_{\downarrow}^c - \bar{\mu}X + U\bar{c}R) \right] \quad [5]$$

With  $X = 4\pi q/\epsilon$  and

$$-[(\Delta G_{\uparrow}^c - \Delta G_{\downarrow}^c)/kT] = -[\Delta \Delta G^c/kT] = b \quad [6]$$

one gets

$$R = \frac{\exp \left[ \frac{8\pi\bar{\mu}q}{\epsilon kT} - \frac{2U\bar{c}R}{kT} + b \right] - 1}{\exp \left[ \frac{8\pi\bar{\mu}q}{\epsilon kT} - \frac{2U\bar{c}R}{kT} + b \right] + 1} \quad [7]$$

The position of the maximum in orientational entropy may be obtained by differentiating Eq. [2] with respect to  $q$  and equating  $dS/dq = 0$ , i.e., at the maximum

$$\frac{1}{2} kN \left[ \ln \frac{1-R}{1+R} \right] \frac{dR}{dq} = 0 \quad [8]$$

Since  $1/2 kN \neq 0$ , either  $\ln[(1-R)/(1+R)] = 0$  or  $dR/dq = 0$ . From Eq. [7]

$$\frac{dR}{dq} = \frac{2Ae^y}{(e^y + 1)^2 + 2Be^y} \quad [9]$$

where

$$A = \frac{8\pi\bar{\mu}}{\epsilon kT}; \quad B = \frac{2U\bar{c}}{kT}; \quad \text{and} \quad y = Aq - BR + b \quad [10]$$

\* Equations [2] and [8] were published by Hills and Hsieh (21) after these authors had been given an early version of the present paper for review by the present authors. The origin of the equations was acknowledged in their paper.



From Eq. [9] and [10] it is evident that  $dR/dq \neq 0$ . Hence Eq. [8] is satisfied only when  $\ln[(1-R)/(1+R)] = 0$ . Thus, the solution of Eq. [8] is  $R = 0$ . Hence from Eq. [7]

$$(q)s = s_{\max} = -\frac{b\epsilon kT}{8\pi\bar{\mu}} \quad [11]$$

The water molecules are preferentially adsorbed at the pzc (13-15) which means  $|\Delta G^c| > |\Delta G^d|$ , i.e.,  $b$  is positive (Eq. [6]). According to Bockris, Devanathan and Müller (11),  $\Delta\Delta G^c$  may be due to a difference in the image interaction in the two orientations favoring the case in which the oxygen atom is towards the metal, since the dipole is then about  $0.05 \times 10^{-8}$  cm closer to the metal (11, 16). Then (11),  $\Delta U_{\text{image}} = -3/2 \mu^2 d/r_w^4$ , where  $d$  is the difference in distances between the metal surface and the centers of "up" and "down" dipoles. With  $\mu = \mu/\sqrt{3}$  (3),  $d = 0.05\text{Å}$ ,  $r_w = 1.38\text{Å}$ , and  $\mu = 1.84D$ , we obtain  $\Delta U_{\text{image}} = -1.42 \text{ kJ mole}^{-1}$ . Due to the difference in positions of the centers of "up" and "down" dipoles, there will be a difference in the dispersion interaction energies of each of these two types of dipoles with the metal surface. The difference from two orientations is then (16),  $\Delta U_{\text{disp}} = C\{1/(\bar{R}-d)^3 - 1/(\bar{R}+d)^3\}$ , where  $\bar{R}$  is the distance between the centers of the adsorbent atom Hg and adsorbate water dipole, and  $C$  is given by (16-18)

$$C = \frac{\pi n m c^2 \alpha_1 \alpha_2}{\alpha_1/\chi_1 + \alpha_2/\chi_2}$$

where  $m$  is the electronic mass;  $c$  the velocity of light;  $\alpha_1, \alpha_2$  are the polarizabilities;  $\chi_1$  and  $\chi_2$  are diamagnetic susceptibilities of the metal and adsorbate atom or molecule, respectively; and  $n$  is the number of adsorbent atoms per  $\text{cm}^3$ . Now (16),  $\alpha_{\text{water}} = 1.44 \times 10^{-24} \text{ cm}^3$ ,  $\alpha_{\text{Hg}} = 5.05 \times 10^{-24} \text{ cm}^3$ ;  $\chi_{\text{water}} = -2.16 \times 10^{-29} \text{ cm}^3$ ,  $\chi_{\text{Hg}} = -5.61 \times 10^{-29} \text{ cm}^3$ ; and  $n = 4.26 \times 10^{22}$  (19). With these values and taking  $d = 0.05 \times 10^{-8}$  cm and  $\bar{R} = r_w + r_{\text{Hg}} = (1.5 + 1.38) \times 10^{-8}$ , one gets  $\Delta U_{\text{disp}} = -1.3 \text{ kJ mole}^{-1}$ . The total energy difference  $\Delta\Delta G^c$  is then  $\Delta\Delta G^c = \Delta U_{\text{image}} + \Delta U_{\text{disp}} = -1.42 - 1.3 = -2.72 \text{ kJ mole}^{-1}$ . Thus,  $b = -\Delta\Delta G^c/kT = 1.1$ . With this value of  $b$  and  $\epsilon = 6$  (20), the position of maximum orientational entropy is found from Eq. [11] to occur at  $q = -3.5 \mu\text{C cm}^{-2}$  at  $25^\circ\text{C}$  [experiment,  $-4 \mu\text{C cm}^{-2}$  (8)]. The position of the entropy maximum is independent of  $U, C$  and  $N$  (Eq. [11]). The orientational entropy as a function of  $q$  as calculated from Eq. [2] is shown in Fig. 1. If, instead of  $0.05\text{Å}$ , the electrical center of "up" dipole is taken as  $0.1 \times 10^{-8}$  cm closer to the metal than that of "down" dipole, then  $\Delta U_{\text{image}} = -2.80 \text{ kJ mole}^{-1}$ , and  $\Delta U_{\text{disp}} = -2.6 \text{ kJ mole}^{-1}$ . With this value of  $\Delta\Delta G = -2.8 - 2.6 = -5.4 \text{ kJ mole}^{-1}$ , the orientational entropy maximum is found to occur at  $q = -6.9 \mu\text{C cm}^{-2}$  (experiment,  $-4 \mu\text{C cm}^{-2}$ ). It follows that the two-state ("up" and "down") water dipole layer is consistent with the experimental findings (6-8) that the position of the maximum of the water component of the entropy of the double layer occurs on the negative side of the pzc, and that the mean of the range of the theoretical calculations of the  $q_{\max}$  is about  $1 \mu\text{C cm}^{-2}$  negative to that observed.

On this basis, interfacial water molecules have zero orientation (i.e., are most loosely bound) at a potential cathodic to the pzc. This is inconsistent with the attribution of a capacitance hump to dielectric saturation, as has been the view of a number of workers (3, 5, 9), because such a hump occurs only at charges positive to the pzc. The alternative model of the anodic capacitance hump, i.e., the anion repulsion model (11, 12) is consistent with the entropy results.

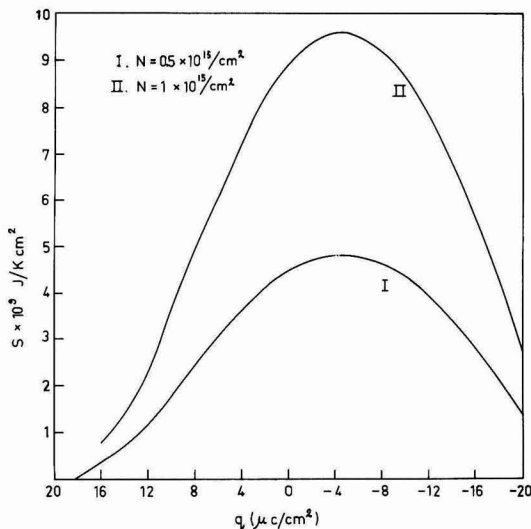


Fig. 1. The orientational entropy of interfacial water as a function of electrode charge.  $\Delta\Delta G = -4.2 \text{ kJ mole}^{-1}$  and  $(Uc/kT) = 2$ .

Any discussion of this paper will appear in a Discussion Section to be published in the December 1976 JOURNAL. All discussions for the December 1976 Discussion Section should be submitted by Aug. 1, 1976.

Publication costs of this article were partially assisted by the Flinders University of South Australia.

#### REFERENCES

1. E. Lange and K. P. Miscenko, *Z. Phys. Chem.*, **A149**, 1 (1930).
2. J. O'M. Bockris and E. C. Potter, *J. Chem. Phys.*, **20**, 614 (1952).
3. R. J. Watts-Tobin, *Phil. Mag.*, **6**, 133 (1961).
4. N. F. Mott and R. J. Watts-Tobin, *Electrochim. Acta.*, **4**, 79 (1961).
5. J. R. MacDonald and C. A. Barlow, *J. Chem. Phys.*, **36**, 3062 (1962).
6. G. J. Hills and R. Payne, *Trans. Faraday Soc.*, **61**, 37 (1965); G. J. Hills, *J. Phys. Chem.*, **73**, 3591 (1969).
7. J. A. Harrison, J. E. B. Randles, and D. J. Schiffrin, *J. Electroanal. Chem.*, **48**, 359 (1973).
8. R. M. Reeves, in "Modern Electrochemistry," Vol. 9, B. E. Conway and J. O'M. Bockris, Editors, Plenum Press, New York (1974).
9. S. Levine, G. M. Bell, and A. L. Smith, *J. Phys. Chem.*, **73**, 3534 (1969).
10. B. E. Conway and G. M. Gordon, *ibid.*, **73**, 3609 (1969).
11. J. O'M. Bockris, M. A. V. Devanathan, and K. Müller, *Proc. Roy. Soc.*, **A274**, 55 (1963).
12. J. O'M. Bockris and M. A. Habib, *J. Res. Inst. Catalysis, Hokkaido Univ.*, **23**, No. 1 (1975).
13. A. N. Frumkin, Z. A. Iofa, and M. A. Gerovich, *J. Phys. Chem. USSR*, **30**, 1445 (1956).
14. J. E. B. Randles and K. S. Whitely, *Trans. Faraday Soc.*, **52**, 1509 (1956).
15. S. Trasatti, *J. Electroanal. Chem.*, **33**, 351 (1971).
16. J. O'M. Bockris, M. Green, and D. A. J. Swinkles, *This Journal*, **111**, 743 (1964).
17. A. Muller, *Proc. Roy. Soc.*, **A154**, 624 (1936); J. G. Kirkwood, *Z. Physik*, **33**, 57 (1932).
18. M. Polanyi, *Trans. Faraday Soc.*, **28**, 316 (1936).
19. C. Kittel, "Introduction to Solid State Physics," 4th ed., John Wiley & Sons, Inc., New York (1971).
20. K. Müller, *J. Res. Inst. Catalysis, Hokkaido Univ.*, **14**, 224 (1966).
21. G. J. Hills and S. Hsieh, *J. Electroanal. Chem.*, **58**, 289 (1975).
22. J. O'M. Bockris and A. K. N. Reddy, "Modern Electrochemistry," Vol. 2, Roseta ed., Plenum Press, New York (1973).





## Low Temperature Oxidation of Silicon Studied by Photosensitive ESR and Auger Electron Spectroscopy

Jerzy Rużyłto,<sup>1</sup> Ikuro Shiota, Nobuo Miyamoto, and Jun-ichi Nishizawa\*

Tohoku University, Research Institute of Electrical Communication, Sendai, Japan

### ABSTRACT

The effect of hydration of silicon oxide surfaces on the thermal oxidation process has been investigated, and the following three-step model for the thermal oxidation of silicon has been proposed: (i) In the temperature range of oxidation up to 600°C the number of Si-OH groups on the surface increases very rapidly with increasing temperature of oxidation, mainly due to the oxidation of Si-H groups from the etched surface; (ii) at 600°-800°C there is a gradual dehydration of the oxide surface due to the transformation of Si-OH into Si-O; and (iii) above 800°C, the oxidation process is little affected by surface hydration but there exists an anomaly in hydration around 800°C.

Electron spin resonance (ESR) absorption studies on the Si-SiO<sub>2</sub> system are known (1, 2) to be very useful for obtaining valuable information on the electronic properties of its interface defects. These investigations have usually been performed on samples with relatively thick oxide layers grown at temperatures above 1000°C. In this work, however, the surfaces of thin silicon oxide layers grown at the low temperature (200°-900°C) are investigated by means of a photosensitive ESR method which is based on a new detection mechanism.

The nature of the ESR centers reported here is not essentially different from that reported previously (3, 4) for the etched silicon surface where the ESR centers were described to be related to adsorbed water on structural surface hydroxyl groups. Nevertheless, the characteristic dependence of photoinduced ESR lines on the oxidation temperature, as referred to in earlier work (3), has to be given a detailed explanation of the mechanism of oxidation of silicon at low temperature. In addition, recent interest in silicon MIOS memory devices and MOS tunnel diodes with a structural feature of having a thin oxide layer grown at low temperature has made this subject of research more important.

The oxide layer was also investigated by Auger electron spectroscopy in order to analyze the oxide composition. This procedure allowed us to establish the relation between the oxide hydration and oxide layer composition and consequently to propose a new model for the thermal oxidation of silicon by taking into account the change of oxide hydration. The rate of this hydration is a critical factor for the determination of oxidation steps.

### Experimental

N-type, (111) oriented, single crystal silicon wafers with high resistivity (250 and 500 ohm-cm) were

\* Electrochemical Society Active Member.

<sup>1</sup> On leave from Instytut Technologii Elektronowej, Politechnika Warszawska, 00-662 Warsaw, Poland, sponsored by Ministry of Education of Japan.

Key words: low temperature oxidation, surface hydration and dehydration, photoinduced ESR, Auger.

used, together with some of the high-resistivity (100) oriented samples. Before oxidation, samples were etched in a 4HNO<sub>3</sub>:2HF:1CH<sub>3</sub>COOH solution and then rinsed in deionized water. Dimensions of the samples after etching were about 1 × 0.3 × 0.02 cm.

The samples were oxidized in an atmosphere of either dry or wet O<sub>2</sub> in the temperature range 200°-900°C and then quenched in air to room temperature within a few minutes after oxidation.

The light with a higher energy than the energy gap of Si was illuminated at right angles to the sample surface which was dipped in liquid nitrogen and located at the center of the TE<sub>102</sub> rectangular resonant cavity. Photostimulated ESR measurements have been made by a Varian Model 4502-15 X-band spectrometer with a sensitivity of 2 × 10<sup>11</sup> spins/gauss.

The appearance of photoinduced ESR lines is based on a mechanism different from the ordinary ESR absorption in which the paramagnetic absorption losses at the resonance are detected as the change in quality factor *Q* of the resonant cavity. In the present case, however, the change in quality factor *Q* is directly related to the phenomenon of spin dependent photoconductivity (5) where the photogenerated free carriers in bulk silicon undergo an enhanced surface recombination through the saturated paramagnetic surface states. Therefore, the reduction of dielectric loss caused by the resonant decrease of free carriers substantially overcomes the ordinary paramagnetic absorption loss. The resulting large photoinduced ESR lines always have an inverted phase of the ordinary ESR absorption lines. This mechanism will be discussed in detail elsewhere (6), but it should be noted that the tunneling of the photogenerated carriers from silicon to paramagnetic surface states distributed both on the oxide surface and inside its layer is essential for the present detection method.

In consequence, the application of this method is limited to the systems where the ESR centers are located within the tunneling distance of carriers photogenerated in silicon. The estimation of the *g*-value has been made by a comparison of obtained ESR lines

with those from the standard samples ( $Mn^{2+}$  in  $MgO$ ) with known parameters.

Analysis of the oxide composition and measurements of the oxide thickness have been performed by means of Auger electron spectroscopy combined with argon sputter etching. Auger spectra were taken in the vacuum range of  $10^{-9}$  Torr immediately after the primary electron beam was collimated on the sample surface in order to avoid the accumulation of the beam-induced effects.

### Results

The detected ESR lines have been found to be the superposition of the two lines with  $g$ -values of 2.007 and 2.004. The most characteristic feature of the observed over-all photoinduced ESR line was the strong dependence of its height on the oxidation temperature (the line height means a peak-to-peak value of the first derivative curve of the absorption type). This dependence is shown in Fig. 1 for both dry and wet oxidation. In Fig. 2 the change in the shape of the over-all ESR line is shown. The results shown in Fig. 1 and 2 reflect that the observed photoinduced ESR lines are sensitive to the content of water in the oxidizing ambient. On the other hand, no influence has been observed by changing the substrate orientation from (111) to (100).

The measurements of Auger electrons from the oxidized surfaces were performed in order to clarify the change in ESR line height with increasing temperature of oxidation. The results revealed that the changes in the Auger peaks of silicon and oxygen are related to the observed behavior of ESR lines. The 91 and 1618 eV Auger peaks which correspond to the  $L_{2,3}VV$  and the KLL Auger transition for elemental silicon, respectively, decrease with increasing temperature of oxidation, while the 1606 eV KLL transition peak for silicon in silicon oxide and the 512 eV oxygen KLL transition peak increase with increasing temperature of oxidation. This relationship is shown in Fig. 3. There is an abrupt increase in the amount of oxygen when the oxidation temperature exceeds  $600^\circ C$ . This phenomenon is accompanied by the increased rate of oxide growth (Fig. 4).

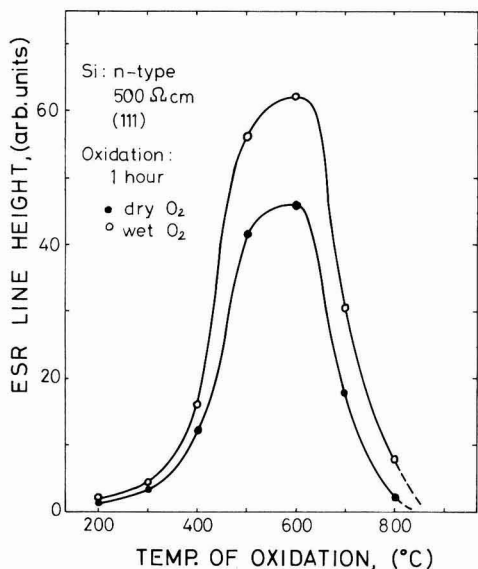


Fig. 1. Change in over-all photoinduced ESR line height with oxidation temperature of silicon in wet and dry  $O_2$  for 1 hr. The curves represent average values from several experimental runs. No ESR signals were observed in the samples oxidized at  $900^\circ C$ .

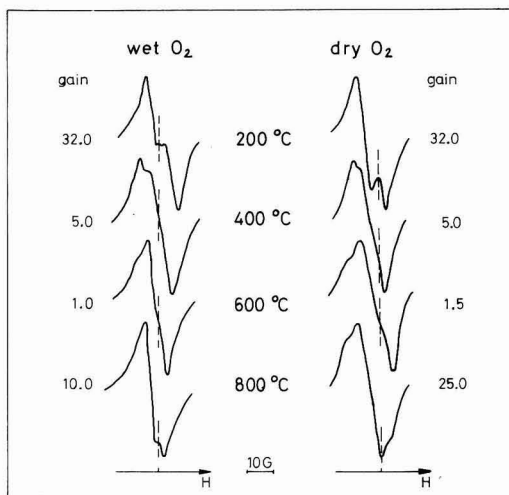


Fig. 2. Changes in line shape of over-all photoinduced ESR lines with oxidation for 1 hr.

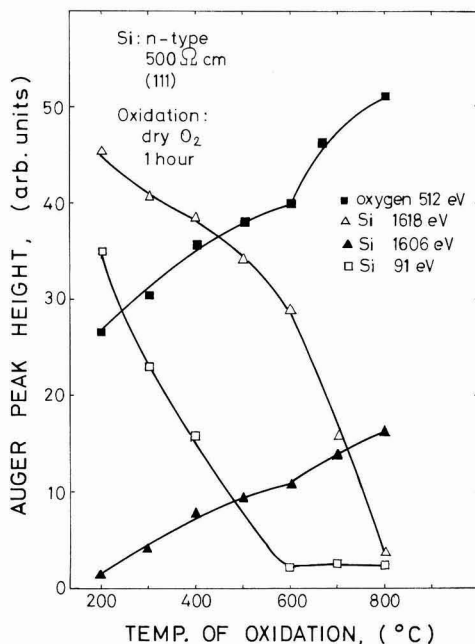


Fig. 3. Relative change in the Auger peak height with oxidation temperature.

The dependence of the ESR line height on the oxidation time at  $600^\circ C$  is presented in Fig. 5, and that at  $800^\circ$  and  $900^\circ C$  in dry  $O_2$  is given in Fig. 6. It can be seen from Fig. 6 that during the oxidation at  $800^\circ C$  the ESR line height remains almost unchanged compared with the case of  $600^\circ$  and  $900^\circ C$  oxidation, although the oxide layer is increased in thickness with increasing oxidation time as shown in Fig. 7. Also, silicon 1606 eV and oxygen Auger peaks are characterized by a smooth and slight increase (10%) with oxidation time at  $800^\circ C$  (from 10 to 60 min). Further information about the investigated centers was obtained by vacuum baking before and after oxidation. In this case, oxidation was 1 hr at  $600^\circ C$  and vacuum baking 1 hr at  $350^\circ C$  in  $10^{-5}$  Torr. ESR measurements

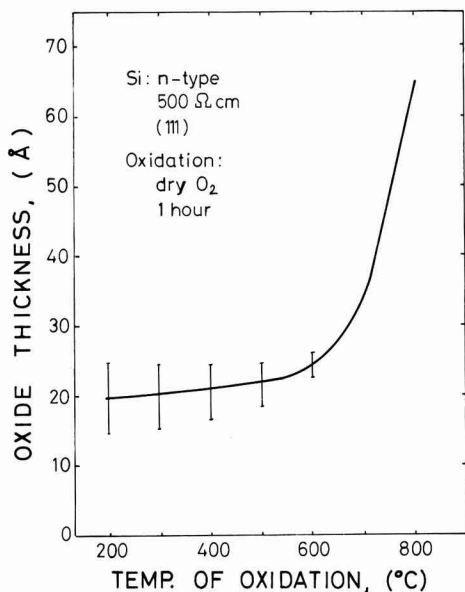


Fig. 4. Silicon oxide thickness vs. oxidation temperature in dry O<sub>2</sub>. The curve is a plot of averaged data points and several experimental runs.

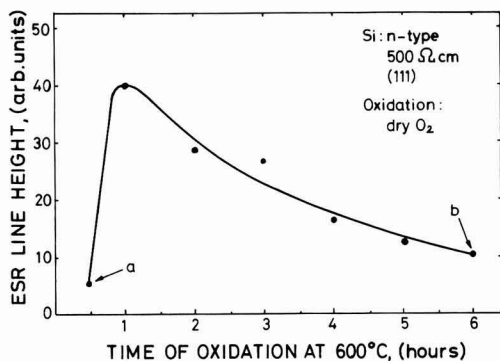


Fig. 5. Change in over-all photoinduced ESR line height with oxidation time at 600°C. At point a and b, the oxide thickness was about 20 and 40 Å, respectively.

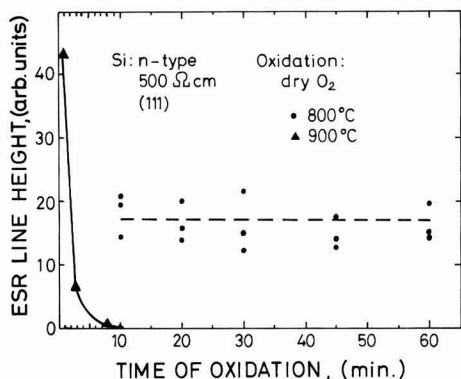


Fig. 6. Change in over-all photosensitive ESR line height with oxidation time at 800°C (broken line shows scattering of data in this case) and 900°C.

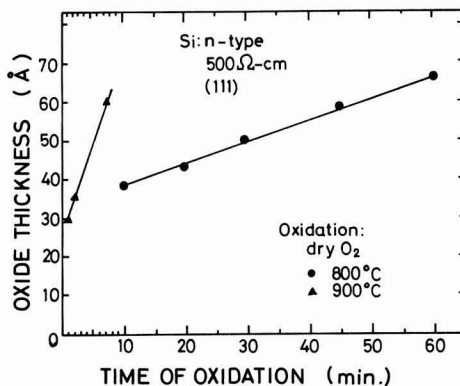


Fig. 7. Silicon oxide thickness vs. oxidation time at 800° and 900°C.

were made after cooling to room temperature, while retaining the samples in vacuum, and no ESR lines were then detected. However, the ESR line appeared again after introducing air into the vacuum system at room temperature, although its intensity was considerably weaker. The effect of the prevacuum baking on the ESR lines is shown in Fig. 8. The gradual decrease of the ESR line height in the oxidized samples after vacuum baking (curve 1) can be attributed to the same effect as in the case of the merely vacuum-baked samples (curve 2) (3, 4). The difference in height of ESR lines between the two cases clearly shows an influence of the oxidation process. It should be noted that no ESR lines are observed from the samples prevacuum baked above 900°C.

#### Discussion

The over-all photoinduced ESR line height may be an adequate measure for the surface hydration, i.e., the number of Si-OH groups on the oxide surface. The reason for the appearance of the two component ESR lines is difficult to clearly establish. In previous work (4), a tentative model was proposed in which the two ESR lines originate from two different structures resulting from the interaction of Si-OH groups with a water molecule adsorbed on the surface. It is well known that Si-OH groups on the surface take the form either isolated from each other or connected through hydrogen bonding (7). Correlating two types of Si-OH groups to the two-component ESR lines may present another possible model.

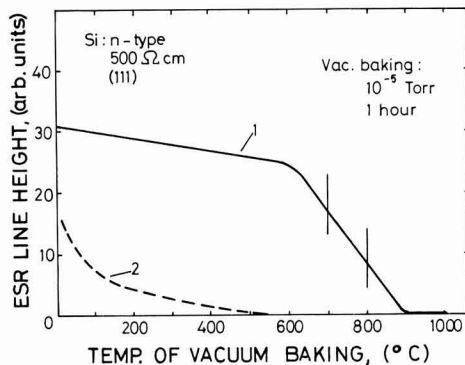


Fig. 8. Effect of vacuum baking; curve 1, vacuum baked and then oxidized at 600°C for 1 hr in dry O<sub>2</sub>; curve 2, vacuum baked only (3).

It is obvious from Fig. 8 that the oxidation process produces an additional amount of Si-OH groups to those originally existing on the etched surface. One of the mechanisms of Si-OH formation is considered to be related to the oxidation of Si-H groups on the etched silicon surface. This reaction does not depend on the water content in the oxidizing atmosphere and occurs at the same rate whether the atmosphere is dry or wet O<sub>2</sub>. In addition, Si-OH groups can also be formed due to the reaction of water with the weakly bonded Si-O-Si which can exist on the etched silicon surface. This phenomenon occurs more preferably in the wet oxidizing atmosphere, which is responsible for the higher ESR line intensity in the samples oxidized in wet O<sub>2</sub> (Fig. 1).

Let us consider the behavior of KLL Auger peaks for silicon and oxygen in the oxide layer with regard to the change in ESR line height with oxidation temperature. In the temperature range of oxidation from 200° to 600°C, the amounts of silicon (1606 eV) and oxygen increase with increasing temperature (Fig. 3). This increase, however, is not accompanied by the rapid growth of the oxide layer (Fig. 4). Therefore, the additional amount of oxygen that appears in the oxide layer is used for both the oxidation of Si-H groups at the oxide surface and the oxidation of unoxidized silicon within the oxide layer. The former is reflected in the increase of ESR line height (Fig. 1), and the latter in the decrease of silicon shown by the 91 and 1618 eV Auger peaks in Fig. 3.

From the above discussion the transformation of Si-H to Si-OH through oxidation appears to be the origin for the rapid increase of ESR line height in the temperature range up to 600°C.

It is known that Si-H bonds, with three oxygens bonded to one silicon, are stable up to about 600°C. This effect might be one of the reasons why the increase of the ESR line height is virtually stopped when the oxidation temperature reaches 600°C (Fig. 1) but a prolonged oxidation at 600°C causes Si-OH bonds to reduce as seen from Fig. 5. The same effect was also observed in the case of the 900°C oxidation, but in this case the destruction of Si-OH bonds proceeds very rapidly and no ESR lines were detected after 10 min oxidation (Fig. 6). At this oxidation temperature an initial increase of the ESR line height (as is in the case of oxidation at 600°C) was not observed, probably because of the immediate destruction of Si-H bonds after oxidation. With regard to these results, an anomalous behavior of the ESR line on isothermal oxidation at 800°C should be emphasized. As can be seen from Fig. 6, the ESR line height remains unchanged up to the 1 hr oxidation, although some scattering of the experimental data is observed. It should be noted that the oxide thickness was about the same in both the 800° and 900°C oxidation (Fig. 7), so that such a different behavior cannot be attributed to the photosensitive ESR method used in this work. Therefore, some peculiar effects are expected to occur at the oxidation temperature of 800°C in terms of surface hydration.

The same approach in terms of surface hydration should be fundamentally made to explain the change in ESR line height above 600°C as shown in Fig. 1, since the tendency of decreasing ESR line height was also recognized in the samples with the same oxide thickness formed at different temperatures above 600°C. In the case of wet oxidation, however, Si-OH groups may exist up to a higher temperature. This might be a reason for the higher ESR line height of the wet oxidized samples. In the case of oxidation for

1 hr, the critical temperature at which the ESR lines completely vanish, is probably close to 900°C (Fig. 1), but this temperature cannot be directly considered as a temperature of complete dehydration of the oxide surface, because of the excessively thick oxide layers of these samples which are beyond the thickness limit for the ESR detection method applied in the present work (6).

### Conclusions

The process of thermal oxidation of silicon below 800°C has been found to be affected by the hydration of the oxide surface and it has been proposed to divide the process into three steps corresponding to each stage of surface hydration, i.e., the temperature ranges of oxidation,  $T \leq 600^\circ\text{C}$ ,  $600^\circ < T < 800^\circ\text{C}$ , and  $T \geq 800^\circ\text{C}$ . In the first temperature range, the number of Si-OH groups on the surface increases very rapidly mainly due to the oxidation of Si-H groups, and reaches the highest value for samples oxidized at 600°C. Simultaneously, the oxidation of the unoxidized silicon in oxide layers on etched surfaces occurs, but very slow oxide growth is observed. The process of oxide surface dehydration, resulting from the destruction of Si-OH bonds, begins in the second range of oxidation, and proceeds through the change of Si-OH into Si-O. The rate of dehydration is lower in the case of wet oxidation. For  $T \geq 800^\circ\text{C}$ , the effect of surface hydration has little influence on the oxidation process but there exists an anomaly around 800°C in terms of surface hydration.

It is suggested that the results presented in this work can be of interest in the fabrication of MNOS memory devices on silicon where the oxide layer is usually formed under conditions similar to those of these experiments. Also the properties of oxide-nitride interfaces are of great importance for the characteristics of the devices. In addition, these results give valuable information on the mechanism of low temperature passivation (8) of silicon surfaces.

### Acknowledgment

The authors wish to thank the staff of Laboratory for Crystal Structure and Lattice Defects, Research Institute of Electrical Communication, Tohoku University, for their assistance during ESR measurements.

Manuscript submitted April 29, 1975; revised manuscript received Aug. 14, 1975.

Any discussion of this paper will appear in a Discussion Section to be published in the December 1976 JOURNAL. All discussions for the December 1976 Discussion Section should be submitted by Aug. 1, 1976.

Publication costs of this article were partially assisted by Tohoku University.

### REFERENCES

1. A. G. Revesz and B. Goldstein, *Surface Sci.*, **14**, 361 (1969).
2. Y. Nishi, *Japan. J. Appl. Phys.*, **10**, 52 (1971); Y. Nishi, K. Tanaka, and A. Ohwada, *ibid.*, **11**, 85 (1972).
3. I. Shiota, N. Miyamoto, and J. Nishizawa, *Surface Sci.*, **36**, 414 (1973).
4. I. Shiota, N. Miyamoto, and J. Nishizawa, Proc. 2nd International Conf. on Solid Surfaces, Kyoto, March 1974, *Japan. J. Appl. Phys. Supplement 2*, Part 2, 417 (1974).
5. D. J. Lepine, *Phys. Rev.*, **B6**, 436 (1972).
6. I. Shiota, N. Miyamoto, and J. Nishizawa, To be published.
7. L. H. Little, "Infrared Spectra of Adsorbed Species," Academic Press, London (1966).
8. H. Iizuka and J. Nishizawa, *JIEE Japan*, **89**, 59 (1969).

# High Quality RF-Sputtered Silicon Dioxide Layers

H.-U. Schreiber<sup>1</sup> and E. Fröschle

Institut für Halbleitertechnik, RWTH Aachen, D-5100 Aachen, Germany

## ABSTRACT

Very homogeneous SiO<sub>2</sub> layers were prepared by rf sputtering of SiO<sub>2</sub> in Ar or Si in O<sub>2</sub> with Ar on Si substrates which had been cleaned *in situ* by sputter etching. After a short anneal in N<sub>2</sub> (20 min at 1050°C and a 10 min postmetallization anneal at 500°C), surface charge, surface-state density, and stability were similar to those reported for good, thermally grown oxides. Best results were obtained with reactively sputtered SiO<sub>2</sub>.

Insulating layers of rf-sputtered silicon dioxide are often used in integrated circuit technology for multi-layer wiring and passivation (1). However, their homogeneity, electrical breakdown strength, and interface quality were, up to the present time, inferior to those of thermally grown oxide films. Some improvement in breakdown strength could be made by bias sputtering, as proposed by Maissel *et al.* (2, 3). In this method sputter etching takes place during deposition. The purpose of the work described here was to investigate whether sputter etching before depositing the SiO<sub>2</sub> also gives improved breakdown characteristics, and to find methods for preparing sputtered oxide layers on Si substrates with an interface quality comparable to that for thermally grown oxide.

## Sputtering Apparatus

For our rf-sputtering experiments we used a commercial MRC apparatus which was somewhat modified to suit our particular requirements. It has a shielded substrate carrier to which the rf power can be switched. This allows sputter etching of the silicon substrate before sputtering SiO<sub>2</sub> onto it. The rf generator with matching network had a maximum output of 1 kW at 13.56 MHz. The diameter of the targets and the substrate electrode was 12.5 cm, their separation 5 cm. The most important differences from the standard design were the following: First, we used a turbomolecular high-vacuum pump instead of the usual oil-diffusion pump. This gives a vacuum free of oil vapor. Next, we added an apparatus for loading and unloading under dust-free conditions. It consisted of a blower with 0.3 μm filter, a plastic hose, and a Plexiglas cylinder with air lock surrounding the sputtering chamber. Third, we inserted a tunable L-C network between substrate and ground for bias sputtering as was also done by Logan (4). The reason for this will become clear from the schematic drawing of the sputtering module and its equivalent circuit shown in Fig. 1. The dark space before the electrodes is represented by a capacitor shunted with a diode.

If the substrate electrode is connected, as usual, directly to ground in the same way as all the metallic parts of the sputtering module, the rf current is distributed through all these surfaces. The current through the substrate electrode is therefore so small that not much bias appears there and sputtering of this surface does not take place. By tuning out the capacitive part of the dark space impedance in front of the substrate electrode, most of the rf current will flow this way, giving it nearly the same bias as the target electrode.

## Experimental

Most of our experiments were done with MOS capacitors having evaporated Al electrodes of 0.3–1.5 mm diameter on SiO<sub>2</sub> films of 0.16 μm thickness which were sputtered onto {111}-orientated n-type silicon wafers

with donor concentrations of 5·10<sup>15</sup> cm<sup>-3</sup>. High quality capacitors were mostly fabricated as follows:

(i) Before sputtering the Si wafers were thoroughly cleaned with standard chemical methods. Rubbing with a cotton pad soaked with detergents before the chemical cleaning and spinning off the quartz-distilled water after the last step reduced the pinhole density significantly.

(ii) Best results were obtained if the wafers were laid onto a SiO<sub>2</sub> disk of 3 mm thickness and 12.5 cm diameter, covering the substrate electrode totally, but lying on it loosely.

(iii) For *in situ* cleaning, 1 μm of the Si wafer was sputter etched away in Ar. At 3 × 10<sup>-3</sup> mm Hg the etch rate with 400W of rf power was approximately 5 × 10<sup>-6</sup> cm/min. To minimize radiation damage the rf power was decreased toward the end in steps of 6 min at 50, 40, 15, and 10W.

(iv) SiO<sub>2</sub> was then sputtered either from a SiO<sub>2</sub> target (impurities << 0.3%, VP grade of MRC) in Ar of 5 × 10<sup>-3</sup> mm Hg pressure or reactively from a Si target (impurities << 0.001%, VP grade of MRC) in a mixture of O<sub>2</sub> (1.5 × 10<sup>-3</sup> mm Hg) and Ar (0.8 × 10<sup>-3</sup> mm Hg). With 300W of rf power the deposition rates were 1.8 × 10<sup>-6</sup> and 5 × 10<sup>-7</sup> cm/min, respectively.

(v) To reduce the radiation damage further, the wafers were annealed 20 min at 1050°C in N<sub>2</sub>. The outermost 0.015 μm SiO<sub>2</sub> was etched away afterwards in buffered HF giving better electrical stability.

(vi) The Al contacts of the MOS diodes were fabricated by high-vacuum evaporation of 0.3 μm Al out of a Na-free tungsten coil using a metal mask with 64 holes.

(vii) As often done with thermally grown oxides, a post-Al annealing of 20 min in N<sub>2</sub> at 500°C followed as the last step.

**Breakdown characteristics.**—For measurement of the current-voltage characteristics we used MOS capacitors of the dimensions shown in Fig. 2. They were probed with whiskers, the Al usually being positive. However, reversing the polarity had little effect on the data. As shown in Fig. 2 the current-voltage characteristics of

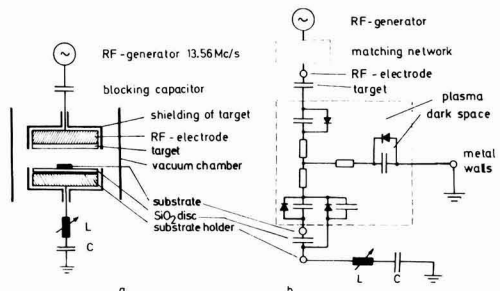


Fig. 1. Schematic (a) and equivalent circuit (b) of the rf sputtering system with L-C tuning network for bias sputtering.

<sup>1</sup> Present address: IV. Ruhr-Universität Bochum, Institut für Elektronische Bauelemente, D-4630 Bochum, Germany.

Key words: MOS diodes, breakdown, flatband voltage.



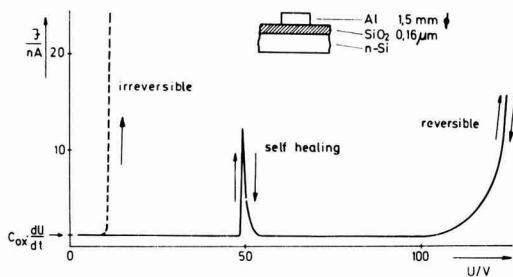


Fig. 2. MOS diode and typical breakdown characteristics

good MOS capacitors, measured by applying a ramp voltage with constant slope, are composed of constant charging currents at small voltages and sharply rising currents at higher ones. The latter are probably caused by the onset of Poole-Frenkel conduction (5) and are reversible, if limited by a high resistance.

Large defects presumably give permanent breakdowns; small pinholes, however, only temporary shorts. Figure 3 shows a scanning electron micrograph of an area where self-healing breakdown has taken place. The breakdown occurred in the middle of the round crater where the Si and the SiO<sub>2</sub> were melted. The heat arising from the breakdown also caused melting of the aluminum in the neighborhood. The metal receded by surface tension, thereby removing the short between Si and Al. The best results were achieved with silicon wafers, cleaned with the procedure described and sputter etched 1 μm before the SiO<sub>2</sub> deposition. The small spread in the characteristics of the 64 MOS diodes on a wafer and their high freedom from defects is apparent from Fig. 4. Less than 3% of them broke down at electric field strengths below 6 MV/cm.

For evaluating the influence of the different treatments, the percentage of diodes showing their first

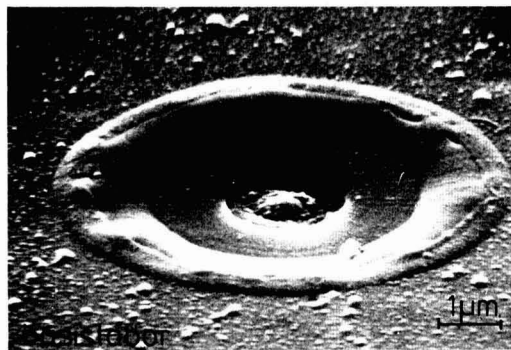


Fig. 3. Scanning electron micrograph of area in an Al-SiO<sub>2</sub>-Si capacitor where self-healing breakdown took place.

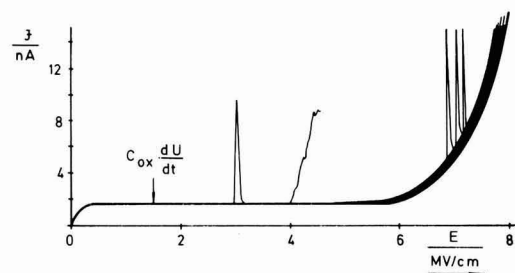


Fig. 4. Measured characteristics of 64 MOS diodes (1.5 mm diam) on a typical wafer after 1 μm sputter etching.

breakdown in a given field interval was plotted as a function of the electric field at breakdown. "First breakdown" was taken to be the first self-healing event which was detected by a very sensitive measuring circuit or a rise of current to more than 10<sup>-8</sup>A. With standard chemical cleaning nearly all MOS diodes broke down at fields below 2 MV/cm, as was also found in Ref. (3), without bias sputtering. By rubbing off the wafers with a cotton pad soaked with detergent before the final chemical cleaning with boiling HNO<sub>3</sub> and by spinning off the quartz-distilled rinsing water as a last step, the breakdown strength could be greatly improved (Fig. 5a).

Very high homogeneity was achieved by removing through sputter etching at least 1 μm of the Si wafer before depositing the SiO<sub>2</sub> (see Fig. 5b, 5c, and 9a). Continued etching did not give further improvement, if the wafers had been cleaned as described before. With standard cleaning a sputter etch of 5 μm was required to obtain the same result (6, 7). The etching was done mostly *in situ*, but no difference was found if the wafer were removed from the apparatus and stored in dust-free air for some minutes before depositing SiO<sub>2</sub>.

*Influence of bias sputtering.*—To test whether these results may also be obtained by etching the substrate during and not before deposition, some experiments with bias sputtering were made. By tuning the inductance as described above, the substrate bias was varied giving a variation of the coefficient of re-emission, K<sub>R</sub>, from 0.3 to 0.9. K<sub>R</sub> was measured by a similar technique as used in Ref. (3). As done by Logan (4) and Maissel (3), we too measured the voltage, U<sub>B</sub>, between the substrate holder and ground (see Fig. 1) and used it as an indicator of bias conditions. U<sub>B</sub>, however, is not identical with the true bias between substrate surface and plasma.

As shown in Fig. 6 the mean field for first breakdown decreased rapidly with increasing bias. Scanning electron micrographs of SiO<sub>2</sub> layers sputtered onto Si with high bias showed partially refilled scratches and craters (Fig. 7). They appear to be caused by breakdown during sputtering because no such structures were observed without bias. Similar effects were found also by McCaughan (11). The difference between our measurements and the results of Maissel *et al.* (3) who reported a distinct improvement by bias sputtering in the range of K<sub>R</sub> = 0.3-0.6 could not be resolved. Perhaps it may be contributed to by the absence of oil and grease vapors in our system which gives reasonably good breakdown characteristics even without sputter etching.

*Interface properties of Ar-sputtered SiO<sub>2</sub> on Si.*—In order to test the usefulness of sputtered SiO<sub>2</sub> for MOS devices oxide charge, interface-state density and stability were measured under various sputtering and

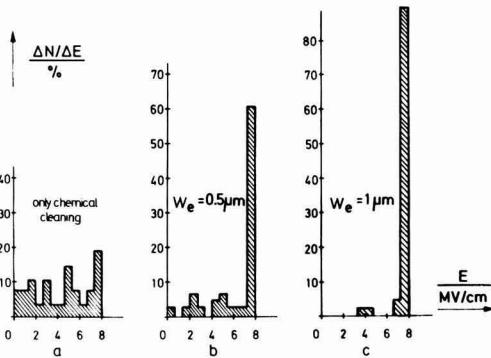


Fig. 5. Breakdown distributions (percentage  $\Delta N/\Delta E$  of first breakdown at fields between  $E$  and  $E + \Delta E$ ) for different thicknesses  $w_e$  of Si removed by sputter etching.



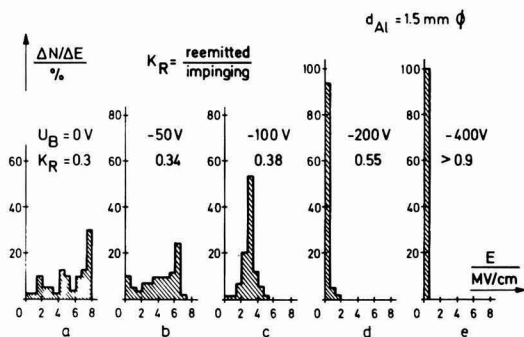


Fig. 6. Dependence of breakdown distributions on substrate holder voltage  $U_B$  during sputtering.

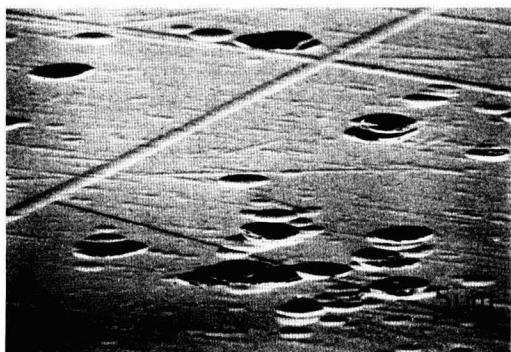


Fig. 7. Scanning electron micrograph of a  $\text{SiO}_2$  layer prepared by bias sputtering at  $U_B = -400\text{V}$ ,  $K_R > 0.9$ .

annealing conditions on MOS diodes with Al electrodes of 0.3 mm diameter. These measurements were made using the conventional high-frequency (3 MHz) capacitance-voltage method. Flatband voltage,  $V_{FB}$ , and oxide-charge density,  $N_{ox}$ , were determined by comparison of experimental with theoretical curves (8). The determination of  $V_{FB}$  of sputtered  $\text{SiO}_2$  films is considerably more accurate than with thermally grown ones because much less impurity redistribution should take place. The interface-state density,  $N_{ss}$ , near the conduction band was estimated after Ref. (9) from C-V measurements at 300°K and 77°K. Stability was measured by the standard temperature-bias test in which the MOS diodes were stressed for 20 min at 200°C with +30V (2 MV/cm) on the Al electrode and subsequently cooled down with the voltage on. The resulting shift of the flatband voltage should be less than 0.1V on good gate oxides for MOS devices.

Without annealing, the densities of surface charge and especially of surface states were very high for sputtered  $\text{SiO}_2$ . Therefore, we used an annealing procedure, which is also often used on thermal oxides. First, we used a high-temperature treatment of 20 min at 1050°C in  $\text{N}_2$ . This was followed by a short etch in buffered HF to remove the outermost 0.015  $\mu\text{m}$  of the  $\text{SiO}_2$  before Al deposition and a 10 min anneal at 500°C in  $\text{N}_2$  after metallization. After this procedure, dry thermal oxides on {111} Si give flatband voltages of 1-2V, shifting less than 0.1V in the stress test if clean, Na-free tungsten filaments are used for evaporating the Al. Their surface-state densities are negligible.

For sputtered  $\text{SiO}_2$  on sputter-etched Si this anneal was not able to reduce the surface-state density below  $10^{11} \text{ cm}^{-2} \text{ eV}^{-1}$  if the rf power was not decreased toward the end of the etching. We usually did this in steps of approximately 6 min at 50, 40, 15, and 10W. The main etching was done at 400W (3.2  $\text{W/cm}^2$ ) in

Ar at a pressure of  $3 \times 10^{-3}$  mm Hg, giving an etch rate of  $5 \times 10^{-6}$  cm/min. Using this process, flatband voltages of 8V corresponding to  $10^{12}$  oxide charges/cm<sup>2</sup>, a shift of 0.5V during the stress test and surface-state densities less than  $3 \times 10^{10} \text{ cm}^{-2} \text{ eV}^{-1}$  were achieved. For obtaining this stability it was necessary to separate the Si wafer from the substrate holder by a  $\text{SiO}_2$  disk which allowed some heating up during sputtering and prevented contamination of the wafer by material etched away from the substrate holder. If the disk was cemented with epoxy to the water-cooled substrate holder, relatively large flatband shifts were observed, even after an anneal at 1050°C.

The effect of the annealing temperature on  $N_{ox}$  and  $N_{ss}$  is shown in Fig. 8. From it can be concluded that an annealing step at a temperature of at least 1050°C is essential for obtaining usable films. The annealing and etching caused some deterioration of the breakdown strength as may be seen from Fig. 9. This effect could possibly be reduced by using cleaner annealing conditions.

**Sputtering in  $\text{O}_2$ -Ar mixtures.**—The relatively high flatband voltage could be reduced by adding a small amount of  $\text{O}_2$  to the sputtering ambient (see Fig. 10). For more than 3 volume per cent (v/o)  $\text{O}_2$  the flatband voltage on {111} Si was less than 1V. The same effect could be achieved by bias sputtering if the bias was higher than 50V (see Fig. 11), but in this case the stability was not as good as without bias.  $\text{O}_2$  addition without bias did not cause the stability to deteriorate. However, the observed shift of 0.5V is too high for good MOS devices. It was probably caused by the Na content of the  $\text{SiO}_2$  target which was only 99.7% pure.

Because targets of very pure silicon are easily available, reactively sputtering of Si in an Ar- $\text{O}_2$  mixture

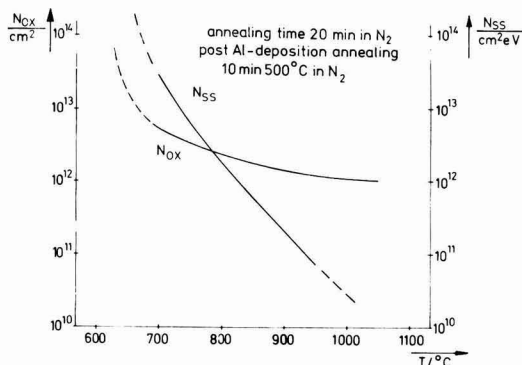


Fig. 8. Influence of annealing temperature on surface-charge density,  $N_{ox}$ , and surface-state density,  $N_{ss}$ , for Ar-sputtered  $\text{SiO}_2$  films.

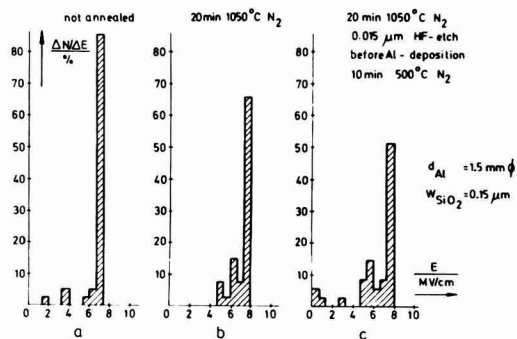


Fig. 9. Effect of annealing and etching on the breakdown distribution.

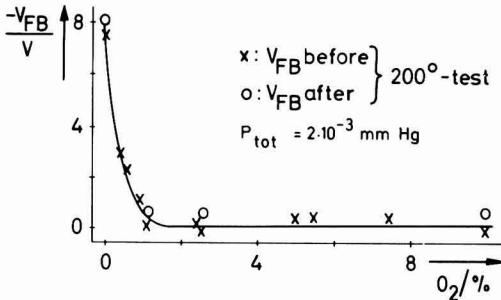


Fig. 10. Lowering of flatband voltage by addition of  $O_2$  during sputtering of  $SiO_2$ .

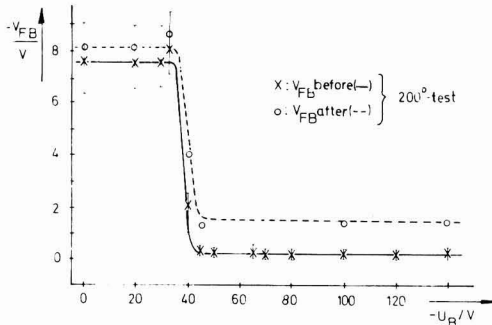


Fig. 11. Lowering of flatband voltage by bias sputtering of  $SiO_2$

was also tried. As may be seen from Fig. 12, very stable  $SiO_2$  layers with low flatband voltage could be made in a range of 40-80%  $O_2$ . The flatband voltage shifted less than 0.1V during the usual  $200^\circ C$ -2 MV/cm temperature-voltage stress tests. Regarding breakdown strength and surface-state density  $N_{ss}$ , we found no difference in layers made by sputtering  $SiO_2$  in Ar.

### Conclusions

The present study has shown that it is possible to deposit, by means of sputtering,  $SiO_2$  layers on Si, which after suitable annealing have the same quality as the best  $SiO_2$  layers prepared by thermal oxidation. The high intrinsic prebreakdown strength, shown in Fig. 4 (7.5 MV/cm at  $10^{-6}$  A  $cm^{-2}$ ), compared with the usual sputtered  $SiO_2$  layers (1) may probably be

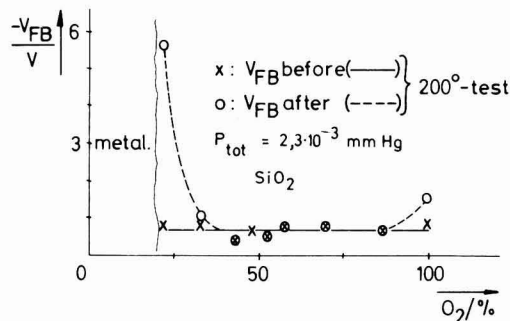


Fig. 12. Flatband voltage of MOS diodes prepared by reactively sputtering Si in an  $O_2$ -Ar mixture.

attributed to the freedom from oil and grease vapors of the sputtering ambient. Very high homogeneity and low densities of weak spots could be achieved by sputter etching approximately  $1 \mu m$  of Si before the deposition, thus removing all dirt and foreign particles from the wafer.

Sputter etching, however, leaves a damaged layer near the surface of the Si and, also, Ar ions are implanted. As shown by Yamamoto (10), with back scattering analysis 20 min annealing in  $N_2$  is sufficient to remove the Ar but does not heal out the damage of the Si completely. This agrees with our results. The rf power had to be reduced toward the end of the etching to keep the damage of the Si so low that it could be removed by the same annealing procedure which is also customarily used on thermal  $SiO_2$ . It is also sufficient to remove enclosed Ar (12) and defects in the sputtered  $SiO_2$  (13). Upon such annealing in  $N_2$  at  $1050^\circ C$  before and at  $500^\circ C$  after Al deposition, MOS diodes of very good quality could be made, especially by reactively sputtering Si in an  $O_2$ -Ar mixture. Their flatband voltage was below 1V and shifted less than 0.1V during a 20 min temperature-voltage stress test with 2 MV/cm at  $200^\circ C$ . The interface-state density was below  $3 \times 10^{10} cm^{-2} eV^{-1}$ .

Rf sputtering from a  $SiO_2$  target in pure Ar resulted in higher surface-charge densities than with reactively sputtered  $SiO_2$ , probably because of oxygen vacancies (14). They could be avoided by adding 3%  $O_2$  to the Ar. Stability during the bias-temperature stress test, however, was not as good as with reactively sputtered  $SiO_2$ , probably because of lower purity of the target.

### Acknowledgments

The authors are indebted to Prof. E. Kubalek and the Basislabor of RWTH for providing the electron micrographs. They would like to acknowledge the support of the Deutsche Forschungsgemeinschaft which enabled these investigations through the Sonderforschungsbereich 56 "Festkörperelektronik."

Manuscript submitted Dec. 27, 1974; revised manuscript received Sept. 8, 1975. This was Paper 116 presented at the Boston, Massachusetts, Meeting of the Society, Oct. 7-11, 1973.

Any discussion of this paper will appear in a Discussion Section to be published in the December 1976 JOURNAL. All discussions for the December 1976 Discussion Section should be submitted by Aug. 1, 1976.

### REFERENCES

1. D. L. Tolliver, Paper 120 presented at The Electrochemical Society Meeting, Boston, Mass., Oct. 7-11, 1973.
2. L. I. Maissel and P. M. Schaible, *J. Appl. Phys.*, **36**, 237 (1965).
3. L. I. Maissel, R. E. Jones, and C. L. Standley, *IBM J. Res. Develop.*, **14**, 176 (1970).
4. J. S. Logan, *ibid.*, **14**, 172 (1970).
5. J. Frenkel, *Phys. Rev.*, **54**, 647 (1938).
6. H.-U. Schreiber and E. Fröschle, 2. Deutsche Sputtering Schule, Rottach-Egern, 30 (1971).
7. H.-U. Schreiber, Thesis, RWTH Aachen, Aachen, Germany (1973).
8. A. Goetzberger, *Bell System Tech. J.*, **45**, 1097 (1966).
9. D. M. Brown and P. V. Gray, *This Journal*, **115**, 760 (1968).
10. Y. Yamamoto, K. Shinada, T. Itoh, and K. Yada, *Jap. J. Appl. Phys.*, **13**, 551 (1974).
11. D. V. McCaughan and R. A. Kushner, *Proc. IEEE*, **62**, 1236 (1974).
12. G. C. Schwartz and R. E. Jones, *IBM J. Res. Develop.*, **14**, 52 (1970).
13. D. V. McCaughan and V. T. Murphy, *J. Appl. Phys.*, **44**, 3182 (1973).
14. J. L. Vossen, *J. Vacuum Sci. Technol.*, **8**, 12 (1972).

# Anodic Processing for Multilevel LSI

G. C. Schwartz\* and V. Platter

IBM System Products Division, East Fishkill Facility, Hopewell Junction, New York 12533

## ABSTRACT

Anodic processing for multilevel LSI is attractive because planar structures can be made. For complete flexibility of design, it is advantageous that portions of the first level of interconnection metallization be isolated initially from silicon, and that the required contact to silicon be made using overpasses on a subsequent level. Anodic processes previously described required that there be a direct contact to silicon for each land to be defined. This restriction can be circumvented by depositing a thin conductive layer before deposition of the interconnection metallurgy and eventually converting it to an insulator. The requirements for a suitable underlay are given, and the choice of hafnium for this purpose is explained. The details of the anodic processing are described and discussed. Conversion of the underlay to an insulator requires both anodization until barrier layer growth ceases and oxidation at elevated temperature; 450°C in steam for 30 min yields excellent results. The leakage current between closely spaced conductors is decreased substantially by the use of this underlay process as compared to the previously described anodic processes.

For multilevel aluminum or aluminum alloy land systems in LSI, anodic processing has two main advantages over conventional subtractive etching. First, planar structures can be fabricated. This eliminates the reliability hazards associated with covering large and often steep metal edges with an insulator. Also photolithography difficulties are reduced. Second, there is substantially less loss in cross-sectional area. Therefore the current-carrying capability of a conductor formed anodically is greater than that formed conventionally using the same mask.

Anodic processing substitutes conversion of the unwanted metal to an insulating film for the removal of unwanted metal. Because relatively thick (10,000Å) metal films are required for the circuitry, the unwanted metal is converted to porous anodic oxide as barrier layer growth is limited. Oxalic acid is used as the electrolyte in the completely planar process (1) since it is compatible with photoresist, it can be decomposed at the completion of anodic processing, and, at the appropriate current densities, the voltages are suitable for semiconductor device fabrication.

All previously described anodic processes (1, 2, 3) had required that there be a direct contact to silicon for every land to be defined. This requirement arises from the need to supply current to the lands after the anodization is apparently complete, so that the residual aluminum which clings to the edges of the lands forming bridges between closely spaced conductors can be converted to insulating anodic oxide. But for complete flexibility of design of integrated circuits with multilevel metallization, it is often desirable to isolate from silicon, initially, portions of the first-level metallization and use "overpasses" on a subsequent level. To be able to isolate, anodically, such electrically "floating" conductors, we have adopted a scheme developed by Romankiw (4) for anodic processing, making the changes necessary to achieve the very low leakage levels required for integrated circuits, but not for the applications for which Romankiw designed his procedure.

Before deposition of the aluminum or aluminum alloy film used for the interconnection pattern, Romankiw proposed that a thin metal film be deposited to carry current to the lands which are not connected to silicon. This film must subsequently be converted to an insulator. We have concluded that the metal used as an underlay must meet certain requirements: (i) it

must be able to be converted to an insulator under conditions compatible with semiconductor device processing and with the presence of the overlying anodic oxide; (ii) it must not react chemically with the electrolyte used to form the porous anodic oxide; (iii) if it can be anodized, it must anodize at or very close to 100% efficiency to avoid oxygen evolution which may cause lifting of the overlying anodic oxide; (iv) it must adhere well to the substrate and the overlying anodic oxide must adhere well to it; and (v) it must not degrade device performance.

The most suitable underlay we have found is hafnium. It forms a barrier layer upon anodization in oxalic acid with no perceptible oxygen evolution. Moreover, the anodization ratio of hafnium is high (11.6Å Hf/V) which means that the final voltage to which the formed structures will be subjected at the completion of anodic processing will be relatively low since underlay films 150-200Å thick are suitable. Hafnium can be oxidized thermally at low temperature. A discrete hafnium layer is maintained when the metals hafnium and aluminum (or aluminum alloy) are deposited sequentially at elevated substrate temperature to insure good adhesion, yet adequate interdiffusion occurs during the final anneal at the completion of the anodic processing. The interdiffusion has been demonstrated by the use of helium ion backscattering. In Fig. 1 is shown the backscattering spectrum for aluminum in a film consisting of 2μ of aluminum with a hafnium layer 1000Å thick on its surface, both before and after heat-treatment in helium at 400°C for 1 hr. It can be seen that after the anneal, aluminum has reached the surface of the film. Adequate interdiffusion occurs even when the hafnium is exposed to air before deposition of the interconnection metallurgy. Individual test transistors made with and without a hafnium underlay have identical electrical characteristics.

The resistivity changes in an aluminum (17,000Å)-hafnium (240Å) film during anneal at 400°C in an inert atmosphere are shown in Fig. 2. When an evaporated aluminum film is annealed at a temperature above its deposition temperature, an initial decrease in resistivity is always observed. This is probably due to a decrease in defects in the grain boundaries. The subsequent small increase in resistivity can be attributed to dissolution of the hafnium and to intermetallic compound formation. However, this increase is very small and would not affect the performance of the interconnection metallization.

Anodic processing is performed as described in a previous paper (1); this method uses a two-current mode

\* Electrochemical Society Active Member.

Key words: multilevel metallization, planar metallization, large-scale integrated circuits, anodic oxidation, aluminum alloy metallurgy.

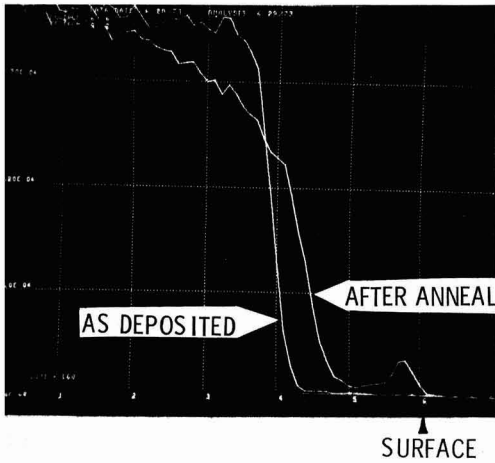


Fig. 1. Energy spectrum obtained by means of helium ion back-scattering of aluminum in a film consisting of  $2\mu$  of aluminum with  $1000\text{\AA}$  of hafnium on its surface before and after anneal in helium at  $400^\circ\text{C}$  for 1 hr.

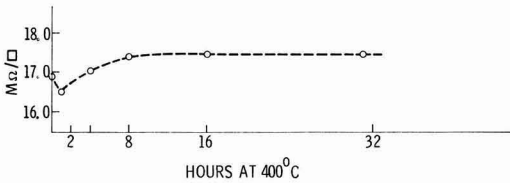


Fig. 2. Resistivity changes in an aluminum-hafnium film during anneal at  $400^\circ\text{C}$  in an inert atmosphere. The film:  $17,000\text{\AA}$  Al/ $240\text{\AA}$  Hf-insulated substrate.

for the isolation anodization of the Al/AlCu film since this had resulted in the best line profile. A typical curve for the isolation anodization in 8% oxalic acid of the metal film Al/AlCu/Hf is shown in Fig. 3.

A current density of  $3.5\text{ mA/cm}^2$  is used at the start of the anodization. At point A in Fig. 3 the aluminum cap has been anodized completely and there is an upward inflection in the voltage curve indicating the beginning of the AlCu layer (5). A control circuit automatically reduces the current (to  $1\text{ mA/cm}^2$ ) when a time which corresponds to the anodization of about two-thirds of the film is reached; i.e., at point B. At point C the anodization is apparently complete because the voltage starts to rise (to a preset limit), and the current starts to decay. Thus, point C is also the beginning of the "decay period." The time it takes to

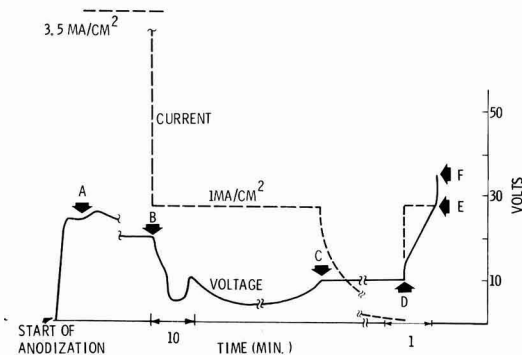


Fig. 3. Constant current anodization in 8% oxalic acid of the film: Al/AlCu/Hf-insulated substrate.

reach point C depends upon the thickness of the film and the copper concentration in the AlCu film. At  $3.5\text{ mA/cm}^2$  aluminum anodizes at about  $750\text{ \AA/min}$ ; an AlCu (4%) film anodizes at about  $450\text{ \AA/min}$  at the same current density.

Point C is also the beginning of the "decay period." In Fig. 4, are shown scanning electron micrographs of three pairs of conductors, separated by 3, 6, and  $15\mu$ ,<sup>1</sup> as they appear after a relatively short "decay period." The anodic aluminum oxide has been removed in phosphochromic acid to reveal any metal particles. It can be seen that the isolated aluminum particles (the "cosmetic defects") are completely converted to anodic aluminum oxide, but that closely spaced lines are bridged. In Fig. 5 the final isolation after suitable "decay" is shown; this would correspond to point D in Fig. 3. From Fig. 4 it is quite clear that the more widely spaced lines are isolated more rapidly, but Fig. 5 shows that the final line width is independent of the spacing. The "decay" time required in any given application will depend on the thickness of the interconnection metallization and the smallest spacing in the pattern being formed. For  $1.5\mu$  metal, 45 min are required to isolate the  $3\mu$  space.

The time interval C-D is preset and, when point D is reached, the voltage is allowed to rise automatically

<sup>1</sup> For the  $15\mu$  spacing, one of the conductors is not shown in the photograph because the spacing was too wide for the second of the pair to be included in the field of view of the SEM at that magnification.

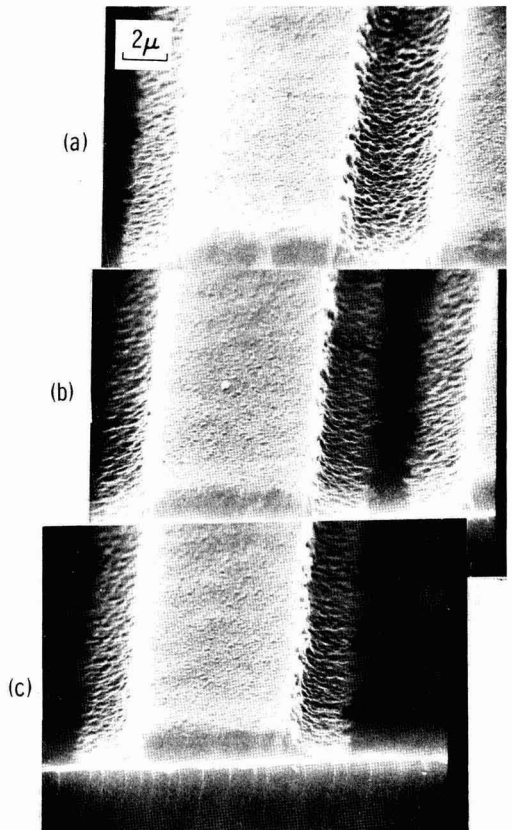


Fig. 4. Scanning electron micrographs showing the effect of a short current decay on the isolation of adjacent conductors. The anodic aluminum oxide has been removed in phosphochromic acid. Three pairs of lines are shown: (a) Space between conductors  $\sim 3\mu$ , (b) Space between conductors  $\sim 6\mu$ , and (c) Space between conductors  $\sim 15\mu$  (second conductor not shown).

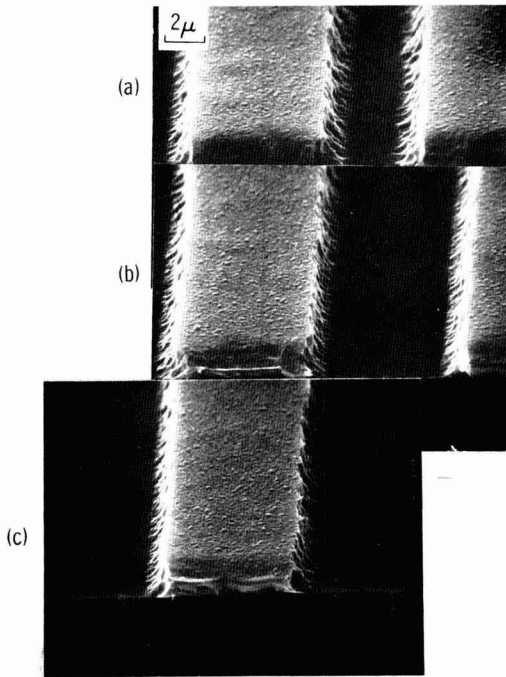


Fig. 5. Scanning electron micrographs showing the effect of adequate current decay on the isolation of adjacent conductors. The anodic aluminum oxide has been removed in phosphochromic acid. Three pairs of lines are shown: (a) Space between conductors  $\sim 3\mu$ , (b) Space between conductors  $\sim 6\mu$ , and (c) Space between conductors  $\sim 15\mu$  (second conductor not shown).

and the hafnium is anodized to form a barrier layer as shown by the linear increase in voltage at constant current ( $1 \text{ mA/cm}^2$ ). At point E, the voltage rises abruptly; when it reaches a preset limit, F, the circuit is opened automatically. Because barrier layer growth ceases at voltage E, it is said that the hafnium is "completely" anodized. The anodizing ratio,  $11.6\text{A Hf/V}$  was determined by anodizing, at  $1 \text{ mA/cm}^2$  in oxalic acid, a series of hafnium films of known thickness and determining the voltage at which the abrupt rise occurred. The voltage E is, within a few volts, the value expected from the known thickness of the hafnium underlay. It should be emphasized that during the "decay period" the voltage should be well below E to insure current flow to the otherwise isolated residual metal.

However, even after the apparent complete anodization of the underlay, adjacent conductors are still electrically shorted, no matter how long the "decay period." Therefore the residue of the underlay metal must be oxidized thermally. The conditions for oxidation of this residual thin layer are much more severe

Table I. Leakage current at 10V (after sufficient decay)  
 $3\mu$  space between conductors  $9 \times 10^{-2} \text{ cm}$  long

Sample	Leakage current
Conductor connected to silicon during processing	$10\text{-}20 \times 10^{-12}\text{A}$
"Floating" lines, no underlay	Short
"Floating" lines, hafnium underlay	Short
Hf anodized to completion only	Short
Hf not anodized: $450^\circ\text{C}$ in $\text{O}_2$ , 1 hr	2-18A
Hf anodized to completion: $450^\circ\text{C}$ in $\text{O}_2$ , 30 min	$40 \times 10^{-9}\text{A}$
Hf anodized to completion: $400^\circ\text{C}$ in steam, 30 min	$50 \times 10^{-9}\text{A}$
Hf anodized to completion: $450^\circ\text{C}$ in steam, 30 min	$0.1 \times 10^{-12}\text{A}$
Hf anodized to completion; $450^\circ\text{C}$ in forming gas, 30 min	Short

than might be predicted from the published data on the low temperature oxidation of such metals (6). The presence of the overlying layer of porous anodic oxide greatly inhibits the oxidation, even though the barrier layer at the base of the pores is quite thin (the anodization is finished at a low voltage) and probably does not have the integrity usually associated with the barrier layer formed on pure aluminum because the copper dissolves in the electrolyte. The residual layer can be oxidized in dry oxygen at  $450^\circ\text{C}$  for 30 min, but using steam as the oxidation medium causes a substantial reduction in leakage current between adjacent conductors. Typical leakage values for a variety of pro-

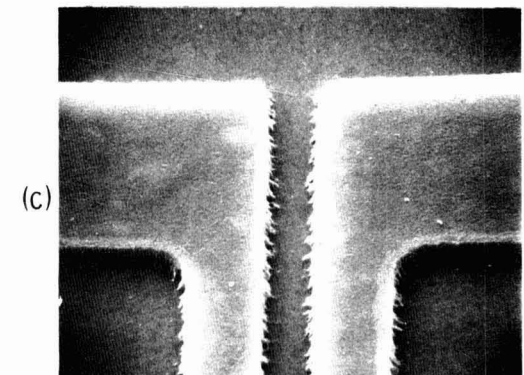
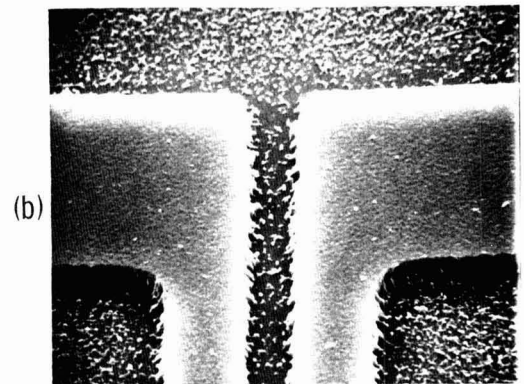
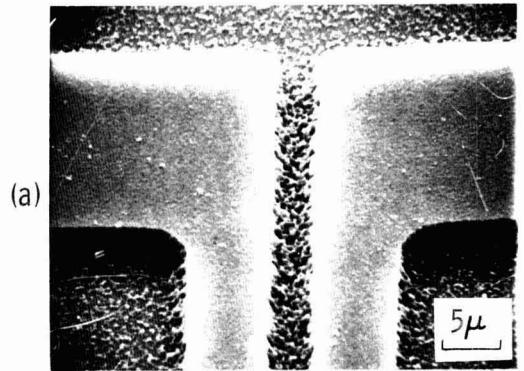


Fig. 6. Scanning electron micrographs of a pattern formed by anodic processing. (a) Floating lines; (b) lines connected to silicon, after decay; and (c) floating lines, hafnium underlay process.



cessing conditions are given in Table I. It can be seen that using the underlay process with steam oxidation results in leakage current about 100 times smaller than that obtained by standard processing, *i.e.*, no underlay, but every conductor connected directly to silicon. During the steam oxidation of the residual underlay, the porous anodic oxide is sealed, making it less vulnerable to attack by the reagents used to form the interlevel via holes.

However, unless the underlay is anodized until barrier layer growth ceases, it is not possible to oxidize it (to achieve suitable leakage values) at a temperature and for a time reasonable for semiconductor devices. We have also shown that the underlay does not react, to any significant extent, with either an SiO<sub>2</sub> underlay or a porous anodic aluminum oxide overlay, since a 450°C anneal in a nonoxidizing atmosphere for the same length of time does not produce any detectable reduction in the leakage current between adjacent conductors.

In Fig. 6 are shown scanning electron micrographs of our standard test structure in which the porous anodic oxide has been removed in phosphochromic acid to reveal the residual aluminum particles. In (a) are anodically processed "floating" lines; in (b) are lines anodically processed in the "standard" way; *i.e.* no underlay, but every line connected directly to silicon; and (c) are anodically processed "floating lines" when the hafnium underlay process is used.

### Conclusions

We have described a method of anodic planarization for LSI which eliminates the necessity of direct contact to silicon for every conductor formed. The method consists of using a hafnium underlay beneath the aluminum or aluminum alloy interconnection metallization and anodizing the hafnium underlay to "completion" after isolation and decay, then oxidizing the

residue of the underlay in steam at 450°C for 30 min. Semiconductor devices with electrical characteristics identical to those made by conventional processing have been made using this technique.

### Acknowledgments

The authors would like to thank R. Lever for performing the helium ion backscattering experiments, and F. Ordóñez for the excellent scanning electron micrographs. We are grateful for J. Van Steenburgh's assistance with the evaporations.

Manuscript submitted June 30, 1975; revised manuscript received Sept. 16, 1975. This was Paper 78 presented at the Toronto, Canada, Meeting of the Society, May 11-16, 1975.

Any discussion of this paper will appear in a Discussion Section to be published in the December 1976 JOURNAL. All discussions for the December 1976 Discussion Section should be submitted by Aug. 1, 1976.

Publication costs of this article were partially assisted by IBM Corporation.

### REFERENCES

1. G. C. Schwartz, Abstract 3, p. 13, The Electrochemical Society Extended Abstracts, Spring Meeting, San Francisco, California, May 12-17, 1974; G. C. Schwartz and V. Platter, *This Journal*, **122**, 1508 (1975).
2. H. Tsunemitsu and H. Shiba, Abstract 18.4, IEEE International Electron Device Meeting, October 1969; *NEC Research and Development*, **74**, April 1972.
3. W. R. McMahon, Abstract 7.1, IEEE International Electron Devices Meeting, October 1970.
4. L. Romankiw, Private communication.
5. G. C. Schwartz, Abstract 80, p. 182, The Electrochemical Society Extended Abstracts, Spring Meeting, Toronto, Canada, May 11-16, 1975.
6. E. A. Guibransen and K. F. Andrews, *This Journal*, **96**, 364 (1949).

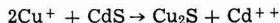
## Ion Backscattering Study of Cu<sub>2</sub>S Formation on Single Crystal CdS

J. A. Borders\*

Sandia Laboratories, Albuquerque, New Mexico 87115

### ABSTRACT

Ion backscattering has been used to study the formation of Cu<sub>2</sub>S layers on single crystal CdS due to the chemical ion exchange reaction



The reaction is found to proceed most rapidly on the A (Cd) face, slower on the B (S) face, with the reaction proceeding slowest on faces perpendicular to the <1120> axis. Reactions on the A and B faces are characterized by a very nonuniform Cu<sub>2</sub>S-CdS interface, whereas the interface for reactions along the <1120> is much more uniform. The reaction in the latter case may be controlled by surface nucleation, and layer formation subsequent to formation of a 300-500Å thick layer is much slower. The formation of Cu<sub>2</sub>S on the A and B faces has an activation energy of 0.9-1.5 eV. Preparation of the surface by polishing leads to a larger rate of Cu<sub>2</sub>S formation and Cu<sub>2</sub>S-CdS interfaces which are more uniform as a function of depth than those in etched samples.

Energetic ion backscattering is a relatively recent tool for the study of the near-surface layers in solids. It is the only nondestructive technique for measuring the depth distribution of atomic composition over

micron-thick layers with significant depth resolution (100-200Å). So far, ion backscattering has been applied mainly to studies of thin-film interdiffusion and interfacial reactions, particularly in the area of semiconductor device technology (1), but there have been few applications to studies of surface chemical reactions.

\* Electrochemical Society Active Member.  
Key words: cadmium sulfide, copper sulfide, thin film solar cells, ion backscattering analysis.

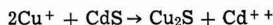
A technologically important system where a surface chemical reaction plays an important role is the CdS-Cu<sub>2</sub>S system. This system is one of the most frequently mentioned candidates for thin-film solar cells and extensive phenomenological information is available. In this paper we report the results of an investigation of the formation of Cu<sub>2</sub>S layers on the surfaces of single crystal CdS using 2.0 MeV He ion backscattering. The ion backscattering provides a direct measure of the depth distribution of atomic composition in the first few thousand angstroms of the sample. Temperature dependences of the depth distributions enable the reaction energetics to be determined over a limited temperature region. The important effects of crystallographic orientation of the CdS substrates have been measured and the effect of surface preparation of the CdS was briefly investigated.

### Experimental

Samples of single crystal CdS were obtained from Eagle-Pitcher and Cleviste Corporation in the form of thin platelets of thickness  $\sim 0.5$  mm. These specimens included both platelets with the C axis in the plane of the platelet and samples with the C axis perpendicular to the platelet. The platelets were cut to the appropriate sample dimensions ( $6.5 \times 6.5$  mm) for the backscattering experiments. The A (0001) and B (000 $\bar{1}$ ) faces of the samples with the C axis perpendicular to the plane of the sample were identified by a 1 min etch in a 50% by volume mixture of HCl and H<sub>2</sub>O. Optical microscope observations indicate that small hexagonal structures begin to form on one of the surfaces. By comparison with known preferential etching (2) behavior in a solution of HNO<sub>3</sub>, CH<sub>3</sub>COOH, and H<sub>2</sub>O in the volume ratios 6:6:1, the surface showing the hexagonal structures was identified as the A (Cd) face. Samples with the C axis in the plane of the platelet were etched for 30 sec in 30% by volume HCl in H<sub>2</sub>O. The crystallographic orientation of these samples was determined by x-ray diffraction to be  $\langle 11\bar{2}0 \rangle$ .

Two samples, an A-face sample and a sample with the C axis in the plane of the surface, were polished to an optically clear finish on a polishing wheel using 0.25  $\mu$ m diamond paste as an abrasive. These samples were then gently swabbed with 30% HCl for 5 min to remove surface damage yet retain the optically smooth surface finish.

The Cu<sub>2</sub>S layers were formed by dipping in a copper chloride solution developed by Fahrenbruck (3). This dipping treatment forms Cu<sub>2</sub>S by the reaction



with the excess cadmium going into solution. Distilled H<sub>2</sub>O was boiled in a flask while argon was bubbled through the H<sub>2</sub>O. After 20 min, 19.8 g/liter CuCl, 37.3 g/liter KCl, and 13.9 g/liter NH<sub>2</sub>OH·HCl were added without disturbing the argon atmosphere in the flask. The solution temperature was then stabilized at the desired dipping temperature and the samples immersed for the desired time while attached to a stainless steel paddle. After dipping, the samples were immediately rinsed with distilled H<sub>2</sub>O, dried, and inserted in the sample holder for the backscattering analysis.

In order to verify that samples reached thermal equilibrium quickly at the shortest dipping times (15 sec), samples of all orientations which had been subjected to two successive 15 sec dips were compared to samples dipped once for 30 sec. For samples of the same orientation there was no difference in the amount or depth distribution of Cu<sub>2</sub>S formed by the two procedures.

All analyses were accomplished with 2.0 MeV He<sup>+</sup> ions at a nominal beam current of 3.0 nA and a beam spot size of  $1.0 \times 1.0$  mm. Scattered ions were de-

tected at a laboratory angle of 160° in a silicon surface barrier detector. Further amplification and analysis was done using standard nuclear spectroscopy electronics, pulse pile-up rejection circuitry, and a PDP-11-based pulse height analysis system (4).

### Data Analysis

A typical ion backscattering spectrum from a CdS sample with a thin layer of Cu<sub>2</sub>S, where  $x \approx 2.0$  as will be discussed, is shown in Fig. 1 (top). These data are for (0001) CdS dipped for 2 min at a solution temperature of 65°C. In Fig. 1 (bottom) is a spectrum taken of an untreated sample of CdS. The formation of the Cu<sub>2</sub>S surface layer is manifested in two ways: (i) the Cd edge is shifted to lower energies due to passage of the ions through and energy loss in the Cu<sub>2</sub>S and (ii) the appearance of scattering due to the Cu atoms themselves. Since the Cu scattering at a given depth occurs at a lower energy than Cd scattering from the same depth, the analysis of the data is more complex than for a heavier atom layer on a lighter atom substrate. It is assumed that the reader is familiar with measurements of the depth dependence of atomic composition by ion backscattering. For a detailed discussion of the principle of the technique and how the information is obtained see Ref. (1). Brice has developed a technique for the extraction of the scattering yields of each component of a binary target (5) and has written a computer code which performs this function. The code as written requires a rather large computer, but by making some restrictions in the capabilities and generality of the code, we have been able to implement this program in a PDP-11 with 28K core. The program is written in an interpretive language and thus requires about five hours to analyze 100 channels.

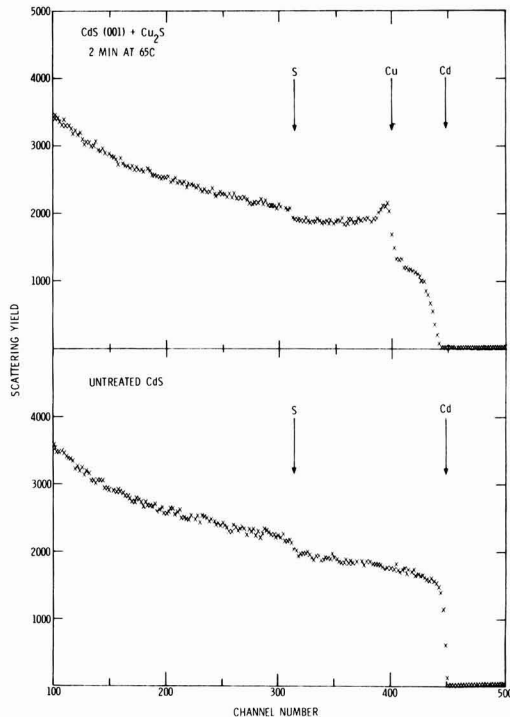


Fig. 1. Backscattering spectra from a sample of CdS (A face) dipped for 2 min at 65°C (top) and an untreated sample of CdS (bottom). The labeled arrows represent the channel where surface scattering from the three constituents will occur.

Several assumptions must be made in order to interpret the data. Since the Brice program is only applicable to binary targets, we have assumed that all the Cd is in the form CdS and all the Cu in the form  $\text{CuS}_{0.5}$ . CdS is the only known compound in the CdS binary system and  $\text{CdCl}_2$ , which would be the reaction product in the dipping reaction, is water soluble. The reasons for the assumption that all the Cu is in the form  $\text{CuS}_{0.5}$  or equivalently  $\text{Cu}_2\text{S}$  are not so obvious. The  $\text{CuS}_{0.5}$  form is used rather than  $\text{Cu}_2\text{S}$  to normalize both molecules to one metallic atom apiece, since we are measuring the helium ion scattering from Cd and Cu and not from S. The solubility of Cu in CdS has been measured by Sullivan (6) and can be expressed as

$$[\text{Cu}] = 6.6 \times 10^{22} \text{ atom/cm}^3 \times \exp[-0.505 \text{ eV}/kT] \quad [1]$$

At the temperatures we are concerned with in this work, 65°–85°C, the solubilities calculated from Eq. [1] vary from  $2.5 \times 10^{15}$  atom/cm<sup>3</sup>. However, the scattering of Cu at the surface in general is superimposed on Cd scattering from deeper in the sample, and the scattering from one atom of Cd is greater than the scattering from one atom of Cu by a factor  $(Z_{\text{Cd}}/Z_{\text{Cu}})^2 = (48/29)^2 = 2.74$ . Because of these problems, we are limited to measuring copper atomic concentrations  $\cong 1/100$  of the Cd atomic concentration. This works out to a practical limit of about  $2 \times 10^{20}$  Cu atom/cm<sup>3</sup>. Thus any copper which we detect must be tied up in a compound, since the maximum solubility of copper in CdS is below our practical detection limits for this system by a factor of 10<sup>5</sup>.

It is well documented that the Cu-S phase diagram is complicated (7). A large number of  $\text{Cu}_x\text{S}$  compounds exist near a value of  $x = 2.0$ . Ion backscattering cannot measure microstructure. At best it measures atomic ratios averaged over the beam area (typically  $\sim 1 \text{ mm}^2$  as a function of depth. Other workers have shown by x-ray diffraction techniques (7) that the  $\text{Cu}_x\text{S}$  compound which forms on single crystal CdS during the dipping reactions is predominantly  $\text{Cu}_2\text{S}$ . For our purpose, however, the exact stoichiometry of the Cu-S compound makes little difference. Thus as we refer to  $\text{Cu}_x\text{S}$ , we have assumed  $x = 2.0$  for calculations. It is possible that ternary Cd-Cu-S compounds are formed, which would change some of the conclusions presented here. However, x-ray diffraction measurements (7) by other workers did not show evidence for such compounds.

Stopping power data for He ions in CdS are limited (8) and none exist for He in  $\text{Cu}_2\text{S}$ , so values for Cd, Cu, and S were used (9) to generate values of the stopping power of CdS and  $\text{CuS}_{0.5}$  for He ions as a function of energy by assuming Bragg's Rule for additivity of atomic stopping powers applied to CdS and  $\text{CuS}_{0.5}$ . These values were then fit to the Brice formula (10) to give an analytic expression for the electronic stopping power,  $\epsilon$ . The values of  $\epsilon$  used, along with the resultant Brice parameters, are listed in Table I.

Since the Brice techniques depend on comparing the scattering from the heaviest component of a two-

component sample to the scattering from a reference sample composed of the pure heaviest component, the amount of the lighter component required to produce the observed reduction in scattering from the heavier component is calculated and its scattering yield is subtracted from the total scattering spectrum at the appropriate energy. The exact choice of this energy is critical. If the energy is slightly too high or too low, a dip or bump will be produced in the calculated scattering yield from the heavier component with a corresponding bump or dip in the calculated scattering yield from this lighter component at a greater depth. Fortunately, if the chosen energy is close to the appropriate energy, these inaccuracies are limited in magnitude and depth and can easily be removed manually. The contribution of the sulfur to the scattering spectrum has been completely neglected in using the Brice extraction technique. This is not a serious error as long as we confine ourselves to analyses of spectra at energies above that expected for scattering from sulfur atoms at the surface.

Figure 2 shows the results of the extraction process for the data of Fig. 1. The upper part of the figure shows the CdS scattering after subtraction of the  $\text{CuS}_{0.5}$  scattering which is shown in the middle section. The lower part of the figure shows the depth distribution of  $\text{CuS}_{0.5}$ .

### Results and Discussion

The effect of crystallographic orientation of the CdS substrate on the rate and nature of  $\text{Cu}_2\text{S}$  formation was rather large. Figure 3 shows backscattering spectra for samples of the three orientations after dipping treatment at 85°C for 45 sec. The A-face and B-face samples show similar behavior with more  $\text{Cu}_2\text{S}$  being formed on the A face than on the B face. Both of these samples have a well-defined surface layer of pure  $\text{Cu}_2\text{S}$ . Behind the surface layer the ratio of  $[\text{Cu}_2\text{S}]/[\text{CdS}]$  as a function of depth decreases mono-

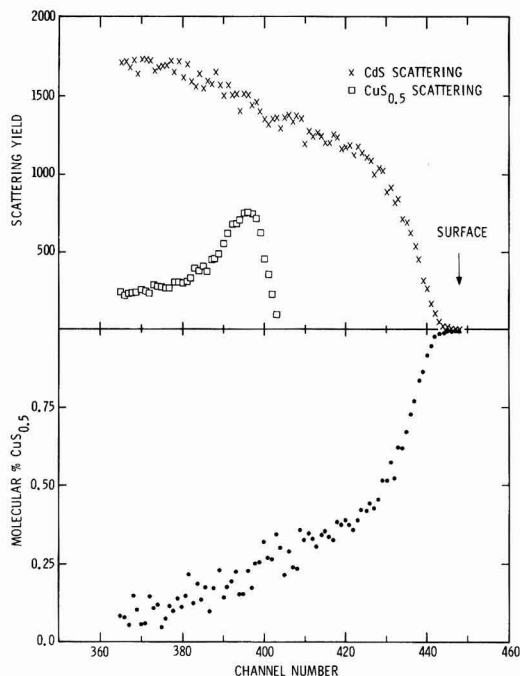


Fig. 2. The top of this figure shows the scattering from Cd (X) and Cu ( $\square$ ) assuming that they are always present in the forms CdS and  $\text{CuS}_{0.5}$ , respectively. The original data is that from the top of Fig. 1. In the bottom of Fig. 2 the molecular concentration of  $\text{CuS}_{0.5}$  is calculated from the separated spectra shown above it.

Table I.  $\epsilon \times 10^{-15} \text{ eV cm}^2/\text{atom}$

Energy (keV)	Cd	Cu	S	Brice parameters		
				CdS	$\text{CuS}_{0.5}$	
400	96.33	62.41	62.12			
600	107.0	68.20	68.61			
800	112.0	71.77	69.72			
1000	113.0	73.58	67.75			
1200	111.4	74.05	64.72	$Z_2$	64	37
1400	108.1	73.50	61.48	$Z$	2.077	2.029
1600	103.8	72.24	58.37	$a$	0.3504	0.3591
2000	94.71	68.48	52.89	$n$	3.249	3.021
2800	84.81	62.0	43.88			
4000	72.53	54.72	35.83			

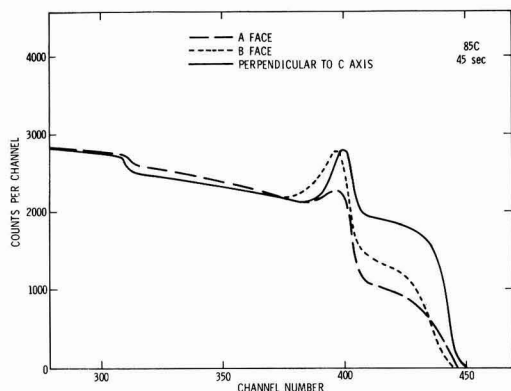


Fig. 3. Backscattering spectra from samples of the three different orientations studied for a dipping treatment of 45 sec at 85°C. The lines were drawn through the actual data points for clarity.

tonically with increasing depth as can be seen from the Cd scattering yield in the energy region between channels 410 and 450. In contrast, the  $\langle 11\bar{2}0 \rangle$  sample shows a surface layer of  $\text{Cu}_2\text{S}$  with no significant Cu scattering at depths beyond the surface layer. This can also be seen in the sharpness of the Cd scattering edge for the  $\langle 11\bar{2}0 \rangle$  sample indicating a  $\text{Cu}_2\text{S}$ -CdS interface at very well-defined depth.

The behavior on the  $\langle 11\bar{2}0 \rangle$  sample can be analyzed without recourse to the Brice subtraction technique. By simply integrating the counts under the copper scattering peak, a measure of the  $\text{Cu}_2\text{S}$  formation is obtained. Data of the formation of  $\text{Cu}_2\text{S}$  on the face perpendicular to the  $\langle 11\bar{2}0 \rangle$  axis are shown in Fig. 4 as a function of dipping time at various temperatures and for both polished and etched samples dipped at 75°C. The general behavior of the curves shows a rapid formation of  $\text{Cu}_2\text{S}$  followed by a period of slower growth. In all cases investigated, the growth slowed at thicknesses between  $1.5$  and  $2 \times 10^{17}$   $\text{CuS}_{0.5}$  molecules  $\text{cm}^{-2}$ . If we assume that this layer is  $\text{Cu}_2\text{S}$  with a bulk density of  $5.6 \text{ g/cm}^3$  (11), the thickness range is 350-500Å. The rapid increase in the amount of  $\text{Cu}_2\text{S}$  observed, followed by a slower growth is most probably related to nucleation of the  $\text{Cu}_2\text{S}$  layer on the surface of the CdS. Such effects have previously been suggested by Fahrenbuck (3). In the spectra which showed very small amounts of  $\text{Cu}_2\text{S}$ , the Cu scattering peak is not energy-resolution limited, but is wide

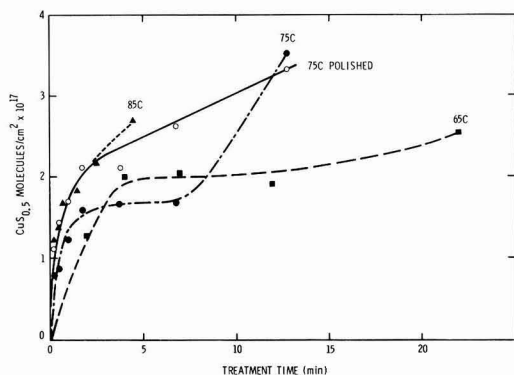


Fig. 4. Total amount of  $\text{CuS}_{0.5}$  formed on  $\langle 11\bar{2}0 \rangle$  samples as a function of time at different dipping temperatures 65°C (■), 75°C (●), 85°C (▲). Also shown are data for a polished sample treated at 75°C (○).

enough to correspond to  $\sim 300\text{Å}$  of  $\text{Cu}_2\text{S}$ . As the treatment time is lengthened, the peak increases in height without appreciable widening, suggesting that  $\text{Cu}_2\text{S}$  nucleates at favorable spots on the surface and the nuclei are about 300Å thick. After a layer of  $\text{Cu}_2\text{S}$  has been formed over the entire surface, the process is no longer controlled by nucleation, but either by the reaction rate for the conversion of CdS to  $\text{Cu}_2\text{S}$  or by diffusion of Cu through the already formed layer of  $\text{Cu}_2\text{S}$ .

As discussed in the previous section, the Brice technique has been applied to the A-face spectra to generate data on the depth distribution of  $\text{Cu}_2\text{S}$  on samples of that orientation. Figure 5 shows data on the depth distribution of  $\text{Cu}_2\text{S}$  subject to the assumptions explained in the previous section. The solid lines are drawn through the actual data points which resemble the data points shown in the bottom half of Fig. 2.

These depth distributions resemble diffusion profiles, but it is important to realize that they cannot be diffusion profiles. The amounts of Cu measured in these experiments are many orders of magnitude above the amounts which can be dissolved in CdS as explained in the previous section. This result suggests that there is lateral variation in  $\text{Cu}_2\text{S}$  formation across the area of the analyzing beam. At any given depth there are regions of  $\text{Cu}_2\text{S}$  and regions of CdS. Since the amount of  $\text{Cu}_2\text{S}$  decreases monotonically with increasing depth in the CdS, a model of cone-shaped regions of  $\text{Cu}_2\text{S}$  growing into the CdS is suggested. Such behavior could easily arise if growth took place preferentially at defects such as dislocations. But whatever the course,  $\text{Cu}_2\text{S}$  growth parallel to the C axis appears to take place with a very non-uniform interface, whereas the interface is much more uniform for growth perpendicular to the C axis.

If the growth of the  $\text{Cu}_2\text{S}$  is limited by the ion-exchange reaction rate, the concentration vs. depth should be linear beyond the initial surface layer. If the limitation is diffusion of Cu through the  $\text{Cu}_2\text{S}$  layer which has already formed, a plot of the logarithm of concentration vs. depth squared should be a straight line. Unfortunately, our data are not sufficiently accurate to distinguish these two forms of kinetic behavior. This does not, however, prevent us from obtaining data on the energetics of the reaction. As has been previously observed (12), by plotting the time-to-equivalent backscattering spectra on an Arrhenius-type diagram, the slope of the line connecting equivalent spectra gives the activation energy

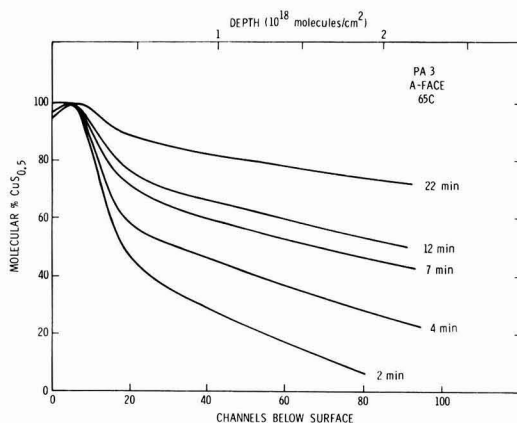


Fig. 5. Depth distributions of  $\text{CuS}_{0.5}$  as a function of energy (lower horizontal axis) and equivalently depth (upper horizontal axis). These concentrations are the average over a 1 mm beam-spot area.

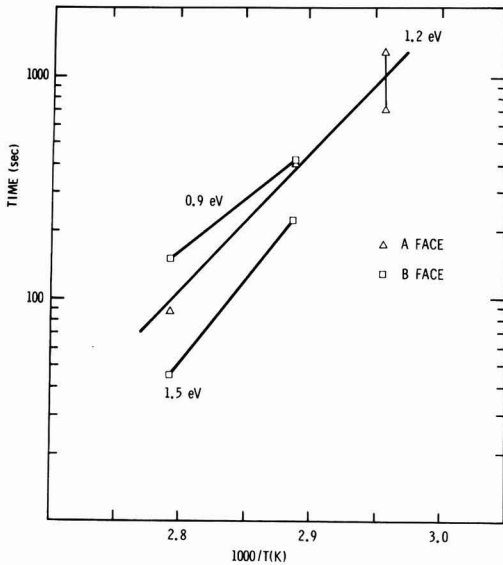


Fig. 6. Arrhenius plot of time to equivalent spectra for A-face ( $\Delta$ ) and B-face ( $\square$ ) samples. The heavy lines connect the equivalent points. The two points at  $65^\circ\text{C}$  connected by a vertical line indicate that the equivalent spectrum fell somewhere between the two points.

of the process. Data for the A and B faces are shown in Fig. 6. There is some scattering in the slope, most probably due to difficulties in picking exactly equivalent spectra, but the data are fairly consistent with an activation energy of 0.9–1.5 eV. It must be cautioned that if more than one process is active during the time taken to produce the spectra, the activation energy derived from Fig. 6 will not be simply related to either individual process, but this is the case in other methods of determining activation energies as well.

Some preliminary results on the effect of surface preparation were obtained on samples which had been polished to an optical finish using  $0.25\ \mu\text{m}$  diamond paste. Figure 4 shows the growth of  $\text{Cu}_2\text{S}$  vs. dipping time for a polished and a normal-etched  $\langle 11\bar{2}0 \rangle$  sample dipped in a  $75^\circ\text{C}$  solution. The short time behavior of the polished sample shows much faster growth than the etched sample, but the curves then cross at high values of  $\text{Cu}_2\text{S}$  layer thickness.

For A-face samples which had been polished, the difference between polished and etched samples is the most apparent. As can be seen in the spectra shown in Fig. 7, the Cu scattering for polished samples shows a less rapid change in  $\text{Cu}_2\text{S}$  concentration vs. depth than for the etched sample. Indeed, the polished sample almost has a uniform layer of  $\text{Cu}_2\text{S}$  which grows linearly in time, but as can be noticed from the Cd scattering remaining in the region between channels 410–450, the layer is not uniform.

We suggest that these results indicate the  $\text{Cu}_2\text{S}$  formation on CdS is very dependent on surface damage and on the crystalline perfection of the near-surface layers of the host CdS crystal.

### Conclusions

The results contained in this paper represent the first application of energetic ion backscattering to the study of an aqueous chemical reaction. While mostly phenomenological, information has been obtained on  $\text{Cu}_2\text{S}$  formation on single crystal CdS in a thickness region of technological importance (0–5000Å). There exist no other data in this region of interest. We

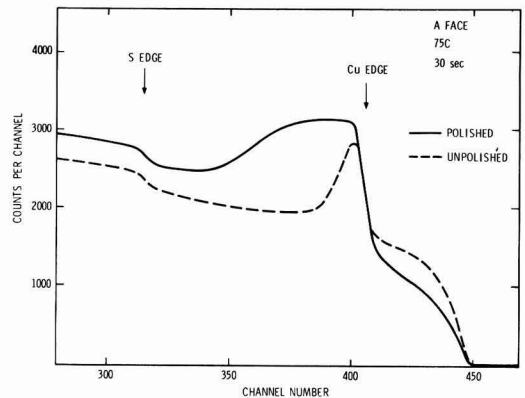


Fig. 7. Backscattering spectra from a polished and an unpolished A-face sample. Both samples were dipped for 30 sec at  $75^\circ\text{C}$ . The lines were drawn through the individual data points.

have demonstrated that the reaction is faster on the A face than the B face, and faster along the C axis than perpendicular to it. Estimates of the energetics of the reaction along the C axis have been obtained. We have shown that the  $\text{Cu}_2\text{S}$  layer formed on single crystal CdS is not uniform in depth, but is propagated into the crystal with great lateral nonuniformity. It is suggested that dislocations may enhance  $\text{Cu}_2\text{S}$  formation due to the local lattice strain. Also, the effects of surface preparation of  $\text{Cu}_2\text{S}$  layer formation have been shown to be quite large.

CdS is a complicated material and samples from different suppliers or samples from the same supplier, but cut from different boules, behaved very differently. However, if we are to ever understand the mechanisms of  $\text{Cu}_2\text{S}$  formation on thin-film CdS where the effects of polycrystallinity and grain morphology may very well be large, we must first attempt to understand what happens in the simpler system of  $\text{Cu}_2\text{S}$  on single crystal CdS.

### Acknowledgments

The author would like to thank J. H. Smalley for his skilled assistance with the experimental work and R. Berg for his valuable comments on the CdS- $\text{Cu}_2\text{S}$  system.

This work was supported by the United States Energy Research and Development Administration (ERDA).

Manuscript submitted July 18, 1975; revised manuscript received Sept. 3, 1975. This was Paper 121 presented at the Toronto, Canada, Meeting of the Society, May 11–16, 1975.

Any discussion of this paper will appear in a Discussion Section to be published in the December 1976 JOURNAL. All discussions for the December 1976 Discussion Section should be submitted by Aug. 1, 1976.

Publication costs of this article were partially assisted by Sandia Laboratories.

### REFERENCES

1. J. A. Borders and S. T. Picraux, *Proc. IEEE*, **62**, 1224 (1974).
2. E. F. Warekois, M. C. Lavine, A. N. Mariano, and H. C. Gatos, *J. Appl. Phys.*, **33**, 690 (1962); see also *ibid.*, **37**, 2203 (1966).
3. A. L. Fahrenbruck, Ph.D. Thesis, Stanford University (1973).
4. Tencomp Systems, Model TP-5000.
5. D. K. Brice, *Thin Solid Films*, **19**, 121 (1973).
6. G. A. Sullivan, *Phys. Rev.*, **184**, 796 (1969).
7. L. R. Shiozawa et al., "Research on the Mechanism of the Photovoltaic Effect in High Efficiency CdS Thin-Film Solar Cells," Aerospace Research-Laboratories Final Report, Contract AF33(615)-5224 (July 1969).



8. P. F. Engel, J. A. Borders, and F. Chernow, *J. Appl. Phys.*, **45**, 38 (1974).  
 9. J. F. Ziegler and W. K. Chu, *Thin Solid Films*, **19**, 281 (1973).  
 10. D. K. Brice, *Phys. Rev.*, **A6**, 1791 (1972).  
 11. Handbook of Chemistry and Physics, 47th ed., The Chemical Rubber Co., Cleveland, Ohio (1966).  
 12. J. A. Borders, *Thin Solid Films*, **19**, 359 (1973).

## The Effects of Processing on Hot Electron Trapping in SiO<sub>2</sub>

R. A. Gdula

IBM System Products Division, East Fishkill Facility, Hopewell Junction, New York 12533

### ABSTRACT

Avalanche injection of hot electrons into the insulator of an MOS capacitor has been used to study electron trapping in SiO<sub>2</sub>. Oxides formed by thermal oxidation in dry O<sub>2</sub>, O<sub>2</sub> + HCl, O<sub>2</sub> + H<sub>2</sub>O, steam, and chemical vapor-deposited (CVD) SiO<sub>2</sub> were subjected to avalanche charging. Pure, dry thermal SiO<sub>2</sub> was found to trap up to  $2.6 \times 10^{12}$  e/cm<sup>2</sup>. The trapping efficiency of SiO<sub>2</sub> varied by three orders of magnitude, depending on forming and annealing conditions.

Goetzberger and Nicollian (1) reported the occurrence of avalanche-produced hot carriers as early as 1966. Subsequently, the conditions under which hot carriers can be produced in MOS structures were outlined (2), and hot carrier injection was used to study high current densities and trapping in SiO<sub>2</sub> (3, 4). At about the same time, it was discovered that hot carrier injection could degrade the performance of silicon planar transistors (5, 6) and produce instabilities in MOSFET's (7). A practical use for the phenomenon was found with the introduction of the FAMOS<sup>1</sup> device (8). These problems induced further studies (9-13).

Avalanche injection of hot carriers into SiO<sub>2</sub> can be conveniently produced using a simple MOS capacitor. A high frequency (> 1 kHz) a-c signal of sufficient amplitude is impressed across the capacitor. Once each cycle the silicon beneath the field plate becomes depleted because the inversion layer cannot form quickly enough. When the field in the silicon becomes strong, large quantities of minority carriers are created by ionization multiplication, and the Si is said to avalanche. These minority carriers are accelerated toward the Si-SiO<sub>2</sub> interface by the field across the depletion region. Some achieve sufficient energy to overcome the potential barrier (~3.25 eV) at the interface and enter the SiO<sub>2</sub>. Most drift through the SiO<sub>2</sub> and are collected on the metal field plate, but some become trapped in the SiO<sub>2</sub>. The details of this trapping and how it is affected by processing are the subject of this paper.

### Experimental Procedures

**Sample preparation.**—Silicon wafers (5.7 cm diameter, boron-doped, p-type, <100> orientation of various resistivities) were quartered, stripped in concentrated HF, and given an inorganic cleaning in hot aqueous solutions of NH<sub>4</sub>OH + H<sub>2</sub>O<sub>2</sub> and HCl + H<sub>2</sub>O<sub>2</sub> finished by copious rinsing in deionized water. SiO<sub>2</sub> films were formed by thermal oxidation at 1000°C in various ambients, or provided by CVD. When required, annealing in N<sub>2</sub> or Ar was performed at 1050°C for various lengths of time. Pure aluminum was evaporated from an e-gun source through metal masks to form  $5.32 \times 10^{-3}$  cm<sup>2</sup> capacitors. Aluminum was also deposited on the wafer back sides and annealed in N<sub>2</sub> at 400°C for 20 min to provide ohmic contacts to the silicon. Mobile charge levels were checked by the I-V loop technique (14, 15) after biasing the capacitors at  $+2 \times 10^6$  V/cm, 200°C, for 10 min. Mobile charge levels in all cases were found to be  $< 3 \times 10^{10}$  charges/cm<sup>2</sup>. SiO<sub>2</sub> film thickness was measured with an ellipsometer.

**Measurement techniques.**—Starting with a virgin (unprobed) capacitor, the high frequency (1 MHz) C-V characteristic was determined. Then the capacitor was avalanched for specified time periods ranging from 1 sec to several thousand seconds using the circuit of Ref. (4). The average d-c current flowing through the sample was monitored by a Keithley Model 615 electrometer operating in the normal mode. The sample was then reconnected to the C-V measuring apparatus through a switch box and the C-V characteristic redetermined. The number of hot electrons injected into and passed through the SiO<sub>2</sub> per unit area and collected on the Al field plate ( $N_{\text{collected}}$ ) was calculated from the area of the field plate and the integrated area under the I vs. time curve. A measure of the number of electron charges trapped per unit area ( $\Delta N_{\text{eff}}$ ) was calculated from the shift between the C-V traces using the equation

$$\Delta N_{\text{eff}} = \frac{\Delta V_{\text{FB}} \epsilon_0 K_{\text{SiO}_2}}{q D_{\text{SiO}_2}} \quad [1]$$

where  $\Delta V_{\text{FB}}$  is the lateral displacement of the C-V traces at the flatband condition in volts,  $\epsilon_0$  is the permittivity of free space (farad/cm),  $K_{\text{SiO}_2}$  is the SiO<sub>2</sub> dielectric constant (taken to be 4),  $q$  is the electronic charge in coulombs, and  $D_{\text{SiO}_2}$  is the SiO<sub>2</sub> thickness (cm). Although Eq. [1] assumes all the trapped charge is located in a uniform sheet at the Si-SiO<sub>2</sub> interface which may not be strictly correct,  $\Delta N_{\text{eff}}$  is useful in predicting the behavior of actual MOSFET devices. For most of the work it was found convenient to keep the current through the oxide constant by continuously adjusting the applied voltage. All measurements were made with the sample in darkness.

### Results and Discussion

**Operating conditions.**—It quickly became apparent that the silicon substrate doping level had a profound effect on sample behavior. The applied voltage necessary to sustain avalanche currents (at  $J_{\text{dc}} = 2 \times 10^{-6}$  A/cm<sup>2</sup>) varied drastically as a function of  $N_A$  as seen in Fig. 1. ( $J$  represents the particle current through the device.) This is in agreement with the work of Goetzberger and Nicollian (2) who considered the edge of the depletion region to be a step junction. According to their data, uniform avalanche behavior can be expected in the  $10^{16}$ - $10^{18}$  atom/cm<sup>3</sup> doping range. At lighter doping levels edge breakdown dominates, and at higher doping levels direct tunneling occurs. For the purposes of this investigation, it was found convenient to use the  $7 \times 10^{15}$  to about  $1 \times 10^{17}$  range; accordingly, most of the samples investigated were constructed on 0.4 or 2 ohm-cm material.

Key words: avalanche injection, hot minority carriers, annealing.  
<sup>1</sup> Floating gate avalanche injection metal oxide semiconductor.

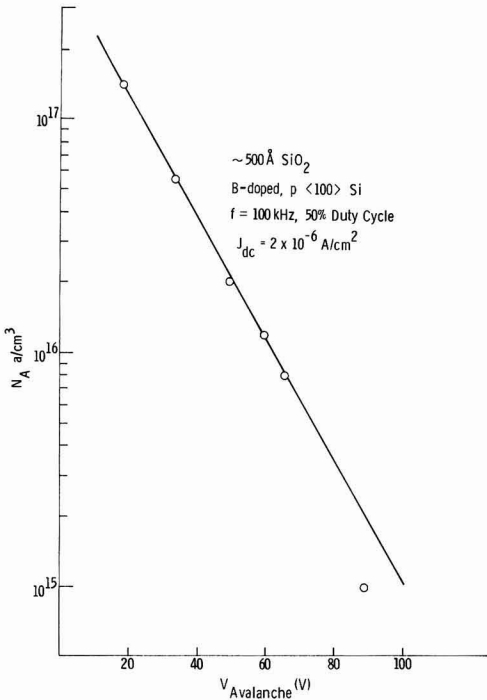


Fig. 1. Applied voltage necessary to sustain an avalanche current of  $2 \times 10^{-6}$  A/cm<sup>2</sup> as a function of Si doping level.

It was also quite apparent that the avalanching conditions affected behavior. For example,  $J_{dc} < 10^{-7}$  A/cm<sup>2</sup> did not cause C-V shifts  $> 10$  mV (the accuracy of the measurements) in reasonable experimental times ( $\sim 100$  sec), while  $J_{dc} > 10^{-3}$  A/cm<sup>2</sup> caused insulator dielectric breakdown or a peculiar damage change in the silicon that shows up as an abnormal C-V trace and gives zero C-V shifts even for passage of very large numbers of electrons. Frequency, duty cycle, and pulse shape also affected  $J_{dc}$ . For the results described here, the apparatus was operated within the following conditions:  $J_{dc} = 2 \times 10^{-7}$  to  $2 \times 10^{-5}$  A/cm<sup>2</sup>,  $f = 100$  kHz, duty cycle = 50%, pulse rise time = 0.8  $\mu$ sec, and pulse fall time = 0.16  $\mu$ sec.

*Typical data and conditions.*—Typical data on a virgin MOS capacitor whose oxide was thermally grown in dry O<sub>2</sub> at 1000°C and subsequently N<sub>2</sub> annealed is shown in Fig. 2. From such a plot the important parameter, instantaneous effective trapping efficiency  $TE$ , defined as

$$TE \equiv \frac{dN_{eff}}{dN_{collected}} \quad [2]$$

may be calculated. It is instructive to note that initially  $TE$  is quite high, trapping 2 electrons for every 100 electrons passing through the oxide, but  $TE$  gradually falls off to very low values. When very large numbers of electrons have passed through the structure, the trapping appears to saturate and then relax as shown in Fig. 3, which shows more extensive data from the identical sample discussed in Fig. 2. This maximum trapping is another important parameter, as it puts an upper bound on the threshold shifts of MOSFET devices and in principle allows a calculation of trapping density in the dielectric film. However, assumptions as to the spatial distribution of the charges are required. Moreover, we expected a saturation of the C-V shift but not a reversal of it. Reversal implies a reduction in the net moment of charge which could be caused

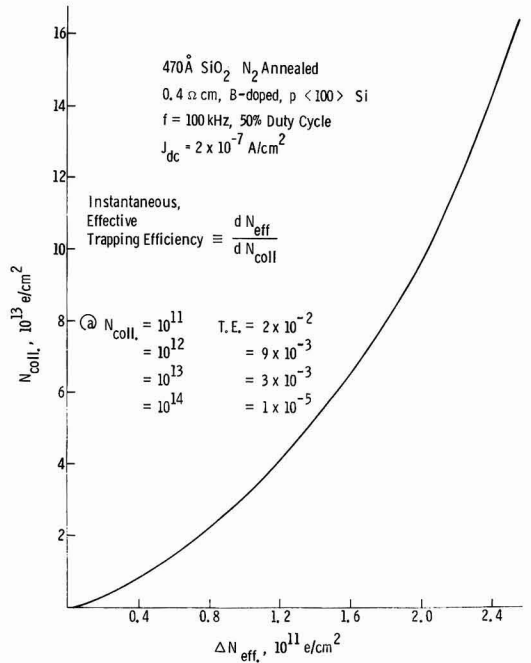


Fig. 2. Typical linear plot of MOS capacitor data

either by detrapping of electrons or compensation by positive charges.

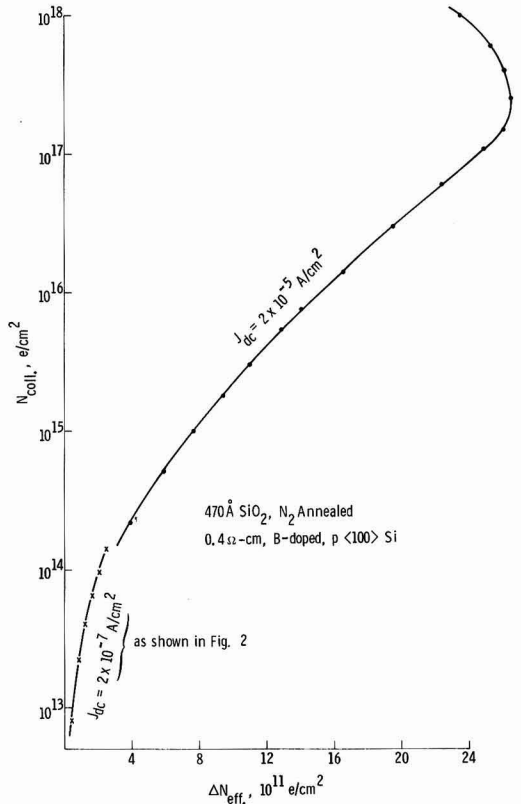


Fig. 3. Typical log-normal plot of MOS capacitor data

A simple experiment was performed to determine the stability of these trapped hot electrons in  $\text{SiO}_2$ . A typical sample of  $\text{N}_2$  annealed, dry thermal oxide  $\sim 570\text{\AA}$  thick had an initial  $N_{\text{eff}} = 0.78 \times 10^{11}$  positive charge/cm $^2$ . It was avalanche charged at  $J_{\text{dc}} = 2 \times 10^{-5}$  A/cm $^2$  for 1000 sec. As quickly as possible (in about 10 sec) the C-V characteristic was retraced and  $N_{\text{eff}}$  was found to be  $11.24 \times 10^{11}$  negative charges/cm $^2$ . Thereafter the C-V trace was redetermined at specified intervals with the capacitor allowed to float in between. The results are given in Fig. 4. Less than 10% of the charge was lost in 270,000 sec and 11 C-V trace sweeps ( $-5$  to  $+5\text{V}$ ) over that time. This sample was also subjected to  $\pm 5 \times 10^6$  V/cm fields for 100 sec with no significant detrapping. This is in agreement with Nicollian *et al.* (9) who also found their trapped electrons to be quite stable.

To assess the magnitude of the oxide field during avalanche charging, a series of samples with  $\text{N}_2$  annealed, dry thermal oxide was made with  $D_{\text{SiO}_2}$  varying from 250 to 1200 $\text{\AA}$ . Under standard conditions ( $f = 100$  kHz, 50% duty cycle) the applied voltage was determined to sustain avalanche in each sample at  $J_{\text{dc}} = 2 \times 10^{-6}$  A/cm $^2$ . These are shown in Fig. 5. By extrapolating the line to zero oxide thickness, the silicon is found to avalanche at 25.7V. Since the field in the silicon cannot exceed the avalanche field, any voltage above  $V_{\text{avalanche}}$  must be dropped in the oxide. The slope of the line yields  $E_{\text{ox}} = 1.7 \times 10^6$  V/cm at the start of avalanche. During long-term avalanching,  $E_{\text{ox}}$  would increase to only about  $3 \times 10^6$  V/cm because  $V_{\text{applied}}$  was continuously increased to keep  $J_{\text{dc}}$  constant. Therefore, detrapping of electrons is unlikely.

For some isolated samples fast surface-state densities were measured by the quasistatic C-V technique (16). Fast state density at  $V_{\text{FB}}$  was found to change little, sometimes decreasing, sometimes increasing for

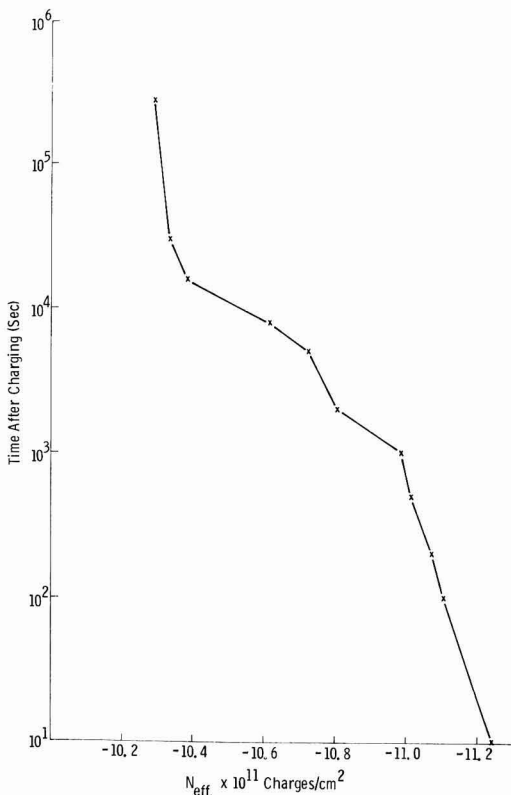


Fig. 4. Detrapping of charge-dry thermal  $\text{SiO}_2$ , floating

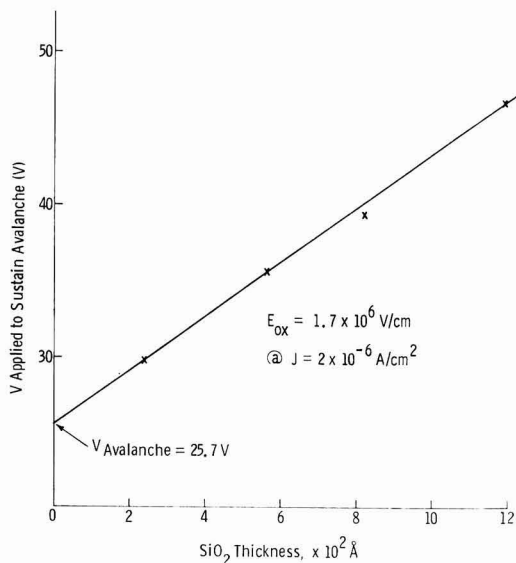


Fig. 5.  $V_{\text{applied}}$  required to sustain avalanche at  $J_{\text{dc}} = 2 \times 10^{-6}$  A/cm $^2$  as a function of oxide thickness.

$N_{\text{collected}} < 10^{16}$  e/cm $^2$ , but increased dramatically in the region where the C-V shifts slowed down and reversed direction. It is likely then that the reversal of  $N_{\text{eff}}$  is due to fast surface-state generation. This severely complicates the task of determining the true number of electrons trapped, and hence the use of  $\Delta N_{\text{eff}}$  for comparative purposes.

**Effects of oxide processing.**—To compare trapping in  $\text{SiO}_2$  formed by various typical processes, a series of samples was made having  $D_{\text{SiO}_2} \approx 500\text{\AA}$ , with no high-temperature annealing. Thermal  $\text{SiO}_2$  films were grown in dry  $\text{O}_2$ , dry  $\text{O}_2 + 3\%$  HCl, dry  $\text{O}_2 + 3\%$   $\text{H}_2\text{O}$ , and steam. CVD oxide films were deposited using the  $\text{SiH}_4 + \text{O}_2$  reaction at  $800^\circ\text{C}$ . BSG films containing  $\sim 5$  weight per cent (w/o)  $\text{B}_2\text{O}_3$  were deposited using the same reaction with diborane as the dopant source, also at  $800^\circ\text{C}$ . These samples were avalanche-charged at  $J_{\text{dc}} = 2 \times 10^{-5}$  A until the trapping saturated. Their behavior is compared in both Fig. 6 and Table I; the results are quite amazing.  $\text{SiO}_2$  was made to accumulate  $> 5 \times 10^{12}$  negative charges/cm $^2$ . Also there is a three order of magnitude difference in the rate of trapping between dry thermal oxide and B-doped CVD oxide. The data suggest that the degree of trapping depends somehow on the OH concentration incorporated in the oxide during forming. The hydroxyl content of the samples listed in Table I was determined from the  $2.73 \mu\text{m}$  absorption peak in the ir spectrum following

Table I. Trapping parameters of  $\text{SiO}_2$  formed by different processes on 0.4 ohm-cm, B-doped,  $p < 100 >$  Si

Oxide type	Initial $V_{\text{FB}}$ (V)	Effective saturated trapping density ( $\times 10^{11}$ /cm $^2$ )	Effective trapping efficiency ( $\times 10^{-9}$ ) <sup>(a)</sup>	Hydroxyl concentration (w/o)
Dry $\text{O}_2$	-1.28	17	5.7	Not detected
Dry $\text{O}_2 + 3\%$ HCl	-1.28	18	16	Not detected
Dry $\text{O}_2 + 3\%$ $\text{H}_2\text{O}$	-1.24	23	58	—
Steam	-1.51	39	180	0.10
CVD	-1.20	56	520	0.44
B-doped CVD	-0.80	57	5000	0.45

<sup>(a)</sup> When  $1 \times 10^{12}$  electrons/cm $^2$  have been trapped.

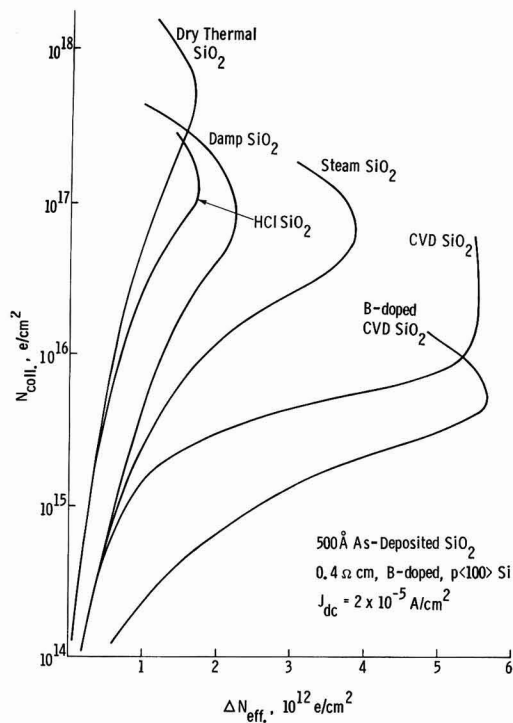
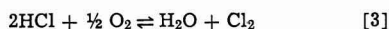


Fig. 6. Trapping behavior of SiO<sub>2</sub> formed by different processes; no high-temperature anneal.

the method of Hetherington and Jack (17). The values for the CVD oxides are well within the levels that can be expected (18). The 0.1 w/o OH measured for the steam oxide is slightly less than that reported by Burkhardt using radio tracer techniques (19). The hydroxyl concentration of the dry O<sub>2</sub> + 3% H<sub>2</sub>O sample was not measured. No OH in the dry O<sub>2</sub> + 3% HCl sample could be detected by our measurements although, by inference, some should be present in the oxide due to the fact that about 15% of HCl dissociates at 1000°C, according to the equilibrium reaction



so the oxidizing ambient contained about 0.5% H<sub>2</sub>O by calculation. There should be no detectable OH concentration in thermal SiO<sub>2</sub> grown in dry O<sub>2</sub> (18). The OH group has been reported (3, 4, 9) to be associated with an electron-capturing center in SiO<sub>2</sub>. It also appears from our current data that boron incorporated in SiO<sub>2</sub> is associated with a strong trapping center. This has been observed by Young for the case of B implanted in SiO<sub>2</sub> (20). If B in SiO<sub>2</sub> is associated with an electron trapping center, this may explain why dry thermal SiO<sub>2</sub> grown on heavily B-doped silicon traps more than SiO<sub>2</sub> grown on lightly B-doped silicon. Figure 7 shows comparisons for two samples processed under identical conditions (oxide grown in dry O<sub>2</sub> at 1000°C, annealed in dry N<sub>2</sub> at 1050°C for 15 min). Because of the favorable segregation coefficient, B is incorporated into the growing SiO<sub>2</sub> film. It is expected that a greater boron concentration in the oxide will result from growth on a more heavily B-doped substrate. The data shows that thermal oxide on 0.4 ohm-cm B-doped silicon traps more efficiently than thermal oxide on 2 ohm-cm, B-doped silicon.

Since the OH group in SiO<sub>2</sub> has been associated with an electron trapping center, and since OH can be expelled from SiO<sub>2</sub> by heating, it is instructive to determine the effects of high-temperature annealing.

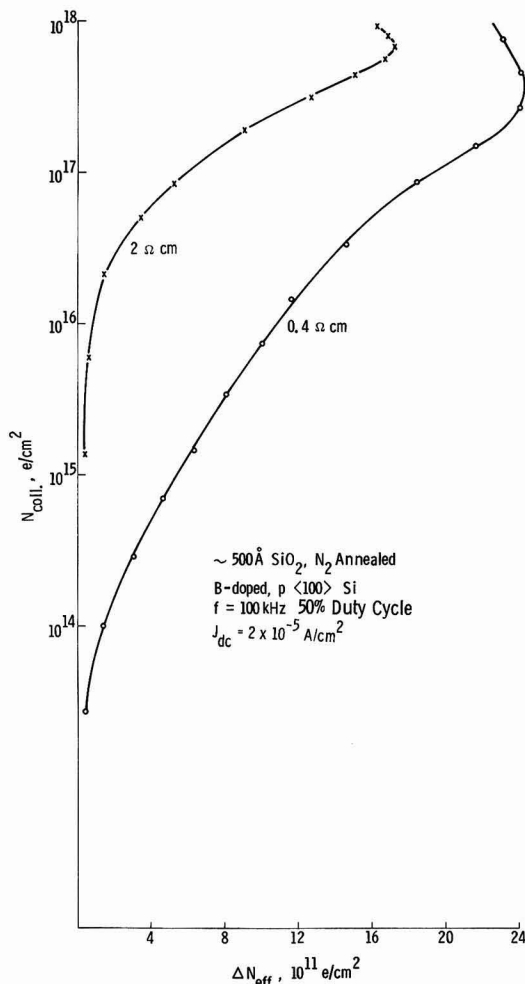


Fig. 7. Trapping in dry, thermal SiO<sub>2</sub> grown on Si of different B-doping levels.

Accordingly, oxide samples from the same experiment as those reported in Fig. 6 and Table I were annealed in dry N<sub>2</sub> at 1050°C for 15 min. The results are reported in Table II. As divergent as the results were before annealing, after N<sub>2</sub> annealing all the SiO<sub>2</sub> films behaved quite similarly. The effect due to OH appears to have been leveled. Trapping decreased in the most efficient films, but increased in the least efficient films. This adverse effect of annealing on the least efficient films may be due to additional boron incorporation into the oxide during annealing. The BSG sample was not tested

Table II. Trapping parameters of SiO<sub>2</sub> after high-temperature N<sub>2</sub> annealing

Oxide type	Initial V <sub>FB</sub> (V)	Effective saturated trapping density (× 10 <sup>15</sup> /cm <sup>2</sup> )	Effective trapping efficiency (× 10 <sup>-6</sup> ) <sup>(a)</sup>
Dry O <sub>2</sub>	-0.91	25	59
Dry O <sub>2</sub> + 3% HCl	-0.85	22	24
Dry O <sub>2</sub> + 3% H <sub>2</sub> O	-0.86	22	29
Steam	-0.77	28	66
CVD	-0.65	24	29

<sup>(a)</sup> When 1 × 10<sup>12</sup> electrons/cm<sup>2</sup> have been trapped.

because boron diffusion occurred during annealing, and no C-V trace could be obtained.

Additional annealing experiments were done with 500Å oxide films grown in dry O<sub>2</sub> + 5% HCl. These samples were annealed for up to 300 min in N<sub>2</sub> and 960 min in Ar at 1050°C. These were then avalanche-charged and the results are shown in Fig. 8 and 9. Clearly annealing reduced trapping; after very long anneals these HCl-SiO<sub>2</sub> samples approached the behavior of dry O<sub>2</sub> SiO<sub>2</sub>.

### Conclusions

1. Hot electron avalanche injection is an effective method to study how processing affects trapping in SiO<sub>2</sub> films on silicon.

2. Pure, dry, thermal SiO<sub>2</sub> was found to trap as many as  $2.6 \times 10^{12}$  electrons/cm<sup>2</sup>.

3. The trapping efficiency of SiO<sub>2</sub> films can vary by three orders of magnitude, depending on the formation method.

4. The trapping ability of SiO<sub>2</sub> varies with its OH concentration, which in turn is affected by the forming process. OH groups in SiO<sub>2</sub> are associated with electron trapping centers.

5. Boron in SiO<sub>2</sub> may also be associated with an electron trapping center.

6. High-temperature annealing in a moisture-free ambient can reduce trapping in SiO<sub>2</sub> due to OH groups.

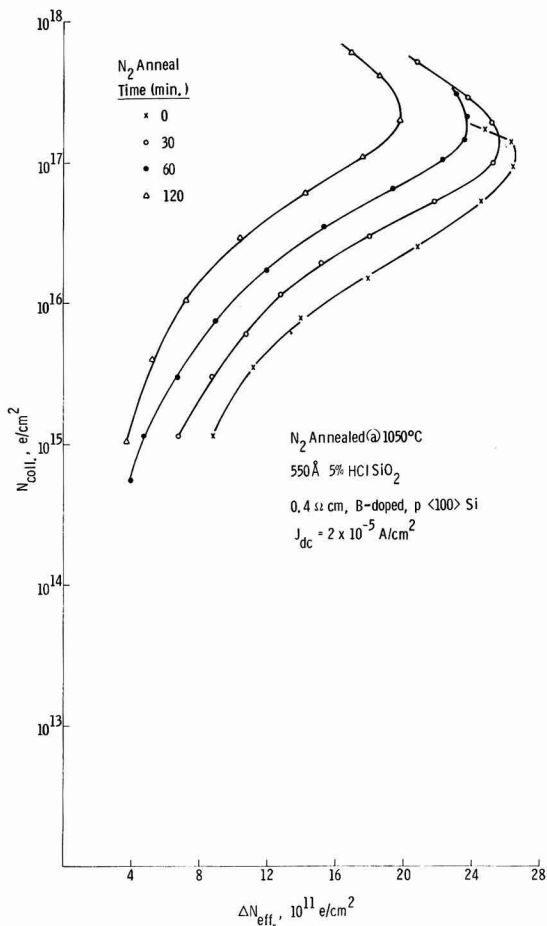


Fig. 8. Trapping in HCl oxide as a function of N<sub>2</sub> anneal time at 1050°C.

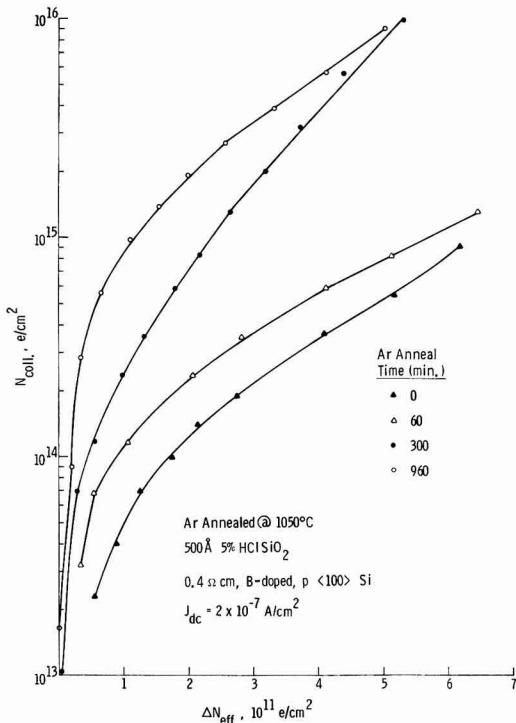


Fig. 9. Trapping in HCl oxide as a function of Ar anneal time at 1050°C.

### Acknowledgments

The author wishes to thank J. C. Hollis, F. J. Hoey, and E. J. Vishnesky for their assistance in sample preparation and electrical measurements, and W. A. Pliskin for ir measurements. Also thanks are due to E. L. Boyd, W. A. Pliskin, M. Shatzkes, and D. Young for many helpful discussions.

Manuscript submitted March 6, 1975; revised manuscript received Aug. 21, 1975.

Any discussion of this paper will appear in a Discussion Section to be published in the December 1976 JOURNAL. All discussions for the December 1976 Discussion Section should be submitted by Aug. 1, 1976.

Publication costs of this article were partially assisted by IBM Corporation.

### REFERENCES

1. A. Goetzberger and E. H. Nicollian, *Appl. Phys. Letters*, **9**, 444 (1966).
2. A. Goetzberger and E. H. Nicollian, *J. Appl. Phys.*, **38**, 4582 (1967).
3. E. H. Nicollian, A. Goetzberger, and C. N. Berglund, *Appl. Phys. Letters*, **15**, 174 (1969).
4. E. H. Nicollian and C. N. Berglund, *J. Appl. Phys.*, **41**, 3052 (1970).
5. J. F. Verwey, *Appl. Phys. Letters*, **15**, 270 (1969).
6. B. A. McDonald, *IEEE Trans. Electron Devices*, **ED-17**, 871 (1970).
7. H. Hara, Y. Okamoto and H. Ohnuma, *Japan. J. Appl. Phys.*, **9**, 1103 (1970).
8. D. Frohman-Bentchkowsky, "Digest of Technical Papers," IEEE Intern. Solid State Circuits Conf., p. 80, Lewis Winner, New York (1971).
9. E. H. Nicollian and C. N. Berglund, *J. Appl. Phys.*, **42**, 5654 (1971).
10. C. A. Neugebauer, J. F. Burgess, R. E. Joynson, and J. L. Mundy, *Thin Solid Films*, **13**, 5 (1972).
11. C. A. Neugebauer, J. F. Burgess, R. E. Joynson, and J. L. Mundy, *J. Appl. Phys.*, **43**, 5041 (1972).



12. J. Bonnet and L. Lassabaterre, *Thin Solid Films*, **22**, 177 (1974).
13. R. Verkuil, Unpublished work.
14. N. J. Chou, *This Journal*, **118**, 601 (1971).
15. M. Kuhn and D. J. Silversmith, *ibid.*, **118**, 966 (1971).
16. M. Kuhn, *Solid State Electron.*, **13**, 863 (1970).
17. G. Hetherington and K. H. Jack, *Phys. Chem. Glasses*, **3**, 129 (1962).
18. W. A. Pliskin and H. S. Lehman, *This Journal*, **112**, 1013 (1965).
19. P. J. Burkhardt, *ibid.*, **114**, 196 (1967).
20. D. Young, Unpublished work.

## Ionic Conductivity of Doped Beta-Lead Fluoride

John H. Kennedy\* and Ronald C. Miles\*

*University of California, Department of Chemistry, Santa Barbara, California 93106*

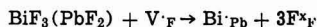
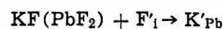
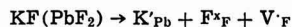
### ABSTRACT

The electrical conductivity of  $\beta$ -PbF<sub>2</sub> in single crystal and pressed pellets was measured by a-c bridge techniques. Alivalent cation fluoride doping was used to elucidate the conductivity mechanism in the extrinsic region, 25°-180°C. Conduction was shown to be via fluoride ion vacancies. Potassium fluoride dopant increased the ionic conductivity of  $\beta$ -PbF<sub>2</sub> from  $5 \times 10^{-7}$  to  $1 \times 10^{-3}$  ohm<sup>-1</sup>cm<sup>-1</sup> at room temperature. However, galvanic cells utilizing the higher conductivity of the doped material failed due to formation of a passivation layer of pure  $\alpha$ -PbF<sub>2</sub> at the anode/electrolyte interface.

Some of the properties of lead fluoride have been known since Tubandt studied the transport number in 1921 (1). However, the solid-state ionic defect formation and conduction mechanisms have only been recently investigated. Lead fluoride occurs in two phases which exist at room temperature. The  $\alpha$ -phase has an orthorhombic unit cell structure and is similar to the lead halides, PbCl<sub>2</sub> and PbBr<sub>2</sub>. Beta-lead fluoride is cubic like CdF<sub>2</sub> and CaF<sub>2</sub>, as are all transition metal fluorides whose cation-to-anion radius ratio is greater than or equal to 0.73. In a previously published part of our study of polycrystalline material we verified Tubandt's finding that at least the  $\beta$ -PbF<sub>2</sub> fluorite structure conducted by anionic migration, and that the  $\alpha$ -PbF<sub>2</sub> structure probably exhibited a similar mechanism (2). We also confirmed Sauka's findings that the  $\alpha$ -phase was metastable at room temperature and atmospheric pressure, while the  $\beta$ -phase is apparently stable up to the melting point. The conductivity of lead fluoride at high temperature near the melting point (822°C) was investigated by Derrington and O'Keeffe (3). They found unusually high values which they attributed to "dynamic ion disorder" of the fluoride sublattice. At lower temperatures, Schoonman *et al.* found two Arrhenius slopes and a knee where they met at about 200°C in single crystals of  $\beta$ -PbF<sub>2</sub> (4). Both Derrington and O'Keeffe (3) and Schoonman *et al.* (4) ascribed the high temperature conductivity of  $\beta$ -PbF<sub>2</sub> to fluoride interstitial ions which were formed by a Frenkel mechanism. The other cubic fluorides are also known to form interstitial defects in that manner (5-7). However, Schoonman stated that the knee he observed at 200°C was most likely a shift from interstitial movement to vacancy movement at lower temperatures, rather than being the usual transition from an intrinsic to extrinsic region. This was based on the fact that the upper slope was too low to be a heat of formation, and the trace impurities present should have generated fluoride vacancies.

In order to understand the low temperature conduction mechanism of  $\beta$ -PbF<sub>2</sub>, alivalent impurities were doped into the  $\beta$ -PbF<sub>2</sub> lattice. The concentration of defects will change with doping in order to maintain charge neutrality. As the following equations show, each KF introduced into  $\beta$ -PbF<sub>2</sub> may create a

fluoride ion vacancy or consume an existing interstitial, while each trivalent cation fluoride such as BiF<sub>3</sub> can consume an existing vacancy or create an interstitial



A change in the conductivity of  $\beta$ -PbF<sub>2</sub> upon doping with known impurities will determine whether the material is conducting via vacancies or interstitial ions.

### Experimental

*Alivalent doping.*—Orthorhombic  $\alpha$ -PbF<sub>2</sub> (ROC/RIC 99.999% pure) was used without further purification. Alivalent cation fluorides were doped into  $\beta$ -PbF<sub>2</sub> by diffusion and by making use of the  $\alpha$ - to  $\beta$ -phase transition. A melt of the mixtures was not used in this study since decomposition of lead fluoride was noted after melting. Also, melting alone does not insure that the dopant has moved into the lead fluoride lattice. Instead, mixtures were heated beyond the phase transition temperature of about 350°C. It was anticipated that during the phase transition the impurities would be incorporated into the new crystal lattice.

The mixtures were made by successive dilution and mixed overnight on a ball mill. They were then loaded into vials and sealed either under nitrogen or vacuum. Each vial was heated to about 500°C. When x-ray analysis showed that the lead fluoride had been converted to the cubic form, pellets were pressed at about 50,000 psi in a Perkin-Elmer evacuable KBr die. This caused some reconversion to the orthorhombic form so that the pellets had to be reheated in sealed vials with PbF<sub>2</sub> packing. No impurity lines or movement of peaks which would indicate a change in lattice spacing were observed in the x-ray spectra.

*Conductivity measurements.*—The experimental procedures used have been reported previously (2). It has since been found that the electrodes which gave the least a-c frequency dependence were those applied by vacuum deposition of lead metal onto surfaces precleaned by glow-discharge followed by an application of graphite (Aquadag) to protect the thin

\* Electrochemical Society Active Member.

Key words: alivalent doping, fluoride ion conductivity, galvanic cells, lead fluoride, solid electrolyte.

film of lead. Single crystals were measured with the Aquadag alone as the electrode material due to their sensitivity to thermal shock. Also the GRC-1650A impedance bridge previously used was modified by addition of an external, parallel variable capacitor which greatly improved the detector nulls. The series equivalent of the cell resistance could be found by (8, 9)

$$R_s = R_B / [1 + (\omega R_B C_B)^2]$$

where  $R_s$  = cell series resistance,  $R_B$  = bridge resistance,  $C_B$  = bridge capacitance, and  $\omega$  = angular velocity.

Only in the case of the single crystals where painted graphite alone formed the electrodes was the  $\omega R_B C_B$  term significant. As previously described, the frequency-dependent terms were separated by use of empirical functions.

**Single crystals.**—Single crystals of pure and doped  $\beta$ -PbF<sub>2</sub> were grown by Stockbarger's technique of pulling from the melt as described by Jones (10). It was necessary to premelt the starting material under a flow of HF to eliminate impurities which would have otherwise caused decomposition. Two single crystals were grown, one of undoped PbF<sub>2</sub> and the other of 1 mole per cent (m/o) KF-doped PbF<sub>2</sub>. Both crystals were extremely brittle and for this reason temperature studies were somewhat limited.

### Results

**Total conductivity.**—NaF, KF, and BiF<sub>3</sub> were used to dope impurity cations into  $\beta$ -PbF<sub>2</sub>. The resulting changes in electrical conductivity determined by the a-c bridge can be seen in Fig. 1. Both NaF and KF increased the conductivity while BiF<sub>3</sub> decreased the conductivity. The slopes of the Arrhenius plots are listed in Table I in terms of a heat of activation. The conductivities and Arrhenius slopes of the NaF-

doped samples were lower and steeper, respectively, than those of the KF-doped samples of the same doping concentration. However both appeared to have activation energies that approached 0.21 eV as the doping was increased.

**Electronic conductivity.**—Wagner polarization cells were made from samples of pure as well as NaF- and BiF<sub>3</sub>-doped samples of  $\beta$ -PbF<sub>2</sub>. The cells were constructed by vacuum deposition of a thin film of lead on one side of a pressed pellet of  $\beta$ -PbF<sub>2</sub> followed by painting the other side with colloidal graphite (Aquadag). Polarization curves were taken at room temperature and under vacuum. An equation relating the observed current to the electronic conductivity and some results for undoped lead fluoride at 150°C were given previously (2). The NaF-doped samples gave currents which were below the detection limit of the apparatus which was about  $1 \times 10^{-10}$  ohm<sup>-1</sup>cm<sup>-1</sup>. New data for undoped cubic lead fluoride at 25°C are shown in Fig. 2 and were ambiguous as to whether the current was carried by electrons or holes. However these new lower conduction values for purer lead fluoride than used previously are in reasonable agreement with those observed by Schoonman (11). The electronic conductivity for BiF<sub>3</sub>-doped  $\beta$ -PbF<sub>2</sub> is shown in Fig. 3 and indicates electron carriers. Except for the BiF<sub>3</sub>-doped material, the electronic conductivity measured was far below the total electrical conductivity observed. At room temperature, the conductivity of 1 m/o BiF<sub>3</sub> in  $\beta$ -PbF<sub>2</sub> was  $6.4 \times 10^{-8}$  ohm<sup>-1</sup>cm<sup>-1</sup>, while the electronic conductivity was  $4.0 \times 10^{-8}$  ohm<sup>-1</sup>cm<sup>-1</sup>. Since the electronic

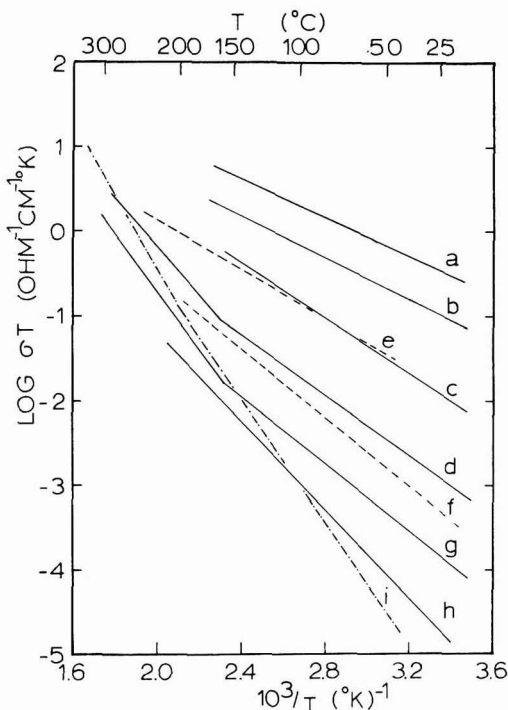


Fig. 1. Ionic conductivity of doped and undoped  $\beta$ -PbF<sub>2</sub>. KF doping: (a) 2 m/o, (b) 1 m/o, (c) 0.5 m/o, (d) 0.1 m/o. NaF doping: (e) 1.5 m/o, (f) 0.5 m/o. Undoped  $\beta$ -PbF<sub>2</sub>: (g) 99.999%  $\beta$ -PbF<sub>2</sub>, (i) results from Ref. (4). BiF<sub>3</sub> doping: (h) 1 m/o.

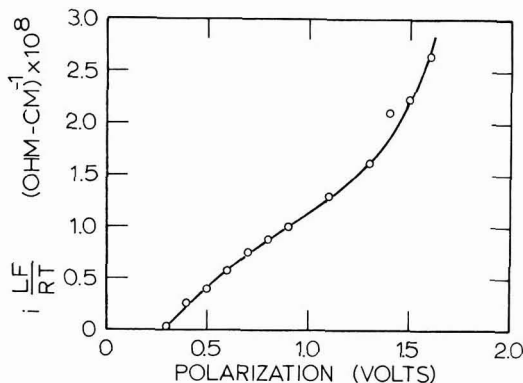


Fig. 2. Electronic current of  $\beta$ -PbF<sub>2</sub> pressed pellet cell vs. applied voltage at 25°C.

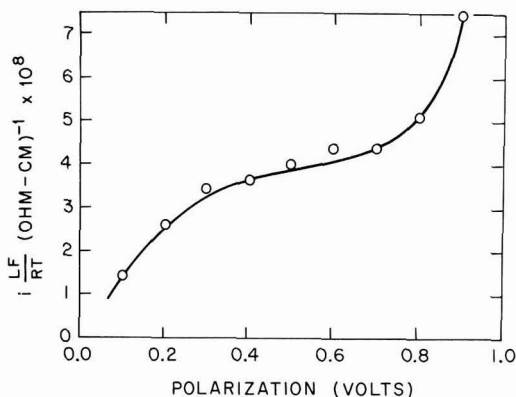


Fig. 3. Electronic current of 1 m/o BiF<sub>3</sub>-doped  $\beta$ -PbF<sub>2</sub> pressed pellet cell vs. applied voltage at 25°C.

contribution to the total conductivity was so large, the Arrhenius plot for the BiF<sub>3</sub>-doped  $\beta$ -PbF<sub>2</sub> was not considered in the elucidation of the ionic conduction mechanism.

### Discussion

The increased conductivity observed when  $\beta$ -PbF<sub>2</sub> was doped with monovalent cation fluorides was due to an increase in ionic conductivity since the electronic conductivity was observed to decline. The extrinsic semiconductor nature of  $\beta$ -PbF<sub>2</sub> which was apparent when BiF<sub>3</sub> was doped into the lattice has been observed before by Chan and Shields (12) and also by Arkhangel'skaya *et al.* (13).

The fact that the ionic conductivity of  $\beta$ -PbF<sub>2</sub> increased upon doping with KF and NaF, while it decreased when BiF<sub>3</sub> was introduced, indicated that the ionic current was carried by mobile, fluoride ion vacancies when the temperature was below about 180°C. Above this transition point the steeper slope may represent an intrinsic region where the conducting defects ( $V_F$ ) are being formed in significant number by thermal generation, or it may represent a shift to a new conduction mechanism, *i.e.*, fluoride interstitials as suggested by Schoonman *et al.* and Derrington and O'Keefe. If both slopes are extrinsic, however, one must assume nonequilibrium between vacancies and interstitials.

If the knee in the Arrhenius slope represented a transition from an extrinsic to an intrinsic region as the temperature increased, then the activation energy of the extrinsic lower slope was  $\Delta H_m$ , the heat of movement, while the intrinsic upper slope was  $\Delta H_m + \Delta H_f/p$ , the sum of the heat of movement and of formation. The constant,  $p$ , represents the number of defects formed, and would be 2 for a Frenkel or 3 for a Schottky mechanism. The values for these two slopes were

$$\text{lowest slope} = \Delta H_m = 0.21 \text{ eV}$$

$$\text{highest slope} = \Delta H_m + \Delta H_f/p = 0.66 \text{ eV}$$

The value for  $\Delta H_f$  would be 0.90 eV (Frenkel) or 1.35 eV (Schottky). Both of these values are rather low and cast doubt on the extrinsic-intrinsic regions hypothesis. Based on the melting point of PbF<sub>2</sub> (822°C) an estimate for  $\Delta H_f$  (Frenkel) is 2.72 eV (4).

Our doping studies show that fluoride ion vacancies are the conductive species, and vacancies can be formed by either a Schottky or Frenkel mechanism. However, studies at higher temperatures (3, 4) have indicated that fluoride ion interstitials are the predominant conductive species. Since interstitials are formed by a Frenkel mechanism and not the normal Schottky mechanism (anti-Schottky defect requires the formation of lead interstitials in addition), it is logical to assume that a Frenkel mechanism prevails at all temperatures with vacancies being the predominant conductive species at low temperature (<200°C) and with interstitials becoming predominant at high temperatures because their heat of movement is higher. However, the possibility of both Schottky and Frenkel mechanisms existing in PbF<sub>2</sub> cannot be ruled out.

It should be noted that a transition from vacancy to interstitial conduction would allow Arrhenius plots of doped samples to cross the undoped line. Potassium fluoride doping would increase the concentration of vacancies and enhance vacancy conduction at low temperature but would decrease the concentration of interstitials and therefore decrease conductivity at high temperature. A transition from extrinsic to intrinsic would not predict such a crossing. Figure 1 shows that the doped lines may cross the undoped lines in the 200°-300°C region. For more data concerning crossing see Ref. (15).

It is dangerous to try and fit results for polycrystalline materials into mathematical models designed for purely bulk effects. Therefore, the doping results were

checked by growing a single crystal of 1 m/o KF-doped  $\beta$ -PbF<sub>2</sub>. It was possible that there might be several pathways by which the conducting species,  $V_F$  and possibly  $F_i$  ions, were moving which would complicate the heats of movement. This effect had been described by Mizuta and Yanagida (14) in the case of CaF<sub>2</sub>, which also conducts by fluoride ion vacancies. They found that the Arrhenius activation energy depended on the history or degree of sintering of the polycrystalline material, and that there were three extrinsic heats of movement: bulk, grain boundary, and grain surface. However, the single crystal of doped PbF<sub>2</sub> gave essentially the same values of conductivity and Arrhenius slope as the polycrystalline material (Table I). Therefore, in this case, the ionic transport mechanism was not dependent on the polycrystalline nature of the material.

A method for calculating the concentration of defects in the undoped material assuming it is extrinsic in nature can be developed from doping studies using the conventional equation

$$\sigma = ne\mu$$

For the undoped material containing an extrinsic concentration of defects,  $n_0$

$$\sigma_0 = n_0e\mu$$

and for the doped material

$$\sigma = (n_0 + n_d)e\mu$$

Since extrinsic conductivity is assumed, the addition of defects by doping ( $n_d$ ) will not affect those present in the undoped material ( $n_0$ ). If we assume for the moment that mobility does not change with doping level then

$$\frac{\sigma}{\sigma_0} = 1 + \frac{n_d}{n_0}$$

A plot of  $\sigma/\sigma_0$  vs.  $n_d$  should be a straight line with a slope of  $1/n_0$ . This plot is shown in Fig. 4. Straight lines were not obtained, and the upward curvature indicated higher conductivities than predicted at high doping levels. If one reviews the activation energies given in Table I it can be seen that the activation energy decreased as alkali metal concentration increased. Thus, the basic assumption which is made in most doping studies that the mobility does not change with doping level was not true in this case. If we take a more general approach, namely

$$\sigma T = \sigma^0 e^{-\Delta H_m/kT}$$

where the preexponential term,  $\sigma^0$ , is directly proportional to the concentration of conductive species, then

$$\sigma_0^0 = kn_0$$

and

$$\sigma^0 = k(n_0 + n_d)$$

Again a ratio of conductivities can be used to give

Table I. Experimental heats of activation

Material	$\Delta H$ (eV)
$\beta$ -PbF <sub>2</sub> , undoped	0.39-0.50, 0.66 <sup>(a)</sup>
$\beta$ -PbF <sub>2</sub> , undoped single crystal	0.80 (25°-150°C)
1 m/o BiF <sub>3</sub>	0.53
0.5 m/o NaF	0.39
1.5 m/o NaF	0.22
0.1 m/o KF	0.33, 0.51 <sup>(a)</sup>
0.5 m/o KF	0.31
1.0 m/o KF	0.22
1.0 m/o KF, single crystal	-0.2 <sup>(b)</sup> (25°-90°C)
2.0 m/o KF	0.21

<sup>(a)</sup> Upper slope at high temperature (>180°C).

<sup>(b)</sup> Slope was frequency dependent.

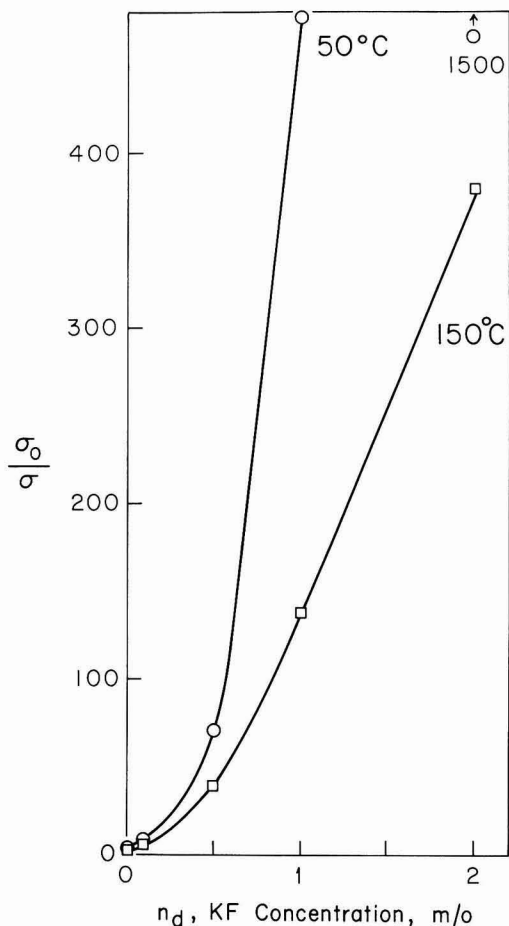


Fig. 4. Conductivity as a function of KF doping level.  $\circ$  50°C,  $\square$  150°C.

$$\frac{\sigma^{\circ}}{\sigma_0} = 1 + \frac{n_d}{n_0}$$

In this case the extrapolated infinite temperature values are used and a plot is shown in Fig. 5. A value of 0.5 m/o for the concentration of extrinsic defects in undoped lead fluoride was obtained from the slope. However, the conductivity was considerably lower than with 0.5 m/o KF doping because the heat of movement was higher for undoped  $\text{PbF}_2$  than for KF-doped  $\text{PbF}_2$ .

A plot of  $\Delta H_m$  as a function of doping level is shown in Fig. 6. It appears that the heat of movement for vacancies can vary from above 0.5 eV in nominally pure  $\text{PbF}_2$  to 0.21 eV in highly doped  $\text{PbF}_2$ . The sensitivity of the activation energy to impurity level explains why several different values have been observed by various investigators for nominally pure  $\beta\text{-PbF}_2$  from below 0.5 eV (2) to 0.7 eV (4).

A change in the extrinsic heat of movement has not been previously reported for analogous solid electrolytes. This may be the result of the high doping levels used in this study or may be specific to  $\text{PbF}_2$ . A concentration of 1 m/o KF is large enough to place a potassium ion within several cell lattice constants of any other ion in the lattice. The difference then between the KF and NaF doping experiments may be the result of different charge densities between sodium and potassium which would affect the energy

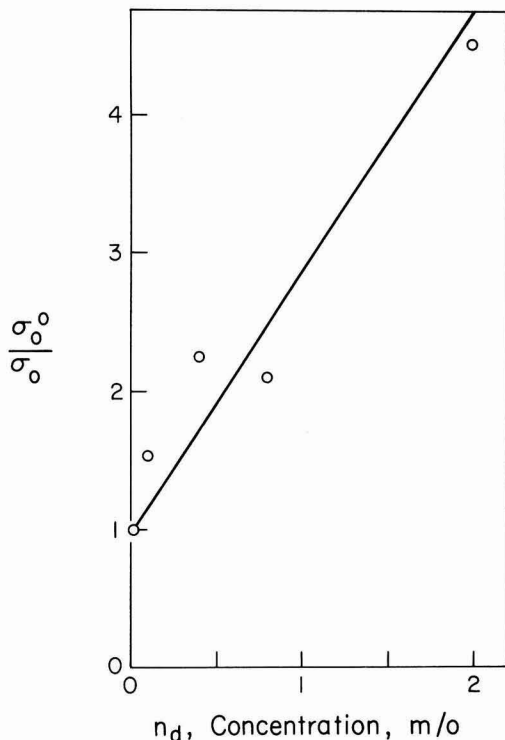


Fig. 5. Preexponential factor as a function of KF doping level

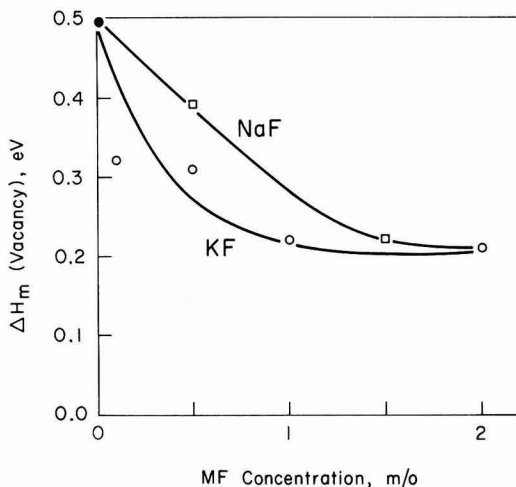


Fig. 6. Heat of motion of vacancy as a function of doping level.  $\circ$  KF,  $\square$  NaF,  $\bullet$  undoped  $\text{PbF}_2$ .

barriers the fluoride ion vacancy experiences at these high doping levels as it migrates.

Recently a paper was published describing similar experiments with lead fluoride (15). Most of the results are in general agreement with those presented here, however some differences were observed. Doping with  $\text{YF}_3$  increased conductivity while our results with  $\text{BiF}_3$  showed a decrease in conductivity. This difference between the  $\text{MF}_3$  compounds should be studied in more detail. Liang and Joshi also described a linear increase in conductivity with doping up to 1 m/o. We have observed more curvature especially

at the higher doping levels (as high as 2 m/o). Finally, we have observed a gradual decrease in activation with increased doping level while Liang and Joshi observed only the high slope for undoped samples and the low slope for doped samples. We agree on both the high and low slope limiting values, but interpretation depends somewhat on whether or not intermediate values are observed. Additional studies should be undertaken to examine these differences and to design experiments which will discriminate between various conductivity mechanisms which have been postulated.

**Galvanic cells.**—Potassium fluoride-doped  $\beta$ -PbF<sub>2</sub> was used as an electrolyte in galvanic cells to test its high conductivity. Solid-state cells were constructed with CuF<sub>2</sub> and AgF as cathode materials. The anticipated open-circuit voltages of 0.70 and 1.30V were achieved, but the cell potentials fell rapidly when placed under load and current drawn.

In order to examine the electrolytic properties exclusive of the galvanic cell configuration, a Pb/PbF<sub>2</sub>/Pb cell was constructed by applying a thin film of lead to serve as a cathode on a pressed pellet (2 m/o KF doped-PbF<sub>2</sub>), and pressing a plate of lead metal against the opposite side of the pellet. In this cell, lead metal would be deposited at the cathode and lead fluoride would be formed at the anode. However, the lead fluoride formed would be pure and would not show the high conductivity of the doped material unless KF were able to diffuse into the newly formed layer. The formation of pure PbF<sub>2</sub> would be similar to the formation of a passivation layer and explain the poor performance of the galvanic cells.

Two Pb/PbF<sub>2</sub>/Pb cells were run, one at 100°C and the other at 250°C. They yielded currents of several hundred microamperes and about 1 mA, respectively, at an applied voltage of one volt. After one day, the current of the cell at 250°C was essentially zero. The cell at 100°C took several more days until the current decayed to near zero. About 9 coulombs of charge passed through the higher temperature cell while about 2 coulombs passed through the lower temperature cell.

Inspection of both lead plate anodes under a microscope revealed deposits, roughly circular in shape. In some places, the deposits had coalesced, but nowhere were they any higher than 40 $\mu$ . There were no corresponding pits in the adjacent pellet surfaces. X-ray analysis of the deposits showed the presence of  $\alpha$ -PbF<sub>2</sub> and Pb<sub>2</sub>O<sub>2</sub> but no  $\beta$ -PbF<sub>2</sub> (Table II). Apparently deposition occurred at a number of preferred active sites and ceased when they were consumed. Possibly these sites were merely high pressure contact points between the lead plate and the pressed pellet of doped electrolyte. It has been shown previously that  $\beta$ -PbF<sub>2</sub> converts to  $\alpha$ -PbF<sub>2</sub> when under pressure (2). This could explain why the lead fluoride was formed in the  $\alpha$ - rather than  $\beta$ -form. Thus, even though doped  $\beta$ -PbF<sub>2</sub> has quite high ionic conductivity its use may not be possible in lead anode galvanic cells because the anode product will be low conductivity pure  $\alpha$ -PbF<sub>2</sub>.

### Conclusion

It has been shown that  $\beta$ -PbF<sub>2</sub> conducts by fluoride ion vacancy movement when at temperatures below 180°C. Furthermore, the conductivity can be considerably enhanced by doping with monovalent cation fluorides. The presence of monovalent cations also appears to decrease the heat of movement for the

Table II. X-ray data of lead anode surface

$2\theta$ , degrees	$d$ , A	$I$	$I/I_0$ (Pb)	$I/I_0$ ( $\alpha$ -PbF <sub>2</sub> )	$I/I_0$ (Pb <sub>2</sub> O <sub>2</sub> )	Assignment
26.83	3.320	56			100	Pb <sub>2</sub> O <sub>2</sub> (3.33)
27.10	3.288	10		100		$\alpha$ -PbF <sub>2</sub> (3.290)
27.70	3.218	3		30		$\alpha$ -PbF <sub>2</sub> (3.222)
29.12	3.064	7			13	Pb <sub>2</sub> O <sub>2</sub> (3.07)
29.20	3.056	7		70		$\alpha$ -PbF <sub>2</sub> (3.058)
31.00	2.882	43			78	Pb <sub>2</sub> O <sub>2</sub> (2.88)
31.26	2.859	58	100			Pb (2.855)
36.28	2.474	20	35			Pb (2.475)
38.15	2.357	8		80		$\alpha$ -PbF <sub>2</sub> (2.364)
42.31	2.134	6		60		$\alpha$ -PbF <sub>2</sub> (2.135)
44.40	2.039	16			29	Pb <sub>2</sub> O <sub>2</sub> (2.03, 2.04)

Comments: Two peaks from Pb<sub>2</sub>O<sub>2</sub> were missing,  $d = 2.86$  ( $I/I_0 = 60$ ) and  $d = 2.70$  ( $I/I_0 = 70$ ). The first was probably masked by the lead at  $d = 2.855$ .  $\alpha$ -PbF<sub>2</sub> was also missing one peak,  $d = 2.475$  ( $I/I_0 = 26$ ). Undoubtedly it was masked by the lead peak at  $d = 2.475$ . Only one x-ray out of three taken showed a very small peak at  $d = 3.423$  which could be attributed to  $\beta$ -PbF<sub>2</sub> at  $d = 3.428$ . X-ray diffraction of a lead plate after being heated at 250°C for several days showed that none of the lead oxide peaks from this spectrum corresponded to the x-ray diffraction pattern shown above.

vacancies. Its usefulness in a solid-state cell, however, is possibly limited due to the formation of an anode passivation layer consisting of low conductivity pure  $\alpha$ -PbF<sub>2</sub>.

### Acknowledgment

This paper was taken in part from the Ph.D. dissertation of RCM, University of California, Santa Barbara, 1974. The authors acknowledge financial support of this project by the National Science Foundation, Grant No. GH-37144. The authors also thank Mr. Neil Nighman for his help in growing single crystals of lead fluoride. One of the authors (JHK) thanks the Japan Society for the Promotion of Science for a visiting professorship grant and Professors T. Takahashi and O. Yamamoto for helpful discussion.

Manuscript submitted March 4, 1975; revised manuscript received July 14, 1975.

Any discussion of this paper will appear in a Discussion Section to be published in the December 1976 JOURNAL. All discussions for the December 1976 Discussion Section should be submitted by Aug. 1, 1976.

Publication costs of this article were partially assisted by the University of California.

### REFERENCES

1. C. Tubandt, *Z. Anorg. Chem.*, **115**, 105 (1921).
2. J. H. Kennedy, R. Miles, and J. Hunter, *This Journal*, **120**, 1441 (1973).
3. C. E. Derrington and M. O'Keeffe, *Nature, Phys. Sci.*, **246**, 44 (1973).
4. J. Schoonman, G. J. Dirksen, and G. Blasse, *J. Solid State Chem.*, **7**, 245 (1973).
5. R. W. Ure, *J. Chem. Phys.*, **26**, 1363 (1957).
6. E. Barsis and A. Taylor, *ibid.*, **45**, 1154 (1963).
7. Y. T. Tau and D. Kramp, *ibid.*, **53**, 3691 (1970).
8. D. O. Raleigh, *J. Phys. Chem. Solids*, **29**, 261 (1968).
9. J. Braunstein and G. D. Robbins, *J. Chem. Ed.*, **48**, 52 (1971).
10. D. A. Jones, *Proc. Phys. Soc.*, **65B**, 165 (1955).
11. J. Schoonman, Private communication.
12. K. K. Chan and L. Shields, *J. Phys. C. (Solid State Phys.)*, **2**, 1978 (1969).
13. V. A. Arkhangel'skaya, V. G. Erofeichev, and M. N. Kiseleva, *Soviet Physics, Solid State*, **14**, 2953 (1973).
14. S. Mizuta and H. Yanagida, *Denki Kagaku*, **40**, 787 (1972).
15. C. C. Liang and A. V. Joshi, *This Journal*, **122**, 466 (1975).



# The Preparation and Properties of (111)Si Films Grown on Sapphire by the SiH<sub>4</sub>-H<sub>2</sub> Process

H. M. Manasevit,\* F. M. Erdmann, and A. C. Thorsen<sup>1</sup>

Rockwell International, Electronics Research Division, Anaheim, California 92803

## ABSTRACT

An experimental study of the effects of various parameters on the properties of (111) and (100)Si films grown on sapphire ( $\alpha$ -Al<sub>2</sub>O<sub>3</sub>) by the SiH<sub>4</sub> pyrolysis CVD method has been carried out. The following were examined: autodoping, growth temperature and growth rate, As-doped n-type films, p-type films doped with B, properties as a function of film thickness, and the effect of reactor configuration. It was determined that at growth rates of  $\sim 2$ -6  $\mu\text{m}/\text{min}$  in a vertical reactor n-type (111)Si films grown at temperatures of 1050°-1100°C on Al<sub>2</sub>O<sub>3</sub> substrates oriented near the (11 $\bar{2}$ 0) plane are electrically superior to those grown on (01 $\bar{1}$ 2)Al<sub>2</sub>O<sub>3</sub> and (10 $\bar{1}$ 4)Al<sub>2</sub>O<sub>3</sub> over the temperature range 950°-1100°C. Films with electron mobilities as high as 600-700 cm<sup>2</sup>/V-sec for carrier concentrations of 10<sup>16</sup>-10<sup>17</sup> cm<sup>-3</sup> were obtained. P-type Si films grown using B<sub>2</sub>H<sub>6</sub> as the dopant source were also electrically better on  $\sim(1120)$ Al<sub>2</sub>O<sub>3</sub> [(111)Si-growth] than on (01 $\bar{1}$ 2)Al<sub>2</sub>O<sub>3</sub> [(100)Si growth], Hall mobilities being  $\sim 2$ -3 times larger for hole concentrations 10<sup>16</sup>-10<sup>17</sup> cm<sup>-3</sup>. A comparison of film properties of n-type films as a function of thickness indicated both the (100) and (111)Si films behave essentially the same way, i.e., the average mobilities show a steady decrease with decreasing film thickness. These studies revealed the strong interrelationships that exist among the various parameters involved in optimizing Si growth on insulators and indicated that growth conditions (i) must be optimized for the particular substrate orientation chosen; (ii) differ for those substrate orientations which lead to the same Si orientation; (iii) are dependent on reactor geometry; and (iv) should be optimized for the particular film thickness desired.

Silicon-on-sapphire (SOS) is now over a decade old, having been first announced by our laboratory in 1963 (1). However, only in the last few years has a pronounced interest in SOS been demonstrated.

A major emphasis has been placed on the use of (01 $\bar{1}$ 2)Al<sub>2</sub>O<sub>3</sub> as the substrate orientation since it controls the growth of (100)-oriented Si, which is preferred for MOS structures in bulk Si because surface states are minimized; however, better electrical properties have been reported for (111)Si/(0001)Al<sub>2</sub>O<sub>3</sub> films grown by chemical vapor deposition (2). The best films were grown at the relatively high temperature of  $\sim 1200^\circ\text{C}$  (2). Two other principal orientations that were identified during our early studies (3) as influencing the growth of (111)Si are (10 $\bar{1}$ 4)Al<sub>2</sub>O<sub>3</sub> and  $\sim(11\bar{2}0)$ Al<sub>2</sub>O<sub>3</sub>. This paper reports the results of a study to compare the properties of (111)Si films grown on these orientations with (100)Si films grown on (01 $\bar{1}$ 2)Al<sub>2</sub>O<sub>3</sub>. Some studies were also performed on (1 $\bar{1}$ 23)Al<sub>2</sub>O<sub>3</sub>, which induces Si growth about 7.5° off the (111)Si plane. Substrates cut  $\sim 5^\circ$  off the (11 $\bar{2}$ 0) plane of Al<sub>2</sub>O<sub>3</sub> toward the [10 $\bar{1}$ 0] direction were used to ensure that the growth was single crystal with the (111) plane of Si parallel to the (11 $\bar{2}$ 0) plane of Al<sub>2</sub>O<sub>3</sub> (3).

## Experimental

Except as noted, the Si growth studies involved the formation of films by the pyrolysis of SiH<sub>4</sub>-H<sub>2</sub> mixtures in the apparatus depicted in Fig. 1. It consists of a vertical 60 mm OD quartz tube 38 cm long, containing a SiC-coated carbon pedestal ("Ti-Kote," Texas Instruments) which could be rotated and inductively heated; a manifold made from 1/4 in. stainless steel (Type 316) tubing; appropriate flow meters (Brooks Instruments) for monitoring the gas flows; Teflon con-

nectors (Beckman Instruments) to facilitate reactor exchange; and provision for separate evacuation of the flow lines and the reactor. During the working day, a continual flow was maintained in the gas lines; only the reactor portion and connections were evacuated between experiments.

The H<sub>2</sub> carrier gas was Pd-purified, and the He was grade 6<sup>TM</sup> from Airco. The dopant sources used contained 200 ppm AsH<sub>3</sub> in H<sub>2</sub> (Airco) and 195 ppm B<sub>2</sub>H<sub>6</sub> in H<sub>2</sub> carrier gas (Scientific Gas). Temperatures of the SiC-coated carbon pedestal were measured with an optical pyrometer and were not corrected for any apparent emissivity changes caused by the intervening quartz chamber wall. Total gas flows of 6 lpm were used in the experiments described.

The substrates, which in most cases possessed an oval shape, were fabricated from 0.5 in. diameter Verneuil and Czochralski rods obtained from Union Carbide (San Diego, California), and Crystal Optics (Ann Ar-

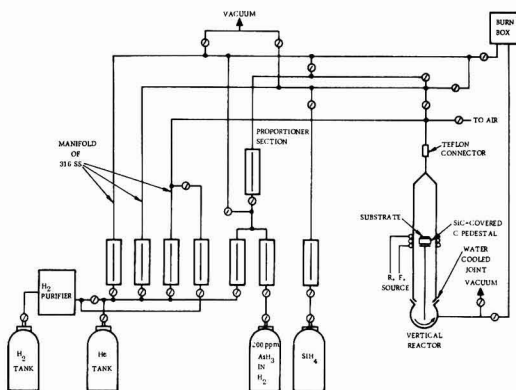


Fig. 1. Schematic diagram of chemical vapor deposition apparatus

\*Electrochemical Society Active Member.

<sup>1</sup> Present address: Rockwell International Science Center, Thousand Oaks, California 91360.

Key words: silicon-on-sapphire, (111)Si films, heteroepitaxy, chemical vapor deposition, anisotropy.

bor, Michigan). They were oriented at Rockwell and cut and polished at Insaco (Quakertown, Pennsylvania), and at Rockwell. Measurements of film conductivity type, resistivity, carrier concentration, and carrier mobility were made utilizing either the van der Pauw method (4) or the more accurate and conventional Hall-effect bridge method. The Hall-effect bridges etched in Si on a given substrate orientation fortunately were, in most cases, placed in the same direction with respect to the crystallographic axes in the plane of the substrates. The importance of this point is discussed later.

### Results and Discussion

**Study of autodoping in (100) and (111)SOS films.**—Autodoping from the  $\text{Al}_2\text{O}_3$  substrates has been shown to cause appreciable doping of epitaxial Si films grown in  $\text{H}_2$  (5, 6). In order to determine more precisely the extent of this doping in our reactor, a number of intentionally undoped (100)- and (111)-oriented,  $\sim 2 \mu\text{m}$  thick films were grown in  $\text{H}_2$  as a function of temperature from 1050° to 1150°C at a growth rate of  $\sim 2 \mu\text{m}/\text{min}$ . The carrier concentration data are shown in Fig. 2 for the unannealed films. Each data point represents an average value for data obtained from 1 to 3 samples. Slight changes in growth temperature appreciably altered the extent of autodoping, since the acceptor concentration varied by over two orders of magnitude for growth temperature changes of just 100°C, i.e.,  $2-3 \times 10^{15}/\text{cm}^3$  at 1050°C to  $\sim 3-5 \times 10^{17}/\text{cm}^3$  at 1150°C. Autodoping appeared to be slightly less in (111)Si on  $\sim (11\bar{2}0)\text{Al}_2\text{O}_3$  than for (100)Si on  $(01\bar{1}2)\text{Al}_2\text{O}_3$  for a given growth temperature. Further studies on the effect of  $\text{Al}_2\text{O}_3$  in a system containing Si are presented as an Appendix to this paper.

**Effect of growth temperature on film properties.**—The electrical properties of As-doped films grown at a rate of  $\sim 2 \mu\text{m}/\text{min}$  in our reactor indicated equivalent quality (111)Si on  $(10\bar{1}4)\text{Al}_2\text{O}_3$  and (100)Si on  $(01\bar{1}2)\text{Al}_2\text{O}_3$  at growth temperatures from 950°-1050°C for donor concentration from  $10^{16}$  to  $10^{18} \text{cm}^{-3}$ . When  $\sim (11\bar{2}0)\text{Al}_2\text{O}_3$  was examined as a substrate for (111)Si

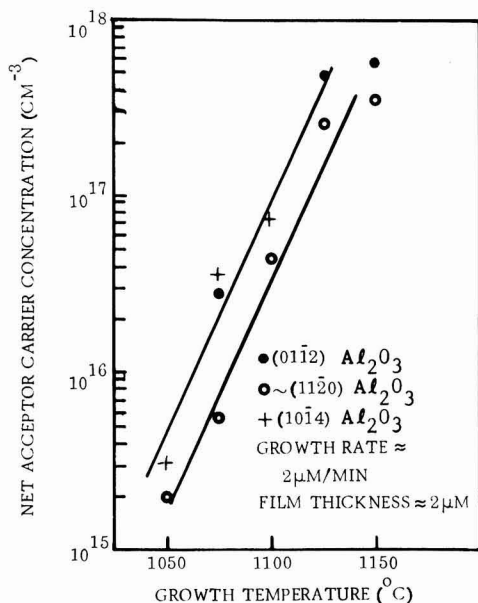


Fig. 2. Variation of net acceptor carrier concentration due to Al autodoping as function of growth temperature for intentionally undoped and unannealed Si/ $\text{Al}_2\text{O}_3$  films. (Data points are averaged values.)

growth, it was found necessary to use temperatures in excess of 1050°C to obtain reflective n-type films. Determination of the correct carrier concentration for films grown at these temperatures was of course complicated by an autodoping species from the  $\text{Al}_2\text{O}_3$  substrate, which served to compensate the As added and had to be removed before the net donor concentration could be established. For this reason, an 1100°C anneal first in  $\text{O}_2$  and then in  $\text{N}_2$  was employed for all films grown at or above 1050°C before measurement in order to render the contaminant electrically inactive.

In Fig. 3, the mobilities of films grown on  $(01\bar{1}2)$  and  $\sim (11\bar{2}0)\text{Al}_2\text{O}_3$  substrates are plotted as a function of growth temperature. At each temperature data for a number of films with net donor concentrations between 1 and  $5 \times 10^{16} \text{cm}^{-3}$  are averaged; the bars indicate the range of mobilities over which the points are averaged, and the number next to the point indicates how many samples contributed to the average value plotted. It was found that for a growth rate of  $\sim 2 \mu\text{m}/\text{min}$  the electron mobility in (100)Si (values of  $\sim 500-550 \text{cm}^2/\text{V-sec}$ ) was nearly independent of growth temperature ( $T_g$ ) for  $1040^\circ\text{C} \leq T_g \leq 1100^\circ\text{C}$ . For (111)Si growth on the  $\text{Al}_2\text{O}_3$  orientation near the  $(11\bar{2}0)$  plane, film mobilities appeared to improve with increasing growth temperature and exceeded those obtained for (100)Si by about 25% (values of 650-700  $\text{cm}^2/\text{V-sec}$ ) at the higher growth temperatures.

Growth of Si on various other  $\text{Al}_2\text{O}_3$  orientations at high growth temperature was also examined. The  $(10\bar{1}4)$  and  $(11\bar{2}3)\text{Al}_2\text{O}_3$  orientations were used as substrates for Si growth at temperatures from 1075° to 1150°C. For film thicknesses of 1.5-1.9  $\mu\text{m}$  and donor concentrations of  $1-2 \times 10^{16} \text{cm}^{-3}$ , the  $(10\bar{1}4)$  and  $(11\bar{2}3)$  orientations yielded films with mobilities of 400-500  $\text{cm}^2/\text{V-sec}$  over the whole temperature range, values inferior to those measured in the better (111)-oriented films grown on  $\sim (11\bar{2}0)\text{Al}_2\text{O}_3$ .

**Effect of growth rate on film properties.**—Growth rate-mobility data for 2  $\mu\text{m}$ -thick films grown at 1075°C on  $(01\bar{1}2)\text{Al}_2\text{O}_3$  and also on  $\sim (11\bar{2}0)\text{Al}_2\text{O}_3$  are plotted in Fig. 4. The data suggest an improvement in film properties at growth rates exceeding 1  $\mu\text{m}/\text{min}$ ; the mobility maxima occur in films grown at a rate of about 4  $\mu\text{m}/\text{min}$  for  $(01\bar{1}2)\text{Al}_2\text{O}_3$  and about 2  $\mu\text{m}/\text{min}$  for films grown on substrates with an orientation near  $(11\bar{2}0)\text{Al}_2\text{O}_3$ . These films were grown under conditions of constant dopant gas flow. However, as shown in Fig. 5, an exponential relationship exists between growth rate and carrier concentration. Such a relationship is not expected since the growth rate is a linear function of  $\text{SiH}_4$  flow rate. That is, a simple dilution of the

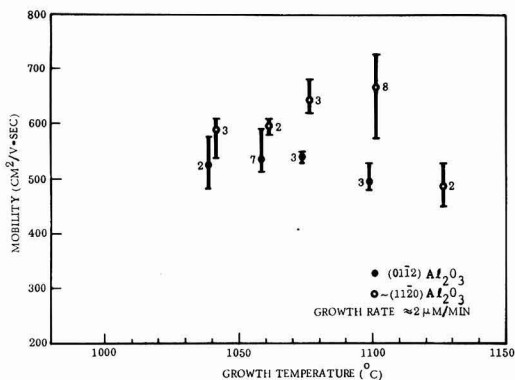


Fig. 3. Variation of Hall mobility with growth temperature for Si/ $\text{Al}_2\text{O}_3$  films having net donor carrier concentration of  $1-5 \times 10^{16} \text{cm}^{-3}$ . (Films were annealed before electrical measurement.)

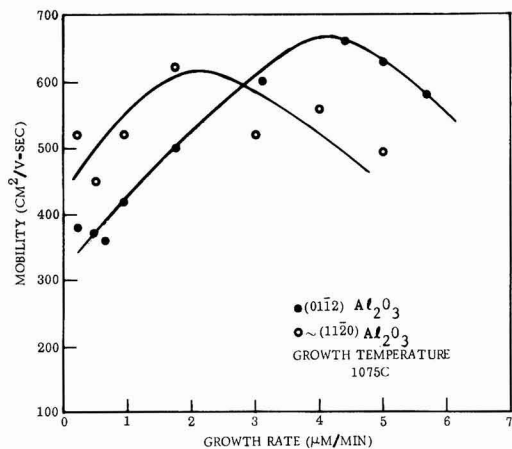


Fig. 4. Variation of Hall mobility with growth rate for n-type Si/Al<sub>2</sub>O<sub>3</sub> films grown at 1075°C. (Annealed at 1100°C in O<sub>2</sub> and N<sub>2</sub>.)

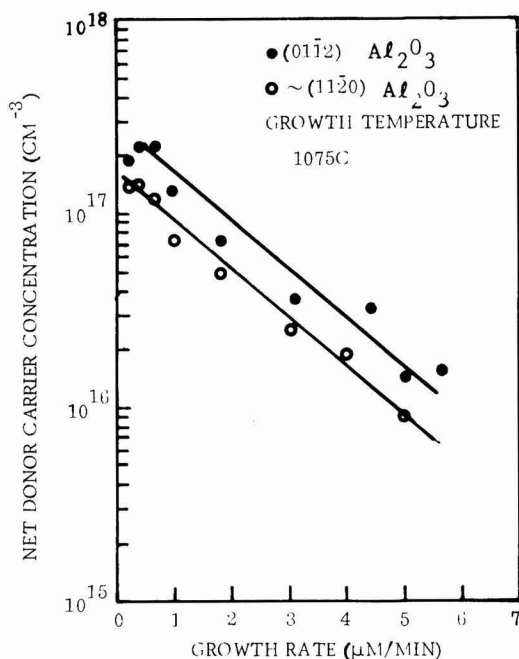


Fig. 5. Variation of net donor carrier concentration with growth rate for Si/Al<sub>2</sub>O<sub>3</sub> films grown at 1075°C with constant dopant-gas flow rate. (Annealed at 1100°C in O<sub>2</sub> and N<sub>2</sub>.)

dopant gas by the increasing silane flow rate would be expected to lead to a linear variation of carrier concentration with growth rate. In any case, a substantial part of the mobility decrease at the low rate is a consequence of an increasing carrier concentration. Unfortunately, studies relating growth rate to mobility at constant donor concentrations and different temperatures were not made in our reactor. The data, however, do indicate the importance of making gas-phase doping concentrations consistent with growth rate when one attempts to grow a homogeneously doped film by a dual-rate growth process (7).

One can also note from Fig. 5 that the donor concentration measured in films on ~ (112̄0) Al<sub>2</sub>O<sub>3</sub> are consistently lower than those grown simultaneously on

(011̄2) Al<sub>2</sub>O<sub>3</sub>. This is consistent with the results on autodoping shown in Fig. 2 and suggests that both donor and acceptor dopants are incorporated less easily into the (111)-oriented Si lattice.

**Properties of p-type, B-doped Si/Al<sub>2</sub>O<sub>3</sub> films.**—Doping experiments with Si films on Al<sub>2</sub>O<sub>3</sub> for the purpose of achieving p-type films were undertaken with diborane (B<sub>2</sub>H<sub>6</sub>) as the source of B. Calibration data for a range of carrier concentrations from  $\sim 3 \times 10^{16}$  to  $\sim 2 \times 10^{20}$  cm<sup>-3</sup> were established for  $\sim 2$  μm thick, p-type Si films grown at  $\sim 2$  μm/min on (011̄2) Al<sub>2</sub>O<sub>3</sub> at 1025°C (unannealed) and on (011̄2), ~ (112̄0), and (101̄4) Al<sub>2</sub>O<sub>3</sub> at 1075°C (annealed); the data are shown in Fig. 6.

Since the data points essentially define a single straight line for both the unannealed and annealed films, the annealing was effective in removing the p-type autodoping species without disturbing the B-species in the film. Hall mobility as a function of hole concentration for the films is shown graphically in Fig. 7. The electrical properties of the B-doped (100)Si are similar to those previously reported in the literature

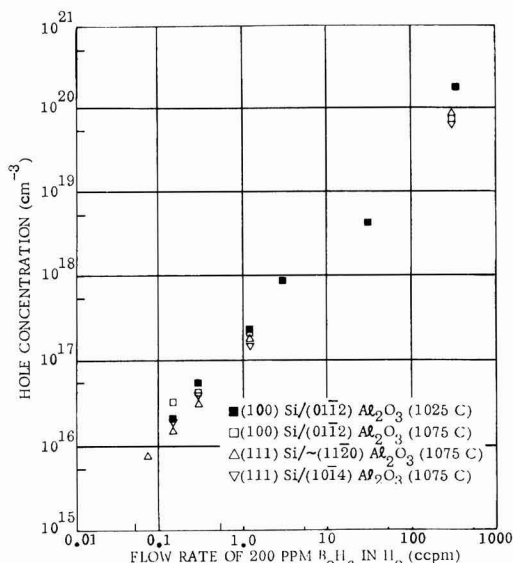


Fig. 6. Calibration curve for growth of p-type Si/Al<sub>2</sub>O<sub>3</sub> films using B<sub>2</sub>H<sub>6</sub> dopant source. The films were annealed at 1100°C in O<sub>2</sub> and N<sub>2</sub>.

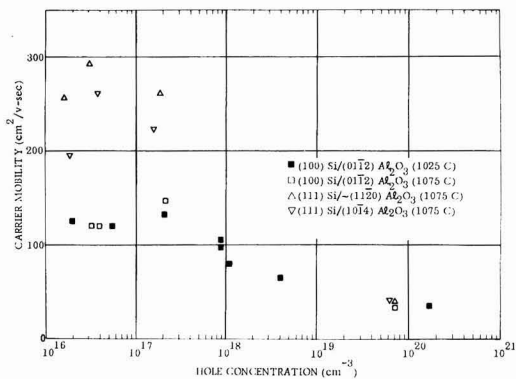


Fig. 7. Electrical properties of p-type Si/Al<sub>2</sub>O<sub>3</sub> films doped with boron.

(8) and are equivalent for films of the same carrier concentration grown at 1025° and 1075°C; therefore, either growth temperature appears to be adequate for p-type (100)Si growth.

The electrical data for the p-type films grown on  $\sim(1\bar{1}\bar{2}0)$  and  $(10\bar{1}4)$   $\text{Al}_2\text{O}_3$  were most encouraging, with mobilities exceeding those measured on  $(01\bar{1}2)\text{Al}_2\text{O}_3$  twofold or more for hole concentrations in the  $10^{16}$ - $10^{17}$   $\text{cm}^{-3}$  range. The results are close to those values for bulk Si and appear to be the largest yet recorded for Si films only 2  $\mu\text{m}$  thick on  $\text{Al}_2\text{O}_3$ . Almost equivalent properties were obtained for p-type (111) films grown on  $(10\bar{1}4)$  and  $\sim(1\bar{1}\bar{2}0)\text{Al}_2\text{O}_3$ . This was surprising since, as previously noted, n-type films grown in  $\text{H}_2$  on  $\sim(1\bar{1}\bar{2}0)\text{Al}_2\text{O}_3$  were superior to those grown on  $(10\bar{1}4)$  substrates. Very high mobilities have also been reported for (111)-oriented p-type films grown on (111) spinel (9). These have been explained by a piezo-resistance effect due to the compressive stress in the films.

**Variations in Si film properties with thickness.**—It has been reported on many occasions that the electrical properties of heteroepitaxial semiconductor films tend to be inferior close to the substrate on which growth occurs (10, 11). A comparison was therefore made of the variation of electrical properties with film thickness for relatively thin, annealed, n-type (100) and (111)Si films grown at 1100°C.

From Fig. 8, it can be observed that the carrier concentration remained relatively constant, decreasing only slightly for thinner films, but the average mobilities showed a more pronounced decrease with decreasing film thickness for both orientations. Films that were reduced stepwise in thickness by polishing and then remeasured electrically also showed the same general thickness dependence on average mobility and carrier concentration. The average mobilities for (111)Si films  $\sim 0.5$ - $1.0$   $\mu\text{m}$  thick grown on  $\sim(1\bar{1}\bar{2}0)\text{Al}_2\text{O}_3$  also appear

to be slightly superior to those found in (100)Si films grown in our vertical apparatus. However, they are essentially the same as those reported by Cullen and Corbo (12) for (100)Si-on-sapphire grown in their reactor at 1000°C. (See next section.)

**Effects of reactor configuration on film properties.**—Because of differences in growth reactors found in various laboratories, several experiments were conducted to investigate the effects that different reactor geometry may have on film properties. Experiments were performed on  $(01\bar{1}2)\text{Al}_2\text{O}_3$  and  $\sim(1\bar{1}\bar{2}0)\text{Al}_2\text{O}_3$  in a horizontal reactor system which normally would accommodate up to four 2 in. diameter wafers per run. Even though the typical growth rate used in this reactor ( $\sim 1$   $\mu\text{m}/\text{min}$ ) was not the same as that used most often in the vertical reactor, and the  $\text{H}_2$  carrier-gas flows ( $\sim 40$  lpm) were substantially greater than those used in the vertical system (6 lpm), the limited data obtained are considered meaningful because they supported the purpose for which the experiments were performed.

The growth temperature was varied from 960° to 1100°C. The visual appearance of those films grown at 1075° and 1100°C indicated a deterioration of film quality; therefore, only those films grown in the range 960°-1075°C were evaluated electrically.

The electrical data shown in Fig. 9 indicate a uniform increase in electron mobility with decreasing growth temperature for 1.0-1.4  $\mu\text{m}$  thick films grown on  $(01\bar{1}2)\text{Al}_2\text{O}_3$ , i.e., from a value of about 325  $\text{cm}^2/\text{V}\text{-sec}$  at 1075°C to approximately 600  $\text{cm}^2/\text{V}\text{-sec}$  at 960°C for carrier concentrations in the range  $\sim 2$ - $6 \times 10^{16}$   $\text{cm}^{-3}$ .

The mobilities of films grown simultaneously on  $\sim(1\bar{1}\bar{2}0)\text{Al}_2\text{O}_3$ , on the other hand, showed a maximum of over 600  $\text{cm}^2/\text{V}\text{-sec}$  at  $\sim 1050^\circ\text{C}$ , with only a slight decrease at 1030° and 1075°C. The results are different from the data obtained on films grown in the vertical reactor system, for in this set of experiments, (100)-oriented Si films were produced with properties essentially as good as those measured in (111)-oriented Si. It is apparent that the determination of optimum film growth parameters relate to the growth apparatus being employed, and a comparison of results from different laboratories must always be made with this fact in mind.

**Anisotropy considerations.**—During the latter part of the studies just described, it was established that the electrical properties of SOS are not isotropic in the plane of the film (13, 14). Using a specifically designed double Hall-bridge pattern etched in the Si film so that independent measurements of Hall mobility were made every 18° in the plane of the films, Hughes and Thorsen determined the amount of anisotropy as described by a parameter  $A$  [ $A \equiv (\mu_{\text{max}} - \mu_{\text{min}})/\mu_A$ , where  $\mu_A = (1/2)(\mu_{\text{max}} \pm \mu_{\text{min}})$ ] of 9% for (100)Si/ $(01\bar{1}2)\text{Al}_2\text{O}_3$  (13) and about 40% for (221)Si/ $(1\bar{1}\bar{2}0)\text{Al}_2\text{O}_3$  (14). Preliminary data indicate anisotropy in mobility for (111)Si films also, averaging 16% for

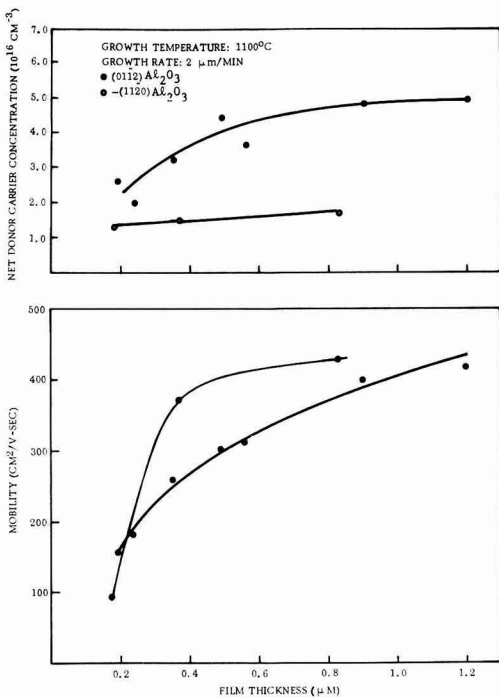


Fig. 8. Variation of film properties with film thickness for thin n-type Si/ $\text{Al}_2\text{O}_3$  films. (All films annealed after growth for 1 hr in  $\text{O}_2$  at 1100°C.)

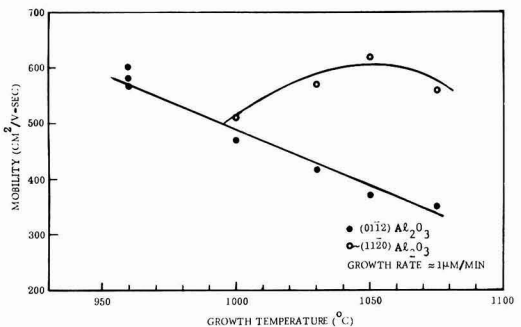


Fig. 9. Variation of Hall mobility with growth temperature for n-type Si/ $\text{Al}_2\text{O}_3$  films grown in a horizontal reactor.

(111)Si growth on  $\sim(1\bar{1}20)\text{Al}_2\text{O}_3$  and 30% for (111)Si growth on  $(10\bar{1}4)\text{Al}_2\text{O}_3$  (15).

These variations in mobility could have led to considerable scatter in the electrical data if circular substrate wafers had been used in these studies prior to the discovery of anisotropy in these films. But, because of the oval shape of the substrate and the operator's tendency to place a square-shaped Hall-effect bridge in approximately the same direction in the Si film relative to the sides of the substrate (and hence to the crystallographic axes of the substrate), it is believed that most of the data obtained can be correlated with the parameter changes made. Since the average anisotropy in mobility for (111)Si on  $\sim(1\bar{1}20)\text{Al}_2\text{O}_3$  is only slightly greater (7%) than that found for (100)Si on  $(01\bar{1}2)\text{Al}_2\text{O}_3$ , we feel that the higher mobilities measured in 2  $\mu\text{m}$  thick (111)Si films on  $\sim(1\bar{1}20)\text{Al}_2\text{O}_3$  grown in the vertical reactor are in fact real and consistent with an improved film quality. A correlation between electrical data and device data is now required to determine if  $\sim(1\bar{1}20)\text{Al}_2\text{O}_3$  is a superior substrate orientation for devices made in silicon-on-sapphire.

### Summary and Conclusions

An experimental study of the effects of various parameters on the properties of (111) and (100)Si films grown on  $\text{Al}_2\text{O}_3$  by the  $\text{SiH}_4\text{-H}_2$  pyrolysis CVD method was carried out in a vertical growth system. It was established that significant autodoping occurs in Si on  $\text{Al}_2\text{O}_3$  at temperatures greater than about 1050°C.

Essentially equivalent (100)- and (111)-oriented, n-type Si films grew on  $(01\bar{1}2)$  and  $(10\bar{1}4)\text{Al}_2\text{O}_3$  substrates at deposition temperatures of 950°-1050°C (below autodoping range) and at growth rates of  $\sim 2 \mu\text{m}/\text{min}$ .

$\text{Al}_2\text{O}_3$  substrates having orientations near the  $(1\bar{1}20)$  plane, which were not previously used in heteroepitaxy growth parameter studies, were also utilized for (111)Si heteroepitaxy, but required temperatures  $> 1050^\circ\text{C}$  for the growth of films with good electrical properties. For growth rates of  $\sim 2 \mu\text{m}/\text{min}$ , films were obtained with electron mobilities of 600-700  $\text{cm}^2/\text{V-sec}$  for net carrier concentrations of  $10^{16}\text{-}10^{17} \text{ cm}^{-3}$ , which exceeded the mobilities we obtained on either  $(01\bar{1}2)\text{Al}_2\text{O}_3$  or  $(10\bar{1}4)\text{Al}_2\text{O}_3$ . At higher Si growth rates (up to  $\sim 6 \mu\text{m}/\text{min}$ ) and deposition temperatures  $T_g$ , good quality films ( $\mu \sim 500\text{-}600 \text{ cm}^2/\text{V-sec}$ ) were also formed on  $(01\bar{1}2)\text{Al}_2\text{O}_3$  ( $1040^\circ\text{C} \leq T_g \leq 1100^\circ\text{C}$ ).

At the high growth temperatures it was found necessary to "homogenize" the electrical properties of the films by an  $\text{O}_2$ ,  $\text{N}_2$  anneal in order to deactivate the autodoping species.

p-type Si films were also grown using  $\text{B}_2\text{H}_6$  as the dopant source. As in the case of the n-type films, better films were obtained on  $\sim(1\bar{1}20)\text{Al}_2\text{O}_3$  [(111)Si growth] than on  $(01\bar{1}2)\text{Al}_2\text{O}_3$  [(100)Si growth]; Hall mobilities were  $\sim 2\text{-}3$  times larger for films with net hole concentrations  $10^{16}\text{-}10^{17} \text{ cm}^{-3}$ .

A comparison of film properties of n-type films as a function of thickness indicated both the (100) and (111)Si films behave the same way, i.e., the average mobilities show a steady decrease with decreasing film thickness. The average mobilities were slightly superior for  $\sim 0.5\text{-}1.0 \mu\text{m}$  films grown  $\sim(1\bar{1}20)\text{Al}_2\text{O}_3$ .

These studies revealed the strong interrelationships that exist among the various parameters involved in optimizing Si growth on insulators. Evaluation of the electrical properties of Si films on those orientations that produce the best Si overgrowths demonstrated that growth conditions (i) must be optimized for the particular substrate orientation chosen; (ii) differ for those substrate orientations which lead to the same Si orientation; (iii) are dependent on reactor geometry; and (iv) probably should be optimized for the particular film thickness desired. In addition, care must be

exercised in measurement techniques when using mobility as a figure of merit because of the differences caused by anisotropy considerations.

### Acknowledgments

The authors wish to thank J. P. Wendt for carrying out the electrical measurements, R. E. Johnson for performing the photolithographic processing, angle-lapping, and staining, Fred Forrest for developing special techniques for producing scratch-free  $(10\bar{1}4)$ -oriented substrates, L. A. Moudy and A. J. Hughes for helpful discussions regarding orientation-relationship data and anisotropy, R. Harada for growth experiments in the horizontal reactor, and R. P. Ruth for a review of the manuscript. The work reported in this paper was supported in part by the Advanced Research Projects Agency under Order No. 1585, and monitored by the U.S. Army Missile Command, Redstone Arsenal, Alabama, under contract No. DAAH01-70-C-1311.

Manuscript submitted Dec. 10, 1974; revised manuscript received Sept. 3, 1975. This was Paper 140 presented at the New York, New York, Meeting of the Society, Oct. 13-17, 1974.

Any discussion of this paper will appear in a Discussion Section to be published in the December 1976 JOURNAL. All discussions for the December 1976 Discussion Section should be submitted by Aug. 1, 1976.

Publication costs of this article were partially assisted by Kockwell International.

### APPENDIX

In order to examine further the effect of the presence of  $\text{Al}_2\text{O}_3$  in a system containing Si, two experiments were performed, one in  $\text{H}_2$ , the other in He. An oval  $\text{Al}_2\text{O}_3$  wafer ( $13 \times 16 \text{ mm}$ ) was placed on a  $\sim 60 \text{ ohm-cm}$  n-type  $\text{H}^+$ -dipped mechanically polished Czochralski-grown Si wafer. The composite was heated in the CVD reactor at a pedestal temperature of  $1100^\circ\text{C}$  for 1 hr in  $\text{H}_2$  or in He, with these carrier gases flowing at a rate of 0.1 pm. For the  $\text{H}_2$  case, after the  $\text{Al}_2\text{O}_3$  was removed, a mesa about 1  $\mu\text{m}$  high which pruned the oval wafer was in evidence, and the Si which had been exposed to the  $\text{H}_2$  was eroded considerably. The Si mesa and surrounding area were p-type and etched. Angle-lapping and staining revealed a relatively uniform p-type layer  $\sim 2.4 \mu\text{m}$  thick at the mesa and a somewhat irregularly shaped layer  $\sim 1.7 \mu\text{m}$  thick in the etched area where the wafer was positioned. A van der Pauw measurement of the mesa, which was cut from the rest of the wafer, gave the following properties:  $\rho = 3.5 \text{ ohm-cm}$ ;  $p = 6.3 \times 10^{15} \text{ cm}^{-3}$ ;  $\mu = 284 \text{ cm}^2/\text{V-sec}$ .

A subsequent anneal for 1/2 hr in  $\text{O}_2$  plus 2 hr in  $\text{N}_2$ , a process which has usually been found sufficient to deactivate the Al-containing impurity species in thin SOS films, diffused the p-type impurity further into the substrate and at the same time converted the top of the p-type layer to n-type. An additional 18 hr of anneal (1/2 hr  $\text{O}_2$  + 17 1/2 hr  $\text{N}_2$ ) almost converted the whole layer to n-type, as evidenced by only a residual stain of the layer at its deepest penetration.

Without  $\text{Al}_2\text{O}_3$  present in the reactor, another unused piece of the same Si wafer used in the above experiment remained n-type and relatively high resistivity after treatment in  $\text{H}_2$  for 1 hr at  $1100^\circ\text{C}$ .

Some attack of the Si by  $\text{Al}_2\text{O}_3$  was also in evidence when He was used as the carrier gas, but the etching was much less severe; essentially no mesa was formed. The Si surface just below the  $\text{Al}_2\text{O}_3$  was converted to p-type, however, as in the  $\text{H}_2$  experiment.

These results demonstrate the need for minimizing the reactions between Si,  $\text{Al}_2\text{O}_3$ , and  $\text{H}_2$ . They also suggest that some reaction products may be generated during the early stages of Si growth which could affect the mode of nuclei formation, be incorporated into the growing film, and affect the crystallinity of the films at the Si- $\text{Al}_2\text{O}_3$  interface. Such impurities may constitute an additional factor in determining the defect structure in SOS films, in addition to that attributed to lattice mismatch and strains at the Si- $\text{Al}_2\text{O}_3$  interface. Autodoping can presumably be minimized by the use of an inert atmosphere, lower growth temperatures, and high growth rates to seal the  $\text{Al}_2\text{O}_3$  surface as fast as possible.



## REFERENCES

1. H. M. Manasevit and W. I. Simpson, *Proc. Am. Phys. Soc.*, Edmonton, Alberta, Canada, Late News Item (1963).
2. D. J. Dumin, *J. Appl. Phys.*, **38**, 1909 (1967).
3. H. M. Manasevit, R. L. Nolder, and L. A. Moudy, *Trans. Met. Soc. AIME*, **242**, 465 (1968).
4. L. J. van der Pauw, *Philips Res. Rept.*, **13**, 1 (1958).
5. D. J. Dumin and P. H. Robinson, *This Journal*, **113**, 469 (1966).
6. J. Mercier, *ibid.*, **117**, 812 (1970).
7. G. E. Gottlieb and J. F. Corboy, Jr., *J. Cryst. Growth*, **17**, 261 (1972).
8. D. J. Dumin and P. H. Robinson, *J. Appl. Phys.*, **39**, 2759 (1968).
9. H. Schlotterer, *Solid State Electron*, **11**, 947 (1968).
10. D. J. Dumin and P. H. Robinson, *J. Cryst. Growth*, **3/4**, 214 (1968).
11. A. C. Ipri, *J. Appl. Phys.*, **43**, 2770 (1972); *Appl. Phys. Letters*, **20**, 1 (1972).
12. C. W. Cullen and J. F. Corboy, *This Journal*, **121**, 1345 (1974).
13. A. J. Hughes and A. C. Thorsen, *J. Appl. Phys.*, **44**, 2304 (1973).
14. A. C. Thorsen and A. J. Hughes, *Appl. Phys. Letters*, **21**, 579 (1972).
15. A. J. Hughes and A. C. Thorsen, Unpublished data.

## Amorphous CVD Al<sub>2</sub>O<sub>3</sub> Films by Ta-Doping and Their Physicochemical Properties

Paul J. Tsang,\* Ronald M. Anderson, and Serge Cvikevich

IBM System Products Division, East Fishkill Facility, Hopewell Junction, New York 12533

### ABSTRACT

Tantalum-doped alumina films were deposited by the pyrolysis of a vapor mixture of TaCl<sub>5</sub> and AlCl<sub>3</sub> in the presence of hydrogen and carbon dioxide in the temperature range of 800°–950°C. The Ta content seems limited to 5.5 mole per cent of Ta<sub>2</sub>O<sub>5</sub>. The films, with only a minute amount of Ta, are crystalline, having the properties of pure alumina films. When the Ta content exceeds a certain level, the films become amorphous. Amorphous films have an optical index of refraction of 1.68 and a dielectric constant ranging from 9.5 to 12.0. Amorphous films are etchable in the diluted, buffered HF<sup>1</sup> solution and show a d-c conduction governed by the Poole-Frenkel effect.

Chemical vapor deposited (CVD) alumina (Al<sub>2</sub>O<sub>3</sub>) films, because of their negative dielectric charges (1), have found applications as gate insulators for the conventional, insulator-gated, field-effect transistors (IGFET) (2–4) and as the field insulators for n-channel MOSFET IC's (5). In addition, it has been shown that electrically alterable read-only memory FET's can be fabricated using layered Al<sub>2</sub>O<sub>3</sub>-SiO<sub>2</sub> gate insulators (6). The capability of alumina to resist radiation damage (7) also makes it attractive for devices used in space applications.

The chemical vapor deposition of alumina films can be achieved by either thermal decomposition of Al organometallic compounds (8) at temperatures below 600°C, or by the pyrolysis of aluminum halides (9, 10) at temperatures higher than 700°C. The alumina films formed at lower temperatures are mostly amorphous, whereas the high temperature films formed by the pyrolysis of Al halides are crystalline.

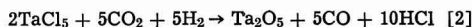
Generally, films used for device fabrication are deposited above 800°C because they are relatively stable during device processing and possess good dielectric strength. Unfortunately, the grain boundaries of the high temperature crystalline films are potential, long-term failure sites. In addition, the high temperature crystalline films are not etchable by the buffered HF solution, the photolithographic etchant most commonly used in microelectronics fabrication. Extra processing steps are required if these films are used. To provide ease of device fabrication and film integrity, amorphous Al<sub>2</sub>O<sub>3</sub> films formed at high temperatures are therefore desired.

Many elements present as impurities are capable of retarding the transformation of the metastable γ-Al<sub>2</sub>O<sub>3</sub> phase into the stable α-phase, due to their preference in occupying the tetrahedral sites in the oxygen lattice

(11). In addition, the introduction of impurity during film formation may also favor the growth of amorphous films due to an increase in configurational entropy (12), and/or due to the impurity-induced change of film nucleation and growth behavior (13). It may therefore be possible to form amorphous CVD Al<sub>2</sub>O<sub>3</sub> films at relatively high temperatures by impurity doping. This paper describes the deposition and physicochemical properties of amorphous Al<sub>2</sub>O<sub>3</sub> films doped with Ta and formed in the temperature range that is normally used for forming crystalline pure alumina films.

### Experimental

*Film deposition.*—It is well known that at temperatures above 700°C, CVD Al<sub>2</sub>O<sub>3</sub> films and Ta<sub>2</sub>O<sub>5</sub> films can be formed by the pyrolysis of AlCl<sub>3</sub> (9) and TaCl<sub>5</sub> (14), respectively, in the presence of H<sub>2</sub> and CO<sub>2</sub> through the following probable reactions



In this work, the formation of Ta-doped alumina was achieved by the pyrolysis of a vapor mixture of AlCl<sub>3</sub> and TaCl<sub>5</sub>. The AlCl<sub>3</sub> and TaCl<sub>5</sub> vapors were generated by heating AlCl<sub>3</sub> and TaCl<sub>5</sub> powders.<sup>1</sup>

The film deposition system is shown in Fig. 1. It consists of a reaction chamber, a TaCl<sub>5</sub> vapor saturator, an AlCl<sub>3</sub> vapor saturator, and feed lines which interconnect the halide vapor saturators through precision flow meters and control valves to allow close control of the AlCl<sub>3</sub> and TaCl<sub>5</sub> mixture flow to the reaction chamber for film deposition. All the feed lines and valves that connect the saturators to the reaction chamber were heated to 145°–160°C to prevent any halide condensation. A rf heated, silicon carbide-coated

\* Electrochemical Society Active Member.

Key words: thin films, dielectric amorphous alumina, Ta-doping, Poole-Frenkel electrical conduction.

<sup>1</sup> AlCl<sub>3</sub> powder of 99.999% pure was purchased from Apache Chemical Company and the high purity resublimed TaCl<sub>5</sub> powder was purchased from Alpha Inorganics (Ventron).

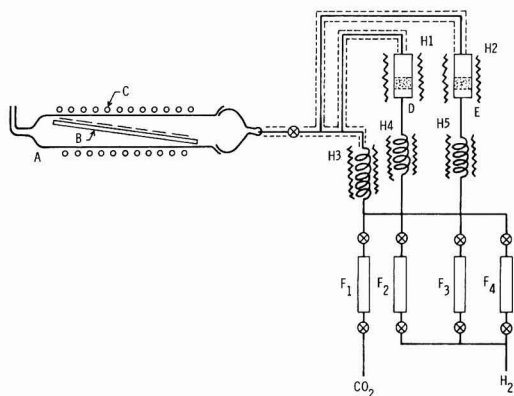


Fig. 1. Film deposition system. A, reactor; B, substrate susceptor; C, rf heating coil; D and E,  $\text{AlCl}_3$  and  $\text{TaCl}_5$  saturators; H1 to H5, heaters; F1 to F4, flow meters.

graphite susceptor was used as a film substrate holder and heater. The temperatures of the substrates were measured by a Leeds and Northrup optical pyrometer and are reported in this paper uncorrected. The "true" substrate temperatures are, in general,  $15^\circ$  higher.

The  $\text{AlCl}_3$  and  $\text{TaCl}_5$  powders in their vapor saturators were heated to  $115^\circ$  and  $130^\circ\text{C}$ , respectively. At these temperatures,  $\text{AlCl}_3$  and  $\text{TaCl}_5$  vapors of approximately the same pressure of 4.3 mm Hg were generated (15, 16), and the vapors were then carried out of the saturators by hydrogen gas, which itself was preheated to the saturator temperatures through separate lines and heaters. The saturation levels of the halide vapors in  $\text{H}_2$  carrier gas were not measured, but the consistencies of their saturation were checked before and after the Ta-doped alumina film deposition by measuring the growth rate of  $\text{Al}_2\text{O}_3$  and  $\text{Ta}_2\text{O}_5$  control films. Hydrogen was also used as a main diluent. It was first mixed with  $\text{CO}_2$  and was then heated to about  $400^\circ\text{C}$ . The preheated  $\text{H}_2$  and  $\text{CO}_2$  mixture, after picking up the halide-carrying  $\text{H}_2$  flows that come out of the saturators, was fed into the reaction chamber for film deposition.

By varying the flow ratio of  $\text{AlCl}_3$  and  $\text{TaCl}_5$  the present system can deposit either pure  $\text{Al}_2\text{O}_3$  or  $\text{Ta}_2\text{O}_5$  films or Ta-doped alumina films in the temperature range of  $800^\circ$ - $950^\circ\text{C}$ . The films were deposited on either bare or slightly oxidized Si substrates (usually p-type  $<100>$ ). In the former case, the as-received substrates were chemically cleaned before film deposition, whereas in the latter case, the substrates were chemically cleaned and then oxidized to form 50-60 Å of  $\text{SiO}_2$  before film deposition. The pure alumina films deposited in this system are polycrystalline and have physicochemical properties similar to those reported by Doo and Tsang (17) and others (18). The pure  $\text{Ta}_2\text{O}_5$  films deposited in this system at  $900^\circ\text{C}$  have an averaged, ellipsoidally measured, index of refraction of  $2.30 \pm 0.10$  and a dielectric constant (measured at 1 MHz) larger than 43. These are in good agreement with the findings reported by Knausenberger and Tauber (14). Transmission electron microscope (TEM) examinations of these  $\text{Ta}_2\text{O}_5$  films show that they are  $\beta$ - $\text{Ta}_2\text{O}_5$  and have a microstructure similar to that observed by Spyridelis *et al.* (19). The Ta-doped alumina [henceforth called (Ta)  $\text{Al}_2\text{O}_3$ ] films are smooth and shiny in appearance but show an orange-peel surface texture when examined by a high-power phase-contrast microscope.

The conditions for film deposition were studied. As in the case of pure alumina films, the most important factor affecting film deposition and film quality was the mole (or volume) ratio of  $\text{CO}_2$  to the halides. It was observed that a  $\text{CO}_2$  to total halide mole ratio of larger than 500 to 1 is required in order to deposit

films with good insulating properties. All the films studied in this experiment were deposited with the  $\text{CO}_2$  to total halide mole ratio equal to or larger than 800 to 1. In order to obtain homogeneous, single modal films with uniform thickness, the total halide content in the feed gas was kept to less than 0.1% by properly adjusting the flow rate ratio of the main  $\text{H}_2$  diluent and the halide-carrying  $\text{H}_2$  gas. With this halide concentration in the gas phase and with the  $\text{TaCl}_5$  to  $\text{AlCl}_3$  mole ratio being kept at less than 1.8 to 1, the (Ta)  $\text{Al}_2\text{O}_3$  film deposition was similar to that of pure alumina films, *i.e.*, the film growth was predominated by the surface reactions. The growth rate of the films was primarily determined by and slightly varied by the  $\text{AlCl}_3$  concentration in the gas flow, and was increased exponentially with the decreasing reciprocals of the deposition temperatures in the range of  $800^\circ$ - $900^\circ\text{C}$  studied, with an apparent activation energy similar to that of pure alumina films as shown in Fig. 2. The addition of  $\text{TaCl}_5$  to the gas flow has an effect of reducing the over-all growth rate of the film. As can be seen in Fig. 3, the film growth rate was decreased monotonically with increasing  $\text{TaCl}_5/\text{AlCl}_3$  mole ratio up to 1.8 to 1. When this halide ratio was increased beyond 1.8 to 1, a drastic increase in film growth rate and a change of film morphology from single modal to bimodal were observed. The study of the film deposition was not pursued beyond the halide ratio of 1.8.

The Ta content of the films was determined by the electron microprobe method, using the pure CVD  $\text{Al}_2\text{O}_3$  and  $\text{Ta}_2\text{O}_5$  films obtained in the present system as standards. The Ta content of the film increases with the increasing volume (or mole) ratio of  $\text{TaCl}_5$  to  $\text{AlCl}_3$  in the feed gas. By assuming full saturation of the halides in the  $\text{H}_2$  carrier gas (*i.e.*, each cubic centimeter of  $\text{H}_2$  passing through the saturator carries out 4.3/760  $\text{cm}^3$

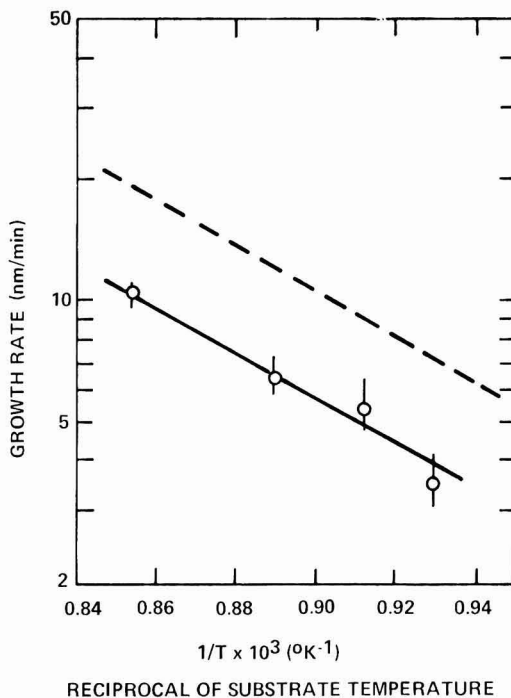


Fig. 2. Arrhenius plot of the growth rate of the (Ta)  $\text{Al}_2\text{O}_3$  films in the temperature range of  $800^\circ$ - $900^\circ\text{C}$  (solid curve). The total halide concentration in the gas phase was  $2.5 \times 10^{-4}$  and the  $\text{TaCl}_5/\text{AlCl}_3$  ratio was kept at 1.3 to 1. The dotted curve in the figure shows the growth rate of pure alumina films in the same temperature range.

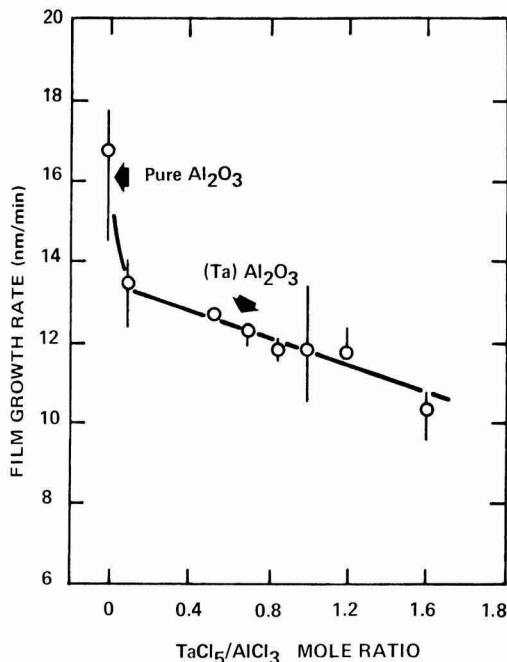


Fig. 3. The growth rate of the  $(\text{Ta})\text{Al}_2\text{O}_3$  film at  $900^\circ\text{C}$  as a function of the  $\text{TaCl}_5/\text{AlCl}_3$  mole ratio in the gas phase. The total halide concentration in the gas phase was varied from  $1.8\text{--}3.0 \times 10^{-4}$ , with the  $\text{AlCl}_3$  concentration in the gas phase kept constant at  $1.8 \times 10^{-4}$ .

halide vapor), we were able to relate the Ta content of the film [in mole per cent (m/o) of  $\text{Ta}_2\text{O}_5$  in the film] with the volume ratio of  $\text{TaCl}_5$  to  $\text{AlCl}_3$  in the feed gas, as shown in Fig. 4.<sup>2</sup> The Ta content of the film rises rather rapidly with the  $\text{TaCl}_5$  to  $\text{AlCl}_3$  ratio and levels off at about 5.5 m/o of  $\text{Ta}_2\text{O}_5$ . The saturation of Ta in the film shown in Fig. 4 may be attributed to system limitations. However, since a drastic increase in film growth rate and a change of film morphology from single modal to bimodal were observed as the  $\text{TaCl}_5/\text{AlCl}_3$  ratio was increased beyond 1.8 to 1, the saturation level in Fig. 4 may also suggest the limitation of incorporating  $\text{Ta}_2\text{O}_5$  into the CVD  $(\text{Ta})\text{Al}_2\text{O}_3$  films. A limited Ta solubility in the amorphous  $(\text{Ta})\text{Al}_2\text{O}_3$  films formed by the pyrolysis of Ta-pentaethoxide [ $\text{Ta}(\text{OC}_2\text{H}_5)_5$ ] and  $\text{AlCl}_3$  was also reported by Matsuo (20).

**Measurements of film properties.**—*Crystal structure.*—X-ray diffractometry and the transmission electron microscope (TEM) were used to study the crystallinity and structure of the films. For the x-ray diffraction study, the as-received films were used. The samples for TEM studies were prepared by back etching the silicon substrate with a mixture of  $\text{HF} + 2\text{HNO}_3 + 3\text{CH}_3\text{COOH}$  through a wax mask. This leaves a 1 mm circle of unsupported film stretched over the etched hole in the silicon wafer which is suitable for TEM examination.

**Film properties.**—The etchability of the film in various chemicals was measured at room temperature by observing thickness change with immersion time in the chemical. The film thickness, before and after etching, and the film optical index of refraction were measured by ellipsometry.

<sup>2</sup> Since good consistency of the halide saturation levels in the  $\text{H}_2$  carrier gas was seen, the effect of less than full halide saturation in Fig. 2 would be the multiplication of a factor of less than unity to the  $\text{TaCl}_5$  to  $\text{AlCl}_3$  ratio. However, the general characteristics of the Ta content vs.  $\text{TaCl}_5$  to  $\text{AlCl}_3$  ratio would still prevail.

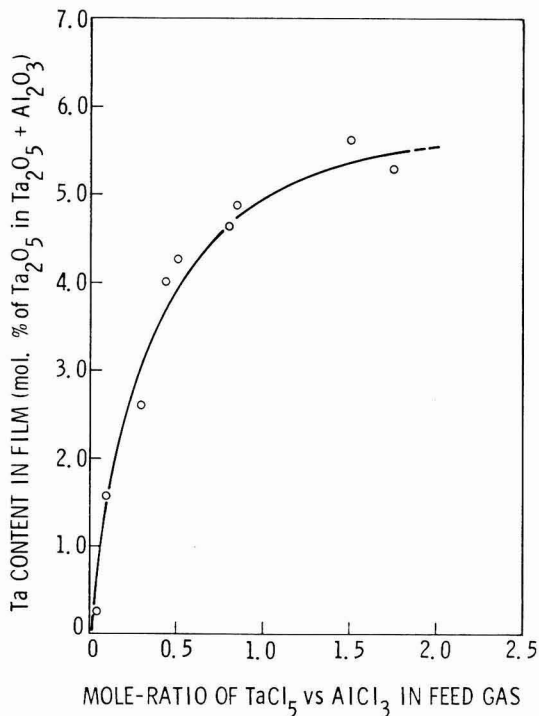


Fig. 4. Ta-content of the  $(\text{Ta})\text{Al}_2\text{O}_3$  film deposited at  $900^\circ\text{C}$  as a function of mole ratio of  $\text{TaCl}_5/\text{AlCl}_3$  in feed gas.

**Electrical characteristics.**—The conventional MIS (metal insulator semiconductor) type samples were fabricated for electrical measurements. In general, pure aluminum was used as the top electrode; however, in the case of d-c conduction measurements, gold top electrodes were used in some samples to study the effect of injecting electrode material on the film's conduction. To provide ohmic contact to the Si substrate, a layer of Al was evaporated onto its back side and the sample was subsequently annealed at  $420^\circ\text{C}$  for 20 min in forming gas. This postmetal anneal also served to reduce surface-state charge of the sample. The capacitance of the MIS samples was measured by a Boonton 710A capacitance meter at 1.0 MHz, while the breakdown strength of the films was measured by the linear I-V ramping technique.

In the film d-c conduction measurements, current transients were observed at lower applied voltages which decay to a quasi steady state in 3-4 min. Therefore, in order to eliminate the transient currents, the I-V characteristics of the films were obtained by applying an incremental stepwise voltage to the sample and measuring the film current 10 min after the voltage application at each voltage step.

## Results and Discussion

**Structure and crystallinity of the films.**—Films deposited at  $900^\circ\text{C}$  with only a minute quantity of Ta doping ( $\text{Ta}_2\text{O}_5 \leq 0.1$  m/o) are crystalline and have the same crystal structure as that of the pure  $\text{Al}_2\text{O}_3$  films examined. X-ray diffractometry performed on these low Ta content films, and the pure alumina films, produced patterns consisting of the few strongest lines of  $\kappa\text{-Al}_2\text{O}_3$ . However, the transmission electron diffraction (TED) pattern of the same films contained a very large number of diffraction lines. The list of interplanar spacings generated from the electron diffraction pattern does not completely match those of any of the alumina phases found in the literature although most of the  $\kappa$ -alumina reflections are accounted for. It is

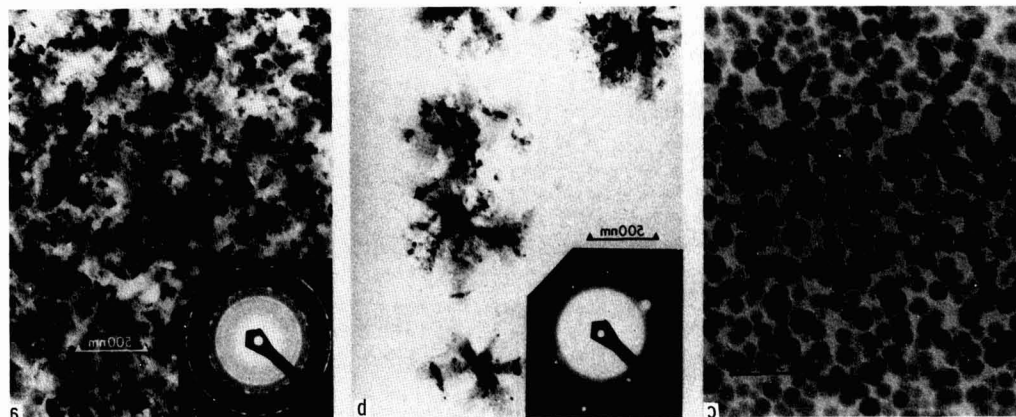


Fig. 5. TEM microstructures of the  $(\text{Ta})\text{Al}_2\text{O}_3$  films deposited on bare silicon: (a) film deposited at  $900^\circ\text{C}$  containing  $\sim 4.1$  m/o  $\text{Ta}_2\text{O}_5$  showing amorphous materials appeared at the film's grain boundaries; (b) film deposited at  $900^\circ\text{C}$  containing  $\sim 5.5$  m/o  $\text{Ta}_2\text{O}_5$ , showing amorphous matrix with  $\kappa'$ -crystallites; and (c) film deposited at  $825^\circ\text{C}$  containing  $\sim 4.8$  m/o  $\text{Ta}_2\text{O}_5$ . No TED pattern was obtainable from this film; the dark dots in the photo, indicated by arrow, are believed to be  $\kappa'$ -embryos.

possible that the extra diffraction lines seen in these CVD alumina films resulted from the occupation by Al atoms of the abnormal octahedral sites of the distorted spinel lattice of the  $\kappa$ -alumina giving rise to  $\kappa$ -alumina structure factor forbidden reflections. Since a complete crystallographical determination of the film is out of the scope of the present experiment, detailed structure analysis was not pursued. However, we were able to obtain the lattice parameters of an orthorhombic unit cell which accounts for the majority of the observed reflections. Calculated interplanar spacings are compared with observed reflections in Table I. We will designate the crystal structure of the films as  $\kappa'$ - $\text{Al}_2\text{O}_3$ , as a variation of  $\kappa$ - $\text{Al}_2\text{O}_3$ , for the convenience of later discussion. These lightly doped films had grain size of the order of 100 nm.

Table I. Crystallographic data

TED measured interplanar spacings	Calculated <sup>(a)</sup> interplanar spacings	Indices	$\kappa$ -alumina interplanar spacings
	6.16	110	6.2
4.72	4.75	101	
	4.53	200	4.5
4.20	4.20	020	4.2
3.14	3.15	121	
	3.02	300	3.04
2.81	2.80	030	2.79
2.76	2.79	002	
	2.70	221	2.70
2.55	2.54	112	2.57
2.42	2.41	131	2.41
2.39	2.38	230	
2.33	2.33	022	2.32
2.28	2.29	212	2.26
	2.18	410	2.16
2.11	2.10	040	
2.08	2.07	222	2.06
2.05	2.05	330	
2.03	2.03	411	
1.99	1.99	420 +	1.99
1.97	1.97	041 +	1.95
1.94	1.93	132 +	
1.87	1.86	003 +	1.87
	1.82	103 +	1.82
	1.75	402 +	1.74
1.64	1.64	341 +	1.64
1.57	1.54	440 +	1.54
1.49	1.49	512 +	1.49
1.45	1.44	052 +	1.44
	1.43	522 +	1.43
1.40	1.40	060 +	
1.395 (100%) <sup>(b)</sup>	1.395	004	1.395 (100%)

<sup>(a)</sup> Interplanar spacings calculated using an orthorhombic unit cell with lattice constants  $a_0 = 9.06$ ,  $b_0 = 8.41$ ,  $c_0 = 5.58\text{\AA}$ .

<sup>(b)</sup> The 1.395 line is the 100% intensity line in the TED pattern and for  $\kappa$ -alumina. In general, the TED intensities differed from the  $\kappa$ -alumina intensities. This is expected, as electron diffraction intensities usually do not track x-ray intensities and the TED pattern shows preferred orientation effect.

A decrease in film crystallinity with increasing Ta content was seen. TEM examination of films deposited at  $900^\circ\text{C}$  showed that diffuse grain boundaries were first formed in the film when a small amount of Ta was added. As the Ta content of the films was increased, the diffuse grain boundaries were replaced by amorphous material, Fig. 5a. At about this point, the film ceased to produce coherent x-ray diffraction patterns, although the  $\kappa'$ -alumina pattern was still obtainable via electron diffraction. The amorphous grain boundary width expanded at the expense of the crystalline grains, as the Ta content of the film was increased. The entire film became amorphous when the  $\text{Ta}_2\text{O}_5$  content of the film reached about 5.5 m/o.

The effects of Ta on the alumina film deposition are, apparently, to inhibit crystal nucleation and to retard grain growth. The effect was more prominent when the films were deposited on oxidized, rather than bare, Si substrates. When the films were deposited directly on bare silicon substrates, there were always some discrete  $\kappa'$ -crystallites included in the film, as shown in Fig. 5b, which, from TEM examination, were nucleated from sites on the silicon surface. The nucleation of the  $\kappa'$ -crystallites was greatly suppressed when the films were deposited on oxidized silicon wafers.

The same crystalline to amorphous structural transition was seen in films deposited at lower temperatures. It was found that by lowering the film deposition temperature the minimum amount of Ta required to produce amorphous films was reduced. At  $800^\circ\text{C}$ , complete amorphous films can be found with  $\text{Ta}_2\text{O}_5$  content as low as 4.5 m/o. Figure 5c shows a near amorphous film deposited at  $825^\circ\text{C}$ , with  $\text{Ta}_2\text{O}_5$  of 4.8 m/o. The film did not show a TED pattern, although TEM revealed bimodal morphology of the film. The dark dots in Fig. 5c are believed to be embryos of  $\kappa'$ -crystallites which were brought out by the silicon etching during TEM sample preparation. Films with the same Ta content would be partly crystalline if deposited at  $900^\circ\text{C}$ . On the other hand, it would be completely amorphous if it were deposited at  $800^\circ\text{C}$ .

Throughout the entire film structure studies, the  $\beta$ -Ta and/or  $\beta$ - $\text{Ta}_2\text{O}_5$  diffraction lines were never observed. Table II summarizes the structural change of the film with its Ta content and the deposition temperature.

*Physicochemical properties of the films.*—As in the case of the pure alumina films, the etchability of the  $(\text{Ta})\text{Al}_2\text{O}_3$  films in concentrated HF and  $\text{NH}_4\text{F}$  buffered HF (BHF) solutions depends on the crystallinity of the film. A highly crystallized film (film with well-defined

Table II. Variation of film crystallinity with Ta content

Sample	$T_{\text{dep}}$ ( $^{\circ}\text{C}$ )	Ta content (m/o $\text{Ta}_2\text{O}_5$ )	Crystallinity of film		
			X-ray	TED	TEM
1101	900	0.00	$\kappa'$	$\kappa'$	Crystalline
1089	900	0.15	$\kappa'$	$\kappa'$	Crystalline
1067	900	4.09	Amor.	$\kappa'$	Xtal. d. gb.(a)
1134	900	4.62	Amor.	$\kappa'$	Xtal. + amor. gb.(b)
1176	900	4.88	Amor.	$\kappa'$	Xtal. + amor. gb.(b)
1154	900	5.61	Amor.	$\kappa'$	Amor. + xtal.(c)
1158	900	5.27	Amor.	$(\kappa')$	Amor. (xtal).(d)
1188	825	4.80	Amor.	Amor.	$(\kappa')$ embryos
1205	800	4.50	Amor.	Amor.	Amorphous

- (a) Crystalline with diffuse grain boundary.  
 (b) Crystalline with amorphous grain boundary.  
 (c) Mixture of crystalline and amorphous phases.  
 (d) Amorphous film matrix with a small number of  $\kappa'$  crystallites.

x-ray and TED patterns) will not be etched by concentrated HF. On the other hand, a completely amorphous film (film structureless under TED examination) can be readily etched by a diluted BHF solution. The etch rate of the amorphous film in a 10:1 BHF solution is about 240 Å/min and seems to be independent of Ta content. The partly crystalline films with a mixture of amorphous and  $\kappa'$ - $\text{Al}_2\text{O}_3$  phases can also be etched with diluted BHF but the differences in etch rates of the two phases yields a rough surface. At room temperature, none of the common acids, such as  $\text{HNO}_3$ ,  $\text{HCl}$ , and  $\text{H}_2\text{SO}_4$ , were found to etch the (Ta) $\text{Al}_2\text{O}_3$  films, whether crystalline or amorphous. In hot (185 $^{\circ}\text{C}$ )  $\text{H}_3\text{PO}_4$ , uniform etchings of all the (Ta) $\text{Al}_2\text{O}_3$  films were observed. The partly crystalline films had an etch rate of approximately 240 Å/min while the etch rate of the amorphous films exceeded 500 Å/min.

The measured values of the index of refraction,  $n$ , of the crystalline and partly crystalline films were scattered; they fell in the range of 1.70–1.80. On the other hand, the index of refraction of the amorphous films remained a consistent value of between 1.66 to 1.68 without regard to the Ta content of the film.

**Dielectric characteristics of the films.**—The dielectric constants of the films were calculated from the capacitance and the thickness of the films. The dielectric constant  $K$  of the crystalline and partly crystalline films ranged from 8.0 to 10.0. No correlation between  $K$  and the Ta content of the film could be found. The dielectric constants of the amorphous films were found to range from 9.5 to 12.0, and seemed to increase slightly with Ta content of the film.

The dielectric breakdown strength  $E_b$  of the films, measured from the Al-(Ta) $\text{Al}_2\text{O}_3$ -Si (MAS) structures, was found to be 5–7 MV/cm.  $E_b$ 's measured on the Al-(Ta) $\text{Al}_2\text{O}_3$ - $\text{SiO}_2$ -Si (MAOS) structures (with 55Å underlying  $\text{SiO}_2$ ) were, in general, larger than 7.0 MV/cm. Table III summarizes the physicochemical properties of the film.

The C-V characteristics of the Al-(Ta) $\text{Al}_2\text{O}_3$ -Si (MAS) diodes are shown in Fig. 6. Curve (a) shows a typical C-V plot of a MAS diode with a highly crystallized, low Ta content (Ta) $\text{Al}_2\text{O}_3$  film. Except for the "sense" of the C-V hysteresis, it is very similar to that of a MAS diode with a pure  $\text{Al}_2\text{O}_3$  film. From the C-V

Table III. Physicochemical properties of film

	Partly crystalline	Amorphous
$n$ (a)	1.70–1.80	1.68 $\pm$ 0.01
$K$ (b)	8.00–10.0	9.5–12.0
BVD(c)	60 mV/cm	5.0–7.0 mV/cm
Etch rate BHF	Slow and uneven	Fast and even
Hot $\text{H}_3\text{PO}_4$	Normal to fast	Fast ( $\sim 10$ Å/sec)

- (a)  $n$  = Index of refraction.  
 (b)  $K$  = Dielectric constant measured at 1 MHz.  
 (c) BVD = Dielectric breakdown strength.

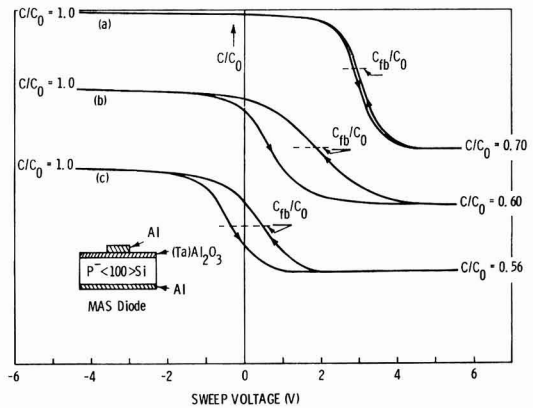


Fig. 6. C-V characteristics of MAS capacitors: (a) with crystalline film; (b) with partly crystalline film; and (c) with amorphous film.

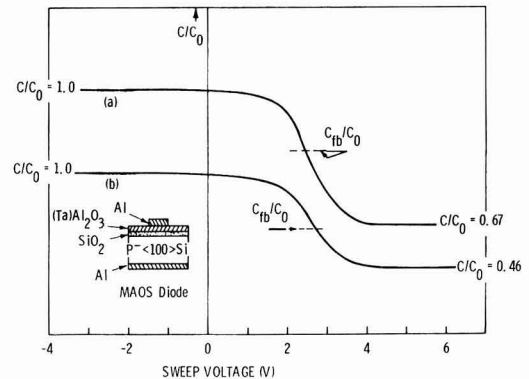


Fig. 7. C-V characteristics of MAOS capacitors: (a) with partly crystalline film; (b) with amorphous film.

hysteresis sense, it appears that acceptor-type, slow surface states exist at the Si-(Ta) $\text{Al}_2\text{O}_3$  interface. The density of these surface states appears to increase with the decreasing crystallinity of the film. This is seen in the extremely large C-V hysteresis in the MAS diodes with the partly crystalline film [Fig. 6, curve (b)] and with the amorphous film [Fig. 6, curve (c)]. The assumption of the existence of surface states at the Si-(Ta) $\text{Al}_2\text{O}_3$  interface is further confirmed by the absence of C-V hysteresis in the MAOS diodes (Fig. 7).

From the positive flatband voltage of the MAS and MAOS diodes examined, it was found that negative charges of the order of  $10^{12}$  q/cm $^2$  exist in the (Ta) $\text{Al}_2\text{O}_3$  film and/or at the  $\text{SiO}_2$ -(Ta) $\text{Al}_2\text{O}_3$  interface. In the MAS diodes, the dielectric charge seems to decrease with the crystallinity of the films. In the MAOS diodes, the crystallinity of the film has little effect on the dielectric charge level, Table IV.

**D-C conduction of the films.**—Figure 8 shows the d-c conduction of an amorphous film deposited at 800 $^{\circ}\text{C}$ . The  $\ln(J/E)$ 's, where  $J$  is the current density and  $E$  is the applied field, were plotted against the square

Table IV. Dielectric charge and crystallinity of films

Sample	Diode	$V_{\text{fb}} - \phi_{\text{ms}}$ (V)	$Q_{\text{eff}}$ (q/cm $^2$ )	Crystallinity of (Ta) $\text{Al}_2\text{O}_3$ film
1053-1	MAS	+2.90	$1.4 \times 10^{12}$	Crystalline
1160-1	MAS	+1.85	$1.05 \times 10^{12}$	Partly crystalline
1206-1	MAS	+0.05	$3.3 \times 10^{11}$	Amorphous
1077-2	MAOS	+1.10	$1.2 \times 10^{12}$	Crystalline
1160-2	MAOS	+2.45	$1.18 \times 10^{12}$	Partly crystalline
1206-2	MAOS	+2.70	$1.10 \times 10^{12}$	Amorphous



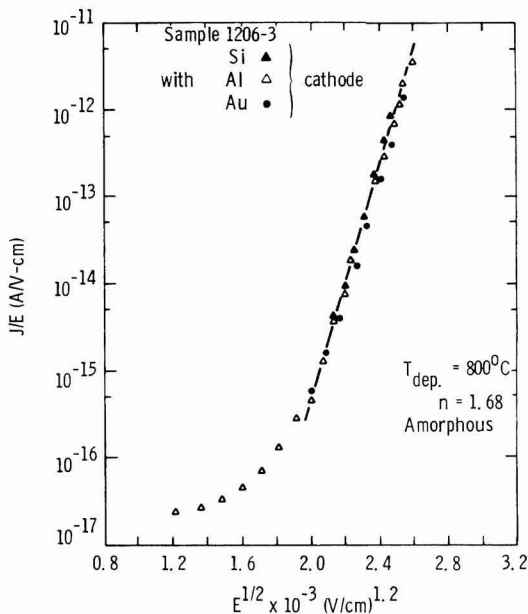


Fig. 8.  $J$ - $E$  characteristics of an amorphous film deposited at  $800^{\circ}\text{C}$ .

root of the applied field. It can be seen that (i) a linear relationship between  $\ln(J/E)$  and  $E^{1/2}$  exists at fields higher than  $3.5 \times 10^6$  V/cm; and (ii)  $J$  is independent of the injecting electrode material. The exponential dependency of film current density on  $E^{1/2}$  and the insensitivity of  $J$  on the electrode material indicate that the conduction is controlled by the Poole-Frenkel (PF) effect (21). The slope  $\mathcal{S}_{PF}$  of the  $\ln(J/E)$  vs.  $E^{1/2}$  plots shown in Fig. 6 yields a value of  $1.6 \times 10^{-2}$ .

It is known that the PF effect (21) arises from the field-assisted thermionic emission of electrons (or holes) from the coulombic traps in the films. The PF conduction of a film that contains only coulombic traps takes the form of Eq. [3] (22), which has a slope  $\mathcal{S}_{PF}$  of the  $\ln(J/E)$  vs.  $E^{1/2}$  plot equals to  $\beta_{PF}/2kT$ , where  $\beta_{PF} = (e^2/\pi\epsilon_0\epsilon_f)^{1/2}$  is the Poole-Frenkel constant

$$J = e\mu E(N_c N_d)^{1/2} \exp -(\psi_d - \beta_{PF} E^{1/2})/2kT \quad [3]$$

where  $e$  = electric charge,  $\mu$  = charge (electron) mobility,  $N_c$  = density of states of the film's conduction band,  $N_d$  = density of the film's coulombic traps,  $\beta_{PF}$  = Poole-Frenkel constant, and  $\psi_d$  = energy of the film's coulombic trap.

The PF constant and the slope of the  $\ln(J/E)$  vs.  $E^{1/2}$  plot, can be calculated by knowing the dynamic dielectric constant  $\epsilon_f$  of the film, or the films' optical index of refraction,  $n$ , since to the first approximation, the dynamic dielectric constant of the film equals the square of the film's optical index of refraction (23). Using the measured value  $n(=1.68)$  of the  $800^{\circ}\text{C}$  film, a theoretical  $\mathcal{S}_{PF}$  of  $0.785 \times 10^{-2}$  is calculated, which is only half of the experimental value. The large experimental  $\mathcal{S}_{PF}$  seen in the film can be explained if, besides the coulombic traps, the existence of neutral traps in the films is assumed (24). In this case, the Poole-Frenkel conduction of the film takes a different form due to the change of the Fermi energy caused by the presence of neutral traps. With the coulomb traps, of density  $N_d$ , and neutral traps, of density  $N_t$ , coexisting in the film, the Poole-Frenkel current density  $J$  takes the form of Eq. [4]

$$J = e\mu N_c (N_d/N_t)^{1/2} \exp -(\psi_d - \beta_{PF} E^{1/2})/kT \quad [4]$$

where  $N_t$  is the density of film's neutral traps, which has a slope of the  $\ln(J/E)$  vs.  $E^{1/2}$  plot equal to  $\beta_{PF}/kT$ , and yields a value of  $1.57 \times 10^{-2}$  if  $n = 1.68$  for the  $800^{\circ}\text{C}$  films is used for calculation. This is in very good agreement with experimentally obtained values.

The current-temperature measurement of the films at constant fields shows an exponential dependency of the conduction current with the reciprocal of the measuring temperature. From the  $\ln(J/E)$  vs.  $1/T$  plots, the apparent activation energy of the film conduction,  $\phi$ , was obtained.  $\phi$  was found to vary linearly with  $E^{1/2}$ , as expected from Eq. [4]. Extrapolating the  $\phi$  vs.  $E^{1/2}$  curve to zero field yields the coulombic trap energy of 1.80 eV below the conduction band of the film.

Similar  $I$ - $V$  characteristics were seen in the films deposited at higher temperatures. However, the slope of their  $\ln(J/E)$  vs.  $E^{1/2}$  plots were smaller, ranging from  $1.14 \times 10^{-2}$  to  $1.3 \times 10^{-2}$ . In addition, a small dependency of  $J$  on the injecting electrode material was also seen. In the films deposited at higher temperatures, some  $\epsilon'$ - $(\text{Ta})\text{Al}_2\text{O}_3$  crystallites were always present in the amorphous film matrix. It is possible then that these crystallites increase either the relative neutral trap density or the dynamic dielectric constant, or both. Both of these effects would result in a reduction of the slope of the Poole-Frenkel plot of the film (24, 25).

### Summary

Present work has shown that Ta-doped  $\text{Al}_2\text{O}_3$  films can be formed by the pyrolysis of a vapor mixture of  $\text{TaCl}_5$  and  $\text{AlCl}_3$  in the presence of hydrogen and carbon dioxide in the temperature range of  $800^{\circ}$ - $950^{\circ}\text{C}$ . The maximum Ta doping level of the  $900^{\circ}\text{C}$  films appears to be limited to 5.5 m/o of  $\text{Ta}_2\text{O}_5$ . With only a minute amount of Ta, the films are crystalline, having the properties of pure alumina films. When the Ta content exceeds a certain level, the film becomes amorphous. The amorphous films have a smaller optical index of refraction and a slightly larger dielectric constant, as compared with pure alumina films. Amorphous films are etchable in diluted, buffered HF solution at room temperature.

Probably due to the smaller energy bandgap (20), the d-c conduction of the amorphous films was found to be governed by the Poole-Frenkel effect. The energy level of the coulombic traps was found to be 1.80 eV from the conduction band of the film.

The films have negative dielectric charge and good dielectric properties in general. The amorphous film's etchability, in buffered HF solution, makes it use more attractive for microelectronic applications.

### Acknowledgment

The authors are indebted to Mr. William N. Patterson for his assistance in film deposition and to Dr. William A. Pliskin and Dr. Morris Shatzkes for their critical review of the manuscript. Mr. J. F. Shepard's suggestion to do this work and his encouragement are also acknowledged.

Manuscript submitted March 21, 1975; revised manuscript received Aug. 4, 1975. This was Paper 18 presented at the San Francisco, California, Meeting of the Society, May 12-17, 1974.

Any discussion of this paper will appear in a Discussion Section to be published in the December 1976 JOURNAL. All discussions for the December 1976 Discussion Section should be submitted by Aug. 1, 1976.

Publication costs of this article were partially assisted by IBM Corporation.

### REFERENCES

- H. E. Nigh et al., *IEEE Trans. Electron Devices*, **ED-14**, 631 (1967).
- P. B. Hart and P. S. Walsh, Paper 113 presented at The Electrochemical Society Meeting, Los Angeles, California, May 10-15, 1970.
- P. J. Tsang, V. Y. Doo, and C. Johnson, Jr., Paper 170 presented at The Electrochemical Society

- Meeting, Atlantic City, New Jersey, Oct. 4-8, 1970.
4. Shigern Nishimatsu and Takashi Takuyama, *Suppl. J. Japan. Soc. Appl. Phys.*, **39**, 125 (1970).
  5. P. J. Tsang and J. F. Shepard, Paper 168 presented at The Electrochemical Society Meeting, Miami Beach, Florida, Oct. 8-13, 1972.
  6. N. J. Chou and P. J. Tsang, *Met. Trans.*, **2**, 659 (1971).
  7. K. H. Zaininger and A. S. Waxman, *IEEE Trans. Electron Devices*, **ED-16**, 333 (1969).
  8. J. Aboaf, *This Journal*, **115**, 948 (1967).
  9. S. K. Tung and R. E. Caffrey, *ibid.*, **117**, 91 (1970).
  10. P. Balk and F. Stephany, *ibid.*, **118**, 1634 (1971).
  11. G. C. Bye and G. T. Simpkin, *J. Am. Ceram. Soc.*, **57**, 367 (1974).
  12. E. O. Jones, "Glass," John Wiley & Sons, Inc., New York (1956); W. H. Zachariassen, *J. Am. Chem. Soc.*, **54**, 38 (1932).
  13. F. C. Eversteyn and B. H. Put, *This Journal*, **120**, 106 (1973).
  14. W. H. Knausenberger and R. N. Tauber, *ibid.*, **120**, 927 (1973).
  15. "Handbook of Chemistry and Physics," R. C. Weast *et al.*, Editors, 45th edition The Chemical Rubber Co. (1964).
  16. H. Schafer and S. Kahleldurg, *Z. Anorg. Allgem. Chem.*, **305**, 184 (1960).
  17. V. Y. Doo and P. J. Tsang, Paper 6 presented at The Electrochemical Society Meeting, New York, New York, May 4-9, 1969.
  18. P. Tsujide, S. Nakanuma, and Y. Ikushima, *This Journal*, **117**, 703 (1970).
  19. J. Spyridelis *et al.*, *Phys. Status Solidi*, **19**, 683 (1967).
  20. Takeshi Matsuo, *Japan. J. Appl. Phys.*, **12**, 1862 (1973).
  21. D. R. Lamb, "Electrical Conduction Mechanisms in Thin Insulating Films," pp. 74, 87, Methuen and Co. Ltd. (1967).
  22. J. R. Yeargan and H. L. Taylor, *J. Appl. Phys.*, **39**, 5600 (1968).
  23. N. F. Mott and R. W. Gurney, "Electronic Process in Ionic Crystals," 2nd edition, Chap. V, Oxford University Press, Fair Lawn, New York (1948).
  24. J. G. Simmons, *Phys. Rev.*, **155**, 657 (1967).
  25. S. M. Hu, D. R. Kerr, and L. V. Gregor, *Appl. Phys. Letters*, **10**, 97 (1967).

## Flame Fusion Growth of Spinel and Sapphire Crystals for ESFI SOS Technology

R. Falckenberg

*Siemens AG, Forschungslaboratorium, München, Germany*

### ABSTRACT

A modified flame fusion process has been developed to grow crystals at low cost for use as substrate for the ESFI® SOS technology. Mg-Al spinel and sapphire single crystals with diameters up to 50 mm have been grown. Differences between both kinds of crystals are described concerning the behavior during the widening phase and the cooling phase of the growth process. Crystalline perfection was investigated in both crystals by the x-ray topography.

Mg-Al spinel as well as sapphire crystals are used as an insulating substrate material for the ESFI® SOS technology (1). For the synthesis of these crystals we investigated the flame fusion process, because it is a technique requiring no crucibles. Therefore it offers a possibility of lower costs compared to the Czochralski method, especially if iridium crucibles have to be used. As compared with crucible-grown crystals, the perfection of Verneuil crystals is worse; the electrical properties, however, of silicon films deposited on both kinds of substrates (2-4) do not show a significant difference. Verneuil sapphire (5) and spinel are produced on a large scale for jewels and bearings; severe limitations, however, exist especially as far as crystals of large diameter and suitable orientation are concerned. The diameter required for substrate wafers is between 50 and 75 mm; the orientation is  $\langle 100 \rangle$  and  $\langle \bar{1}012 \rangle$  for Mg-Al spinel and sapphire, respectively.

Two phenomena can be observed, if such crystals are grown by the flame fusion process: (i) cracking of the crystals during the cooling down phase and (ii) melt runover during the widening phase of the growth process.

With spinel crystals, it could be shown that cracking can be avoided by modifying the technique (6). The idea of the modification is to essentially exclude the temperature shock a crystal suffers at the end of the growth process when the flame is quenched. This is done by a ceramic furnace insert which deflects the flame gases immediately below the growth front of the growing crystal; from the beginning of the growth process, the bulk of the crystal is in thermal equilib-

rium with this insert. During the cooling down, the cooling rate is determined by the heat capacity of the insert. By this method, even the stoichiometric variation of Mg-Al spinel could be grown (Fig. 1).

The phenomena of melt runover can be understood by considering a model which explains the mechanism of crystal widening (9). According to this model an increase in flame power leads to remelting of a thin layer of already crystallized matter immediately below the growth front. The excess melt runs down at the crystal rim and forms a protrusion along the solid-liquid transition line. This line goes around the top of the crystal. The lower part of the protrusion solidifies. This model conception requires the radial temperature gradient at the solid-liquid transition line to stay below a certain critical magnitude, if the formation of a protrusion that is widening of the crystal is to occur.

Now alone the fact that a large crystal diameter requires a large growth chamber leads to low wall temperatures inside the growth chamber and consequently to an increase of the temperature gradient in question. Device parameters affecting the gradient are furnace insulation, multiple burners (10-12), displaceable heat shields and additional heating of the side walls of the growth chamber. An example of a displaceable insert device and additional heating for the modified flame fusion technique is shown schematically in Fig. 2. In contrast to afterheaters (13-16), which are thought for an *in situ* annealing of a crystal after the growth process, additional heating during crystal growth has to be confined to side walls of the growth chamber situated at (and above) the level of the solid-liquid transition line of the crystal. Additional heating below this level

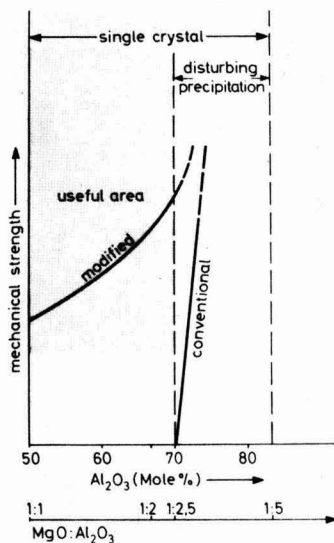


Fig. 1. Spinel substrate growth by flame fusion. The useful area is limited by too low mechanical strength (7) and by precipitations (8) arising during thermal treatment which disturb the epitaxial growth of silicon films.

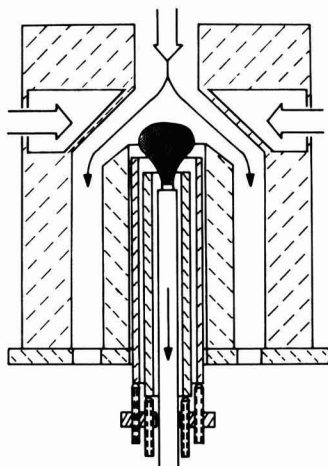


Fig. 2. Furnace with telescopic insert and additional heating of the side walls of the growth chamber for the growth of large diameter crystals.

would, at the high temperatures required, lead to an unstable growth situation due to the decrease of the axial temperature gradient along the crystal.

In Table I the results are shown which were obtained with spinel of a molar composition  $\text{MgO}:\text{Al}_2\text{O}_3 = 1:2$  and with sapphire. All the changes of the device parameters shown are acting in a direction as to keep the radial temperature gradient at the level of the solid-liquid transition line below a critical value. Above this value widening of the crystal would not be possible without melt runaway. In a displaceable heat shield device as depicted in Fig. 2 but without additional heating, spinel crystals could be grown up to a diameter of 50 mm (Fig. 3). In the identical device, sapphire crystals could be grown only up to a diameter of 38 mm; trying to enlarge the diameter further led to melt runaway. According to the model of crystal widening, the radial temperature gradient had to be further decreased. With the device shown in Fig. 2 we

Table I. Influence of device parameters on the diameter of Mg-Al spinel and sapphire crystals

Device parameters	Maximum crystal diameter [mm]	
	spinel	sapphire
poor furnace insulation, 2-tube burner	20	—
furnace insulation reinforced, 2-tube burner	35	—
furnace insulation reinforced, 3-tube burner	40	—
furnace insulation reinforced, 3-tube burner, telescopic insert	50	38
additional heating of side walls	—	53

used additional oxyhydrogen burners heating the side walls of the growth chamber. In this way sapphire crystals with a diameter up to about 50 mm could be grown (Fig. 3). A further enlargement was not possible in this device because of the inner diameter of the growth chamber being only 60 mm.

At the end of the growth process the flame was quenched. The spinel crystals obtained were mechanically stable; annealing before machining was not necessary. Sapphire crystals of  $\langle 10\bar{1}2 \rangle$  orientation cracked if the diameter was larger than  $\sim 45$  mm; strength and diameter could be increased further by choosing a different orientation, e.g.,  $\langle \bar{1}010 \rangle$ .

For x-ray topography spinel and sapphire crystals were cut into wafers perpendicular to the growth axis. The spinel samples were lapped with SiC, polished with  $\text{Al}_2\text{O}_3$ , thoroughly cleaned with Ultrasonics, etched with hot phosphoric acid, treated with sulfuric acid, and rinsed with distilled water. The final thickness of the samples was  $300 \mu\text{m}$ . With the sapphire slices, lapping as well as polishing was done with diamond paste. Figure 4 shows the x-ray topographies demonstrating the crystal quality. The spinel crystal shows a number of subgrains with deviations in orientation from the growth axis  $\langle 100 \rangle$  of up to  $2^\circ$ . The sapphire crystal essentially shows only tensions with a deviation from the growth axis not exceeding  $1^\circ$ .

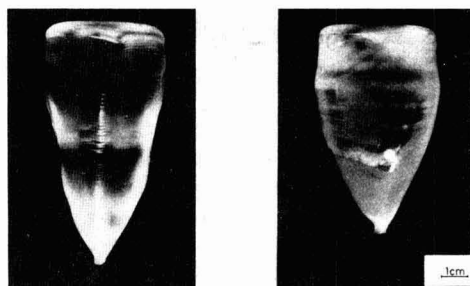


Fig. 3. Mg-Al spinel single crystal (molar composition  $\text{MgO}:\text{Al}_2\text{O}_3 = 1:2$ ) and sapphire crystal, grown by the modified flame fusion process. Orientation  $\langle 100 \rangle$  and  $\langle \bar{1}012 \rangle$ , respectively.

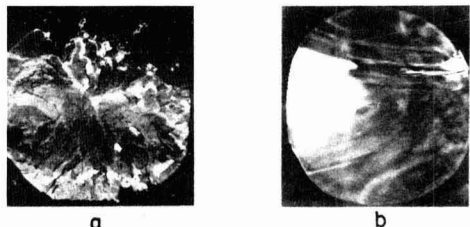


Fig. 4. X-ray topographies (Lang mode) of Mg-Al spinel (a) and sapphire (b), the reflecting planes being  $\{400\}$  and  $\{012\}$  respectively. Radiation Mo K $\alpha_1$ .

Growing spinel and sapphire distinct differences have been found in the way the crystals behaved during the widening phase as well as during the cooling down phase of the growth process. Different behavior in the diameter increasing may be due to differences in the thermal conductivities, emissivities, and IR absorptions; values which apply at high temperatures are known only for the IR absorption which indeed is lower for sapphire than for spinel. About the sensitivity of cracking measurements with polycrystalline  $\text{Al}_2\text{O}_3$  material have been conducted by Schwartz (17), there are however no investigations of Mg-Al spinel, which could be compared with these results.

#### Acknowledgments

The author wishes to acknowledge the work of J. v. Ivanits who assisted in crystal growth and of H. Grienauer who did the x-ray topography. For valuable discussions the author would like to thank Dr. E. Preuß.

Manuscript submitted July 24, 1975; revised manuscript received Sept. 18, 1975. This was Paper 223 presented at the Toronto, Canada, Meeting of the Society, May 11-16, 1975.

Any discussion of this paper will appear in a Discussion Section to be published in the December 1976 JOURNAL. All discussions for the December 1976 Discussion Section should be submitted by Aug. 1, 1976.

Publication costs of this article were partially assisted by Siemens AG.

#### REFERENCES

1. H. Schlötterer, *Electronics*, **42**, 113 (1969).
2. M. Druminski and Ch. Kühl, Paper presented at the GdCh-meeting "Grundlagen der Epitaxie," Erlangen, Germany, Sept. 1974.
3. M. Druminski, Ch. Kühl, E. Preuß, H. Splitterger, D. Takacs, and J. Tihanyi, Paper presented at ESSDERC, Nottingham, Sept. 74.
4. G. W. Cullen and F. C. Dougherty, *J. Cryst. Growth*, **17**, 230 (1972).
5. J. Ricard and A. Cioccolani, *ibid.*, **13/14**, 718 (1972).
6. R. Falckenberg, *ibid.*, **13/14**, 723 (1972).
7. J. G. Grabmaier and R. Falckenberg, *J. Am. Ceram. Soc.*, **52**, 648 (1969).
8. R. Falckenberg, *Mater. Res. Bull.*, **8**, 171 (1973).
9. R. Falckenberg, *J. Cryst. Growth*, **29**, 195 (1975).
10. J. A. Adamski, *J. Appl. Phys.*, **36**, 1784 (1965).
11. R. A. Lefevew, *Rev. Sci. Instr.*, **33**, 769 (1962).
12. Ch. H. Moore, *Trans. Am. Inst. Mining Met. Eng.*, **184**, 194 (1949).
13. W. Seifert, *J. Cryst. Growth*, **12**, 17 (1972).
14. R. S. Mitchell, *Rev. Sci. Instr.*, **36**, 1667 (1965).
15. R. H. Arlett and M. Robbins, *J. Am. Ceram. Soc.*, **50**, 273 (1967).
16. L. Merker, *ibid.*, **45**, 366 (1962).
17. B. Schwartz, *ibid.*, **35**, 325 (1952).

## MOS (Si-Gate) Compatibility of RF Diode and Triode Sputtering Processes

A. K. Sinha

Bell Laboratories, Murray Hill, New Jersey 07974

#### ABSTRACT

Using a Si-gate CMOS tester the MOS compatibility has been demonstrated of a metallization process involving triode sputter etch cleaning of Si prior to PtSi contact formation, triode sputter deposition of Ti/TiN/Pt layers, and rf diode sputter etching of the Pt using Ni as a sputter etch mask. The radiation damage induced in the gate regions of CMOS capacitors by each step of this metallization process has been evaluated, and the surface states and oxide charge resulting from the damage have been shown to be completely annealable using hydrogen. Triode sputter etch cleaning of the Si prior to PtSi formation was found to introduce considerable radiation damage. All of this damage could be removed after sintering and stripping the unreacted Pt by a hydrogen anneal at a temperature in the range of 375°-400°C and for times in the range of ½ to 1 hr. Subsequent triode sputter deposition of Ti/TiN/Pt leads to the generation of only a small peak ( $\sim 1.2 \times 10^{10} \text{ cm}^{-2} \text{ eV}^{-1}$ ) in the  $N_{ss}$  distribution in the lower half of the bandgap. Sputter etching of Au and Pt in an rf-diode system at rf power levels of 2 W  $\text{cm}^{-2}$  (sputter etch rate  $\sim 900 \text{ Å/min}$  for Au) also leads to considerable radiation damage. However, for a lower rf power of  $\sim 1.2 \text{ Wcm}^{-2}$ , which is practical if Pt only is sputter etched, little additional damage is observed over and above that induced during triode sputter deposition of Ti/TiN/Pt. Our results indicate that if a hydrogen anneal is performed prior to the final metal deposition (i.e., prior to the structure being sealed if a  $\text{Si}_3\text{N}_4$  layer is used), then excess hydrogen can be trapped in the  $\text{SiO}_2$  and poly-Si layers. A low temperature inert ambient anneal (e.g., 325°C, 1 hr, vacuum) can then be used subsequent to final metal deposition, during which hydrogen is redistributed, neutralizing any surface states at the Si/ $\text{SiO}_2$  interface.

A recent technology for  $\text{Si}_3\text{N}_4$ -sealed MOS-LSI devices utilizes chemical vapor deposited (CVD) poly-Si for the first level conductor (gates) separated from the second level metallization (contacts and interconnections) by an intermediate dielectric layer consisting of CVD  $\text{SiO}_2$  followed by  $\text{Si}_3\text{N}_4$  (1). The second level metallization processing involves the use of filament evaporation to form  $\text{Pd}_2\text{Si/Ti/Pd}$ . Evaporation was

chosen over sputtering because (i) sputtering as opposed to filament evaporation can cause radiation-induced damage (2), leading to unwanted interface states and trapped charge in the MOS structures, and (ii) it was considered very difficult to anneal out any radiation damage since the combination of metal contacts and  $\text{Si}_3\text{N}_4$  in the intermediate dielectric layer seals the device from the hydrogen required for low temperature ( $< 450^\circ\text{C}$ ) annealing of the interface states (3, 4). Sputter deposition has certain obvious advan-

tages though, an important one being that the step coverage is better than that usually obtained by evaporation (5). Poor step coverage by second level metallization is especially undesirable in the contact areas, since it can provide paths for migration of impurities such as Na and Au.

The objective of the present work was (i) to characterize any radiation-induced damage in Si-gate MOS structures due to triode sputter deposition and etching, and rf diode sputter etching, and (ii) to devise annealing schemes that would eliminate such damage in Si-gate devices sealed with  $\text{Si}_3\text{N}_4$ . For this purpose, a realistic test vehicle was used in which most of the thin gate oxide areas are covered by layers of poly-Si and intermediate level dielectrics.<sup>1</sup> The uniform gold process (7) was utilized for metal pattern generation for second level metallization. This process has been successfully used for metal gate MOS and bipolar devices. For bipolar devices, the metallization scheme consists of PtSi/Ti/TiN/Pt/Au which is metallurgically more reliable than the  $\text{Pd}_2\text{Si}/\text{Ti}/\text{Pd}/\text{Au}$  system. The uniform gold process is LSI compatible, since only one critical photoresist step is required as opposed to two for the standard Pd or Pt etch processes. The process studied involves triode sputter etching prior to PtSi contact formation, triode sputter deposition of Pt for PtSi, triode sputter deposition of Ti, TiN, and Pt layers, and electroplating of Au and Ni. The Au and Pt layers are removed by sputter etching in an rf diode system using selectively plated Ni as the mask. Each of the steps and combinations, thereof, have been evaluated with regard to the radiation-induced damage they produce in the above-mentioned MOS structure. An effective annealing scheme has been devised which utilizes intentionally trapped hydrogen to anneal out interface states in sealed MOS structures.

### MOS Test Structure and Processing

Figure 1 (a) shows a photomicrograph of a completed chip of the CMOS tester; the upper left corner shows the MOS capacitors on n-Si substrates and on the p-tub. Details of the MOS capacitors including metal contacts (rectangular-shaped pads,  $4 \times 10$  mil, over square window,  $3 \times 3$  mil) to the poly-Si electrodes

<sup>1</sup> Extensive studies were recently carried out by McCaughan et al. (2) on apparently "unannealable-degradation" of thin oxide films and interfaces due to various sputter deposition and back-sputtering processes; however, their test structures involved direct exposure of the gate oxide to various plasmas, following which the gate electrodes were evaporated.

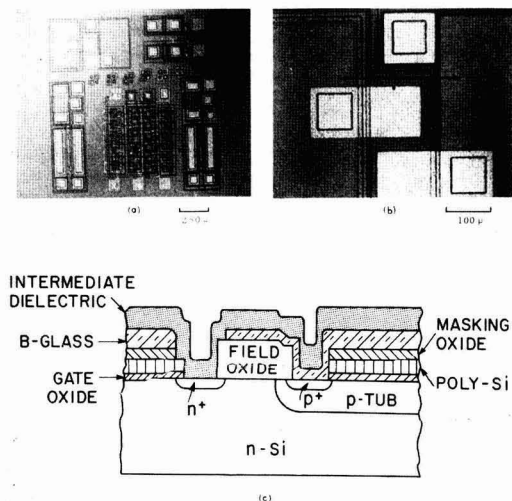


Fig. 1. (a) Photomicrograph of the CMOS tester. (b) Details of the p- and n-channel MOS capacitors. (c) Schematic cross section through the unmetallized portion of (b).

(area =  $10^{-3}$  cm<sup>2</sup>) and that (square-shaped pad,  $4 \times 4$  mil over window,  $3 \times 3$  mil) to the p-tub are shown in Fig. 1 (b), whereas Fig. 1 (c) shows schematically a cross section through the unmetallized portion of the two capacitors, including the n<sup>+</sup> and p<sup>+</sup> guard rings. The Si substrates consisted of  $\langle 100 \rangle$  n-type material doped with As to  $N_D \approx 1.5 \times 10^{15}$  cm<sup>-3</sup> whereas the p-tubs were doped with B to  $N_A \approx 1.5 \times 10^{16}$  cm<sup>-3</sup>. The gate oxide (1000Å thick) was grown on a freshly exposed Si surface prepared by stripping  $1\mu$  thick steam-oxide off the gate areas. The oxidation was done in HCl-cleaned quartz tube furnaces in a dry O<sub>2</sub> ambient at 1100°C (40 min) following which the oxidized Si wafers were annealed in Ar, also at 1100°C (30 min) using the same furnace. The first level (gate) metallization consisted of poly-Si doped with P to a sheet resistance of  $\sim 10$  ohm/□. The poly-Si electrodes were defined using steam-grown oxide (2500Å) as a mask. The p<sup>+</sup> areas ( $N_A \sim 2 \times 10^{19}$  cm<sup>-3</sup>) were formed using 1000Å of B-doped "Silox" oxide (followed by 2000Å of undoped SiO<sub>2</sub>, both made by reacting SiH<sub>4</sub> and O<sub>2</sub> at 480°C) as a diffusion source, with a drive-in at 1100°C (2 hr, N<sub>2</sub>). Next, n<sup>+</sup> areas ( $N_D \sim 10^{20}$  cm<sup>-3</sup>) were doped using PBr<sub>3</sub> (1100°C, 30 min). The intermediate dielectric layer separating the first level poly-Si metallization from the second level metallization normally consists of a composite layer of  $1\mu$  SiO<sub>2</sub> and 1-2000Å Si<sub>3</sub>N<sub>4</sub> through which windows are opened down to the diffused Si areas as well as to the poly-Si. In the present experiments, the Si<sub>3</sub>N<sub>4</sub> layer was omitted. However, the annealing schemes were devised keeping this Si<sub>3</sub>N<sub>4</sub>-sealing layer in mind.

The second level (contact and interconnection) metallization consists of PtSi ohmic contacts to n<sup>+</sup> and p<sup>+</sup> Si areas and to poly-Si, Ti/TiN/Pt/Au interconnections up to the termination areas, where a third level of metallization (beam leads) is built up by selectively electroplating thick Au beams ( $\sim 12\mu$ ). The characteristics of the sputtering stations (8) used in our experiments are given in Table I.

Finally, the back side of the Si wafers was cleaned and metallized with evaporated Al to form a large area ohmic contact to the n-Si substrate. Contacts to the p-tub were provided on front side of the wafer, along side each n-channel capacitor as shown in Fig. 1 (b).

### MOS Measurement Technique

For MOS measurements, the test facility consisted of an Electroglas 910 prober equipped with a Trompton TP35 thermochuck; the whole apparatus was completely enclosed in a dry N<sub>2</sub> glove box containing air interlocks. High frequency (1 MHz) C-V measurements were made at sweep rates of 100 mV/sec and quasi-static measurements were made at sweep rates of 20 mV/sec using the slow-ramp technique described by Kuhn (9). On a limited number of samples, mea-

Table I. Characteristics of the triode and rf diode machines/processes used in the present work

(A)	Triode machine
	Plasma in the Ti confinement tube: 80V, d.c., 10A
	Ta filament (cathode of confinement tube): 54A, a.c.
	Ar pressure: 2μ
(a)	Sputter etch cleaning mode
	Substrate table (Al coated with Pt): 500V peak-to-peak, rf (~250W rf power)
	Catch plate (stainless steel) grounded
	Si sputter etch rate $\sim 400$ Å/min
(b)	Sputter deposition mode
	Target (Ti or Pt, 12 in. diam): -500V, d.c.
	Substrate table: grounded through the rf power supply
	pN <sub>2</sub> for TiN: $7 \times 10^{-3}$ Torr
	Deposition times: 1 min for 500Å Pt
	3½ min for 1000Å Ti
	2 min for 100Å TiN
	3 min for 1500Å Pt
(B)	Rf diode sputter etching machine
	Rf power: 2 Wcm <sup>-2</sup> at 13.7 MHz (14 in. diam cathode)
	Cathode self-bias: 1800V peak-to-peak, -900V, d.c.
	Pressure: 20μ (80% Ar, 20% air)
	Cathode/anode spacing: 2 in.
	Au sputter etch rate: 900 Å/min



measurements were also made of the minority carrier storage time, oxide breakdown voltage, and the mobile charge density. The storage times were determined by pulsing the MOS capacitors into deep depletion and then plotting the recovery of inversion capacitance as a function of time.

The high frequency and quasi-static C-V data were analyzed in the manner described, e.g., by Wagner and Berglund (10). The Si-doping level  $N_{D,A}$  was estimated from the measured inversion capacitance,  $C_{inv}$  ( $Fcm^{-2}$ ) and the flatband voltage,  $V_{FB}$ , was estimated from the calculated flatband capacitance  $C_{FB}$ . For nonideal C-V curves, the net oxide charge,  $Q_t$  ( $cm^{-2}$ ) at flatband can be calculated using the relationship (11)

$$Q_t = (\phi_{MS} - V_{FB}) \cdot \frac{C_{ox}}{q} \quad [1]$$

where  $\phi_{MS}$  is the work function difference between the metal gate and the Si-substrate (for  $n^+$  poly-Si, its Fermi level was assumed to coincide with the Si-conduction band edge),  $C_{ox}$  is the oxide capacitance ( $Fcm^{-2}$ ), and  $q$  is the electronic charge. This simple equation does not allow one to separate the true fixed charge,  $Q_{SS}$  (always positive) from charges ( $N_{st}$ , positive or negative) trapped in the surface states. The latter are responsible for distortions in the high frequency C-V curves. The interface states density,  $N_{SS}$  ( $cm^{-2} eV^{-1}$ ) was calculated from the dispersion in the quasi-static and high frequency curves, in accordance with the relationship (12)

$$N_{SS} = \frac{C_{ox}}{q} \cdot \left[ \frac{1}{1/C_{qs} - 1} - \frac{1}{1/C_{hf} - 1} \right] \quad [2]$$

where  $C_{qs}$  and  $C_{hf}$  are normalized values (on a scale of 1.0, which represents the accumulation capacitance) of the quasi-static and the high frequency capacitances, respectively, at a given gate bias. The  $N_{SS}$  results from Eq. [2] are truly valid only in the potential range extending from about flatband point to the midgap. In a number of cases, the quasi-static C-V curves were analyzed in detail to give  $N_{SS}$  as a function of the relative surface potential,  $\psi_s$ , which was calculated from the area under the quasi-static curve (12)

$$\psi_s = \int_{V_0}^{V} [1 - C_{qs}] \cdot dV \quad [3]$$

The  $N_{SS}$  vs.  $\psi_s$  results for p- and n-channel capacitors were plotted on the same graph labeling  $\psi_s = 0$  at midgap, so that  $\psi_s(FB) \approx +|\phi_F|$  for the p-channel and  $-|\phi_F|$  for the n-channel capacitor. Positive values of  $\psi_s$  then signify the upper half of the bandgap and the negative values represent the lower half of the bandgap.

### The Over-all Metallization Process

Figure 2 shows typical high frequency C-V curves (solid lines) for p- and n-channel capacitors subjected to the over-all metallization process outlined in Table I. Also shown for comparison are the dashed C-V curves (high frequency and quasi-static), which correspond to well-annealed CMOS capacitors. The solid C-V curves reflect certain obvious effects of radiation damage; they are greatly distorted indicating a high density of surface states,  $N_{SS}$ . The negative shift of both C-V curves is taken as an indication of a large positive charge  $Q_{SS}$ . One consequence of the large  $Q_{SS}$  and high  $N_{SS}$  is to significantly decrease the apparent threshold voltage for the corresponding MOS transistor from the intended values of approximately  $\mp 1.5V$  (for p- and n-channel, respectively) to about  $-5.0$  and  $-1.0V$ , respectively, as indicated in Fig. 2.

For an understanding of the MOS damage shown in Fig. 2, the effects were studied of each of the three radiation-damage inducing steps in the metallization process, namely, sputter etch cleaning of Si, sputter deposition, and sputter etching of the deposited metallization. These results are considered below.

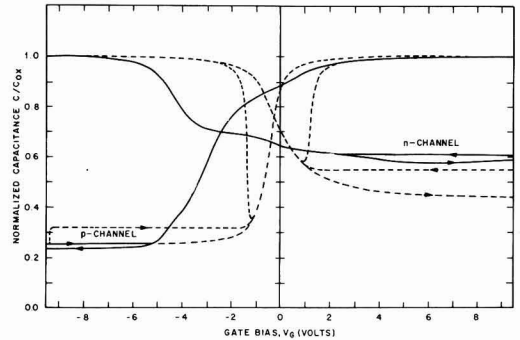


Fig. 2. High frequency C-V curves for CMOS capacitors subjected to the standard metallization process (solid lines). The dashed lines show C-V curves (high frequency and quasi-static) for well-annealed capacitors, with no radiation damage.

**Sputter etch cleaning.**—The preferred practice of forming PtSi ohmic contacts to Si (13) involves *in situ* rf-sputter etch cleaning of the exposed Si areas (e.g., source, drain, and guard rings in the Si substrate, and contact areas of the  $n^+$  poly-Si gate); this is followed by sputter deposition of Pt and sintering of the Pt layer to form PtSi ohmic contacts. For sputter etching, an rf potential is applied to the substrates, and the substrates achieve a negative self-bias equal to approximately one-half the peak-to-peak rf potential. As a result of this potential, the substrates are subjected to bombardment by energetic  $Ar^+$  ions extracted from the plasma. With no metal barriers present yet, direct damage can occur, in the case of IGFT's (insulated gate field effect transistors), at the edge of the gate oxide/Si interface which gets exposed when windows are formed in the source and drain areas. In the case of test capacitors, a similar situation arises at the  $p^+$  contacts to the p-tub. Moreover, indirect damage can result from  $Ar^+$ -ion bombardment of the poly-Si layer over the Si/SiO<sub>2</sub> interface. Although the exact mechanisms are not apparent, sputter etch cleaning was found to be the most severe radiation-damage inducing step of the metallization process.

The radiation damage induced by sputter etching is expected to be cumulative, i.e., it will depend upon the product of the intensity of radiation and time of exposure. The effect of the duration of sputter etch cleaning is shown in Fig. 3 and 4 which show complete C-V curves (high frequency and quasi-static, p- and n-channel) for samples sputter etch cleaned for 3 min and 1 min, respectively. Subsequent to sputter etching but prior to C-V measurements both of these samples were coated with 500Å of sputtered Pt, sintered at 650°C (20 min) in Ar/10% air ambient and the unre-

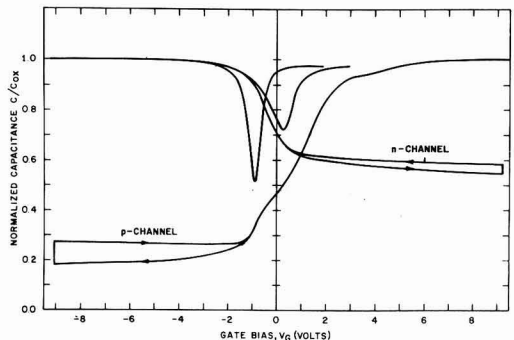


Fig. 3. C-V curves for CMOS capacitors processed through 3 min of sputter etch cleaning and PtSi formation in the contact windows.

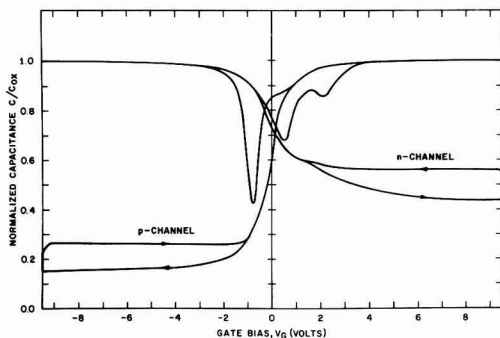


Fig. 4. C-V curves for CMOS capacitors processed through 1 min of sputter etch cleaning and PtSi formation in the contact windows.

acted Pt was etched away using hot *aqua regia*. The high frequency C-V curve for the p-channel capacitor of Fig. 3 is severely distorted and shifted in the positive direction. The positive shift of the p-channel C-V curve is also seen for the sample of Fig. 4 which was sputter cleaned for 1 min, but it is considerably less in extent. These positive shifts (apparent negative  $Q_t$ ) appear to be the result of a large  $N_{SS}$  effect.

The data in Fig. 3 and 4 were analyzed to give a distribution of surface states density  $N_{SS}$  with the relative surface potential  $\psi_S$  (Fig. 5). In both cases, i.e., for 3 and 1 min back-sputter cleaning, the  $N_{SS}$  vs.  $\psi_S$  distributions are similar; they show a shallow minimum near the mid-gap and a well-defined peak near the p-channel flatband point in the upper half of the forbidden band. The area under the peak of Fig. 5(a) was used to estimate  $N_{st}$ , the (negative) charge ( $-6.5 \times 10^{11} \text{ cm}^{-2}$ ) associated with the interface traps which, in the present case, act as acceptor states. Moreover, the shift in high frequency C-V curves for p-channel capacitors gives  $Q_t$  ( $= Q_{SS} + N_{st}$ ) as  $-3.4 \times 10^{11} \text{ cm}^{-2}$ , so that the radiation-induced  $Q_{SS}$  appears to be  $\sim 3 \times 10^{11} \text{ cm}^{-2}$ . A similar calculation for the case of Fig. 5(b) gives the trapped charge  $N_{st}$  as  $-10^{11} \text{ cm}^{-2}$  and the radiation-induced  $Q_{SS}$  as  $\sim 2 \times 10^{10} \text{ cm}^{-2}$ . In both cases, negative  $N_{st}$  dominates  $Q_{SS}$ , but only for p-channel capacitors presumably because the portion of the forbidden gap available for occu-

pancy by negative charges increases on going from midgap to flatband of p-channel capacitors; a reverse situation holds for n-channel capacitors.

Nearly ideal MOS characteristics are restored, i.e., the surface states are completely neutralized upon hydrogen annealing either of the above two samples at, e.g.,  $380^\circ\text{C}$  for  $\frac{1}{2}$  hr. This is evident from the data shown in Fig. 6 according to which both p- and n-channel capacitors have a  $Q_{SS} \sim 0$  (i.e.,  $< 10^{10} \text{ cm}^{-2}$ ) and midgap  $N_{SS} < 10^{10} \text{ cm}^{-2} \text{ eV}^{-1}$ . In the case where the intermediate oxide is covered with  $\text{Si}_3\text{N}_4$ , the  $\text{H}_2$  annealing would primarily occur by lateral migration of the H atoms across the wall of the contact windows, i.e., in the region between the top  $\text{Si}_3\text{N}_4$  layer and the PtSi layer present at the bottom of the contact apertures. The device is not fully sealed (against  $\text{H}_2$ ) until the contact windows are covered with Ti/TiN/Pt metallization upon subsequent sputter deposition.

**Ti/TiN/Pt triode sputter deposition.**—Triode sputter deposition of Ti/TiN/Pt was carried out on wafers which contained sintered PtSi ohmic contacts and were  $\text{H}_2$ -annealed for times in excess of those required to neutralize the previously present interface states. Metal pads were then defined over the contact areas by chemical etching in conjunction with usual photolithographic techniques. During the sputter deposition step, most of the particle bombardment is due to low energy neutrals, however, during the early stages of deposition, until a continuous layer (1000-2000Å) of metal film is formed, the Si-gate areas ( $\sim 5000\text{Å}$  thick) are exposed to the u.v. radiation and voltages of the plasma, which can produce radiation damage (14).

The effect of triode sputter deposition is shown in Fig. 7 in the form of high frequency and quasi-static C-V plots. It may be seen that sputter deposition after PtSi formation and  $\text{H}_2$  anneal does not appreciably distort the high frequency C-V curves, but the quasi-static C-V curves show evidence of interface states, whose distribution is shown in Fig. 8. This  $N_{SS}$  distribution has a peak in the lower half of the bandgap; however, the  $N_{SS}$  values are relatively low (in the range of  $1-7 \times 10^{10} \text{ cm}^{-2} \text{ eV}^{-1}$ ) so that the effects of any charge trapping are not reflected by appreciable distortion of the high frequency C-V curves.

**Sputter etching for metal pattern generation.**—The radiation damage induced in MOS Si-gate structures by rf diode sputter etching for metal pattern genera-

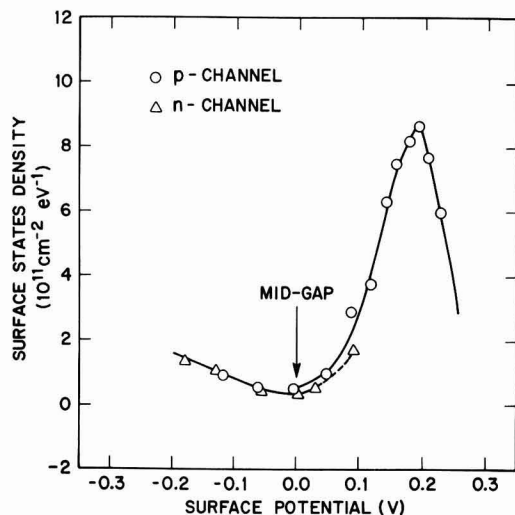
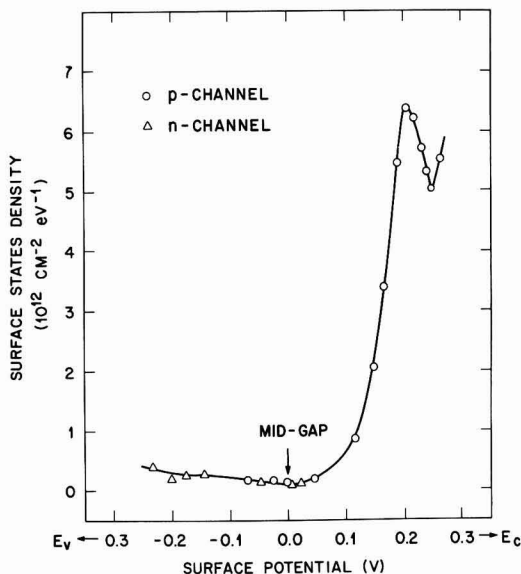


Fig. 5(a) and (b). Interface states density vs. surface potential curve for CMOS capacitors of Fig. 3 and 4, respectively

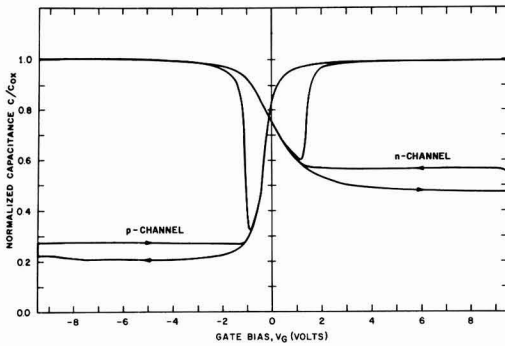


Fig. 6. Effect of  $H_2$  anneal ( $380^\circ C$ ,  $1/2$  hr) on the CMOS capacitors of Fig. 3 or 4.

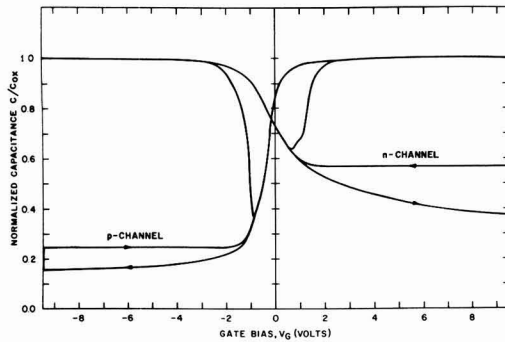


Fig. 7. Effect of Ti/TiN/Pt triode sputter deposition on the CMOS capacitors containing PtSi contacts and  $H_2$  annealed prior to triode sputter deposition.

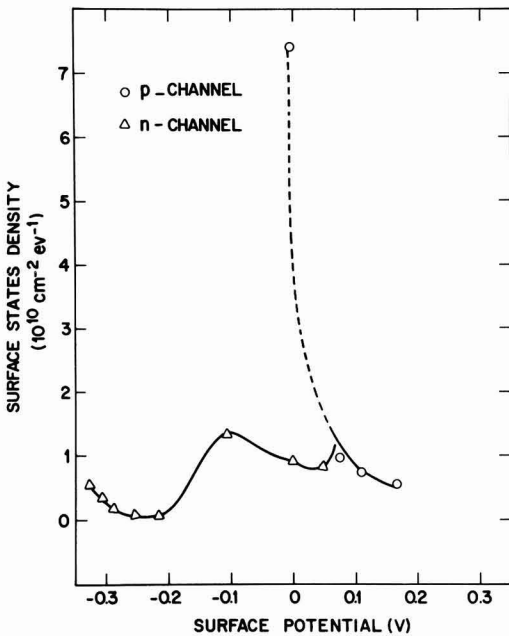


Fig. 8. Surface states density vs. surface potential for the CMOS capacitor of Fig. 7.

tion (uniform gold process) has been recently investigated (15). It was concluded that the damage is primarily due to x-rays (bremsstrahlung and character-

istic) generated by secondary electrons accelerated from the cathode which strike the anode. Since many types of MOS SIC's may require gold only on the beam leads and not on the intrachip metallization, sputter etch processes for metal patterning with and without gold (i.e., those utilizing high and low rf power levels, see below) on the intrachip metallization were compared. Two sets of conditions were evaluated. First, samples containing PtSi/Ti/TiN/Pt and  $H_2$ -annealed after PtSi formation were uniformly plated with gold ( $1\mu$ ) and selectively plated with a Ni mask. The Au and Pt layers were removed by sputter etching for 30 min at an incident rf power to the cathode of  $2 Wcm^{-2}$ . This condition corresponds to a cathode d-c self-bias of  $-900V$ , an rf peak-to-peak voltage of  $1800V$ , and a gold sputter etch rate of  $\sim 900 A/min$ . Second, samples, containing PtSi/Ti/TiN/Pt were selectively plated directly with Ni and the Pt removed by sputter etching for 20 min at an incident rf power to the cathode of  $1.2 Wcm^{-2}$ . This corresponds to a cathode self-bias of  $-500V$ , d.c., and an rf peak-to-peak voltage of  $1000V$ . Elimination of Au on the intrachip metallization makes it practical to consider sputter etching at lower power levels which should be milder conditions as far as MOS damage is concerned.

The C-V data for the sample sputter etched at a power of  $2 Wcm^{-2}$  are shown in Fig. 9. Considerable damage has occurred to the CMOS capacitors as reflected in the large positive  $Q_t$  ( $4-5 \times 10^{11} cm^{-2} eV^{-1}$ ) and  $N_{SS}$  values. The distribution of  $N_{SS}$  vs.  $\psi_S$  is shown in Fig. 10. The  $N_{SS}$  shows a peak in the upper half of the bandgap near the flatband point for the p-channel capacitor. From the area under this peak, the charge  $N_{st}$  trapped in the surface states is estimated as  $\sim 10^{11} cm^{-2}$ . This is relatively small compared to  $Q_t$  ( $= Q_{SS} + N_{st}$ ) so that irrespective of the sign of  $N_{st}$ ,  $Q_{SS}$  will be a large positive number ( $3-6 \times 10^{11} cm^{-2}$ ). Thus, in contrast with the case of sputter etch cleaning, here the radiation-induced positive  $Q_{SS}$  dominates  $N_{st}$ . At this stage, it is not possible to determine whether the  $N_{st}$  is associated with acceptor states (i.e.,  $N_{st} \sim -10^{11}$ ,  $Q_{SS} \sim 5-6 \times 10^{11} cm^{-2}$ ) or with donor states (i.e.,  $N_{st} \sim 10^{11}$ ,  $Q_{SS} \sim 3-4 \times 10^{11} cm^{-2}$ ).

The effect of sputter etching at the lower power of  $1.2 Wcm^{-2}$  is shown in Fig. 11. Although this sample shows only a slight increase in  $Q_t$ , the MOS degradation is manifested by an order of magnitude increase in  $N_{SS}$  over that characteristic of well-annealed samples (see, e.g., results given below). The resulting distribution of  $N_{SS}$  with  $\psi_S$  is shown in Fig. 12. It is characterized by a minimum near the midgap. These  $N_{SS}$  values are comparable to those induced by sputter deposition of Ti/TiN/Pt layers (Fig. 8) so that it appears that the simple expedient of reducing the rf power used for sputter etching was effective in mini-

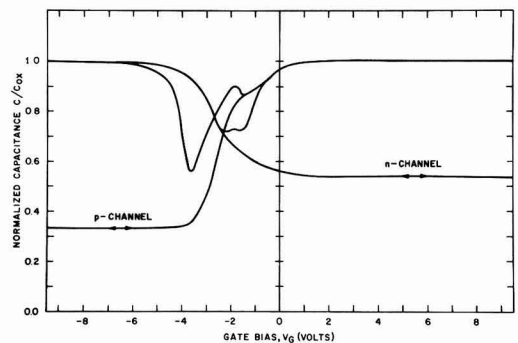


Fig. 9. C-V curves for CMOS capacitors processed through PtSi contacts,  $H_2$  anneal, Ti/TiN/Pt sputtering, Au electroplating, and sputter etching at high powers ( $2 Wcm^{-2}$ ).

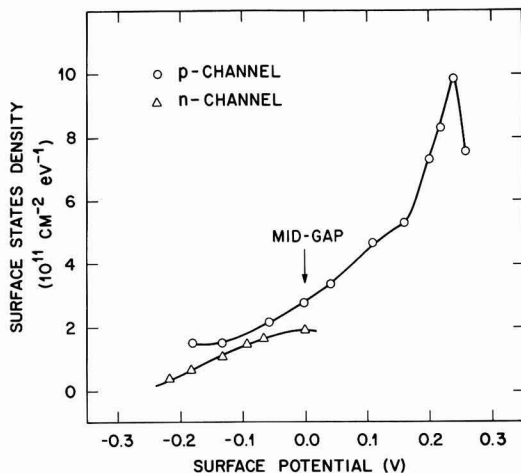


Fig. 10. Surface states density distribution curve for the CMOS capacitor of Fig. 9.

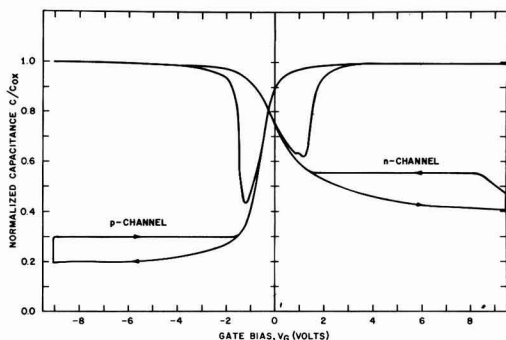


Fig. 11. C-V curves for CMOS capacitors processed through PtSi contact formation,  $H_2$  anneal, Ti/TiN/Pt sputtering, and sputter etch through Pt at low powers ( $1.2 \text{ Wcm}^{-2}$ ).

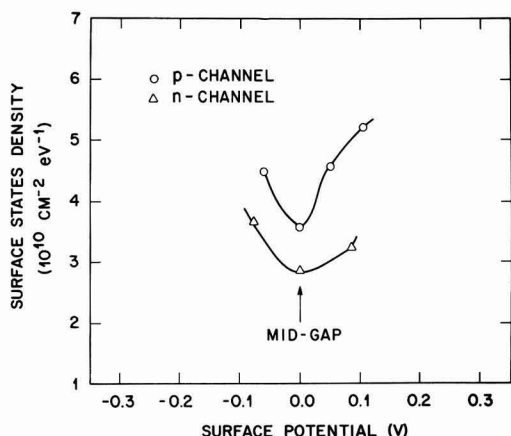


Fig. 12. Surface states density distribution curve for the CMOS capacitor of Fig. 11.

mizing additional damage during the sputter etch step. Furthermore, a partial annealing<sup>2</sup> of the  $N_{SS}$  due to trapped  $H_2$  (see below) might have also occurred dur-

<sup>2</sup> Although the Si wafers are clamped to a water-cooled cathode plate for efficient cooling during sputter etching, surface temperatures in the range  $100^\circ\text{--}200^\circ\text{C}$  are attained.

ing sputter etching to give the appearance of only a small net increase in  $N_{SS}$ .

### Use of Trapped Hydrogen for Annealing Interface States

The combination of a  $Si_3N_4$  seal and sputtered Ti/TiN/Pt metallization in the contact windows would render devices impervious (at practical postmetallization processing temperatures) to hydrogen which is required to neutralize the surface states associated with dangling bands at the Si/SiO<sub>2</sub> interface (16). Although the upper limit of postmetallization  $H_2$ -annealing temperature can be set by a variety of reasons, for systems containing Au, it will definitely be below the Au-Si eutectic point ( $370^\circ\text{C}$ ), and in the case of Al thin films it will be  $\leq 450^\circ\text{C}$  because of excessive hillock formation and grain growth. Our results indicate that part of the hydrogen previously introduced (during  $380^\circ\text{C}$ , 1/2 hr  $H_2$  anneal) in the devices after PtSi formation in the contacts gets trapped into the SiO<sub>2</sub> and poly-Si layers of the device. A subsequent anneal in an inert ambient such as *vacuo*<sup>3</sup> causes this trapped hydrogen to redistribute and anneal out the additional interface states produced by Ti/TiN/Pt sputter deposition and Pt sputter etching steps. The results of a vacuum anneal at  $325^\circ\text{C}$  (1 hr) are shown in Fig. 13 for a sample that received triode Ti/TiN/Pt sputter deposition and Pt removal by diode sputter etching. Nearly ideal MOS characteristics have been restored after the  $325^\circ\text{C}$  "redistribution anneal." The midgap surface states density is reduced by about an order of magnitude  $\sim 4 \times 10^9 \text{ cm}^{-2} \text{ eV}^{-1}$  for the p-channel device and to  $\sim 9 \times 10^9 \text{ cm}^{-2} \text{ eV}^{-1}$  for the n-channel device. The resulting  $Q_{SS}$  is nearly zero (i.e.,  $< 10^{10} \text{ cm}^{-2}$ ) for both cases and the calculated threshold voltages are found to be approximately  $\mp 1.5\text{V}$ , respectively, for the p- and n-channel devices, as expected.

Additional measurements of storage time, oxide breakdown voltage, and mobile charge were made on a limited number of MOS capacitors subjected to the hydrogen-redistribution anneals. Figure 14 shows typical plots of the normalized MOS capacitance as a function of time after the capacitors were driven into deep depletion by a pulse voltage of  $-10\text{V}$  or  $+10\text{V}$  for the p- and n-channel devices, respectively. The capacitors gradually recovered to the equilibrium state of inversion. The resulting transients were analyzed by the procedure suggested by Heiman (17). For the p-channel capacitors, the  $\tau$  was estimated at midpoint of the transient as 0.1 and 0.23 msec whereas for the n-channel capacitor on diffused p-tubs,  $\tau$  was found to be

<sup>3</sup> Vacuum annealing was initially tried to ensure moisture-free samples. Equally good results have been obtained by annealing in  $N_2$  or forming gas but only provided the samples had earlier received a  $H_2$ -annealing treatment prior to sputter deposition.

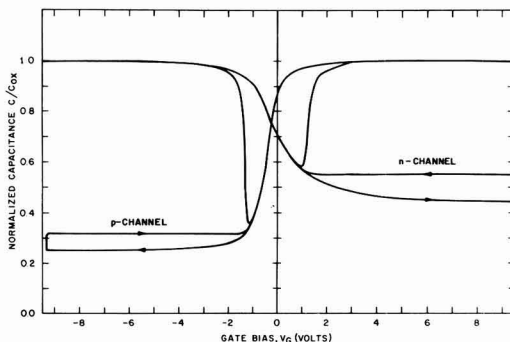


Fig. 13. Nearly ideal C-V curves of CMOS capacitors processed through PtSi contacts,  $H_2$  anneal, Ti/TiN/Pt sputtering, Pt sputter etch, and a final vacuum anneal ( $324^\circ\text{C}$ , 1 hr) to redistribute the previously trapped  $H_2$ .

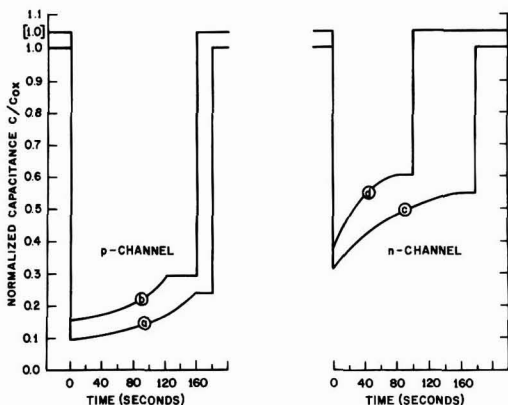


Fig. 14. Normalized MOS capacitance vs. time for capacitors of Fig. 13 driven into deep depletion: (a) and (b) p-channel; (c) and (d) n-channel.

much shorter at 9 and 5  $\mu\text{sec}$ . These values are generally representative of those expected for well-annealed MOS samples.

Gate-oxide breakdown voltages were also measured for a limited number of capacitors after the H-redistribution anneal. These ranged from 30 to 65V (for 1000Å thick gate oxide) with a median of about 50V.

Bias-stress aging experiments were carried out ( $\pm 10\text{V}$  on gate oxide,  $250^\circ\text{C}$ , 30 min) on the annealed samples with a view to determine any mobile charge ( $\text{Na}^+$ ) in the gate oxide. The total flatband shifts were always less than 0.1V indicating that the present CMOS device processing (which included a  $1000^\circ\text{C}$   $\text{PBr}_3$  getter step) was effective in keeping the mobile charge density acceptably below  $10^{10}$  atom  $\text{cm}^{-2}$ , and that mobile charges were not activated in the gate oxide as a result of the above processing steps.

Long-term negative bias-temperature aging studies (4) were not carried out, but they would be required to verify the permanence of the anneal. In view of the low values of  $N_{\text{SS}}$  that were achieved, there is reason to believe that significant charge trapping and consequent shifts in threshold voltage should not occur.

### Conclusions

Using a Si-gate CMOS structure, the MOS compatibility has been demonstrated of a process involving (i) triode sputter etch cleaning of contact areas, triode sputter deposition of Pt (for PtSi) and Ti, TiN, Pt layers, and rf diode sputter etching of the Pt layer and (ii) use of trapped hydrogen for annealing interface states in sealed MOS structures. The conclusions reached should be of general validity to Si-gate MOS devices, even though details of the radiation damage may depend critically on the specific structure employed.

1. The dominant modes of damage were found to be generation of surface states, radiation-induced  $Q_{\text{SS}}$ , and lifetime degradation, all of which are annealable using hydrogen.

2. The triode sputter etch cleaning step introduces surface states whose distribution shows a peak in the upper half of the bandgap. A large negative charge in the surface traps appears to dominate the (positive) radiation-induced  $Q_{\text{SS}}$ .

3. The triode sputter deposition process (following PtSi contact formation and  $\text{H}_2$  annealing) of Ti/TiN/Pt layers leads to a small peak in  $N_{\text{SS}}$  in the lower half of the bandgap.

4. Rf diode sputter etching (of Au and/or Pt) at high powers ( $2 \text{ W cm}^{-2}$ ) produced a peak in  $N_{\text{SS}}$ , also in the upper half of the bandgap. In this case a large positive radiation-induced  $Q_{\text{SS}}$  dominates any charges associated with surface traps. For low power sputter etching ( $1.2 \text{ W cm}^{-2}$ ), the  $N_{\text{SS}}$  distribution contains no peaks, only a shallow minimum is present near the midgap and no charge trapping is observed.

5. In sealed MOS structures which are impervious to hydrogen during postdamage annealing, hydrogen can be introduced and trapped in the oxide layer prior to the deposition of the final metallic layer seal. A low temperature, inert ambient anneal (e.g.,  $325^\circ\text{C}$ , 1 hr vac) can then be employed, subsequent to sputter deposition of the metallic layer, whereby the hydrogen redistributes by migration to the Si/SiO<sub>2</sub> interface and repairs the MOS damage.

6. MOS structures subjected to the above H-redistribution anneal have midgap  $N_{\text{SS}}$  in the  $10^9 \text{ cm}^{-2} \text{ eV}^{-1}$  range, nearly zero  $Q_{\text{SS}}$  (i.e.,  $< 10^{10} \text{ cm}^{-2}$ ), and lifetime of 10-100  $\mu\text{sec}$ . With careful processing, no mobile charges are introduced or activated by the above processes.

### Acknowledgments

The author is indebted to E. F. Labuda for many helpful suggestions in the course of this work, and for reviewing the manuscript. Appreciation is also extended to L. B. Fritzing for his generous assistance with metallization processing, to T. E. Smith for technical assistance with the MOS measurements, and to E. H. Nicollian, H. J. Levinstein, and R. S. Wagner for their suggestions.

Manuscript submitted July 16, 1975; revised manuscript received Sept. 22, 1975.

Any discussion of this paper will appear in a Discussion Section to be published in the December 1976 JOURNAL. All discussions for the December 1976 Discussion Section should be submitted by Aug. 1, 1976.

Publication costs of this article were partially assisted by Bell Laboratories.

### REFERENCES

1. J. T. Clemens, Unpublished.
2. D. V. McCaughan and R. A. Kushner, *Proc. IEEE*, **62**, 1236 (1974).
3. B. E. Deal, E. L. MacKenna, and P. L. Castro, *This Journal*, **116**, 997 (1969).
4. E. H. Nicollian, 12th Annual IEEE Proc. Rel. Physics, p. 267, 1974.
5. A. K. Sinha, Proc. 6th Int. Vac. Congress, Japan. *J. Appl. Phys., Suppl.* **2**, 487 (1974).
6. W. T. Lynch and W. J. Bertram, Unpublished.
7. E. F. Labuda, G. K. Herb, W. D. Ryden, L. B. Fritzing, and J. M. Szabo, Jr., Abstract 78, p. 195, The Electrochemical Society Extended Abstracts, Spring Meeting, San Francisco, California, May 12-17, 1974.
8. L. B. Fritzing, To be published.
9. M. Kuhn, *Solid-State Electron.*, **13**, 873 (1970).
10. S. Wagner and C. N. Berglund, *Rev. Sci. Instr.*, **43**, 1775 (1972).
11. A. S. Grove, B. E. Deal, E. H. Snow and C. T. Sah, *Solid-State Electron.*, **8**, 145 (1965).
12. C. N. Berglund, *IEEE Trans. Electron. Devices*, **ED-13**, 701 (1966).
13. A. K. Sinha, *This Journal*, **120**, 1767 (1973).
14. A. S. Grove, "Physics and Technology of Semiconductor Devices," John Wiley & Sons, Inc., New York (1967).
15. W. D. Ryden, E. F. Labuda, and J. T. Clemens, To be published.
16. E. Kooi, *Philips Res. Rept.*, **21**, 477 (1966).
17. F. P. Heiman, *IEEE Trans. Electron. Devices*, **ED-14**, 781 (1967).



# Characterization of Thin Anodized Films on Aluminum with Soft X-ray Spectroscopy

W. L. Baun

Air Force Materials Laboratory (MBM), Wright-Patterson AFB, Ohio 45433

and T. J. Wild and J. S. Solomon

University of Dayton Research Institute, Dayton, Ohio 45469

## ABSTRACT

Two methods utilizing x-ray spectra from the electron microbeam probe for the determination of aluminum oxide film thickness for a broad range of thicknesses are described. One method uses the direct measurement of oxygen K emission while the other uses the changes in fine features of the x-ray spectra with changes in oxide film thickness. For oxides formed by the barrier anodization technique, films as thin as 20-30Å and as thick as several thousand angstroms could be measured by these methods.

The thickness of thin films is usually determined by optical methods such as ellipsometry or interferometry or by an indirect method such as calculation from the evaporation of a known weight of material in a vacuum evaporator. Depth profiling techniques in which an inert gas ion beam sputters away surface layers while the surface is sampled are being used increasingly. Such depth profiling is done with ion scattering spectroscopy (ISS), secondary ion mass spectroscopy (SIMS), Auger electron spectroscopy (AES), and electron spectroscopy for chemical analysis (ESCA). Both the optical methods and techniques depending on sputter etching give good results in selected cases. However, the optical methods suffer greatly when the film is not uniform and the substrate is not flat (macroscopic) and smooth (microscopic). Other factors such as the film being a color which absorbs the probing radiation also can interfere with optical measurements such as ellipsometry. The accuracy of methods using sputter etching depends on a knowledge of the film sputtering rate, which even for pure materials varies greatly (depending on experimental conditions, especially ion beam voltage). There are also problems due to ion beam crater shape (sampling from the sides as well as the bottom of the crater), redeposition of sputtered material back into the crater, surface roughness, and other factors.

Each of the aforementioned techniques gave good results on idealized aluminum oxide films on aluminum. Such samples were prepared by vacuum evaporating aluminum on glass microscope slides and anodizing under barrier conditions at low voltages. When real samples which had been cut by shear techniques from bulk sheet stock subjected to surface oxidizing etches or to standard surface preparation prior to anodization were investigated, very poor results were often obtained probably due to surface roughness. X-ray emission technique similar to that used by Sewell *et al.* (1, 2) for thin films of Ta<sub>2</sub>O<sub>5</sub> on Ta by means of oxygen K measurement looked attractive for determining thickness of aluminum oxide on aluminum. In addition, the striking changes in the fine features of aluminum K spectra with changes in chemical combination (3, 4) showed promise for characterizing these films, both from the standpoints of thickness and structure.

## Experimental

The Hitachi XMAS electron microbeam probe analyzer equipped with a dispersing KAP crystal and an

ultrathin polypropylene-windowed flow proportional detector was used for results on oxygen K radiation shown here. For aluminum K spectra high resolution was provided by use of an ADP dispersing crystal. The electron beam potential was 10 kV with  $1 \times 10^{-6}$ A electron beam current using approximately  $5 \mu\text{m}^2$  beam. X-ray data was collected by step-scan techniques on paper tape and inputted to a time-share computer, X and Y intercepts for each point were calculated, and plots were prepared by a digital plotter. Samples were prepared in a stirred bath of 1% ammonium borate in ethylene glycol. Except as discussed later, anodizing voltages were maintained (constant voltage) in a range which gave a barrier anodized film.

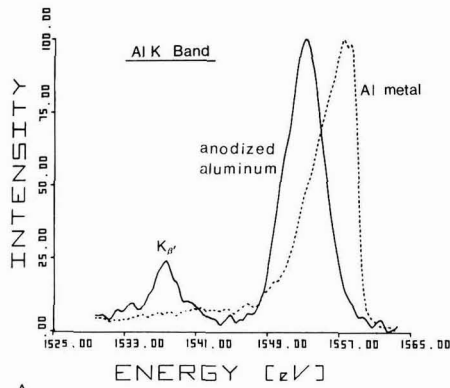
## Background on X-ray Spectra

The fine features of x-ray emission spectra may be used to determine chemical bonding. By operation at low voltages and other techniques the method can provide near-surface characterization on areas as small as  $1 \mu\text{m}^2$ . Aluminum K spectra are especially sensitive to changes in chemical bonding. Figure 1 shows the K band ( $K_{\beta}$ ) from aluminum metal and an anodized film. The large shift in the band as well as the appearance of  $K_{\beta}'$  in the oxide due to a molecular orbital transition forms the basis of using these fine features. Also shown in Fig. 1 is the K satellite group, the principal lines of which are stronger than  $K_{\beta}$  and are thus usually easier to use. The use of these features assumes that the oxide is on the surface and that a uniform change from "metal" to "oxide" spectra will take place when going from no film on the surface to a point where all x-ray emission emanates from the oxide film. This upper limit was about 4000Å in this work where 10 keV electrons were used but could be increased by an increase in operating voltage.

## Results

The most obvious method of using x-rays to determine oxide thickness is that of direct measurement of oxygen K intensities similar to the method of Sewell *et al.* (1, 2, 5). Such results are shown in Fig. 2 where the OK intensities obtained from anodized films on aluminum are plotted *vs.* the anodizing voltage. The anodization constant was determined to be 14 Å/V using ellipsometric techniques on vacuum-evaporated Al films anodized under the same conditions as the samples described earlier. Note that the intercept is not at zero, probably due to oxygen in solution in the bulk and to the natural oxide film which immediately covers an aluminum surface. The linear

Key words: films, x-ray, Al<sub>2</sub>O<sub>3</sub>, spectroscopy, anodization.



A

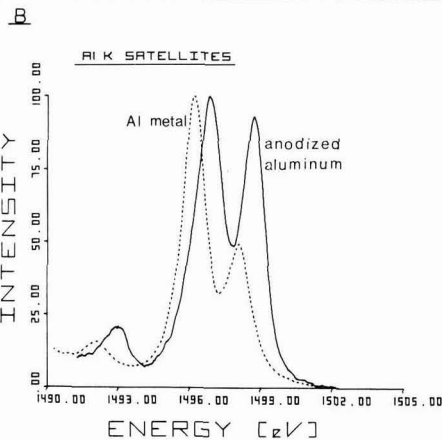


Fig. 1. Changes in fine features of x-ray emission spectra with changes in chemical combination; spectra from Al metal and aluminum oxide (anodized aluminum). A. the Al K band, B. the Al K satellites  $K\alpha_3$  and  $K\alpha_4$ .

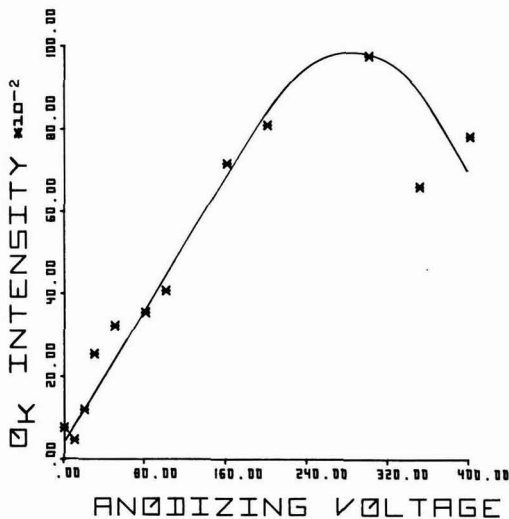


Fig. 2. Oxygen K x-ray intensities vs. anodizing voltage for aluminum (1% ammonium borate in ethylene glycol).

portion of the curve may be more nearly exponential if more points were added and better precision were achieved. Such a shape would be in keeping with elec-

tron and x-ray attenuation in the films, and would be in better agreement with the data of Mitchell and Sewell (5) on aluminum. However, data shown here, because of the use of a higher take-off angle and higher electron energies, would be less susceptible to absorption effects compared with the results of Mitchell and Sewell.

The changes in Al K x-ray spectra provide another method of determining oxide film thickness. Figure 3 shows the orderly change in the K band which involves valence electrons in going from Al metal to a thick 400V film. For reference, a spectrum is also shown for sapphire. Sapphire, the corundum structure, exhibits two maxima on the main K band, while anodized films show only one, indicating that the anodized film is not corundum structure and that x-ray fine features are sensitive not only to nearest neighbors, but also to the way in which they are arranged in the compound.  $K\beta$  originates only from the oxide due to a molecular orbital transition, and therefore becomes stronger with increasing oxide thickness in relation to the K band as seen in Fig. 4. Work is continuing to determine if the observed scatter is due to statistical measurement problems such as surface

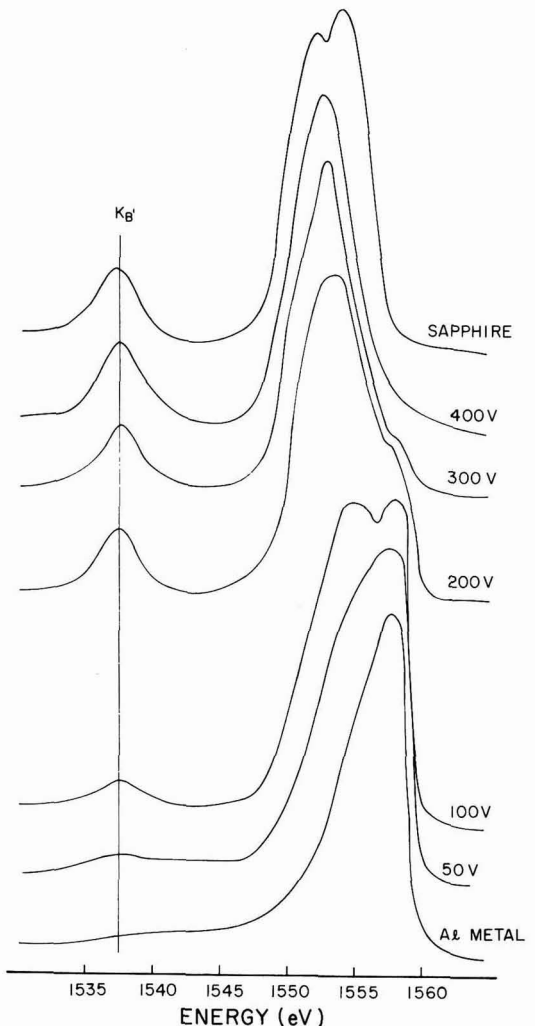


Fig. 3. The Al K band for samples anodized at various voltages compared to  $Al_2O_3$ , sapphire.

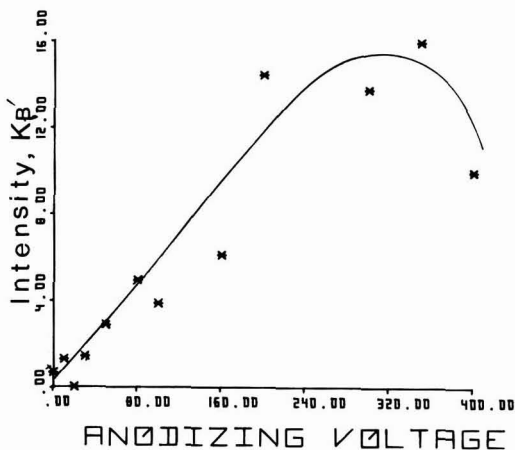


Fig. 4. The relationship of Al  $K_{\beta'}/K_{\beta}$  to anodizing voltage for aluminum.

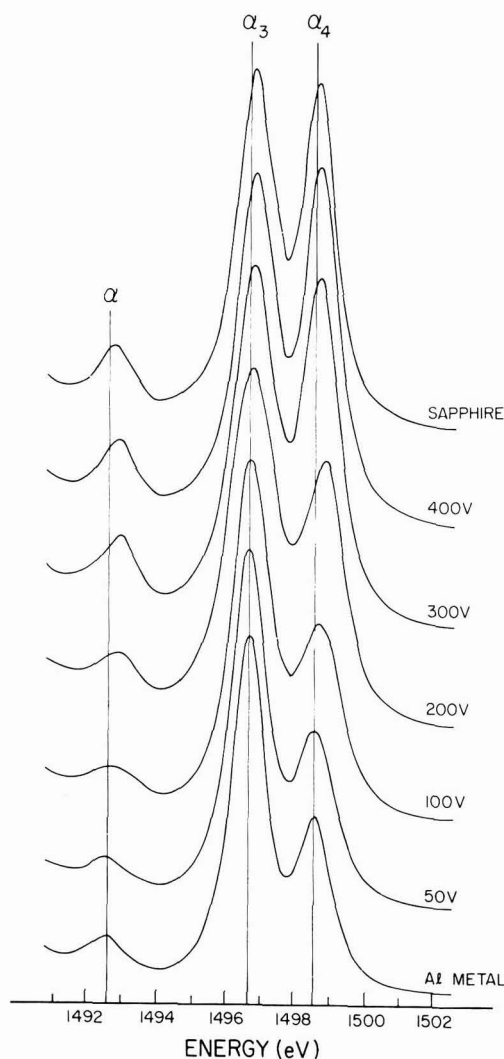


Fig. 5. Al K satellites for samples anodized at various voltages compared to  $Al_2O_3$ , sapphire.

charging or whether changes in anodization conditions or inhomogeneities in the film are responsible.

The strong satellites  $K\alpha_3$  and  $K\alpha_4$  which originate from multiply ionized states, provide another method of measuring film thickness as seen by the continuous change in the spectra in going from pure metal to a thick 400V film as seen in Fig. 5. The spectrum from sapphire in this case is virtually identical to the spectrum from the thick anodized film indicating that the satellite lines are not sensitive to structural changes. The ratio  $K\alpha_4/K\alpha_3$  is shown in Fig. 6. Notice in this plot the curve comes to a maximum and remains constant once the ratio has attained a value of approximately unity representing emission from only oxide. In measurements of OK intensities a similar effect was seen except that a maximum was reached followed by a decline giving the appearance that the film was becoming thinner with increasing anodizing voltage. It was suspected that a change in mechanism of anodization was responsible for the curve shape and current vs. time recordings were made at constant voltage for both high and low voltages. It was found for this electrolyte concentration that barrier oxide films are formed up to 250V; above this voltage a combination of barrier and porous film exists. Hoar and Yahalom (6) have shown detailed results of current density vs. time for aluminum anodization in which the curves may be analyzed as having one component which is due to barrier film forming and a superimposed component due to pore formation. Figure 7 illustrates this phenomenon for the electrolyte used here where A is current-time relationship for 50V and shows a typical curve for a barrier film while B is obtained at 300V and shows first barrier formation during the early sharp surge followed by a break in the curve indicating porous oxide formation. Electron micrographs of replicas at high magnification show the increase of the pore structure in the higher voltage oxide. Therefore, apparently the bend in the OK intensities represents a change in oxide bulk density rather than the oxide becoming thinner at higher voltages. That is, because of the pores, there are fewer oxygen sites per unit area. In addition it is possible that in the porous oxide the stoichiometric ratio between oxygen and aluminum is different from the barrier oxide. How-

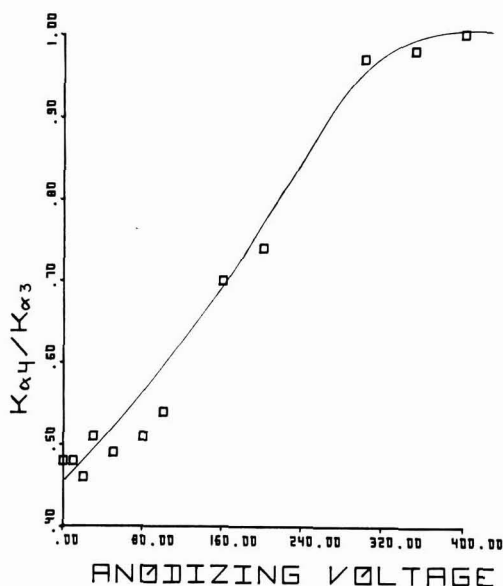


Fig. 6. The relationship of Al  $K\alpha_4/K\alpha_3$  to anodizing voltage for aluminum.

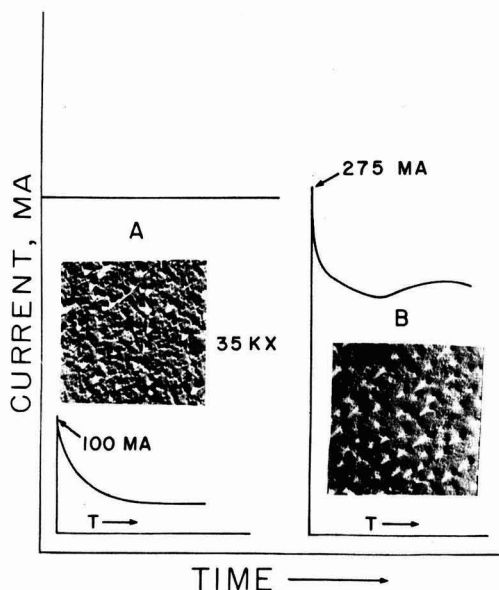


Fig. 7. Current vs. time curves and electron micrographs (35,000 $\times$ ) for aluminum anodized at voltages of 50V (A) and 300V (B) in 1% ammonium borate in ethylene glycol.

ever, in a nonaqueous system such as used here, this is unlikely.

### Conclusions

The x-ray emission method, either the direct measurement of oxygen K intensities, or the measurement of changes in the fine features of x-ray spectra, gives thickness information on aluminum oxide on aluminum over a wide range of thickness from about 20Å to several thousand Å. The technique lends itself to practical samples which are not amenable to measurement by methods enumerated earlier. The range of thickness could be increased compared to the results shown here. That is, much thicker films could be measured by using higher electron beam voltage.

### Acknowledgments

The ellipsometry measurement of film thickness of oxides on vacuum-evaporated films by Neil T. McDevitt is appreciated by the authors.

Manuscript submitted Feb. 25, 1975; revised manuscript received Aug. 16, 1975.

Any discussion of this paper will appear in a Discussion Section to be published in the December 1976 JOURNAL. All discussions for the December 1976 Discussion Section should be submitted by Aug. 1, 1976.

Publication costs of this article were partially assisted by The Air Force Materials Laboratory.

### REFERENCES

1. P. B. Sewell, D. F. Mitchell, and M. Cohen, *Surface Sci.*, **29**, 173 (1972).
2. P. B. Sewell and D. F. Mitchell, *J. Appl. Phys.*, **42**, 5879 (1971).
3. D. W. Fischer and W. L. Baun, *ibid.*, **36**, 534 (1965).
4. W. L. Baun, *ibid.*, **40**, 4210 (1969).
5. D. F. Mitchell and P. B. Sewell, *Thin Solid Films*, **23**, 109 (1974).
6. T. P. Hoar and J. Yahalom, *This Journal*, **110**, 614 (1963).

## Synthesis and Luminescence Properties of Europium-Activated Yttrium Oxysulfide Phosphors

Markus Koskenlinna, Markku Leskelä, and Lauri Niinistö

Department of Chemistry, Helsinki University of Technology, SF-02150 Otaniemi, Finland

### ABSTRACT

A new method of preparing brightly emitting Eu:Y<sub>2</sub>O<sub>2</sub>S phosphors is described. Yttrium sulfite doped with Eu is used as starting material and the Eu-activated oxysulfide is obtained from it either directly by reducing the sulfite with carbon monoxide, or by first oxidizing sulfite and then reducing the obtained oxysulfate. The properties of the phosphors and the effect of impurities on their luminescence spectra are briefly discussed.

Due to its bright luminescence under cathode ray excitation, europium-activated yttrium oxysulfide is a widely used red-emitting phosphor in color television picture tubes (1). Several methods have been reported for the synthesis of rare earth (RE) oxysulfides; they include reaction of RE oxides with various sulfur-containing reagents (e.g., H<sub>2</sub>S, CS<sub>2</sub>, NH<sub>4</sub>SCN) (2-4), reduction of RE sulfates by hydrogen (5, 6) and by carbon monoxide (7), reaction between RE oxides and sulfides (8), and methods employing sulfurizing fluxes (9, 10).

Key words: luminescence, phosphors, yttrium oxysulfide, europium oxysulfide.

In our previous study concerning the thermal decomposition of RE sulfites it was found that under certain conditions they form oxysulfides in reducing atmospheres (11). Based on that reaction, this report describes a new method for the preparation of brightly emitting europium-activated yttrium oxysulfide phosphors. Their properties are also briefly discussed, with special emphasis on the effect of impurities on the luminescence brightness.

### Experimental

*Materials and analytical methods.*—Three different grades of yttrium oxide (99.9, 99.99, and 99.999% with

respect to RE impurities) were used in the experiments. The purity of europium oxide was 99.9%. Both oxides were produced by Kemira Oy, Oulu, Finland.

The purity of the starting materials as well as that of the phosphors was analyzed with an AEI MS702 mass spectrometer, using spark-source excitation and electrical detection. The amount of europium present in the sulfites and phosphors was analyzed by atomic absorption spectrometry with a Perkin-Elmer 303 instrument. The purities of deionized water, ethanol, ether, and acetic acid used for washing the phosphors were also checked by AAS.

**X-ray diffraction.**—The homogeneity and crystallinity of the sulfites and oxysulfides were checked by x-ray diffraction using a Philips powder diffractometer with Ni-filtered  $\text{CuK}\alpha$  radiation. The accurate unit cell parameters of the synthesized oxysulfides were calculated by a least-squares procedure from x-ray diffraction photographs taken with a Guinier camera (Enraf-Nonius FR 552). Potassium chloride was used as internal standard, and the films were measured with a microdensitometer.

**Thermal analysis.**—The formation of  $\text{Eu: Y}_2\text{O}_2\text{S}$  from the sulfite was investigated in a Mettler Thermoanalyzer by simultaneously recording the TG, DTG, and DTA curves. The flow rate of CO was  $90 \text{ cm}^3/\text{min}$ . The sample holder was an aluminum oxide crucible (diam-8 mm, depth 20 mm). The stability of the activated phosphor in vacuum ( $4 \cdot 10^{-5} \text{ atm}$ ) was checked in another experiment where it was heated from  $25^\circ$  to  $1000^\circ\text{C}$ . The heating rate in both experiments was  $6^\circ/\text{min}$ .

**Luminescence measurements.**—Luminescence spectra of the phosphors were measured with a Hitachi Perkin-Elmer fluorescence spectrometer, Type MPF-3A. In relative intensity measurements the instrumental parameters were as follows: sensitivity: 2; slit:  $2 \mu\text{m}$ ; filter: UV-D25 (excitation), UV-39 (emission); wave length: 324 nm (excitation), 500-700 nm (emission).

**Scanning electron microscopy.**—SEM pictures were taken with a JEOL scanning electron microscope, Type JSM-U3.

**Synthesis of the oxysulfide phosphors.**— $\text{Y}_2\text{O}_3$  containing the desired amount of  $\text{Eu}_2\text{O}_3$  was suspended in water. A slow stream of sulfur dioxide was led into this suspension until the RE oxides dissolved. Complete precipitation of RE ions as sulfites was achieved by boiling the solution and simultaneously leading nitrogen gas through to remove excess sulfur dioxide. Due to the small difference in solubilities of yttrium and europium sulfites, the crystalline precipitate contained europium sulfite homogeneously dispersed in yttrium sulfite. It was washed with deionized water and dried with ethanol and ether. As an example of the amounts of reagents and the time required the following values can be given:  $\text{Y}_2\text{O}_3$  1.5g,  $\text{Eu}_2\text{O}_3$  0.149g [6 mole percent (m/o)],  $\text{H}_2\text{O}$   $150 \text{ cm}^3$ ,  $\text{SO}_2$   $100 \text{ cm}^3/\text{min}$  for 1.5 hr, and boiling time 1 hr.

The sulfites obtained can be reduced to oxysulfides by the action of carbon monoxide at  $600^\circ$ - $900^\circ\text{C}$ . In a typical experiment, 0.5g of sulfite was reduced in a quartz reaction vessel (volume  $80 \text{ cm}^3$ ) by leading in carbon monoxide ( $100 \text{ cm}^3/\text{min}$ ) for 60 min at  $750^\circ\text{C}$ .

An alternative route, requiring slightly higher reduction temperatures, consists of the oxidation of sulfites in air to oxysulfates and then their reduction by carbon monoxide to oxysulfides. For example, 0.5g of sulfite was fired in air at  $950^\circ\text{C}$  for 1 hr and the oxysulfate thus obtained was reduced by CO ( $100 \text{ cm}^3/\text{min}$ ) at  $830^\circ\text{C}$  during 1 hr.

Finally, in order to improve the crystallinity and luminescence properties of the oxysulfide, it was fired in nitrogen for 1 hr at a temperature  $50^\circ$ - $100^\circ\text{C}$  higher

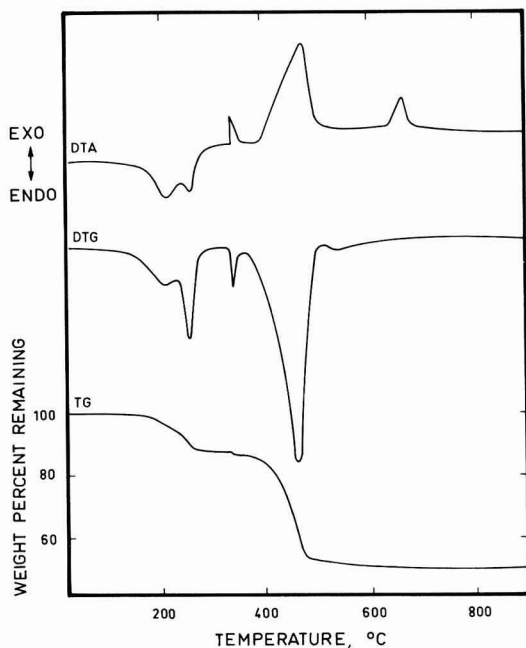


Fig. 1. Results of thermal analysis showing the formation of oxysulfide by carbon monoxide reduction of yttrium sulfite trihydrate containing 6 m/o Eu.

than the reduction temperature. Cooling was also carried out under nitrogen in order to avoid the formation of oxysulfate by oxidation.

## Results and Discussion

**Preparation of phosphors.**—Results of thermal analysis indicated that first an endothermic dehydration reaction takes place in the temperature range  $150^\circ$ - $270^\circ\text{C}$  (Fig. 1). The observed weight loss corresponds to three molecules of water. The anhydrous sulfite is then reduced to oxysulfide in a two-stage exothermic process. The first step, at  $330^\circ$ - $340^\circ\text{C}$ , clearly visible in both DTA and TG curves, is due to the reduction of europium sulfite; yttrium sulfite is reduced at the higher temperature range of  $360^\circ$ - $490^\circ\text{C}$ . The exothermic peak not involving a weight change at  $640^\circ\text{C}$  is probably due to recrystallization of the phosphor.

The over-all weight loss (46.60%) calculated from the TG curve is smaller than the theoretical value (47.90%), indicating the formation of other sulfides besides the desired oxysulfide. The sulfides may be washed from the product by dilute acetic acid in which they are readily soluble (12). This lowers the yield, however, because oxysulfide is slightly soluble in acetic acid.

In this work the reaction temperature was optimized with respect to luminescence intensity and yield. Figure 2 shows the amount of material soluble in 2.5M acetic acid (mainly sulfides) and the luminescence intensity of the remaining oxysulfide phosphor. Temperatures around  $700^\circ\text{C}$  seem to be best for oxysulfide formation, but the optimum temperature with respect to both yield and intensity is somewhat higher, around  $750^\circ\text{C}$ . If an alternative preparative route employing the reduction of oxysulfate is used, the amount of material soluble in acetic acid remains fairly constant (approx. 5%), but the optimum intensity is obtained with reaction temperatures of  $800^\circ$ - $850^\circ\text{C}$  and a post-synthesis  $\text{N}_2$  anneal at  $900^\circ$ - $950^\circ\text{C}$ . There seem to be no significant differences in luminescence properties of phosphors prepared by the two alternative methods.



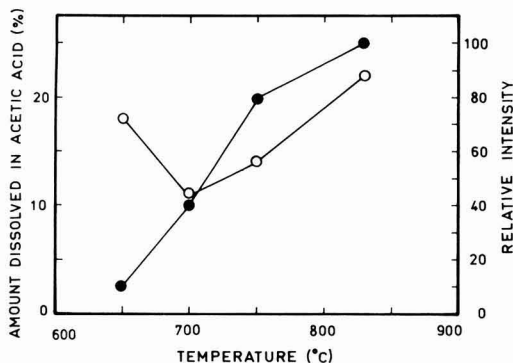


Fig. 2. The amount of material soluble in acetic acid (2.5M) in phosphors prepared by direct reduction of sulfites (open circles) and their relative brightnesses (filled circles) as functions of the reducing temperature.

*Properties of the phosphors.*—The phosphors prepared were pale brown. Their thermal stability in the absence of oxygen was good; heating in vacuum ( $4 \cdot 10^{-5}$  atm) up to 1000°C caused the weight to drop only 0.8%.

According to x-ray diffraction patterns the phosphors were well crystallized. The unit cell parameters for Eu: Y<sub>2</sub>O<sub>2</sub>S with different Eu contents are given in Table I; they show a slight increase with increasing europium concentration.

Firing in nitrogen improves the luminescence properties significantly by increasing the crystallite size of the phosphor. This was visible in the line widths of the powder patterns taken before and after firing in nitrogen. The increase of particle size was also observed in SEM pictures. The intensity obtained after 1 hr firing may be as high as 5-10 times the original.

*Effect of impurities on the luminescence spectra.*—In the present study yttrium oxides of three different purities were employed in order to study the effect of impurities in the starting materials on the luminescence properties. Table II lists results of a mass spectrometric analysis of these starting materials, numbered I to III in order of increasing purity. Oxysulfide phosphors prepared under similar conditions from these oxides showed a relative luminescence intensity of 40, 50, and 100 for samples I/a, II/a, and III/a, respectively.

Much higher impurity levels, however, may be introduced during the preparation and subsequent handling. Table II also lists the results of mass spectrometric analyses for Eu: Y<sub>2</sub>O<sub>2</sub>S phosphors prepared from these starting materials by (a) direct reduction of yttrium sulfite by carbon monoxide, (b) reduction after oxysulfate conversion and, for comparison, by (c) sulfurization of Eu: Y<sub>2</sub>O<sub>3</sub> in a sulfur-sodium carbonate-potassium carbonate flux (10), or (d) by method same as (c) but with mechanical dispersion (13). When comparing the analytical results for different phosphors it should be kept in mind that although spark source mass spectrometry is a very sensitive method of analysis, its precision with the logarithmic

Table I. Unit cell parameters of europium-activated yttrium oxysulfides. Estimated standard deviations are given in parentheses.

Europium content (m/o)	a (Å)	c (Å)
0	3.7910(7)	6.5959(19)
3	3.7936(7)	6.5977(16)
6	3.7947(7)	6.5995(14)
9	3.7967(7)	6.6029(22)

Table II. Mass spectrometric analyses (in ppm) of three yttrium oxides and phosphors prepared therefrom

Element	Sample*										
	I	II	III	I/a	II/a	III/a	III/b	I/b	III/c	II/d	
Yb	5			10					10		
Ho	6	4	4	6	4	5	4	7	4	4	
Dy	10	40	5	20	50	20	20	15	20	30	
Tb	5	25		3	40	1	2	5	2	25	
Gd	25	10	6	40	30	20	10	30	20	20	
Sm	40	15	15	50	20	25	15	60	20	20	
Nd	20	3	4	20	10	4	8	10	10	10	
Pr	8			7	5	2	4	6	5	5	
Ce	25	1	4	25	15	6	10	20	10	15	
La	20	8	5	35	20	10	35	30	20	15	
Mo									600	200	
Zn	35	10	5	50	40	20	20	20	200	200	
Cu	20	10	10	100	50	50	50	100	200	200	
Ni	2	1		30	20	20	20	30	300	100	
Fe	20	20	10	100	100	40	70	400	>1000	1000	
Mn	10	10	10	10	10	10	10	200	1000	>500	
Cr	30	30	20	30	30	30	30	300	100	1000	
Ca	15	15	15	40	40	30	30	40	300	>300	
K	15	15	15	100	100	50	100	200	>1000	>1000	
Si	100	50	30	800	1000	200	600	600	>3000	1000	
Al	10	10	10	30	50	30	10	30	>100	70	
Na	100	10	10	100	200	50	100	200	>2000	>4000	

\* Roman numbers I, II, and III refer to Y<sub>2</sub>O<sub>3</sub> of 99.9, 99.99, and 99.999% purity, respectively. Small letters after the solidus indicate the method of preparation: (a) reduction of sulfite, (b) reduction after conversion to oxysulfate, (c) use of sulfurizing flux with dispersion of Eu in Y<sub>2</sub>O<sub>3</sub> by oxalate precipitation, and (d) use of sulfurizing flux with mechanical dispersion of Eu in Y<sub>2</sub>O<sub>3</sub>. In the preparation of the three last phosphors, a quartz boat inside a steel reactor was employed; in other preparations apparatuses made entirely of quartz were used. The impurities originating from the activator (6 m/o Eu in all phosphors) have been taken into account in the values for the yttrium oxides.

scanning method can be estimated to be at best only  $\pm 20\%$ .

The results show clearly that the use of a quartz boat significantly increases the silicon content. Nevertheless, the impurity levels for the present method are generally lower than those associated with the flux method, where in spite of careful washings, high contents of alkali and alkaline earth metals originating from the flux are introduced into the phosphor in addition to the high content of silicon from the quartz vessel. The presence of steel, even though not in direct contact with the sample, causes the Fe and Mn contents to rise significantly, as can be seen in the values for the last three phosphors prepared in the quartz vessel inside a steel reactor (Table II).

It is well known that minute amounts of other rare earths influence the luminescence properties of Eu: Y<sub>2</sub>O<sub>2</sub>S phosphors. Only Tb and Pr have been reported to increase the luminescence intensity (14), all other RE's reduce the brightness and/or lead to other undesired effects; e.g., dysprosium increases the decay time (15).

Much less information is available on the effect of ions other than RE's on the luminescence properties of europium-activated yttrium oxysulfide phosphors. Mathers (15) reports that alkali metals are not usually considered detrimental to the spectra in amounts less than 100 ppm. At higher amounts they have been found to increase the brightness somewhat; the upper limit of alkali concentration has been reported to be 3000 ppm (16). Conversely, too high calcium and iron concentrations lower the brightness (15); no reports seem to be available on the effect of silicon on the spectra.

Table III lists the luminescence spectra with line identification of the same samples for which mass spectrometric analyses were performed (17). The effect of other rare earths on the spectra of Eu: Y<sub>2</sub>O<sub>2</sub>S phosphors is noticeable in a few cases. For instance, the  $^5D_2 \rightarrow ^7F_4$  transition, which is the strongest line due to terbium (18), is only present in the spectra of phosphors prepared from the 99.99% yttrium oxide, which contained 25 ppm terbium (Tables II and III).

The most striking feature of the spectra is, however, the differences in the relative line intensities of the

Table III. Relative intensities for different emission fluorescent wavelengths in samples of Eu: Y<sub>2</sub>O<sub>3</sub>S. Excitation wavelength 312.0 nm.

Wave-length (nm)	Sample*							Corresponding transition (7)
	I/a	II/a	III/a	I/b	III/b	III/c	II/d	
626.9	100	100	100	100	100	100	74.5	<sup>5</sup> D <sub>0</sub> → <sup>7</sup> F <sub>2</sub>
617.0	48.2	50.0	42.3	48.0	44.1	50.5	36.7	<sup>5</sup> D <sub>0</sub> → <sup>7</sup> F <sub>1</sub>
596.0	67.2	56.7	43.3	55.2	53.7	71.0	50.2	<sup>5</sup> D <sub>0</sub> → <sup>7</sup> F <sub>3</sub>
587.8	14.8	12.6	12.4	13.7	12.1	14.4	42.7	<sup>5</sup> D <sub>0</sub> → <sup>7</sup> F <sub>5</sub>
583.7	24.6	27.5	22.5	23.7	24.3	26.5	21.0	<sup>6</sup> D <sub>1</sub> → <sup>7</sup> F <sub>0</sub>
571.0	0.5	0.2	0.1	0.2	0.1	0.4	1.6	<sup>5</sup> D <sub>2</sub> → <sup>7</sup> F <sub>5</sub>
565.6	1.7	0.6	0.2	0.5	0.2	1.1	3.9	<sup>5</sup> D <sub>1</sub> → <sup>7</sup> F <sub>2</sub>
556.3	10.6	5.3	5.5	6.9	3.4	6.9	26.0	<sup>5</sup> D <sub>1</sub> → <sup>7</sup> F <sub>3</sub>
545.0	—	2.3	—	—	—	—	15.6	<sup>5</sup> D <sub>2</sub> → <sup>7</sup> F <sub>4</sub>
540.0	39.1	23.2	22.8	29.1	14.5	26.9	100	<sup>5</sup> D <sub>1</sub> → <sup>7</sup> F <sub>1</sub>
529.6	—	0.5	0.3	0.6	0.3	0.8	3.3	<sup>5</sup> D <sub>2</sub> → <sup>7</sup> F <sub>6</sub>
513.7	12.0	6.3	4.3	4.1	4.1	9.8	49.8	<sup>5</sup> D <sub>2</sub> → <sup>7</sup> F <sub>3</sub>
497.0	9.1	5.5	5.2	8.5	4.3	7.5	39.4	<sup>5</sup> D <sub>2</sub> → <sup>7</sup> F <sub>5</sub>
491.0	4.7	4.1	5.5	7.2	3.9	4.2	20.5	<sup>5</sup> D <sub>2</sub> → <sup>7</sup> F <sub>2</sub>
483.0	1.2	2.2	5.2	5.5	3.4	1.3	4.7	**
476.0	3.3	3.4	6.7	7.1	4.5	3.0	14.5	<sup>5</sup> D <sub>2</sub> → <sup>7</sup> F <sub>1</sub>
470.0	10.1	9.2	16.0	19.7	11.4	8.9	—	<sup>5</sup> D <sub>3</sub> → <sup>7</sup> F <sub>1</sub>
							52.9***	<sup>5</sup> D <sub>2</sub> → <sup>7</sup> F <sub>0</sub>
465.0	2.3	4.6	10.8	12.1	7.2	2.5	4.9	**
452.9	1.2	2.6	6.7	8.7	4.3	1.5	4.9	<sup>5</sup> D <sub>3</sub> → <sup>7</sup> F <sub>5</sub>
446.5	1.1	2.1	5.6	5.1	3.3	1.4	4.1	**
440.0	—	—	—	—	—	—	2.6	**
429.9	0.9	1.6	4.3	—	2.7	1.2	3.2	<sup>5</sup> D <sub>3</sub> → <sup>7</sup> F <sub>2</sub>
423.1	0.9	1.7	4.3	4.0	2.8	1.2	3.6	**
417.1	1.6	3.2	8.1	9.2	6.4	2.0	7.3	<sup>5</sup> D <sub>3</sub> → <sup>7</sup> F <sub>1</sub>
414.0	—	—	—	—	—	0.7	2.1	**
409.9	—	—	—	—	1.6	—	—	**

\* The sample numbering is explained in Table II. In each sample the strongest line has been given the value of 100. The relative intensity values for different samples determined with instrumental parameters described in the text, were as follows (sample III/a 100): I/a 40, II/a 50, III/a 100, I/b 48, III/b 90, III/c 90, and II/d 2.

\*\* Unassigned.

\*\*\* Unresolved.

sample containing most impurities (II/d) as compared with the other spectra. This sample also had the lowest relative brightness, a value of only 2, whereas III/a had the highest value of 100, and III/c had a value of 90. The difference between the samples III/c and II/d is certainly due not only to impurities in the starting materials but also to different dispersion methods of the activator. In sample II/d Eu<sub>2</sub>O<sub>3</sub> was mechanically dispersed in Y<sub>2</sub>O<sub>3</sub> (13); in the other sample (III/c), oxalate precipitation and subsequent firing were employed in obtaining the oxide (10).

The iron concentrations introduced in the phosphors by the steel reactor seem not to be so high as to have a distinct effect on the over-all brightness. This can be seen by comparing, for instance, the samples I/a (relative brightness 40) and I/b (relative brightness 48) prepared in quartz and steel reactors, respectively (Tables II and III). However, the effect of an individual element other than a RE on the spectra is difficult to evaluate on the basis of present material and it would require a further study.

### Summary

The reduction of Eu-doped yttrium sulfite hydrate by carbon monoxide offers a new possibility for the

preparation of Eu: Y<sub>2</sub>O<sub>3</sub>S phosphors. The reaction and annealing temperatures required are not significantly lower than in the case of sulfate reduction. However, an advantage of the present method over the sulfate route lies in the ease and completeness of precipitating homogenous starting materials for the synthesis.

The rare earth impurities in the starting materials as well as other impurities mainly introduced during processing can seriously degrade the luminescent properties of the phosphors.

### Acknowledgments

The authors are indebted to Dr. I. Yliruokanen and Mr. L. Hiltunen, M.Sc. for valuable aid in mass spectrometric analyses. Kemira Oy has supported this work by providing the rare earth oxides.

Manuscript submitted June 3, 1975; revised manuscript received Aug. 25, 1975.

Any discussion of this paper will appear in a Discussion Section to be published in the December 1976 JOURNAL. All discussions for the December 1976 Discussion Section should be submitted by Aug. 1, 1976.

### REFERENCES

- M. R. Royce, U.S. Pat. 3,418,246 (1968).
- P. N. Yocom, U.S. Pat. 3,418,247 (1968).
- H. A. Eick, *J. Am. Chem. Soc.*, **80**, 43 (1958).
- E. J. Yarembash, E. S. Vigileva, A. A. Reshchikova, A. I. Zachatskaya, G. N. Novikova, and E. J. Boev, *Izv. Akad. Nauk. SSSR, Neorg. Mater.*, **7**, 1551 (1971).
- J. W. Haynes and J. J. Brown, *This Journal*, **115**, 1060 (1968).
- J. J. Pitha, A. L. Smith, and R. Ward, *J. Am. Chem. Soc.*, **69**, 1870 (1947).
- V. P. Surgutskii and V. V. Serebrennikov, *Russ. J. Inorg. Chem.*, **9**, 435 (1964).
- P. Khodadad, T. Tek, J. Flahaut, and L. Domange, *C. R. H. Acad. Sci.*, **260**, 2235 (1965).
- L. Ozawa and M. Jaffe, *This Journal*, **117**, 1297 (1970).
- M. R. Royce, S. M. Thomsen, and P. N. Yocom, U.S. Pat. 3,502,590 (1970).
- M. Koskenlinna and L. Niinistö, *Suomen Kemistilehti*, **B46**, 326 (1973).
- J. Flahaut, M. Guittard, and M. Patrie, *Bull. Soc. Chim. France*, **1958**, 990.
- L. G. van Uitert, U.S. Pat. 3,243,723 (1966).
- H. Yamamoto, T. Kano, Y. Otomo, and K. Urabe, "Proceedings of the Ninth Rare Earth Research Conference," Blacksburg, Virginia, p. 503 (1971).
- J. E. Mathers, in "Analysis and Applications of Rare Earth Materials," O. B. Michelson, Editor, p. 241, Universitetsforlaget, Oslo (1973).
- W. H. Byler, J. J. Mattis, S. A. Ring, L. E. Sobon, K. A. Wickersheim, and M. Tecotzky, U.S. Pat. 3,515,675 (1970).
- C. W. Struck and W. H. Fonger, *J. Luminescence*, **1**, 456 (1970).
- M. R. Royce and A. L. Smith, Abstract 34, p. 94, Electrochemical Society Extended Abstracts, Spring Meeting, Boston, Massachusetts, May 5-9, 1968.

# On the Kinetics of the X-Ray Irradiation-Caused Degradation of Photoluminescence of Some Phosphors

George T. Bauer\*

Webster Research Center, Xerox Corporation, Rochester, New York 14644

## ABSTRACT

The growth of absorption and the degradation of photoluminescence of calcium tungstate and zinc silicate phosphors have been studied as functions of x-ray exposure. The characteristics of the growth curves are observed to be very similar to those reported for F centers in alkali halides. Based on the theoretical analysis of the kinetics, the fast initial growth of the absorption is interpreted as arising from the imperfections present in the phosphors prior to irradiation, while the following slow linear rise is attributed to the effect of new radiation-induced imperfections. From the two stages of growth curves, the two periods of degradation of photoluminescence observed could be quantitatively explained. These results indicate that the u.v. and visible absorption of radiation-produced color centers is the major cause of degradation of the phosphors studies. The observed dark recovery of absorption and of luminous efficiency after ceasing the irradiation of the phosphors was also found to be a correlated effect.

The degradation of phosphors as the effect of exciting irradiation is known to be a limiting factor in many applications. The degradation of the luminescence of some x-ray or u.v.-irradiated single crystals and phosphors has been attributed to the absorption of the irradiation-produced color centers (1, 2). In a previous publication, we reported results on the effects of x-ray and ultraviolet irradiation on different types of phosphors (3). We found that a decrease of luminous efficiency of the irradiated phosphors was always accompanied by increased absorption. In most cases, the absorption coefficient increased in the absorption band as well as in the emission band. The absorption bands could be partially or completely bleached out by a one-hour heat-treatment at 400°C. The reflectance data and glow curves of x-ray-irradiated phosphors were very similar to the ones obtained after long-term u.v. irradiation. These results indicate that the formation of color centers by irradiation in phosphors is a quite common phenomenon and is not restricted to those few basic types that had been studied in this respect by other authors (1, 2).

Our work also resulted in some increased insight into the various processes which are going on in the phosphors when irradiated. In certain phosphors, such as calcium tungstate and zinc silicate, the irradiation-caused degradation could be completely interpreted in terms of the absorption of irradiation-produced absorbing centers. Some part of the exciting energy in this phosphor is absorbed in radiation-produced color centers instead of being absorbed in the luminescent centers. A part of the emitted luminescent light is also absorbed by color centers. According to the experiments, the light emitted by color centers—if any—did not contribute to the luminous efficiency of these phosphors. In some other materials (for example, phosphate-type phosphors) glow curve measurements indicated an additional loss (3) which seemed to be connected with an energy transfer process between activator and color centers. In these cases, the induced traps should give rise to radiationless transitions or to emission outside the visible range.

In our previous measurements (3), the irradiation times did not vary over a wide range, and, consequently, did not yield enough information concerning the time dependence of the degradation of the phosphors. It appeared that for those particular phosphors

in which the absorption of radiation-produced color centers is the only cause of degradation, the time dependence of this process should be described by the time-dependent change of their absorption coefficient. Thus, the problem can be reduced to interpreting the growth of absorption of these phosphors.

The growth of absorption of x-ray-irradiated alkali halides, a classical problem of color center research, has been studied by a number of authors (4, 5). In general, the physical processes which result in the growth of absorption were found to be rather complicated. However, in several cases, good agreement between theory and experiments (6, 7) was reported. Such detailed studies, although they might provide a better understanding of the degradation process, were not conducted for irradiated phosphors. The reason for the lack of such efforts should be attributed not only to the well-known complexity of the problem, but also to the difficulties encountered in measuring the absorption coefficient of powder phosphors. However, the absorption coefficient can be determined accurately enough for such purposes from measurements of diffuse optical properties of phosphor layers (8, 9). The problem can be simplified further because, as has been shown previously (3), only the relative values of the absorption coefficients of phosphors as a function of exposure are needed to interpret quantitatively the effect of color centers in the degradation process.

In this work, we study the time-dependent degradation of x-ray-irradiated  $\text{CaWO}_4$ :Pb and  $\text{Zn}_2\text{SiO}_4$ :Mn,Pb,As. The phosphors were made available to us by Westinghouse Corporation. The main effect of irradiation in these phosphors seems to be that it changes the visible and ultraviolet absorption of the phosphors. Long-term x-ray exposure induces only barely detectable new glow peaks over room temperature. Therefore, those other effects of x-rays which are related to energy transfer processes are neglected.

The choice of x-rays for irradiation was based on practical considerations. The irradiation time needed with x-rays is relatively short and the penetration depth is large, making it possible to use known techniques for the measurement of optical properties of powder phosphors.

However, based on the similarity of the effects of x-rays and u.v. on optical characteristics of phosphors, we may expect the results obtained here to hold also for degradation produced by other forms of excitation.

The theory and the experimental work can be divided into two major parts: the first is concerned with

\* Electrochemical Society Active Member.  
Key words: luminescence, phosphor degradation kinetics, color centers.

the growth of absorption; the second is the basic problem, the time-dependent degradation of the selected phosphors. Some efforts have also been concentrated on the study of dark recovery of the absorption and luminescence.

### Theory

*Calculation of the growth of the absorption.*—We suppose that the growth of absorption of the irradiated phosphors can be attributed to the increase in concentration of the irradiation-produced color centers. As it is known from the extensive literature (4), the presence of imperfections in the crystal (e.g., vacancies, interstitials, impurities) gives rise to color center formation. In the two sample phosphors, the concentrations of the activator and the color centers before and after the irradiation are small; that is, the absorption is in the "weak" region. Also, as indicated by relatively high quantum efficiency of the photoluminescence of the phosphors (10), absorption by impurities is negligible. The phosphor prior to irradiation already contains electron or hole-type imperfections of concentration  $N_0$ , and the irradiation produces new imperfections. The concentration of the new imperfections is proportional to  $I_0$ , the intensity of the x-rays, and to the elapsed time,  $\tau$ , of irradiation. The total imperfection concentration,  $N$ , can be expressed by Eq [1]

$$N = N_0 + a_2 I_0 \tau \quad [1]$$

The growth of  $C_1(\tau)$ , the color center concentration, can be described by Eq. [2]

$$\frac{dC_1(\tau)}{d\tau} = a_1 I_0 [N_0 + a_2 I_0 \tau - C_1(\tau)] - a_3 I_0 C_1(\tau) - a_4 C_1(\tau) \quad [2]$$

According to the first term in Eq. [2], the irradiation produces new color centers and the rate of the concentration growth is proportional to the intensity of irradiation,  $I_0$ , and to the concentration of the available unfilled imperfections. The second term indicates that the radiation destroys color centers and that the rate of destruction is proportional to their instantaneous concentration,  $C_1(\tau)$ , and to  $I_0$ . The third term on the right of the equation expresses the fact that spontaneous recovery which does not depend on the intensity of the radiation may also occur,  $a_1$ ,  $a_2$ ,  $a_3$ , and  $a_4$  are rate constants in Eq. [1] and [2].

The integral of Eq. [2], taking into account the boundary condition, is

$$C_1(\tau) = f_0(1 - e^{-g_0\tau}) + h_0\tau \quad [3]$$

where

$$f_0 = \frac{I_0^2(a_1^2 N_0 + a_1 a_3 N_0 - a_1 a_2) + a_1 a_4 I_0 N_0}{[I_0(a_1 + a_3) + a_4]^2} \quad [4]$$

$$g_0 = I_0(a_1 + a_3) + a_4 \quad [5]$$

$$h_0 = \frac{I_0^2 a_1 a_2}{I_0(a_1 + a_3) + a_4} \quad [6]$$

From the  $C_1(\tau)$  concentration and  $\sigma_1(\lambda)$ , the capture cross section of the color centers for absorption, the induced absorption coefficient can be expressed (3) as  $C_1(\tau)\sigma_1(\tau)$ . Adding the induced absorption to the value of the initial absorption of the phosphor prior to the irradiation,  $a(\lambda, \tau = 0)$ , the whole absorption is

$$a_{ir}(\lambda, \tau) = a(\lambda, \tau = 0) + C_1(\tau)\sigma_1(\lambda) \\ \equiv a(\lambda, \tau = 0) + f_0\sigma_1(\lambda)(1 - e^{-g_0\tau}) + h_0\sigma_1(\lambda)\tau \quad [7]$$

Based on the experimental fact that no reciprocity failure was found within the applied exposure range, we introduce the exposure,  $E = \tau$ , instead of  $\tau$ , where  $i$  is the anode current in the x-ray tube. The relative absorption coefficient [ $a_{ir}(\lambda, \tau)$ ] expressed with  $E$  from Eq. [7] is

$$a_{ir}(\lambda, E) = a_r(\lambda, E = 0) + f(1 - e^{-gE}) + hE \quad [8]$$

The coefficients  $f$ ,  $h$ , and  $g$  differ from  $f_0\sigma_1$ ,  $h_0\sigma_1$ , and  $g_0$ , respectively, only by numerical factors.

*The decrease of the luminous efficiency.*—As shown previously (3), the luminous efficiency,  $L_i$ , of an x-ray-irradiated phosphor can be expressed in terms of the unirradiated one,  $L$ , by the initial absorption coefficient  $a_r(\lambda, E = 0)$  and by the absorption coefficient of the irradiated phosphor  $a_{ir}(\lambda, E)$  both measured at the wavelength of excitation

$$\frac{L_i}{L} = m_v(E) \frac{a_r(\lambda, E = 0)}{a_{ir}(\lambda, E)} \quad [9]$$

where  $m_v(E)$  is that part of the loss which is caused by self-absorption of the emitted light by the irradiation-produced color centers. An approximate expression for  $m_v(E)$  is given in Ref. (3). The exposure-dependent change of the  $L_i/L$  relative efficiency with respect to  $\lambda$  wavelength excitation is from Eq. [8] and [9]

$$\frac{L_i}{L} = m_v(E) \frac{a_r(\lambda, E = 0)}{a_r(\lambda, E = 0) + f(1 - e^{-gE}) + hE} \quad [10]$$

*Spontaneous recovery of the absorption coefficient and of the luminous efficiency.*—In Eq. [2], the rate constant,  $a_4$ , is related to the spontaneous bleaching of the phosphor at room temperature. In phosphors in which such a phenomenon actually occurs, both the absorption and the luminous efficiency might recover partially or return to their original values after the irradiation has stopped. Based on Eq. [2], the change in the concentration of the color centers at a time  $\tau^*$  elapsed after ceasing the irradiation at time  $\tau_0$  is

$$\frac{dC_1(\tau^*)}{d\tau} = -a_4 C_1(\tau^*) \quad [11]$$

The integral of Eq. [11] is

$$C_1(\tau) = C_1(\tau_0) e^{-a_4\tau^*} \quad [12]$$

Let  $a_{ir}(\lambda, \tau^*)$  be the relative absorption coefficient of the phosphor after  $\tau^*$  elapsed time of dark recovery. Multiplying Eq. [12] by the capture cross section of the color center related to  $\lambda$ , the wavelength of excitation, and adding the initial absorption of the phosphor prior to the irradiation  $a_r(\lambda, E = 0)$  to the induced absorption, we obtain for the time dependence of the relative absorption coefficient

$$a_{ir}(\lambda, \tau^*) = a_r(\lambda, E = 0) + \sigma_1(\lambda) C(\tau_0) e^{-a_4\tau^*} \\ \equiv a_r(\lambda, E = 0) + a_{ir}(\lambda, E = i\tau_0) e^{-a_4\tau^*} \quad [13]$$

Let us consider that the visible absorption does not change during the recovery. That is

$$m_v(\tau_0) = m_v(\tau_0 + \tau^*) \quad [14]$$

Then, based on Eq. [9] from Eq. [13] and [14], we obtain for the recovery of the luminous efficiency

$$\frac{L_i}{L} = \frac{a_r(\lambda, E = 0)}{a_{ir}(\lambda, \tau^*)} \\ = \frac{a_r(\lambda, E = 0)}{a_r(\lambda, E = 0) + a_{ir}(\lambda, E = i\tau_0) e^{-a_4\tau^*}} \quad [15]$$

### Experimental

*Irradiation and optical measurements.*—The phosphors were irradiated by 50 kV unfiltered tungsten x-rays. The measurements of the relative absorption coefficient and of the luminous efficiency of the phosphors were based on diffuse reflectance measurements made on 2 mm-thick powder layers. The apparatus used for the irradiation, excitation, and optical measurements of the phosphors was described previously

(3). An important aspect of the optical measurements is that they were carried out on two characteristic wavelengths: one of these wavelengths is in the tail of the absorption band of the phosphors, the other is within the emission band. The absorption of the irradiation-induced color centers in a wavelength which corresponds to the tail of the absorption band can be quite high compared to the absorption of the phosphor prior to irradiation. The decrease of luminous efficiency related to excitation occurs in the peak of the absorption band, and it is easier to measure this change (3). Some measurements have been also made near the peak of the excitation band.

The absorption coefficients of the irradiated phosphors used in this study, as measured by diffuse reflectance,  $R(\lambda)$ , were small enough to use the weak absorption limit of the expression (9) for the relative absorption coefficient

$$a_r(\lambda) = \frac{(1 - R(\lambda))^2}{R(\lambda)} \quad [16]$$

The relative luminous efficiency of the irradiated phosphor in terms of the unirradiated one,  $L_i/L$ , can be expressed using the relative brightness  $I$  and  $I_i$ , and reflectances,  $R(\lambda)$  and  $R_i(\lambda)$ , of the phosphor before and after irradiation, respectively (10)

$$\frac{L_i}{L} = \frac{I_i}{I} \frac{1 - R(\lambda)}{1 - R_i(\lambda)} \quad [17]$$

### Results

*The growth of absorption.*—The change of the relative absorption coefficient of calcium tungstate was measured at three different wavelengths. One of these wavelengths (2537Å) is well within the absorption band of the phosphor while another one (3120Å) falls in the tail of the absorption band. Measurements were also carried out at 4358Å, a wavelength inside the emission band. Two series of measurements with different irradiation times were made; the first using 50 kV, 40 mA, and the second using 50 kV, 4 mA tungsten x-rays. Figures 1 through 4 show  $a_{ir}(\lambda, E)$ , the measured relative absorption vs. the relative exposure,  $E = i\tau$ , where  $i$  is the anode current in mA and  $\tau$  is the elapsed time of irradiation in minutes. Figure 1 shows the growth of the relative absorption coefficient measured at 3120Å in the exposure range 0–40 mA·min. Some measurements were made by irradiation with 50 kV, 40 mA tungsten x-rays (solid points) while others were made with 50 kV, 4 mA tungsten x-rays (open points). The geometrical configurations of the samples were the same for both exposures. As this and following figures indicate, the relative absorption co-

efficients can be considered as a function of the product,  $i\tau$ . That is, within the anode current range applied in this work, the reciprocity failure is negligible. Therefore, in the following figures, the absorption as well as the luminous efficiency of the phosphors is plotted vs. the relative exposure,  $E$ .

The absorption coefficient of calcium tungstate measured at this wavelength suddenly increases right after beginning the irradiation. Figure 2 shows that this part of the fast growth of absorption is followed by a very slow linear rise. This initial sudden rise of the growth curve is characteristic for both phosphors studied at every measured wavelength.

Figures 3 and 4 show the exposure dependence of absorption of the calcium tungstate measured at 4358Å. The curve has the same characteristic as the one measured at 3120Å. However, the absorption of the phosphor prior to the irradiation is near zero at this wavelength. The growth of absorption is also smaller than on the curve measured at 3120Å. According to our model, this means that the capture cross section for absorption of the radiation-induced color centers is smaller in the visible than well inside the absorption band. Here, too, the sudden rise of the absorption at low exposures is followed by a slow linear rise (Fig. 4). The value of reflectance of the calcium tungstate was found to be very small ( $R \approx 0.07$ ) at 2537Å and did not show any change within the applied range of exposure. Obviously, the capture cross section and concentration of the activators are much higher than

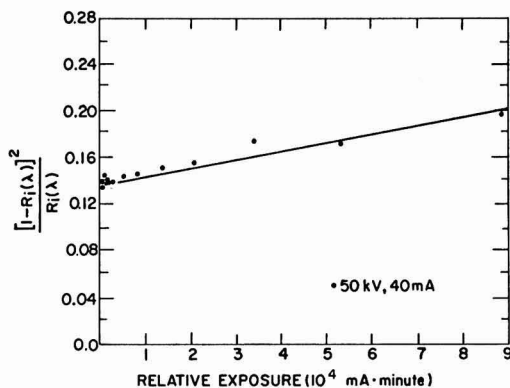


Fig. 2. X-ray-exposure dependence of the relative absorption coefficient of calcium tungstate at 3120Å (long-term exposures). Dots measured; line calculated.

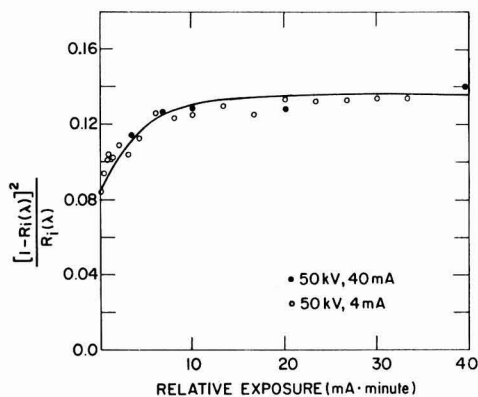


Fig. 1. X-ray-exposure dependence of the relative absorption coefficient of calcium tungstate at 3120Å (short-term exposures). Dots measured; line calculated.

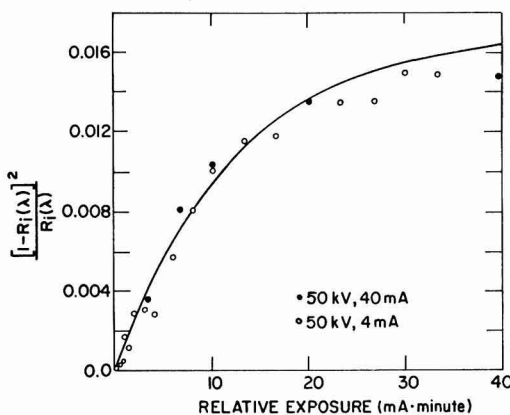


Fig. 3. X-ray-exposure dependence of the relative absorption coefficient of calcium tungstate at 4358Å (short-term exposures). Dots measured; line calculated.



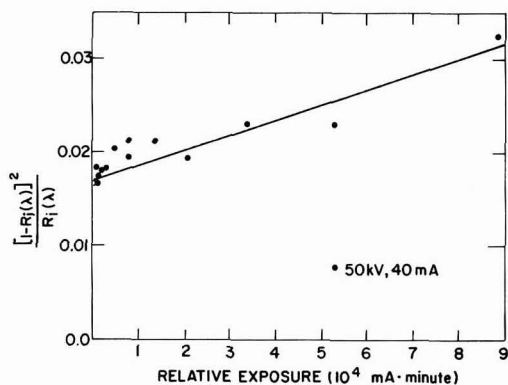


Fig. 4. X-ray-exposure dependence of the relative absorption coefficient of calcium tungstate at 4358Å (long-term exposures). Dots measured; line calculated.

those of the induced color centers and the latter cannot significantly contribute to the whole absorption.

The exposure dependency of the change of the relative absorption coefficient of zinc silicate samples has been measured at 3650Å (Fig. 5) and 4358Å (Fig. 6). The growth of absorption of the zinc silicate is similar to that of the calcium tungstate. Again, a sudden rise is followed by a slower, more gradual growth. If we

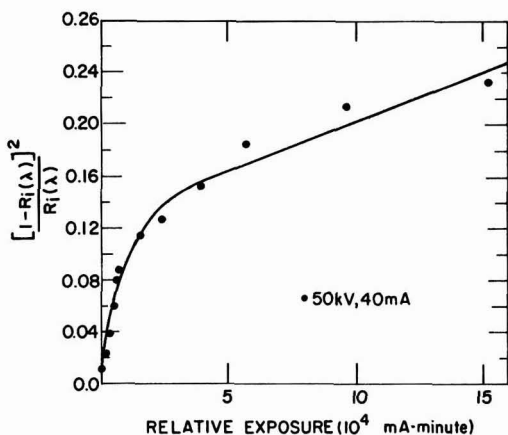


Fig. 5. X-ray-exposure dependence of the relative absorption coefficient of zinc silicate at 3650Å. Dots measured; line calculated.

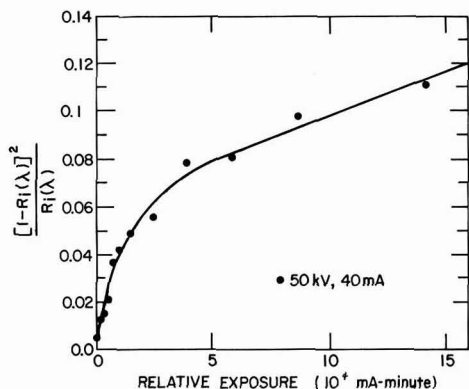


Fig. 6. X-ray-exposure dependence of the relative absorption coefficient of zinc silicate at 4358Å. Dots measured; line calculated.

compare Fig. 5 to Fig. 6, we can see that if the same exposure is applied, the increase of the absorption coefficient is smaller at 4358Å than at 3650Å. 40 mA for 63 hr x-ray exposure causes only a very slight change (from  $R \approx 0.08$  to  $R \approx 0.07$ ) in the reflectance of zinc silicate measured at 2537Å.

*The degradation of the luminous efficiency.*—The brightness of the irradiated samples was measured while exciting the phosphors at the same wavelength at which the reflectance measurements were completed. The changes of the luminous efficiency of calcium tungstate related to excitation at 2537 and 3120Å are shown in Fig. 7 and 8. The luminous efficiency is again a function of the exposure only, that is, the reciprocity failure is negligible, as was also found for the absorption.

Comparing the absorption and luminous efficiency results, Fig. 1 and 7 and Fig. 2 and 8, respectively, it

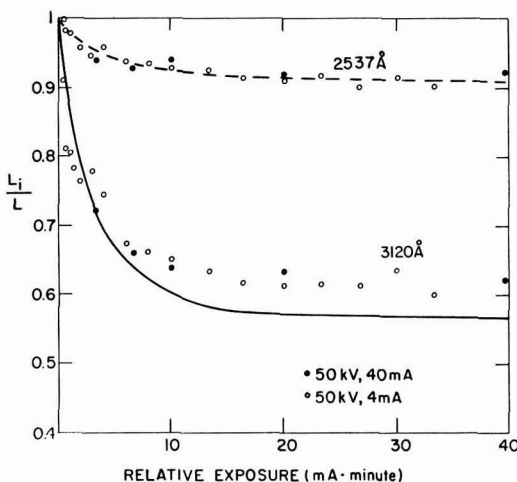


Fig. 7. X-ray-exposure dependence of the relative luminous efficiency of calcium tungstate related to excitation at 2537 and 3120Å (short-term exposures). Dots measured; continuous line calculated.

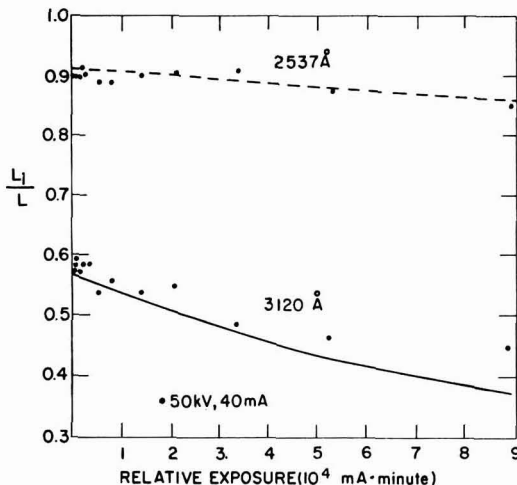


Fig. 8. X-ray-exposure dependence of the relative luminous efficiency of calcium tungstate related to excitation at 2537 and 3120Å (long-term exposures). Dots measured; continuous line calculated.

is noticeable that the sudden increase of the absorption measured at 3120Å (within the exposure range 0-10 mA·min) coincides with a sudden decrease of the luminous efficiency. After 10 mA·min of exposure, the decrease of luminous deficiency slows down, which corresponds to the slower rise of absorption which also occurs at longer exposures. The decrease of the luminous efficiency is significantly smaller at 2537Å than at 3120Å.

The degradation of zinc silicate is more extensive and the close correlation between the radiation-induced change of absorption and luminous efficiency can also be seen in this case. After several minutes of irradiation, the luminous efficiency of zinc silicate related to 3650Å excitation drops below 10% of its initial value (Fig. 9). This is obviously connected with the change of the absorption which increases after the same exposure to about ten times its initial value (Fig. 5).

*Spontaneous bleaching.*—The stability of color centers is known to be dependent on the temperature of their environment. The observed connection between degradation and color center formation of irradiated phosphors suggested a study of the dark recovery of irradiated calcium tungstate at room temperature. In order to avoid the possible bleaching effect of the sources used for excitation, each sample was used for only one measurement. The samples studied were irradiated by 50 kV, 40 mA x-rays for 10 min and kept in the dark until the time of measurement. As Fig. 10 shows, the absorption of the sample measured at 3120Å suddenly decreases after the irradiation ceases. Later, the change slows down. The same character of recovery was observed when the relative absorption of the samples was measured at 4358Å (Fig. 11). The dark recoveries of the measured luminous efficiencies related to 2537 and 3120Å excitation are shown in Fig. 12. The decrease of the absorption after the interruption of irradiation is accompanied by an increase of luminous efficiency of the phosphor. The extent of the recovery related to 3120Å excitation is greater than that related to excitation at 2537Å.

*Comparison of the experiments with theory.*—The exposure dependence of the relative absorption coefficient,  $a_{ir}(\lambda, E)$  was calculated for the studied phosphors at the wavelength of the measurements from Eq. [8]. Applying the least squares method, the best fits for calcium tungstate could be achieved with constants

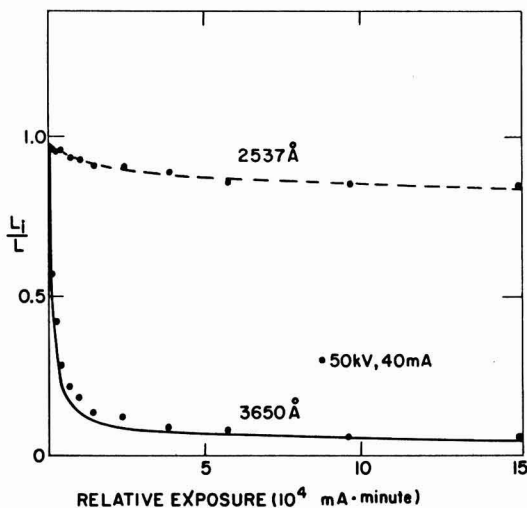


Fig. 9. X-ray-exposure dependence of the relative luminous efficiency of zinc silicate related to excitation at 2537 and 3650Å. Dots measured; continuous line calculated.

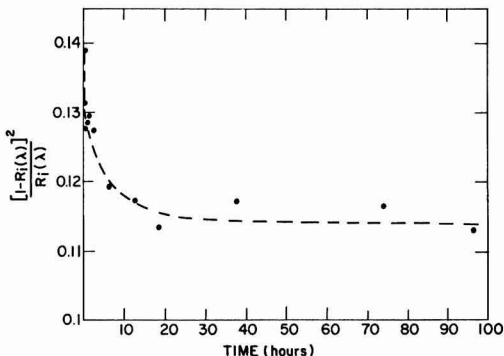


Fig. 10. Spontaneous recovery of the relative absorption coefficient of calcium tungstate at 3120Å after an exposure of 40 mA, 10 min by 50 kV x-rays.

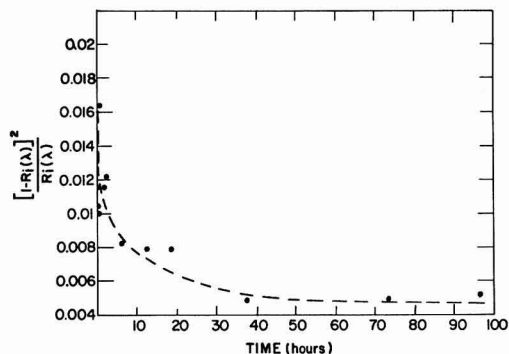


Fig. 11. Spontaneous recovery of the relative absorption coefficient of calcium tungstate at 4358Å after an exposure of 40 mA, 10 min by 50 kV x-rays.

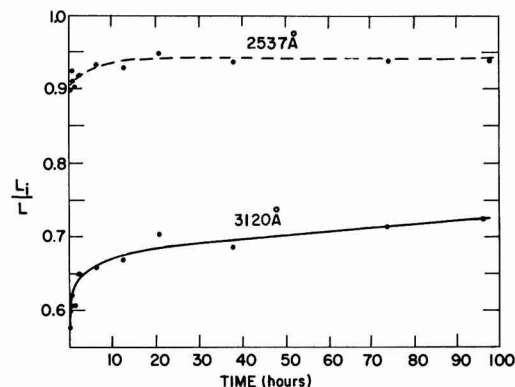


Fig. 12. Spontaneous recovery of the relative luminous efficiency related to excitations at 2537 and 3120Å, respectively, after an exposure of 40 mA, 10 min by 50 kV x-rays. Dots measured; continuous line calculated from absorption data.

shown in Table I. The calculated curves together with the measured points are shown in Fig. 1-4. The curves calculated for zinc silicate with the constants shown in Table II are plotted in Fig. 5 and 6. The calculation of the exposure-dependent change of the luminous efficiencies of calcium tungstate (Fig. 7 and 8) and zinc silicate phosphors (Fig. 9) were based on Eq. [10]. The values of  $m_v(E)$  in Eq. [10] were calculated from the measurements (3). Within the range of exposures, the variation of  $m_v(E)$  was found to be very small com-

Table I. Calcium tungstate

	$\lambda = 3120\text{\AA}$	$\lambda = 4358\text{\AA}$
$f$	$5.18 \cdot 10^{-2}$	$1.69 \cdot 10^{-2}$
$g$ (in mA · min)	$2.33 \cdot 10^{-1}$	$8.03 \cdot 10^{-2}$
$h$ (in mA · min)	$7.68 \cdot 10^{-7}$	$1.64 \cdot 10^{-7}$

Table II. Zinc silicate

	$\lambda = 3650\text{\AA}$	$\lambda = 4358\text{\AA}$
$f$	$1.14 \cdot 10^{-1}$	$5.7 \cdot 10^{-2}$
$g$ (in mA · min)	$1 \cdot 10^{-4}$	$8 \cdot 10^{-5}$
$h$ (in mA · min)	$7.53 \cdot 10^{-7}$	$3.3 \cdot 10^{-7}$

pared to the change of the relative absorption  $a_{1r}(\lambda, E)$ . The other parameters that appear in Eq. [10] were taken from the absorption data shown on Table I or II.

Except for the initial region, the recovery of the absorption of calcium tungstate after 10 min of irradiation by 50 kV, 40 mA x-rays cannot be fitted by Eq. [13]. However, as Fig. 12 shows, the recovery of  $L_i/L$  luminous efficiency can be fitted well applying Eq. [15], using the measured values of the relative absorption coefficients  $a_{1r}(\lambda, \tau^*)$  and  $a_r(\lambda, E = 0)$ .

### Discussion

Theoretical interpretation of the experimental results gives a more complete understanding of the degradation kinetics of the model phosphors studied. Let us discuss first the growth of absorption. The initial fast period and the slow linear rise of the growth curves which follows can be correlated with the imperfections originally present in the phosphors and the ones formed by the radiation, respectively. If  $a_2$  in Eq. [2] is equal to 0, then, from Eq. [4], [5], [6], and [7],  $h$  in Eq. [8] is also equal to 0, but  $f$  and  $g$  do not vanish. The second linear section,  $hE$ , of the growth of absorption curves (Fig. 2, 4, 5, 6) is connected with the new imperfections because, in Eq. [1],  $a_2$  is the rate constant of the generation of new imperfections by the radiation. The first fast rise of the curves (Fig. 1, 3, 5, 6) that corresponds to the second term,  $f(1 - e^{-gE})$ , in Eq. [8] is connected mainly with the imperfections already present in the phosphors prior to the irradiation. This second term approaches the value of  $f$  to within 1% after an exposure of  $E > 60$  mA·min for calcium tungstate and  $E > 4.6 \cdot 10^4$  mA·min for zinc silicate.

These results are very similar to those obtained for the growth of F centers in KCl by other authors (5, 6, 7). The accuracy of our measurements was not enough for a definite identification of an inflection point on the growth curves (6) which would indicate that the initial and the radiation-induced vacancies behave differently (7). In Ref. (5-7), the optical density measurements were made near the peak of the characteristic band of the F centers in the alkali halide crystals studied. The concentration of the F centers could be determined from absorption measurements (11). In our case, the types of centers are not yet identified; the reflectance measurements (3) indicate that several different types could have formed in the phosphors by irradiation, and their absorption bands might overlap. There is another indication from this work that in calcium tungstate at least two different color centers are produced by the irradiation. Comparing Eq. [7] and [8] if only one type of color centers was formed,  $g$  in Eq. [8] would not be a function of the wavelength-dependent, capture cross section of the color centers, but would be related only to their concentration. In calcium tungstate,  $g$  was found to be a function of the wavelength of measurement (Table I) while in zinc silicate, within the error of measurement,  $g$  had the same value at both measured wavelengths.

The calculated curves of degradation which are based on the calculated growth of absorption curves

fit the measured values for zinc silicate reasonably well (Fig. 9), while there is some deviation from the measured values in the case of calcium tungstate (Fig. 7 and 8). We attribute these deviations to the error of the measurement rather than to other unknown effects. We can rather safely say that the u.v. and visible absorption of irradiation-produced color centers is the major cause of the degradation of the photoluminescence of these phosphors. Other effects of the irradiation, if any, are negligible in this respect. Comparing the results obtained for the degradation to the analysis (above) of the growth of absorption curves, it is quite obvious that according to our model the initial fast degradation is connected with the imperfections prior to the irradiation of the phosphors while the following slow change can be attributed to new imperfections formed by the irradiation. A closer model of the absorption (12) and the energy levels involved could not be determined from our measurements which are related to the time-dependent change of the absorption and of the luminescence only.

We do not completely understand why the recovery of absorption follows the calculated values, Eq. [13], only during the initial period of recovery. In order to explain the experimental findings that the absorption (Fig. 10 and 11) and luminous efficiency (Fig. 12) do not completely regain the original value after irradiation stops, further study is needed. However, calculating the recovery of the luminescence from Eq. [15] with the experimentally measured absorption values during the recovery, good agreement with the experiments could be obtained (Fig. 12). The recovery phenomenon in general and this result in particular are additional proof that degradation is strictly connected with the absorption of color centers produced in the phosphors.

A reasonable approach to slowing down the initial fast degradation of phosphors should be the elimination of the imperfections originally present by annealing, by charge compensation, or by other methods. The rate and extent of the dark recovery should also be important in most applications, although it is not yet known how it can be influenced. Enhancing the absorption of the luminescent centers by increasing the activator concentration also seems feasible. However, it is restricted by the phenomenon of concentration quenching.

### Acknowledgments

The author wishes to thank Drs. Esther Conwell, Gustav Pfister, and Richard Zallen for their comments on the manuscript.

Manuscript submitted Aug. 7, 1974; revised manuscript received Sept. 5, 1975. This was Paper 46 presented at the Washington, D.C., Meeting of the Society, May 9-13, 1971.

Any discussion of this paper will appear in a Discussion Section to be published in the December 1976 JOURNAL. All discussions for the December 1976 Discussion Section should be submitted by Aug. 1, 1976.

Publication costs of this article were partially assisted by the Xerox Corporation.

### REFERENCES

- H. N. Hersch, *J. Chem. Phys.*, **30**, 790 (1959); L. Suchow, *This Journal*, **108**, 847 (1961); J. H. Singleton and L. Suchow, *ibid.*, **110**, 36 (1963); E. F. Apple, *ibid.*, **110**, 374 (1963); L. E. Vrenken, T. H. DeVette, and R. W. Van der Wolf, *Illumin. Engr.*, **59** (1964).
- B. Segall, G. W. Ludwig, H. H. Woodbury, and P. D. Johnson, *Phys. Rev.*, **128**, 76 (1962); R. K. Swank, *ibid.*, **135A**, 266 (1964); W. W. Piper, L. C. Kravitz, and R. K. Swank, *ibid.*, **138A**, 1802 (1965).
- G. T. Bauer, *This Journal*, **115**, 1176 (1968).
- K. Przibram, "Irradiation Colors and Luminescence," Pergamon Press, London (1956).
- I. L. Mador, R. F. Wallis, M. C. Williams, and R. C.

- Herman, *Phys. Rev.*, **96**, 617 (1954); R. B. Gordon and A. S. Nowick, *ibid.*, **101**, 977 (1956); A. S. Nowick, *ibid.*, **111**, 16 (1958).
6. H. W. Etzel and J. G. Allard, *Phys. Rev. Letters*, **2**, 452 (1959).
  7. P. V. Mitchell, D. A. Wiegand, and R. Smoluchowski, *Phys. Rev.*, **121**, 484 (1961).
  8. P. D. Johnson and F. J. Studer, *J. Opt. Soc. Am.*, **40**, 121 (1950); Z. Bodo, *Acta Phys. Hung.*, **1**, 135 (1951); P. D. Johnson, *J. Opt. Soc. Am.*, **42**, 978 (1952); O. P. Girin and B. J. Stepanov, *Zh. Eksperim. i Teor. Fiz.*, **27**, 281 (1954); G. T. Bauer, G. Gergely, and J. Adam, "Festkörperphysik," Akademie Verlag, Berlin (1961); G. T. Bauer, *Acta Phys. Hung.*, **14**, 311 (1962); N. T. Melamed, *J. Appl. Phys.*, **34**, 560 (1963); G. Kör-tum, "Reflectance Spectroscopy," Springer-Verlag, New York (1969).
  9. V. V. Antonov-Romanovskii, *Zh. Eksperim. i Teor. Fiz.*, **26**, 459 (1954); I. Masuda, *J. Phys. Soc. Japan*, **16**, 105 (1961); I. Masuda, *Oyo Butsuri*, **28**, 147 (1959).
  10. G. T. Bauer, *Acta Phys. Hung.*, **11**, 225 (1960); A. Brill, in "Luminescence of Organic and Inorganic Materials," H. P. Kallman and G. M. Spruch, Editors, p. 479, John Wiley & Sons, Inc., New York (1962).
  11. A. Smakula, *Z. Physik*, **59**, 603 (1930); D. L. Dexter, *Phys. Rev.*, **101**, 48 (1956).
  12. P. D. Townsend and F. C. Kelly, "Colour Centres and Imperfections," Crane, Russak and Company, Inc., New York (1973).

## Low Energy Ion-Electron Luminescence: A New Technique for the Excitation of Inorganic Phosphors

Jerry Kramer

GTE Laboratories Incorporated, Waltham, Massachusetts 02154

### ABSTRACT

A new technique for the excitation of inorganic phosphors by low kinetic energy ions (<40 eV) and low kinetic energy electrons (<20 eV) has been demonstrated and characterized. The characteristic light output of the phosphor has been used as a probe of the excitation mechanism. An empirical relationship between the light output and the ion and electron currents has been determined and used to ascertain the change in light output as a function of ion and electron kinetic energy and ionization potential. The excitation mechanism starts with the formation of holes by the ion beam. Although the holes are mobile in the lattice, some of the holes get trapped. In a second step electrons interact with these trapped holes to create an excited state(s) of the phosphor. Energy is transferred to the luminescent centers resulting in the characteristic emission of the phosphor. The slow or rate-limiting step in the production of light by low energy ions and electrons is the emission of light. Of the ten phosphors examined for low energy ion-electron excitation, six showed detectable levels of light output and, hence, we conclude that this excitation technique is quite general. The efficiency of light production observed for  $Y_2O_3$ -Eu is  $\sim 1$  photon per 40  $N_2^+$  ions and no effort has been made to increase this efficiency. We refer to the light produced by this excitation technique as low energy ion-electron luminescence (LEIEL).

This paper presents a new technique for the excitation and subsequent characteristic emission of an inorganic phosphor. This new technique is based upon the interaction of low kinetic energy ions (<40 eV kinetic energy) and electrons (< 20 eV kinetic energy) with a phosphor.

Two schemes which are widely employed today for phosphor excitation involve electromagnetic radiation or charged particles with high kinetic energy, usually in excess of 1 keV (1). In the case of electromagnetic radiation, the exciting species are generally u.v. photons or higher energy x-rays. For charged particles, the exciting species are either negatively charged electrons (cathodoluminescence) or positively charged ions (ionoluminescence). For both electrons and ions the luminous output is kinetic energy dependent, increasing with kinetic energy.

A third excitation scheme is radical recombination luminescence (RRL), a phenomenon often referred to in the early literature as candoluminescence (2). RRL was initially observed when flames, a rich source of radicals, were "played upon" phosphor surfaces. More recent work has utilized microwave discharges as radical sources and confirmed the validity of radical excitation. RRL involves the recombination of two neutral species (which may be the same) on a phosphor surface. The energy of excitation can be thought of,

naively, as equal to the recombination energy of the two radicals, or, equivalently, to the bond energy of the molecular bond formed in the recombination. As an example, in the case of two hydrogen atoms, the excitation energy would be 4.5 eV. For the sake of comparison, a 4.5 eV photon would have a wavelength of  $\sim 2750\text{\AA}$ . The efficiency of RRL is quite low. Typical efficiencies for RRL of about 1 photon/ $10^5$  radicals are found experimentally. These low efficiencies relate, in part, to an excitation mechanism involving many steps, only one of which involves the formation of a bond between the two radicals.

An interesting extension of these ideas involves the use of oppositely charged species to excite luminescent materials. The available recombination energy of low kinetic energy ions and electrons can be thought of as approximately equal to the ionization potential of the neutral atom or molecule formed in the recombination. The ionization potentials of most neutrals range from about 10 to 25 eV. The corresponding wavelengths of photons of that energy span the range from about 1250 to 5000 $\text{\AA}$ . Conceptually, the excitation of phosphors by ions and electrons can be thought of as primarily a potential energy phenomenon, rather than a kinetic energy process.

The idea that ions and electrons could excite a phosphor has been speculated upon in the literature of flame-excited luminescence (2). However, controlled

experiments to test this hypothesis have not been reported to date.

We present the first experiments on the excitation of luminescence in inorganic phosphors by low kinetic energy ions and electrons. The phenomenon is found to be complex, being very much dependent upon the interaction of the ions and electrons with the phosphor. The phosphor does not act as a simple third body which accepts the recombination energy of the ions and electrons. In contrast to RRL, the efficiency of light production by low kinetic energy ions and electrons is quite high.

### Experimental

The low energy ion-electron luminescence (LEIEL) apparatus is shown schematically in Fig. 1. The glass outer envelope of the system is connected to glass-to-metal seals and copper-gasketed stainless steel flanges which are used for supports and feedthroughs. The use of flanges permitted independent removal of the following four main components: (i) the ion source, (ii) the electron source, (iii) the phosphor support, and (iv) the vacuum system. Positive ions, generated in the ion source, and electrons from the electron source interacted with a phosphor sample. The light produced was spectrally analyzed by a monochromator and detected by a photomultiplier tube. Modulation of the charged beam(s) discriminated against the background d-c light signal as well as metastables and allowed measurement of the phase shift of the modulated light signal relative to the modulated charged beam.

The ion source and ion optics are from a Process Analyzers, Incorporated Quad 1200 RGA ionizer with electronic circuitry from a Quad 250B ionizer controller. The ion source potential was positive with respect to ground and determined the ion kinetic energy (maximum 40 eV). The first and third grids of the Einzel lens were at ground potential and the second grid at  $-90\text{V}$  to discriminate against electrons. The ion beam was modulated by applying a square wave potential (positive with respect to the ion source) to the first grid of the Einzel lens. Ions left the third grid and drifted  $\sim 5\text{ cm}$  to a phosphor plate oriented at a  $45^\circ$  angle to the axis of the ion beam. The only modification of the ion source consisted of replacing the tungsten filament with a directly heated oxide filament. This change significantly reduced background light. With an oxide filament emission current of  $150\ \mu\text{A}$ , 50 eV ionizing energy, and a source pressure of  $6 \times 10^{-4}$  Torr of  $\text{N}_2$ , an ion current of  $\sim 6 \times 10^{-8}\text{ A}$  was detected at the phosphor plate. The detected ion current was not significantly altered when a phosphor was on the plate. A baffle, attached to the third grid, served to reduce the pressure in the phosphor region, relative to the source region, by a factor of  $\sim 20$ .

Since mass discrimination has not been incorporated into the apparatus, ion beams derived from diatomic neutrals will contain some monatomic ions. All experiments, however, were run with an ion source ionizing energy of 50 eV and were reproducible. For simplicity, we shall refer to an ion beam, derived from  $\text{N}_2$  neutrals, as  $\text{N}_2^+$  ions with the understanding that  $\text{N}^+$  ions are also present.

The electron source consisted of the heater, Ba/SrO cathode, and the first two grids from a Sylvania ST 4716 A CRT electron gun. The indirectly heated cathode was at a negative potential with respect to ground (normally  $-3\text{V}$ ). The first grid was negative with respect to the cathode and was used to control the electron current. The second grid was positive with respect to the cathode and a square wave potential on grid two produced a modulated electron beam. The electron beam, which is normal to the phosphor plate and elevated  $45^\circ$ , originated  $\sim 3\text{ cm}$  from the phosphor plate.

At the low electron source cathode to phosphor potentials used in these experiments, the electron kinetic energy is dependent upon the contact potential of the phosphor and the oxide cathode as well as the cathode bias. These contact potentials are, in general, not known and we report the cathode bias which, within an additive constant, equals the electron kinetic energy. Since our results are correlated with a change in electron kinetic energy, knowledge of the actual electron kinetic energy is not necessary. We also note that surface charging will change the electron kinetic energy at a given cathode bias.

All phosphors, except one, have been obtained from GTE Sylvania. The exception,  $\text{SrAl}_2\text{O}_4\text{-Eu}$ , has been synthesized and characterized previously (3-5). Phosphors are settled from acetone onto a stainless steel flat and baked at  $\sim 400^\circ\text{-}500^\circ\text{C}$  for 15 min. Typical calculated phosphor thicknesses were about  $10\ \mu$ . The stainless steel flat was attached to an insulating ceramic block and a lead from the flat connected to an electrometer to ground.

The apparatus was evacuated by a 4 in. oil diffusion pump filled with Convalex 10 pump oil. A Freon-cooled baffle above the pump reduced backstreaming and a gate valve isolated the system from the pump. Pressures below  $1 \times 10^{-7}$  Torr, as measured by an ionization gauge in the ion source region, were obtained routinely and provision existed for baking the apparatus to  $400^\circ\text{C}$ .

The detection scheme is shown schematically in Fig. 2. A modulated electron beam plus an unmodulated ion beam produced a modulated light signal from the phosphor. The light was passed through a  $\frac{1}{4}$  meter Jarrell-Ash monochromator and detected by a 1P28 PMT. The photomultiplier tube current generated a voltage across a  $10^4$  ohm resistor to ground and the a-c voltage was detected by a PAR HR-8 lock-in amplifier.

The phase of the modulated light was determined relative to an external reference from the Tektronix 161. The phase of the modulated current signal was also determined relative to the same external reference and the difference between these two phases was taken as the phase shift.

Modulation techniques, in addition to providing phase shift data which can be correlated with radiative lifetimes for first order processes, discriminate against background d-c light from filaments and possible effects from metastables. Modulation of both beams with continuously variable phase provides mechanistic information about the interaction of the ions and electrons with the phosphor.

In general, the charging of phosphor surfaces by low energy electrons necessitated the following experimental sequence. The ion source was turned on and an initial ion current  $I_T^+$ , was detected by the electrometer. (It is assumed that the ion current detected at the electrometer is proportional to the ion current which strikes the phosphor surface.) Electrons were then added in incremental amounts and the decrease in  $I_T^+$  was taken equal to the electron current,  $I_e$ , an indirectly measured quantity. At each new value of  $I_e$ , the light output was measured and the phase shift could be determined.

As arbitrary standard conditions, we have studied the interaction of a beam of electrons modulated at 100 Hz with the electron source cathode biased 3V nega-

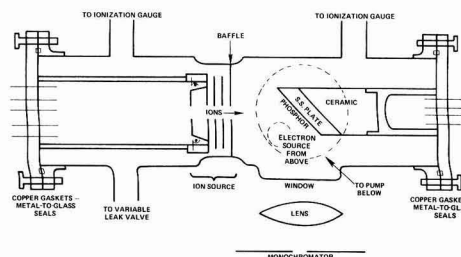


Fig. 1. Schematic diagram of the low energy ion-electron luminescence apparatus (viewed from above).



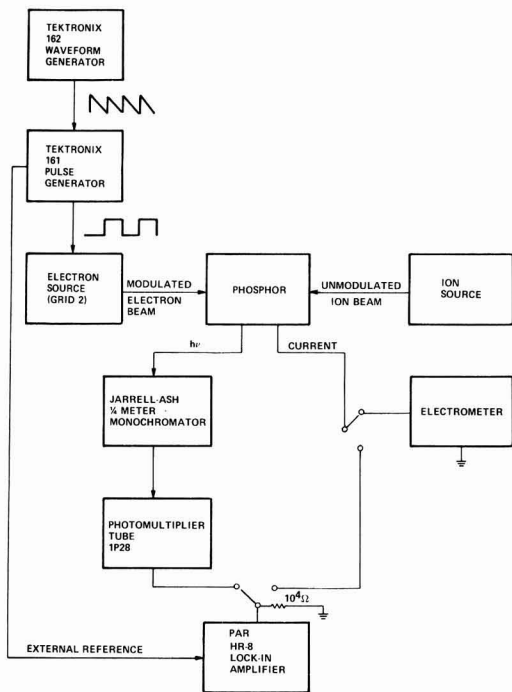


Fig. 2. Schematic diagram of the detection schemes. Modulation of the ion beam instead of the electron beam requires that the square wave go to grid 1 of the ion source rather than grid 2 of the electron source. Incorporation of a second Tektronix 161, triggered by the same 162, generates a modulated ion beam as well, with continuously variable phase with respect to the modulated electron beam.

tive with respect to the phosphor plate, and an unmodulated beam of 40 eV kinetic energy  $N_2^+$  ions. Typical ion currents,  $I_T^\circ$ , were in the range of  $1-10 \times 10^{-8}$  A and almost all data was determined for  $|I_T^\circ| > |I_e|$ .

## Results

We find that the interaction of a beam of low kinetic energy electrons and ions with a phosphor leads to the production of visible light characteristic of that phosphor. This light output has been used as a probe of the excitation mechanism: to probe the mechanism we measured the change in light output as a function of the external variables of the experiment. Initially, the quantitative relationship between light output and ion and electron currents was determined. This relationship provided a basis of comparison for the effect of variables such as electron and ion kinetic energy and ionization potential on the light output. Most of the experiments involved the interaction of ions and electrons with a  $Zn_2SiO_4$ -Mn phosphor. However, nine other phosphors were also studied in order to determine: (i) the generality of the phenomenon, which we shall refer to as low energy ion-electron excitation (LEIEE), (ii) the relative efficiencies of the different phosphors, and (iii) whether the quantitative relationships observed for  $Zn_2SiO_4$ -Mn held for the other phosphors.

The LEIEL spectrum of  $Zn_2SiO_4$ -Mn was the same as the emission spectrum observed by the more conventional excitation schemes of photoexcitation or cathode-ray excitation of the same phosphor. In the quantitative results which follow, the light output for  $Zn_2SiO_4$ -Mn was measured without slits on the monochromator ( $\sim 300\text{\AA}$  bandpass) and centered at 5280\AA.  $Zn_2SiO_4$ -Mn has a broad emission, peaking at 5280\AA, and a bandwidth at half-height of 410\AA (6).

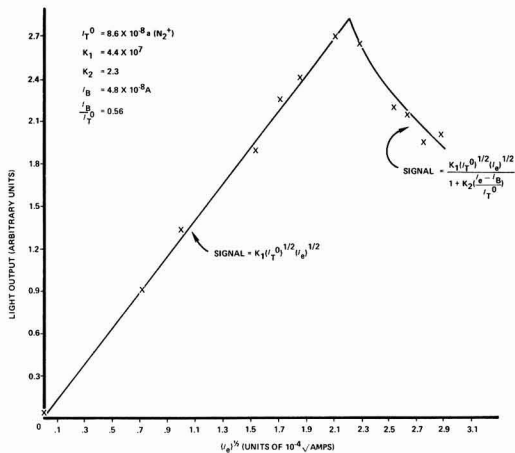


Fig. 3. Light output vs.  $(I_e)^{1/2}$ . Experimental conditions:  $Zn_2SiO_4$ -Mn; 40 eV  $N_2^+$  ions, unmodulated; electrons modulated at 100 Hz, cathode biased 3V negative. Crosses refer to the experimental points and the solid line to the empirical equation.

The light output of  $Zn_2SiO_4$ -Mn vs.  $(I_e)^{1/2}$  is shown in Fig. 3 for our arbitrary standard conditions. Qualitatively, the light output increased with increasing  $I_e$  and then started to fall off. This falloff was not associated with a change in the emission spectrum. The electron current at which falloff began was arbitrarily called  $I_B$ . The dependence of light output on  $I_T^\circ$  was determined by running experiments at different initial ion currents. The initial ion current could be varied by changing the neutral gas pressure or the emission current of the filament in the ion source and equivalent results were obtained with each method.

The relationships observed for ions at 40 eV were

$$S = \text{light output} = K_1(I_T^\circ)^{1/2}(I_e)^{1/2} \text{ for } (I_e < I_B) \quad [1a]$$

and

$$S = \frac{K_1(I_T^\circ)^{1/2}(I_e)^{1/2}}{1 + K_2 \frac{(I_e - I_B)}{I_T^\circ}} \text{ for } (I_e > I_B) \quad [1b]$$

$K_1$  is the scaling factor for output at values of  $I_e < I_B$ , the constant  $K_2$  determines the magnitude of the falloff, and  $I_B/I_T^\circ$  relates to when the falloff begins.

In Table I we tabulate the constants  $K_1$ ,  $K_2$ , and  $I_B/I_T^\circ$  (95% confidence levels) determined for our arbitrary standard conditions at a large number of different initial ion currents and also the constants determined at an ion kinetic energy of 20 eV. For our standard conditions we found that the falloff began when 55% of the initial ion current had been neutralized. Halving the ion kinetic energy to 20 eV resulted in a marked

Table I. Light output equation constants

$$S = \text{light output} = K_1(I_T^\circ)^{1/2}(I_e)^{1/2} \text{ for } (I_e < I_B)$$

$$S = \frac{K_1(I_T^\circ)^{1/2}(I_e)^{1/2}}{1 + K_2 \frac{(I_e - I_B)}{I_T^\circ}} \text{ for } (I_e > I_B)$$

	$K_{1 \pm .b}$	$K_{2 \pm .c}$	$I_B/I_T^\circ \pm .a$
$N_2^+$ (KE = 40 eV) Modulate electrons—100 Hz	$4.2 \pm 0.2 \times 10^7$	$2.9 \pm 0.5$	$0.55 \pm 0.02$
$N_2^+$ (KE = 20 eV) Modulate electrons—100 Hz	$1.9 \pm 0.2 \times 10^7$	—	—

<sup>a</sup> 95% confidence levels.  
<sup>b</sup> Units of  $(A)^{-1/2}$ .  
<sup>c</sup> Dimensionless.

decrease ( $\sim$  half) in the light output ( $K_1$ ) at  $I_e < I_B$  and, in addition, the falloff was not observed in four out of five runs. Hence, at 20 eV ion kinetic energy,  $I_B/I_T^\circ$  approaches unity.

In Fig. 4 we plot the light output vs.  $(I_e)^{1/2}$  for ion kinetic energies of 20 eV, 30 eV, and 40 eV. We see that whereas no falloff is observed at 20 eV and the 40 eV curve follows the relationships of Eq. [1], the results at 30 eV indicate that the light output has saturated.

More negative values of electron source cathode bias led to increased electron kinetic energy and, as shown in Fig. 5, increasing electron kinetic energy led to a linear increase in the light output ( $K_1$ ) at  $I_e < I_B$ . Also, increasing electron kinetic energy resulted in larger values of  $I_B/I_T^\circ$ . In comparing the effect of increasing electron and ion kinetic energy, we found that both led to an increase in light output. However, the behavior observed for  $I_B/I_T^\circ$  was opposite: increasing electron kinetic energy increased  $I_B/I_T^\circ$  while increasing ion kinetic energy decreased  $I_B/I_T^\circ$ .

Ions, derived from  $N_2$  neutrals, were used in most of our experiments. In order to explore the effect of ionization potential on the light output we examined

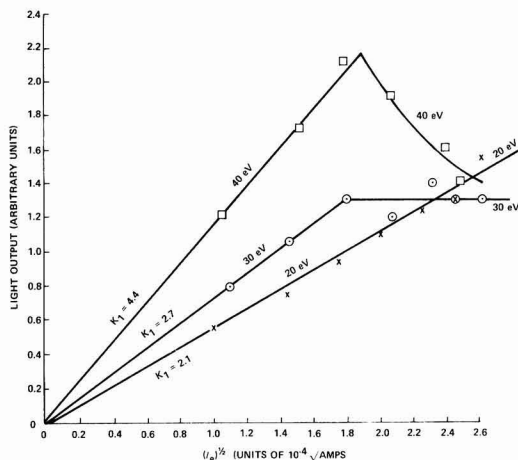


Fig. 4. Light output vs.  $(I_e)^{1/2}$  for different ion kinetic energies. Experimental conditions:  $Zn_2SiO_4$ -Mn; electrons modulated at 100 Hz, cathode biased 3V negative;  $N_2^+$  ions unmodulated, 40 eV ( $\square$ ),  $I_T^\circ = 7.0 \times 10^{-8}A$ , 30 eV ( $\circ$ ),  $I_T^\circ = 6.9 \times 10^{-8}A$ , and 20 eV ( $\times$ ),  $I_T^\circ = 7.2 \times 10^{-8}A$ .

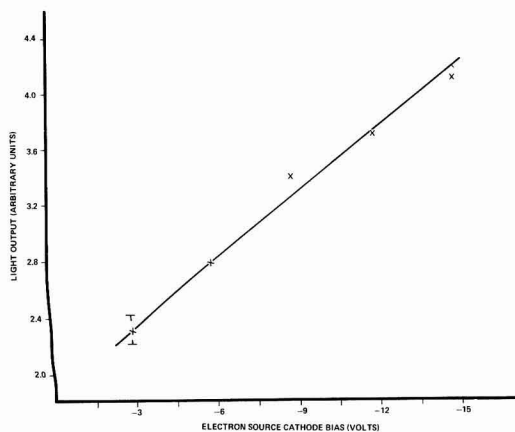


Fig. 5. Light output vs. electron kinetic energy. Experimental conditions:  $Zn_2SiO_4$ -Mn; 40 eV  $N_2^+$  ions, unmodulated; electrons modulated at 100 Hz.

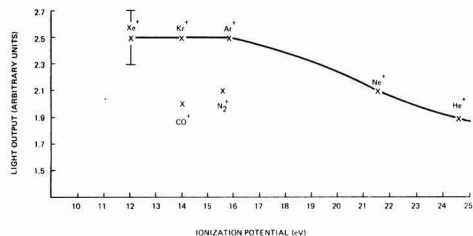


Fig. 6. Light output vs. ionization potential. Experimental conditions:  $Zn_2SiO_4$ -Mn; 40 eV ions, unmodulated; electrons modulated at 100 Hz, cathode biased 3V negative.

the light output for all the inert gas ions and  $CO^+$ . Polyatomic neutral sources could not be used because mass separation was lacking and  $O_2$  was excluded because of potential damage to the oxide filaments. The light output for the various ions used showed the same dependence on  $I_T^\circ$  and  $I_e$  (including falloff) as observed with  $N_2^+$ . In Fig. 6 the light output,  $K_1$ , for  $I_e < I_B$  is shown vs. the ionization potential of the neutrals (7). A gradual increase in light output ongoing from  $He^+$  to  $Ne^+$  to  $Ar^+$  (decreasing IP) was observed and then the signal remained constant through  $Xe^+$ . The ions derived from diatomic neutrals,  $N_2^+$  and  $CO^+$ , showed lower light outputs than the monatomic ions,  $Ar^+$  and  $Kr^+$ , respectively, with comparable ionization potentials.

The interaction of two charged beams with a phosphor allowed each beam to be modulated separately or to modulate both beams with continuously variable phase between them. We have shown the results of four different modulation schemes in Table II. As our basis of comparison, we considered the constants  $K_1$ ,  $K_2$ , and  $I_B/I_T^\circ$  for unmodulated 40 eV  $N_2^+$  ions and electrons modulated at 100 Hz. We observed that modulating both beams, in phase and out of phase, did not have a large effect on the constants in the light output equation. A small decrease in  $K_1$  for the case of both beams modulated out of phase was most apparent. In addition, note that the falloff was observed for both of these modulation schemes. In contrast, modulating the ion beam with an unmodulated electron beam resulted in very weak light output, too weak to be quantitatively measured. Finally, it was noted that modulating both beams out of phase at 20 Hz still produced a strong signal relative to both beams modulated in phase at 20 Hz.

Modulation of the electron beam plus an unmodulated ion beam produced a modulated light output.

Table II. Light output equation constants for different modulation schemes

$$S = \text{light output} = K_1(I_T^\circ)^{1/2}(I_e)^{1/2} \text{ for } (I_e < I_B)$$

$$S = \frac{K_1(I_T^\circ)^{1/2}(I_e)^{1/2}}{1 + K_2 \frac{(I_e - I_B)}{I_T^\circ}} \text{ for } (I_e > I_B)$$

	$K_{1a,b}$	$K_{2a,c}$	$I_B/I_T^\circ$
$N_2^+$ (KE = 40 eV) Modulate electrons—100 Hz	$4.2 \pm 0.2 \times 10^7$	$2.9 \pm 0.5$	$0.55 \pm 0.02$
$N_2^+$ (KE = 40 eV) Modulate electrons and $N_2^+$ 100 Hz—in phase	$4.0 \pm 0.6 \times 10^7$	$2.8 \pm 0.9$	$0.53 \pm 0.05$
$N_2^+$ (KE = 40 eV) Modulate electrons and $N_2^+$ 100 Hz—out of phase	$3.7 \pm 0.6 \times 10^7$	$2.7 \pm 0.9$	$0.50 \pm 0.06$
$N_2^+$ (KE = 40 eV) Modulate ions—100 Hz	—	—	—

a 95% confidence levels.

b Units of (A)<sup>-1</sup>.

c Dimensionless.

This light output was phase shifted with respect to the current beams and the magnitude of the phase shift was dependent upon the modulation frequency. The phase shift could be determined for each incremental addition of electron current to the initial ion current,  $I_T^\circ$ . The magnitude of the phase shift was also dependent upon whether  $I_e$  was less than  $I_B$  or greater than  $I_B$ .

Before the falloff,  $I_e < I_B$ , the phase shift was approximately constant for each incremental addition of  $I_e$ . The quantitative relationship between phase shift,  $\theta$ , and the modulation frequency,  $f = \omega/2\pi$ , was

$$\frac{\omega}{\tan \theta} = \frac{1}{\tau} = \frac{1}{\tau_0} + c\omega \quad [2]$$

where  $c$  is a constant and  $\tau$  is a first-order decay time. In the limit of zero frequency,  $\tau_0$  equals  $2.6 \times 10^{-3}$  sec. Rearrangement of Eq. [2] yields

$$\tan \theta = \frac{\omega\tau_0}{1 + c\omega\tau_0} \quad [3]$$

These results are shown in Fig. 7.

After the falloff, the phase shift gradually decreased. Associated with this change was a change in the phase of the current beam and the light as well as the difference between them. Phase shifts determined near  $|I_T^\circ| \approx |I_e|$  did not show the same dependence upon frequency as shown in Eq. [2]. Near  $|I_T^\circ| \approx |I_e|$  the phase shift data could be fit to the equation

$$\frac{\omega}{\tan \theta} = \frac{1}{\tau} \quad [4]$$

and  $\tau \approx 1.5 \times 10^{-3}$  sec.

When both beams were modulated, the phase shift of the light correlated with the modulated electron beam, rather than the modulated ion beam. The magnitude of the phase shift was the same for modulation of both beams or the electron beam alone.

Nine other phosphors were examined for their LEIEL properties (8). A list of the phosphors studied and their relative efficiencies are shown in Table III. The luminescence observed showed no deviation from the normal emission spectrum. All phosphors, with sufficient emission to be quantitatively examined, showed the same dependence on  $I_T^\circ$  and  $I_e$ , including falloff, as  $Zn_2SiO_4$ -Mn. This relationship, (Eq. [1a]), with corrections for phosphor bandpass, PMT spectral response, and phosphor decay time, was used to determine the relative efficiencies. Selected checks of the effect of ion and electron kinetic energy and ionization potential on the light output revealed the same behavior as ob-

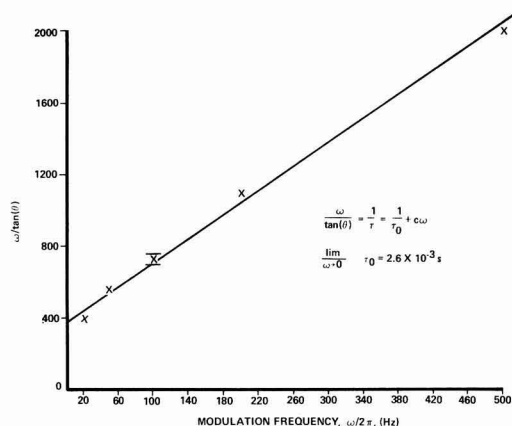


Fig. 7. Relationship between phase shift and modulation frequency ( $I_e < I_B$ ). Experimental conditions:  $Zn_2SiO_4$ -Mn; 40 eV  $N_2^+$  ions, unmodulated; electrons modulated, cathode biased 3V negative.

Table III. The relative LEIEL efficiency of different phosphors

Phosphor	Efficiency <sup>a, b</sup>
$Y_2O_3$ -Eu	10
$YVO_4$ -Eu	5
$Zn_2SiO_4$ -Mn	5
$Ba_2P_2O_7$ -Ti	3
$MgWO_4$	2
$SrAl_2O_4$ -Eu	1
$ZnCdS$ -Cu <sup>c</sup>	Very weak (?)
$CaF_2(PO_4)_3$ -Sb, Mn	Very weak (?)
$CaSiO_3$ -Mn-Pb	Not observed
$ZnS$ -Ag <sup>c</sup>	Not observed

<sup>a</sup> Light output corrected for emission bandpass, PMT spectral response, and lifetime. Experimental conditions: 40 eV  $N_2^+$  ions, unmodulated,  $I_T^\circ = 8 \times 10^{-8}$ A; electrons modulated, cathode biased 3V negative.

<sup>b</sup> Arbitrary units.

<sup>c</sup> These samples were not baked in air to prevent formation of an oxide coating on the surface.

served with  $Zn_2SiO_4$ -Mn. The only deviation from the results observed with  $Zn_2SiO_4$ -Mn related to phase shifts. Neither  $Y_2O_3$ -Eu nor  $YVO_4$ -Eu showed the linear frequency dependence on lifetime of Eq. [2] observed with  $Zn_2SiO_4$ -Mn at  $I_e < I_B$ .

When both beams were modulated at 20 Hz out of phase, the first six phosphors in Table III showed significant light outputs relative to in-phase modulation at 20 Hz. This was true even for  $SrAl_2O_4$ -Eu with a decay time of  $\sim 10$   $\mu$ sec to 10% initial brightness (3). By way of comparison, LEIEL in  $SrAl_2O_4$ -Eu was also observed at an electron beam modulation frequency of 10 kHz, the limit of the square wave generator.

$SrAl_2O_4$ -Eu and  $Y_2O_3$ -Eu both had sufficient conductivity to conduct a modulated low kinetic energy electron beam (cathode = -15V) without significantly charging the phosphor surface. In both cases, no evidence of light was observed at the normal sensitivity used for LEIEL, even though the electron current was  $\sim 5$ -10 times the initial ion current normally used in an experiment.

In order to obtain a rough measure of the absolute quantum efficiency of the LEIEL process we have utilized ZnO. ZnO is excited by very low kinetic energy electrons and the quantum efficiency for 10 eV electrons is about 1 photon per 200 electrons (9). The ZnO light output, which is proportional to  $I_e$ , was measured at a modulated current of  $8 \times 10^{-8}$ A and 10 eV kinetic energy (cathode-phosphor bias) and corrected for PMT response, bandpass, and phosphor decay time. We have compared the light output of ZnO with the light outputs of the various phosphors in Table II at the experimental conditions given. The light output of ZnO was approximately equal to the light output for  $MgWO_4$ . Hence, we conclude that at an initial ion current,  $I_T^\circ$ , of  $8 \times 10^{-8}$ A  $MgWO_4$  has a maximum light output upon the addition of electrons corresponding to about 1 photon per 200  $N_2^+$  ions. No effort has been made to increase the yields for any phosphor.

## Discussion

We begin our discussion by considering the effect of electrons and ions alone on the phosphor, followed by the development of a model and subsequent refinements derived from quantitative data.

**Electron-phosphor interactions.**—When electrons interact with a phosphor, secondary electrons are emitted from the phosphor (10). The secondary electron emission coefficient, defined as the ratio of secondary electrons to primary electrons, is dependent upon the electron kinetic energy. At low kinetic energy the secondary electron emission coefficient of the phosphor is less than unity and in time the phosphor charges to the negative bias of the electron source cathode. For many phosphors, at approximately 50-200 eV, the secondary emission coefficient rises above unity and no negative charging is observed (11). Finally, at still higher kinetic energies ( $\sim 1$ -60 keV) the secondary electron

emission coefficient falls below unity again (11). In addition to producing secondary electrons, primary electrons also interact with a phosphor to produce visible light *via* cathode ray excitation (1). The kinetic energy threshold for the production of light is typically several hundred electron volts, however, notable exceptions such as ZnO have thresholds below 3 eV (9). For the continuous production of light, the phosphor must not charge negatively. In two phosphors used for the LEIEL experiments, charging did not occur at the typical electron kinetic energies of our experiments. It is significant that no light was detected in these two phosphors.

**Ion-phosphor interactions.**—The interpretation of ion-phosphor interactions is more complicated than electron-phosphor interactions. The complications arise because an ion has potential as well as kinetic energy by virtue of its ability to recombine with an electron. At high-ion kinetic energies (for example  $>1000$  eV), the ion bombards the phosphor and the interaction is dominated by the kinetic energy. As with the primary electrons, one observes secondary electron emission (12) and the production of light (ionoluminescence) (1). At low ion kinetic energies, the ion spends a much greater time near the surface of the phosphor and, hence, the potential energy of the ion can play a more dominant role. When low kinetic energy ions, with sufficient potential energy, approach within a few angstroms of a phosphor surface, neutralization of the ion can occur before the ion strikes the phosphor surface in a process involving the phosphor, the ion, and an electron from the valence band of the phosphor. Ion neutralization and the subsequent effect on the phosphor are best considered by reviewing some of the elementary theory of ion neutralization spectroscopy (12-14).

In Fig. 8 we see a diagram of the interaction of an ion with a phosphor surface (15).  $E = 0$  represents the vacuum level of the phosphor as well as a free electron and ion separated to infinity. The incoming ion approaches the phosphor surface and at some critical distance,  $s$ , dependent upon the ion kinetic energy, an electron from the valence band tunnels through the potential barrier to neutralize the incoming ion. The neutralized ion retains much of its kinetic energy (velocity) and continues toward the phosphor, striking the surface as a neutral. For neutralization to occur, the recombination energy of the ion, which in first order neglects the interaction with the phosphor and can be taken as the ionization potential (IP), must be greater than the energy from the top of the valence band to free space ( $\phi^*$ ). The valence electron, upon tunneling from the valence band, creates a hole and generally this hole is formed very close to the surface. If the IP  $> \phi^*$ , excess energy must be dissipated and if IP  $> \phi^* + \Delta E_g$  (the bandgap), a second electron from the valence band can be excited into the conduction band in an Auger-type process creating an electron-hole pair. Finally, if the IP  $> 2\phi^*$ , secondary electrons can be emitted.

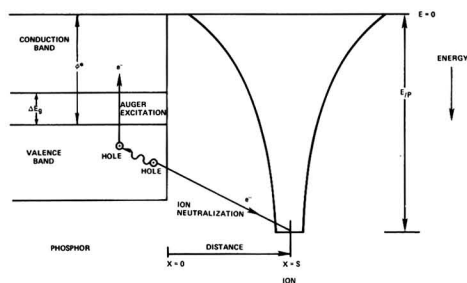


Fig. 8. Schematic energy diagram of low kinetic energy ion-phosphor interaction.

In semiconductors the secondary electron emission coefficient is only very weakly dependent upon ion kinetic energy, but the secondary electron yield increases dramatically for ions with increasing ionization potentials (16). Because of the high conductivity of the semiconductors, no surface charging was observed. For an insulator such as amorphous selenium, surface charging is most apparent (14). In the case of SiO<sub>2</sub> films, ion neutralization processes lead to degradation of the MOS quality SiO<sub>2</sub> films (17) and impurity migration from the surface to the Si substrate (18).

In our experiments on phosphors, surface charging, if present, was not pronounced enough to repel the incoming unmodulated ion beam. Compared to an unmodulated ion beam, square wave modulation halved the detected ion current with the phosphor present. For identical settings of the ion source, nearly the same ion current was detected by the electrometer with and without a phosphor present. From these observations we conclude that most of the holes formed upon neutralization have sufficient mobility to reach the electrometer and prevent charge buildup.

**Formation of a trapped hole.**—In the LEIEL experiments luminescence was only observed when ions as well as electrons interacted with the phosphor. By modulating both beams out of phase it was determined that the two charged species did not have to be coincident for light to be produced. This result suggested two possible roles for the ions. The first was that the electrons excited the phosphor *via* a conventional cathodoluminescent type excitation and that ions passively provided charge neutrality. A second mechanism assumes a more active role for the ion in the excitation process. Our results suggest that the active role for the ions is dominant.

Low energy ions ( $>100$  eV) interacting with metal surfaces show almost a 100% neutralization efficiency:  $\sim 0.1\%$  reflected ions and metastable atoms are observed (19). At the opposite end of the conductivity scale, the insulator, amorphous Se, shows a 100% charging efficiency in the region of low surface charge, and no difference was observed in charging behavior among any of the ions at any energy ( $<200$  eV) in the limit of zero surface charge (14). If we make the logical assumption that all the different ions are neutralized with 100% efficiency at the phosphor surface, then the observed differences in light output as a function of ionization potential indicate an active role for the ions. The square root dependence on the ion current in the light output equation is also suggestive of an active ion role. For two phosphors, electron charging did not occur at low electron kinetic energy and no luminescence was observed when the positive ion current was zero. Thus, for these two phosphors, the ions must play an active role and this strongly suggests that the ions take an active role in all the other phosphors.

One could argue that the decreased light output observed when only the ions are modulated is indicative of a passive role for the ions. The ions could preserve charge neutrality and the electrons produce a d-c light signal undetected by the lock-in amplifier. A more likely explanation, which preserves the active role, involves the formation of a trapped hole by the ion. If the ion beam creates a trapped hole whose lifetime is long with respect to the modulation frequency, then modulation of the ion beam at that frequency will lead to a decreased a-c light signal (20). This explanation requires that the ion beam creates an intermediate excited state of the phosphor which cannot luminesce. When both beams are modulated out of phase, the phase of the light output correlates with the electron beam rather than with the ion beam. Hence, we conclude that the electron beam interacts with the trapped hole of the phosphor to create an excited state(s) that leads to luminescence.

In the case of phosphors, temporary trapping of holes has been shown to lead to luminescence in SrAl<sub>2</sub>O<sub>4</sub>-Eu (5). Although the Eu<sup>+2</sup> emission in SrAl<sub>2</sub>O<sub>4</sub>-Eu has a

fast (10  $\mu$ sec) decay to 10% of initial brightness, a long-lasting persistence of many seconds is observed (3). This luminescence has been shown to be associated with trapped holes that are thermally deactivated. We note that LEIEL was observed in  $\text{SrAl}_2\text{O}_4\text{-Eu}$ . In  $\text{SrAl}_2\text{O}_4\text{-Eu}$  the hole trapping levels are associated with defects in the lattice. In general, a second possibility for a hole trap is the activator ion itself. For example,  $\text{Mn}^{+2}$  could act as a hole trap by forming  $\text{Mn}^{+3}$ . Upon deactivation of the  $\text{Mn}^{+3}$  to  $\text{Mn}^{+2}$  with an electron, the  $\text{Mn}^{+2}$  could be left in an excited state and hence, might luminesce. A third possibility is that two mobile holes will dimerize and be trapped. This concept has been postulated with regard to  $\text{CaF}_2$  and will be amplified later (21).

All our results point to the formation of a trapped hole by the ion beam. The correlation between the electron beam and the light output, determined from the phase shift, and the ability to produce light with the beams out of phase supports the idea that electrons interact with the trapped holes in a second step to produce an excited state(s) of the phosphor. The light emission from LEIEL agrees with the other conventional excitation schemes and, hence, the same emitting state is most probably involved in the different excitation schemes. This is entirely reasonable, in that most phosphor excitation schemes with widely varying energy inputs lead to the same emission spectrum of the phosphor. Finally, the phase shift in  $\text{Zn}_2\text{SiO}_4\text{-Mn}$  extrapolated to zero modulation frequency yields a first order decay time of  $2.6 \times 10^{-3}$  sec which is similar to the value of  $2.5 \times 10^{-3}$  sec at  $15^\circ\text{C}$  determined by photoexcitation of the same sample (22).

*Possible mechanisms and kinetic energy dependence.*—The light output equations for ions at 40 eV are  $S = \text{light output} = K_1(I_T^\circ)^{1/2}(I_e)^{1/2}$  for  $(I_e < I_B)$  [1a] and

$$S = \frac{K_1(I_T^\circ)^{1/2}(I_e)^{1/2}}{1 + K_2 \frac{(I_e - I_B)}{I_T^\circ}} \text{ for } (I_e > I_B) \quad [1b]$$

We note that the falloff does not begin when electrons are first added to the phosphor, but only after a significant fraction of the initial ion current has been neutralized. As seen in Fig. 4, the falloff at 30 eV is different, being better represented by a term in the denominator of the light output equation which reflects saturation, and that at 20 eV no falloff is observed. Common to the results at these three kinetic energies, however, is the light output equation,  $K_1(I_T^\circ)^{1/2}(I_e)^{1/2}$ , for  $I_e < I_B$ . We start by discussing a possible mechanism which might give rise to the square root behavior of the ion and electron currents.

Ions interact with the phosphor at low kinetic energy and are neutralized when they approach within a few angstroms of the phosphor surface. The neutralized ion continues its path toward the phosphor and strikes the phosphor surface as a neutral with some kinetic energy. Results on low energy ions (25–600 eV) interacting with a tungsten wire indicate that at the energies used in those experiments approximately 50% of the kinetic energy of the ion is transferred to the tungsten lattice by the neutralized ion (23). The incoming ion is neutralized when an electron from the valence band of the phosphor tunnels to the approaching ion leaving a hole at the surface of the phosphor. In the case of metals or semiconductors, the mobility of the holes formed (or electrons) is high enough to prevent charge buildup at the surface, while in the case of insulators such as amorphous selenium, rapid charge buildup with an initial 100% efficiency is observed at the surface. For phosphors with conductivities between insulators such as amorphous selenium and semiconductors, we postulate that positive charge buildup at the surface is kept down because the kinetic energy of the neutralized ion frees the hole from the surface of the

phosphor and creates a mobile hole. Recent experiments in low energy ion bombardment effects in  $\text{SiO}_2$  have also postulated this "knock-on" effect with regard to impurity migration (17). The increasing ability to free holes from the surface of the phosphor may explain the increase in light output before falloff observed with increasing ion kinetic energy.

Holes, once freed from the surface region, are mobile and can migrate to the phosphor substrate and be collected by the electrometer or they may be trapped along the way. The square root dependence on the ion current in the light output equation mechanically suggests that two mobile holes combine to form a trapped hole. The rate of production of trapped holes,  $dp_t/dt$ , is proportional to the rate of creation of holes,  $I_T^\circ$ , minus the rate at which trapped holes are formed in a process dependent upon the square of the hole concentration,  $p$ . Thus

$$\frac{dp_t}{dt} = \beta I_T^\circ - kp^2 \quad [5]$$

and at steady state  $dp_t/dt = 0$  and

$$[p] \propto (I_T^\circ)^{1/2} \quad [6]$$

The dimerization of holes has been postulated previously in work done on  $\text{CaF}_2$  (21). X-irradiation of  $\text{CaF}_2$  doped with  $\text{Tm}^{+3}$  produces self-trapped ( $V_K$ ) centers at liquid  $\text{N}_2$  temperatures.  $\text{Tm}^{+3}$  ions enhance  $V_K$  production by trapping electrons and hence, are converted to  $\text{Tm}^{+2}$  ions. Upon warming the crystal to room temperature, about 90% of the  $V_K$  centers are changed to nonparamagnetic hole centers (24). The nonparamagnetic nature and complex decay kinetics of these room temperature hole centers are compatible with the formation of hole pairs as the stable hole centers.

In analogous fashion, the dependence of the light output on the square root of the electron current suggests that two electrons may be involved in the production of light. The light output would be expected to increase with increasing electron kinetic energy if the excitation of a valence electron were involved in initiating the luminescence. This may explain the results of Fig. 5 which shows the light output vs. electron kinetic energy. Two other factors which might be relevant are that increasing electron kinetic energy will lead to less negative surface charging of the phosphor because of the increasing secondary electron emission coefficient, and that different electron kinetic energies will lead to different penetration depths of the electrons into the phosphor. Also at very low electron kinetic energy, cathodoluminescent processes show a "dead layer" effect which has been attributed to surface recombination (25). Our understanding of LEIEL, however, is not sufficiently developed to examine these three effects in any detail.

In order that the light output be proportional to the square roots of the two currents the light output must also be proportional to the first power of the hole concentration and the first power of the electron concentration. From the analysis above, however, the light output should be proportional to the square of the hole and electron concentrations. At this time we cannot resolve this discrepancy, nor can we suggest an alternative mechanism which might fit the data better. We might also add that the influence of the hole concentration gradient from surface to substrate on the light output is not known, nor is the effect of the diffusion of the holes and electrons.

*Falloff.*—The falloff in light output is shown in Fig. 4 for a number of different ion kinetic energies. The falloff represents a competition between radiative and nonradiative processes. Interestingly, this competition does not begin at the start when electrons are added, but only after a finite percentage of the ion current has been neutralized. This suggests that the falloff in light output must be triggered by some state of the system.



Secondly, the functional form of the falloff changes dramatically with ion kinetic energy and does not even occur at an ion kinetic energy of 20 eV.

The triggering of the falloff is kinetic energy dependent. For electrons, increasing the kinetic energy increases the percentage of the ion current which is neutralized before falloff occurs. In contrast, increasing the ion kinetic energy from 20 to 30 eV decreases the percentage of the ion current which is neutralized before falloff occurs. This opposite behavior for oppositely charged species suggests that an electrostatic phenomenon may be responsible for the falloff. We also note that when the falloff occurs, the phase of the ion and electron beams change with respect to a reference. Charging of the phosphor surface would lead to distortion of the square wave ion plus electron signal and, hence, produce a phase shift.

**Effect of ionization potential.**—Our results show that the kinetic energy of the ion beam has a much greater effect on the light output than the chemical identity of the ion, i.e., the ionization potential. However, when the ionization potential is less than  $\phi^*$  (Fig. 8), insufficient energy is available for neutralization by an electron tunneling from the valence band, and, hence, the light should be very low or nonexistent. In contrast to our results, the secondary electron emission observed in ion neutralization spectroscopy is strongly dependent upon the ionization potential, increasing with increasing ionization potential, and very weakly dependent upon the ion kinetic energy (16). This suggests that for LEIEL the ability of an ion with high ionization potential to form an electron-hole pair in a secondary Auger process either does not lead to luminescence, or that any luminescence obtained from the Auger process is swamped by a different luminescent process which has a weak inverse dependence on the ionization potential.

The hole produced by the incoming ion, once freed from the surface of the phosphor, can either migrate to the substrate and be neutralized or be trapped in the bulk. A competition exists between these possibilities. One factor which may influence this competition is the energy of the hole initially formed, relative to the top of the valence band. Those holes formed closer to the top of the valence band may have a higher probability of being trapped. For a given ion current, ions with smaller ionization potentials capable of being neutralized by valence electrons will produce a greater percentage of holes closer to the top of the valence band, and hence more light will be produced per unit ion current.

The decreased light output of  $N_2^+$  relative to  $Ar^+$ , and  $CO^+$  relative to  $Kr^+$ , may relate to the ability of diatomic species to vibrate and rotate (26). Excitation of vibrational and rotational modes of  $N_2$  and  $CO$  at the time of neutralization may decrease the percentage of the ion kinetic energy which is transferred to the phosphor relative to monatomic species. In general, some of the effect of ionization potential on light output may also relate to the inherent efficiency of kinetic energy transfer by the neutral to the lattice.

Although holes may be trapped either at the surface or in the bulk, our results suggest that the trapped holes responsible for luminescence are in the bulk. If a surface phenomenon were involved, one would expect that vacuum conditions, sample preparation, and time would play a major role in the light output obtained. Reproducible results were obtained, however, over periods of months without changing samples or baking the apparatus. In addition, fresh samples could be inserted into the system and, with no other preparation than evacuating the system, luminescence could be observed. Surely, by the modern standards of surface science, our phosphor surfaces were not clean.

Mass sputtering by ion beams with kinetic energies in excess of 500 eV is commonly used to clean surfaces. Low energy ion-surface collisions have produced optical radiation which arises from sputtered material

(27). Some samples showed thresholds as low as  $\sim 50$  eV (27). Although sputtering could be occurring in our experiments during ion irradiation, the low ion currents and low kinetic energies argue against significant amounts of sputtering.

**Phase shifts.**—The phase shift of the light output in  $Zn_2SiO_4$ -Mn vs.  $\omega$  before the falloff is shown in Fig. 7. We will only consider the region before falloff because of possible electrostatic complications that arise after falloff.

The relationship between the phase shift and  $\omega$  in  $Zn_2SiO_4$ -Mn before falloff (assuming that  $\tau$  is a constant independent of  $\omega$ ) is

$$\theta = \tan^{-1} \frac{\omega\tau_0}{1 + c\omega\tau_0} \quad [7]$$

where  $c$  is a constant. This differs from the normal equation for a first-order decay process by the  $1 + c\omega\tau_0$  term in the denominator. Extrapolation of the phase shift to zero frequency to eliminate frequency dependent effects yields a first-order decay time,  $\tau_0$ , of 2.6 msec.  $Zn_2SiO_4$ -Mn shows a first-order decay to below 10% of initial brightness and photoluminescent decay data from this laboratory on the same sample yields a first-order decay time of 2.5 msec at 15°C (22). The excellent agreement between these two values implies that the slow step in the production of light by LEIEL is the emission of light. In support of this conclusion, the first-order decay times for  $YVO_4$ -Eu and  $Y_2O_3$ -Eu were in reasonable agreement with the values obtained by other methods. Also the transit time of the ions to the phosphor is much faster than the luminescent decay times.

The  $1 + c\omega\tau_0$  term in the denominator of the phase shift, although unusual, is reproducible. It may, however, be unique for  $Zn_2SiO_4$ -Mn in that it was not observed with  $Y_2O_3$ -Eu or  $YVO_4$ -Eu. The fact that the  $1 + c\omega\tau_0$  term was not observed with  $Y_2O_3$ -Eu or  $YVO_4$ -Eu also tends to rule out experimental artifacts as the origin of the  $1 + c\omega\tau_0$  term. A mechanism which might explain the physical origin of the  $1 + c\omega\tau_0$  term is not apparent.

An alternative interpretation of the experimental data is that the phase angle,  $\theta$ , is equal to  $\tan^{-1}(\omega\tau)$  as expected for a first-order process, but that  $\tau$  changes with frequency. This interpretation, however, requires that increasing frequency leads to apparent radiative lifetimes which are increasingly shorter than the natural lifetime obtained by photoluminescence. It is unreasonable that the lifetime could decrease by a factor of 5 ongoing from a modulation frequency of 20 to 500 Hz, especially with no indication that the lifetime was reaching a steady value.

**Other phosphors.**—Of the ten phosphors studied, six showed detectable levels of light by the LEIE excitation technique. From this result we conclude that LEIEL is a reasonably general phenomenon and that the technique should be capable of exciting a large number of phosphors. The fact that all six phosphors showed the same functional dependence on  $I_1^+$ ,  $I_0$ , and  $I_B$  in the light output equations as well as the same qualitative effect of electron and ion kinetic energies and ionization potential on light output indicates that the same general excitation mechanism leading to light production is operative in all of these phosphors. The linear frequency dependence of the emitting state lifetime observed in  $Zn_2SiO_4$ -Mn may be peculiar to that material.

Calibration of the light output with a ZnO standard shows that the LEIEL process is quite efficient.  $Y_2O_3$ -Eu has a maximum light output (just before falloff begins) with 40 eV  $N_2^+$  ions and cathode bias of  $-3V$  which corresponds to about 1 photon per 40  $N_2^+$  ions. No effort was made to maximize the light output of these phosphors by altering the phosphor itself. There seems no reason to believe that a phosphor optimized for u.v. or electron excitation will be optimized for LEIE excitation.

### Acknowledgments

The author wishes to thank Drs. Adam Heller and Joseph Lester for their many helpful discussions. This work was sponsored in part by the Office of Naval Research.

Manuscript submitted June 11, 1975; revised manuscript received Sept. 2, 1975.

Any discussion of this paper will appear in a Discussion Section to be published in the December 1976 JOURNAL. All discussions for the December 1976 Discussion Section should be submitted by Aug. 1, 1976.

Publication costs of this article were partially assisted by GTE Laboratories Incorporated.

### LIST OF SYMBOLS

LEIEL	low energy ion-electron luminescence
LELEE	low energy ion-electron excitation
$I_T^\circ$	the initial ion current passing through the phosphor and detected by an electrometer
$I_e$	the electron current determined from the decrease in $I_T^\circ$ upon the addition of electrons
$I_B$	the electron current at which the light output starts to deviate from a $K_1(I_T^\circ)^{1/2}(I_e)^{1/2}$ dependence
$f$	the frequency at which the ion or electron beams, or both, are modulated
$\omega$	the modulation frequency, $f$ , divided by $2\pi$
$\theta$	the phase shift of the light output signal relative to the modulated current signal
$\tau$	the first-order decay time to $1/e$ of initial value
$\phi^*$	the energy difference from the top of the valence band to free space
$\Delta E_g$	the bandgap

### REFERENCES

- For a general discussion on phosphors the reader is referred to H. W. Leverenz, "An Introduction to Luminescence of Solids," John Wiley & Sons, Inc., New York (1950).
- For a recent review see H. F. Ivey, *J. Luminescence*, **8**, 271 (1974).
- F. C. Palilla, A. K. Levine, and M. R. Tomkus, *This Journal*, **115**, 642 (1968).
- G. Blasse and A. Brill, *Philips Res. Rept.*, **23**, 201 (1968).
- V. Abbruscato, *This Journal*, **118**, 930 (1971).
- "Zinc Orthosilicate: Mn, Type 2282," Sylvania Phosphors, Technical Information Bulletin.
- J. L. Franklin *et al.*, "Ionization Potentials, Appearance Potentials, and Heats of Formation of

- Gaseous Positive Ions," National Standard Reference Data System, NBS-26, 1969.
- A tenth phosphor, ZnO, showed the usual property of being excitable by a low energy ion beam by itself. The results for this phosphor will be reported on elsewhere.
  - P. Wachter, *Z. Physik*, **161**, 62 (1961).
  - For a discussion of secondary electron emission see A. Van der Ziel, "Solid State Physical Electronics," Chapter 10, Prentice Hall, Inc., Englewood Cliffs, N.J. (1957).
  - H. W. Leverenz, "An Introduction to Luminescence of Solids," p. 435, John Wiley & Sons, Inc., New York (1950).
  - See, for example: I. A. Abroyan, M. A. Ereemeev, and N. N. Petrov, *Soviet Phys. Usp.*, **10**, 332 (1967).
  - H. D. Hagstrum, *Phys. Rev.*, **122**, 83 (1961).
  - D. W. Vance, *J. Appl. Phys.*, **42**, 5430 (1971).
  - We consider the phosphor as a semiconductor or insulator, depending upon its conductivity, with special radiative properties which do not affect the ion neutralization results observed in semiconductors and insulators.
  - See, for example: Y. Takeishi and H. D. Hagstrum, *Surface Sci.*, **3**, 175 (1965).
  - D. V. McCaughan and V. T. Murphy, *I.E.E.E. Trans. Nucl. Sci.*, **19**, 249 (1972).
  - D. V. McCaughan, R. A. Kushner, and V. T. Murphy, *Phys. Rev. Letters*, **30**, 614 (1973).
  - H. D. Hagstrum, *Phys. Rev.*, **96**, 325 (1954).
  - The relationship among modulation frequency, first-order decay time, and signal intensity is discussed in J. Perel, R. H. Vernon, and H. L. Daley, *J. Appl. Phys.*, **36**, 2157 (1965).
  - Z. J. Kiss and D. L. Staebler, *Phys. Rev. Letters*, **14**, 691 (1965).
  - R. Pappalardo and J. Moore, Private communication.
  - H. F. Winters and D. Horne, *Phys. Rev.*, **B-10**, 55 (1974).
  - J. H. Beaumont, W. Hayes, D. L. Kirk, and G. P. Summers, *Proc. Roy. Soc. (London)*, **Ser. A 315**, 69 (1970).
  - G. Gergely, *J. Phys. Chem. Solids*, **17**, 112 (1960).
  - Decreased secondary electron emission yields for diatomic ions vs. monatomic ions with the same ionization potential have been observed in the ion neutralization spectroscopy of metals. Calculations have shown that the decreased yield is consistent with the ability of the diatomic ion to vibrate and rotate. See J. B. French and R. H. Prince, in "The Structure and Chemistry of Solid Surfaces," G. Somorjai, Editor, Chapter 48, John Wiley & Sons, Inc., New York (1969).
  - C. W. White and N. H. Tolk, *Phys. Rev. Letters*, **26**, 486 (1971).

# Structures and Optical Properties of Rf-Sputtered Bi<sub>12</sub>GeO<sub>20</sub> Films

Tsuneo Mitsuyu, Kiyotaka Wasa, and Shigeru Hayakawa

Wireless Research Laboratory, Matsushita Electric Industrial Company, Limited, Kadoma, Osaka, Japan

## ABSTRACT

Thin films of Bi<sub>12</sub>GeO<sub>20</sub> were prepared on glass and silicon substrates by rf-sputtering with the growth rate of 0.04–1.5 μm/hr. The crystalline structure of the films varied mainly with the substrate temperature: the amorphous state was obtained below 150°C of the substrate temperature; polycrystalline with fcc form between 150° and 350°C; and polycrystalline with bcc form above 400°C. The (111)-oriented aluminum films deposited on glass substrates were found to enhance the preferred orientation of the bcc films in the <321> direction. These sputtered films exhibited the near ultraviolet optical absorption edges at 460–620 mμ, and a broad absorption at about 20 μm in the infrared region.

Bi<sub>12</sub>GeO<sub>20</sub> (BGO) in the body-centered cubic (bcc) system is strongly piezoelectric, optically active, photoconductive, and exhibits an electro-optic effect. Large single crystals of BGO are made by the Czochralski method (1) and are studied for fabricating ultrasonic devices (2).

Thin films of BGO are usable for the fabrication of thin-film surface acoustic wave devices. The BGO films reduce the dimension of the acoustic devices owing to their low sound velocities (3) and also have a potential in the fabrication of thin-film optical devices such as light modulators, deflectors, and switches (4). Several processes are used to make the BGO film: chemical vapor deposition (CVD), liquid phase epitaxial growth, and cathodic sputtering. The CVD method was examined to deposit the single crystal BGO films on a surface of monocrystalline substrates by Silvestri *et al.* (5). In addition, several workers have succeeded in fabricating highly oriented or single crystalline films of multicomponent oxides such as ferroelectric Bi<sub>4</sub>Ti<sub>3</sub>O<sub>12</sub> and LiNbO<sub>3</sub> by cathodic sputtering (6–8). The cathodic sputtering process has the advantage that a wide variety of materials can be deposited on various substrates with little cross contamination.

Recently we have fabricated thin films of BGO on heterogeneous substrates by rf sputtering. This paper describes the structure and some optical properties of rf-sputtered BGO films.

## Experimental Procedures

An rf diode sputtering apparatus of a hemispherical electrode system was used for depositing the BGO films. The electrode configuration of the sputtering apparatus is schematically shown in Fig. 1. A polycrystalline BGO hemispherical target 25 mm in diameter was used as cathode. The target was prepared as follows: First, powder of Bi<sub>2</sub>O<sub>3</sub> (purity, 99.8%) and GeO<sub>2</sub> (purity, 99.99999%) mixed at the mole ratio of 6:1 was pressed into a column and the column was prebaked in air for about 4 hr at 800°C in order to synthesize BGO grains. Then, the grains were pressed into a column again and were sintered in air at the same firing condition to the prebaking process. Finally, the sintered column was formed into a hemispherical shape. The x-ray diffraction pattern and the corresponding lattice constant of the target well agreed with the ASTM data (card No. 23-71) for the bcc phase of the BGO. Borosilicate glass and (111)-oriented single crystal wafers of Si were used as substrates. These substrates were placed on a holder

Key words: bismuth germanium oxide, rf sputtering, piezoelectric film, optical absorption.

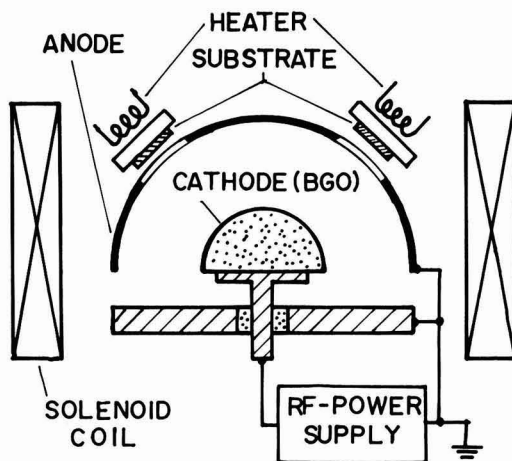


Fig. 1. Electrode configuration of rf-sputtering system

located behind the anode. Table I shows typical sputtering conditions for the film preparation. Under these conditions the BGO films were prepared with a growth rate of 0.04–1.5 μm/hr. The sputtered films were 0.15–3.0 μm thick.

Crystalline structures of the films sputtered on the glass and Si substrates were determined by x-ray diffraction and reflection electron diffraction (RED). Optical transmission spectra were examined at room temperature. The glass substrates were used in the visible region and the Si substrates, in the infrared region.

## Results and Discussion

It was observed that the crystalline structure of the sputtered films scarcely depended on the substrate material or the growth rate, but strongly depended on the substrate temperature during the sputtering process. At the substrate temperature below 150°C

Table I. Sputtering conditions for the film preparation

Target area	9 cm <sup>2</sup>
Target-substrate spacing	2–3 cm
Sputtering gas	Ar (50%) + O <sub>2</sub> (50%)
Gas pressure	5 × 10 <sup>-2</sup> Torr
Background pressure	2 × 10 <sup>-6</sup> Torr
Rf power	5–20W
Magnetic field	100G
Substrate temperature	100°–500°C

(not deliberately heated) the sputtered films were amorphous. These films were yellow and transparent. At the substrate temperature between  $150^\circ$  and  $350^\circ\text{C}$ , the sputtered films were dark brown and showed a different x-ray diffraction pattern with that of the bcc phase. From the x-ray analyses, this phase is found to be the impure phase of  $\text{Bi}_2\text{O}_3$  with a face-centered cubic (fcc) form which has been designated as  $\delta^*-\text{Bi}_2\text{O}_3$  by Gattow and Schröder (9). A comparison of the x-ray diffraction data for the film obtained in our experiment with the data for  $\delta^*-\text{Bi}_2\text{O}_3$  prepared from a composition  $6\text{Bi}_2\text{O}_3 \cdot \text{GeO}_2$  by Gattow and Fricke (10) (listed as  $\text{Bi}_{12}\text{GeO}_{20}$  in ASTM card No. 17-812) is given in Table II. The lattice constant  $a = 5.55\text{\AA}$  for the former is slightly smaller than  $a = 5.57\text{\AA}$  for the latter. This fcc phase is considered to be a metastable state since it has transformed easily into the bcc phase by annealing at  $400^\circ\text{C}$  for 1 hr. This consideration is confirmed by the fact that the bcc phase is found to be stable at any temperature below the melting point of  $935^\circ\text{C}$  (11). In the bulk BGO, the fcc phase can be obtained only by quenching a melt (10). It is noted that in the sputtering film growth process, the metastable fcc phase can be easily grown without any additional quenching process.

Films of the bcc phase were obtained at the substrate temperature above  $400^\circ\text{C}$ . The films of the bcc phase were pale yellow and semitransparent. X-ray data for these films and the ASTM data for the pulled single crystal BGO are also given in Table II. The lattice constant for the film is  $a = 10.16\text{\AA}$  which is slightly greater than the ASTM data,  $a = 10.146\text{\AA}$ . At the substrate temperature of  $350^\circ\text{--}400^\circ\text{C}$ , sputtered films were mixtures of the fcc and bcc phases.

Figure 2 shows typical RED patterns and electron micrographs for the BGO films of the amorphous, fcc, and bcc phases on the glass substrates. It is observed that the crystallites of the bcc phase are much larger than that of the fcc phase. The RED patterns indicate that all these films are polycrystalline and scarcely exhibit a preferred orientation. Similar results were obtained for the films on Si substrates. But a slight tendency of the (321) orientation was observed for the bcc films as shown in Fig. 3 when the glass substrate was coated with a thin (111)-oriented Al layer (vacuum deposited), the growth rate was very low ( $0.04 \mu\text{m/hr}$ ), and the sputtered film was very thin ( $0.15 \mu\text{m}$ ).

The crystalline structures of the BGO films sputtered on glass or Si substrates are summarized in Table III.

Table II. X-ray diffraction data for  $\text{Bi}_{12}\text{GeO}_{20}$

fcc $\text{Bi}_{12}\text{GeO}_{20}$ ( $\delta^* - \text{Bi}_2\text{O}_3$ )				bcc $\text{Bi}_{12}\text{GeO}_{20}$			
Films		ASTM 17-812		Films		ASTM 23-71	
d(Å)	I	d(Å)	hkl	d(Å)	I	d(Å)	hkl
3.204	100	3.21	100	3.591	19	3.57	30
2.776	19	2.78	45	3.211	100	3.20	100
1.960	31	1.965	65	2.930	26	2.922	40
1.674	19	1.681	70	2.718	64	2.702	90
1.600	8	1.605	18	2.540	3	2.569	5
1.386	1	1.393	10	2.395	5	2.384	10
1.272	7	1.278	25	2.272	8	2.265	10
1.240	4	1.244	20	2.167	13	2.158	20
				2.074	8	2.066	20
				1.992	12	1.986	40
				1.855	5	1.852	30
				1.742	22	1.738	80
				1.693	13	1.690	50
				1.647	15	1.644	70
						1.564	10
						1.529	10
				1.531	3	1.495	70
				1.498	12	1.464	10
						1.434	60
				1.437	4	1.416	10
						1.379	60
						1.355	20
						1.332	50
				1.289	1	1.288	40
						1.267	5
						1.249	40
						1.231	30
				1.215	3	1.212	100
						653	

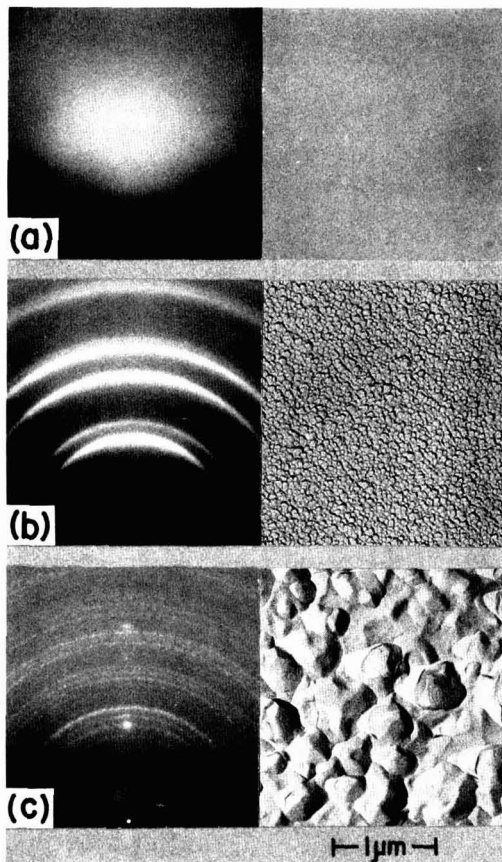


Fig. 2. Typical reflection electron diffraction patterns and electron micrographs of  $\text{Bi}_{12}\text{GeO}_{20}$  films sputtered onto glass substrates: (a) film sputtered at about  $100^\circ\text{C}$  with growth rate of  $0.25 \mu\text{m/hr}$ , amorphous state; (b) film sputtered at  $200^\circ\text{C}$ ,  $0.20 \mu\text{m/hr}$ , fcc form; (c) film sputtered at  $400^\circ\text{C}$ ,  $0.15 \mu\text{m/hr}$ , bcc form.

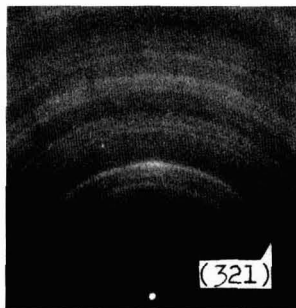


Fig. 3. Reflection electron diffraction pattern of bcc  $\text{Bi}_{12}\text{GeO}_{20}$  film about  $0.15 \mu\text{m}$  thick sputtered onto thin (111)-oriented Al layer on glass substrate with growth rate of  $0.04 \mu\text{m/hr}$  and substrate temperature of  $400^\circ\text{C}$ .

Optical absorption spectra in the visible and infrared region were measured for the three types of film. The results are shown in Fig. 4 and 5. In the visible region, although absorption edges of the films are not sharp, the absorption edges can be approximately estimated at  $510$ ,  $620$ , and  $460 \text{ m}\mu$  for the amorphous, fcc, and bcc phases, respectively. The absorption edge at  $450 \text{ m}\mu$  was reported for single crystal BGO (bcc phase)

Table III. Crystalline structures of  $\text{Bi}_{12}\text{GeO}_{20}$  films sputtered on glass or Si substrates under various conditions

Sample No.	Substrate material	Substrate temperature ( $^{\circ}\text{C}$ )	Growth rate ( $\mu\text{m}/\text{hr}$ )	Film thickness ( $\mu\text{m}$ )	Crystalline structure
M5G-M	Glass	100	1.0	3.0	amorphous
M7G-M	Glass	100	0.25	1.8	amorphous
M2S	Si	100	0.64	2.1	amorphous
M7G	Glass	200	0.20	1.5	fcc
M5G	Glass	275	0.60	1.8	fcc
M5S	Si	300	0.60	1.8	fcc
M25G-B	Glass	350	1.2	1.2	fcc
M26G-B	Glass	350	0.17	0.6	fcc
M23G-B	Glass	375	1.2	1.2	fcc + bcc
M26G-A	Glass	375	0.17	0.6	fcc + bcc
M24G-A	Glass	400	0.44	1.2	bcc
M14G	Glass	400	0.15	0.6	bcc
M15S	Si	400	0.30	1.2	bcc
M20A	Al*	400	0.04	0.15	bcc**
M24S	Si	500	0.44	1.2	bcc

\* Thin (111)-oriented Al layer vacuum deposited on a glass substrate.

\*\* A slight tendency of the (321) orientation was observed.

(1), which well agreed with our results for films of the bcc phase. In the infrared region, a broad absorption at a wavelength of about  $20\ \mu\text{m}$  was observed for all the three types of film. In the films of the bcc phase, several remarkable peaks were superposed on the absorption band. These peaks may correspond to vibration modes peculiar to the bcc structure of BGO.

The refractive index  $n$  was determined from the number of optical interference fringes in the visible transmission spectrum by using the well-known relation  $n = m\lambda_1\lambda_2/2t(\lambda_1 - \lambda_2)$ , where  $m$  denotes the number of fringes between optical wavelength  $\lambda_1$  and  $\lambda_2$ , and  $t$  is the film thickness. Taking  $m = 5$  for  $\lambda_1 = 720\ \text{m}\mu$ ,  $\lambda_2 = 583\ \text{m}\mu$ , and  $t = 3.0\ \mu\text{m}$  for the sputtered amorphous BGO films, we have  $n = 2.6$ , which is nearly equal to the single crystal value of 2.55 (1). The values for the crystalline BGO films, however, cannot be determined due to their high optical absorption in the visible region.

### Summary

We attempted to grow thin films of  $\text{Bi}_{12}\text{GeO}_{20}$  on glass and silicon substrates by rf sputtering with the growth rates of  $0.04\text{--}1.5\ \mu\text{m}/\text{hr}$ . The structure of the sputtered films varied mainly with the substrate temperature  $T_s$  as follows: for  $T_s \lesssim 150^{\circ}\text{C}$  films were

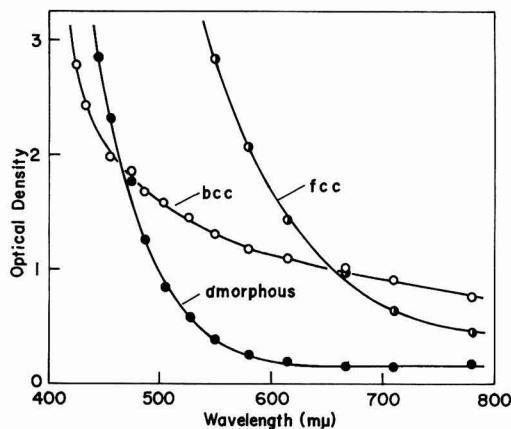


Fig. 4. Optical absorption spectra in the visible region for three types of sputtered  $\text{Bi}_{12}\text{GeO}_{20}$  films.

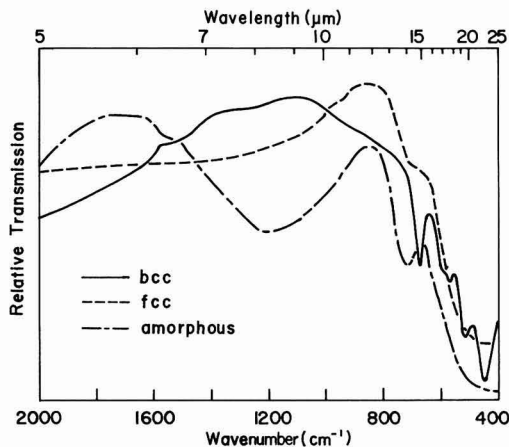


Fig. 5. Infrared transmission spectra for three types of sputtered  $\text{Bi}_{12}\text{GeO}_{20}$  films.

amorphous; for  $150^{\circ}\text{C} \lesssim T_s \lesssim 350^{\circ}\text{C}$  films were polycrystalline with the fcc structure which was the metastable impurity form of  $\text{Bi}_2\text{O}_3$  designated as  $\delta^*\text{-Bi}_2\text{O}_3$ ; for  $T_s \geq 400^{\circ}\text{C}$  films were polycrystalline with the bcc structure which was the normal phase of BGO; for  $350^{\circ}\text{C} \lesssim T_s \lesssim 400^{\circ}\text{C}$  the films were a mixed phase of the fcc and bcc structures. Optical transmission study indicated that the ultraviolet absorption edges were located at  $510, 620,$  and  $460\ \text{m}\mu$  for the amorphous, fcc, and bcc phases, respectively, and a broad absorption, at about  $20\ \mu\text{m}$  for all films. Although highly oriented BGO films of the bcc phase could not be obtained on glass or silicon substrates, (111)-oriented aluminum films deposited on the glass substrates were found to enhance the preferred orientation of the BGO films.

### Acknowledgments

The authors wish to thank Dr. S. Mori and Mr. H. Yamao for their electron microscopic analyses.

Manuscript submitted June 30, 1975; revised manuscript received Sept. 17, 1975.

Any discussion of this paper will appear in a Discussion Section to be published in the December 1976 JOURNAL. All discussions for the December 1976 Discussion Section should be submitted by Aug. 1, 1976.

Publication costs of this article were partially assisted by the Matsushita Electric Industrial Company, Limited.

### REFERENCES

1. A. A. Ballman, *J. Cryst. Growth*, **1**, 37 (1967).
2. E. G. Spencer, P. V. Lenzo, and A. A. Ballman, *Proc. IEEE*, **55**, 2074 (1967).
3. M. Onoe, A. W. Warner, and A. A. Ballman, *IEEE Trans. Sonics Ultrasonics*, **SU-14**, 165 (1967).
4. S. E. Miller, *IEEE J. Quantum Electron.*, **QE-8**, 199 (1972).
5. V. J. Silvestri, T. O. Sedgwick, and J. B. Lander-mann, *J. Cryst. Growth*, **20**, 165 (1973).
6. W. J. Takei, N. P. Formigoni, and M. H. Francombe, *J. Vacuum Sci. Technol.*, **7**, 442 (1969).
7. S. Takada, M. Ohnishi, H. Hayakawa, and N. Miko-shiba, *Appl. Phys. Letters*, **24**, 490 (1974).
8. S. Fukunishi, A. Kawana, N. Uchida, and J. Noda, *Japan. J. Appl. Phys. Suppl.*, **2**, 749 (1974).
9. G. Gattow and H. Schröder, *Z. Anorg. Allgem. Chem.*, **318**, 176 (1962).
10. G. Gattow and H. Fricke, *ibid.*, **324**, 287 (1963).
11. E. M. Levin and R. S. Roth, *J. Res. Nat. Bur. Std.*, **A68**, 197 (1964).



# An Optically Effective Intermediate Layer Between Epitaxial Silicon and Spinel or Sapphire

Ch. Kühn, H. Schlötterer,\* and F. Schwidewsky

Siemens AG, Forschungslaboratorien, München, Germany

## ABSTRACT

The existence of an optically effective intermediate layer between epitaxial silicon and spinel or sapphire has been proved. By measuring the optical and geometric thickness of the films as a function of film thickness a difference in the thickness values was found which could be interpreted as the thickness of an intermediate layer. This layer was also measured directly with a stylus tracer yielding a thickness of about 40 nm. Reflection electron diffraction and secondary ion mass spectroscopy were performed. A growth model for the silicon films is proposed which assumes that aluminum silicates will be formed due to reactions with the substrate as long as the substrate surface is uncovered. Despite or possibly because of this existing intermediate layer good epitaxial silicon films are obtained.

The fact that strong orientation relationships can be found in the case of epitaxial silicon films on insulating substrate crystals has already been discussed in numerous papers (1, 2). A one-to-one coordination of the atoms of the two corresponding net planes of film and substrate, respectively, is in most cases given as an explanation (3, 4), and the substitution of atoms of the substrate surface by silicon atoms resulting in a Si-O bonding is discussed in literature. To overcome the relatively great mismatch or misfit of the lattice constants and distances which is frequently encountered, multiple fits had been used to match these differences (2, 4), a practice often adopted for epitaxy (5). Especially in the case of silicon-on-sapphire, some disagreement between different investigators was found (4) concerning the exact orientation relationships. Considering all these and similar aspects, one gains the impression that the existence of symmetry elements, especially symmetry axes like three- or fourfold rotation axes perpendicular to the surface plane, is more relevant to achieving good epitaxy than an exact atom-to-atom matching. This impression is confirmed by the fact that transition or intermediate layers are often discovered in connection with the epitaxy of vapor-deposited films (6).

Mercier (7) has used infrared spectroscopy to confirm the presence of Si-Al and Si-O bonds in silicon, films, but it was not possible to determine whether these were situated near the interface or in the silicon film itself. In the case of silicon on Mg-Al spinel and sapphire, we had experimental findings that suggest the existence of an intermediate layer which is in any case optically effective. We therefore studied this system in more detail in order to prove this hypothesis.

## Experimental Methods and Results

The epitaxial silicon films on spinel or sapphire studied were produced by chemical vapor deposition in the  $\text{SiH}_4/\text{H}_2$  system in a water-cooled horizontal reactor at substrate temperatures of 1080° and 1000°C and at growth rates of 1.5 and 2.5  $\mu\text{m}/\text{min}$ , respectively. The substrates were single crystals of magnesium-aluminum spinel (Verneuil) with (100) surfaces and single crystals of sapphire (Czochralski) with  $(\bar{1}012)$  surfaces.

**Thickness measurements.**—A simple experimental procedure was adopted, which is shown schematically in Fig. 1. After the epitaxial deposition a mask is applied and the unmasked part of the silicon film has been etched away by an acid etch of 95 ml 65%  $\text{HNO}_3$ , 5 ml 40% HF, and 1g  $\text{NaNO}_2$  (8) resulting in a step.

\* Electrochemical Society Active Member.  
Key words: optical interferences, thickness measurement, absorption, electron diffraction, SIMS.

The step height, i.e., the geometric film thickness  $d_G$ , is measured with a Perthen stylus tracer, Model ECW-L. The measured value may be a little less than the real distance of the silicon surface from the substrate since the acid may not remove all of the film also at the unmasked parts. The optically determined average film thickness,  $d_0$ , is calculated by evaluating the extrema of the interference fringes caused by reflection at the assumed optically effective interfaces air/film and film/substrate (9). The refractive index of the silicon films has been assumed to be that of bulk silicon. This assumption is suggested by earlier results and will be justified by the results discussed later on. The reflectance measurements were carried out in the wavelength range 1-2.5  $\mu\text{m}$  with a Zeiss two-beam spectrophotometer, Model DMR 21, which was adapted by the construction of a reflection attachment.

Comparing the film thicknesses obtained with the different methods one observes that in all cases the optical thickness was less than the geometric thickness. We therefore assumed the existence of an intermediate layer giving rise to the difference in height between the substrate surface and the optically effective film boundary. To prove this hypothesis, we thinned several films with an initial thickness of about 1-2  $\mu\text{m}$  in steps of about 0.2  $\mu\text{m}$  by means of an alkaline etch of 30% KOH, 15 ml isopropanol at 84°C (8). After each step thickness measurements were performed with both methods.

In order to avoid falsifications caused by surface roughness, the surface of the film was carefully polished and cleaned after each thinning step.

Figure 2 shows the difference between both types of thickness values as a function of the optical thickness. Though there is a large spread of the values due to experimental error, a systematic positive difference is evident, which we interpret as the thickness of an intermediate layer between film and substrate; the thickness of this layer varies between 40 and 70 nm for different silicon-on-spinel samples. With silicon-on-sapphire, values were found (20-40 nm), which

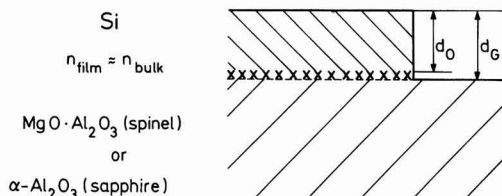


Fig. 1. Optical and geometrical thickness of an epitaxial silicon film on spinel or sapphire (xxx intermediate layer).

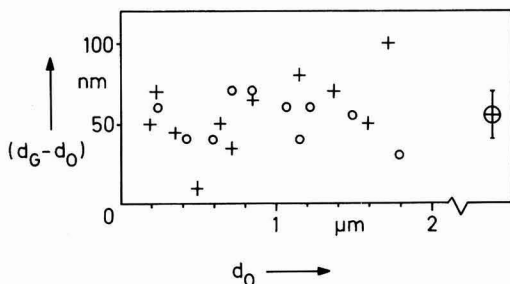


Fig. 2. Thickness of the intermediate layer on spinel vs. optical silicon thickness (+ sample 1, O sample 2, ⊕ mean value).

were systematically lower than those of spinel but which also showed some scatter.

Since the difference between geometric and optical thickness turns out to be independent of the film thickness, the refractive index of the film which had been assumed to be that of bulk silicon can be regarded as constant in all parts of the film. In principle, at a given film thickness, one could equalize the results of both measurements by assuming a refractive index  $n'$  smaller than that of bulk silicon. But in an earlier paper (10) it had already been shown that this should only be possible if a relatively high oxygen content is present, which is not the case with our films being produced in a reducing hydrogen atmosphere. On the other hand, if the geometric thickness is used for evaluation,  $n'$  should decrease strongly with decreasing thickness, but no signs of such a decrease have been found.

But the existence of the intermediate layer could also be proved directly: after the last etching step a scarcely visible layer remained showing a remarkably reduced etch rate compared to the silicon etch rate. In one case it was possible to measure this residual layer employing the step method, as described above. The result was a geometric thickness of about 40 nm. The spectral reflectance of this layer showed no difference compared to the substrate. Therefore, we assume that the optical constants of the intermediate layer scarcely differ from those of the substrate (sapphire:  $n = 1.76$ ,  $k = 0$ ; spinel:  $n = 1.71$ ,  $k = 0$  at  $\lambda = 1 \mu\text{m}$ ).

**Absorption measurements.**—We also calculated the average absorption constant  $\alpha$  at the different steps of film thickness according to a method described in a previous paper (11). The results are shown in Fig. 3. We observed a distinct increase in the absorption constant as we approached the substrate/silicon interface ( $d_0 = 0$ ). Other measurements, e.g., lifetime and mobility measurements in the silicon films, also indicate a poor crystal quality near the interface (12).

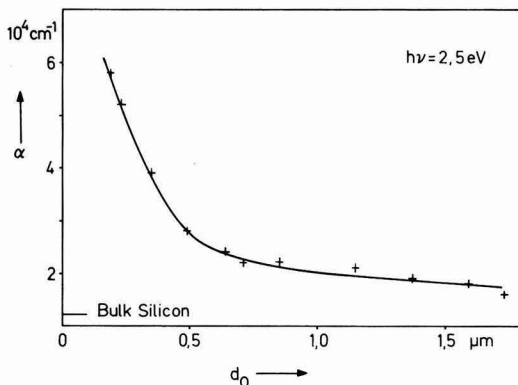


Fig. 3. Absorption constant vs. optical film thickness for a successively thinned epitaxial silicon film on spinel.

These results lead us to assume that a disordered region exists near the bottom of the silicon film, which can be correlated with the intermediate layer.

**Analysis of the intermediate layer.**—**Secondary ion mass spectroscopy.**—In order to analyze the composition of the intermediate layer, secondary ion mass spectroscopy (SIMS) was performed (13) using Balzers equipment. The primary beam consisted of  $\text{Ar}^+$  ions with an energy of 450 eV and a current density of  $10^{-8} \text{ A cm}^{-2}$ . The target area was  $0.1 \text{ cm}^2$ . The surface of three samples was investigated, i.e., a thin silicon film of about 100 nm, an intermediate layer with a thickness of about 40 nm, and a spinel surface as it appears after the acid etch. The most important results are shown in Fig. 4. With decreasing film thickness the magnesium and aluminum signals increase, whereas those of silicon and silicon compounds decrease. It is also seen that the spinel surface is giving signals of silicon and silicon oxides after the removal of the silicon film by the acid etch. This shows that on top of the substrate a thin film has remained containing those materials besides the components of the substrate. So even  $d_G$  does not correspond to the real distance between the silicon film surface and the true substrate crystal. That can be understood by the

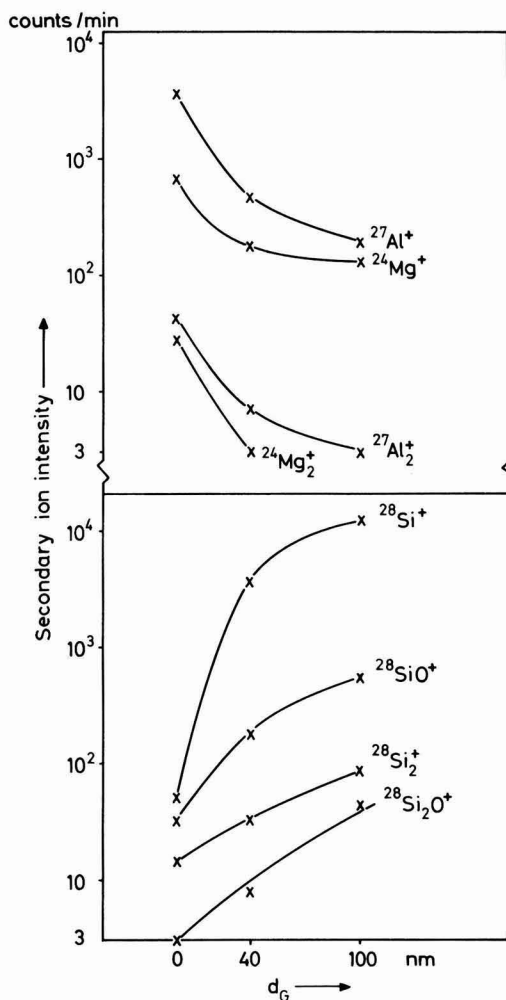


Fig. 4. SIMS analysis of the intermediate layer: intensity of characteristic signals vs. geometric thickness. Upper (lower) part: complex ions originating from the spinel substrate (silicon film).

experimental fact that highly doped silicon has a very small etch rate, even with the acid etch.

At a first glance the SIMS result obtained with the silicon compounds is not in agreement with the decrease of the oxygen content expected with increasing distance from the oxide-substrate interface. But here we have to remember that we do not have a true profile measurement, but only the surface investigation of three samples. We therefore assume that the oxygen has not been incorporated during the epitaxial growth, but that the silicon near the surface has been oxidized during and after the etching process. Consequently the concentration of the silicon oxides decreases in the same way as the concentration of silicon itself. Similar results are obtained with silicon films on sapphire.

**Electron diffraction.**—In order to see a possible structural difference between the substrate and the intermediate layer, reflection electron diffraction was performed with a Siemens Elmiskop (electron energy 80 keV). Figure 5 (a) shows the diffraction pattern of the intermediate layer, whereas for the purpose of comparison, Figure 5 (b) shows the pattern of a spinel substrate, and Figure 5 (c) the pattern of an epitaxial

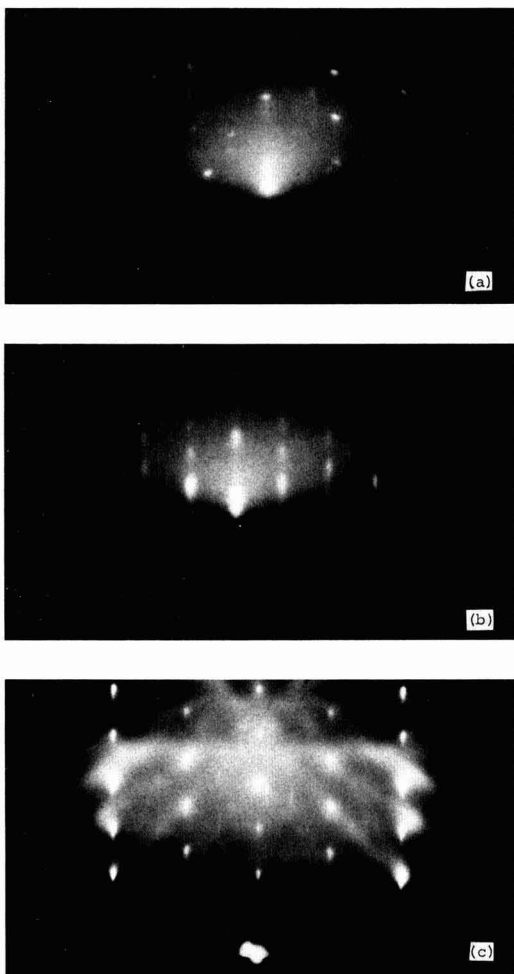


Fig. 5. (a) Electron diffraction pattern of the intermediate layer, (b) electron diffraction pattern of the spinel substrate, (c) electron diffraction pattern of the epitaxial silicon film on spinel. All obtained with (100) surfaces, the incident beam being parallel to [011].

silicon film. In the latter case, besides the Bragg reflection spots, we also see rather distinct Kikuchi lines, indicating the good quality of the film.

Only part of the reflection spots in Fig. 5 (a) can be identified either as spinel [Fig. 5 (b)] or silicon [Fig. 5 (c)], whereas the other spots are probably due to some crystalline Al-Mg silicates. Unfortunately these spots could not easily be related to the generally known silicates. Nevertheless, the electron diffraction results, together with the SIMS data, suggest that the intermediate layer contains crystalline compounds differing both from the spinel substrate and the silicon film. More exhaustive experiments will have to be conducted to investigate the properties of the intermediate layer.

### Discussion

The present investigations have shown that there is a gradual transition from the  $\text{Al}_2\text{O}_3$  and  $\text{MgO}$  of the substrates to the pure silicon of the final film, the thickness of the transition layer in the case of sapphire being somewhat smaller than with spinel. The formation of the transition layer obviously is in connection with the well-known chemical reactions during the nucleation phase in the epitaxial growth (14).

For explanation we therefore make use of the following growth model: during the first phase of growth volatile reaction products like  $\text{SiO}$  and  $\text{Al}_2\text{O}$  are produced and partly included into the growing film (15). The amount of these reaction products will be proportional to the uncovered surface of the substrate since the reaction cannot take place below the silicon nuclei and islands. Therefore this amount decreases with increasing silicon coverage of the surface and, consequently, the concentration of the included compounds will also decrease. At the moment at which the surface is completely covered with silicon, the situation drastically changes as no more oxygen will be included in the silicon film. The consequence is a change of the composition due to the lack of oxygen. As long as oxygen is present, we will have some kind of aluminum silicates, which all indeed have optical constants (16) similar to those of the substrates ( $\text{Al}_2\text{O}_3$ ,  $\text{MgO}$ - $\text{Al}_2\text{O}_3$ ). Therefore the optically effective interface will be located at a thickness containing so much silicon and so little magnesium, aluminum, and oxygen that it is rather the optical behavior of probably highly doped silicon than that of oxide compounds.

The different etch behavior of the alkaline and acid etch is in agreement with the differences in the ratio of etch rates for silicon and silicon oxide films (8). The alkaline etch rate is much more reduced by oxygen than that of the acid etch.

Using the expression "intermediate layer" rather than "transition layer" is, therefore, really appropriate because from the optical point of view it is a layer of definite thickness between substrate and silicon film (15). The experimental observation that this thickness is somewhat less with sapphire than with spinel can be explained by the different nucleation behavior of the two materials. The average thickness which is necessary to cover the substrate completely is smaller in the case of sapphire (15, 17), so that the thickness of the intermediate layer is also smaller. It seems that the intermediate layer matches the differences between substrate and silicon lattice. On the other hand, Distler *et al.* (18) found that the orienting influence of a single crystal substrate can be transmitted even through an amorphous intermediate layer. They studied, among other things, the oriented growth of PbS on top of amorphous carbon on NaCl. The authors give as an explanation of their observation the existence of long-range active centers on the substrate surface which induce epitaxial growth at a remarkable distance. However, Chopra (19) supports the hypothesis that epitaxial growth is an interfacial phenomenon and that the orienting influence of a substrate is confined to its surface plane only and the atoms located in it. Despite Chopra's argument we get good epitaxial silicon films on spinel or sapphire, as can be seen in Fig. 5 (c)

(Kikuchi lines) although an intermediate crystalline layer does exist. We could even assume that the intermediate layer is responsible for the achieved good epitaxial relation since the rather great mismatch between the lattice parameters of film and substrate will be reduced by such a layer.

#### Acknowledgments

The authors wish to express their thanks to Dr. R. Falckenberg for providing the spinel substrates and to Dr. M. Druminski and Mrs. S. Rheinboldt for providing the epitaxial silicon films. We also wish to thank Dr. R. Buhl, Balzers AG, for SIMS measurements and helpful discussions.

This work has been supported by the technological program of the Federal Department of Research and Technology of the FRG. The authors alone are responsible for the contents.

Manuscript submitted June 9, 1975; revised manuscript received Sept. 22, 1975. This was Paper 27 RNP presented at the San Francisco, California, Meeting of the Society, May 12-17, 1974.

Any discussion of this paper will appear in a Discussion Section to be published in the December 1976 JOURNAL. All discussions for the December 1976 Discussion Section should be submitted by Aug. 1, 1976.

Publication costs of this article were partially assisted by Siemens AG.

#### REFERENCES

1. H. M. Manasevit and W. I. Simpson, *J. Appl. Phys.*, **35**, 1349 (1964).
2. J. D. Filby and S. Nielsen, *Brit. J. Appl. Phys.*, **18**, 1357 (1967).

3. R. Nolder and I. Cadoff, *Trans. Met. Soc. AIME*, **233**, 549 (1965).
4. H. Seiter and C. Zaminer, *Z. Angew. Phys.*, **20**, 158 (1965).
5. D. Pashley, *Phil. Mag. Suppl.*, **5**, 174 (1956).
6. H. Mayer, in "Advances in Epitaxy and Endotaxy," H. G. Schneider and V. Ruth, Editors, p. 63, VEB Deutscher Verlag für Grundstoffindustrie, Leipzig (1971).
7. J. Mercier, *This Journal*, **117**, 666 (1970).
8. Ch. Raetzel, S. Schild, and H. Schlötterer, Paper 142 presented at the Electrochemical Society Meeting, New York, New York, Oct. 13-17, 1974.
9. J. F. Hall and W. F. C. Ferguson, *J. Opt. Soc. Am.*, **45**, 714 (1955).
10. R. Hezel and F. Schwidetsky, *Siemens Forsch.-Entw.-Ber.*, **1**, 297 (1972).
11. Ch. Kühn, H. Schlötterer, and F. Schwidetsky, *This Journal*, **121**, 1496 (1974).
12. M. Druminski, Ch. Kühn, E. Preuss, F. Schwidetsky, J. Tihanyi, and K. Schmid, Paper 139 presented at the Electrochemical Society Meeting, New York, New York, Oct. 13-17, 1974.
13. A. Benninghoven, in "Ergebnisse der Hochvakuumtechnik und der Physik Dünner Schichten," M. Auwärter, Editor, p. 81, Wissenschaftl. Verlagsges. mbH, Stuttgart (1971).
14. H. M. Manasevit, A. Miller, F. L. Morritz, and R. Nolder, *Trans. Met. Soc. AIME*, **233**, 540 (1965).
15. H. Schlötterer, *J. Vacuum Sci. Technol.*, To be published.
16. Powder Diffraction File of the JCPDS.
17. G. W. Cullen and J. F. Corboy, *This Journal*, **121**, 1345 (1974).
18. G. I. Distler, S. A. Kobzareva, and Y. M. Gerasimov, *J. Cryst. Growth*, **2**, 45 (1968).
19. K. L. Chopra, *J. Appl. Phys.*, **40**, 906 (1969).

## A New Fast Technique for Large-Scale Measurements of Generation Lifetime in Semiconductors

Wolfgang R. Fahrner<sup>1</sup> and Christian P. Schneider

IBM System Products Division, East Fishkill Facility, Hopewell Junction, New York 12533

#### ABSTRACT

This paper describes a technique that permits measurements of generation lifetime in the range of  $\geq 1$  msec to  $\ll 0.1$  nsec. For the measurements, a metal oxide semiconductor (MOS) capacitor is biased into strong inversion and subsequently switched into deep depletion. An appropriate experimental setup prints out or displays a typical recovery time, which is introduced into a computer fed by the theoretical generation model and the wafer data. The technique is suitable for process characterization.

The determination of lifetime in silicon (Si) is of great technological importance. Since the basic paper by Zerbst (1), important contributions to the literature have been made by others (2-4). Large-scale measurements of minority carrier lifetime have become desirable for many applications. The usual technique, described by Zerbst, is too cumbersome for large-scale measurements. Faster techniques (5) very often do not give the same results as a Zerbst plot. This paper describes a technique capable of rapid measurements of generation lifetime with good precision. Three, slightly modified, measurement setups using this technique allow coverage in silicon of the wide spectrum of lifetimes which are of practical interest. The measurements are carried out on metal

oxide semiconductor (MOS) capacitors. [We used thermally grown oxides 1000 to 5000Å thick. The  $\langle 100 \rangle$  oriented substrates (mostly p-type) had resistivities of 1-20 ohm-cm. The p-type samples were selected so that no lateral currents occurred due to channel injection. Aluminum dots were evaporated onto the oxide to form MOS capacitors.] A voltage,  $V_a$ , is applied to a metal dot, and a steady-state inversion regime is established. Then a voltage step or pulse,  $\Delta V_a$ , is added. This creates a depletion layer underneath the dot, thus reducing the value of the total measured capacitance and increasing the (absolute) value of the voltage drop across the interface. The time difference,  $t$ , between switching ( $t = 0$ ) and reaching a preselected percentage of the equilibrium value is printed or displayed on a counter. This value is fitted to the thermal generation model by computer.

<sup>1</sup> Present address: Institute for Applied Solid-State Physics, D-78 Freiburg i. Br., Eckerstrasse 4, West Germany.

Key words: lifetime, MOS process control, silicon characterization.

**Theoretical**

This technique is not bound to a specific model of relaxation. For the sake of simplicity, we use the well-known equations given by Zerbst (1) and re-write them in a convenient form. The applied voltage is the sum of the voltage drop,  $V_{ox}$ , across the oxide and the surface potential,  $\phi_s$

$$V_a + \Delta V_a = V_{ox} + \phi_s \quad [1]$$

Differentiation with respect to time and the use of equations

$$\phi_s = q \cdot N_A \cdot \epsilon_{si} / (2C_{D^2}) \quad [2]$$

$$V_{ox} = (Q_D + Q_I) / C_{ox} \quad [3]$$

and

$$dQ_D/dt = C_D \cdot d\phi_s/dt \quad [4]$$

yields

$$(q \cdot \epsilon_{si} \cdot N_A / 2) d(1/C_{D^2})/dt + (C_D \cdot q \cdot N_A \epsilon_{si} / 2 \cdot C_{ox}) \cdot d(1/C_{D^2})/dt + (1/C_{ox}) dQ_I/dt = 0 \quad [5]$$

The integration of Eq. [5] requires knowledge of the generation current,  $I_{Gen} = dQ_I/dt$ . Most commonly, the thermal generation model

$$dQ_I/dt = qn_i(x_D - x_{Df})/2\tau = I_{th} \quad [6]$$

is adopted. This model is not always valid. Discrepancies are found, especially for long-lifetime silicon at the end of the  $C$ - $t$  return curve, where a faster generation mechanism might exceed the decreasing thermal generation. The origins for these deviations may be channel injection, enhanced generation due to inhomogeneities, or defects in both the oxide and the silicon.

In the case of channel injection or injection due to inhomogeneities, a simple model for  $dQ_I/dt$  can be assumed, namely

$$dQ_I/dt = I_{Gen} = I_{th} + \alpha I_1$$

where

$$I_1 = \begin{cases} I_0 = \text{const for } C < C_f \\ 0 \text{ otherwise} \end{cases}$$

measures the contribution of the injection to the total current.

Note that Eq. [6] does not contain any surface contribution  $I_s = n_i \cdot q \cdot s_0$  for the following reason: In a comparison of  $I_s$  and  $I_{th}$ ,  $s_0$  values in the order of 10-700 cm/sec were reported (6). These data are obtained from techniques based on switching the MOS structure from accumulation to deep depletion. By switching from inversion to deep depletion, as done in this technique, one obtains  $s_0$  values in the order of  $10^{-2}$  cm/sec. The reason for the reduction is the screening of the surface by an inversion layer. The lifetimes are found to be in the range of 1 nsec-1 msec. The space-charge width,  $x_D$ , depends on the doping concentration,  $N_A$ , and the applied voltage. Assuming typical values  $x_D = 10^{-4}$  cm  $\gg x_{Df}$ ,  $s_0 = 10$  cm/sec, and  $\tau = 50$   $\mu$ sec, one obtains  $I_s/I_{th} = 10$ , whereas, with the "inversion screened"  $s_0$  value of  $10^{-2}$  cm/sec,  $I_s$  is small compared with  $I_{th}$ , even for very long lifetimes and small space-charge widths.

In this paper, we adopt the thermal generation model. The reason is shown below, where Eq. [5] is solved for different models for the generation current  $dQ_I/dt$ . Combining Eq. [5] and [6], we obtain

$$\frac{C_{ox} + C_D}{C_{Df} - C_D} \cdot \frac{1}{C_{D^2}} dC_D = \frac{n_i}{2\tau N_A} \frac{1}{C_{Df}} dt \quad [7]$$

This equation can easily be solved by normalization (replacing  $C_D$  by  $C_D/C_{Df} = C_{DR}, C_{ox}$  by  $C_{ox}/C_{Df} = C_{DR}(1 - C_{DR})$  and by changing twice the variable  $C_{DR} = 1/x_R = 1/\sqrt{\phi_R}$ , where  $x_R = x_D/x_{Df}$  and  $\phi_R = \phi_s/\phi_{sf}$ . The final result is

$$\sqrt{\phi_R} + (C_{Df}/C_{ox} + 1) \ln(\sqrt{\phi_R} - 1) = -t_R \quad [8]$$

where

$$t'_R = \frac{n_i}{2N_A\tau} \cdot \frac{C_{Df}}{C_{ox}} (t - t_0)$$

This is the basic equation for the measurement of the short lifetimes (low-frequency measurement).

When the MOS capacitance is measured with a high-frequency signal, the total capacitance is  $C = C_{ox}C_D/(C_{ox} + C_D)$ . In this case, Eq. [7] can be rewritten

$$\frac{1}{C_R^2(1 - C_R)} \frac{dC_R}{dt} = \frac{C_f}{C_{ox}} \frac{n_i}{2\tau N_A} \quad [9]$$

and its solution is

$$\left[ \ln \frac{C_R}{1 - C_R} \right] - \frac{1}{C_R} = t''_R \quad [10]$$

where  $C_R$  is the normalized capacitance,  $C_R = C/C_f$ . Equation [10] is essentially the same as Heiman's result (5). Heiman, however, did not use this result, but its differential form (Eq. [9]). Furthermore, he switched from accumulation to inversion. For silicon with lifetimes  $\tau \geq 10$   $\mu$ sec, a Heiman plot gives satisfactory results only during a very short range of the measuring time, as shown below. Equation [10] is used here to measure longer lifetimes (high-frequency measurement). Both Eq. [8] and [10] are plotted in Fig. 1 and 2. In Fig. 1, we reverse the  $\phi_R$  axis because we do the same in the measurement (cf. Eq. [12a], below). Equation [5] has been integrated for

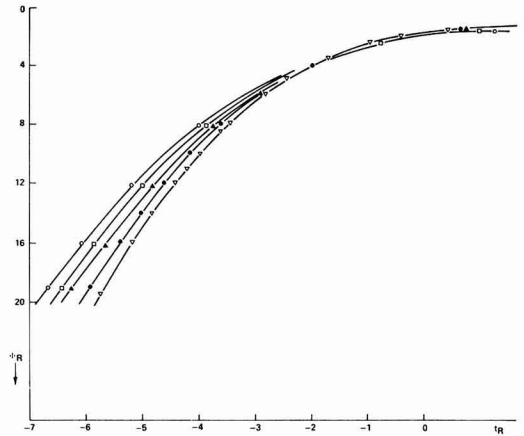


Fig. 1. Relaxation of the surface potential  $\phi_R$  for different values of  $C_{Df}/C_{ox}$ .  $\nabla$ ,  $C_{Df}/C_{ox} = 0.1$ ;  $\bullet$ ,  $C_{Df}/C_{ox} = 0.3$ ;  $\blacktriangle$ ,  $C_{Df}/C_{ox} = 0.5$ ;  $\square$ ,  $C_{Df}/C_{ox} = 0.7$ ;  $\circ$ ,  $C_{Df}/C_{ox} = 0.9$ .

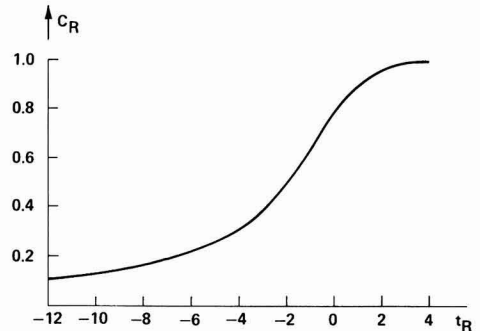


Fig. 2. Relaxation of an MOS capacitance already in inversion to which a voltage step is applied.



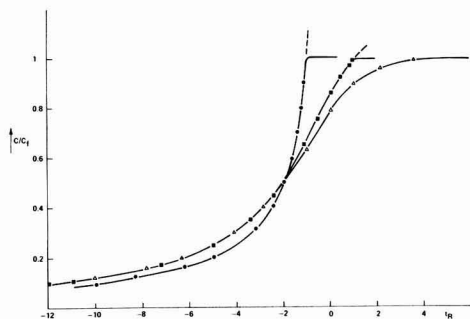


Fig. 3. Relaxation of the capacitance for  $I_{Gen} = I_{th} + \alpha I_0$ .  $\Delta$ ,  $\alpha = 0$ ;  $\blacksquare$ ,  $\alpha = 0.1$ ;  $\bullet$ ,  $\alpha = 1$ .

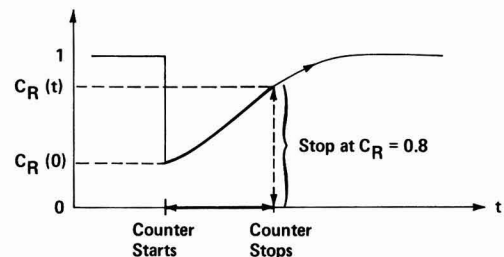


Fig. 4. Representative C-t plot.  $t_0 = 0$ ;  $C_R = C/C_i$

several other modes of relaxation. Of these, we present one example (Fig. 3), where we add a constant current to the thermal current. The parameter,  $\alpha$ , is a measure for the contribution of these additional currents;  $\alpha = 0$  means a pure thermal generation. It can be seen that for  $C_R \leq 0.9$ , if the  $t_R$  axis is expanded or compressed, the curves will be similar. On the other hand, a variation of  $\tau$  has the same effect. Thus, an additional generation current is equivalent to a reduction of the lifetime in the thermal generation model. This observation is valid for any reasonable generation current that decreases toward zero when the capacitance approaches  $C_f$ .

We use Eq. [10] (high-frequency measurement) to demonstrate this technique. When we measure two capacitance values  $C_R(t)$  and  $C_R(t_0)$  at the corre-

Fig. 6a. Block diagram of the long-lifetime case.

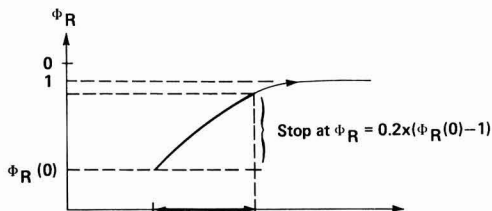
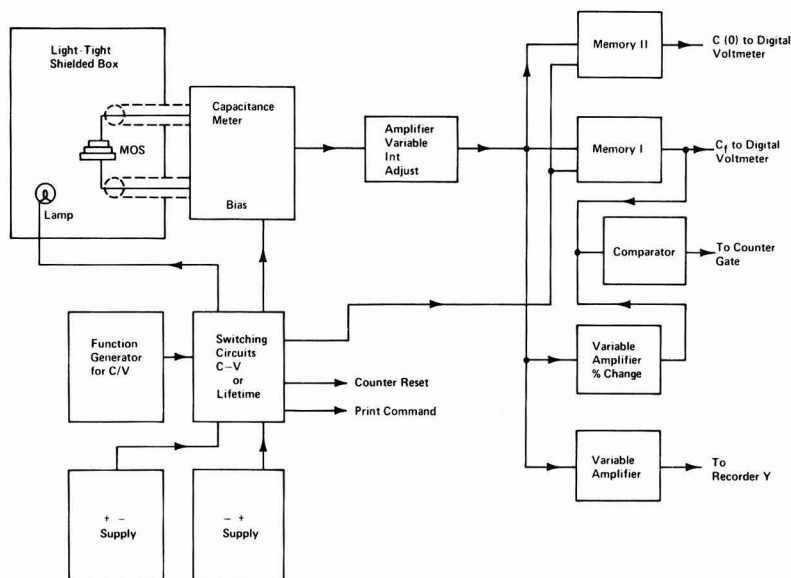


Fig. 5. Representative  $\phi$ -t plot.  $t_0 = 0$

ponding times  $t$  and  $t_0$ , we can calculate  $\tau$ , because the other parameters involved are easily available.  $C_{ox}$  and  $C_f$  can be obtained by standard C-V measurements. From these values,  $N_A$  can be calculated. The room temperature value of  $n_i$  is  $1.4 \times 10^{10} \text{ cm}^{-3}$ . For  $t_0$ , we choose the onset of the step or pulse ( $t_0 = 0$ ). Rather than measure the capacitance after a fixed time  $t$ , we select a fixed capacitance value, e.g.,  $C_R = 0.8$ , and measure the time,  $t$ , between switching and reaching the selected capacitance level. Figure 4 shows a schematic C-t plot and the measured time interval.

An analog technique is used in the low-frequency case. Instead of  $C_R$ , a specific change of  $\phi_R$  (and its time duration) is measured. Only the counting of the time is slightly different; for example, we count now between  $t = 0$  and the time when  $\phi_R = 0.2 \times (\phi_R(0) - 1)$  (Fig. 5). This alteration is caused by the experimental conditions (see below).

Experimental and Results

As shown in Fig. 6a and b, the first, high-frequency, measurement setup essentially consists of a 1 MHz capacitance meter, two power supplies, two memories, a voltage comparator, a plotter, and a printer. Care must be taken that one does not switch the voltage through zero, because the majority carrier response is much faster than any switching time. This setup can be used for relaxation times  $T = 2\tau N_A/n_i \geq 100$  msec. This lower limit is caused by the transient time of the bridge.

A similar setup is used for  $T$  values  $> 1$  msec (Fig. 7). The block diagram of this setup has been published by Princeton Applied Research, Princeton, New Jersey (7). In this case, the output of a lock-in is proportional to  $C_R$ . For  $T \leq 1$  sec, the plotter must be replaced by an oscilloscope. We use a Tektronix sam-

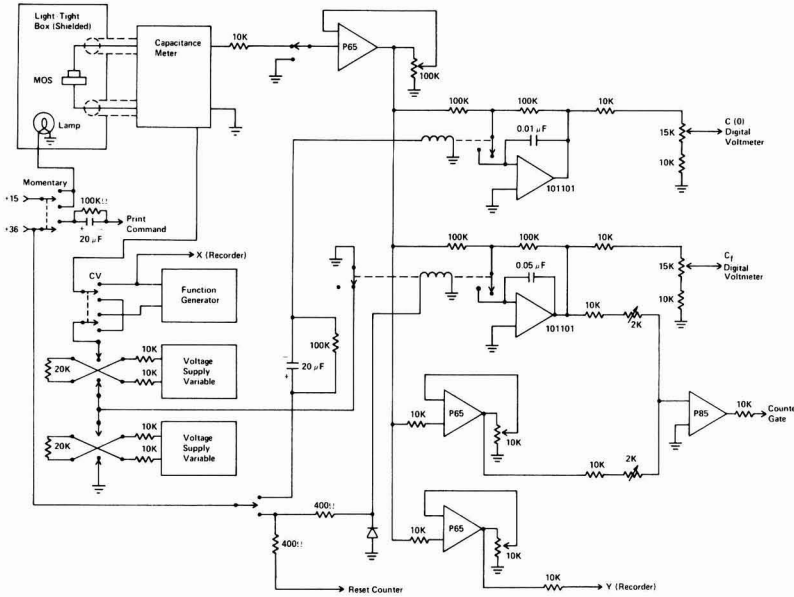


Fig. 6b. Schematic of the long-lifetime case.

pling oscilloscope, which can be connected to a digital counter. We count the time between  $t = 0$  and the instant  $C_R = 0.8 \times (1 - C_R(0))$  (as an example).

The third setup is used for the "short" lifetime case  $T < 4$  sec. As shown in Fig. 8, it consists of a series combination of the MOS capacitor,  $C$ , and a standard capacitor,  $C_{st} \gg C$ . The voltage drop,  $V_{st}$ , across  $C_{st}$  is measured with an operational amplifier. The large parallel resistor,  $R$ , defines the d-c potential for the amplifier. The condition  $R \gg 1/\omega C_{st}$  yields the upper limit for the measurable  $T$  values:  $T \ll R \cdot C_{st} \cdot 2\pi$ . It is favorable to choose a large value of  $R$  rather than of  $C_{st}$ , because an increase in  $C_{st}$  implies a loss in resolution. We can write

$$V_{st} = V_a(1/C_{st}) / (1/C + 1/C_{st})$$

$$V_{st} \approx V_a \cdot C/C_{st} \quad [11]$$

However,  $C$  is a mixture of the high- and low-fre-

quency capacitance and relaxes finally to  $C_{ox}$ . Though it might be possible to calculate  $C(t)$  analytically, we prefer a different, more convenient interpretation. We write the voltage drop,  $V_{MOS}$ , across  $C$  as

$$V_{MOS} = V_{ox} + \phi_s$$

Thus

$$V_a = V_{st} + V_{ox} + \phi_s$$

Because  $C_{st}$  and  $C_{ox}$  are linear capacitors

$$V_{st} \cdot C_{st} = V_{ox} \cdot C_{ox}$$

$$V_a = V_{st}(1 + C_{st}/C_{ox}) + \phi_s$$

and, finally

$$V_{st} = (V_a - \phi_s) / (1 + C_{st}/C_{ox}) \quad [12a]$$

$$\phi_s = V_a - V_{st}(1 + C_{st}/C_{ox}) \quad [12b]$$

By measuring  $V_{st}$ , we know  $\phi_s$  and can use Eq. [8]. Note that, in Eq. [11] and [12],  $V_a$  assumes two different values. For this reason, we do not obtain the same final values before and during the pulse as in Fig. 4, but two values as shown in Fig. 9. The time measurement is again performed with a digital counter connected to a sampling scope. The advantage

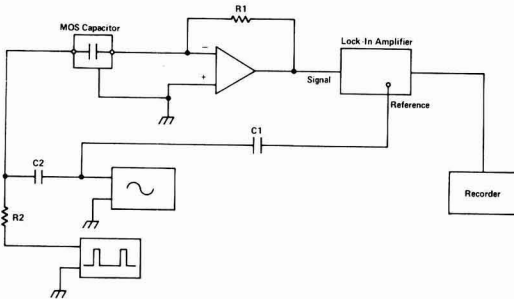


Fig. 7. Block diagram of the medium-lifetime case

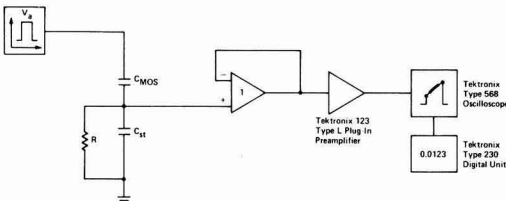


Fig. 8. Block diagram of the short-lifetime case

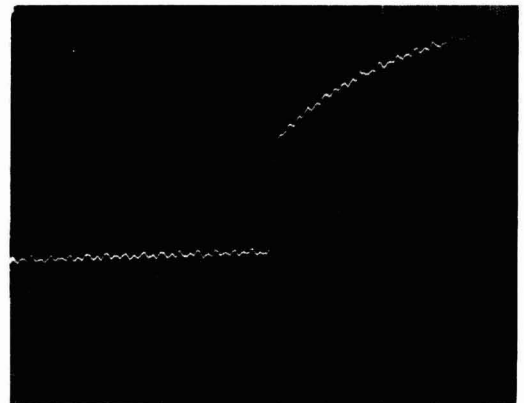


Fig. 9. Photograph of a  $C$ - $t$  trace of a low-frequency measurement. Note that the scale factor  $V_a$  changes when the pulse is switched on (50 msec/horizontal division).

in using the scope and counter is the speed and accuracy of the reading. The error in reading without the counter can be larger than 100%, especially for small  $\Delta V_a$  signals. Figure 10 shows how the time marks of the counter are set. The left time mark is set at the onset of the pulse and indicates the start of the counting (left arrow). The stop time mark can be seen at the end of the pulse (right arrow). The time of an 80% vertical transition between the zones is measured as indicated by the heavy line. Note that we are within the upper limit for the  $RC_{st}$  ( $10^7 \text{ ohm} \times 10^{-7} \text{F}$ ) combination, as shown by the slight tilt of the last horizontal line.

In Fig. 11 and 12, the results of two measurements are fitted to the thermal relaxation curve described by Eq. [10]. Good agreement is obtained in Fig. 11, whereas, for the long-lifetime silicon in Fig. 12, the agreement is merely satisfactory. This is in accord with the general observation that in this range ( $\tau \approx 1 \text{ msec}$ ) the error becomes 100%. A Zerbst plot (Fig. 13) taken from Fig. 11 gives  $\tau = 2.5 \times 10^{-3} \text{ sec}$  and  $s_0 = 3.7 \times 10^{-2} \text{ cm/sec}$ . This technique yields  $\tau = 1.3 \cdot 10^{-3} \text{ sec}$  with  $C_{ox} = 130 \text{ pf}$ ,  $C_f = 75 \text{ pf}$ ,  $C_R(0) = 0.339$ , and  $t = 1060 \text{ sec}$  for a selected level  $C_R(t) = 0.8$ .

These experiments were repeated with different samples. Following are typical results obtained

$\tau$  (Zerbst) = 420  $\mu\text{sec}$  -  $\tau$  (this technique) = 252  $\mu\text{sec}$   
 $\tau$  (Zerbst) = 144  $\mu\text{sec}$  -  $\tau$  (this technique) = 108  $\mu\text{sec}$   
 $\tau$  (Zerbst) = 5.6  $\mu\text{sec}$  -  $\tau$  (this technique) = 4.6  $\mu\text{sec}$   
 $\tau$  (Zerbst) = 1 msec -  $\tau$  (this technique) = 850  $\mu\text{sec}$

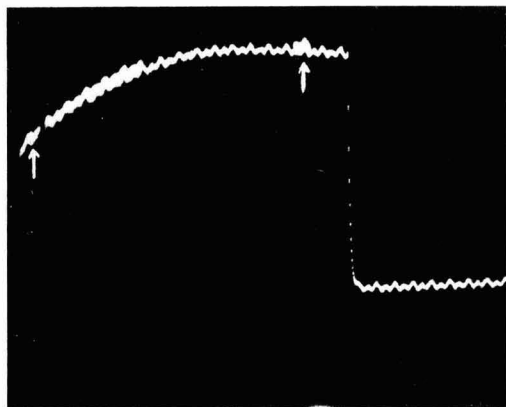


Fig. 10. Photograph of the same sample as in Fig. 9. The time marks and the portion of the curve during which the counter operates are intensified. The sequence of the pulse is reversed compared with Fig. 9.

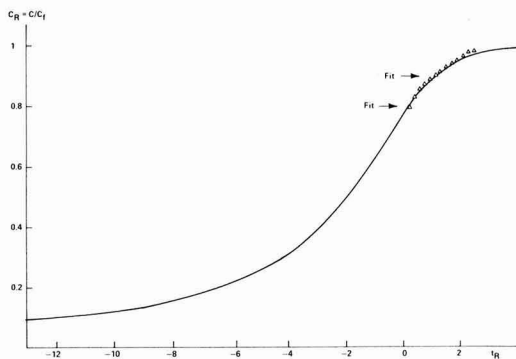


Fig. 11. C-t plot of a sample fitted to the thermal relaxation curve.

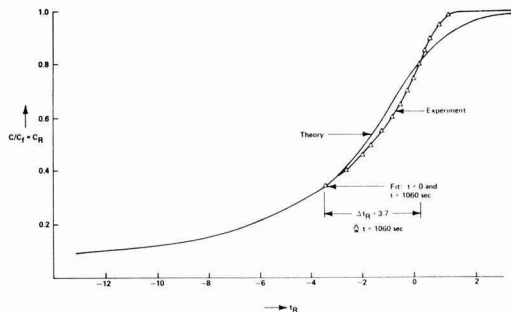


Fig. 12. Same curve as in Fig. 11, taken from another sample

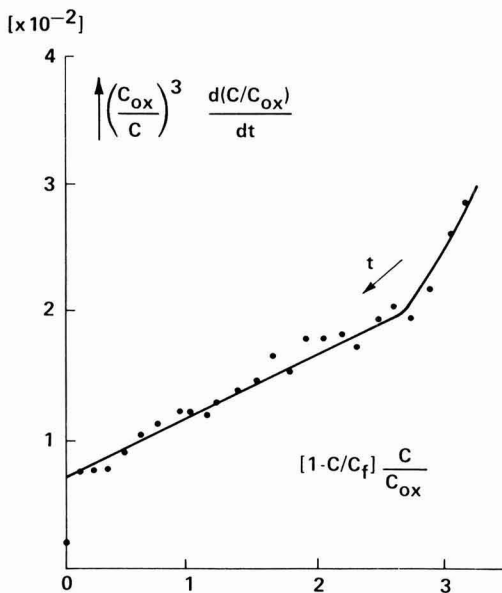


Fig. 13. Zerbst plot for the sample of Fig. 12

Furthermore, we examine how a nonthermal generation mechanism affects the reliability of this technique. This is done by shining controlled intensities of light on the sample or by using mechanically or chemically stressed substrates for the MOS fabrication. The general result is as follows: Whenever a reasonable Zerbst plot is obtained, a lifetime results which agrees with the value of our technique. However, when the Zerbst plot fails, our technique still reports at least an "effective" lifetime, which can be used for process monitoring.

In Fig. 14, we show an example of a Heiman plot. (We define a Heiman plot as the  $\tau$  vs.  $t$  curve, where  $\tau$  has been obtained from a C-t plot with the procedure proposed by Heiman (5); cf. Eq. [9].) The data are taken from the sample used in Fig. 12. It can be seen that the agreement is poor.

It is possible to make the measurements and the data evaluation even more expedient by calculating, rather than measuring,  $C_R(0)$ . For this purpose, we use the following model: A fast-increase  $dV_a$  of the applied voltage displaces a charge  $dQ = C(V_a) \cdot dV_a$  across the capacitor, C. Only the majority carriers can follow, and a space charge  $q \cdot N_A \cdot dx_{DI}$  matches  $dQ$ . Thus, C consists of the series combination  $C_{ox}$  and  $\epsilon_{Si}/x_{DI}$  with the initial condition  $x_{DI} = x_{D0}$  or  $C = C_f$  for  $t = 0$ . (Because of this initial condition, we cannot assume  $\epsilon_{Si}/x_{DI} \gg C_{ox}$  as done by others (8) in solving Eq. [7].) The solution of the differential

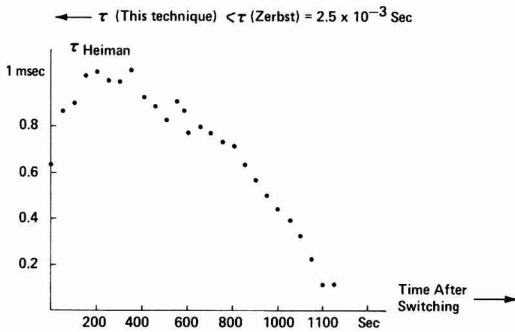


Fig. 14. Heiman plot for the sample of Fig. 12

equation

$$N_A \cdot q \cdot dx_{DI} = (1/C_{ox} + x_{DI}/\epsilon_{Si})^{-1} \cdot dV_a$$

is

$$N_A \cdot q x_{DI}^2 / (2 \cdot \epsilon_{Si}) + N_A q x_{DI} / C_{ox} \\ = \Delta V_a + N_A q x_{D0}^2 / (2 \epsilon_{Si}) + N_A \cdot q \cdot x_{D0} / C_{ox}$$

or

$$x_{DI} = (-\epsilon_{Si}/C_{ox}) \\ + \sqrt{2\Delta V_a \cdot \epsilon_{Si}/(N_A \cdot q) + ((\epsilon_{Si}/C_{ox}) + x_{D0})^2} \quad [13]$$

We obtain a depletion capacitance

$$C_D(0) = \epsilon_{Si}/x_{DI}$$

and

$$C_R(0) = (C_{ox} \cdot C_D(0) / (C_{ox} + C_D(0))) / C_f \quad [14]$$

We check this model by switching an MOS capacitance with  $\Delta V_a$  values = 1, 2, 3 . . . 10V. The bias  $V_a$  is 20 and 40V. The results and the comparison with the theoretical values according to Eq. [14] can be seen in Fig. 15. As expected, there is no measurable difference between the 20 and 40V measurements. The systematic discrepancy between the experimental and theoretical values can be explained by the error in determining the doping concentration. Different measurements give a value between  $8 \cdot 10^{14}$  and  $1.3 \cdot 10^{15}/\text{cm}^3$ . The same model can be used to calculate  $\phi_R(0)$ . It must be emphasized that this model ignores some effects that might reduce the value of  $C_R(0)$ . Among these, the lateral current paths and the finite thickness of the inversion layer, probably, are most important.

### Summary

A new fast technique for large-scale measurements of silicon lifetimes is described. The error limit, compared with a Zerbst plot, is less than 20% for  $\tau \leq 10$

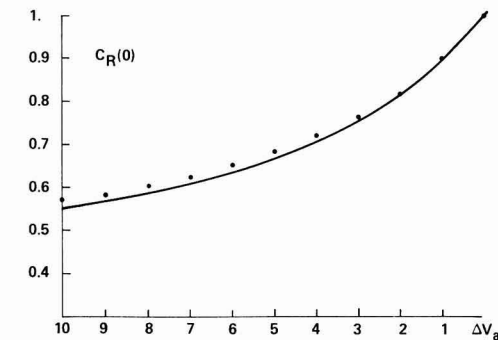


Fig. 15.  $C_R(0)$  vs.  $\Delta V_a$  experiment. Theory: solid line.  $C_{ox} = 123 \text{ pf}$ ;  $A = 1.765 \cdot 10^{-2} \text{ cm}^2$ ;  $N_A = 9 \times 10^{14} \text{ cm}^{-3}$ .

$\mu\text{sec}$  and increases to  $\approx 100\%$  for  $\tau \approx 1 \text{ msec}$ . This error limit can be reduced by choosing a smaller stopping level  $C_R(t)$ . For the long-lifetime case, the measurement time is determined by the setting of the selected level and by the  $\tau$  value of the silicon itself. For the short-lifetime case, it is determined by the time required to find the optimum pulse frequency. The computer time can be disregarded.

### Acknowledgments

The authors are grateful to Dr. G. H. Schwuttke for his continuous encouragement and support of this work. A setup similar to our low-frequency setup has been developed independently by K. Ziegler and E. Klausmann for the measurement of equilibrium surface potentials. We are obliged to them for communicating their results in advance of publication.

This research was supported, in part, by the Advanced Research Projects Agency of the Department of Defense under contract DAHC-15-72-0274. The views and conclusions contained in this document are those of the authors and should not be interpreted as necessarily representing the official policies, either expressed or implied, of the Advanced Research Projects Agency or the U.S. Government.

Manuscript submitted Dec. 16, 1974; revised manuscript received Aug. 27, 1975.

Any discussion of this paper will appear in a Discussion Section to be published in the December 1976 JOURNAL. All discussions for the December 1976 Discussion Section should be submitted by Aug. 1, 1976.

Publication costs of this article were partially assisted by IBM Corporation.

### LIST OF SYMBOLS

$C$	measured capacitance
$C_f$	minimum capacitance of high-frequency C-V curve
$C_D$	depletion capacitance
$C_{ox}$	oxide capacitance
$C_i$	inversion capacitance
$C_{st}$	standard capacitance
$\phi_s$	surface potential
$V_a$	applied voltage
$V_{ox}$	voltage drop across the oxide
$Q_i$	inversion charge
$Q_D$	depletion charge
$N_A$	doping density
$\epsilon_{Si}$	dielectric constant of silicon
$q$	elementary charge
$x_D$	depletion width
$\tau$	lifetime
$t$	time
$s_o$	surface generation velocity
$n_i$	intrinsic carrier density

### Subscripts

a	applied
ox	oxide
f	final, in equilibrium
th	thermal
Gen	generation
s	surface
R	in reduced units
D	depletion

### REFERENCES

1. M. Zerbst, *Z. Angew. Phys.*, **22**, 1, 30 (1966).
2. P. Tomanek, *Solid-State Electron.*, **12**, 301 (1969).
3. S. R. Hofstein, *IEEE Trans. Electron Devices*, **ED-14**, 785 (1967).
4. D. K. Schroder and H. C. Nathanson, *Solid-State Electron.*, **13**, 577 (1970).
5. F. P. Heiman, *IEEE Trans. Electron Devices*, **ED-14**, 11, 781 (1967).
6. Y. Kano and A. Shibata, *Japan. J. Appl. Phys.*, **11**, 8, 1161 (1972).
7. Princeton Applied Research, Tech. Note TN102.
8. J. S. T. Huang, *Proc. IEEE*, **58**, 11, 1489 (1970).

# Deposition and Properties of Silicon on Graphite Substrates

T. L. Chu,\* H. C. Mollenkopf, and Shirley S. C. Chu

Southern Methodist University, Dallas, Texas 75275

## ABSTRACT

Polycrystalline silicon has been deposited on low-cost graphite substrates by the thermal decomposition of silane and thermal reduction of trichlorosilane with hydrogen in a gas flow system. The microstructures and crystallographic properties of deposited silicon were studied over a wide range of deposition conditions by metallographic and x-ray techniques, respectively. The observed differences in the properties of silicon layers deposited by silane and trichlorosilane processes were attributed to the difference in the chemical reversibility of the reactions. The microstructure of silicon deposited by the trichlorosilane process was improved by the addition of hydrogen chloride to the reactant mixture. Solar cells were prepared from silicon layers deposited on graphite substrates by a one-step process using silane or trichlorosilane and appropriate dopants, and AMO efficiencies of up to 1.5% were obtained.

The current interest in the terrestrial utilization of solar energy by photovoltaic converters has stimulated considerable research and development efforts in low-cost solar cells. Silicon solar cells which have been used reliably in spacecrafts for many years are manufactured from semiconductor-grade silicon and are far too expensive for terrestrial applications. The use of polycrystalline silicon layers on suitable substrates is considered as a promising approach for the fabrication of low-cost solar cells (1). In this approach, the selection of the substrate is an important consideration. Steel is the most economical choice for a large area substrate; however, polycrystalline silicon solar cells deposited on steel substrates were found to have low conversion efficiencies because of the incompatibility of the properties of iron and silicon (2). Graphite is more compatible with silicon in properties than steel. Several types of low-cost graphite have a thermal expansion coefficient similar to that of silicon. Graphite is relatively inert toward silicon at temperatures used for the deposition of silicon. Also, graphite has high thermal and electrical conductivities and may be used as an ohmic contact to the solar cell. Thus, graphite appears to be the most promising substrate for low-cost silicon solar cells at present.

In this work, the thermal decomposition of silane and the thermal reduction of trichlorosilane with hydrogen have been used for the deposition of silicon on graphite substrates. The microstructure and crystallographic properties of silicon deposited under a wide range of conditions were studied. Using appropriate dopants during the deposition process, p-n junction solar cell structures were prepared and characterized. The experimental procedures used for the deposition process and the properties of deposited silicon and solar cells are discussed in this paper.

## Deposition of Silicon on Graphite Substrates

The thermal decomposition of silane and the thermal reduction of trichlorosilane have been used extensively for the deposition of silicon. The relative merits of these two processes are fairly well established (3). The decomposition of silane is thermochemically and kinetically more favorable than the reduction of trichlorosilane. Silane is thermochemically unstable at room temperature and higher, and decomposes rapidly at temperatures above 700°C, thus enabling the deposition of silicon at lower temperatures (4). However, the thermal instability of silane tends to promote nucleation by pyrolysis in the gas phase, and the gas-phase nucleation must be suppressed by optimizing the experimental conditions, such as the use of water-cooled reaction tube, low partial pressure of silane in the reactant mixture, etc (3). Furthermore, the reduction of

trichlorosilane with hydrogen is chemically reversible while the decomposition of silane is essentially irreversible. Because of these differences, the properties of silicon are sometimes dependent on the chemical reaction used. The thermal reduction of trichlorosilane was emphasized in this work because of its economic advantages.

The deposition of silicon was carried out by using the apparatus shown schematically in Fig. 1. The flow of various gases was directed by appropriate valves and measured by flowmeters. Hydrogen purified by diffusion through a palladium-silver alloy was used as a carrier gas to introduce trichlorosilane into the reaction tube and as a diluent in all deposition reactions. Trichlorosilane was kept in a double-wall stainless steel cylinder with gas inlet and outlet tubes, and a constant temperature fluid was circulated through the jacket of the container to maintain the temperature of trichlorosilane at  $15.5 \pm 0.5^\circ\text{C}$ . The reactant mixture of the desired composition was introduced into a fused silica reaction tube of 55 mm ID. In the reaction tube, the graphite substrates (PLC graphite supplied by POCO Graphite, Incorporated and CMB graphite supplied by Union Carbide Corporation) were supported on a susceptor, and the susceptor was heated externally by an rf generator. The chemical reaction takes place on the substrate surface, depositing silicon.

The substrate temperature was in the range of  $950$ - $1250^\circ\text{C}$ . In all experiments, the flow rate of hydrogen was maintained at 20 liter/min, and the concentration of the silicon compound in the reactant mixture was adjusted to yield deposition rates in the range of  $0.2$ - $3 \mu\text{m}/\text{min}$ . In the silane process, for example, the average deposition rate of silicon at  $1050^\circ\text{C}$  was about  $0.3$  and  $1.3 \mu\text{m}/\text{min}$  when the reactant mixture contained  $0.03$  and  $0.13\%$  silane respectively. At silane concentrations below about  $0.2\%$ , the deposition rate was essentially a linear function of the concentration of silane in the reactant mixture. The average deposition rate of silicon

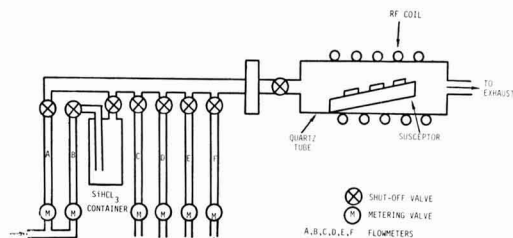


Fig. 1. Schematic diagram of the apparatus for the deposition of silicon.

\* Electrochemical Society Active Member.

Key words: graphite, silane, silicon, solar cells, trichlorosilane.



was essentially independent of temperatures in the range of 1050°-1150°C. At higher temperatures, 1200°C for example, the contribution of gas-phase nucleation becomes noticeable. The deposition of silicon by the trichlorosilane process can be carried out at higher temperatures, 1250°C for example, and at higher rates, 3  $\mu\text{m}/\text{min}$  for example, with negligible contribution of gas-phase nucleation. The average deposition rate of silicon at 1250°C can be increased from about 0.25 to 2  $\mu\text{m}/\text{min}$  by increasing the concentration of trichlorosilane in the reactant mixture from 0.1 to 1%.

### Microstructure of Silicon

Silicon deposited on graphite substrates by silane and trichlorosilane processes was all polycrystalline, and its microstructure was found to depend strongly on the substrate temperature and deposition rate. In general, silicon deposited at low temperatures and high rates consisted of micrometer-size crystallites, and the size of crystallites increased with increasing deposition temperature or decreasing deposition rate.

Silicon layers deposited on graphite substrates at 1000°C or above by the silane process usually consisted of crystallites with well-developed faces, particularly when low deposition rates were used. An example is shown in Fig. 2 where the scanning electron micrograph of the as-deposited surface of a silicon layer deposited on a graphite substrate at 1100°C at a rate of 1  $\mu\text{m}/\text{min}$  is reproduced. The grown surface of most crystallites is hexagonal and has been shown to be of a  $\{110\}$  orientation by x-ray diffraction. The six side faces of the crystallites are therefore of  $(111)$ ,  $(\bar{1}\bar{1}\bar{1})$ ,  $(1\bar{1}\bar{1})$ ,  $(\bar{1}\bar{1}1)$ ,  $(11\bar{1})$ , and  $(\bar{1}\bar{1}1)$  orientations. The edges of the hexagons are along  $[110]$ ,  $[\bar{1}\bar{1}2]$ , and  $[11\bar{2}]$  directions, and the angle between  $[110]$  and  $[\bar{1}\bar{1}2]$  is 54.74°, and that between  $[\bar{1}\bar{1}2]$  and  $[11\bar{2}]$  is 70.53°. These relations have also been verified. The vertical cross section of silicon/graphite specimens was studied by conventional metallographic techniques. Figure 3 shows the mechanically polished and chemically etched  $[\text{Sirtl etch (5), 30 sec}]$  surface of the vertical cross section of a silicon/graphite specimen deposited at 1100°C. The etching process has revealed the grain boundaries, and it is seen that the structural perfection of the silicon layer improved with increasing thickness.

The microstructure of silicon deposited by the thermal reduction of trichlorosilane with hydrogen was studied in more detail. At 950°C and below, the silicon deposit was found to consist of very small crystallites, less than 1  $\mu\text{m}$  in diameter. As the substrate temperature was increased, the size of silicon

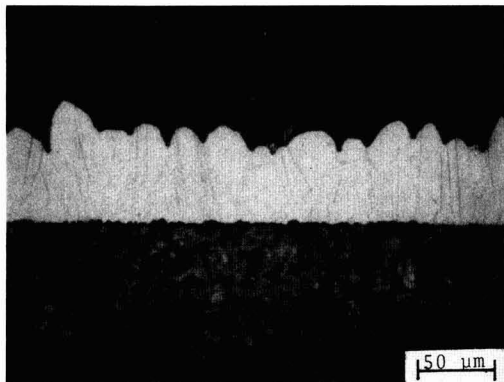


Fig. 3. Mechanically polished and chemically etched surface of the vertical cross section of a silicon/graphite specimen prepared by the pyrolysis of silane at 1100°C.

crystallites increased, and the deposition rate was found to have a very pronounced effect on the microstructure of silicon, particularly at high substrate temperatures. Figure 4 (A and B, respectively) shows the scanning electron micrograph of the as-deposited surface and the mechanically polished and chemically etched surface of the vertical cross section of a silicon sample deposited on graphite at 1000°C at about 1  $\mu\text{m}/\text{min}$ . The average size of the crystallites is 3-5  $\mu\text{m}$ , smaller than those obtained by the thermal decomposition of silane. Furthermore, the crystallites in silicon layers from the trichlorosilane process were less uniform in size; considerably larger crystallites were sometimes intermingled with the smaller ones. The presence of crystallites of widely differing sizes could be due to (i) the inhomogeneities on the substrate surface affecting the nucleation and growth of silicon or (ii) the chemical transport of silicon between neighboring crystallites due to the difference in surface energy or temperature. The transport of silicon does not occur in the silane process since the thermal decomposition of silane is essentially irreversible. When silicon was deposited at 1250°C at about 1  $\mu\text{m}/\text{min}$ , the microstructure of the silicon was very similar to that shown in Fig. 4B, except that the average size of crystallites was increased to 8-10  $\mu\text{m}$ . By reducing the deposition rate to 0.25-0.3  $\mu\text{m}/\text{min}$ , crystallites as large as 30  $\mu\text{m}$  were frequently obtained. Examples of the as-deposited and cross-sectioned surfaces are shown in Fig. 4C and D, respectively. However, the as-deposited surface became very irregular due presumably to the nucleation and transport processes discussed earlier. The transport process becomes more pronounced at low deposition rates. In extreme cases, the silicon layer was not continuous with gaps between crystallites even when the average thickness of the layer was greater than 50  $\mu\text{m}$  (Fig. 5).

Since large crystallites in silicon layers are preferred for solar cell purposes, high substrate temperatures and low deposition rates must be used. However, silicon layers deposited by the trichlorosilane process under these conditions exhibited such surface roughness that the formation of large-area, uniform, shallow p-n junctions becomes extremely difficult. To modify the nucleation and growth of silicon on graphite substrates, hydrogen chloride was added to the reactant mixture. It has been shown that at low Si/Cl ratios in the reactant mixture, preferential deposition into surface depressions can be achieved (6, 7). This is due presumably to the thermochemical nature of the reaction that at low Si/Cl ratios, the transport of silicon takes place from a low temperature region to a higher temperature zone, opposite to the direction of transport at high Si/Cl ratios (8). Since silicon at the surface of tall crystallites is at a lower temperature than that

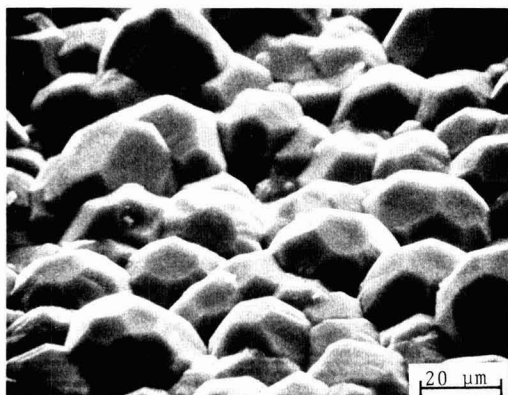
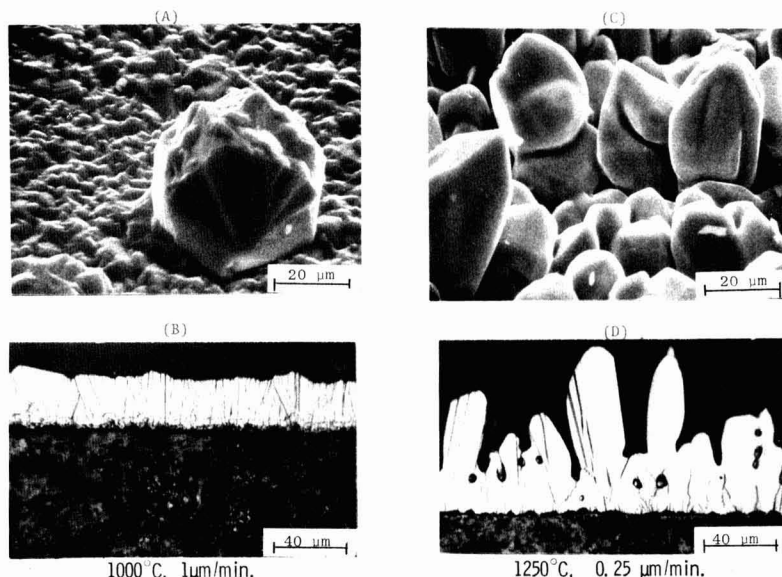


Fig. 2. Scanning electron micrograph of the as-grown surface of a silicon layer deposited on graphite substrates at 1100°C by the pyrolysis of silane at a rate of 1  $\mu\text{m}/\text{min}$ .

Fig. 4. Scanning electron micrographs of the as-deposited surface (A and C) and optical micrographs of the polished and etched cross-sectioned surface (B and D) of silicon deposited on graphite by the trichlorosilane process under different conditions.



of shorter ones, the transport process will reduce the surface irregularity of the deposited silicon layer.

A number of silicon layers were deposited on graphite substrates by the thermal reduction of trichlorosilane containing various concentrations of hydrogen chloride. High substrate temperatures and low deposition rates were used in order to obtain large crystallites. As expected, the addition of hydrogen chloride to the reactant mixture was found to decrease the deposition rate of silicon. For example, the average deposition rate of silicon at 1250°C using a reactant mixture containing 0.13% trichlorosilane and 0.4% hydrogen chloride was about 0.2  $\mu\text{m}/\text{min}$ , as compared with an average deposition rate of 0.3–0.35  $\mu\text{m}/\text{min}$  without using hydrogen chloride. However, the addition of hydrogen chloride to the reactant mixture has reduced considerably the surface roughness of the deposited silicon. Figure 6 shows the mechanically polished and chemically etched surface of the vertical cross section of such a specimen. A comparison of Fig. 6 and 4D or 5 indicates clearly the advantage of using hydrogen chloride in the deposition process. Once a reasonably uniform silicon layer is formed on the graphite substrate, higher deposition rates may be used without degrading the microstructure of the deposited silicon.

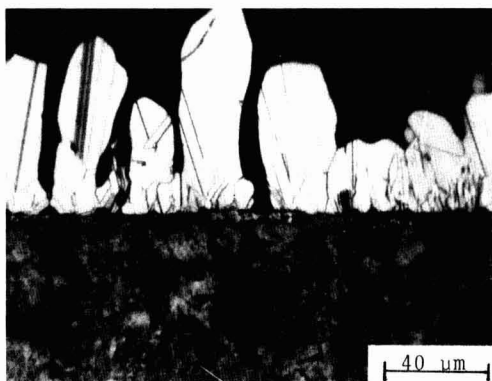


Fig. 5. Mechanically polished and chemically etched surface of the vertical cross section of a silicon layer deposited on a graphite substrate 1250°C at a rate of 0.2  $\mu\text{m}/\text{min}$ .

### Crystallographic Properties of Silicon

The crystallographic properties of a number of silicon layers deposited on graphite substrates by the silane and trichlorosilane processes under a wide range of substrate temperatures, deposition rates, and dopant concentrations were examined by the x-ray diffraction technique using a General Electric Model XRD-6 diffractometer with  $\text{CuK}\alpha$  radiation. Polycrystalline silicon powder of random orientations is known to show three strong diffraction peaks associated with  $\{111\}$ ,  $\{220\}$ , and  $\{311\}$  reflections with  $2\theta$  values of 28.4°, 47.3°, and 56.1° and relative intensities of 100, 60, and 35, respectively (9). The diffraction spectra of the silicon layers were obtained by scanning  $2\theta$  in the range of 20°–60°. When the thermal decomposition of silane was used for the deposition of silicon, the  $\{220\}/\{111\}$  intensity ratio was found to depend strongly on the substrate temperature, deposition rate, and the extent of doping. In general, unintentionally doped silicon layers deposited at low temperatures and high rates exhibited very large  $\{220\}/\{111\}$  intensity ratios, up to about 1000 indicating that the silicon crystallites show a very strong  $\{110\}$  preferred orientation. This ratio was found to decrease with increasing substrate temperature, decreasing deposition rate, or the introduction of a high concentration of dopants. The crystallographic properties of silicon on graphite substrates are very similar to those on borosilicate/steel substrates (10). However, when the thermal reduction of trichlorosilane was used for the deposition of silicon of various doping levels on graphite at 1000°–1250°C and at 0.2–2  $\mu\text{m}/\text{min}$ , the  $\{220\}/\{111\}$  intensity ratio was found to be in the range of 0.4–5, indicating

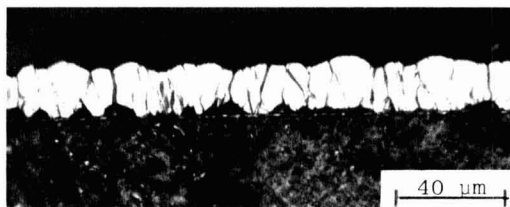


Fig. 6. Mechanically polished and chemically etched surface of the vertical cross section of a silicon/graphite specimen deposited at 1250°C by using a reactant mixture containing 0.13% trichlorosilane and 0.4% hydrogen chloride.

no significant preferred orientation in the crystallites of the silicon deposit. In some silicon layers deposited at 1250°C, crystallites exhibited a slight preferred {111} orientation, as indicated by the {220}/{111} intensity ratios. Figure 7 shows typical diffraction spectra of silicon layers deposited by the silane and trichlorosilane processes. Figure 7A shows the diffraction spectrum of a boron-doped silicon layer deposited on a graphite substrate at 1100°C by the thermal decomposition of silane, where the {220}/{111} intensity ratio is about 150 (the {111} reflection was measured at a considerably magnified scale). Figure 7B shows the diffraction spectrum of an unintentionally doped silicon layer deposited on a graphite substrate at 1000°C and at 0.25  $\mu\text{m}/\text{min}$  by the thermal reduction of trichlorosilane, where the {220}/{111} intensity ratio is about 2.8. The difference in the crystallographic properties of silicon deposited by the silane and trichlorosilane processes is presumably also related to the difference in the reversibility of the chemical reactions.

### Preparation and Characterization of Solar Cells

Silicon deposited on graphite substrates at temperatures of 1150°C or lower by the silane and trichlorosilane processes without intentional doping was always of high electrical resistivity, due at least in part to the grain boundary effects. When the trichlorosilane process was used for the deposition of silicon at higher temperatures, the deposit was always p-type with an electrical resistivity dependent on substrate temperature and deposition rates. For example, silicon deposited at 1250°C at a rate of 1  $\mu\text{m}/\text{min}$  had a resistivity of 5-10 ohm-cm, and the resistivity was decreased to 1 ohm-cm or less when the deposition rate was reduced to about 0.25  $\mu\text{m}/\text{min}$ . These results strongly suggest the diffusion of impurities from the graphite substrate into the silicon deposit at high temperatures.

The electrical resistivity of silicon deposited on graphite substrates by both silane and trichlorosilane

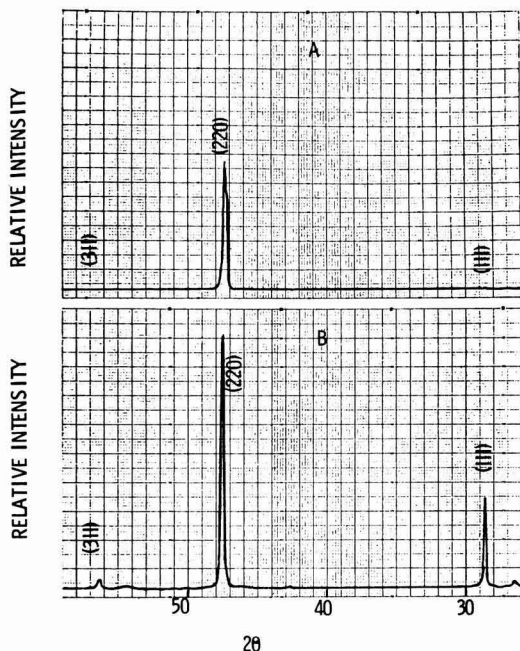


Fig. 7. X-ray diffraction spectra of (A) a boron-doped silicon layer deposited on a graphite substrate at 1100°C by the thermal decomposition of silane, and (B) an undoped silicon layer deposited on a graphite substrate at 1000°C by the thermal reduction of trichlorosilane.

processes was controlled by using phosphine and diborane as dopants. Polycrystalline silicon p-n junction solar cell structures were prepared on graphite substrates, 3 cm  $\times$  3 cm in area, by depositing successively 10-40  $\mu\text{m}$  of 0.002-0.003 ohm-cm p-type silicon, 8-10  $\mu\text{m}$  of 0.2-2 ohm-cm p-type silicon, and 0.2-0.4  $\mu\text{m}$  of 0.001-0.002 ohm-cm n-type silicon. The use of a relatively thick, boron-doped layer at the initial stage of silicon deposition was to improve the microstructure of silicon in the junction region without contributing appreciatively to the series resistance of the device. The thickness and resistivity of the p<sup>+</sup> and p-silicon layers were obtained by measuring the resistivity profile along the angle-lapped surface of the specimen using a spreading resistance probe. During the angle-lapping process, however, the n<sup>+</sup>-silicon layer was always removed due to its small thickness and rough surface. The thickness of the n<sup>+</sup>-silicon layer was deduced from the duration of deposition under conditions established for a low deposition rate, and its resistivity was determined by the four-point probe technique.

The electrical resistivity of silicon layers deposited by the silane process was readily controlled by introducing an appropriate amount of the desired dopant into the reactant mixture. When the thermal reduction of trichlorosilane was used for the deposition of silicon, the resistivity of the p-layer was found to be less uniform. Furthermore, the addition of hydrogen chloride to the reactant mixture severely interfered with the control of dopant distribution in the p-silicon layer. This is again due to the chemical transport associated with the reversibility of the trichlorosilane process. During the deposition of the p<sup>+</sup>-silicon layer, low resistivity boron-doped silicon was also deposited on the susceptor. Since the susceptor was at a higher temperature than the substrates, silicon and boron were transported from the susceptor onto the substrate by hydrogen chloride during the subsequent deposition, and this transport process resulted in the low and non-uniform resistivity in the p-silicon layer. Therefore, hydrogen chloride was added to the reactant mixture only during the initial deposition of the p<sup>+</sup>-silicon layer. Figure 8 shows the mechanically polished and chemically etched surface of the vertical cross section of a solar cell structure on a graphite substrate deposited by using a hydrogen-trichlorosilane-hydrogen chloride mixture and appropriate dopants. The etching process has delineated the p-p<sup>+</sup> junction due to their difference in chemical potentials (11); however, the n<sup>+</sup>-silicon layer, about 2000Å in thickness, was removed by etching.

Mesa diodes were isolated from the above structures by evaporating titanium-silver dots of 0.75 mm diameter on the silicon surface followed by masking and etching. Typical current-voltage characteristics of these diodes deposited by the silane process are shown in Fig. 9. The "n" value in the diode equation, cal-

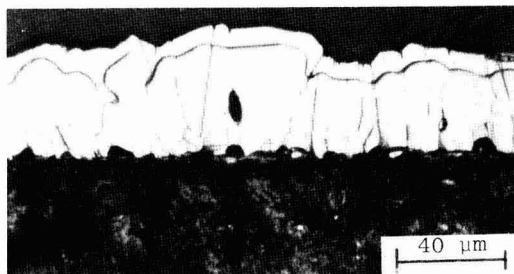


Fig. 8. Mechanically polished and chemically etched surface of the vertical cross section of a polycrystalline silicon solar cell deposited on a graphite substrate by using a hydrogen-trichlorosilane-hydrogen chloride mixture (the n<sup>+</sup>-layer was removed by etching).

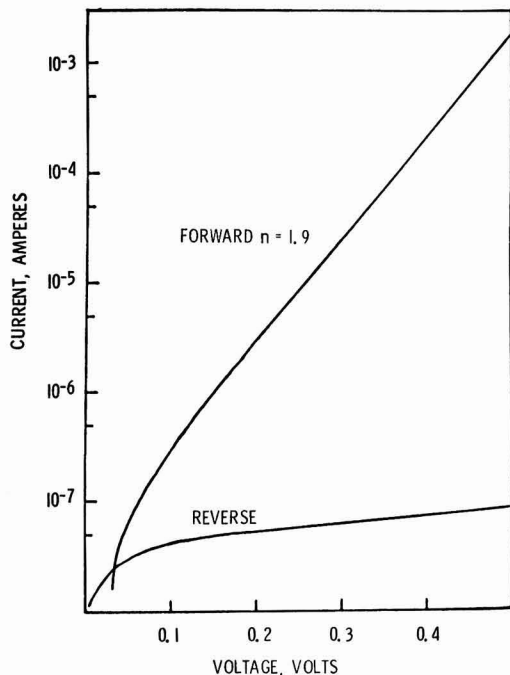


Fig. 9. Current-voltage characteristics of a polycrystalline silicon p-n junction of 0.75 mm diameter deposited on a graphite substrate by the silane process.

culated from the forward characteristics, is 1.9, very similar to that for single crystalline silicon p-n junctions, indicating that the grain boundaries in polycrystalline silicon on graphite substrates do not play a significant role in current conduction. The reverse current density, however, is considerably higher than that in single crystalline silicon p-n junctions.

A number of solar cells were fabricated from n<sup>+</sup>-silicon/p-silicon/p<sup>+</sup>-silicon/graphite structures deposited by both silane and trichlorosilane processes. A grid contact of about 1500Å titanium and 5 μm silver was evaporated onto the n<sup>+</sup>-silicon surface, and the graphite substrate served as the other ohmic contact to the solar cell. The four sides were cut off to remove the silicon deposit on the periphery. The current-voltage characteristics of resulting solar cells, 2.5 cm × 2.5 cm in area, were measured under illumination with an AMO solar simulator at room temperature. The conversion efficiencies of cells prepared by the silane and trichlorosilane processes were similar and were in the range of 1.0-1.5%. An example of the current-voltage characteristics of a polycrystalline silicon solar cell on a graphite substrate prepared by the trichlorosilane process is shown in Fig. 10. The open-circuit voltage, short-circuit current density, and fill factor are 0.33V, 13 mA/cm<sup>2</sup>, and 0.47, respectively, corresponding to a conversion efficiency of 1.5%.

### Summary and Conclusions

Polycrystalline silicon layers have been deposited on graphite substrates by the thermal decomposition of silane and the thermal reduction of trichlorosilane under a wide range of conditions. Because of the difference in the chemical reversibility of these two reactions, silicon layers deposited by silane and trichlorosilane processes had different microstructures and crystallographic properties. The microstructure of silicon deposited by the trichlorosilane process may be improved by adding hydrogen chloride to the reactant mixture. Silicon layers containing crystallites with an average size of 20-30 μm can thus be obtained by

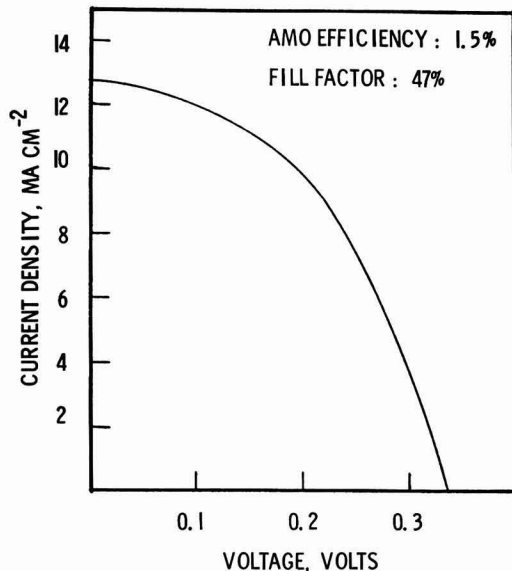


Fig. 10. Current-voltage characteristics of a polycrystalline silicon solar cell on a graphite substrate, deposited by the trichlorosilane process, under illumination with an AMO simulator.

either process. Solar cells with AMO efficiencies of up to 1.5% were obtained by controlling the dopant distribution in deposited silicon in a one-step deposition process. No appreciable differences in the characteristics of solar cells prepared by the two processes were observed.

### Acknowledgments

The authors wish to thank Mr. Bill Parker for most of the photomicrographs reported in this paper.

This work was supported by the National Science Foundation, Research Applied to National Needs (RANN), under Grant AER 73-07843 (GI-38981).

Manuscript submitted June 16, 1975; revised manuscript received Sept. 15, 1975.

Any discussion of this paper will appear in a Discussion Section to be published in the December 1976 JOURNAL. All discussions for the December 1976 Discussion Section should be submitted by Aug. 1, 1976.

Publication costs of this article were partially assisted by Southern Methodist University.

### REFERENCES

1. T. L. Chu, in "Workshop Proceedings—Photovoltaic Conversion of Solar Energy for Terrestrial Applications, Cherry Hill, N. J., Oct. 23-25, 1973," Vol. I, p. 17, NTIS PB-1213.
2. T. L. Chu, J. C. Lien, H. C. Mollenkopf, S. C. Chu, K. W. Heizer, F. W. Voltmer, and G. F. Wakefield, *Solar Energy*, **17**, 229 (1975).
3. T. L. Chu and G. A. Gruber, *This Journal*, **114**, 522 (1967).
4. C. H. Lewis, H. C. Kelly, M. B. Giusto, and S. Johnson, *ibid.*, **108**, 1114 (1961).
5. E. Sirtl and A. Adler, *Z. Metallk.*, **52**, 529 (1961).
6. W. R. Runyan, E. G. Alexander, and S. E. Craig, *This Journal*, **114**, 1154 (1967).
7. R. K. Smeltzer, Abstract 224, p. 555, The Electrochemical Society Extended Abstracts, Fall Meeting, New York, New York, Oct. 13-17, 1974.
8. L. P. Hunt and E. Sirtl, *This Journal*, **119**, 1941 (1972).
9. H. E. Swanson and R. K. Fuyat, NBS Circular 539, p. 8, 1953.
10. T. L. Chu, H. C. Mollenkopf, and Shirley S. Chu, *This Journal*, **122**, 1681 (1975).
11. T. L. Chu and J. R. Gavalier, *Electrochim. Acta*, **10**, 1141 (1965).



# Preparation and Properties of SiO<sub>2</sub> Films from SiH<sub>4</sub>-CO<sub>2</sub>-H<sub>2</sub>

A. K. Gaid,\* G. K. Ackermann,<sup>1</sup> V. J. Lucarini,\* and R. L. Bratter

IBM System Products Division, East Fishkill Facility, Hopewell Junction, New York 12533

## ABSTRACT

This paper presents the results of chemical vapor deposited (CVD) silicon dioxide films on silicon from an SiH<sub>4</sub> + CO<sub>2</sub> + H<sub>2</sub> system. The kinetics of this reaction have been studied with a barrel reactor. The activation energy ( $\Delta E$ ) of the SiH<sub>4</sub>, CO<sub>2</sub> reaction in hydrogen is 106.7 J/g mol (25.4 kcal/g mol) in the temperature range 800°-1050°C. The SiH<sub>4</sub> and CO<sub>2</sub> reaction in hydrogen is shown to be a first-order reaction with respect to SiH<sub>4</sub> (CO<sub>2</sub>:SiH<sub>4</sub>  $\approx$  20). The deposition rates of SiO<sub>2</sub> are dependent only on deposition temperature and on SiH<sub>4</sub> mole fraction. They are independent of the CO<sub>2</sub>:SiH<sub>4</sub> ratio in the experimental range of 7:1-120:1. Electrical characterization was carried out on MOS capacitors of  $\sim$ 1300Å dielectric thickness. The breakdown field was found to be  $(7.8 \pm 0.1 \times 10^6$  V/cm). Measurements of oxide charges, of mobile charges, and of fast surface-state density show that these oxides are stable under positive and negative bias, with maximum shifts of 250 mV after 50 hr stress at 200°C and  $\pm 2 \times 10^6$  V/cm electrical field. Postdeposition high-temperature anneal deteriorates the V<sub>FB</sub> stability under negative-bias temperature stress. The index of refraction depends on the CO<sub>2</sub>:SiH<sub>4</sub> ratio, going above 1.46 at a ratio  $<$ 10. Ratios of CO<sub>2</sub>:SiH<sub>4</sub>  $\geq$  50 give reproducible results at an average index of  $1.454 \pm 0.001$ . Etch rates in "P-etch" for 1000°C deposited samples are  $\sim$ 50% faster than thermal oxides grown at the same temperature.

Chemical vapor deposited (CVD) SiO<sub>2</sub> films have several advantages in planar semiconductor device processing over the oxidation of silicon. Since no silicon of the substrate is consumed, the junction movement, pileup, or depletion of dopants at SiO<sub>2</sub>-Si interfaces is minimized. Thick films of SiO<sub>2</sub>, which may be used in the field region of integrated FET circuits, can be deposited with greater ease than thermal oxidation because the deposition rates are not diffusion-limited in the solid. One application of CVD oxides where the thermal oxide does not compete is the use of CVD oxides as photolithographic masks for films not etched in fluorides, such as silicon nitride. Finally, CVD oxides lend themselves to *in situ* processing where two or more films are required and one of these films is SiO<sub>2</sub>.

Silica films have been deposited by a variety of chemical systems, at both high and low temperatures (1-10). It was desirable in this case to select a process that would produce SiO<sub>2</sub> films with etch rates close to those of thermal SiO<sub>2</sub>, so as to avoid excessive undercutting during etching. Since etch rate is inversely proportional to deposition temperature, the process had to be carried out at a high temperature (1000°C). SiH<sub>4</sub> was preferred over other silicon-bearing compounds (e.g., SiCl<sub>4</sub> or SiBr<sub>4</sub>) because of its gaseous nature and resulting ease of metering control. *In situ* processing also favors SiH<sub>4</sub> because one has only to replace the oxidant with NH<sub>3</sub> to deposit silicon nitride or discontinue the oxidant flow to deposit polysilicon. It was also desirable to use an oxidant that would have a minimal gas-phase reaction with SiH<sub>4</sub> so as to keep the reactor down time to a minimum. This led to the investigation of the SiH<sub>4</sub> and CO<sub>2</sub> reaction. Swann and Payne (4) and Kroll *et al.* (5) reported on the SiH<sub>4</sub>-CO<sub>2</sub> system. Our purpose is to investigate further the deposition kinetics, to obtain an empirical rate expression, and to examine the physical and electrical properties of the resulting SiO<sub>2</sub> films.

## Experimental

**Equipment.**—The equipment used for the entire experimental investigation was a vertical, cold-wall, barrel-type, induction-heated reactor (11). The silicon "wafers" were placed on an SiC-coated graphite susceptor. Figure 1 gives a schematic cross-sectional view of the reactor. The fused-quartz chamber is 18 in.

( $\sim$  45 cm) long, with an internal diameter of 9 in. ( $\sim$  23 cm). The susceptor is placed in the chamber so that its leading edge is  $\sim$  5 in. (12.7 cm) from the molybdenum distributor. The susceptor is hexagonal and is divided into three tiers, or "rings." Each of the six faces of the susceptor makes an angle of  $\sim$ 3° with the central vertical axis. The susceptor is placed on a fused-quartz plate, which in turn is supported by a fused-quartz pedestal. The susceptor, approximately 8.25 in. (21 cm) long, was rotated at about 8 rpm throughout this experimental work. The volume of the annulus between the susceptor and the chamber (*i.e.*, the volume of the deposition zone) is  $\sim$ 5 liters.

The temperature was measured with an optical pyrometer.<sup>2</sup> All temperatures reported were corrected for system transmission losses and for emissivity (12). The reacting and the carrier gases were introduced from the top of the reactor after each had been metered through a separate rotometer. Each rotometer was calibrated. The silane used was a 5% mixture in nitrogen or hydrogen. The SiH<sub>4</sub>, CO<sub>2</sub>, and the carrier gas (either H<sub>2</sub> or N<sub>2</sub>) were filtered (submicron filters) before they passed through their respective rotometers.

**Typical deposition conditions and measurement technique.**—Three, 2¼ in. (5.7 cm) Si, 11-25 ohm-cm, p-type,  $<$ 100 wafers were processed in each experimental run, unless otherwise indicated. One wafer each

<sup>2</sup> The temperature along the susceptor length is  $\pm$ 10°C of any reported value.

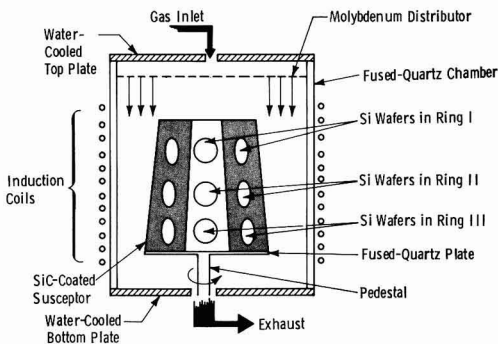


Fig. 1. Schematic cross-sectional view of barrel reactor

\* Electrochemical Society Active Member.

<sup>1</sup> Present address: IBM Deutschland Boeblingen (Lab) 0711 Boeblingen, Germany.

Key words: silicon dioxide, dielectric films, MOS, CVD, thin films.



was placed in rings 1, 2, and 3, at a predetermined fixed position. The remaining positions on the susceptor were filled with dummy wafers. Before loading in the reactor, wafers were cleaned ultrasonically in hot (85°C) deionized water (for 5 min), followed by  $H_2SO_4/HNO_3$  (3:1, at 120°C) cleaning (for 10 min), followed by 10:1 dilute HF dip (10 sec). The wafers were then rinsed in running deionized water (for 5 min) and subsequently spin-dried. The wafer surface was hydrophobic after this cleaning.

During the experimental work, the carrier gas flow rate ( $H_2$  in most cases) was varied between 60 and 120 liters/min and the  $SiH_4$  flow rate (5% in  $H_2$  or  $N_2$ ) between 60 and 1000  $cm^3/min$ . The  $SiH_4:CO_2$  ratio was changed between 7:1 and 120:1. The deposition temperature range was 800°–1050°C; the deposition time was never less than 5 min or greater than 25 min.

The resulting  $SiO_2$  film thicknesses were measured by CARIS<sup>3</sup> (>1500Å) and by ellipsometry (≤1500Å). The index of refraction was always measured by ellipsometry. Five thickness measurements were taken per wafer; these five readings cover ~80% of the total wafer area. Peripheral readings were taken 0.125 in. (3.18 mm) away from the edge of the wafer. The typical within-a-run deposition uniformity was ≤±5% at 1000°C and at a total flow rate of ~110 liters/min; the worst case within-a-run uniformity at any temperature and flow (within the experimental range) was ~±15%. The deposition rates used in this report are therefore average deposition rates over three rings (i.e., 15 measurements); thus, as a first approximation, we neglected the silane concentration variations along the susceptor length.

### Experimental Results

**Preliminary experiments.**—Preliminary experiments were performed using an  $H_2$  and  $N_2$  mixture as a carrier gas at a deposition temperature of 1000°C. The  $H_2/N_2$  ratio was varied from 0.03:1 to 1.5:1, with similar results. The films deposited were dendritic in appearance. When these films were etched in 5:1 diluted HF, a brown film was left on the silicon surface. Swann and Payne (4) reported similar observations when they used argon as a carrier gas. The brown film on the silicon surface was etchable only in I-etch,<sup>4</sup> suggesting that the brown film is a silicon-rich film (mostly polysilicon).

The use of pure  $H_2$  as a carrier gas prevented the formation of either "dendritics" or the silicon-rich brown film. The  $SiO_2$  films thus deposited were etchable in diluted HF (5:1) and left the silicon surface clean (hydrophobic). The remaining investigations used  $H_2$  as a carrier gas.

**Deposition rates ( $SiH_4-CO_2-H_2$  system).**—The parameters whose effect on deposition rate of  $SiO_2$  has been investigated are  $SiH_4$  mole fraction,  $SiH_4:CO_2$  ratio, deposition temperature, and  $H_2$  flow rate.

**Deposition rate vs.  $SiH_4$  mole fraction.**—Figure 2 shows the log of  $SiO_2$  deposition rate as a function of the entering gas composition ( $X_{SiH_4}^0$ ), as determined by the entering gas composition. The slope of the graph is very nearly 1, which shows that the  $SiH_4-CO_2$  reaction in  $H_2$  is a first-order reaction with respect to  $SiH_4$ . For Fig. 2, the deposition temperature and the  $H_2$  and  $CO_2$  flow rates were kept constant. Note that the  $CO_2:SiH_4$  ratio varied from ~20 to 200 during this experiment; however, it is important to point out that only the  $SiH_4$  concentration is a variable for Fig. 2. Hence, Fig. 2 is the result of a classical experiment to isolate the order of the reaction with respect to  $SiH_4$  (13).

**Deposition rate vs.  $SiH_4:CO_2$  ratio.**—Figure 3 graphs the deposition rate as a function of  $CO_2/SiH_4$  ratio for the two  $SiH_4$  mole fractions. The deposition tempera-

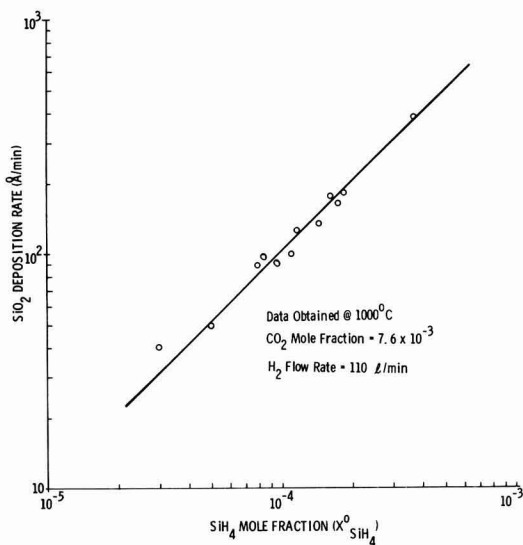


Fig. 2. Deposition rate as a function of  $SiH_4$  mole fraction in the feed. Deposition temperature,  $H_2$  flow, and  $CO_2$  flow kept constant.

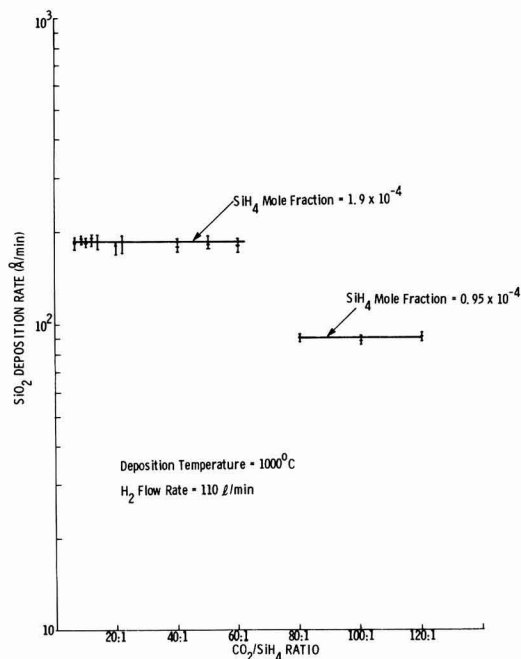


Fig. 3. Deposition rate as a function of  $CO_2:SiH_4$  ratio at two silane mole fractions, at 1000°C and at constant  $H_2$  flow rate.

ture and the  $H_2$  flow rate were kept constant. The deposition rate is independent of the  $CO_2:SiH_4$  ratio in the experimental range of 7:1–120:1. Note that, for a fixed  $SiH_4$  mole fraction (e.g.,  $1.9 \times 10^{-4}$ ), the deposition rate is independent of the  $CO_2$  concentration.

These results are consistent with the classical "method of excesses" or "isolation technique" (14); i.e., when a large excess of one chemical is used as compared with another, the reaction rate is independent of the concentration of the chemical being used in large excess. The lack of dependence of deposition rate on  $CO_2$  concentration, however, is in total disagreement with

<sup>3</sup> Constant angle reflection interference spectroscopy.

<sup>4</sup> I-etch is a mixture of stock solution and  $HNO_3$  in the ratio of 1:5. The stock solution is a mixture of  $CH_3COOH$ , HF,  $HNO_3$  in a 1:2:5 ratio, saturated with iodine and allowed to settle overnight (14 hr).

the results reported by Swann and Payne (4) and by Kroll *et al.* (5). Both papers reported an increase in deposition rate with increasing CO<sub>2</sub>:SiH<sub>4</sub> ratio. The likely reason for this discrepancy is the difference in reactor design. In both papers, a pedestal or pancake-type reactor was used where the flow of gas is at right angles to the wafer surface. In our reactor, the flow of gases is nearly parallel to the wafer surface. These two very different flow patterns will have a markedly different mass and energy transfer and, hence, possibly, different results.

**Deposition rate vs. deposition temperature.**—Figure 4 shows the deposition rate as a function of reciprocal temperature at a constant injected SiH<sub>4</sub> mole fraction of  $1.9 \times 10^{-4}$ . Two CO<sub>2</sub>:SiH<sub>4</sub> ratios were used, 12 and 40, and the H<sub>2</sub> flow rate was kept constant at 110 liters/min. The activation energy obtained from Fig. 4 is 25.4 kcal/g mol (106.7 J/g mol).

**Deposition rate vs. flow rate.**—To determine whether the deposition rate of SiO<sub>2</sub> is limited by the surface chemical reaction rate or controlled by mass transfer, an experiment was performed in which the H<sub>2</sub> flow rate was varied from 60 to 115 liters/min. The deposition temperature was kept constant at 1000°C. The SiH<sub>4</sub> and CO<sub>2</sub> mole fractions were also constant at  $1.9 \times 10^{-4}$  and  $1.14 \times 10^{-2}$ , respectively. Figure 5 shows the results, with the deposition rate plotted against the square root of the flow rate.

For all practical purposes, the deposition rate is independent of the flow rate, and, hence, the SiH<sub>4</sub>-CO<sub>2</sub> reaction in H<sub>2</sub> is limited by the surface-chemical-reaction rate, with the experimental flow range 60–115 liters/min.

**Rate expression (empirical).**—Following the standard procedure for obtaining an empirical rate expression for any heterogeneous reaction (13), and knowing that the reaction is (i) independent of CO<sub>2</sub> concentration (Fig. 3), (ii) first order with respect to SiH<sub>4</sub>

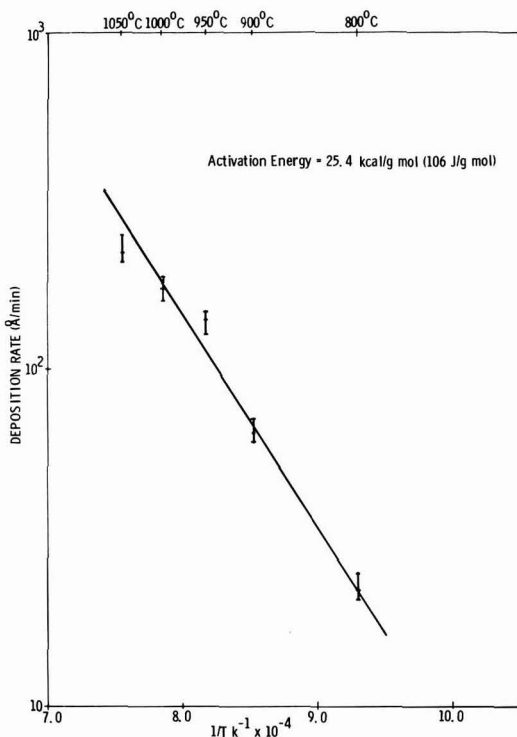


Fig. 4. Deposition rate as a function of  $1/T$ , at constant H<sub>2</sub> flow rate and SiH<sub>4</sub> mole fraction. Two CO<sub>2</sub>:SiH<sub>4</sub> ratios, 12 and 40.

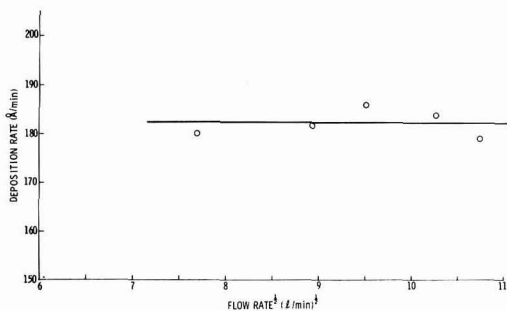


Fig. 5. Deposition rate as a function of square root of flow rate at 1000°C. SiH<sub>4</sub> mole fraction constant at  $1.9 \times 10^{-4}$ . Constant CO<sub>2</sub>:SiH<sub>4</sub> ratio of 60.

(Fig. 2), and (iii) surface-chemical-reaction-limited (Fig. 5), we can arrive at the following rate expression

$$r_{\text{SiO}_2} = K_s C^0_{\text{SiH}_4} [1 - Y_{\text{SiH}_4}] \quad [1]$$

where  $r_{\text{SiO}_2}$  = deposition rate of SiO<sub>2</sub> (moles/min),  $C^0_{\text{SiH}_4}$  = silane concentration in the feed (moles/liter),  $K_s$  = the rate constant for surface chemical reaction (liters/min), and  $Y_{\text{SiH}_4}$  = fraction of silane converted to deposit.

The fraction of SiH<sub>4</sub> converted to SiO<sub>2</sub> can be calculated by mass-balance, and its value is small, *i.e.*, 0.02–0.15, depending on the deposition temperature. Thus, neglecting  $Y_{\text{SiH}_4}$  and expressing deposition rate in Å/min and concentration as mole fraction, we can rewrite Eq. [1] as

$$d_{\text{SiO}_2} = K'_s X^0_{\text{SiH}_4} \quad [2]$$

where  $d_{\text{SiO}_2}$  is the deposition rate in Å/min,  $X^0_{\text{SiH}_4}$  is the mole fraction of silane in the feed, and  $K'_s$  is the rate constant in Å/min. The value of  $K'_s$  has been calculated from the data of Fig. 2, at 1000°C, to be approximately equal to  $10^6$  Å/min.

Now

$$K'_s = K'_0 \exp [-\Delta E/RT] \quad [3]$$

where  $K'_0$  is the frequency factor in Å/min and  $\Delta E$  the activation energy. The activation energy is 25.4 kcal/g mole (Fig. 4), and the calculated value of  $K'_0$  is  $2 \times 10^{10}$  Å/min.

Thus, the empirical rate expression for SiO<sub>2</sub> deposition is

$$d_{\text{SiO}_2} = 2 \times 10^{10} \cdot \exp [-25400/RT] \cdot X^0_{\text{SiH}_4} \quad [4]$$

where  $R$  is the gas constant (1.98 cal/g mole °K) and  $T$  is temperature in °K.

**Physical properties.**—Table I lists the physical properties of SiO<sub>2</sub> grown from the SiH<sub>4</sub>-CO<sub>2</sub>-H<sub>2</sub> system as a function of deposition parameters and anneal conditions.

**Refractive index.**—The refractive index was measured by ellipsometry at 5460 Å (mercury-light wavelength). The refractive index of deposited SiO<sub>2</sub> is very close to that of the thermal SiO<sub>2</sub> (1.462) (15). Owing to densification, the annealing treatment increases the refractive index of as-deposited samples. There also appears to be some effect due to the CO<sub>2</sub>:SiH<sub>4</sub> ratio. However, although CO<sub>2</sub>:SiH<sub>4</sub> ratios greater than 20:1 do not seem to affect the refractive index within measurement accuracy, for a deposition temperature of 1050°C and a low CO<sub>2</sub>:SiH<sub>4</sub> ratio of 12, the refractive index goes up, indicating that the film may be silicon-rich. As Table I shows, only the third-place decimal in the refractive index was affected by the CO<sub>2</sub>:SiH<sub>4</sub> ratio from 20:1 to 120:1. Ratios of SiH<sub>4</sub>:CO<sub>2</sub>  $\geq$  50:1 are preferred because the run-to-run refractive index reproducibility is considerably improved (*i.e.*,  $\pm 0.001$  run-to-run).

Table I. Physical properties of SiO<sub>2</sub> grown from SiH<sub>4</sub>-CO<sub>2</sub>-H<sub>2</sub>

Deposition temperature (°C)	CO <sub>2</sub> /SiH <sub>4</sub>	Densification in N <sub>2</sub> ambient		Refractive index (5460Å)	Etch rate in P-etch at 25°C (Å/sec)	Etch rate in 5:1 HF at 25°C (Å/sec)	Density* (g/cm <sup>3</sup> )	Sample thickness (μm)
		Temp (°C)	Time (min)					
950	12	—	—	1.460	3.21	9.5	2.19	0.36
950	12	1100	30	1.462	2.1	7.2	2.28	0.38
1000	12	—	—	1.458	2.97	7.9	2.25	0.33
1000	12	1100	30	1.462	2.07	7.2	2.30	0.33
1050	12	—	—	1.469	—	8.2	2.10	0.21
1050	20	—	—	1.458	2.92	8.5	2.20	0.40
1050	20	1100	30	1.462	2.06	7.2	2.24	0.40
1000	20	—	—	1.458	—	8.8	—	0.10
1000	50	—	—	1.455	—	8.5	—	0.12
1000	60	—	—	1.454	—	9.1	—	0.12
1000	120	—	—	1.453	—	9.1	—	0.10

\* By weight loss method.

Infrared absorption spectra of a limited number of as-deposited samples were taken. All samples were deposited at 1000°C. First absorption maxima lay at ~1070 cm<sup>-1</sup> for all samples.

**Etch rate.**—Etch rate was determined by etching the samples in P-etch (15) [15 parts HF (49%), 10 parts HNO<sub>3</sub> (70%), and 100 parts H<sub>2</sub>O]. Typically, SiO<sub>2</sub> deposited at 1000°C etched ~50% faster than thermal oxide. In P-etch, the etch rate appears to be a function of deposition temperature (Table I). Sample-to-sample variations in etch rate decreased as the deposition temperature was increased. All samples when annealed in N<sub>2</sub> at 1100°C for a half-hour had an etch rate of between 2.1 and 2.06 Å/sec. The etch rate in 5:1 diluted HF also showed a drop upon annealing; however, this etchant did not delineate the etch rate as a function of deposition temperature.

**Density.**—Film density was measured by the weight-loss method; i.e., deposited wafers were weighed and then stripped and reweighed. The density of as-deposited samples appears consistently lower than that of annealed samples. The density of all samples varied between 2.1 and 2.3 g/cm<sup>3</sup>. The density of the annealed sample approached that of thermal oxide (2.27 g/cm<sup>3</sup>) within measurement accuracy.

**Electrical properties.**—Several samples were prepared from the SiH<sub>4</sub>-CO<sub>2</sub>-H<sub>2</sub> system at 1000°C, with the CO<sub>2</sub>:SiH<sub>4</sub> ratio varying from 40:1 to 60:1. All wafers were n-type Si, <100>, 8.5–20 ohm-cm, 5.72 cm (2¼ in.) diameter. The total SiO<sub>2</sub> thickness deposited was ~1350Å. Most wafers were split in half after the SiO<sub>2</sub> deposition. One portion of each wafer was then annealed at 1050°C for 15 min in N<sub>2</sub> (standard anneal for thermal SiO<sub>2</sub>). Then, clean 20-mil aluminum dots were evaporated on both halves of the wafers. The metallized wafers were annealed at 400°C for a half-hour in N<sub>2</sub>.

Following are the results of measurements on MOS capacitors.

**Dielectric strength.**—Twenty MOS capacitor dots in each sample were biased in accumulation, and the bias voltage was ramped at a rate of approximately 1 V/sec. The capacitor leakage current was monitored with a picoammeter. The dielectric breakdown was considered to have occurred when the leakage was greater than or equal to 2 nA. All samples exhibited the same dielectric breakdown field (E<sub>B</sub>). There was no dependence on CO<sub>2</sub>:SiH<sub>4</sub> ratio or the postdeposition anneal. The E<sub>B</sub> value obtained was 7.8 × 10<sup>6</sup> V/cm, and the breakdown distribution obtained was very tight in every case, with a standard deviation σ<sub>EB</sub> ≤ 0.1 × 10<sup>6</sup> V/cm.

**Dielectric constant.**—The thickness measured by ellipsometry and C-V measurements agreed within 50Å in all cases. This leads to the conclusion that the dielectric constant lies between 3.8 and 4.0. Annealed halves of wafers were thinner by ~30Å than the nonannealed halves. This means that there is densification of the order of 2–3% upon annealing.

**Oxide fixed charges (Q<sub>ox</sub>).**—The fixed oxide charges were measured by means of the C-V technique. There was no influence of CO<sub>2</sub>:SiH<sub>4</sub> ratio on the fixed charges; however, annealing showed the expected reduction in fixed charges. The Q<sub>ox</sub> for nonannealed wafers was 2.8 (±0.2) × 10<sup>11</sup> cm<sup>-2</sup>, and the Q<sub>ox</sub> for annealed wafers was 1.3 (±0.5) × 10<sup>11</sup> cm<sup>-2</sup>.

**Mobile charges (Q<sub>m</sub>).**—Mobile charges were measured by applying ±2 × 10<sup>6</sup> V/cm for 10 min at 200°C. This technique is similar to the one used by Kriegler *et al.* (16). The shift in flatband under positive bias was converted into mobile charge. In no case was the shift in the flatband under negative bias taken into account, for two reasons:

1. In most cases, the shift in the flatband under negative bias was negligible (i.e., ≤25 mV). This also means that the mobile charges were present at the metal/SiO<sub>2</sub> interface.

2. In some cases, the flatband shift was significant under negative bias (i.e., ≥50 mV), but the direction of the shift was wrong, i.e., as if more positive charges were being accumulated at the SiO<sub>2</sub>/Si interface. This effect (discussed in greater detail under Stability) is due to fast surface-state generation at the SiO<sub>2</sub>/Si interface (17).

There was no measured effect of CO<sub>2</sub>:SiH<sub>4</sub> ratio on mobile charge. The annealed wafers had a mobile charge of <1 × 10<sup>10</sup>, whereas the nonannealed wafers showed a mobile charge of 2.7 (±0.5) × 10<sup>10</sup> cm<sup>-2</sup>. The apparent higher mobile charges in nonannealed wafers are most likely due to run-to-run variations of the Al evaporator. The nonannealed halves of wafers were metallized first. Thermal oxide monitor wafers in the above two metallization runs were checked and showed the same general trend as the CVD oxide wafers.

**Fast surface states (N<sub>FS</sub>).**—Fast surface states were determined by the quasistatic technique of Kuhn (18). This technique was modified after Castagne (19) and Kerr (20). The modification involved the use of a high-frequency C-V trace in place of the ideal. The N<sub>FS</sub> was obtained from accumulation to onset of inversion by comparison of the high- and low-frequency C-V traces.

$$N_{FS} = \frac{C_{FS}}{q} = \left[ \frac{C_{LF} \cdot C_{OX}}{C_{OX} - C_{LF}} - \frac{C_{HF} \cdot C_{OX}}{C_{OX} - C_{HF}} \right] \frac{1}{q} \quad [5]$$

where C<sub>FS</sub> = capacitance due to fast surface states, C<sub>OX</sub> = oxide capacitance, C<sub>LF</sub> = low-frequency capacitance at a given voltage on the metal electrode, C<sub>HF</sub> = high-frequency capacitance at a given voltage on the metal electrode, and q = electronic charge 1.6 × 10<sup>19</sup>.

Equation [5], in which all capacitances are per unit area, determines N<sub>FS</sub> as a function of applied electrode voltage. This voltage can be readily converted into surface potential [e.g., Kuhn (18)], so N<sub>FS</sub>, as a function of surface potential, is given in this investigation.

The fast surface-state densities are generally small in all samples. Annealed samples show somewhat higher N<sub>FS</sub> than nonannealed samples. The difference in the two cases, however, is not considered significant,

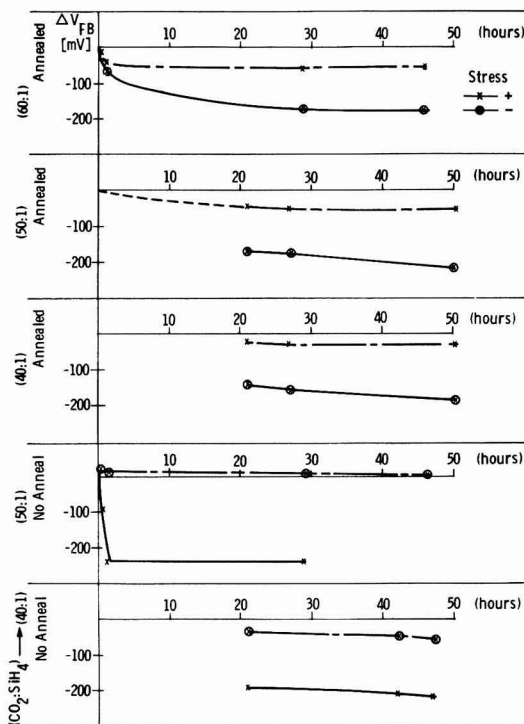


Fig. 6. Change of flatband voltage under the influence of temperature-bias stressing.

and all samples measured can be adequately represented by an  $N_{FS}$  value of  $1.5 (\pm 0.5) \times 10^{10} \text{ cm}^{-2} \cdot \text{eV}^{-1}$  (at mid-bandgap).

**Stability**—As shown in Fig. 6, 50-hr stress data on some samples were accumulated at 200°C and  $2 \times 10^6$  V/cm with both polarities on the metal of the MOS capacitor. The positive-bias data confirm the short-term stress data. There is a shift in the flatband voltage within the first hour and then a fast leveling off. This can be explained by the movement of mobile ions. Under negative bias, there is again a negative shift, the final value of which is larger for the annealed wafers than for the nonannealed wafers. There was no discernible dependency of  $V_{FB}$  shift on the CO<sub>2</sub>:SiH<sub>4</sub> ratio. Negative shifts under negative bias are commonly attributed to an increase of fast surface-state density (17). It was not expected that the nonannealed wafers would display fewer fast surface states after temperature bias stressing.

To check the above expectation, several MOS capacitors on both annealed and nonannealed wafers were stressed for 20 hr at  $\pm 2 \times 10^6$  V/cm and 200°C. Most of the observed shift in  $V_{FB}$  occurs within this time span (Fig. 6). Table II presents the initial and final values of the  $N_{FS}$  at mid-bandgap. Note that there is a significant difference between annealed and nonannealed

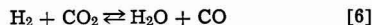
annealed samples and, contrary to the above expectation, the annealed samples show higher, fast surface-state density after temperature- and negative-bias stressing. The behavior of the annealed samples is much like the dry, O<sub>2</sub>-grown thermal oxides (17), whereas the nonannealed wafers appear to characterize the CVD oxides.

The behavior of the CVD oxides investigated is not believed to be limited to oxides deposited in SiH<sub>4</sub>-CO<sub>2</sub>-H<sub>2</sub>. This effect is most likely due to the deposition temperature used in this case (i.e., 1000°C). Thus, the high-temperature postdeposition anneal deteriorates the stability of the CVD oxides under temperature- and negative-bias stressing.

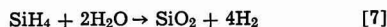
### Discussion

It has been shown that the SiH<sub>4</sub>-CO<sub>2</sub> reaction is first order with respect to SiH<sub>4</sub>. This was determined by using the "method of excesses," or "isolation," technique (14); i.e., CO<sub>2</sub> had considerably larger concentration than SiH<sub>4</sub>. Therefore, as expected, the reaction rate was independent of the CO<sub>2</sub> concentration. The same technique (i.e., excess SiH<sub>4</sub> compared with CO<sub>2</sub>) or the use of molar ratios of SiH<sub>4</sub> and CO<sub>2</sub> cannot isolate the reaction order with respect to CO<sub>2</sub>, because, in both cases, silicon-rich films are deposited (i.e., no longer SiO<sub>2</sub>). There is no other known technique that would isolate reaction order with respect to CO<sub>2</sub>. Thus, the experimental data cannot firmly support a reaction mechanism, and none will be postulated here. However, we shall discuss our results in the light of the mechanism previously postulated.

Tung and Caffrey (1), Steinmaier and Bloem (21), and Rand and Ashworth (8) proposed a two-step kinetic mechanism for SiO<sub>2</sub> deposition from SiCl<sub>4</sub>-CO<sub>2</sub>-H<sub>2</sub> and SiBr<sub>4</sub>-CO<sub>2</sub>-H<sub>2</sub>. The first step involves so-called "water-gas" reaction



The second step involves oxidation (hydrolysis) of silicon halides with H<sub>2</sub>O. Similar two-step kinetics may also be written for SiH<sub>4</sub>, the second step being



These authors realized that intermediate-reaction steps must exist, e.g., that reactions [6] and [7] may proceed via a free-radical chain mechanism or any other equally probable path. It is also generally accepted that the water-gas reaction is the slower and, hence, the rate-controlling step.

Then, Tingey (22) experimentally determined the forward rate expression of reaction [6] in the temperature range of 800°-1050°C. The experimentally determined activation energy for H<sub>2</sub>O formation from H<sub>2</sub> and CO<sub>2</sub> is 78 kcal/g mole (22). Therefore, if the water-gas reaction is rate controlling for SiO<sub>2</sub> deposition from SiH<sub>4</sub>-CO<sub>2</sub> reaction in H<sub>2</sub>, the observed activation energy should be of the order of 78 kcal/g mole. We have obtained an activation energy of 25.4 kcal/g mole for SiO<sub>2</sub> deposition. These results are inconsistent with the water-gas mechanism. Only the Steinmaier and Bloem (21) results are consistent with water-gas reaction. These authors obtained an activation energy of 82 kcal/g mole for SiCl<sub>4</sub>-CO<sub>2</sub>-H<sub>2</sub>. However, Tung and Caffrey (1), who also studied the SiCl<sub>4</sub>-CO<sub>2</sub>-H<sub>2</sub> system, reported an activation energy of 51.6 kcal/g mole. Similarly, Rand and Ashworth (8) reported an activation energy of 30 kcal/g mole for the SiBr<sub>4</sub>-CO<sub>2</sub>-H<sub>2</sub> system in the temperature range of 800°-950°C. Thus, hardly any of the activation energy data involving CO<sub>2</sub> and H<sub>2</sub> support the so-called water-gas mechanism.

The inconsistency of the activation energy data led us to perform several experiments, with hopes of answering a two-part question: (i) Does H<sub>2</sub>O form in our reactor under the experimental conditions of flow? (ii) What physical evidence would be produced if H<sub>2</sub>O were to form in the reactor? It was assumed that, if H<sub>2</sub>O were formed, the thermal oxidation of silicon would occur in the absence of SiH<sub>4</sub>. In the presence of SiH<sub>4</sub>,

Table II. Fast surface states as a function of temperature-bias stress and postdeposition high temperature (1050°C, 15 min, N<sub>2</sub>) anneal

Sample	$N_{FS} \text{ cm}^{-2} \text{ eV}^{-1}$ (at mid-bandgap) $\times 10^{10}$		
	Initial	After 20 hr of $+2 \times 10^6$ V/cm and 200°C	After 20 hr of $-2 \times 10^6$ V/cm and 200°C
As deposited	1.1 ( $\pm 0.3$ )	1.2 ( $\pm 0.3$ )	2.5 ( $\pm 0.3$ )
Annealed	1.8 ( $\pm 0.2$ )	3.1 ( $\pm 0.5$ )	6.6 ( $\pm 0.7$ )

\* Note: Values in parentheses are twice the standard deviation.

we expected some homogeneous reaction (manifested by reaction-chamber clouding) besides the usual heterogeneous reaction. Several experiments, with results, are presented below.

Cleaned Si wafers were exposed to an  $H_2$  and  $CO_2$  ambient ( $\leq 1.2\% CO_2$ ) at  $1000^\circ C$  for 1 hr. The wafers were hydrophobic before and after exposure to the  $H_2$  and  $CO_2$  ambient. Ellipsometric measurements showed that the wafers had  $\leq 15\text{Å}$  of  $SiO_2$  before and after. Now the question arose whether other oxidants produced similar results. This led us to repeat the above experiment with  $N_2O$  which resulted in the growth of  $\approx 600\text{Å}$   $SiO_2$  on the silicon wafers (23). To check whether the formation of  $SiO_2$  from the  $N_2O$  and  $H_2$  reaction was due to the  $H_2O$  formation or to the decomposition of  $N_2O$  and subsequent oxidation of silicon by oxygen, we repeated the experiment with  $N_2O$  and  $N_2$ . The resulting film was only  $\sim 150\text{Å}$  thick (23). Clearly,  $H_2O$  is formed when wafers are heated in  $N_2O$  and  $H_2$ , whereas  $H_2O$  is not likely to form from  $CO_2$  and  $H_2$  under the flow conditions of the reactor. This conclusion is consistent with, and supported by, two facts: (i) when the  $SiH_4$ - $N_2O$ - $H_2$  system is used for  $SiO_2$  deposition ( $850$ - $1000^\circ C$ ), the reaction chamber clouds very rapidly (23), whereas when the  $SiH_4$ - $CO_2$ - $H_2$  system is used there is no evidence of reaction-chamber clouding; (ii) the deposition rate of  $SiO_2$  from the  $SiH_4$ - $N_2O$ - $H_2$  system is  $\sim 2$ - $10$  times higher than the  $SiH_4$ - $CO_2$ - $H_2$  system, depending on deposition temperature ( $850$ - $1000^\circ C$ ) for identical  $SiH_4$  and oxidant mole fraction (23).

Experiments with mixtures of  $H_2$  and  $O_2$  and of  $N_2$  and  $O_2$  showed results similar to those of  $H_2$  and  $N_2O$  and of  $N_2$  and  $N_2O$ ; i.e., a higher thickness of thermal  $SiO$  was grown with the  $H_2$  and  $O_2$  mixture. Clearly,  $H_2O$  was being produced by the reaction of hydrogen and oxygen. We then attempted to study the rate of reaction of  $SiH_4$  with  $H_2O$  using the  $SiH_4$ - $O_2$ - $H_2$  system. The task, however, was nearly impossible because of the chamber clouding which necessitated reactor cleaning after every run. We were able to obtain deposition-rate data at  $800$ - $850^\circ C$ , however, before abandoning the effort. The deposition rate of  $SiO_2$  from the  $SiH_4$ - $O_2$ - $H_2$  system was nearly an order of magnitude greater than that obtained from the  $SiH_4$ - $CO_2$ - $H_2$  system for identical temperature,  $SiH_4$ , and oxidant mole fractions (24). The results of the experiments with  $SiH_4$ - $O_2$ - $H_2$  and  $SiH_4$ - $N_2O$ - $H_2$  are at variance with the water-gas mechanism for the  $SiH_4$ - $CO_2$ - $H_2$  system because, if  $H_2O$  is produced from  $CO_2 + H_2$ , which subsequently reacts with  $SiH_4$  to produce  $SiO_2$ , then the deposition rate of  $SiO_2$  should not significantly change, irrespective of the source of  $H_2O$ .

Finally, Tingey (22) experimentally showed that the water-gas reaction is homogeneous, i.e., that  $H_2O$  is produced in the gas phase. This should result in the homogeneous reaction of  $SiH_4$  and  $H_2O$ ; yet the  $SiH_4$ - $CO_2$ - $H_2$  reaction is singularly characterized by the lack of homogeneous reaction, i.e., no clouding of the reaction chamber by gas-phase reaction. The above experimental and activation energy data neither support nor are consistent with the water-gas reaction mechanism for  $SiH_4$ - $CO_2$ - $H_2$ . It is therefore probable that the  $SiH_4$ - $CO_2$  reaction could proceed via direct oxidation of silane, as suggested by Swann and Payne (4), some complex free-radical chain mechanism, as alluded to by Rand and Ashworth (8), or any other mechanism that does not include water-gas reaction as a step.

### Summary and Conclusion

We have presented the results of  $SiH_4$ - $CO_2$  reaction in  $H_2$  in the temperature range  $850$ - $1050^\circ C$ . We have used a multiple-wafer reactor in sharp contrast to Swann and Payne's single-wafer reactor. Our results should find more application in CVD practice because the flow of gases is nearly parallel to the wafer surface. Unlike Swann and Payne, we have been able to isolate the order of the  $SiH_4$ - $CO_2$  reaction with respect to  $SiH_4$

and the activation energy and frequency factor of the reaction. However, care should be exercised in extrapolating and using these results to predict the  $SiO_2$  deposition rate for  $SiH_4$  concentrations larger than  $0.06$ - $0.07\%$  because, at higher concentrations than these, the  $SiO_2$  films become silicon-rich; i.e., codeposition of Si and  $SiO_2$  occurs.

We have shown that the physical and electrical properties of  $SiO_2$  deposited at  $1000^\circ C$  are comparable to those of steam-grown oxide. In fact, the fast surface-state densities are considerably lower in these CVD oxides than in steam-grown oxides. The low level of fast surface-state density may be attributed to the use of  $H_2$  during deposition. The stability of these oxides under temperature ( $200^\circ C$ ) and bias  $\pm 2 \times 10^6$  V/cm has been demonstrated. The negative effects of post-deposition anneal in  $N_2$  at a temperature higher than the deposition temperature have also been shown.

The use of  $CO_2$  does not result in a homogeneous reaction, especially at higher temperatures, i.e., of the order of  $1000^\circ C$ . This is a significant advantage, since it keeps the reactor down time to a minimum. However, the use of  $CO_2$  has often raised the possibility of carbon inclusion. Though we do not have any direct evidence of the presence or absence of carbon in  $SiO_2$  films deposited from  $SiH_4$ - $CO_2$ - $H_2$ , trace quantities of carbon may well be incorporated in these films. None of the measured physical and electrical properties, however, show any unusual or detrimental effects of these trace impurities, if present.

Finally, the CVD  $SiO_2$  film from  $SiH_4$ - $CO_2$ - $H_2$  could be readily used as a photolithographic mask for films like  $Si_3N_4$  and in the field or the gate region of an integrated FET circuit.

### Acknowledgments

The authors are indebted to A. A. Kozul and T. O. Williams for preparing the samples.

Manuscript submitted April 10, 1974; revised manuscript received July 16, 1975. This was Paper 50 presented at the San Francisco, California, Meeting of the Society, May 12-17, 1974.

Any discussion of this paper will appear in a Discussion Section to be published in the December 1976 JOURNAL. All discussions for the December 1976 Discussion Section should be submitted by Aug. 1, 1976.

Publication costs of this article were partially assisted by IBM Corporation.

### REFERENCES

1. S. K. Tung and R. E. Caffrey, *Trans. Met. Soc. AIME*, **233**, 572 (1965).
2. M. J. Rand, *This Journal*, **114**, 274 (1967).
3. T. L. Chu, J. R. Szedon, and G. A. Gruber, *Trans. Met. Soc. AIME*, **242**, 532 (1968).
4. R. C. G. Swann and A. E. Payne, *This Journal*, **116**, 1014 (1969).
5. W. J. Kroll, R. L. Titus, and J. B. Wagner, Abstract 13, p. 31, The Electrochemical Society Extended Abstracts, Spring Meeting, Houston, Texas, May 7-11, 1972.
6. M. L. Barry, in "Chemical Vapor Deposition, 2nd International Conference," John M. Blocher, Jr. and James C. Withers, Editors, The Electrochemical Society Softbound Symposium Series, New York (1970).
7. T. Miyazaki, I. Yoshida, M. Horiuchi, and T. Tokuyama, *ibid.*, p. 571.
8. M. J. Rand and J. L. Ashworth, *This Journal*, **113**, 48 (1966).
9. L. V. Gregor, in "Physics of Thin Films," Vol. 3, p. 133, Georg Hass and R. E. Thun, Editors, Academic Press, Inc., New York (1966).
10. V. Y. Doo, D. W. Boss, R. Valletta, and W. A. Pliskin, Paper 42, presented at Electrochemical Society New York, New York, Meeting, May 4-9, 1969.
11. E. O. Ernst, D. J. Hurd, and G. Seeley, U. S. Pat. 3, 424,629, Assigned IBM Corporation.
12. F. G. Allen, *J. Appl. Phys.*, **28**, 1510 (1957).
13. O. Levenspiel, "Chemical Reaction Engineering," John Wiley & Sons, Inc., New York (1967).



14. G. W. Castellan, "Physical Chemistry," p. 607, Addison-Wesley Publishing Co., Inc., Reading, Mass. (1964).
15. W. A. Pliskin and H. S. Lehman, *This Journal*, **112**, 1013 (1965).
16. R. J. Kriegler, Y. C. Cheng, and D. R. Colton, *ibid.*, **119**, 388 (1972).
17. A. Goetzberger, A. D. Lopez, and R. J. Strain, *ibid.*, **120**, 90 (1973).
18. M. Kuhn, *Solid-State Electron.*, **13**, 873 (1970).
19. R. Castange, C. Y. Lebd. *Se'anc, Acad. Sci. (Paris)*, **267**, 866 (1968).
20. D. R. Kerr, Private communication.
21. W. Steinmaier and J. Bloem, *This Journal*, **111**, 206 (1964).
22. G. L. Tingey, *J. Phys. Chem.*, **70**, 1406 (1966).
23. R. L. Bratter and A. K. Gaind, Unpublished work.
24. R. L. Bratter, Unpublished work.

## Fabrication of P-Channel Silicon Gate LSI Devices with Si<sub>3</sub>N<sub>4</sub>/SiO<sub>2</sub> Gate Dielectric

Alfred P. Turley,\* R. M. McLouski,\* P. R. Reid, and D. H. McCann

*Westinghouse Advanced Technology Laboratory, Baltimore, Maryland 21203*

### ABSTRACT

Processing of p-channel silicon gate devices with a Si<sub>3</sub>N<sub>4</sub>/SiO<sub>2</sub> gate dielectric is described in detail. Some attractive features of this particular process include polysilicon to silicon contacts, improved metal step coverage obtained with a glass flow anneal, low fast surface-state density for good 1/f noise performance, and high parasitic field threshold voltages obtained by ion implantation of arsenic.

Because of the work function difference between p-type polycrystalline silicon gate electrodes and lightly doped n-type silicon substrates, most p-channel silicon gate devices have been fabricated on <111> oriented silicon substrates. This avoids the possibility of very low threshold or depletion mode devices which can result if <100> oriented substrates are used. This result is a direct consequence of the lower fixed positive charge density at the SiO<sub>2</sub>-Si interface of <100> oriented silicon substrates. However, for devices used in analog signal processing, the use of <111> material will degrade the 1/f noise performance of such IGFET'S because of the high fast surface-state density associated with this orientation. To take advantage of the better 1/f noise performance obtained on <100> material and still maintain a reasonable threshold voltage (-1.3V), silicon gate devices can be fabricated with a Si<sub>3</sub>N<sub>4</sub>/SiO<sub>2</sub> gate dielectric. The desired threshold voltage can be obtained by controlling the amount of fixed positive charge at the nitride-oxide interface formed during the nitride deposition. Other advantages of the dual dielectric structure are: (i) Si<sub>3</sub>N<sub>4</sub> is superior to SiO<sub>2</sub> as a boron diffusion barrier (2), (ii) the composite structure has better integrity than a SiO<sub>2</sub> gate, and (iii) higher transconductance FET's result from the higher dielectric constant of Si<sub>3</sub>N<sub>4</sub>.

Other attractive features of this particular process are polysilicon-silicon contacts which allow very high packing densities because they take up less area than metal-silicon contacts, improved metal step coverage obtained with a glass flow anneal (4), and high parasitic field threshold voltages obtained by ion implantation of the surface (except active regions) with arsenic.

### Process Sequence

An outline of the process is given in the flow chart in Table I. The starting wafer material is 4-8 ohm-cm, <100>, n-type. The first step is the formation of the gate oxide. This is thermally grown in an atmosphere of 10% HCl + 90% O<sub>2</sub> for 13 min at 1000°C. The resulting oxide thickness is about 300Å. This is followed by the deposition of the gate nitride. About 800Å of

silicon nitride is deposited at 750°C with an ammonia to silane ratio of 250:1. In the next step, the first photoengraving operation is performed. A mask is applied to define islands of nitride which will ultimately become the active devices. A photoresist mask is used and the silicon nitride is plasma etched (5). The 300Å of oxide under the nitride stops the plasma etching process. With the photoresist still on the wafer, an arsenic implant is next performed at an energy of 80 keV and a dose of  $5 \times 10^{11}$  cm<sup>-2</sup>. The photoresist acts as a mask which prevents penetration of the arsenic into active device regions. After photoresist removal, a cross section of a transistor structure appears as in Fig. 1. The transistor gate, source, and drain will be formed in the region defined by the island of silicon nitride. The arsenic implant in the surrounding regions will prevent parasitic transistor action by keeping the surface from inverting at voltages less than -35V. The next processing step forms the field oxide region by steam oxidation at 1100°C.

About 10 kÅ of SiO<sub>2</sub> is grown in 2.5 hr in the regions surrounding the nitride islands. Only about 300Å of the nitride is oxidized. This is removed by dip etching for 30 sec in a 10:1 HF solution. At this point in the process, the structure is annealed in dry O<sub>2</sub> for 30 min at

Table I. Process flow chart

1. Starting material: 4-8 ohm-cm, <100>, n-type
2. Gate oxidation: 300Å (10% HCl + 90% O<sub>2</sub>, 13 min at 1000°C)
3. Gate nitride: 800Å (NH<sub>3</sub>/SiH<sub>4</sub> = 250 at 750°C)
4. Device window mask (plasma etch Si<sub>3</sub>N<sub>4</sub>)
5. Ion implant arsenic (E = 80 keV, dose =  $5 \times 10^{11}$  cm<sup>-2</sup>)
6. Steam oxidation: 10 kÅ (H<sub>2</sub> + O<sub>2</sub>, 150 min at 1100°C)
7. Etch oxidized nitride (~300Å)
8. O<sub>2</sub> anneal (30 min at 1050°C)
9. Polysilicon-silicon contact window mask
10. Polysilicon deposition (4 kÅ at 700°C)
11. Polysilicon gate and interconnect mask (plasma etch poly and nitride, chem. etch gate oxide to define self-aligned gate)
12. Boron diffusion (diborane source)
  - a. Deposition: 18 min at 980°C
  - b. Drive: 60 min, O<sub>2</sub> at 1000°C
13. Phosphorus-doped oxide deposition (~5% phosphorus, 15 kÅ)
14. Via and contact window mask
15. Glass flow anneal (O<sub>2</sub>, 20 min at 1050°C)
16. Hydrogen anneal (30 min H<sub>2</sub> at 800°C)
17. Dip etch 30 sec in 10:1 HF (removes oxide from windows in doped glass)
18. Metallization (10 kÅ of Al-Si)
19. Metal interconnect mask
20. Sinter metal (30 min, N<sub>2</sub> at 500°C)

\* Electrochemical Society Active Member.

Key words: polysilicon, insulator, MOSFET, noise.

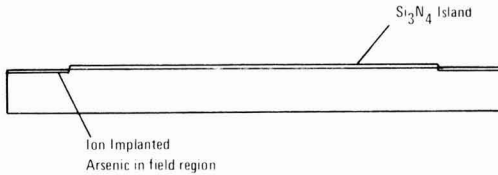


Fig. 1. Device cross section after ion implantation of arsenic in field regions. Step 5 in process flow chart.

1050°C. This anneal converts about 50Å of the nitride surface to oxide and has the effect of stabilizing the structure (6). Figure 2 shows the transistor structure cross section at this point of the process. The device is now ready for opening contact windows for the polysilicon-silicon contacts. Again, a photoresist mask is used and the silicon nitride is plasma etched followed by an oxide etch. Figure 3 shows the device cross section at this point. Polysilicon is now deposited to a thickness of 4000Å with a deposition temperature of 700°C. A mask to define the polysilicon interconnect pattern and the self-aligned gate structure is next applied. A photoresist mask is used and the polysilicon is plasma etched. The plasma etching continues through the polysilicon and the silicon nitride around the gate electrode. A short oxide etch (~300Å) then completes the self-aligning gate definition. The transistor cross section at this point is shown in Fig. 4. A boron diffusion now forms the source and drain and also dopes the polysilicon conductor lines. Reoxidation in dry O<sub>2</sub> for 60 min at 1000°C during the boron drive forms about 700Å of SiO<sub>2</sub> over the polysilicon and source-drain regions. This oxide prevents counterdoping of the p-type regions by the phosphorus-doped oxide deposited in the next step.

This doped oxide is about 15 kÅ thick and contains about 5-6% phosphorus. The structure at this point is shown in Fig. 5. Contact windows and vias are opened in the doped oxide. An anneal is performed on the phosphorus-doped oxide under the following conditions: (i) 20 min, O<sub>2</sub> at 1050°C; (ii) 30 min, H<sub>2</sub> at 800°C. This high temperature anneal causes the viscosity of the doped oxide to decrease to the point where it begins to flow, giving rise to smooth oxide

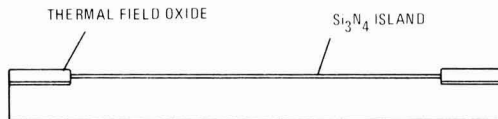


Fig. 2. Device cross section after formation of field oxide and anneal. Step 8 in process flow chart.

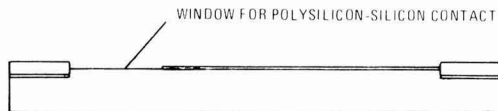


Fig. 3. Device cross section after etching of contact windows for polysilicon-silicon contacts. Step 9 in process flow chart.

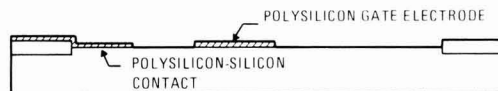


Fig. 4. Device cross section after definition of polysilicon conductor lines. Step 11 in process flow chart.

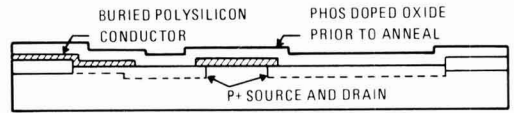


Fig. 5. Device cross section after source-drain diffusion and deposition of phosphorus-doped oxide insulator. Step 13 in process flow chart.

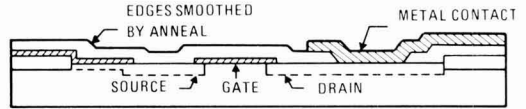


Fig. 6. Device cross section at completion of process

edges over polysilicon steps and via and contact windows. A small amount of oxide is formed in the open windows during the anneal. This can be removed by a short dip etch before metallization. The hydrogen part of the anneal is the last high temperature step before metallization greatly reduces the number of fast surface states at the Si-SiO<sub>2</sub> interface in the gate regions, which in turn produces devices with excellent 1/f noise characteristics. The effects of the glass flow anneal are shown in the SEM photograph of Fig. 7. Note the excellent metal coverage of oxide steps.

The processing is completed with a metal deposition (10 kÅ of Al-Si), interconnect photoengraving, and sintering. The completed cross-section transistor structure is shown in Fig. 6. A photograph of a section of a completed device is shown in Fig. 8.

### Device Characteristics

The threshold voltage of transistors fabricated by this process is greatly influenced by fixed positive charge formed at the silicon nitride-silicon dioxide interface in the gate dielectric. The magnitude of this charge is strongly influenced by the silicon nitride deposition parameters. Our nitride is deposited at 750°C with an ammonia/silane ratio of 250:1. The parameters that influence charge magnitude are deposition rate and deposition temperature. Temperature has by far the strongest effect with deposition rate being a second-order effect. Figure 9 shows the deposition temperature effect by comparing the C-V characteristics of MOS capacitors formed at deposition temperatures of 750° and 800°C. The negative shift of the 800°C curve indicates a larger fixed positive inter-

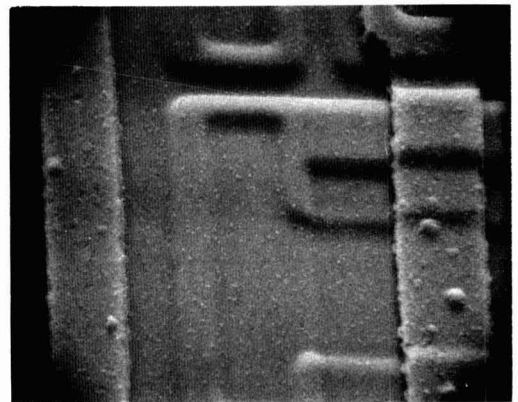


Fig. 7. SEM photograph showing the effects of the glass flow anneal on smoothing oxide edges and sloping oxide steps.

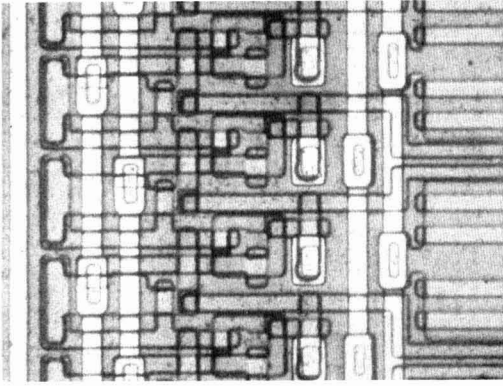


Fig. 8. Photograph of a portion of a completed LSI device. Shown are several stages of a dynamic shift register.

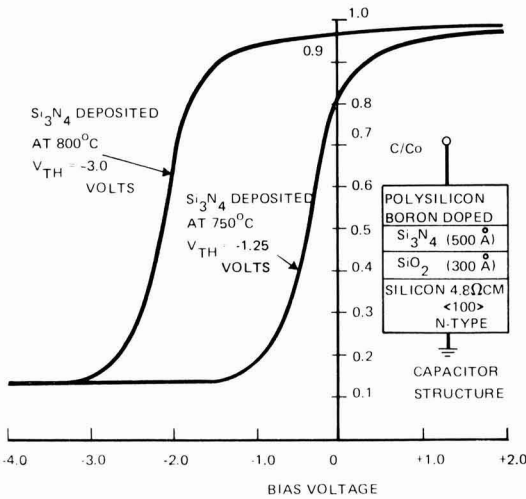


Fig. 9. MOS C-V curves showing the effect of nitride deposition temperature on the magnitude of the fixed charge formed at the nitride-oxide interface.

face charge. This data indicates a nitride charge of  $2 \times 10^{12}$  charges/cm<sup>2</sup> at the 800°C deposition temperature and  $7 \times 10^{11}$  charges/cm<sup>2</sup> at the 750°C deposition temperature. The charge at the nitride-oxide interface is transformed to a charge at the silicon surface ( $Q_{eff}$ ) by the following equation

$$Q_{eff} = \frac{\frac{\epsilon_{ox}}{\epsilon_n} t_n}{t_{ox} + \frac{\epsilon_{ox}}{\epsilon_n} t_n} Q_n \quad [1]$$

In this equation, one can think of the term  $(\epsilon_{ox}/\epsilon_n) t_n$  as an effective oxide thickness of the nitride as far as its dielectric properties are concerned. Since  $\epsilon_{ox}/\epsilon_n \sim 0.6$ , one sees that 500Å of nitride is equivalent to 300Å of oxide for capacitance calculations.

The threshold voltage is given by the equation

$$V_{th} = \phi_{GS} - \frac{1}{C_i} (Q_{eff} + Q_{ss} + \sqrt{2\epsilon_s q N_d (2\phi_F)}) \quad [2]$$

Thus one concludes that increasing  $Q_{eff}$  will make the threshold voltage more negative. The threshold voltage of 24 devices from different wafers in different runs was measured. The mean and standard deviation were

-1.31 and 0.17V, respectively. The transconductance at  $V_{GS} = -5V$  was also measured and normalized to unity width to length ratio. The mean and standard deviation were 32 and 3.84  $\mu$ -mhos, respectively.

The stability of the threshold voltage was examined by making temperature-bias stressed C-V measurements. Figure 10 shows the flatband voltage shift vs. time for a +15V bias at 200°C. The instabilities noted are not caused by ionic contamination but by the difference in the resistivity of the nitride and oxide (6). The resistivity of the silicon nitride is less than the oxide resistivity; hence, when bias is applied, the nitride oxide layers form a resistive divider and charge slowly accumulates at the nitride oxide interface. One can increase the nitride resistivity by oxidizing its surface. This small amount of oxide on the nitride surface effectively increases the nitride resistivity and improves stability. This effect is shown in Fig. 10 where

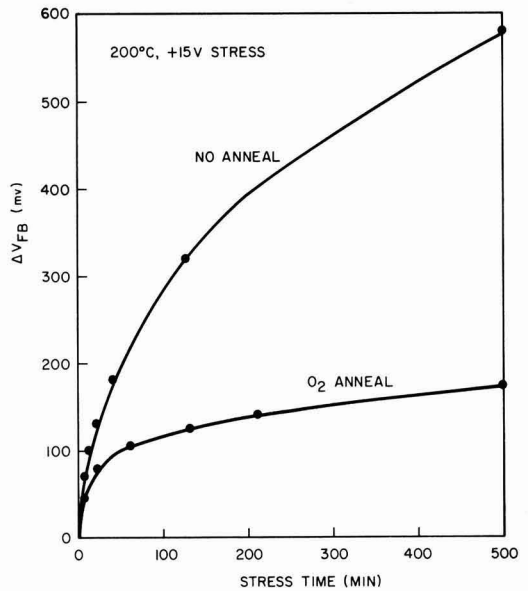


Fig. 10. Flatband voltage shift under temperature-bias stress

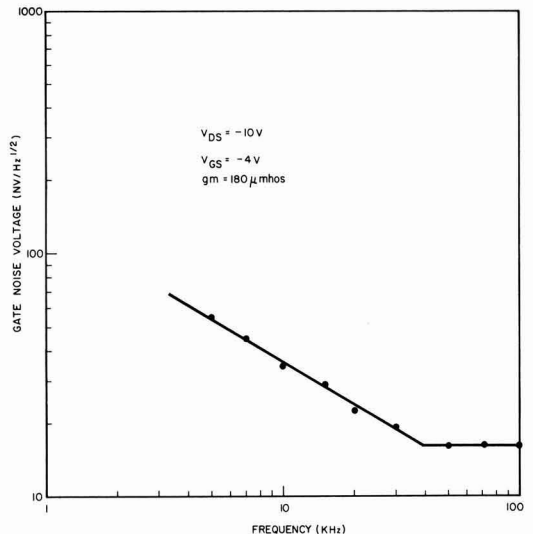


Fig. 11. Noise spectra of typical transistor

oxidized and nonoxidized samples are compared. This is the reasoning behind the oxygen anneal in step 8 of the process as indicated in Table I. Under a negative bias stress of  $-15\text{V}$  at  $200^\circ\text{C}$ , the oxidized samples shifted only 20 MV and saturated to this value after 5 min of stress. The nonoxidized sample shifted 40 MV under the same conditions.

The noise performance achieved with these devices is shown in Fig. 11. Here is plotted the noise voltage referred to the gate vs. frequency. The  $1/f$  portion of the noise spectra shows about a 12% improvement over the performance attained with an equivalent device made with a metal gate and an oxide insulator.

### Conclusion

We have devised and demonstrated a process for fabrication of p-channel silicon gate MOS devices with a silicon nitride/silicon dioxide gate dielectric for both digital and analog LSI applications. The process features include small area polysilicon-silicon contacts; smoothed, sloped oxide steps for excellent metal coverage; low fast surface-state density with a  $\text{H}_2$  anneal; good threshold stability with an  $\text{O}_2$  anneal; high parasitic field threshold voltages from ion implantation of arsenic in the field oxide regions.

### Acknowledgments

The authors wish to acknowledge the help in process development given by D. A. Tremere, P. D. Blais, P. L.

Hower, P. Rai-Choudhury, and R. N. Ghostagore of the Westinghouse Research and Development Center, Pittsburgh, Pennsylvania. The authors also wish to thank Dr. M. Lonky for the noise measurements.

Manuscript submitted April 16, 1975; revised manuscript received Aug. 21, 1975. This was Paper 189 presented at the New York, New York, Meeting of the Society, Oct. 13-17, 1975.

Any discussion of this paper will appear in a Discussion Section to be published in the December 1976 JOURNAL. All discussions for the December 1976 Discussion Section should be submitted by Aug. 1, 1976.

Publication costs of this article were partially assisted by Westinghouse Electric Corporation.

### REFERENCES

1. H. C. Lin, J. L. Halsor, and P. J. Hayes, *IEEE Trans. Electron Devices*, **ED-19**, 1199 (1972).
2. V. Doo, *ibid.*, **ED-13**, 561 (1966).
3. S. Abbas, A. Nagarajan, and P. Stern, Paper 171 presented at The Electrochemical Society Meeting, Miami Beach, Florida, Oct. 8-13, 1972.
4. W. E. Armstrong and D. L. Tolliver, *This Journal*, **121**, 307 (1974).
5. L. L. Fritz, *Solid State Technol.*, **14**, No. 12, 43 (1971).
6. R. C. Dockerty, C. A. Barile, A. Nagarajan, and S. M. Zalar, *Rel. Phys. Symp.*, 159 (1973).
7. R. C. Dockerty and M. D. Cowan, Paper 51 presented at The Electrochemical Society Meeting, San Francisco, California, May 12-17, 1974.

## Studies of the Ti-W Metallization System on Si

J. M. Harris,\* S. S. Lau, and M.-A. Nicolet

California Institute of Technology, Pasadena, California 91125

and R. S. Nowicki\*<sup>1</sup>

Fairchild Camera and Instrument Corporation, Research and Development Laboratory,  
Palo Alto, California 94304

### ABSTRACT

MeV backscattering spectrometry and x-ray diffraction are used to investigate the behavior of sputter-deposited Ti-W mixed films on Si substrates. During vacuum anneals at temperatures of  $700^\circ\text{C}$  for several hours, the metallization layer reacts with the substrate. Backscattering analysis shows that the resulting compound layer is uniform in composition and contains Ti, W, and Si. The Ti:W ratio in the compound corresponds to that of the deposited metal film. X-ray analyses with Reed and Guinier cameras reveal the presence of the ternary  $\text{Ti}_2\text{W}_{(1-x)}\text{Si}_2$  compound. Its composition is unaffected by oxygen contamination during anneal, but the reaction rate is affected. The rate measured on samples with about 15% oxygen contamination is linear, of the order of  $0.5 \text{ \AA}/\text{sec}$  at  $725^\circ\text{C}$ , and depends on the crystallographic orientation of the substrate and the d-c bias during sputter deposition of the Ti-W film.

Titanium and tungsten have both been used for many years as materials for metallizing integrated circuits (1). Tungsten is used because its coefficient of expansion closely matches that of silicon, and titanium is used because of its strong adherence to oxides. A metallization scheme has also been developed which uses a mixture of titanium and tungsten (2). Like many of the transition materials, Ti and W both form silicides. The formation of  $\text{WSi}_2$  from thin tungsten films on Si has been studied by several authors (3, 4). The formation of  $\text{TiSi}_2$  by thin films on Si has also been studied (5), though not to as great an extent as  $\text{WSi}_2$ . To our knowledge, the present investigation is the first to con-

sider the interaction of a mixed thin film with silicon. This study shows that, like Ti and W individually, a thin composite layer of Ti and W deposited on Si by sputtering and annealed in vacuum forms a disilicide. This ternary disilicide is studied using the techniques of x-ray diffraction,  $^4\text{He}$  backscattering spectrometry (BS), and Auger electron spectrometry (AES).

### Sample Preparation

Films of 1000-1500Å were deposited by RF sputtering from an arc-melted  $\text{Ti}_{0.3}\text{W}_{0.7}$  target onto silicon and carbon substrates. The silicon substrates were n- or p-type, 1-10 ohm-cm single crystal wafers of  $\langle 111 \rangle$ ,  $\langle 110 \rangle$ , or  $\langle 100 \rangle$  orientations which had been mechanically polished and chemically etched. The polycrystalline carbon substrates were 0.5 in. squares and were polished and cleaned prior to sputter deposition.

\* Electrochemical Society Active Member.

<sup>1</sup> Present address: Hewlett-Packard Advanced Product Division, Cupertino, California 95014.

Key words: thin-film reactions, silicide formation, Ti-W metallization,  $^4\text{He}$  backscattering.

During deposition, the substrates rested on a water-cooled pallet and the deposition temperature was monitored by a shielded iron-constantan thermocouple placed on the substrate surface. Substrates were loaded through a side loader which was evacuated by a cryogenic pumping station so as to prevent contamination of the target during loading.

Prior to loading, the silicon substrates were dipped in HF, rinsed in deionized water, and dried with high purity isopropanol. After loading, the sputtering chamber was evacuated to a background pressure of  $1 \times 10^{-6}$  Torr. Argon of 5N purity which had passed through a titanium purifier was used to backfill the chamber. The Ti-W target was given a short presputter to insure a clean surface, and the substrates were sputter cleaned immediately before deposition. During deposition the substrates were held at a negative bias ranging from 0 to 50V with respect to ground. The maximum temperature measured during deposition was about 300°C. The Ti-W films deposited on Si have a resistivity of about 80  $\mu\text{ohm-cm}$ , irrespective of the substrates or bias voltage. The films deposited on carbon were analyzed by BS to check for possible contaminants. Carbon substrates rather than Si were used for these measurements so that the BS signal from the substrate would not interfere with signals from possible nitrogen or oxygen impurities. No oxygen or nitrogen could be detected. The samples deposited with -50V bias showed the largest amount of contamination, which consisted of Ar and was less than 2 atomic per cent (a/o). Examination of the films on silicon substrates by SEM at 30K magnification revealed a featureless surface.

Anneals were performed in an evacuated quartz-tube furnace. The furnace was pumped from one end by a LN<sub>2</sub> trapped oil diffusion pump and from the other end by a water-cooled titanium sublimation pump. The vacuum during anneals was typically  $7 \times 10^{-7}$  Torr. The temperature in the center of the furnace was measured by a Chromel-Alumel thermocouple which had been calibrated to an accuracy of  $\pm 1^\circ\text{C}$  against a mercury thermometer to a temperature of 350°C. The thermometer was calibrated against the freezing point and the boiling point (corrected for barometric pressure) of H<sub>2</sub>O. The temperature stability of the furnace was measured to be  $\pm 2^\circ\text{C}$  over a period of 20 hr. The furnace was constructed so that many samples could be loaded and annealed sequentially during a single pump-down, and samples were always placed at the position within the furnace where it had been calibrated. Samples could be grouped and annealed simultaneously in the furnace.

### Analytical Techniques

**Backscattering spectrometry (BS).**—The experimental setup and analytical method for BS have been reviewed elsewhere (6). In brief, the technique consists of placing a sample in a beam of monoenergetic <sup>4</sup>He<sup>+</sup> ions and energy analyzing those He atoms which are scattered from the sample. BS with MeV <sup>4</sup>He<sup>+</sup> ions provides information on concentration profiles in depth with a resolution of about 200Å and to depths of about 3000-5000Å. In thicker films, the depth resolution degrades due to energy straggling within the target. The beam spot is typically 1-2 mm<sup>2</sup> and hence backscattering analysis required samples whose lateral composition is uniform over at least such a dimension.

**X-ray analysis.**—Two types of x-ray diffraction analyses were performed. The first type uses the Reed Camera (7) geometry which is basically a glancing angle x-ray diffraction setup with a fixed angle of incidence. The structure of the thin-film samples is identified in a manner similar to that employed with the Debye-Scherrer camera. Because of the glancing angle of incidence of the x-rays (8-14° with respect to the specimen surface), a relatively large volume is examined although the samples are thin. For example, at an incident angle of 10° the x-ray path length is 6

times the film thickness. The incident x-ray beam used for the exposure was CuK<sub>α</sub> radiation collimated through two pinholes. The diffraction pattern is recorded on film placed along a 5 cm radius from the sample center.

The second type of x-ray diffraction analysis performed used a Guinier camera (8). This is a transmission x-ray diffraction apparatus in which the sample rotates with respect to the beam during exposure. CuK<sub>α</sub> radiation was used in conjunction with x-ray film to record the diffraction patterns. The Guinier camera requires thin samples so as to not substantially attenuate the diffracted x-rays. To this end, the rear side of a reacted sample was lapped until the sample thickness was reduced to between 50-60 $\mu$ . The sample was then ultrasonically cleaned and rinsed in diluted HF. A similar sample of the bare silicon substrate was also prepared in this way. By comparing the x-ray diffraction patterns from both samples, the diffraction lines due to the silicide could be identified.

Given the camera constant and an accurate measurement of the silicide diffraction line spacing, determination of the cell parameters can be made. The camera constant was determined by measurement of the camera radius and verified using the diffraction lines from a strain-free sample of polycrystalline silicon powder. The silicide diffraction line spacing was measured with an optical comparator to  $\pm 0.01$  mm, which gave an uncertainty of  $\pm 0.01\text{Å}$  in the unit constants. The advantage of the Guinier technique is to enable an accurate determination of the cell constants, whereas the Reed camera can detect the presence of phases without special preparation of the specimens.

**Auger electron spectroscopy (AES).**—AES has been reviewed recently in the literature (9). This technique uses the decay by electron emission of sample atoms which experience inner shell ionization by an energetic electron beam. Energy analysis of these emitted Auger electrons allows one to perform an elemental analysis of the sample surface. Typically, sensitivities of about 1 a/o can be obtained.

Auger electrons originate only from atoms excited in the outermost atomic layers. Hence, elemental depth profiling requires a sequential removal of thin layers between measurements. This can be accomplished by sputtering. To obtain the depth profile of a sample requires knowledge of the sample's sputtering rate and the sputtering time. BS can be used conveniently to determine the film thickness and thereby calibrate the sputtering rate.

AES and BS nicely complement each other. AES is more sensitive than BS for profiling light elements in heavy matrixes, and BS can be used to measure the thickness and composition of the film quantitatively in a relatively short time ( $\sim 10$ -20 min).

### Results

**Characterization of ternary silicide.**—Films of Ti-W having about 30 a/o Ti (10% by weight) prepared as described above were vacuum annealed at 800°C for 20 min. The surface changed from the smooth metallic luster of Ti-W to a deep silver-gray. Examination by SEM at 4500 $\times$  magnification revealed a uniform and gently undulating surface. The undulations were typically 2.5  $\mu\text{m}$  across and  $< 0.05 \mu\text{m}$  in height (as determined by measurement with a Sloan Dektak).

X-ray diffraction analysis by Reed camera revealed the presence of only one compound (Fig. 1). The diffraction pattern corresponds to that described by the ASTM powder diffraction compilation No. 6-0599. This compound has a chemical formula of Ti<sub>2</sub>W<sub>3</sub>Si<sub>2</sub>, where  $x + y = 1$ , with a hexagonal CrSi<sub>2</sub>-type (C-40) structure. X-ray analysis by the Guinier camera supported the Reed camera results in that no crystal structures other than the C-40 type were detectable. The line spacings from the Guinier photographs gave cell parameters of  $a_0 = 4.61 \pm 0.01\text{Å}$  and  $c_0 = 6.48 \pm 0.01\text{Å}$ .



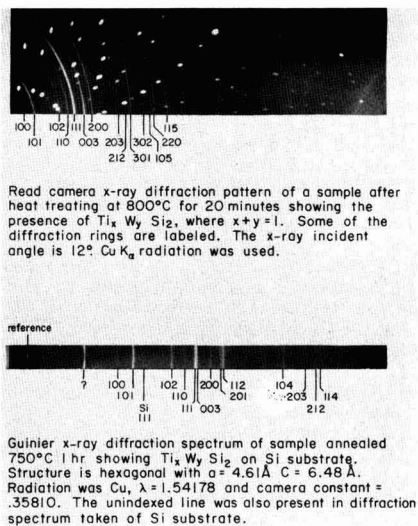


Fig. 1. X-ray diffraction pattern taken with Reed camera (top) and Guinier camera (bottom) of reacted samples.

2 MeV  $^4He^+$  BS analysis of films reacted at 725°C for 40 min revealed that the atomic concentration ratio of the films is  $Ti:W:Si = 0.3:0.7:2.0$  (Fig. 2). The compound maintains this composition at temperatures ranging from 675° to 900°C. Additional experiments established that the compound formed was independent of substrate orientation, doping type, substrate bias during sputter deposition, and the sample contamination by oxygen during annealing.

Once formed, the compound adheres strongly to the silicon substrate. The compound seems unaffected by hot  $H_2O_2$ , HF, or CP-4, and dissolves only slowly in aqua regia. Indium solder would not adhere to the compound.

**Kinetics of silicide formation.**—The reaction rate of the compound formation was investigated by BS on samples annealed in vacuum for increasing periods of time. To translate the energy scale of a BS spectrum into a depth scale, we assumed a density of  $7.54 \times 10^{22}$  atom/cm<sup>3</sup> for the compound, as calculated from the measured unit cell parameters. Using this density, 10 keV in a BS spectrum corresponds to about 106Å of compound.

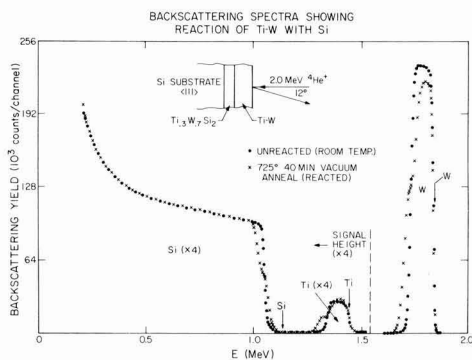


Fig. 2. Backscattering spectra showing a virgin (room temperature) and a covered, annealed (725°C, 40 min,  $7 \times 10^{-7}$  Torr) sample of Ti-W on Si. The Si substrate is  $\langle 111 \rangle$  single crystal n-type with resistivity of 10 ohm-cm. The Ti-W film was deposited with  $-50V$  bias. Arrows indicated the position of signals from Si, Ti, and W on the sample surface.

Films deposited on  $\langle 111 \rangle$  silicon at  $-50V$  bias and annealed at  $5 \times 10^{-6}$  Torr and 725°C were found to have reaction rates of about 9.7 Å/min. Improving the vacuum to  $7 \times 10^{-7}$  Torr and covering the metallized side of the sample with a clean Si wafer during anneal increased the reaction rate by approximately a factor of 2 (Fig. 5). Figure 3 shows a  $\langle 111 \rangle$  silicon sample of which half of the metallized side was covered with a Si wafer during an anneal at  $7 \times 10^{-7}$  Torr and 725°C for 45 min. The uncovered side (top) shows little reaction whereas the covered side (bottom) is almost completely reacted. A subsequent AES analysis of this sample (Fig. 4) reveals that the uncovered half of the sample has a larger concentration of oxygen than does the covered half.

In Fig. 2 the ratio of the signal height of the remaining unreacted tungsten to that of the unreacted silicon substrate is smaller than that same ratio measured on the virgin sample. This was true for partially reacted samples which had been covered and annealed in the highest vacuum attainable. If this difference is attributed to oxygen contamination, then the samples annealed in the cleanest vacuum still contained up to 15 a/o oxygen. Since oxygen has been shown to influence rates, the kinetics studies performed here are to be interpreted with caution and the results should be regarded as preliminary.

Reaction rate studies at 750°, 725°, and 700°C were performed on covered samples annealed at  $7 \times 10^{-7}$  Torr. Samples annealed at each temperature were all cut from the same wafer and loaded simultaneously. The samples were then annealed sequentially. When precautions to reproduce the vacuum were taken, the results were reproducible. The analysis of the backscattering yields established that after anneal all the samples were contaminated 15-20%, presumably by

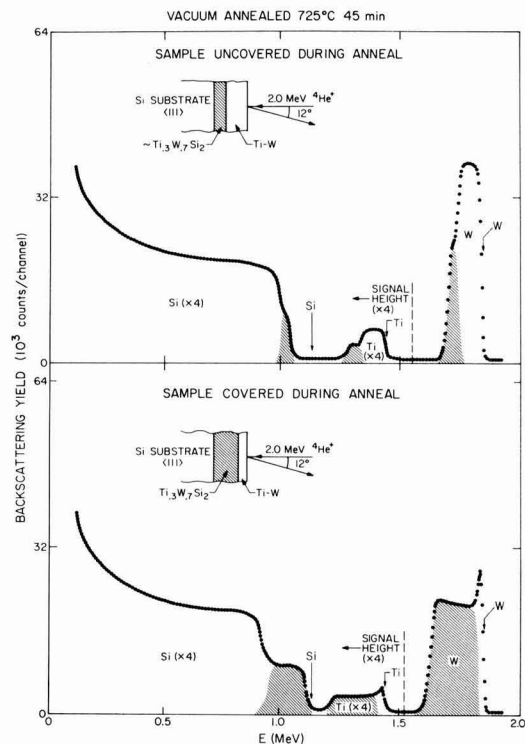


Fig. 3. Backscattering spectra of a partially covered sample annealed at 725°C for 45 min. Top shows portion of sample which was uncovered during anneal and bottom shows covered part. Arrows indicate the position of signals from Si, Ti, and W on the sample surface.

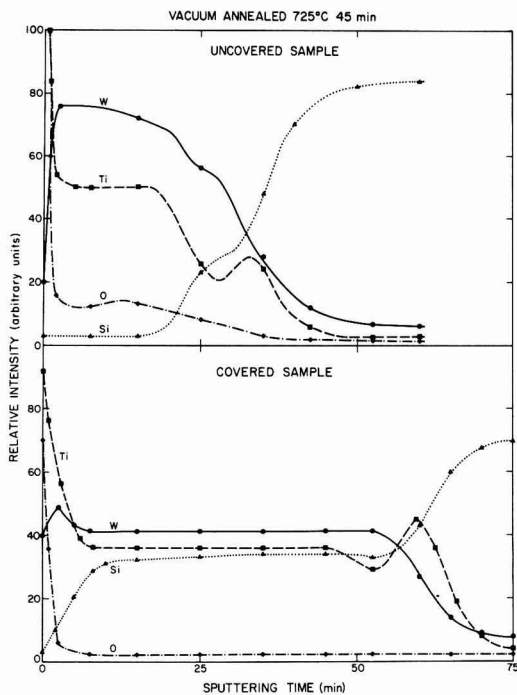


Fig. 4. AES depth profile of W, Ti, Si, and O in the uncovered (top) and covered (bottom) parts of the sample in Fig. 3.

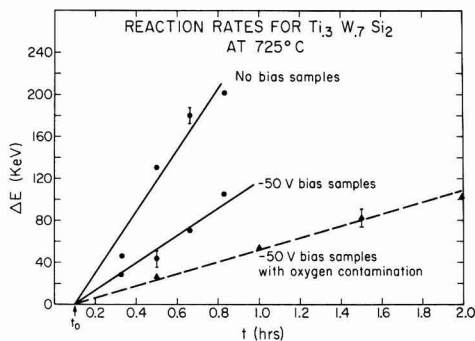


Fig. 5. A plot of compound thickness (expressed in terms of backscattering energy loss) vs. anneal time. The warm-up time for a sample placed in the vacuum furnace is denoted by  $t_0$ . Lines marked "No bias samples" and "-50 V bias samples" were annealed covered at a vacuum of  $7 \times 10^{-7}$  Torr. Line marked "-50V bias samples with oxygen contamination" refers to samples annealed uncovered at a vacuum of  $5 \times 10^{-6}$  Torr. (10 keV corresponds to about 106Å of compound).

oxygen. The reaction has a linear time dependence at all temperatures and over the entire range of oxygen contamination. An apparent activation energy of 4.5 eV is determined from the reaction rate vs. temperature (Fig. 6).

The rate of reaction is influenced by several parameters. This fact was established by comparing two samples which differed only in the parameter of interest. These sample pairs were sandwiched together with the metallized sides face to face and annealed in a vacuum similar to that used in the rate vs. temperature studies. This procedure also gave reproducible results. From such comparison, it was established that the reaction rate is influenced by the bias applied during sputter deposition (Fig. 5). Samples deposited on

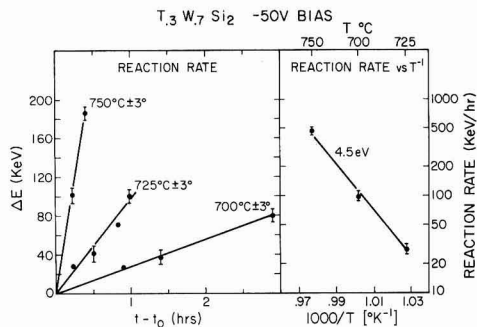


Fig. 6. (Left) plot of compound thickness (expressed in terms of backscattering energy loss for 2.0 MeV  $^4\text{He}^+$  ions, 10 keV corresponds to about 106Å of compound) vs. anneal time,  $t$ , minus warm-up time  $t_0$ . (Right) plot of log of reaction rate vs. reciprocal anneal temperature (yields activation energy of 4.5 eV).

$\langle 111 \rangle$  silicon substrates react slower than those deposited on  $\langle 110 \rangle$ , and samples prepared on  $\langle 100 \rangle$  react the fastest. On the other hand, the dopant type of the Si substrate had no measurable effect on the reaction rate, nor did changes of the doping level from 2 to 10 ohm-cm.

### Discussion and Conclusion

Transition metal silicides typically form complete solid solutions when the two constituting binary silicides are isomorphous. A partial solid solution or ternary compound forms when the two binary silicides are nonisomorphous (10).  $\text{TiSi}_2$  has an orthorhombic (C-54) structure with a packing sequence ABCD, but  $\text{WSi}_2$  has a tetragonal (C-11b) structure with a packing sequence ABAB. Hence one expects that a ternary compound will form with Ti, W, and Si. Formation of ternary compounds has also been reported in both the Ti-Mo-Si system and the Ti-Re-Si system (10).

The Ti-W-Si system has been studied by Nowotny (11). He reports a ternary disilicide of composition  $\text{Ti}_2\text{W}_{1-x}\text{Si}_2$  for  $x > 0.6$  but a mixture of  $\text{TiSi}_2$  and  $\text{WSi}_2$  for  $x < 0.6$ . In the present case,  $x = 0.3$ ; compound formation is observed nevertheless. This discrepancy between Nowotny and the present work could possibly be due to the fact that Nowotny investigated bulk samples prepared by high pressure sintering at 1300°C while we consider thin-film samples prepared near 750°C.

We attribute the surface distortion after compound formation to the volume expansion the film experiences as a result of Si inclusion. This expansion is substantial since the film undergoes only a small atomic density change (approximately  $6.14 \times 10^{22}$  atom/cm<sup>2</sup> for the initial Ti-W layer, as calculated from the weighted sum of the elemental densities; approximately  $7.54 \times 10^{22}$  atom/cm<sup>3</sup> for  $\text{Ti}_{0.3}\text{W}_{0.7}\text{Si}_2$  calculated from the x-ray data).

A reduction of reaction rates by oxygen contamination has been observed by Kräutle (12) in the formation of  $\text{VSi}_2$  by thin films of V on Si. It is remarkable that the rate of reaction is closely linear in spite of considerable oxygen contamination (Fig. 5). The observations that the rate remains linear at reduced oxygen contamination and that the substrate crystal orientation also influences the rate, is consistent with a reaction-limited mechanism. This hypothesis is further supported by the fact that Borders (4) reports linear rates for the  $\text{WSi}_2$  formation. No published data exist for reaction rates of Ti films on Si substrates.

The observed activation energy of 4.5 eV is high. Sinha (13) also reported a high activation energy of 4.4 eV for  $\text{WSi}_2$  growing at the expense of PtSi. On the other hand, the activation energies quoted for the formation of  $\text{WSi}_2$  films on Si range from 2 to 3 eV (4). Our value of 4.5 eV may thus be the result of

Ti<sub>0.3</sub>W<sub>0.7</sub>Si<sub>2</sub> growing at the expense of an oxide of titanium and/or tungsten. An argument against this hypothesis is the fact that no oxides of Ti or W were detected in the x-ray photographs. The x-ray analysis, however, is not very sensitive to small oxide concentrations over narrow regions such as the reaction interface. At present, the high value of the activation energy is not understood.

The influence of deposition bias on the reaction rate may also be a contamination effect. The samples with -50V deposition bias had both lower reaction rates and higher argon contamination levels than the sample deposited at zero bias. However, certain parameters of the films such as stress or crystal grain size which could influence the reaction rate, were not well characterized. Differences in these parameters could also contribute to variations in reaction rates between samples prepared at different biases.

Since we were unable to perform anneals without introducing detectable amounts of contamination, the kinetics data presented here are to be considered preliminary. It would also be worthwhile to extend this study to Ti-W films with various initial compositions, or to other disilicide-forming bimetal combinations. The results would be of value to the subject of ternary silicides in general, and to their possible application in silicon device technology in particular.

#### Acknowledgments

We wish to thank Paul Turner for allowing the use of his sputtering system. We also thank Dr. C. A. Evans, Jr., University of Illinois, Urbana, for his Auger analysis, and Dr. Sten Samson for the use of his Guinier camera and for his help in the x-ray analysis. We express our appreciation to the Kellogg Radiation Laboratory for the use of their 3 MeV accelerator and to Dr. C. A. Barnes for his continuous assistance.

This work was supported in part by the National Aeronautics and Space Administration (J. Maserjian and J. Boreham, Jet Propulsion Laboratory) and by

the Air Force Cambridge Research Laboratories (D. E. Davies).

Manuscript submitted June 11, 1975; revised manuscript received Aug. 18, 1975. This was Paper 108 presented at the Toronto, Canada, Meeting of the Society, May 11-16, 1975.

Any discussion of this paper will appear in a Discussion Section to be published in the December 1976 JOURNAL. All discussions for the December 1976 Discussion Section should be submitted by Aug. 1, 1976.

Publication costs of this article were partially assisted by the California Institute of Technology.

#### REFERENCES

1. J. L. Vossen, *J. Vacuum Sci. Technol.*, **11**, 60 (1974).
2. J. A. Cunningham, *IEEE Trans. on Reliability*, **R19**, 182 (1970).
3. L. D. Locker and C. D. Capiro, *J. Appl. Phys.*, **44**, 4366 (1973); A. K. Sinha, M. H. Reed, and T. E. Smith, *This Journal*, **120**, 1775 (1973).
4. J. A. Borders and J. N. Sweet, in "Proceedings of the International Conference on Applications of Ion Beams to Metals," S. T. Picraux, E. P. Eer-Nisse, and F. L. Vook, Editors, p. 179, Plenum Press, New York (1974).
5. H. Kräutle, M.-A. Nicolet, and J. W. Mayer, *ibid.*, p. 193. See also, *Phys. Status Solidi*, (a)**10**, k33 (1973).
6. W. K. Chu, J. W. Mayer, M.-A. Nicolet, T. M. Buck, G. Amsel, and F. Eisen, *Thin Solid Films*, **17**, 1 (1973).
7. S. S. Lau, W. K. Chu, J. W. Mayer, and K. N. Tu, *ibid.*, **23**, 205 (1974).
8. A. Guinier, "X-ray Crystallographic Technology," Hilgar and Watts, Limited, London (1952).
9. C. C. Chang, in "Characterization of Solid Surfaces," Kane and Larrabee, Editors, p. 509, Plenum Press, New York (1974).
10. H. J. Goldschmidt, "Interstitial Alloys," p. 323, Plenum Press, New York (1967).
11. H. Nowotny, R. Kieffer, and H. Schachner, *M. L. Chem.*, **83**, 1243 (1952).
12. H. Kräutle, M.-A. Nicolet, and J. W. Mayer, *J. Appl. Phys.*, **45**, 3304 (1974).
13. A. K. Sinha and T. E. Smith, *ibid.*, **44**, 3465 (1973).

## Isochronal Annealing of Silicon-Phosphorus Solid Solutions

P. Ostoj, D. Nobili, A. Armigliato, and R. Angelucci

C.N.R. Laboratorio Lamel, 40126 Bologna, Italy

#### ABSTRACT

Isochronal annealings of 500 hr per pulse, in steps of 25°C, have been performed in the range 400°-800°C on silicon single crystals of well-known composition bulk-doped with phosphorus. Dopant concentrations were 1.7, 3.3, 3.7, 5, 5.8, and 7.5 × 10<sup>19</sup> at/cm<sup>3</sup>. The annealing curves, determined by electrical resistivity measurements, are reported and discussed. A resistivity increase, attributed to phosphide precipitation, takes place above 400°C in the dopant richest alloy. It is noticed that a high density of dislocations (about 10<sup>8</sup> cm<sup>-2</sup>) does not alter the kinetics of this process. At 550°C coherent precipitates of interstitial character have been observed by TEM; their density and mean size are consistent with a SiP composition. The features of the defects associated with the dissolution process are also reported. Phosphorus diffusivity for precipitation, calculated at 550°C, turns out to be about five orders of magnitude higher than expected from extrapolation of well-known high temperature values. The solubility of phosphorus in silicon, determined by the kinetics of recovery of resistivity, results as about 7 × 10<sup>19</sup> at/cm<sup>3</sup> at 650°C.

Phase equilibria and the related kinetics in the binary systems of silicon and its substitutional dopants are important for basic knowledge. Further, this information presents a relevant interest for the technology and failure physics of silicon devices. Our laboratory is involved in a research program concerning

Key words: silicon, phosphorus-doped, annealing, precipitation, solubility.

the Si-B and the Si-P systems (1, 2). The present study deals with the precipitation of phosphorus by isochronal annealing of bulk-doped silicon single crystals. The formation of phosphide precipitates in silicon has been observed by several authors, mainly by TEM examinations (3-10). This technique has also been used, together with x-ray topography, in our laboratory (11, 12). All the above studies were carried out

on specimens doped by diffusion which, therefore, presented concentration gradients. As a consequence, the kinetics of the process have never been analyzed.

Isochronal kinetics constitute an obvious step in determining the temperature above which precipitation takes place at a measurable rate. They can give information on the diffusivity, as well as on the influence of lattice defects on the nucleation of the new phase. The purpose of our work was also the determination of reliable values of phosphorus solubility at low temperature. The status of knowledge in the whole range below the eutectic temperature is lacking: values at 900°C and above are widely scattered (a single research has reported data below this temperature) and no data are available below 700°C (13).

The annealing and quenching method is widely used in phase diagram determinations; its precision can be improved by increasing the annealing time and comparing precipitation and dissolution results. The experimental procedures of this method unambiguously satisfy the condition that both the primary solid solution and its conjugate phase must be competing for equilibrium. It is open to question if this basic thermodynamic condition has been fulfilled in solubility determinations based on measurements of surface concentration of the dopant after predeposition in an oxidizing atmosphere (14).

In the silicon-phosphorus system below the eutectic temperature, the conjugate phase is Si<sub>3</sub>P<sub>2</sub>, base-centered orthorhombic (14, 15). This structure has recently been confirmed on small phosphide precipitates by electron diffraction studies carried out in our laboratory (12).

### Experimental

Our experiments were carried out on (111)-oriented, bulk-doped silicon single crystals. Six compositions were studied. The corresponding phosphorus concentrations are reported in Table I. Slices were nominally dislocation free, with an actual density  $< 10^8 \text{ cm}^{-2}$ . These alloys have been the subject of previous investigations concerning the dependence on phosphorus concentration of electrical resistivity and mobility (16, 17), as well as of lattice parameter (18). The concentration of dopant has been determined by neutron activation analysis; by this technique and gamma-scintillation spectrometry we also performed the analysis of about forty metallic impurities. The results of these analyses are reported in a previous paper (16). Oxygen, as well as carbon and nitrogen content, was determined by ion activation analysis. The content of carbon was about  $4 \times 10^{17}$  and that of nitrogen about  $1.5 \times 10^{17} \text{ at/cm}^3$ . Oxygen concentration was found to range between  $6 \times 10^{15}$  and  $3.7 \times 10^{17} \text{ at/cm}^3$ ; the figures for each composition are reported in Table I. Precise lattice parameter determinations were carried out along the diameter of some representative wafers. Lattice parameter oscillations, although increasing with dopant concentration, turned out to be small, and a homogeneity of  $10^{-3}\%$  was ensured near the wafer center from where we obtained our samples. The techniques of chemical analysis and of structural examinations have been described in detail in the above-mentioned papers (16, 18).

Isochronal annealings were performed in the temperature range 400°-800°C in steps of 25°C, by using a vacuum furnace ( $10^{-8}$  Torr) for shorter times (21 hr

per pulse), and quartz tubes sealed under the same vacuum for longer treatments (500 hr per pulse). The temperature stability was kept better than  $\pm 0.5^\circ\text{C}$  even for the longer times by using a CAT control system. The heating and cooling times of our specimens were of the order of some minutes. To follow the annealing behavior, we performed room temperature electrical resistivity measurements after each heating pulse. Our previous work (16) allowed us to obtain a reliable relationship between resistivity and the concentration of electrically active phosphorus in the heavy doping range. Repeatability of our resistivity determinations turned out to be  $\pm 0.5\%$ ; this was confirmed by measuring in each run unannealed reference dummy samples of composition similar to that of the specimens. Moreover, the experiments were carried out on several samples, at least ten, of each composition. Half of the most heavily doped specimens were deformed by a four-point bending technique (19) in order to observe the influence of the high density of dislocations introduced (about  $10^8 \text{ cm}^{-2}$ ). At the end of selected annealing steps, samples were thinned with the jet-etching technique and observed by TEM in order to follow the structural modifications induced by the annealing process. Our instrument was a Siemens Elmiskop 101 equipped with a  $\pm 45^\circ$  double tilting cartridge.

### Results

*Electrical measurements.*—The resistivity curves after isochronal annealing of 500 hr per pulse of the samples with phosphorus concentrations 1.7, 3.3, 3.7, 5, and  $5.8 \times 10^{19} \text{ at/cm}^3$  are reported in Fig. 1. The resistivity values of the unannealed reference dummy sample, also reported in this plot, refer to electrical measurements performed in the same run as the corresponding annealed specimens. The most diluted compositions clearly exhibit a negative resistivity variation in the temperature range 450°-575°C, with two minima centered at 500° and 550°C, respectively. The

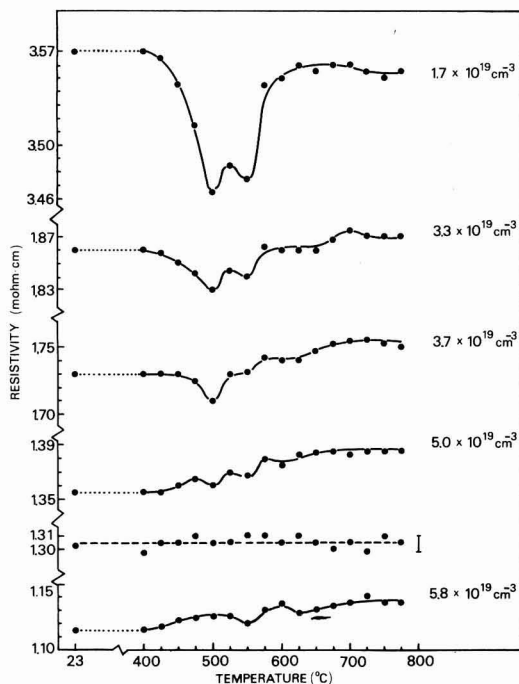


Fig. 1. Electrical resistivity vs. temperature for 500 hr per pulse annealing of Si samples bulk-doped with increasing P concentrations (solid lines). The behavior of the unannealed reference dummy sample is also reported (broken line).

Table I.

Samples	Resistivity (ohm · cm)	Phosphorus conc (at/cm <sup>3</sup> )	Oxygen conc (at/cm <sup>3</sup> )
W/na	$3.5 \times 10^{-3}$	$1.7 \times 10^{19}$	$6.1 \times 10^{15}$
A/na	$1.9 \times 10^{-3}$	$3.3 \times 10^{19}$	$7.9 \times 10^{15}$
M/n4	$1.7 \times 10^{-3}$	$3.7 \times 10^{19}$	$3.7 \times 10^{17}$
M/n3	$1.3 \times 10^{-3}$	$5.0 \times 10^{19}$	$3.7 \times 10^{17}$
M/n2	$1.1 \times 10^{-3}$	$5.8 \times 10^{19}$	$3.7 \times 10^{17}$
M/n1	$8.5 \times 10^{-4}$	$8.5 \times 10^{19}$	$3.7 \times 10^{17}$

amplitude of this effect decreases with increasing phosphorus, and the minimum at 500°C is not observed in the alloys with dopant concentration exceeding  $5 \times 10^{19}$  at/cm<sup>3</sup>. A third slight inflection, centered at about 625°C, is also noticed and is significant considering the reproducibility that we observed between the specimens with the same composition as well as the behavior of the different alloys.

The isochronal annealing kinetics for the P-richer composition ( $7.5 \times 10^{19}$  at/cm<sup>3</sup>) are reported in Fig. 2. A resistivity increase can be clearly seen above 400°C. The amplitude of this effect is higher as the annealing time is longer, and is of about 11% in curve (a), which corresponds to 500 hr of annealing per pulse. Two small resistivity minima, superimposed on the main peak, are in any case noticed. In curve (a) they are centered at 550° and 625°C, that is, corresponding to the minima observed in Fig. 1. In curve (b), which corresponds to 21 hr annealing per pulse, they are shifted to about 575° and 675°C, respectively. After high temperature annealing the resistivity recovers approximately its original value. At the end of the heat-treatment of 21 hr per pulse [curve (b)], the samples were isochronally annealed for the same time per pulse, at decreasing temperatures. A resistivity increase has been obtained also in this case, thus indicating that the phenomenon is reversible. As will be discussed later, the resistivity peak in Fig. 2 is attributed to a decrease of the concentration of the charge carriers due to precipitation of phosphorus in a super-saturated solid solution. Finally, it is worthwhile to remark that the behavior of the deformed specimens, which contain a high density of dislocations, is indistinguishable from that of the undeformed ones.

**TEM examinations.**—Due to the destructive character of electron microscopy, a limited number of situations have been studied by TEM in bright and dark field two-beam conditions, as well as by using the weak beam dark field technique (20). Our observations on the most heavily doped specimens, isochronally heated 500 hr per pulse, were carried out after annealing up to 500°, 550°, and 775°C, respectively. Prior to annealing the specimens did not exhibit the presence of any crystallographic defect.

(i) *Specimens annealed up to 500°C.*—Images taken in different areas of these specimens did not reveal any defect, either in bright or dark field two-beam conditions. Images taken with the weak beam dark field technique clearly displayed, as shown in Fig. 3, a large density of small defects, typically about 50Å in diameter. It was, in any case, difficult to decide from con-

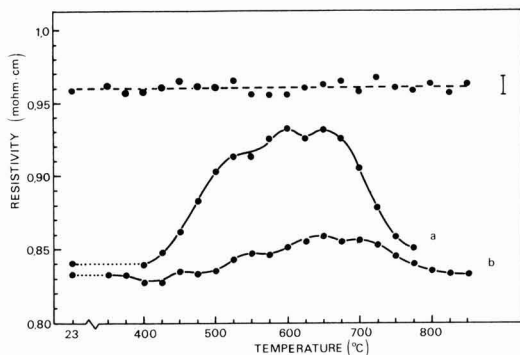


Fig. 2. Electrical resistivity vs. temperature for 500 hr per pulse, curve (a), and 21 hr per pulse, curve (b), annealing of Si samples bulk-doped with P ( $7.5 \times 10^{19}$  at/cm<sup>3</sup>). The same curves hold also for specimens containing a high density ( $\sim 10^8$  cm<sup>-2</sup>) of dislocations. The broken line refers to the unannealed reference dummy sample.

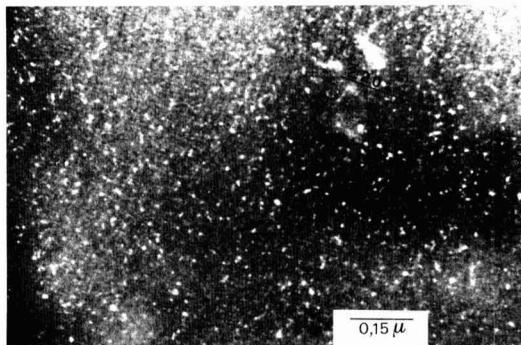


Fig. 3. Small defects in one of the most heavily doped samples annealed up to 500°C. Weak beam ( $-g, g$ ) image.

trast experiments whether such defects were precipitates or dislocation loops.

(ii) *Specimens annealed up to 550°C.*—As reported in previous papers (1, 2), the observations carried out on these samples revealed the presence of a high density (about  $6 \times 10^{13}$  cm<sup>-3</sup>) of coherent precipitates which, from dark field images, were found to be interstitial in character, with strain parameter  $\epsilon = 2.5 \times 10^{-2}$ . A typical bright field image of these particles is shown in Fig. 4. From the Ashby and Brown theory it was possible to compute their average radius which came out at about 130Å. These figures, compared with the amount of electrically inactive phosphorus deduced from resistivity data, are consistent with the hypothesis that the particles are SiP precipitates. Weak beam images taken in the same areas revealed again, as shown in Fig. 5, the presence of the small defects already observed in the samples annealed up to 500°C.

(iii) *Specimens annealed up to 775°C.*—Images taken both from deformed and undeformed specimens exhibited a large amount of dislocation loops. A typical micrograph is reported in Fig. 6, which also evidences one of the dislocations introduced by bending the unannealed specimen. The loops displayed in this picture are of interstitial type, and the same holds for the loops in Fig. 7. Loops like the ones marked B and D in Fig. 6 and M in Fig. 7 are perfect loops with Burgers vectors of the type  $a/2 \langle 110 \rangle$ . Those marked A and C in Fig. 6 and L in Fig. 7 are stacking fault loops with Burgers vectors of the type  $a/3 \langle 111 \rangle$ . This latter statement becomes apparent if one looks at the weak beam micrograph of Fig. 8, taken in the ( $-g, g$ ) orientation. The fringes observed in this figure are spaced by 36Å, which is in very good agreement with the

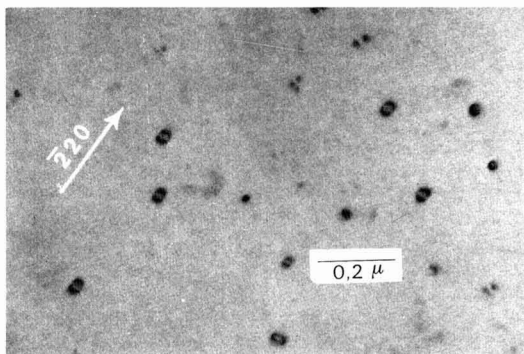


Fig. 4. Coherent precipitates in one of the most heavily doped samples annealed up to 550°C. Bright field image.



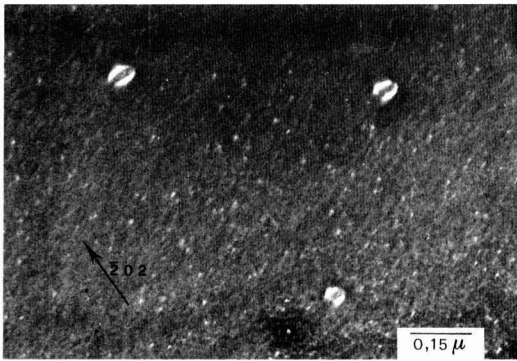


Fig. 5. Coherent precipitates and small defects in the same sample as Fig. 4. Weak beam  $(-g, g)$  image.

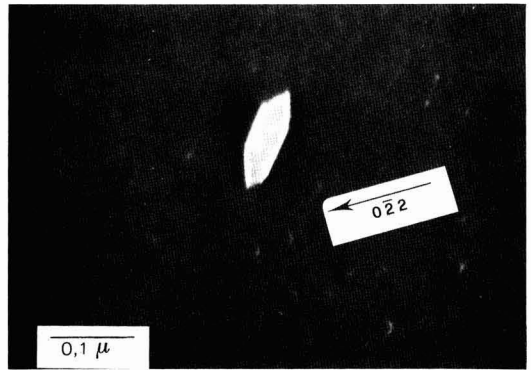


Fig. 8. Weak beam  $(-g, g)$  image of the stacking fault loop (L) of Fig. 7, showing the  $36\text{\AA}$  spaced fringes given by the  $02\bar{2}$  reflection.

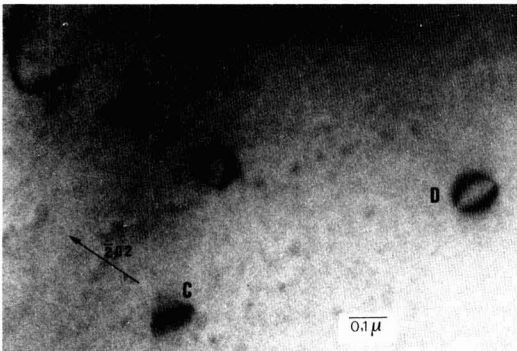


Fig. 6. Perfect dislocation loops (B and D) and stacking fault loops (A and C) in one of the most heavily doped samples annealed up to  $775^\circ\text{C}$ . One of the dislocations introduced by bending is also visible. Bright field image.

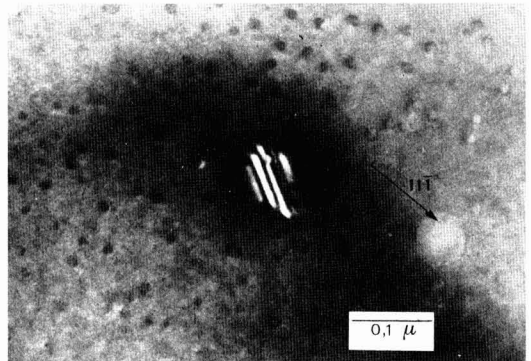


Fig. 9. Weak beam  $(-g, g)$  image of the stacking fault loop (L) showing the  $144\text{\AA}$  spaced fringes, given by the  $11\bar{1}$  reflection.

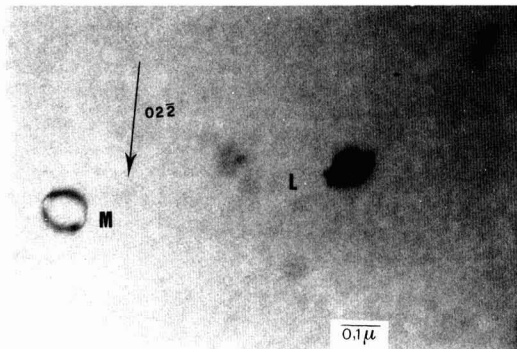


Fig. 7. Perfect dislocation loop (M) and stacking fault loop (L) in the same sample as Fig. 6. Bright field image.

theoretical fringe spacing  $d$  obtained from the formula  $d = \frac{1}{S'} \cot \alpha$ , where  $S'$  is the deviation of the  $02\bar{2}$  reciprocal lattice point from the sphere of reflection, and is given by  $1/S' = 1/\lambda g^2$ .  $\lambda$  is the electron wavelength that, in our case, corresponds to  $369 \times 10^{-4}\text{\AA}$ , and  $\alpha$  is the angle between the surface of the specimen and the  $(11\bar{1})$ -inclined plane of the fault ( $\alpha = 70.5^\circ$ ) (21). A further check is given by the calculation of the spacing of the fringes observed in Fig. 9, taken with  $g =$

$11\bar{1}$ , still in weak beam orientation. One gets  $d = 144\text{\AA}$ , in good agreement with the theoretical value of  $142\text{\AA}$ . A certain number of vacancy loops were also observed, like the ones labeled A and C in Fig. 10, found near the loop G which is of interstitial type. Finally, we notice that the small defects like those shown in Fig. 3 are rare at this stage of annealing; nevertheless they are actually present, although with lower concentration.

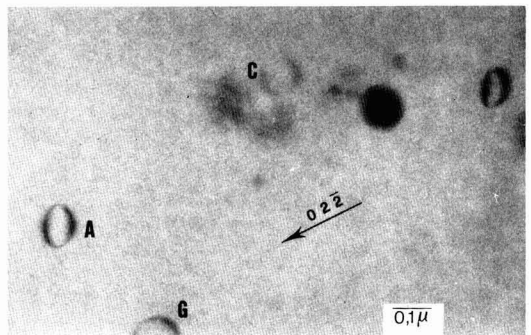


Fig. 10. Vacancy dislocation loops (A and C) together with an interstitial one (G) in the same sample as Fig. 6-9. Bright field image.

### Discussion and Conclusion

We consider, first, the resistivity peaks in Fig. 1. The influence of the concentration of phosphorus in the range from  $1.7$  to  $3.8 \times 10^{19}$  at/cm<sup>3</sup>, as well as that of the content of carbon and oxygen, has been studied in a previous work based on isochronal annealing of 21 hr per pulse. It was observed that the amplitude of the peaks does not depend on the concentration of carbon and oxygen (22). Further, these previous results are in agreement with the observation that the amplitude of the main negative peaks, centered at 500° and 550°C, respectively, in Fig. 1, decreases with the increasing phosphorus concentration. Moreover, it can be seen that by increasing the annealing time per pulse the amplitude of the peaks increases, and they result in being more clearly resolved and slightly shifted toward lower temperatures.

These observations suggest that the resistivity peaks in Fig. 1 are probably due to rearrangements of point defects, giving rise to complexes which are dissolved again with increasing temperature, as can be seen from the resistivity recovery at the end of each peak. In fact, if one computes from our experimental data the contribution to the conductivity due to the donors involved in such complexes, one gets a value which remains nearly constant, at least within the experimental errors, throughout the range of concentrations of phosphorus. This consideration allows us to conclude that these donor complexes should not depend on the P content, although the relative amplitude of the dips in Fig. 1 is lower as the resistivity decrement due to the increasing P concentration is higher. Further information on the nature of these phenomena should be obtained by comparing the annealing behavior of n- and p-doped crystals. We shall report in a further work the results of a research in progress on silicon doped with boron.

The resistivity peak in Fig. 2 can be attributed to phosphide precipitation followed by redissolution at high temperature. In fact it is observed only in the most heavily doped alloy; the compositions with a comparable amount of impurities, but less rich in phosphorus, do not show this phenomenon. These conclusions are in agreement with the formation of coherent precipitates of the type shown in Fig. 4. The mean size and density of these precipitates are in keeping with a SiP composition. In addition they are dissolved after annealing up to 775°C, when the resistivity has recovered its original value.

It is unlikely that the small defects shown in Fig. 3 are phosphide precipitates; if so, they should be unstable with respect to the larger ones. On the contrary, a considerable fraction of these defects is still present after annealing up to 775°C. The dislocation and stacking fault loops previously analyzed show the formation of excess point defects, mainly interstitials. They are associated with the dissolution of phosphide precipitates; in fact, these defects are absent in less-doped alloys annealed in the same way. The formation of dislocation loops takes place also in specimens undergoing isothermal precipitation of phosphorus, as evidenced by TEM observations which are at present in progress. The amount of inactive phosphorus resulting from the 500 hr per pulse annealing [Fig. 2, curve (a)] and the onset of the redissolution process at 650°C allows determination of the solid solubility of phosphorus in silicon at this temperature, which is about  $7 \times 10^{19}$  at/cm<sup>3</sup>. This figure should be practically unaffected by the interface effects, which can greatly increase the solubility of very fine particles. In fact, the 500 hr per pulse annealing gives rise, as shown in Fig. 4, to a high density of precipitates with radius larger than 100Å. The above solubility is in good agreement with the value of  $7 \times 10^{19}$  at/cm<sup>3</sup> at 700°C reported by Abrikosov *et al.* (23).

All experiments on the heavily doped alloy have shown that the kinetics of precipitation and redissolution are unaffected by the presence of dislocations. This result is interesting also in the aging of electronic devices. A reasonable hypothesis is that the available point defects provide more suitable centers competing for the formation of critical nuclei.

To account for these precipitation phenomena, the diffusivity of phosphorus has to be much higher than that expected. In fact, the diffusion length  $\sqrt{Dt}$  calculated at 550°C using diffusivity values determined in our laboratory (24) or well-known data found in literature (13, 25) and taking  $t = 1000$  hr turns out to be only a few angstroms. A calculation, albeit crude, of the diffusivity involved in our experiments can be performed using the model of Ham (26), considering the spherical symmetry and the radius ( $\sim 130\text{Å}$ ) of our coherent precipitates, admitting that the composition is SiP, and assuming, from extrapolation of our experimental data on the isochronal curve (a) in Fig. 2, a solubility of  $6 \times 10^{19}$  at/cm<sup>3</sup> at 550°C. This calculation gives  $D \approx 5 \times 10^{-17}$  cm<sup>2</sup>sec<sup>-1</sup>, that is, five orders of magnitude higher than the diffusivity value at 550°C calculated by extrapolation of our high temperature data, as well as of the above-cited data found in literature.

Actually, preliminary results of the data analysis on the isochronal curve, combined with those of isothermal annealing in progress, suggest that the activation energy for diffusion is substantially reduced. The discrepancy could be explained either by a completely different diffusion mechanism, active at low temperature, or by an excess of point defects associated with the precipitation process. Further research is in progress on isothermal annealing followed by TEM observations and lattice parameter determinations with the aim of contributing to the clarification of the precipitation process.

### Acknowledgments

Thanks are due to Dr. J. W. Steeds of the H. H. Wills Physics Laboratory, Bristol University, and Drs. P. G. Merli and M. Servidori for useful suggestions and discussion on the electron microscopy results. The skillful technical assistance of Mr. L. Dori and Mr. G. Ruffini is also acknowledged.

Manuscript submitted July 23, 1975; revised manuscript received Sept. 12, 1975. This was Paper 222 presented at the New York, New York, Meeting of the Society, Oct. 13-17, 1974.

Any discussion of this paper will appear in a Discussion Section to be published in the December 1976 JOURNAL. All discussions for the December 1976 Discussion Section should be submitted by Aug. 1, 1976.

Publication costs of this article were partially assisted by C.N.R.-Lamel.

### REFERENCES

1. R. Angelucci, A. Armigliato, D. Nobili, and P. Ostoja, Abstract 222, p. 548, The Electrochemical Society Extended Abstracts, Fall Meeting, New York, New York, Oct. 13-17, 1974.
2. A. Armigliato, D. Nobili, and P. Ostoja, Proceedings of the 8th International Congress on Electron Microscopy, Vol. I, p. 668, Canberra, 1974.
3. R. Stickler and P. F. Schmidt, *This Journal*, **111**, 1188 (1964).
4. M. L. Joshi, *ibid.*, **112**, 912 (1965).
5. T. W. O'Keefe, P. F. Schmidt, and R. Stickler, *ibid.*, **112**, 878 (1965).
6. M. L. Joshi, *ibid.*, **113**, 45 (1966).
7. C. G. Beck and R. Stickler, *J. Appl. Phys.*, **37**, 4683 (1966).
8. M. L. Joshi and S. Dash, *IBM J. Res. Dev.*, **11**, 271 (1967).
9. E. Levine, J. Washburn, and G. Thomas, *J. Appl. Phys.*, **38**, 87 (1967).
10. R. J. Jaccodine, *ibid.*, **39**, 3105 (1968).
11. C. Ghezzi and M. Servidori, *J. Mater. Sci.*, **9**, 1797 (1974).

12. M. Servidori and A. Armigliato, *ibid.*, **10**, 306 (1975).
13. V. M. Glazov and V. S. Zemskov, "Physico-Chemical Principles of Semiconductor Doping," p. 141, JPST Press, Jerusalem (1968).
14. R. P. Elliott, "Constitution of Binary Alloys," p. 716, McGraw-Hill Book Co., New York (1965).
15. T. Wadsten, *Univ. Stockholm Chem. Communic.*, **7**, 1 (1973).
16. F. Mousty, P. Ostoja, and L. Passari, *J. Appl. Phys.*, **45**, 4576 (1974).
17. G. Baccarani and P. Ostoja, *Solid-State Electron.*, **18**, 579 (1975).
18. G. Celotti, D. Nobili, and P. Ostoja, *J. Mater. Sci.*, **9**, 821 (1974).
19. E. Susi, L. Dori, and M. Servidori, *Met. Ital.*, **65**, 147 (1973).
20. D. J. H. Cockayne, I. L. F. Ray, and M. J. Whelan, *Phil. Mag.*, **20**, 1265 (1969).
21. R. Bicknell, *J. Microsc.*, **98**, 165 (1973).
22. P. Ostoja, D. Nobili, and A. Armigliato, *Met. Ital.*, **65**, 65 (1973).
23. N. Kh. Abrikosov, V. M. Glazov, and C.-Y. Liu, *Russ. J. Inorg. Chem.*, **7**, 429 (1962).
24. G. Masetti, S. Solmi, and G. Soncini, *Solid-State Electron.*, **16**, 1419 (1973).
25. D. L. Kendall and D. B. De Vries, in "Semiconductor Silicon," B. R. Haberecht and E. L. Kern, Editors, p. 358, The Electrochemical Society Softbound Symposium Series, New York (1969).
26. F. S. Ham, *J. Phys. Chem. Solids*, **6**, 335 (1958).

## Solid-State Ionics—High-Conductivity Solid Copper Ion Conductors

### Organic Ammonium Halide-Copper (I) Halide Double Salts

Takehiko Takahashi,\* Noboru Wakabayashi, and Osamu Yamamoto

*Department of Applied Chemistry, Faculty of Engineering, Nagoya University, Nagoya 464, Japan*

#### ABSTRACT

The copper ion conductivities of the system organic substituted ammonium halide-copper (I) halide have been measured in the solid state, and the relation between the formation of high conductivity compounds and the conformation of organic substituted ammonium halides was examined. No high copper ion conductivity was found in the system unsaturated azacyclic substituted ammonium halide-copper (I) halide, while high copper ion conductivity was found in the saturated azacyclic substituted ammonium halide-copper (I) halide system. For example, the system 1-methylpiperidinium bromide-copper (I) bromide at the composition of 84 mole per cent CuBr gave the conductivity of  $8.2 \times 10^{-3}$  (ohm-cm)<sup>-1</sup> at room temperature.

Ionic conduction in the system substituted ammonium iodide-silver iodide was studied extensively by Owens (1), Owens, Christie, and Tiedeman (2), and Beradelli *et al.* (3), and many compounds were reported to have the ionic conductivities in the range of  $8 \times 10^{-4}$  to  $6 \times 10^{-2}$  (ohm-cm)<sup>-1</sup> at 25°C. From the conductivity measurements of a large number of the systems, Owens *et al.* (2) concluded that the formation of ion conductive compounds was related to the size of organic ammonium ions. Recently, double salts formed by the combination of copper (I) halide with N-alkyl-hexamethylenetetramine halide (4), and N,N'-dialkyl-triethylenediamine dihalide (5) have been found to exhibit high ionic conductivity at room temperature. In order to extend the area of high copper ion conductivity solid electrolytes, the electrical conductivities of the products formed by the reaction between copper (I) halides and organic ammonium halides have been measured (6, 7). The relations between the formation of copper ion conductive compounds and the size and conformation of the organic substituted ammonium ion are discussed.

#### Experimental

**Materials.**—Copper (I) halides were purified by recrystallizing in the corresponding hydrohalogenic acid. The substituted ammonium halide salts were prepared by the method A used generally, except for ethane-1, 2-bis-piperidinium bromide, and pentane-1,5-bis-morpholinium bromide which were prepared by the method B (8). The typical examples of synthesis are as follows:

**Method A:** To a solution containing 10 mliters (0.10 mole) of piperidine in 50 mliters of ethyl alcohol were slowly added 14g (0.098 mole) of a methyl iodide solution in 10 mliters of ethyl alcohol and the mixture was refluxed for 1 hr. After being filtered, the precipitate was dried in vacuo on P<sub>2</sub>O<sub>5</sub>. A yield of 1.5g of product (about 10% yield) was obtained.

**Method B:** To 3.8g (0.44 mole) of morpholine a solution containing 15g (0.065 mole) of 1,5-dibromopentane in benzene were added slowly at 0°C and the mixture was allowed to stand at room temperature for 2 days. After being filtered, the precipitate was dried in vacuo on P<sub>2</sub>O<sub>5</sub>. A yield of 22g of product (80% yield) was obtained.

The electrolytes were prepared by combining copper (I) halides (CuX) with substituted ammonium halides (QX). The appropriate quantities of CuX and QX were thoroughly ground together before being pressed to form a pellet under a pressure of 4000 kg/cm<sup>2</sup>, and then heated in a sealed, evacuated Pyrex vessel. The reactions were carried out below the decomposition temperatures of the starting materials, which were determined by thermogravimetric analysis.

**Electrical conductivity.**—The conductivity was measured with a 1000 Hz conductance bridge. The frequency dependence of the resistance was not observed in the frequency range of 1000-10,000 Hz. The conductivity measurement cell was as follows

Cu, Sample (2:1 weight ratio)/Sample/  
Cu, Sample (2:1 weight ratio)

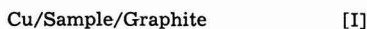
The sample of about 0.8g was stacked between two

\* Electrochemical Society Active Member.

Key words: solid electrolyte, copper ion conductor, copper (I) halide, organic ammonium halide.

electrodes and pressed into a pellet of 13 mm diameter under a pressure of 4000 kg/cm<sup>2</sup>. The conductivity was measured in nitrogen gas flow.

**Electronic conductivity.**—The electronic conductivities of some of the samples have been measured by the Wagner polarization method (9). To cell [I] with a copper anode and a graphite cathode, d.c. was applied at a voltage less than the decomposition voltage of the samples



The sample was pressed in the shape of pellet, 13 mm in diameter and 3 mm thick. A constant current supplier was used and the resulting voltage was measured with a high impedance digital voltmeter.

**Thermogravimetric analysis (TGA).**—The decomposition temperatures of the samples were determined by thermogravimetric analysis, the heating rate of which was 3.3°C/min.

## Results and Discussion

The electrical conductivities at room temperature for the organic ammonium iodide-copper(I) iodide systems, viz., tetramethyl ammonium iodide ((CH<sub>3</sub>)<sub>4</sub>NI), 1-methyl pyridinium iodide (C<sub>5</sub>H<sub>5</sub>NCH<sub>3</sub>I), 1-methyl pyrrolidinium iodide (C<sub>4</sub>H<sub>9</sub>NCH<sub>3</sub>I), 1-methyl piperidinium iodide (C<sub>5</sub>H<sub>11</sub>NCH<sub>3</sub>I), and 1-methyl morpholinium iodide (C<sub>4</sub>H<sub>9</sub>ONCH<sub>3</sub>I)-copper(I) iodide systems, are shown in Table I, where  $\sigma_e$  and  $\sigma_i$  are the electronic and ionic conductivity, respectively. The ionic conductivities of the silver iodide-organic ammonium iodide systems shown in this table were measured by Owens *et al.* (1, 2). In the silver iodide-organic ammonium iodide and copper(I) halide-organic ammonium halide systems as the high silver and copper ion conductivities (1, 2, 4, 5) were found at the composition between 80 and 90 mole per cent (m/o) silver iodide and copper halide, it may be assumed in the present investigation that if high conductivity materials could be formed, they would contain almost the same percentage of copper(I) iodide. So the thermal reaction products containing about 84 m/o copper iodide were examined. Table I shows that the C<sub>5</sub>H<sub>11</sub>NCH<sub>3</sub>I-CuI and C<sub>4</sub>H<sub>9</sub>ONCH<sub>3</sub>I-CuI systems give relatively high conductivities of  $8.6 \times 10^{-4}$  (ohm-cm)<sup>-1</sup> and  $5.8 \times 10^{-4}$  (ohm-cm)<sup>-1</sup> at room temperature, respectively. According to x-ray investigation, these systems did not give the diffraction patterns of the starting materials but gave the new phase diffraction patterns, which showed that the new conductive double salts were obtained in these systems at the composition of about 84 m/o CuI. In the (CH<sub>3</sub>)<sub>4</sub>NI-CuI, C<sub>5</sub>H<sub>5</sub>NCH<sub>3</sub>I-CuI, and C<sub>4</sub>H<sub>9</sub>NCH<sub>3</sub>I-CuI systems, however, no conductive

double salts were formed, and the conductivities of these systems were the same order of magnitude as that of CuI and the conduction was mainly due to electrons. The x-ray diffraction patterns of these systems were the same as those of the starting materials. In other unsaturated azacyclic substituted ammonium iodide (the derivatives of the 1-methyl pyridinium iodide)-copper(I) iodide systems, no high conductive material was found in all the systems investigated: 1-hydro pyridinium iodide, 1,4-dimethyl pyridinium iodide, 1,3-dimethyl pyridinium iodide, 1,2,6-trimethyl pyridinium iodide, 1-hydro-3,5-dimethyl pyridinium iodide, 1,3,5-trimethyl pyridinium iodide, 1-methyl quinolinium iodide, and 1-ethyl quinolinium iodide-copper(I) iodide systems, and 1-hydro-2-methyl quinolinium bromide-copper(I) bromide system.

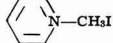
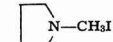
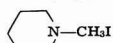
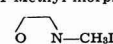
It is of interest to define by what parameters the existence of the conductive compounds were determined. It was suggested by Owens *et al.* (2) that in the silver iodide-organic ammonium iodide systems, the formation of high ionic conductivity compounds was related to the size of the organic ammonium ions. Table I indicates that in the copper(I) iodide-organic ammonium iodide systems, though C<sub>5</sub>H<sub>5</sub>NCH<sub>3</sub><sup>+</sup> and C<sub>5</sub>H<sub>11</sub>NCH<sub>3</sub><sup>+</sup> have almost the same size, only the latter gave high conductive materials. Therefore, the parameters other than the size of organic ammonium ions may be important to obtain high copper ion conductivity materials. One of these parameters may be the flexibility of organic ammonium ions; 1-methyl pyridinium ion has a plane structure, while 1-methyl piperidinium ion and 1-methyl morpholinium ion have flexible structures. Further, 1-methyl pyrrolidinium ion has a plane structure and tetramethyl ammonium ion has a rigid tetrahedral structure. That is, the flexible organic ammonium ions give a high ionic conductivity compound when they combine with copper(I) iodide. The other alkyl piperidinium halide, alkyl morpholinium halide, and alkyl piperidinium halide-copper(I) halide systems were examined also and the results of the electrical conductivity obtained are shown in Table II. Of these systems, the highest conductivity of  $8.2 \times 10^{-3}$  (ohm-cm)<sup>-1</sup> at 20°C is found in 1-methyl piperidinium bromide-copper(I) bromide, the conductivity value of which is comparable to that of N-alkyl hexamethylene-tetramine halide-copper(I) halide double salts reported previously (4) and one order of magnitude higher than that of the copper(I) iodide-1-methyl piperidinium iodide system. Gamma-copper(I) iodide and  $\gamma$ -copper(I) bromide have zinc blende structures, and the structure of copper(I) bromide is more open than that of copper(I) iodide. These results suggest that in the high ionic conductivity compounds, the structure of metal halide may play an important role.

In the 1,2- and 1,4-dimethyl piperidinium bromide-copper(I) bromide systems, the reaction products which gave the x-ray diffraction patterns of new compounds have lower conductivities than the compound in 1-methyl piperidinium bromide-copper(I) bromide system at room temperature, which suggested that the steric effect of substituted groups in the 1,2- and 1,4-dimethyl piperidinium bromide-copper(I) bromide systems may interrupt the diffusion of copper(I) ions.

**Conductivity.**—The composition dependence of the electrical conductivity was determined for three systems, viz., the 1-methyl piperidinium bromide-copper(I) bromide, 1-methyl piperidinium iodide-copper(I) iodide, and 1-methyl morpholinium iodide-copper(I) iodide systems. Figure 1 shows the conductivity as a function of mole per cent of copper(I) halide. The highest values of conductivity are  $8.2 \times 10^{-3}$ ,  $8.6 \times 10^{-4}$ , and  $5.8 \times 10^{-4}$  (ohm-cm)<sup>-1</sup> for the C<sub>5</sub>H<sub>11</sub>NCH<sub>3</sub>Br-CuBr, C<sub>5</sub>H<sub>11</sub>NCH<sub>3</sub>I-CuI, and C<sub>4</sub>H<sub>9</sub>ONCH<sub>3</sub>I-CuI systems, respectively, at the composition of about 84 m/o CuX.

The conductivities of C<sub>5</sub>H<sub>11</sub>NCH<sub>3</sub>Br 16 m/o-CuBr 84 m/o and C<sub>5</sub>H<sub>11</sub>NCH<sub>3</sub>I 16 m/o-CuI 84 m/o were mea-

Table I. Electrical conductivity of the copper(I) iodide-organic ammonium iodide systems and silver iodide-organic ammonium iodide systems at room temperature

	CuI	AgI
Tetramethyl ammonium iodide (CH <sub>3</sub> ) <sub>4</sub> NI	$\sigma_e \gg \sigma_i$	$4 \times 10^{-3}$
1-Methyl pyridinium iodide 	$\sigma_e \gg \sigma_i$	$1 \times 10^{-3}$
1-Methyl pyrrolidinium iodide 	$\sigma_e \gg \sigma_i$	$8 \times 10^{-3}$
1-Methyl piperidinium iodide 	$8.6 \times 10^{-4}$	
1-Methyl morpholinium iodide 	$5.8 \times 10^{-4}$	



**Table II. Electrical conductivity of the copper(I) halide-derivatives of 1-methyl piperidinium iodide systems at room temperature**

		(ohm-cm) <sup>-1</sup>
1-Methyl piperidinium iodide		$8.61 \times 10^{-4}$
1-Ethyl piperidinium iodide		$2.70 \times 10^{-7}$
Piperidinium bromide		$2.18 \times 10^{-7}$
1-Methyl piperidinium bromide		$8.24 \times 10^{-8}$
1-Ethyl piperidinium bromide		$4.24 \times 10^{-6}$
1,2-Dimethyl piperidinium bromide		$9.25 \times 10^{-5}$
1,4-Dimethyl piperidinium bromide		$1.15 \times 10^{-5}$
Ethane-1,2-bis-piperidinium bromide		$1.2 \times 10^{-7}$
Morpholinium iodide		$\sigma_e \gg \sigma_i$
1-Methyl morpholinium iodide		$5.80 \times 10^{-4}$
1-Ethyl morpholinium iodide		$7.62 \times 10^{-5}$
Morpholinium bromide		$\sigma_e \gg \sigma_i$
1-Ethyl morpholinium bromide		$2.66 \times 10^{-7}$
Pentane-1,5-bis-morpholinium bromide		$< 10^{-9}$
Piperadinium iodide		$\sigma_e \gg \sigma_i$
1,4-Dimethyl piperadinium iodide		$3.22 \times 10^{-5}$

sured at different temperatures. These samples were not decomposed up to 110°C in nitrogen atmosphere. The logarithmic conductivity vs. the reciprocal of the absolute temperature curves for these samples are shown in Fig. 2. These curves give straight lines in the range of temperature studied. The activation energies for conduction calculated from these curves are 3.7 kcal/mole for C<sub>5</sub>H<sub>11</sub>NCH<sub>3</sub>Br 16 m/o-CuBr 84 m/o and 5.1 kcal/mole for C<sub>5</sub>H<sub>11</sub>NCH<sub>3</sub>I 16 m/o-CuI 84 m/o; these values are almost the same as those of previously reported high copper ion conductivity solid electrolytes (4).

**Electronic conductivity.**—Electronic conductivity for some systems has been measured by Wagner's polarization method. According to Wagner's theoretical analysis (9) the current density  $J$  in cell [I] is given by

$$J = I/A = (RT/LF) [\sigma_e \{1 - \exp(-EF/RT)\} + \sigma_h \{\exp(EF/RT) - 1\}] \quad [1]$$

where  $I$  is the current,  $A$  the cross-sectional area,  $L$  the thickness of the sample,  $E$  the applied voltage, and  $F$  the Faraday constant, and  $\sigma_e$  and  $\sigma_h$  are the excess electron and hole conductivities of the sample which is in equilibrium with metallic copper. The plots of  $\log I$  vs.  $E$  give virtually straight lines whose slopes are close to the value of  $F/2.30RT$  at each temperature. Since the excess electron conduction is negligible, Eq. [1] may be written as

$$\log I = \log \sigma_h ART/LF + EF/2.30RT \quad [2]$$

if  $EF/RT \gg 1$ . The values of  $\sigma_h$  were then calculated

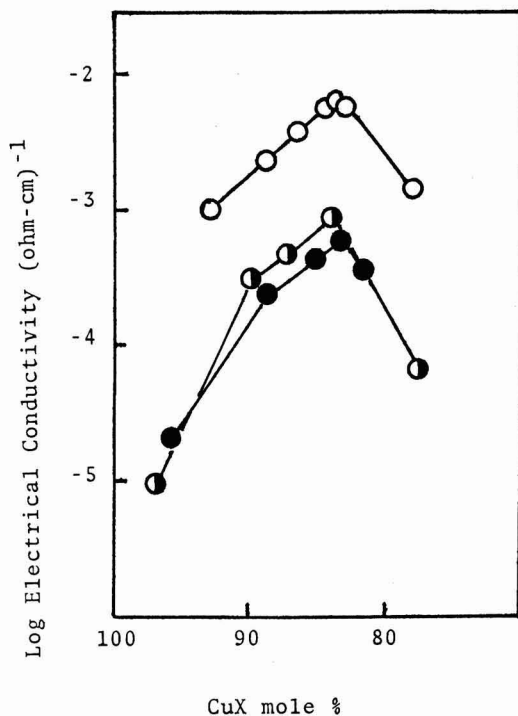


Fig. 1. Composition dependence of electrical conductivity of the binary solid electrolyte systems C<sub>5</sub>H<sub>11</sub>NCH<sub>3</sub>Br-CuBr (○), C<sub>5</sub>H<sub>11</sub>NCH<sub>3</sub>I-CuI (●), and C<sub>4</sub>H<sub>9</sub>ONCH<sub>3</sub>I-CuI (●) at 25°C.

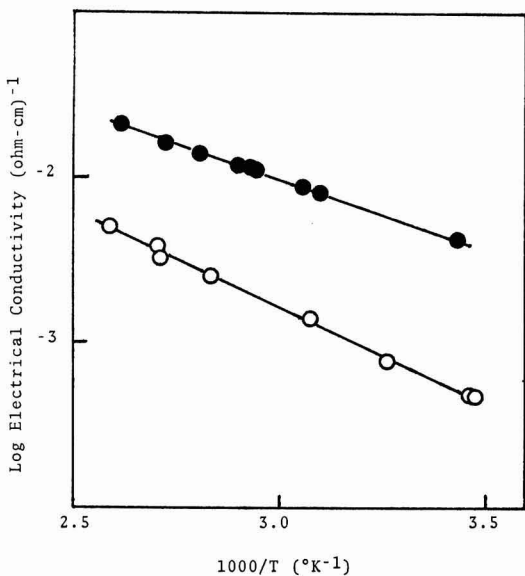


Fig. 2. Temperature dependence of the electrical conductivity of 6CuBrC<sub>5</sub>H<sub>11</sub>NCH<sub>3</sub>Br (●) and 6CuIC<sub>5</sub>H<sub>11</sub>NCH<sub>3</sub>I (○).

from Eq. [2]. Figure 3 shows the values of  $\sigma_h$  for the C<sub>5</sub>H<sub>11</sub>NCH<sub>3</sub>Br-CuBr, C<sub>5</sub>H<sub>11</sub>NCH<sub>3</sub>I-CuI, and C<sub>4</sub>H<sub>9</sub>ONCH<sub>3</sub>I-CuI systems as a function of the composition of CuX at 110°C. The electronic conductivity for these systems decreases with decreasing copper(I) halide content. The conductivity of C<sub>5</sub>H<sub>11</sub>NCH<sub>3</sub>Br 16 m/o-CuBr 84 m/o is lower than  $3.2 \times 10^{-12}$  (ohm-cm)<sup>-1</sup> at 110°C. The temperature dependence of the



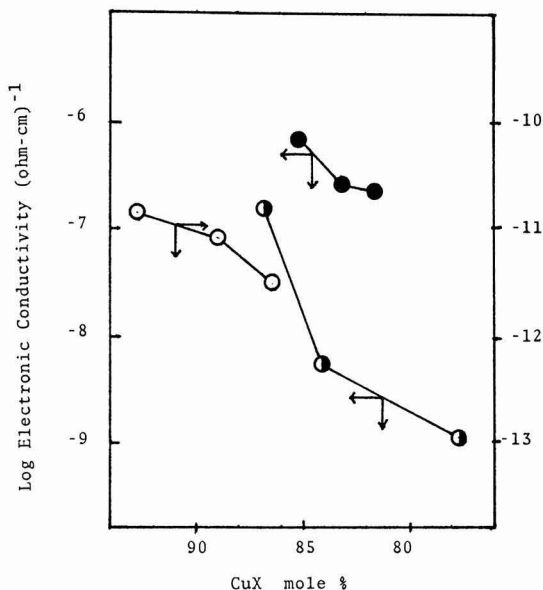


Fig. 3. Composition dependence of the electronic conductivity of the binary solid electrolyte systems  $C_5H_{11}NCH_3Br-CuBr$  (○),  $C_5H_{11}NCH_3I-CuI$  (◐), and  $C_4H_9ONCH_3I-CuI$  (●).

electronic conductivity of the  $C_5H_{11}NCH_3Br-CuBr$  system is shown in Fig. 4. Thus, it is concluded that the conduction in the systems  $C_5H_{11}NCH_3Br-CuBr$ ,  $C_5H_{11}NCH_3I-CuI$ , and  $C_4H_9ONCH_3I-CuI$  is essentially ionic.

### Conclusion

It is concluded from the experimental results that the formation of high copper ion conductivity solids in the organic ammonium halide-copper(I) halide system is related to not only the size of ammonium ion, but also to its flexibility.

Manuscript submitted June 2, 1975; revised manuscript received Aug. 16, 1975.

Any discussion of this paper will appear in a Discussion Section to be published in the December 1976 JOURNAL. All discussions for the December 1976 Discussion Section should be submitted Aug. 1, 1976.

Publication costs of this article were partially assisted by the authors.

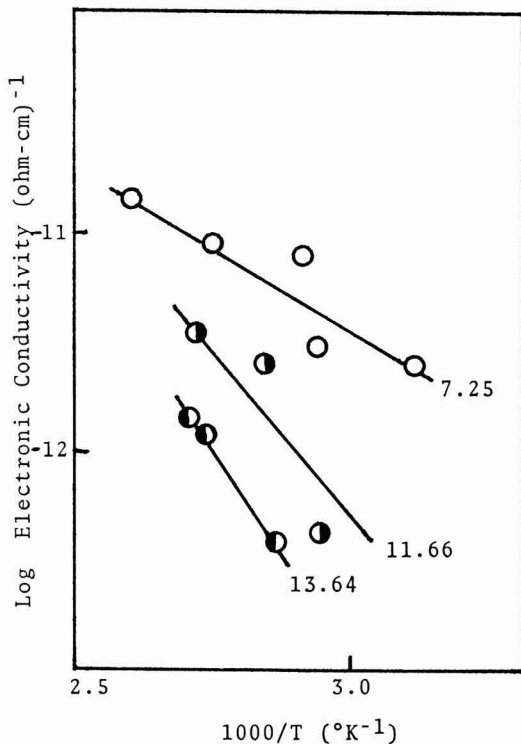


Fig. 4. Temperature dependence of the electronic conductivity of  $C_5H_{11}NCH_3Br-CuBr$ .  $C_5H_{11}NCH_3Br$  (m/o): (○) 7.25, (◐) 11.66, (●) 13.64.

### REFERENCES

1. B. B. Owens, *This Journal*, **117**, 1536 (1970).
2. B. B. Owens, J. H. Christie, and G. T. Tiedeman, *ibid.*, **118**, 1144 (1971).
3. M. L. Berardelli, C. Biondi, M. De Rossi, G. Fonseca, and M. Giomini, *ibid.*, **119**, 114 (1972).
4. T. Takahashi, O. Yamamoto, and S. Ikeda, *ibid.*, **120**, 1431 (1973).
5. T. Takahashi and O. Yamamoto, *ibid.*, **122**, 83 (1975).
6. T. Takahashi, N. Wakabayashi, O. Yamamoto, and S. Ikeda, Abstracts, 40th Meeting Electrochem. Soc. Japan, Satsuporo, August 1973.
7. A. F. Sammells, Ext. Abst. Fall Meeting Electrochem. Soc., Oct. (1974) New York.
8. K. Sanada, A. Iwasawa, E. Tsuchida, and I. Shinohara, Abstracts, vol. I, p. 1, 27th Fall Meeting of the Chemical Society of Japan, Nagoya, October 1972.
9. C. Wagner, Proc. 7th Meeting C.I.T.C.E., Lindau, 1955, p. 361, Butterworths, London (1957).

# Mass Spectrometric Investigation of the Reaction Velocities of $\text{BCl}_3$ and $\text{BBr}_3$ with Oxygen and Water Vapor in a Diffusion Furnace

V. Geiss<sup>1</sup> and E. Frösche

Institut für Halbleitertechnik, RWTH Aachen, D-51 Aachen, Germany

## ABSTRACT

The velocities of the reactions of  $\text{BCl}_3$  and  $\text{BBr}_3$  with  $\text{O}_2$  and  $\text{H}_2\text{O}$  were measured in a diffusion tube. The conditions (gas composition, gas velocity, temperature) were those commonly used in the open tube diffusion process. For the analysis the gaseous reaction products were sampled with a quadrupole mass spectrometer at different locations in the tube. The measurements indicate that with  $\text{H}_2\text{O}$  the reaction proceeds rapidly, but with  $\text{O}_2$  very slowly. Therefore, with  $\text{O}_2$  present in the gas mixture, large variations of the gas composition occur along the length of the tube. The time behavior of this reaction is described by its half-life and its dependence on temperature and  $\text{O}_2$  partial pressure.

A commonly employed method for the diffusion of boron into silicon is the "open tube" technique, using nitrogen with a small percentage of oxygen as a carrier gas and boron halides such as boron trichloride ( $\text{BCl}_3$ ) (2) or boron tribromide ( $\text{BBr}_3$ ) (3-6). If surface concentrations below saturation are desired, the diffusion process is performed in two steps, a boron deposition step at temperature below  $1000^\circ\text{C}$  and a drive-in step above  $1000^\circ\text{C}$ . The reproducibility of the results depends mainly on the boron deposition step. The oxygen reacts with the boron halides and the silicon to produce  $\text{B}_2\text{O}_3$  and  $\text{SiO}_2$ .  $\text{B}_2\text{O}_3$  and  $\text{SiO}_2$  form a borosilicate glass (BSG), which functions as a secondary dopant source during deposition and drive-in.

When using the process in the fabrication of semiconductor devices, a relatively long (typically 10 in.) zone of constant  $\text{B}_2\text{O}_3$  supply is mandatory in order to obtain uniform deposition on the many silicon substrates in the same run. The quality of BSG which is formed on the silicon wafers at each position in the diffusion tube is strongly dependent on the temperature, gas composition, and gas velocity. In fact, for an arbitrarily chosen set of conditions, the zone where appreciable deposition occurs may even fall entirely upstream or downstream of the position of the sample support. This suggests that the time necessary for carrying the  $\text{B}_2\text{O}_3$  formation reaction to completion is comparable to that required for the flow of the gas through the tube of the diffusion furnace (6). Thus it appears that the kinetics of  $\text{B}_2\text{O}_3$  formation play a decisive role in the boron diffusion process. Therefore, we have studied the kinetics by analyzing the gas composition in a diffusion tube using a mass spectrometer. It will be shown that the data obtained lead to a clearer understanding of the system and facilitate optimization of the diffusion process.

## Reactions and Equilibrium States

The compositions of the gas phases in thermodynamic equilibrium at  $973^\circ$  and  $1053^\circ\text{C}$  were calculated for the diffusion systems  $\text{BCl}_3\text{-O}_2$  and  $\text{BBr}_3\text{-O}_2$  using the JANAF Tables (1). The results of these calculations are shown in Tables I and II. Here the partial pressure of the main reaction products which result from reactions of the doping gases with the oxygen are listed. The initial pressures of the doping gases and oxygen correspond to the values which were used in the gas analysis experiments.

<sup>1</sup> Present address: Institut für Werkstoffe der Elektrotechnik, Ruhr-Universität Bochum, D-463 Bochum, Germany.

Key words: gas analysis, doping gases, boron, silicon.

At the temperature used,  $\text{Cl}_2$  is dissociated partially and  $\text{Br}_2$  largely according to



and



At equilibrium the gas phase consists entirely of the reaction products and residual oxygen. The partial pressure of all boron containing gaseous species is small compared to the boron content of the input gas. From this one can conclude that the main part of the

Table I. Initial and equilibrium partial pressures of the system  $\text{BCl}_3\text{-O}_2$  (1)

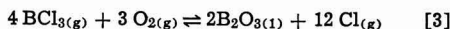
Initial partial pressures							
	$P_{\text{BCl}_3(\text{g})}/\text{atm}$						$P_{\text{O}_2(\text{g})}/\text{atm}$
$T = 973^\circ\text{C}$	$1.6 \cdot 10^{-4}$						$1 \cdot 10^{-2}$
$T = 1053^\circ\text{C}$	$6.5 \cdot 10^{-5}$						$1 \cdot 10^{-2}$
Equilibrium partial pressures							
Substance	Cl	$\text{Cl}_2$	$\text{BO}_2$	$\text{B}_2\text{O}_3$	$\text{BClO}$	$\text{BCl}_3$	$\Sigma \text{ Bor}/\%$ as $\text{B}_2\text{O}_3$ liquid
$P/\text{atm at } T$	1	1.9	2.9	3.9	3.4	8.4	99.8
$= 973^\circ\text{C}$	$10^{-4}$	$10^{-4}$	$10^{-7}$	$10^{-8}$	$10^{-8}$	$10^{-11}$	
$P/\text{atm at } T$	1	4.6	1.5	3.8	8.6	3.1	96.4
$= 1053^\circ\text{C}$	$10^{-4}$	$10^{-5}$	$10^{-9}$	$10^{-7}$	$10^{-8}$	$10^{-11}$	

Table II. Initial and equilibrium partial pressures of the system  $\text{BBr}_3\text{-O}_2$  (1)

Initial partial pressures							
	$P_{\text{BBr}_3(\text{g})}/\text{atm}$						$P_{\text{O}_2(\text{g})}/\text{atm}$
$T = 973^\circ\text{C}$	$3.5 \cdot 10^{-5}$						$1 \cdot 10^{-2}$
$T = 1053^\circ\text{C}$	$3.4 \cdot 10^{-5}$						$1 \cdot 10^{-2}$
Equilibrium partial pressures							
Substance	Br	$\text{Br}_2$	$\text{BO}_2$	$\text{B}_2\text{O}_3$	$\text{BBrO}$	$\text{BBr}_3$	$\Sigma \text{ Bor}/\%$ as $\text{B}_2\text{O}_3$ liquid
$P/\text{atm at } T$	1	2.8	1.9	3.9	8.0	5.2	99.2
$= 973^\circ\text{C}$	$10^{-4}$	$10^{-6}$	$10^{-7}$	$10^{-8}$	$10^{-11}$	$10^{-10}$	
$P/\text{atm at } T$	1	9.5	1.1	3.8	3.2	7.7	94.6
$= 1053^\circ\text{C}$	$10^{-4}$	$10^{-7}$	$10^{-9}$	$10^{-7}$	$10^{-10}$	$10^{-10}$	

boron injected into the diffusion system is deposited as a condensed phase, probably as liquid  $B_2O_3$ .

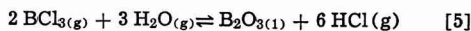
Therefore, good approximations of the over-all reactions are



and



Calculations of the equilibrium pressures in the systems  $BCl_3-H_2O$  and  $BBr_3-H_2O$  are given in Tables III and IV. For a very small surplus of water vapor ( $P_{H_2O} < 10^{-6}$  atm), as a good approximation the following over-all reactions are valid



A larger surplus of water vapor would reduce the amount of the  $B_2O_3$  in favor of  $HBO_2$ .

### Experimental

For the experiments a three-zone resistance-heated diffusion furnace was used. The nitrogen carrier gas passed through the full length of the tube and could be mixed with oxygen and water vapor (Fig. 1). A smaller part of nitrogen carried the doping gases  $BCl_3$  or  $BBr_3$  through an extra tube to the beginning of the constant temperature zone, where the gases were mixed. Both gases were preheated while flowing through the heated front part of the furnace. Thus the chemical reactions would start at a well-defined position. The temperature was kept uniform, within  $2^\circ C$  over the range of  $5 < L < 60$  cm. The velocity of the  $N_2$  carrier gas was mostly  $v = 1$  cm/sec. All gases except water vapor were dried to the extent that the residual partial pressure of water vapor was less than  $10^{-6}$  atm. In this way, unwanted reactions of the doping gases already in the supply tubes could be pre-

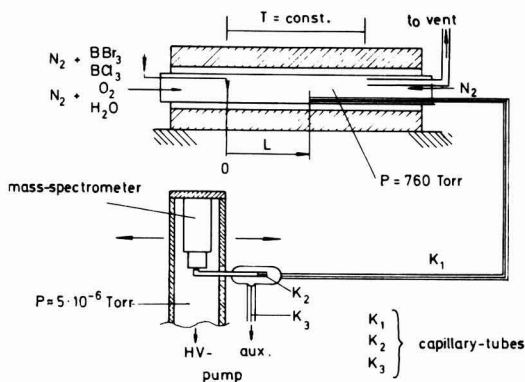


Fig. 1. Diffusion furnace and gas sampling system

vented. To avoid contamination of the colder end zone of the quartz tube by condensation, the reaction products were exhausted from the hot zone and dry nitrogen was blown in from the downstream side to provide a gas buffer.

For the analysis of the gas composition in the tube, a small part of the gas was pumped through a quartz capillary tube into a quadrupole mass spectrometer. The gas transport through the capillary tube to the spectrometer took about 0.2 sec. It cannot be excluded that during this time the reaction could reverse itself due to cooling. In fact although the stable form of bromine at the temperatures and concentrations in the reaction tube is  $Br_2$ , it was always measured as  $Br$ , the stable form at room temperature. The calibration of the mass spectrometer was done by controlled dilution of  $Cl_2$ ,  $Br_2$ ,  $BCl_3$ , and  $BBr_3$  with an error of less than  $\pm 10\%$ . The reproducibility of the concentration measurements in the  $10^{-4}$  atm range was about  $\pm 3\%$ . The amount of condensed material could be determined from the differences between the partial pressures of the gaseous species at input and their measured value after reaction. The vacuum system together with the capillary tube could be moved in such a way that sampling of the gas was possible in the range  $-10 < L < 60$  cm. Changes of the gas composition along the tube could thus be measured as a function of the distance from the doping gas inlet or as a function of time, since the gas velocity was known.

### Results

An example of such a mass spectrometric measurement of the reaction of  $BCl_3$  with  $O_2$  at  $1057^\circ C$  is shown in Fig. 2. The decrease of the  $BCl_3$  partial pressure and the increase of the  $Cl_2$  partial pressure are

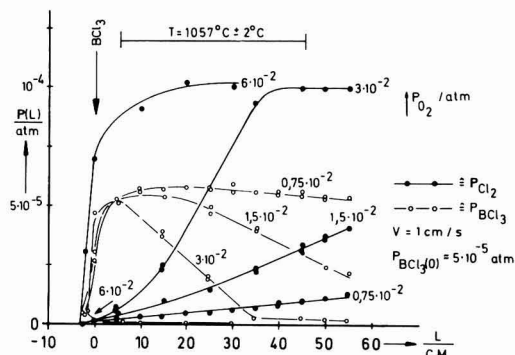


Fig. 2. Reaction of  $BCl_3$  with  $O_2$  as a function of the location in the tube at  $1057^\circ C$  for different  $O_2$  partial pressures.

Table III. Initial and equilibrium partial pressures of the system  $BCl_3-H_2O$  (1)

Initial partial pressures		
	$P_{BCl_3(0)}/\text{atm}$	$P_{H_2O(0)}/\text{atm}$
$T = 973^\circ C$	$3.3 \cdot 10^{-5}$	$5.1 \cdot 10^{-5}$
$T = 1053^\circ C$	$3.3 \cdot 10^{-5}$	$5.2 \cdot 10^{-5}$
Equilibrium partial pressures		

Substance	HCl	$H_2O$	$BHO_2$	$B_2O_3$	$BCl_3$	$B(OH)_3$	$\Sigma \text{ Bor}/\%$ as $B_2O_3$ liquid
$P/\text{atm}$ at $T$	1	1	2.7	3.9	2.6	1.2	93.3
$P/\text{atm}$ at $T$	$10^{-4}$	$10^{-6}$	$10^{-9}$	$10^{-8}$	$10^{-11}$	$10^{-11}$	
$P/\text{atm}$ at $T$	1	1	4.7	3.8	5.9	1.3	83.5
$P/\text{atm}$ at $T$	$10^{-4}$	$10^{-6}$	$10^{-9}$	$10^{-7}$	$10^{-11}$	$10^{-11}$	

Table IV. Initial and equilibrium partial pressures of the system  $BBr_3-H_2O$  (1)

Initial partial pressures		
	$P_{BBr_3(0)}/\text{atm}$	$P_{H_2O(0)}/\text{atm}$
$T = 973^\circ C$	$3.3 \cdot 10^{-5}$	$5.1 \cdot 10^{-5}$
$T = 1053^\circ C$	$3.3 \cdot 10^{-5}$	$5.2 \cdot 10^{-5}$
Equilibrium partial pressures		

Substance	HBr	$H_2O$	$BHO_2$	$B_2O_3$	$B(OH)_3$	$BBr_3$	$\Sigma \text{ Bor}/\%$ as $B_2O_3$ liquid
$P/\text{atm}$ at $T$	1	1	1.8	3.9	1.5	1.5	94.4
$P/\text{atm}$ at $T$	$10^{-4}$	$10^{-6}$	$10^{-9}$	$10^{-8}$	$10^{-11}$	$10^{-12}$	
$P/\text{atm}$ at $T$	1	1	4.7	3.8	1.4	3.7	83.7
$P/\text{atm}$ at $T$	$10^{-4}$	$10^{-6}$	$10^{-9}$	$10^{-7}$	$10^{-11}$	$10^{-12}$	

represented as a function of the distance  $L$  from the doping gas inlet with the  $\text{O}_2$  pressure as a parameter. The input pressures of  $\text{BCl}_3$  and the gas velocity were kept constant for these series of measurements. Increasing the  $\text{O}_2$  partial pressure caused an increase of the reaction velocity.

In spite of a considerable surplus of oxygen and the fact that at equilibrium the gas phase contains only the oxidation products, the reaction velocity is remarkably low. The decrease in the partial pressure of  $\text{BCl}_3$  is balanced by the increase in that of  $\text{Cl}_2$ . Other chlorine containing gaseous compounds could not be measured. This appears to confirm Eq. [3] as the correct expression for the over-all reaction. It must be remarked that only the gaseous compounds  $\text{BCl}_3$ ,  $\text{O}_2$ , and  $\text{Cl}_2$  can be analyzed with the mass spectrometer.  $\text{Cl}$  reacts during sampling to  $\text{Cl}_2$ .  $\text{B}_2\text{O}_3$  could not be detected because at the temperatures used it is a liquid and condensed at the tube walls. Figure 3 shows data for the reaction of  $\text{BCl}_3$  with  $\text{O}_2$  at the lower temperature of  $973^\circ\text{C}$ . As expected, lower temperatures cause smaller reaction velocity.

Similar measurements were done with  $\text{BBr}_3$  as a dopant (Fig. 4). They agree with the assumption that Eq. [4] represents the over-all reaction. Comparing the  $\text{BBr}_3$  and  $\text{BCl}_3$  data, it may be seen that for the same  $\text{O}_2$  partial pressure and temperature the reaction velocity is very much higher with  $\text{BBr}_3$ .

In order to characterize the reaction velocity we used the half-life  $\tau_h$ , i.e., the time in which the initial concentration of the doping gas has been reduced by 50%. The values of  $\tau_h$  were read or extrapolated from Fig. 2-4 and plotted as a function of the initial  $\text{O}_2$  partial pressure (Fig. 5). Similar experiments were done for other initial partial pressures of the doping gases in the region  $2 \cdot 10^{-5} < P < 2 \cdot 10^{-4}$  atm. They showed that in this region  $\tau_h$  is independent of the initial doping gas pressure. This indicates that the reaction is first order in the doping gas. Assuming the

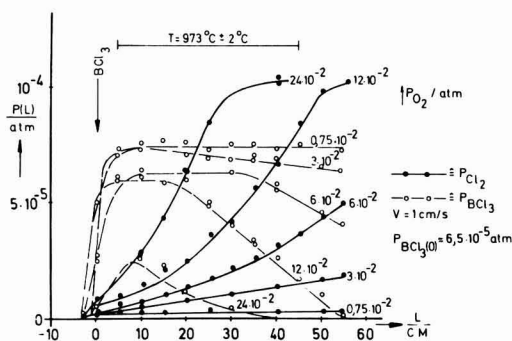


Fig. 3. Reaction of  $\text{BCl}_3$  with  $\text{O}_2$  as a function of the location in the tube at  $973^\circ\text{C}$  for different  $\text{O}_2$  partial pressures.

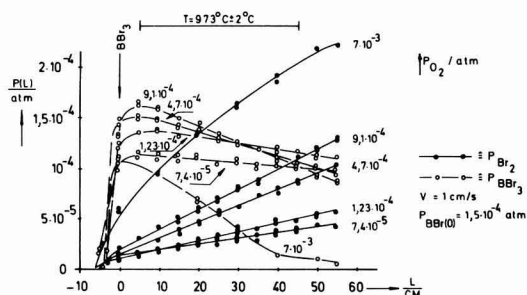


Fig. 4. Reaction of  $\text{BBr}_3$  with  $\text{O}_2$  as a function of the location in the tube at  $973^\circ\text{C}$  for different  $\text{O}_2$  partial pressures.

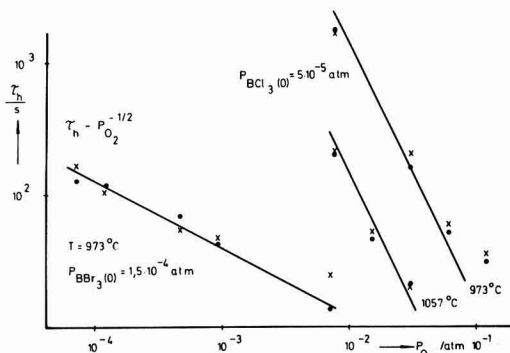


Fig. 5. Half-life  $\tau_h$  of  $\text{BBr}_3$  and  $\text{BCl}_3$  as a function of the  $\text{O}_2$  partial pressure; left-hand side:  $\text{BBr}_3$ , right-hand side:  $\text{BCl}_3$ ; ● calculated from  $\text{BCl}_3$ ,  $\text{BBr}_3$ ; × calculated from  $\text{Cl}_2$ ,  $\text{Br}_2$  partial pressures.

commonly observed exponential temperature dependence, the following expression can be obtained from Fig. 5 for the half-life of  $\text{BCl}_3$  reacting with  $\text{O}_2$

$$\tau_h/\text{sec} = 2.2 \cdot 10^{-17} (P_{\text{O}_2}/\text{atm})^{-2} \exp(3.9 \text{ eV}/kT) \quad [7]$$

The dependence of the time constant on the oxygen partial pressure is that of a third order reaction in  $\text{O}_2$ .

The reaction rate of  $\text{BBr}_3$  with oxygen was determined only at the lower temperature of  $973^\circ\text{C}$ . The dependence of the half-life of  $\text{BBr}_3$  on  $\text{O}_2$  partial pressure may be expressed as

$$\tau_h/\text{sec} = 1.3 \times (P_{\text{O}_2}/\text{atm})^{-1/2} \quad [8]$$

It is somewhat surprising that the pressure dependence of this reaction is very different from the  $\text{BCl}_3$  reaction and corresponds to a reaction order between the first and second. At higher temperatures ( $T > 1000^\circ\text{C}$ ), the reaction of  $\text{BBr}_3$  with nitrogen starts, which makes the measurement of the oxygen reaction rate impossible.

In order to determine if the walls of the tube had any effect on the reaction rate, some measurements were made after the diffusion tube had been partially filled (up to 20 cm) with quartz wool. No difference in the reaction profiles could be noticed, which proves that the reactions are volume processes.

Using water vapor instead of oxygen, the reaction with both doping gases was found to go to completion near  $L = 0$  for all gas velocities investigated even at  $973^\circ\text{C}$ . The time constants  $\tau_h$  were too small to be measured.

## Discussion

The foregoing data show that under the commonly used conditions for boron deposition the doping gases  $\text{BCl}_3$  and  $\text{BBr}_3$  react rather slowly with oxygen, though at equilibrium only the oxidation products are left in the system. Figure 5 shows that at  $973^\circ\text{C}$  and with an oxygen pressure of  $5 \cdot 10^{-2}$  atm the half-life  $\tau_h$  for the reaction of  $\text{BCl}_3$  with oxygen is about 100 sec. This means that for a gas velocity of 1 cm/sec the reaction cannot be completed within the length of a typical diffusion tube. With  $\text{BBr}_3$  more favorable results can be expected since for the above-mentioned conditions the time  $\tau_h$  is about 6 sec.  $\text{BBr}_3$  does not dissociate thermally into boron and bromine at temperatures as low as  $200^\circ\text{C}$ , as was hypothesized in Ref. (5). Such a dissociation could not even be noticed at  $973^\circ\text{C}$ .

A quantitative comparison between the mass spectrometric measurements and published diffusion measurements is not possible, since in the literature generally no information is given concerning the distance between the doping gas inlet and the first silicon wafer, the linear gas velocity and the temperature pro-

file of the tube. Nevertheless a qualitative comparison can be made.

Parekh and Goldstein (6) describe diffusion investigations in an oxidizing atmosphere using  $BBr_3$  as dopant. In the direction of flow of the gas, they first observed in the diffusion tube an area with decreasing sheet resistance, then one with constant sheet resistance, and finally an area with rising sheet resistance. They showed that the interesting area of constant sheet resistance moves toward the doping gas inlet for rising temperatures and oxygen partial pressures and decreasing gas velocities.

The same behavior was observed in our mass spectrometric investigations for the reaction zone with decreasing dopant pressures and increasing pressures of the reaction products (Fig. 3). Taking our results and those of Parekh and Goldstein together, it follows that constant sheet resistances can be expected when a major part of the doping gas has reacted to form  $B_2O_3$ . The  $B_2O_3$  is carried by the gas stream and will condense at the same time on the quartz walls and the silicon wafers. As long as the BSG layer formed in this way has an adequate thickness, constant sheet resistances are obtained upon the drive-in. Since the reaction proceeds very slowly, the amount of the  $B_2O_3$  formed is insufficient in the part of the tube near the inlet. In the third zone the supply of  $B_2O_3$  is depleted because of the continuous condensation of this compound.

Using water vapor instead of oxygen, the doping gases react immediately. When a small surplus of water is used mainly  $B_2O_3$  will be formed. This reaction proceeds even in low temperatures. Therefore all carrier

gases must be dried thoroughly to prevent unwanted reactions in the supply tubes.

### Acknowledgments

The authors are indebted to Professors P. Balk and E. Kubalek for helpful discussions. They would like to acknowledge the support of the Deutsche Forschungsgemeinschaft, which enabled these investigations in the Sonderforschungsbereich 56 "Festkörperelektronik."

Manuscript submitted Dec. 27, 1974; revised manuscript received Sept. 8, 1975.

Any discussion of this paper will appear in a Discussion Section to be published in the December 1976 JOURNAL. All discussions for the December 1976 Discussion Section should be submitted by Aug. 1, 1976.

### REFERENCES

1. JANAF Thermochemical Tables, Dow Chemical Co., Midland Michigan (1965).
2. K. D. Kang, R. R. Burgess, and Y. D. Kwon, Paper 520 presented at The Electrochemical Society Meeting, Montreal, Canada, Oct. 6-11, 1968.
3. J. F. Shepherd, R. J. Dendall, and P. Balk, Paper 196 presented at The Electrochemical Society Meeting, Philadelphia, Pennsylvania, Oct. 9-14, 1966.
4. H. D. Pawlowski and J. C. Brixey, Paper 173 presented at The Electrochemical Society Meeting, Chicago, Illinois Oct. 15-19, 1967.
5. G. M. Oleszek and W. M. Whittemore, Paper 303 presented at The Electrochemical Society Meeting, New York, New York, May 4-9, 1969.
6. P. C. Parekh and D. R. Goldstein, *Proc. IEEE*, **57**, 9 (1969).

## Thermodynamic Domains of the Various Solid Deposits in the B-C-H-Cl Vapor System

M. Ducarroi

Laboratoire des Ultra-Réfractaires, C.N.R.S., Odeillo, 66120 Font-Romeu, France

and C. Bernard

Centre d'Information de Thermodynamique Chimique Minérale, E.N.S.E.E.G., 38401 Saint Martin d'Herès, France

### ABSTRACT

Calculations have been made of the equilibrium conditions under which chemical deposition of  $B_4C$  from  $BCl_3$ - $CH_4$ - $H_2$  mixtures takes place. Pure  $B_4C$  is mainly obtained for gas-phase mixtures in which  $BCl_3/CH_4 > 1$  and  $H_2/BCl_3 > 1$ . The maximum yield is obtained in the range 1675°-2075°K for the initial composition  $BCl_3 = 0.1$ ,  $CH_4 = 0.02$ ,  $H_2 = 0.88$ . The dependence of the hydrogen partial pressure on the equilibrium composition is discussed. At high temperatures with a large excess of hydrogen, the tendency is to form gaseous  $BH_2$  and  $BH_3$  instead of condensed species. With decreasing the amount of hydrogen, graphite begins to deposit under  $CH_4/BCl_3 \ll 1/4$  ratios. At lower temperatures the equilibrium content of  $BCl_2H$  increases as the  $H_2/BCl_3$  ratio falls. The results of the calculations are confirmed by experimental data.

Chemical vapor deposition is a complex process in which many factors affect the deposition, and thus the process is difficult to optimize. Nevertheless it can be analyzed in terms of thermodynamic, transport, and kinetic factors to find a set of deposition conditions which will produce the desired goal.

The thermodynamic system evaluation is the first step of a complete analysis. The equilibrium composition is obtained by such calculations and sometimes

Key words: boron carbide, vapor deposition, efficiency, boron trichloride, methane.

unsuspected reactions may be deduced from atomic balances equations. The thermodynamic analysis has been used by many authors in order to predict the preparation conditions of doped layers, solid solutions, binary or ternary compounds (1-9).

The conclusions obtained from the thermodynamic evaluation may be useful to describe a reaction mechanism. Using a thermodynamic approach, the presence of  $BCl_2H$  in the B-Cl-H system was demonstrated at equilibrium, this fact has been used by Carlton (10) to postulate a kinetic model taking into account this



species. The present paper is concerned with a thermodynamic analysis of the B-C-H-Cl vapor system in order to define optimum conditions for deposition of  $B_4C$  from  $BCl_3$ - $CH_4$ - $H_2$  gas mixtures. This compound has interesting properties (light weight, extreme hardness, resistance to abrasion, resistance to chemical attack) and is employed in the nuclear, metallurgical, and watch industries.

A number of investigators have attempted to prepare it as coatings, but in most cases the chemical vapor deposition of  $B_4C$  seems to be difficult. According to different authors, deposits may be either boron rich or carbon rich depending on the composition of the initial gas phase. Deposits of pyrolytic carbon +  $B_4C$  or pyrolytic carbon only may be produced (11-16). Furthermore, there exists no thermodynamic study which gives the solid deposit domains in this system.

### Procedure

The computation procedure employed for the determination of the equilibrium in a system taking into account several condensed species is based on the minimization of the free energy and is detailed in a previous paper (18). It is a time-sharing program. The necessary starting data are the free-energy function and the standard heats of formation of the chemical species considered. In calculations of the equilibrium of the system B-C-H-Cl, the following species were chosen:  $BCl_3$ ,  $CH_4$ ,  $H_2$ ,  $BCl_2H$ ,  $BH$ ,  $BH_2$ ,  $BH_3$ ,  $B_2H_6$ ,  $B_3H_9$ ,  $B_2Cl_4$ ,  $Cl_2$ ,  $HCl$ ,  $C_2H_2$  in the gas phase, and  $B_4C$ , C (graphite), B (a) in the condensed phase. In addition, we define the total pressure, the temperature, and the initial gas-phase composition (number of moles of species), that is, in our case, for the total pressure  $P = 1$  atm

$$BCl_3 : a \text{ moles} \equiv P_0 BCl_3$$

$$CH_4 : b \text{ moles} \equiv P_0 CH_4$$

$$H_2 : 1-a-b \text{ moles} \equiv P_0 H_2$$

Most of our results are presented in terms of efficiency  $\eta$ .  $\eta$  is defined with respect to the content of  $BCl_3$  for all components of boron

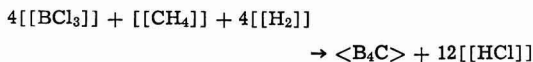
$$\eta_{BCl_3} = \frac{BxCyClzHw}{a} \frac{Bx'Cy'Clz'Hw'}{100} 100$$

For C,  $CH_4$ , and  $C_2H_2$  the coefficient of conversion is defined with respect to the initial methane

$$\eta_{CH_4} = \frac{CyHw}{b} \frac{Cy'Hw'}{100} 100$$

### Results and Discussion

The general behavior of the equilibrium is shown in Fig. 1-9. The variation of the boundaries of the deposition ranges as a function of the initial partial pressures is shown in Fig. 1-3 for three temperatures (1400°, 1800°, 2200°K). The calculation precision is of  $10^{-8}$  molecule and in this case it follows a same order precision for the individual boundary line evaluations. The dotted line, for the case of B and C atomic balances, represents the stoichiometry of the following reaction



So the diagram is divided in two regions: the upper part which represents all the input values of composition with an excess of boron (with respect to the above-mentioned reaction); the lower part in which are the reactant concentrations with an excess of carbon.

The  $B_4C$  deposit domain is very narrow but it extends into a wide range of initial compositions: into

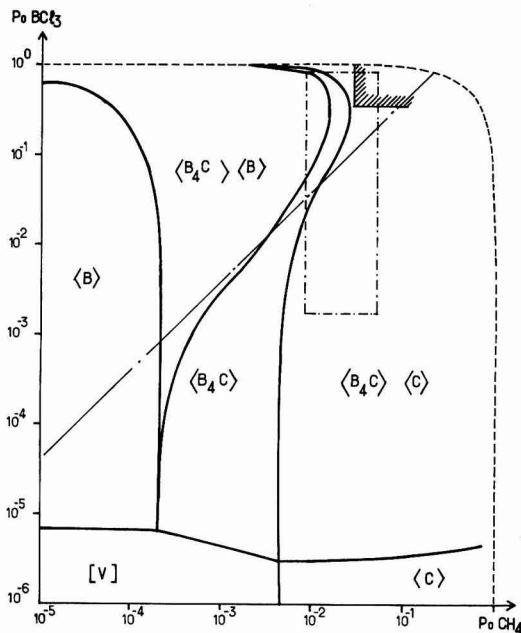


Fig. 1. Deposition domains of the solid species at  $T = 1400^\circ K$ ,  $P = 1$  atm. / / / = composition range of Fitzer and Röhms (16), - - - = composition range of Moore and Volk (15).

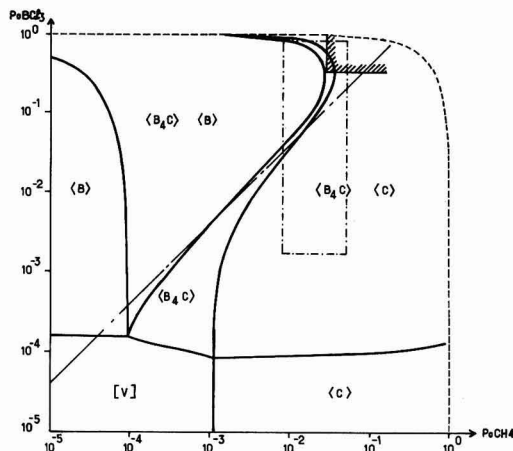


Fig. 2. Deposition domains of the solid species at  $T = 1800^\circ K$ ,  $P = 1$  atm. / / / = composition range of Fitzer and Röhms (16), - - - = composition range of Moore and Volk (15).

the carbon-excess side for the low partial pressures of  $BCl_3$  and  $CH_4$ , that is a large excess of hydrogen; into the boron-excess side for initial mixtures with a moderate dilution with  $H_2$ . The domain of pure  $B_4C$  is neighbored by the two-phase domains  $B_4C$ -C and  $B_4C$ -B, it is limited at the lowest part by the gas phase and at its limits by the pure solid-phases B and C.

An increase in the temperature greatly favors the stability of the gas phase and the pure carbon domain. At 2200°K these two phases appear in the upper part of the diagram for high partial pressures of  $BCl_3$  ( $BCl_3 > 0.7$ ). Figure 4 shows the details of this zone. At lower temperature the results of the calculations indicate the same phenomenon. According to Table I we can see the phase boundaries at 1400°-1800°K for different initial concentrations of  $CH_4$ . This table shows

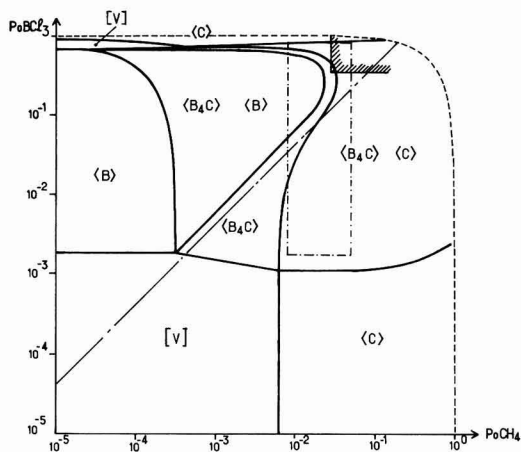


Fig. 3. Deposition domains of the solid species at  $T = 2200^\circ\text{K}$ ,  $P = 1 \text{ atm}$ .  $////$  = composition range of Fitzner and Röhlm (16),  $- \cdot -$  = composition range of Moore and Volk. (15).

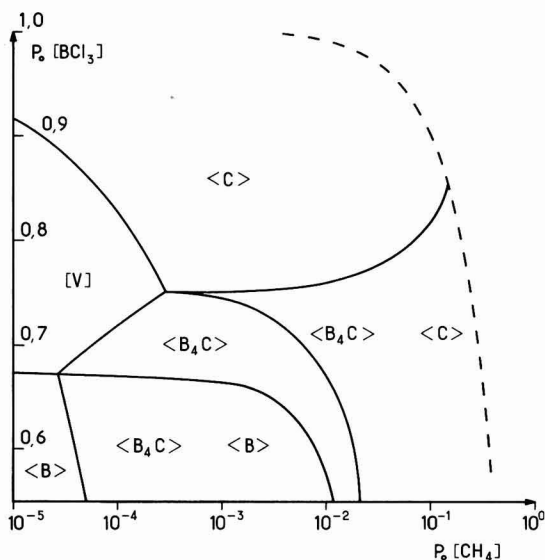


Fig. 4. Details of the deposition domains at  $2200^\circ\text{K}$ ; [V] = vapor phase.

us the precision that the method provides. As a result of the thermodynamic calculation we obtained the gas-phase equilibrium composition. The equilibrium values depend markedly both on the temperature and the excess of hydrogen (that is the ratio  $\text{H}_2/\text{BCl}_3$ ).

In the low temperatures side, the predominant species in the gas phase are  $\text{H}_2$ ,  $\text{HCl}$ ,  $\text{CH}_4$ ,  $\text{BCl}_3$ , and  $\text{BCl}_2\text{H}$ . Dilution with a large excess of  $\text{H}_2$  insures the complete reduction of  $\text{BCl}_3$  producing free boron; the decomposition of  $\text{CH}_4$  is inhibited. As  $\text{H}_2/\text{BCl}_3$  decreases, the formation of  $\text{BCl}_2\text{H}$  increases. When the value of this ratio is unity,  $\text{BCl}_3$  is still present but  $\text{CH}_4$  completely disappears to give free carbon and boron carbide.

In the high temperatures side,  $\text{H}_2$ ,  $\text{HCl}$ ,  $\text{C}_2\text{H}_2$ ,  $\text{CH}_4$ ,  $\text{BH}_2$ ,  $\text{BH}_3$ ,  $\text{BCl}$ ,  $\text{BCl}_2$ , and  $\text{BCl}_3$  are the major species with a trend to the formation of molecules with B-H or C-H bonds as the excess of hydrogen increases. Then the condensed phases completely disappear. If there is no excess of hydrogen, the molecules with B-Cl bonds are mainly formed in the vapor state and solid

Table I. Examples of phase boundaries at  $T = 1400^\circ\text{K}$  and  $1800^\circ\text{K}$ , vs. initial concentrations\*

$\text{BCl}_3$	$T = 1400^\circ\text{K}$		$T = 1800^\circ\text{K}$	
	$\text{CH}_4$ $1 \cdot 10^{-5}$	$\text{CH}_4$ $1 \cdot 10^{-4}$ Phases	$\text{CH}_4$ $2 \cdot 10^{-5}$	$\text{CH}_4$ $1 \cdot 10^{-5}$ Phases
0.6	x			
0.65	•			
0.7	•			
0.95	"	"	•	•
0.96	"	"	"	"
0.97	"	"	○	○
0.9755	"	"	"	○
0.9757	"	"	"	○
0.976	"	"	"	○
0.99	•	"	■	■
0.995	•	•	"	"
0.997	•	"	"	"
0.9977	○	○	"	"
0.997999	○	"	"	"
0.998	○	■	"	"
0.9985	○	"	"	"
0.99885	■	"	////	"
0.999	△	"	////	"
0.999	△	"	////	"
0.9991	△	△	////	△
0.9999	"	"	////	////
0.99999	△	////	////	////

\* x = <B>, • = <B<sub>4</sub>C><B>, ○ = <B<sub>4</sub>C>, ■ = <B<sub>4</sub>C><C>, △ = <C>, \* [V] //// = end of calculation.

$\text{B}_4\text{C}$  and  $\text{C}$  tend to deposit. Figure 5 details the phenomenon shown in Fig. 4. If the input partial pressure of  $\text{BCl}_3$  is 0.8 atm, deposition of pure  $\text{B}_4\text{C}$  is impossible for a partial pressure of  $\text{CH}_4$  ranging from  $1 \times 10^{-5}$  to  $7 \times 10^{-2}$ . The homogeneous equilibrium is due to the pressure of  $\text{C}_2\text{H}_2$ ,  $\text{BCl}_2$ ,  $\text{BCl}$ , and  $\text{BCl}_2\text{H}$  and to the high content of  $\text{BCl}_3$  in the equilibrium vapor. The carbon is easily obtained as soon as the amount of  $\text{CH}_4$  in the initial gas is very low (e.g.,  $\text{CH}_4/\text{BCl}_3 = 2.5 \cdot 10^{-4}$ ).

Consequently, it is intended to optimize the input composition of the reactants for a given constant partial pressure of  $\text{CH}_4$  ( $P_0\text{CH}_4 = 2 \cdot 10^{-2}$ ) and a range of  $P_0\text{BCl}_3$  ( $0.1 < P_0\text{BCl}_3 < 0.75$ ), that is, in the widest part of the region in which the deposition of pure  $\text{B}_4\text{C}$  occurs. Variation of the equilibrium yield of each vapor species and condensed phases is shown in Fig. 6-8 for

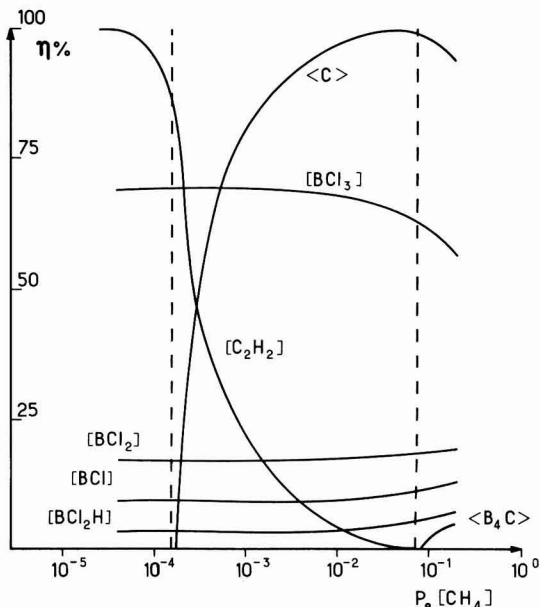


Fig. 5. Variation of the equilibrium yields with  $P_0\text{CH}_4$ ;  $P_0\text{BCl}_3 = 0.8 \text{ atm}$ ,  $T = 2200^\circ\text{K}$ .

1400°, 1800°, and 2200°K. The plots illustrate the evolution of the gas phase reactions as a function of temperature. At 1400°K the pure B<sub>4</sub>C is expected to deposit inside a wide concentration range of boron trichloride (from 0.17 to 0.55). At 1800°-2200°K, this range is becoming narrower and is divided in two parts (0.08 <

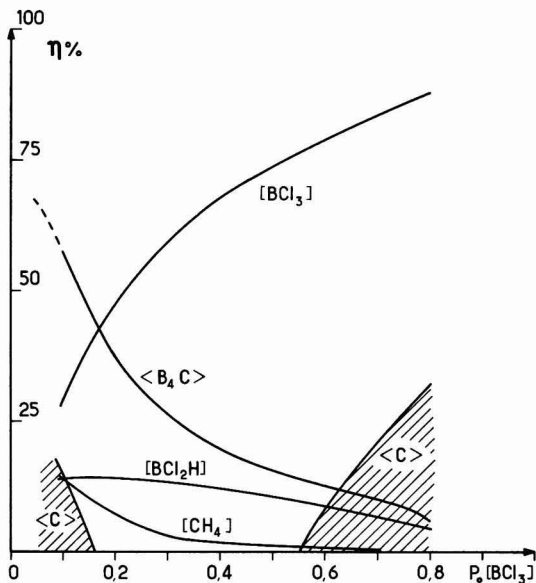


Fig. 6. Variation of the equilibrium yields with  $P_0\text{BCl}_3$ ;  $P_0\text{CH}_4 = 0.02 \text{ atm}$ ,  $T = 1400^\circ\text{K}$ .

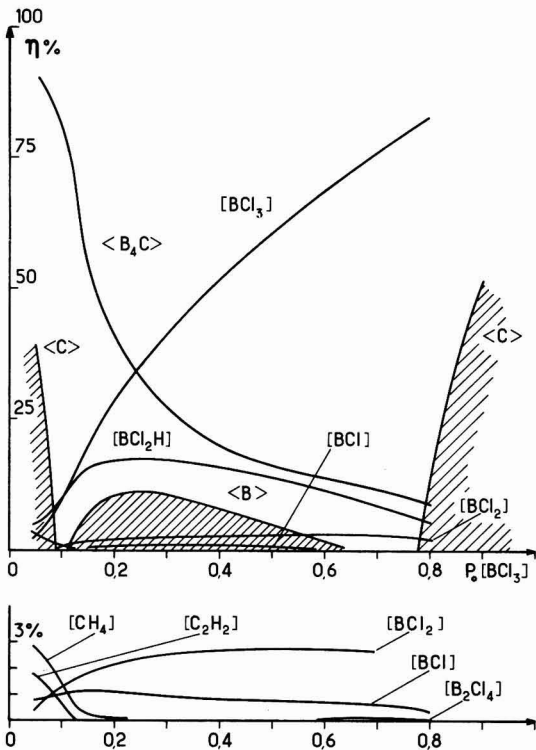


Fig. 7. Variation of the equilibrium yields with  $P_0\text{BCl}_3$ ;  $P_0\text{CH}_4 = 0.02 \text{ atm}$ ,  $T = 1800^\circ\text{K}$ .

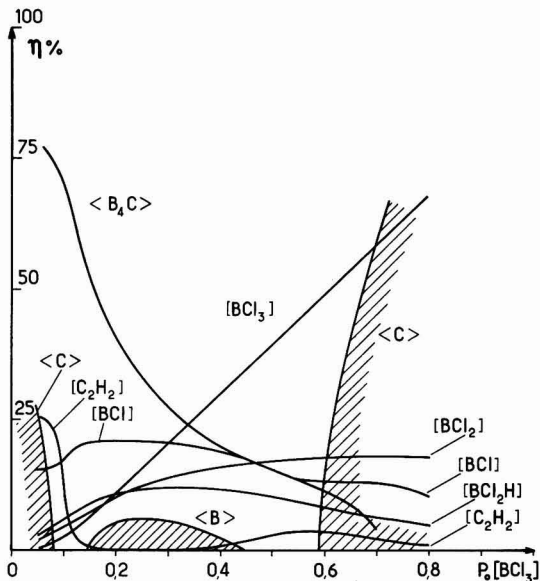


Fig. 8. Variation of the equilibrium yields with  $P_0\text{BCl}_3$ ;  $P_0\text{CH}_4 = 0.02 \text{ atm}$ ,  $T = 2200^\circ\text{K}$ .

$P_0\text{BCl}_3 < 0.12$ ;  $0.64 < P_0\text{BCl}_3 < 0.78$ ) due to the presence of a boron deposit. As shown in Fig. 6-8, the equilibrium amount of boron carbide depends markedly on the initial BCl<sub>3</sub>; there is a significant trend toward increasing the solid yield with decreasing the inlet BCl<sub>3</sub> partial pressure. Therefore we choose  $P_0\text{BCl}_3 = 0.1 \text{ atm}$  to study the amount of thermodynamically available B<sub>4</sub>C in relation to the temperature of deposition. The maximum is found at 1900°K for the input partial pressures,  $P_0\text{BCl}_3 = 0.1$ ,  $P_0\text{CH}_4 = 0.02$ ,  $P_0\text{H}_2 = 0.88$  (Fig. 9). In the temperature range 1675°-2075°K, the solid yield is around 75-80%. One must remember that high efficiencies and quality of the deposit may not occur together. Therefore, if a continuous layer is desired, it would be necessary to lower the temperature under 1225°K to be out of a two solid deposit domain.

It is interesting to check the results of the theoretical analysis with experimental data. The work of Moore and Volk concerning the chemical vapor deposition of B<sub>4</sub>C from BCl<sub>3</sub>, CH<sub>4</sub>, H<sub>2</sub> with various concentrations  $a, b, c \geq 0$  has been employed for comparison. Three types of experiments were performed by these authors. The deposition without hydrogen in the temperature range 1823°-2373°K at low pressures lead to B<sub>4</sub>C-C deposits. At 2473°K, under precise experimental conditions, C (graphite) is obtained. With moderate dilu-

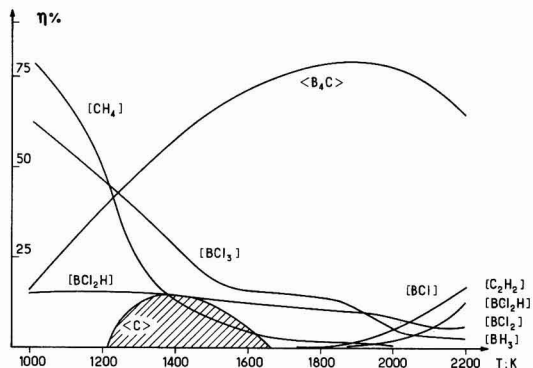


Fig. 9. Temperature dependence of the equilibrium yields;  $P_0\text{CH}_4 = 0.02 \text{ atm}$ ,  $P_0\text{BCl}_3 = 0.1 \text{ atm}$ .

Table II. Comparison of some experimental results (15) and calculations

BCl <sub>3</sub>	CH <sub>4</sub>	H <sub>2</sub>	Moore and Volk			T <sub>K</sub>	Calculations		
			T <sub>K</sub>	P <sub>Torr</sub>	Phases		P <sub>Torr</sub>	Phases	
0.604	0.396	0	1823	1	B <sub>4</sub> C-C	1800	1	B <sub>4</sub> C-C	
0.2	0.8	0	2473	3.5	C	2200	3.5	C	
0.211	0.789	0	2223	4	B <sub>4</sub> C-C	2200	15	B <sub>4</sub> C-C	
							10	C	
0.251	0.749	0	2223	4	B <sub>4</sub> C-C	2200	15	B <sub>4</sub> C-C	
							10	C	
0.604	0.396	0	2223	2.5	B <sub>4</sub> C-C	2200	65	B <sub>4</sub> C-C	
							20	C	
0.248	0.152	0.6	2223	0.5	B <sub>4</sub> C-C	2200	10	B <sub>4</sub> C-C	
							20	C	
0.284	0.146	0.570	2223	0.83	B <sub>4</sub> C-C	2200	25	B <sub>4</sub> C-C	
							20	C	

tion of reactants with H<sub>2</sub>, B<sub>4</sub>C-C deposits are formed. Deposition with a large excess of H<sub>2</sub> above 1300°K at low pressures can produce massive B<sub>4</sub>C and boron- or carbon-rich structures depending on the value of CH<sub>4</sub>/BCl<sub>3</sub>.

The comparison of some experimental and calculated results for initial compositions without H<sub>2</sub> and with a moderate dilution is presented in Table II. Agreement is good for the first two cases though the conditions of calculation are slightly different. In Fig. 1-3 a temperature rise produces a wide enlargement of the range of pure carbon, in addition this boundary shift is favored with a decrease in pressure; subsequently, a pure C deposit would be obtained for BCl<sub>3</sub> = 0.2, CH<sub>4</sub> = 0.8, and T > 2200°K. In the other cases the computer results are a bit different. The general trend is to find B<sub>4</sub>C-C deposition for higher values of total pressure than in the experiments of Moore and Volk, but nevertheless of the same order of magnitude. When large excesses of hydrogen are used, the nature of the deposit in relation to the experimental conditions is not sufficiently specified by these authors to allow a valid comparison with calculations. Nevertheless, the deposition of B<sub>4</sub>C-B, B<sub>4</sub>C, and B<sub>4</sub>C-C above 1300°K, for 0.0098 < a < 0.785, 0.0079 < b < 0.049, and 0.166 < c < 0.9823, as a function of the BCl<sub>3</sub>/CH<sub>4</sub> ratio must be compared with Fig. 1-3. They show, in the zone defined by the previous values a, b, and c, the possibility of depositing the different condensed phases. In addition, in this zone, it has been checked that a large reduction of total pressure does not much affect the deposition range of B<sub>4</sub>C; that is, Fig. 1-3 can probably be used for lower pressures.

Moreover, in a recent work, Fitzer and Röhm mention that deposit structures consisting alternatively of boron and boron carbide can be obtained due to an oscillating chemical reaction influenced by mass transport phenomena. Though the deposition conditions are imprecisely defined (BCl<sub>3</sub> 35%, BCl<sub>3</sub>/CH<sub>4</sub> ratios between 10:1 and 1:2, H<sub>2</sub>, 1473° < T < 1973°K, P = 1 atm) this experimental observation can be compared with the fact that the range of input compositions used by these authors extend from the B<sub>4</sub>C single-phase region to the B<sub>4</sub>C-C two-phase region (Fig. 2-3). Thus the different solid phases would be generated by small fluctuations in the initial partial pressures.

## Conclusions

This paper has shown the narrowness of the thermodynamic range of deposition of pure boron carbide and has defined the variation of that range with temperature. The solid phases obtained from the system depend strongly on the initial concentration, in contrast to the phenomenon shown in the previous study of the Ti-C-H-Cl vapor system in which the deposition range of TiC was very wide. The thermodynamic approach is very useful for forecasting the best conditions for deposition, and for determining the influence or different parameters on the gas and solid phases. The maximum yield of B<sub>4</sub>C (75-80%) is obtained between 1675° and 2075°K for the following partial pressures: P<sub>0</sub>BCl<sub>3</sub> = 0.1; P<sub>0</sub>CH<sub>4</sub> = 0.02; P<sub>0</sub>H<sub>2</sub> = 0.88. In addition, the thermodynamic results agree with some previous experiments. Thus, it seems that a real deposition system would be near an equilibrium system.

Manuscript received May 20, 1975; revised manuscript submitted Sept. 16, 1975.

Any discussion of this paper will appear in a Discussion Section to be published in the December 1976 JOURNAL. All discussions for the December 1976 Discussion Section should be submitted by Aug. 1, 1976.

Publication costs of this article were partially assisted by C.N.R.S.

## REFERENCES

1. F. A. Kuznetsov, *Thin Solid Films*, **13**, 303 (1972).
2. H. Nagai, T. Shibata, and H. Okamoto, *Japan J. Appl. Phys.*, **10**, 1337 (1971).
3. S. Minagawa, H. Seki, and H. Eguchi, *ibid.*, **11**, 855 (1972).
4. M. E. Weiner, *This Journal*, **119**, 496 (1972).
5. R. F. Lever, *IBM J. Res. Develop.*, **8**, 460 (1964).
6. L. P. Hunt and E. Stirl, *This Journal*, **120**, 806 (1973).
7. V. S. Kilin, A. I. Evstyukhin, and V. S. Dergunova, *Russ. J. Phys. Chem.*, **42**, 410 (1968).
8. S. Minagawa and H. C. Gatos, *Japan J. Appl. Phys.*, **19**, 844 (1971).
9. D. W. Shaw, Second International Spring School on Crystal Growth, L 11-12, Tokyo, March 31-April 7, 1974.
10. H. E. Carlton, J. H. Oxley, E. H. Hall, and J. M. Blocher, in "Chemical Vapor Deposition: Second International Conference," J. M. Blocher, Jr. and J. C. Withers, Editors, p. 209, The Electrochemical Society Softbound Symposium Series, New York (1970).
11. K. Ploog, *J. Cryst. Growth*, **24**, 197 (1974).
12. S. Mierzejewska and T. Niemyski, *J. Less-Common Metals*, **8**, 368 (1965).
13. A. A. Cochran, J. B. Stephenson, and J. G. Donaldson, *J. Metals*, **22**, 37 (1970).
14. R. G. Bourdeau, U.S. Pat. 3,334,967 (1967).
15. A. W. Moore and H. F. Volk, U.S. Clearinghouse Fed. Sci. Tech. Inform., AD-693882 (1969).
16. E. Fitzer and M. Röhm, in "Chemical Vapor Deposition: Fourth International Conference," G. F. Wakefield and J. M. Blocher, Jr., Editors, p. 133, The Electrochemical Society Softbound Symposium Series, Princeton, N. J. (1973).
17. P. Vay, Ph.D. Thesis, Grenoble (1971).
18. C. Bernard, Y. Deniel, A. Jacquot, P. Vay, and M. Ducarroir, *J. Less-Common Metals*, **40**, 165 (1975).



## Flux Growth of the Gallium Analog of Beta-Al<sub>2</sub>O<sub>3</sub>

L. M. Foster\* and J. E. Scardefield

IBM Thomas J. Watson Research Center, Yorktown Heights, New York 10598

The importance of the alkali aluminate,  $\beta$ -Al<sub>2</sub>O<sub>3</sub>, as a solid electrolyte in secondary batteries and other electrochemical applications is well known (10). The gross features of the  $\beta$ -Al<sub>2</sub>O<sub>3</sub> structure that allow the high mobility of the alkali ions are clearly recognized, and detailed mechanisms of the conduction process have been proposed (2-7). It is recognized that neither Na<sup>+</sup>, Al<sup>+++</sup>, nor perhaps even oxygen itself is specifically required for the high conduction in this structure, but rather an open, highly defective layer in the lattice is necessary through which an ion species can move with a low activation energy *via* a vacancy mechanism. In beta-alumina the requisite structure must result in part from charge compensation by Na<sup>+</sup> and vacancies when the Mg<sup>++</sup> of spinel (MgAl<sub>2</sub>O<sub>4</sub>) is replaced by Al<sup>+++</sup>, but the process is complex and not completely understood.

There is a very large number of other crystals with the spinel structure, and the process of fast ion conduction should be common to many of them if the same charge compensating substitutions can be made. In 1951, Foster and Stumpf (8) described the extensive isomorphism between the alumina and gallia systems and, in particular, prepared the gallium analogs of sodium and potassium beta-alumina.<sup>1</sup> Fast ion conduction has recently been demonstrated in this material (9-11), and it is apparent that it has the same highly defective structure as  $\beta$ -Al<sub>2</sub>O<sub>3</sub>.

In spite of the similarities between  $\beta$ -Al<sub>2</sub>O<sub>3</sub> and its gallium analog, subtle differences are expected which can be exploited to increase our understanding of this interesting class of materials. For example, because Ga<sup>+++</sup> is slightly larger than Al<sup>+++</sup>, the slot width—the distance across the conducting plane—is slightly greater in the gallium analog. This should result in higher conductivity for the gallium compound, especially for the larger alkali ions. The uptake of water in the conduction plane, which has a profound effect on the stability and conductivity of the beta-aluminas (12), is also likely to be quantitatively and perhaps qualitatively different in the gallium analogs. Finally, subtle differences between the Al<sub>2</sub>O<sub>3</sub>-Na<sub>2</sub>O and Ga<sub>2</sub>O<sub>3</sub>-Na<sub>2</sub>O systems should make it possible to elucidate features of these complex phase diagrams by providing an alternative system to study.

It is desirable to employ high quality monocrystals in a study of the properties of a new material. The present paper describes progress toward producing such crystals of the gallium analog of  $\beta$ -Al<sub>2</sub>O<sub>3</sub> by a flux growth method. With growth parameters thus determined, it should also be possible to prepare monocrystalline layers by a liquid-phase epitaxial technique if a suitable substrate can be found.

\* Electrochemical Society Active Member.

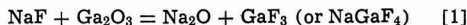
Key words: solid electrolytes, crystal growth, flux growth.

<sup>1</sup> The unfortunate nomenclature error that gave rise to  $\beta$ -Al<sub>2</sub>O<sub>3</sub> is compounded in the gallia system. The metastable phase, alpha-gallia, was named to show the isomorphism with  $\alpha$ -Al<sub>2</sub>O<sub>3</sub>. If this pattern were continued, the high-temperature-stable phase of Ga<sub>2</sub>O<sub>3</sub> would have been called theta to show the analogy to  $\theta$ -Al<sub>2</sub>O<sub>3</sub>. This was not done, however, and, instead, stable Ga<sub>2</sub>O<sub>3</sub> was designated  $\beta$ -Ga<sub>2</sub>O<sub>3</sub> throughout the literature. The gallium isomorphs of  $\beta$ -Al<sub>2</sub>O<sub>3</sub> thus remain nameless and will be referred to herein simply as alkali gallates.

### Experimental

It is known that foreign ions substitute readily in the  $\beta$ -Al<sub>2</sub>O<sub>3</sub> structure, both in the conduction plane and in the spinel body (13, 14). We wished to avoid that complication in the present study and so were restricted to the use of a sodium salt for the flux. However, the use of pure sodium carbonate was known to produce solids far to the Na<sub>2</sub>O side of Ga<sub>2</sub>O<sub>3</sub>-Na<sub>2</sub>O phase diagram, and sodium borate produces a series of complex borates. NaCl exhibits very low solubility for oxides and is not suitable for that reason. NaF emerged, therefore, as the most logical choice.

Early experiments had shown that Na<sub>2</sub>O·xGa<sub>2</sub>O<sub>3</sub> with the  $\beta$ -Al<sub>2</sub>O<sub>3</sub> structure was formed to varying degrees depending on conditions from Ga<sub>2</sub>O<sub>3</sub>-NaF melts (8). Since some Na<sub>2</sub>O was required to produce the gallate, it obviously resulted from partial reaction of the Ga<sub>2</sub>O<sub>3</sub> with the flux, thus



The details of the complex ternary or quaternary system that results are not known. However, it was established empirically that 7.5 weight per cent (w/o) of Ga<sub>2</sub>O<sub>3</sub> will completely dissolve in NaF at 1350°C, and that the liquidus at that composition is about 1300°C. When the Ga<sub>2</sub>O<sub>3</sub> content was higher than about 8%, primary bar-shaped crystals of  $\beta$ -Ga<sub>2</sub>O<sub>3</sub> were found admixed with the Na<sub>2</sub>O·xGa<sub>2</sub>O<sub>3</sub> product. When it was appreciably lower, small needlelike crystals appeared. Their composition was approximately Na<sub>2</sub>O·2.5Ga<sub>2</sub>O<sub>3</sub>, and not the 3Na<sub>2</sub>O·5Ga<sub>2</sub>O<sub>3</sub> phase reported by Boilot *et al.* (9).

Contrary to most solvents that are employed for flux growth of oxides, the NaF in the present case is not the most volatile species. Consequently, one of the preferred growth practices, isothermal vaporization of the flux, is not possible. The most volatile species is GaF<sub>3</sub>, or possibly NaGaF<sub>4</sub>, the gallium analog of aluminum atmolite, NaAlF<sub>4</sub>. Loss of this material by vaporization forces reaction [1] to the right with the formation of more Na<sub>2</sub>O, and changes the composition of the Na<sub>2</sub>O·xGa<sub>2</sub>O<sub>3</sub> product to lower values of x. In fact, control of the GaF<sub>3</sub> activity was absolutely essential for reproducibility in the present experiments. This could be accomplished by employing a controlled "leak," such as a hole of predetermined size in an otherwise sealed container. However, we found it more satisfactory to try to assure zero leak rate by use of tightly pressed-in crucible covers or, in some cases, welded closures.

**Growth procedure.**—A suitable charge composition was 78.0 NaF, 6.3 Ga<sub>2</sub>O<sub>3</sub>, and 15.7 NaCl w/o. The NaCl was an inert diluent that was added to facilitate the removal of the flux from the product through formation of the NaF-NaCl eutectic (mp 674°C), and by increasing the solubility of the flux in water.

The dried components were placed into a standard 110 ml conical platinum crucible, and an inverted lid pressed in. If a leak was suspected, the lid was autogeneously welded in. Total charge weights of both 80 and 160g were employed. The charge was held at



1350°C for about 2 hr, then the temperature was lowered at approximately 4°C/hr to 1200°C. The crucible was then inverted so that most of the flux drained away from the crystal product, which generally adhered to the crucible bottom.

When cold, the flux was broken out of the top and the crucible was filled with granular NaCl which was melted and held at approximately 900°C for an additional 2 hr. This further removed residual flux that adhered to the crystals.

Some  $\text{Na}_2\text{O} \cdot x\text{Ga}_2\text{O}_3$  product could be removed at this stage, but generally the crystals adhered tightly to the platinum and, since they are very friable, it was difficult to remove them without damage. Generally it was necessary to boil water in the crucible for an hour or two in order to free them.

**Description of product.**—Typical flux-grown crystals are shown in Fig. 1. The figure illustrates one of the remaining problems with the method: recovery of the product without damage. Although a profusion of small (1–5 mm), free crystals could be recovered that were excellent for x-ray and optical studies, etc., larger ones generally cracked during cooldown because of differential contraction between the platinum or adhering flux and the crystals. This is a common problem of flux growth of most materials and presumably can be alleviated by further manipulation of the heat flow pattern during growth.

The crystals had the  $\beta\text{-Al}_2\text{O}_3$  structure. A comparison of their properties with those of a "standard"  $\beta\text{-Al}_2\text{O}_3$  sample obtained from the Carborundum Company is given in Table I. No fluorine was detectable in the crystals by electron microprobe analysis

### Discussion and Summary

It has been demonstrated that the gallium analog of  $\beta\text{-Al}_2\text{O}_3$  can be grown from a NaF flux. The problems common to most flux growth processes, uncontrolled nucleation and difficulty of recovery of the product, are thought to be solvable with design changes so that larger perfect crystals can be grown. The growth parameters have been sufficiently well established for liquid phase epitaxy to be undertaken as an alternative procedure if a suitable substrate can be found.

The practice of boiling the crystals in water to free them from the crucible, although undesirable, appears not to alter them. An electron microprobe analysis of



Fig. 1. Crystals of  $\text{Na}_2\text{O} \cdot 7.43\text{Ga}_2\text{O}_3$  grown from a NaF flux

Table I.

	$\text{Na}_2\text{O} \cdot x\text{Ga}_2\text{O}_3$	$\text{Na}_2\text{O} \cdot 8\text{Al}_2\text{O}_3$
Composition*	$x = 7.43 \pm 0.37$	—
Space group	$R\bar{3}m/mmc$	—
a	5.81Å	5.61Å
c	23.13Å	22.41Å
Slot width	4.87Å	4.76Å
Index of refraction ( $n_o$ )	1.85	1.66

\* By electron probe analysis.

a water-treated surface gave the same sodium content as an analysis of an internal surface exposed by cleaving. It is possible, of course, that sodium might have been extracted from the very outer atomic layers of the crystal and not be detected by this technique.

The Ga analog of the three-block  $\beta''\text{-Al}_2\text{O}_3$  structure was never observed in our experiments, even though the growth temperature was below that where  $\beta''$  transforms irreversibly to  $\beta$  (approximately 1380°C). The reason cannot be insufficient soda content, as is sometimes stated with respect to the alumina system, since when large volatile losses were permitted, the sodarich phase of composition approximately  $\text{Na}_2\text{O} \cdot 2.5\text{Ga}_2\text{O}_3$  appeared, still without any evidence of a  $\beta''$  phase. As in the aluminum system, the conditions for stability of the three-block phase are unclear, and this is further evidence that the  $\beta''$  phase is metastable, although stabilization of the  $\beta$  phase by traces of fluoride cannot be excluded.

Manuscript submitted June 17, 1975; revised manuscript received Sept. 17, 1975. This was Paper 4 presented at the Toronto, Canada, Meeting of the Society, May 11–16, 1975.

Any discussion of this paper will appear in a Discussion Section to be published in the December 1976 JOURNAL. All discussions for the December 1976 Discussion Section should be submitted by Aug. 1, 1976.

Publication costs of this article were partially assisted by IBM Corporation.

### REFERENCES

- See, for example: J. T. Kummer, in "Progress in Solid State Chemistry," Vol. 7, Reiss and McCaldin, Editors, Chap. 5, Pergamon Press, Inc., New York (1972); "Fast Ion Transport in Solids—Solid State Batteries and Devices," W. van Gool, Editor, American Elsevier, New York (1973); M. S. Whittingham and R. A. Huggins, in "Solid State Chemistry, Proceedings of 5th Materials Research Symposium," Special Publication No. 364, p. 139, National Bureau of Standards, Washington, D.C. (1972).
- M. J. Rice and W. L. Roth, *J. Solid State Chem.*, **4**, 294 (1972).
- H. Sato, *J. Chem. Phys.*, **55**, 677 (1971).
- W. van Gool, *Ann. Rev. Phys. Chem.*, **25**, 311 (1974).
- R. D. Armstrong, R. S. Bulmer, and T. Dickinson, "Fast Ion Transport in Solids—Solid State Batteries and Devices," W. van Gool, Editor, p. 269, American Elsevier, New York (1973).
- R. Kikuchi, *ibid.*, p. 249.
- H. Rickert, *ibid.*, p. 3.
- L. M. Foster and H. C. Stumpf, *J. Am. Chem. Soc.*, **73**, 1590 (1951).
- J. P. Boilot, J. Thery, and R. Collongues, *Mater. Res. Bull.*, **8**, 1143 (1973).
- H. C. Brinkhoff, *J. Phys. Chem. Solids*, **35**, 1225 (1974).
- R. J. Chicotka, Abstract 5, p. 16, The Electrochemical Society Extended Abstracts, Spring Meeting, Toronto, Canada, May 11–16, 1975.
- Ford Motor Company Contract Report No. NSF-C805 (AER-73-07199) for period June 30, 1974 to Dec. 31, 1974, p. 106.
- Y. Y. Yao and J. T. Kummer, *J. Inorg. and Nucl. Chem.*, **29**, 2453 (1967).
- J. T. Kummer, in "Progress in Solid State Chemistry," Vol. 7, Reiss and McCaldin, Editors Chap. 5, Pergamon Press, Inc., New York (1972).

# The Cathodic Corrosion of Aluminum

E.P.G.T. van de Ven and H. Koelmans

Philips Elcoma H.O.C. Laboratory and Philips Research Laboratories, Eindhoven, The Netherlands

When hydrogen is cathodically evolved at a metal in an electrolyte, an increase of the hydroxyl ion concentration at the electrode surface results. This alcalization effect (1) is responsible for the cathodic corrosion of an amphoteric metal like Al (2). Though this phenomenon has been known for decades, detailed information about how the cathodic corrosion depends on current density, ionic composition of the electrolyte, and especially on temperature is still lacking. The present work, in which we consider the influence of these parameters, is part of an effort aimed at a better understanding of the electrolytic corrosion of the Al metallization tracks on integrated circuits during temperature-humidity-bias tests. The corrosion observed after these tests is often mainly cathodic (3, 4).

## Experimental

The experiments were done with thin disks of 99.99% Al which formed the end faces of a cylindrical cell of polymethylmethacrylate. The Al disks had a diameter of 2 cm and a thickness of 100  $\mu\text{m}$ . The design of the cell is sketched in Fig 1. During the experiments the current was kept constant. The amount of corrosion produced at both the cathode and the anode was determined from weight-loss measurements. The corrosion products were removed with an aqueous solution of  $\text{H}_3\text{PO}_4$  and  $\text{CrO}_3$ .

## Results and Discussion

Figure 2 shows, in an Arrhenius plot, how the rate of electrolytic corrosion at both the cathode and anode depends on temperature. The experiments were done in  $5 \times 10^{-4}\text{N}$  NaCl at a number of constant currents. The rate of corrosion at the anode is independent of temperature at all current densities used. In agreement with others(5) we found that for every three electrons flowing in the external circuit slightly more than one Al atom is oxidized. In our experiments we found 3e equivalent to 1.16 Al.

Corrosion at the cathode is more complicated. In the range of low temperatures the lines for the cathodic attack run parallel to the line found for chemical dis-

**Key words:** integrated circuits, aluminum metallization, temperature-humidity-bias tests.

solution of the same Al disks in NaOH (see Fig. 2), which suggests that in this temperature range cathodic corrosion is similar to dissolution in an NaOH solution of constant concentration. At higher temperatures the lines for the cathodic corrosion level off to a constant value corresponding to a situation where for every three electrons flowing three atoms of Al pass into solution. Our interpretation is that at higher temperatures all the hydroxyl ions formed by the electrochemical reaction  $\text{H}_2\text{O} + e \rightarrow \text{OH}^- + 1/2\text{H}_2$  are used up in the ensuing chemical dissolution reaction  $\text{OH}^- + \text{Al} + \text{H}_2\text{O} \rightarrow \text{AlO}_2^- + 3/2\text{H}_2$ . In the high-temperature range the rate of cathodic corrosion is limited by the electrochemical production of  $\text{OH}^-$ , i.e., by the current density, independent of temperature. At these high temperatures the over-all reaction is  $\text{Al} + 2\text{H}_2\text{O} + e \rightarrow \text{AlO}_2^- + 2\text{H}_2$ , hence, for every electron one Al atom dissolves, as observed. At lower temperatures the rate of corrosion is limited by the chemical dissolution reaction, part of the  $\text{OH}^-$  ions produced are carried away from the cathode into the bulk of the electrolyte by diffusion and electrical migration. The simple dissolution of Al in NaOH is also limited by the chemical surface reaction  $\text{OH}^- + \text{Al} + \text{H}_2\text{O} \rightarrow \text{AlO}_2^- + 3/2\text{H}_2$ . Therefore, in the low temperature range, the temperature dependence of cathodic corrosion is described by an activation energy (0.47 eV/at = 10.8 kcal/mole) equal to that observed for the chemical dissolution of Al in NaOH.

The results of Fig. 2 also show that in the lower temperature range the influence of current density is rather weak, an increase in current density by a factor of ten produces an increase in the rate of cathodic corrosion by a factor of only about two. Apparently in the range of the steady-state  $\text{OH}^-$  concentrations produced at the current densities used in our experiments, the influence of  $\text{OH}^-$  concentrations on the chemical dissolution reaction is not very pronounced. The results of Caldwell and Albano (2) also indicate that at low  $\text{OH}^-$  concentration the influence of concentration is rather small.

We next investigated the influence of ionic composition of the electrolyte on cathodic corrosion. The results for a number of electrolytes, all in a concentra-

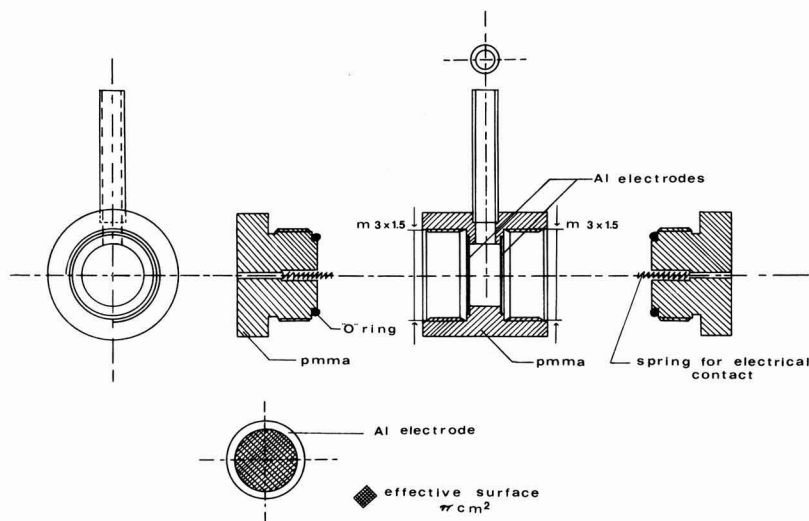
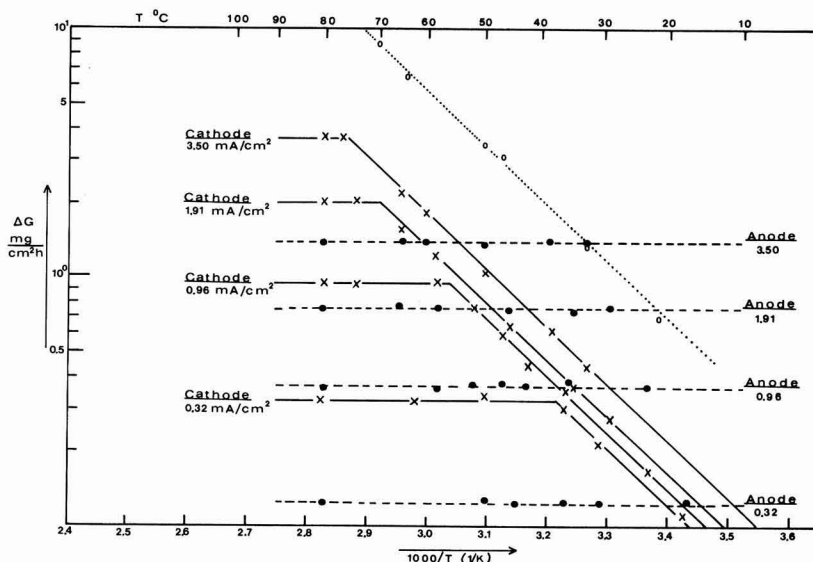


Fig. 1. Design of the cell used in the cathodic corrosion experiments. Cell volume  $\pi \text{ cm}^3$ .

Fig. 2. Arrhenius plot of the rate of cathodic (—) and anodic (-----) corrosion of Al at various current densities in NaCl  $5 \times 10^{-4}N$ . Also shown is the line for dissolution of Al in  $2.5 \times 10^{-2}N$  NaOH (.....).



tion of  $5 \times 10^{-4}M$  are summarized in Table I. The results of Table I show that the rate of cathodic Al corrosion does not depend on the nature of the anion used and remains unchanged in an acid medium down to a pH of at least 3.3. In both the neutral and the acid solutions the addition of a drop of phenolphthalein gave a red color at the cathode when the current was switched on. This means that for the current density used (1.91 mA/cm<sup>2</sup>), even in the acid solutions the pH at the surface of the cathode rises to at least 8.5.

### Conclusions

In summary we conclude:

1. The influence of temperature, current density, and ionic composition of the electrolyte on the cathodic corrosion of Al can be interpreted on the basis of the alcalization theory.

2. With regard to the influence of temperature two regions were found: (i) a low-temperature region where the increase in cathodic corrosion with rising temperature is governed by an activation energy equal

to that observed for the chemical dissolution of Al in NaOH, and (ii) a high-temperature region where cathodic corrosion is independent of temperature.

3. In the high-temperature region the cathodic corrosion of Al is proportional to the current density, whereas in the low-temperature region the influence of current density is rather weak.

4. Our experiments show that the cathodic corrosion of Al does not depend on the type of anion used and does not require the presence of large amounts of cations capable of forming a strong base.

Manuscript submitted April 24, 1975; revised manuscript received Aug. 17, 1975.

Any discussion of this paper will appear in a Discussion Section to be published in the December 1976 JOURNAL. All discussions for the December 1976 Discussion Section should be submitted by Aug. 1, 1976.

Publication costs of this article were partially assisted by Philips Research Laboratories.

### REFERENCES

- K. J. Vetter, "Electrochemical Kinetics," p. 183, Academic Press, New York (1967).
- B. P. Caldwell and V. J. Albano, *Trans. Electrochem. Soc.*, **76**, 271 (1939).
- W. M. Paulson and R. W. Kirk, 12th Annual IEEE Reliability Physics Symposium, Las Vegas, Nevada, April 1974, pp. 172-179.
- H. Koelmans, 12th Annual IEEE Reliability Physics Symposium, Las Vegas, Nevada, April 1974, pp. 168-171.
- M. E. Straumanis and K. Poush, *This Journal*, **112**, 1185 (1965).

Table I. Cathodic corrosion of Al in various electrolytes, current density 1.91 mA/cm<sup>2</sup>; T = 25°C

Electrolyte $5 \times 10^{-4}M$	Cathodic corrosion (mg/cm <sup>2</sup> hr)	Electrolyte $5 \times 10^{-4}M$	Cathodic corrosion (mg/cm <sup>2</sup> hr)
NaCl	$0.19 \pm 0.015$	HCl	0.19
NaNO <sub>3</sub>	0.19	HNO <sub>3</sub>	0.18
Na <sub>2</sub> PO <sub>4</sub>	0.19	H <sub>2</sub> PO <sub>4</sub>	0.18

# Impurity Striations during Faceted Crystal Growth

W. Bardsley and D. T. J. Hurlle

Royal Radar Establishment, Great Malvern, Worcestershire, England

The occurrence of impurity striations in melt-grown crystals due to crystal rotation and/or nonsteady convective motion in the melt is now well established. [See, for example, reviews by Hurlle (1) and by Gatos and Witt (2).] Recent elegant work by Witt and co-workers (3,4) has shown that while striations occur on both faceted and nonfaceted portions of the growth surface, the operative mechanisms are different. Specifically, in nonfaceted regions striations result from modulation of the microscopic growth rate (3) and are particularly pronounced if "melt-back" occurs during part of the periodic growth cycle. Clearly, the striations arise from modulation of the height of the impurity boundary layer by the varying growth rate. In contrast, on faceted growth surfaces the microscopic growth rate appears to be sensibly constant (4) despite the presence of temperature fluctuations or oscillations in the bulk of the melt and the occurrence of striations is ascribed to modulation of the thickness of the impurity boundary layer by the nonsteady convective motion.

In recent experiments under conditions of near-zero gravity aboard Skylabs III and IV where gravity-induced convection was suppressed, Witt *et al.* (5) demonstrated that striations were eliminated in melt-grown Te-doped InSb except that they observed irregularly spaced striations remaining on peripheral facets [Fig. 17 and 18 of Ref. (5)]. The authors ascribed these anomalous striations to the occurrence of nucleation at the exterior edge of the facet where its rate would be sensitive to vibration or to the arrival of a foreign particle.

The purpose of this note is to report the occurrence of similar striations on an earth-grown single crystal of Ga-doped Ge grown some years ago by the authors during a study of the effects of constitutional supercooling (6-8). However, these striations occurred on microfaceted regions of the crystal growth surface well away from its free surface and had a relatively regular periodicity (Fig. 1). The crystals were grown on a  $\langle 110 \rangle$  axis by pulling from the melt without rotation of either the crystal or the crucible. The pull rate was

Key words: crystal growth, growth striations, germanium, semiconductor single crystal.

9 cm/hr and the concentration of Ga was adjusted so as to produce a cellular structure over the whole of the growth surface. This cellular structure consisted of a corrugated array composed of  $\{111\}$  microfacets. The section shown in Fig. 1 contains the growth axis and is orthogonal to the axis of the corrugations. Some of the cells exhibit bands of striations. The distribution of the bands and their extent are apparently quite random. They start and stop quite abruptly. The etchant used was 1.3 HF:HNO<sub>3</sub> at 70°C; it is of course possible that other etchants might have revealed additional striae, but in any event it is clear that two different modes of growth can occur in any given cell. The fact that the striations start and stop at the same time on each of the pair of facets which make up the cell suggests that nucleation of layer growth on both faces is occurring at the line of intersection, *i.e.* at the apex of the cell. These observations suggest that the process is a fundamental one involving some form of oscillatory coupling between the nucleation event and the solute and thermal fields rather than due simply to foreign particles. The temporal spacing of the striae is of the order of 1 sec. The fact that neighboring cells do not show the same effect at the same time implies that the process must be very sensitive to the longer range solute field. It seems likely that the explanation must involve a mechanism for the periodic growth of the cell apex which modulates the rate of supply of layer sources; an explanation involving step bunching [see, for example, Parker's review (9) on the kinematic theory of layer growth] seems less probable.

Manuscript submitted Aug. 18, 1975; revised manuscript received Sept. 22, 1975.

Any discussion of this paper will appear in a Discussion Section to be published in the December 1976 JOURNAL. All discussions for the December 1976 Discussion Section should be submitted by Aug. 1, 1976.

## REFERENCES

1. D. T. J. Hurlle, *J. Cryst. Growth*, **13/14**, 39 (1972).
2. H. C. Gatos and A. F. Witt, in "Recent Advances in Science and Technology of Materials," Vol. I,

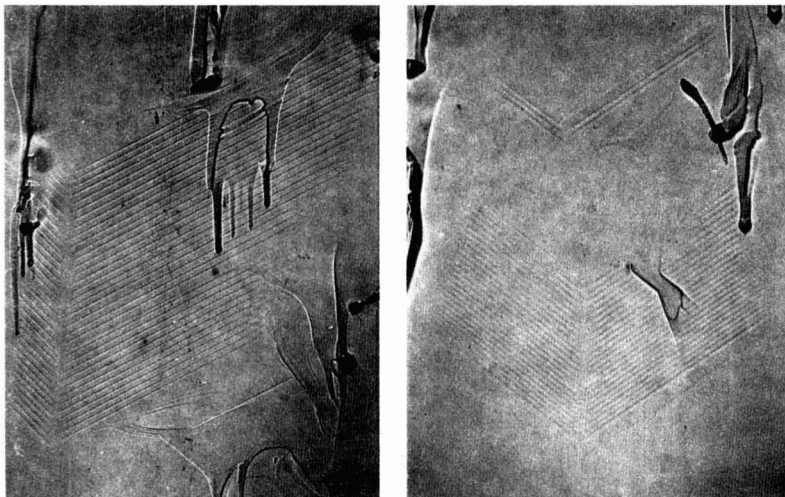


Fig. 1. Two nonadjacent regions of  $\langle 110 \rangle$  Ga-doped Ge single crystal showing striations on the  $\{111\}$  microfaceted cells (the growth axis is vertically downward). The "paint tears" effect is the result of the migration of trapped liquid gallium droplets (8). Magnification: X70.

- A. Bishay, Editor, p. 59, Plenum Publishing Co., New York (1974).
3. A. F. Witt, M. Lichtensteiger, and H. C. Gatos, *This Journal*, **120**, 1119 (1974).
  4. *Ibid.*, **112**, 787 (1974).
  5. A. F. Witt, H. C. Gatos, M. Lichtensteiger, M. C. Lavine, and C. J. Herman, *ibid.*, **122**, 276 (1975).
  6. D. T. J. Hurle, *Solid-State Electron.*, **3**, 37 (1961).
  7. W. Bardsley, J. M. Callan, H. A. Chedzey, and D. T. J. Hurle, *ibid.*, **3**, 142 (1961).
  8. W. Bardsley, J. S. Boulton, and D. T. J. Hurle, *ibid.*, **5**, 395 (1962).
  9. R. L. Parker, in "Solid State Physics: Advances in Research and Applications," Vol. 25, H. Ehrenreich, F. Sietz, and D. Turnbull, Editors, p. 151, Academic Press, Inc., New York (1970).
  10. D. T. J. Hurle, J. B. Mullin, and E. R. Pike, *Phil. Mag.*, **9**, 423 (1964).

## Brief Communications



### The Effect of a Prior Sirtl Etch on Subsequent Thermally Induced Processing Damage in Silicon Wafers

W. A. Porter, D. L. Parker, and L. G. Reed

*Institute for Solid State Electronics, Texas A&M University, College Station, Texas*

Sirtl etch (1) has traditionally been used to identify the presence and density of dislocations in silicon. The relationship between the levels of stress in silicon, and the formation of dislocations by thermal cycling has previously been established (2). Furthermore, it has been shown that residual impurities such as chromium left by Sirtl etching can be removed (3), reducing dangers of contamination. This note reports that prior Sirtl etching of silicon wafers results in reduced dislocation densities after subsequent thermal cycling.

#### Experimental

The photographs in Fig. 1, 2, and 3 are x-ray topographs of the same 2 in. silicon wafer. A modified Berg-Barrett type camera was used with copper radiation and the (440) reflection. The topograph in Fig. 1

Key words: defects, damage, processing, silicon.

was made after diamond scribing a line across the front (polished) side of the wafer, two triangles on the front side, two triangles on the backside (unpolished), and the S-3 nomenclature on the front side. (The two fainter triangles in the topograph are on the back side of the wafer.) The topograph in Fig. 2 was made after the right half of the wafer was given a 5 min Sirtl etch. Note that the scribe marks in the Sirtl etched half are now barely visible. This illustrates the well-known ability of the etch to relieve stress due to lattice damage.

The topograph shown in Fig. 3 was made after an 8200Å oxide was grown in steam at 1100°C. The wafer was processed horizontally on a flat quartz boat with the edges of the wafer near the ends of the scribed line overhanging the edges of the carrier about ¼ in. on each side. Of course, the maximum thermal

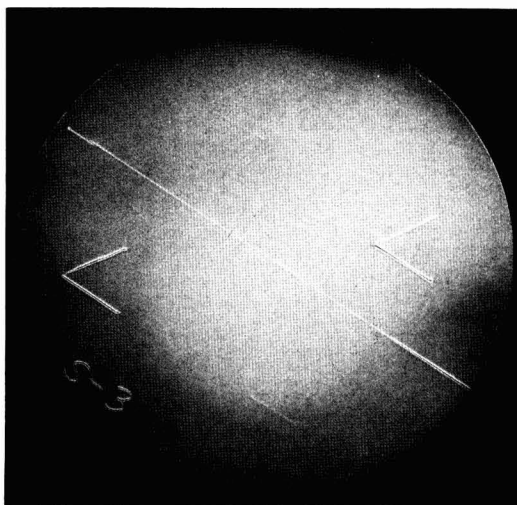


Fig. 1. An x-ray topograph of the 2 in. silicon wafer after scribing.

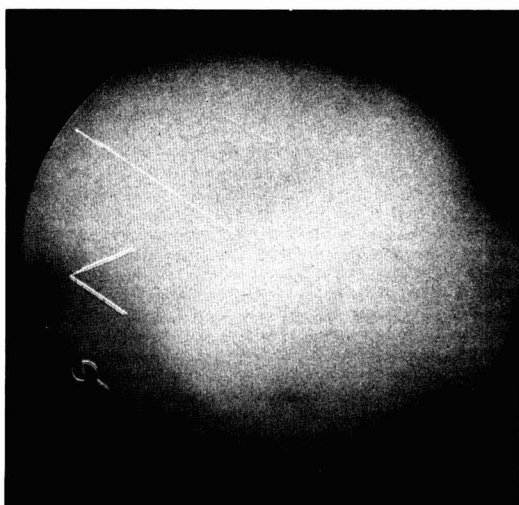


Fig. 2. An x-ray topograph of the same wafer after the right half was given a 5 min Sirtl etch.



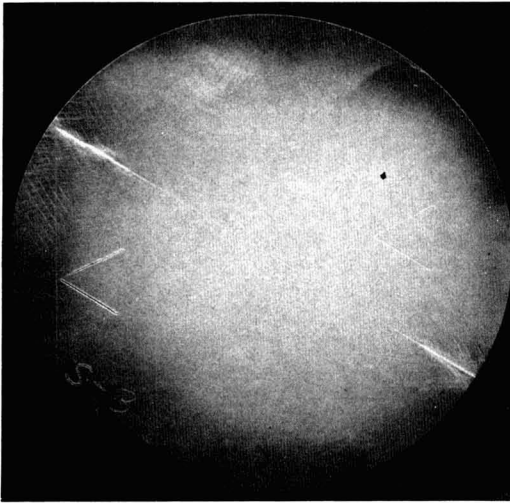


Fig. 3. An x-ray topograph of the wafer after a thermal oxidation step. Note the relative abundance of processing damage on the half of the wafer that was not stress relieved.

stress during insertion and withdrawal from the furnace is produced in the overhanging area of the wafer. Note that there is considerably less process-induced slip damage in the etched half of the wafer. Careful examination of this topograph will reveal the location

of the meniscus produced in the etch solution. It is seen at the wafers edge between the S and the 3 and extends to the opposite edge of the wafer.

### Conclusion

Visual demonstration using x-ray topography has been given to demonstrate the reduction in thermally generated defects in silicon when a stress relief Sirtl etch is used prior to thermal processing. The potential influence and application of this technique to silicon devices is presently being studied and is the objective of a masters thesis, where preliminary results indicate that a Sirtl etch as short as 30 sec provides significant reduction in subsequent process-induced damage.

### Acknowledgments

This research was supported by NASA and the Air Force under NASA contract NAS8-26379.

Manuscript received July 17, 1975.

Any discussion of this paper will appear in a Discussion Section to be published in the December 1976 JOURNAL. All discussions for the December 1976 Discussion Section should be submitted by Aug. 1, 1976.

Publication costs of this article were partially assisted by Texas A&M University.

### REFERENCES

1. V. E. Sirtl and A. M. Adler, *Z. Metallk.*, **52H**, 529 (1961).
2. W. A. Porter, D. D. Drew, and J. S. Linder, *J. Appl. Phys.*, **47**, 1477 (1972).
3. W. A. Porter, A. Gupta, and D. L. Swindle, *This Journal*, **120**, 589 (1973).

## Vapor-Phase Growth of Thin GaAs Multilayer Structures

K.-H. Bachem and M. Heyen

*Institute of Semiconductor Electronics/Sonderforschungsbereich 56, Technical University, Aachen, Germany*

The ability to deposit multilayer epitaxial structures has become an essential requirement for the fabrication of properly functioning GaAs devices. As an example, conventionally constructed MESFET's using a single epitaxial layer grown directly on a semi-insulating substrate exhibit loops and poor saturation behavior in their I-V characteristics. It has been found recently, in this laboratory as well as by other workers (1-3), that these undesirable effects are greatly reduced by depositing an undoped buffer layer between substrate and active film. In the present report we will describe the special technique which we have successfully employed to obtain sequences of differently doped epitaxial layers in one run under well-defined conditions.

A schematic diagram of the apparatus for deposition of epitaxial layers from the  $\text{AsCl}_3\text{-H}_2\text{-Ga}$  system, as used in this work, is shown in Fig. 1. The reactor is distinguished from conventional systems by the design of the substrate holder (4), as will become clear in the description of a typical loading and deposition sequence. After chemically etching in an aqueous  $\text{H}_2\text{SO}_4\text{-H}_2\text{O}_2$  solution and cleaning in organic solvents, the GaAs substrate is subsequently inserted into the depression of the base plate. It is covered by the quartz plate and  $\text{H}_2$ -flushed cap and introduced into the apparatus. The entire reactor is flushed with  $\text{H}_2$  and heated up. The Ga source is saturated with As at  $880^\circ\text{C}$  under formation of a GaAs crust. As a next step the source temperature is slowly decreased during which

time the reactor is being etched using the upper gas inlet. When the deposition conditions (substrate temperature  $750^\circ\text{C}$ , source temperature  $850^\circ\text{C}$ ) have been reached, the etching is terminated and the deposition flow switched on. The gas phase is allowed to reach a stable composition. At this point, cap and plate are removed to the position shown by the dashed lines, thereby initiating the deposition process. After the desired growth has been effected, the cover is put back in place, thus terminating the deposition. New deposition conditions are now established in the system and the

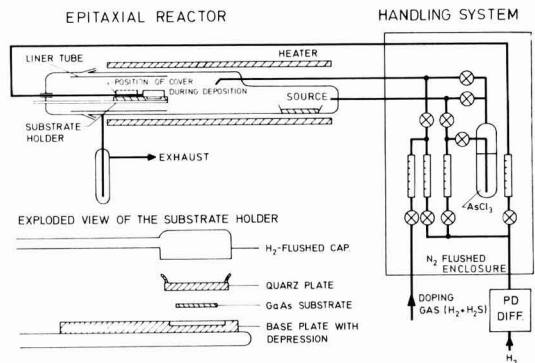


Fig. 1. Schematic diagram of the epitaxial deposition system

\* Electrochemical Society Active Member.

Key words: gallium arsenide submicron multilayer, gallium arsenide MESFET, gallium arsenide steady-state growth and doping.

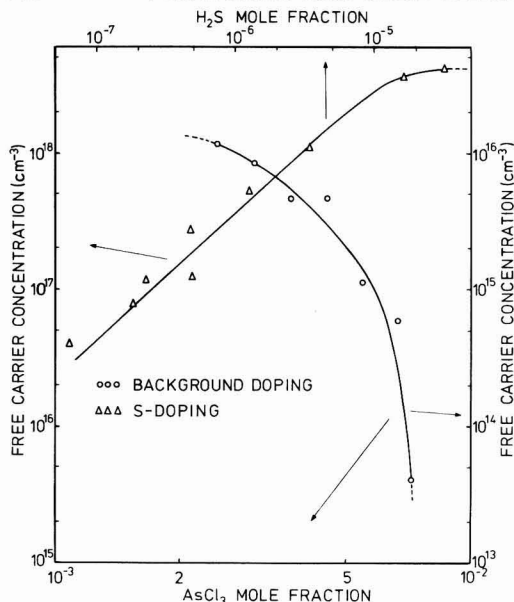


Fig. 2. Variation of the free carrier concentration  $n$  ( $\text{cm}^{-3}$ ) with  $\text{AsCl}_3$  mole fraction (background doping) and  $\text{H}_2\text{S}$  mole fraction at  $\text{AsCl}_3$  mole fraction of  $6.67 \cdot 10^{-3}$  (S-doping).

apparatus is ready for growth of a next layer for a preset gas-phase composition.

Because the growth rates in the  $\text{AsCl}_3$ - $\text{H}_2$ -Ga system are relatively high, the growth of submicron layers requires the ability to select well-defined, very short deposition times. The ability to remove and close the cover in approximately 2 sec means that this second condition is also fulfilled in our apparatus.

In the apparatus, doping levels from the  $10^{13}$  to the  $10^{18} \text{ cm}^{-3}$  range have been reproducibly obtained, and one can grow a low-doped layer immediately after a high-doped layer without contamination of the former by the latter. The range below  $1 \cdot 10^{16} \text{ cm}^{-3}$  is controlled by the well-known  $\text{AsCl}_3$  mole fraction dependence of the background doping (2, 6, 7). The larger values are realized by injecting a  $\text{H}_2\text{S}$ - $\text{H}_2$  mixture into the gas stream (Fig. 2). For each run the doping gas was pre-mixed in a stainless steel container from  $\text{H}_2$  and a 1000 ppm  $\text{H}_2\text{S}$ -in- $\text{H}_2$  source. It was injected into the reactor at a constant flow rate in all experiments. The concentration in the container was determined photometrically using the methylene blue method (8) after extracting the  $\text{H}_2\text{S}$  from a predetermined volume of doping gas with an aqueous zinc acetate solution.

A typical example of the structures prepared by this method is the following double layer epitaxial film for MESFET application. At the before-mentioned system temperatures, an  $\text{AsCl}_3$  mole fraction of  $7.1 \cdot 10^{-3}$ , and a flow rate of 950 ml/min (tube diameter: 60 mm), the film growth rate of  $0.3 \mu \text{ min}^{-1}$  is obtained. Since the structure consists of a  $1.5 \mu$  thick buffer layer ( $n = 4 \cdot 10^{13} \text{ cm}^{-3}$ ) and a  $0.1 \mu$  active layer ( $n = 2 \cdot 10^{17} \text{ cm}^{-3}$ ), a deposition time of only 20 sec is required for the second film. The doping profile obtained from C-V measurements shows a steep transition between the layers; it drops from  $1 \cdot 10^{17}$  to  $1 \cdot 10^{16}$  in  $0.054 \mu$ , which is very close to the value calculated by Johnson and Panousis (5) for an idealized steplike doping profile. For the transition between active layer and substrate in the conventional structure, the considerably larger distance of  $0.12 \mu$  was found for the same drop. This observation is indicative of the boxlike impurity profile attainable with the present apparatus in the case of the double layer structure.

Results on these and other device applications of the described deposition technique will be published elsewhere.

Manuscript submitted Jan. 23, 1975; revised manuscript received Aug. 15, 1975. This was Paper 264RNP presented at the New York, New York, Meeting of the Society, Oct. 13-17, 1974.

Any discussion of this paper will appear in a Discussion Section to be published in the December 1976 JOURNAL. All discussions for the December 1976 Discussion Section should be submitted by Aug. 1, 1976.

Publication costs of this article were partially assisted by the Technical University, Aachen.

#### REFERENCES

1. L. Hollan, "GaAs 1974 Symposium Proceedings," Institute of Physics and the Physical Society, p. 22 (1975).
2. T. Nozaki, M. Ogawa, H. Terao, and H. Watanabe, *ibid.*, p. 46.
3. M. J. Cardwell, I. Goddridge, and J. A. Turner, Paper presented at ESSDERC 1974, Nottingham, England (1974).
4. K.-H. Bachem, G. Erlaki, and W. Markert, "Chemical Vapor Deposition, Fourth International Conference," G. F. Wakefield and J. M. Blocher, Jr., Editors, p. 296, The Electrochemical Society Soft-bound Symposium Series, New York (1973).
5. W. C. Johnson and P. T. Panousis, *IEEE Trans. Electron. Devices*, **ED-18**, 965 (1971).
6. J. V. Dilorenzo, *J. Cryst. Growth*, **17**, 189 (1972).
7. D. J. Ashen, P. J. Dean, D. T. J. Hurle, J. J. Mullin, A. Royle, and A. M. White, "1974 GaAs Symposium Proceedings," Institute of Physics and the Physical Society, p. 229 (1975).
8. M. S. Budd and H. A. Bewick, *Anal. Chem.*, **24**, 1536 (1952).



## Energy—The Short and Long of It<sup>1</sup>

John S. Foster, Jr.

TRW Incorporated, Redondo Beach, California 90278



Thank you very much, President Beck, for that very generous and flattering introduction. At the outset I want to express my appreciation for the honor and privilege of being invited to present the semiannual Electrochemical Society Lecture.

I should begin with a few words about the title chosen for this lecture. Each of you has been called upon to make presentations and speeches from time to time. In addition you are asked to supply a subject and title. In my case the subject came easily—ENERGY. The rest of the title, however, was born out of a sense of frustration—frustration being experienced by almost everyone involved in energy; those who search for new sources and development and production, processes, distribution, and final use. And also those who are frustrated by the difficult and tedious social, political, economic, environmental, legislative, and legal aspects. This frustration has been growing for the last twenty years.

Perhaps it started with the debates in the early 1950's culminating in the 1954 congressional decision to regulate the price of gas at the wellhead. The subsequent controls to keep the price of gas low held down prices for oil and reduced our use of coal. We went to

the Middle East for cheaper oil and became dependent on that source to fuel the future growth of America. And all the while we have been debating the pros and cons of our actions. We chose the course of enforcing cheaper fuel prices for energy at the risk of not facing up to the costs of energy for the long haul. In 1973 OPEC pulled the string on our short-term strategy realizing that by then we were ill prepared to do without them. So in spite of two decades of debate, the short and the long of it is that we are drifting deeper and deeper into trouble. It was the sense of frustration that despite endless debates we have stuck to the wrong course that prompted me to assume it might be possible to say something succinct, hence the title, "Energy—The Short and Long of It."

America and the rest of the world may have finally awakened to the fact that we have an energy crisis on our hands, and that it's going to get worse before it gets better.

Our energy needs are increasing while our supplies of oil and gas are dwindling. We're at the mercy of the petroleum exporting countries, more so today than we were at the time of the embargo back in 1973. We may have to deal with a shortage of natural gas this winter. And both oil and gas supplies are limited. One day they're going to be gone.

It's everyone's problem—government, industry, universities, the man on the street. The solution is going to be devilishly difficult, and everyone is going to have to get involved.

We need a plan of action, for both the short term and long term, if we're going to solve the dilemma. And that's a part of what I want to talk about today, at the risk perhaps of belaboring the obvious. Some things do bear repeating, lest we get so busy fighting alligators that we forget that our original objective was to drain the swamp.

It seems to me that the energy crisis and the way out of it can best be understood if we look at three fairly well-defined aspects of the problem. First off, there is the people problem, which has to do with the general public and its relationship to the energy crisis. Make no mistake about it, if we can't solve this one, if we can't get the public behind us, then "Project Independence" isn't likely to be any more successful than "Project Prohibition" was half a century ago.

Second, we have the problem of method and approach; how we're going to attack the energy crisis, arrive at decisions about what to do, the associated risks, and how best to use the nation's capabilities.

Third, there are the specific programs, schedules, and approvals for achieving our objectives. If the schedule slips too much, if we make too many wrong guesses about what we ought to be doing, the crisis is going to turn into a full-scale disaster.

Now let's look at the short and long of it for each of these categories.

*The people problem.*—Some of the shorts and longs of the "people problem" are: we're short on energy

<sup>1</sup>This is The Electrochemical Society Lecture delivered at the Dallas, Texas, Meeting of the Society, October 6, 1975.

resources, long on waste. Short on action and decisions, long on proposals, ideas, and schemes. Short on trust, long on suspicion. Short on personal concern and commitment, long on fingerpointing and accusations. Short on enabling legislation, long on restrictive legislation. Long on political profit, short on economic profit.

It's very difficult to get people, except those already deeply and professionally involved with energy, to realize that we do have a crisis. To most people, the energy crisis has come and gone. They want to keep their heavy and low-mileage cars. They want the thermostat up to 75° or 80° in the winter and down to 70° or 75° in the summer. We're short on the long view, long on the short view.

What we're going through right now is kind of like a remission in cancer: some of the symptoms have disappeared, but the disease is still there. We'd better do something to treat it, because it can be terminal.

The people are recovering, or trying to recover, from a series of painful blows. In the past few years, we've seen America all but torn apart by the controversy over Vietnam. We've lived through the shame and shambles of Watergate. We've held our breath and tried to resolve the Middle East crisis before it blows up in our faces. We've tried and are still trying to cope with runaway inflation in the midst of a recession. (Perhaps recession is not the right word. If your neighbor is out of work, that's an "economic readjustment." If you're out of work, that's a "recession." And if your wife is out of work, that's a "depression.")

Now, after all these overlapping traumas and crises, we're told that we have to learn to live with less oil for our furnaces and cars and electric power plants. Is it any wonder that people are either apathetic about the energy problem, or simply refuse to believe that it is a problem? Or that some are convinced that it's another high-level conspiracy designed to line the pockets of the "haves" at the expense of the "have-nots"?

Of course, it's actually a cop-out to even talk about the problem in the context of our own country exclusively. The fact is, and we all know this even though we may not like to admit it, the energy problem is a global one. Anything we do to cope with it on a national basis is only going to be a stopgap measure at best. We already consume 35% of the world's energy with only 6% of its population. How much longer can we get away with that?

There are some very tough choices that have to be made. President Ford realized this when he began to review the Project Independence Blueprint during his Christmas vacation last year. Every alternative seemed to have two or three unacceptable aspects to it. Some alternatives would play hell with the economy, others would further degrade the environment, almost all of them present severe economic problems. Everything interacts with everything else. We don't just have an energy problem, we have the Four Big E's: Energy, Environment, Economics, and Education.

Everyone who tries to cope with these problems suffers from some kind of built-in bias. Any program the President proposes has, of necessity, a political aspect and requires negotiation and compromise with the Congress. Each member of Congress has a constituency back home to answer to, with their own sets of built-in biases and regional interests. The same applies to industry; any changes they propose have to be evaluated in terms of profit-and-loss and accountability to the stockholders. Who among us is going to volunteer to become a nonprofit corporation in order to save a few barrels of oil? But the fact is we can save energy and make more profit.

It comes down to this: we're short on self-sacrifice, long on self-interest. That's what created the energy problem in the first place, and that's what's delaying the solution. It's going to take nothing less than a restructuring of all the old thought patterns, from the top down and from the bottom up. We've got to start living by the Golden Rule instead of just giving it lip

service. And since America has been the biggest consumer of energy, I think it's pretty much up to us to take the lead in alleviating the crisis.

*The method and approach.*—How should we approach this amorphous mass known as the energy crisis? Some of the shorts and longs that apply here are: we're short on incentives, long on requests. Short on trained people, long on unemployed people. We're short on coordinated, integrated programs, long on individual pet projects. Worst of all, we're short on time, long on problems to be solved in time.

Dr. Edward Teller, in his report to the Energy Panel of the Commission on Critical Choices for Americans, said that we should not try to solve the energy problem forever. We can't expect to provide answers to all the new problems and possibilities that may show up in the 21st century. I think that's an important point to remember. It provides a sharper focus and makes the over-all problem a little more manageable.

We need to look at the whole picture, the four Big E's that I mentioned. In one sense, there's no such thing as solving the energy problem, the environmental problem, the economic problem, the education problem any more than we can expect to solve the old age problem or the health care problem. We can only improve the situation in each case by solving hundreds and thousands of individual problems, one at a time.

It's different than going to the moon or fighting a war and it's even more complex. But some of the same tools and skills can be used and are being used. The systems approach, computer modeling and synthesis, these techniques help identify key elements of the problem, analyze various functions and how they interact, but the name of the game is to spot the leverage points that can increase the energy supply, reduce the cost, improve the environment, and motivate people to do their part.

There are a lot of dedicated people in industry, government, and education working on these problems. Of these the most immediate and pressing burden falls on those in government, for without question it is their judgments and actions which will chart our course toward energy independence. Unfortunately, almost all of these civil servants are terribly overloaded. Those at the top are very able people who must be involved in an enormously complicated and demanding range of activities. The coordination of government agencies, preparation and presentation of testimony, speaking engagements, program development and review are just part of the burden. To the levels below them falls the responsibility for creating analyses of important questions, program detail, endless meetings with support contractors, etc. With such heavy loads there is a tendency to handle each problem as it comes up and not be able to devote the time necessary to address and resolve the major problems.

It seems to me that the effectiveness of various agencies could be significantly improved, particularly in the energy areas, if the largest or more important efforts could be identified, and government/industry teams selected to give them the attention they deserve. While this may seem to be quite a departure from present practice, it is just the method we have used in the past—in World War II to produce synthetic rubber, in the late fifties to overcome the missile gap, and in the sixties to go to the moon and return successfully. In the same way, it seems to me we can forge government/industry teams to accelerate the development of *in situ* coal and shale, liquefaction and gasification of coal, and other areas where the name of the game is to reduce technical and economic uncertainties. In this regard one of the things our government does best is to take those actions necessary to improve the market environment by the removal of technical risk, provision of front end capital, etc. One of the things that government frequently does not do well is the implementation of programs; hence, the reason for suggesting a government/industry team.



It will take years to perform a complete analysis of the over-all energy problem and all the alternative solutions. But in the meantime, we can and must begin working on some of the major requirements that have already been identified, like expanding our coal production and usage, building more nuclear power plants, intensifying the search for new oil and gas deposits, and doing extensive research and development on new energy sources such as oil from shale, gas from coal, and solar energy conversion.

Of course the energy problem is nothing new to electrochemists. You've been working on more efficient ways to convert and store energy ever since the discovery of electricity back in the 18th century, and the contributions of electrochemists include batteries, fuel cells, and solar cells. Your work has made possible self-starting cars, portable radios, flashlights, calculators, manned flight, and long-term planetary probes. And today, electrochemistry still faces a host of challenges. The world needs low-cost, efficient ways of reducing our dependence on fossil fuels. Fuel cells, for example, can nearly double the efficiency of converting fossil fuels to electricity, provided low-cost, long-life catalysts can be found. Inexpensive photogalvanic or photovoltaic devices can provide us with an almost inexhaustible supply of energy. And economical, long-life, efficient secondary batteries can provide the load leveling needed to operate large coal and nuclear power plants at maximum efficiency. There's no doubt about it, you've got your work cut out for you. We all have.

*Programs and schedules.*—The things we have to do to deal with the energy crisis are related to our two major objectives: reduce energy demands and find new energy resources. It sounds a lot simpler than it really is.

For the short term, I see at least six steps that need to be taken, all of which will help for the long term, too. They are: conservation, building a reserve supply, finding new gas and oil deposits, switching from petroleum to coal wherever possible, stepping up construction of nuclear power plants, and, last but by no means least, training the necessary talent. For the long term, we have only one step to take, but it's a giant one: we have to find new substitutes, in addition to nuclear power and coal, to replace the oil and gas which will all be gone within the next generation or two unless of course we can gain a little time through the unlikely discovery of major new deposits that we don't yet know about.

Eliminating waste through conservation can relieve the energy crunch faster than any other single step. This will also alleviate the economic crunch to some extent and, in many cases, ease the environmental pollution problem. It's amazing but true that even a one per cent saving or improvement in efficiency would reduce our oil consumption by 100 million barrels each year. At today's prices, that's more than a billion dollars saved. There are other fringe benefits, too. For instance, the 55 mile-per-hour national speed limit, even though it's pretty loosely enforced, not only saved a lot of gas but reduced highway fatalities by 20% in 1974. (Apparently this idea of taking things slower is catching on with the younger generation. My secretary tells me that the kids are not only driving slower, they're even dancing slower, and closer, too.)

The automotive industry has finally embarked on a program of conversion to energy-saving cars. It's been a slow and painful process, but it's working. To the rest of industry, conservation means planning for the future in new ways like more efficient heating and cooling systems, more efficient machines and equipment and use of materials. To labor, conservation may mean the loss of some jobs for the short term, but it will mean more jobs in the long run as more energy becomes available for critical industrial needs, and as new sources of energy are developed.

But what about the man on the street again? What can be done on an individual basis to make people stop wasting energy? The whole thrust of the American way of life has been the idea of upward mobility, increasing our standard of living, and that means burning up more energy. But we must have the cooperation of the general public or we're not going to solve the energy problem. Government and industry need the public's support and confidence. We've got to work like the devil to restore the people's faith in their leaders and in science and technology. Beyond that, we've got to somehow get people to do what's best for the greater number, even if it means giving up some of their personal conveniences. This may require rationing and enforced scarcity, unless we can find the kinds of incentives that will make it happen voluntarily.

Close on the heels of this conservation program, we need to begin building a reserve stockpile of gas and petroleum. We should start small, say, a six-month supply, while continuing to study the situation to figure out whether we really need a six-month, two-year, four-year supply or whatever. This will help take us out of the panic mode and also put us in a little better negotiating position. Naturally, this plan is not going to work unless we can make the first step, conservation, work.

We've got to keep looking for more oil and gas, that goes without saying. We need to explore the outer continental shelf, in spite of the risk of pollution. The techniques to avoid blowouts and spills or to minimize their consequences are improving every day. The risk is small, but in my view it is one that we have to take. It is, after all, a much smaller risk than the one we're already taking—the risk of running out of oil altogether before we have a viable substitute.

Further, we need to switch from oil and gas to coal wherever possible and to step up production of coal, for which the supply is numbered in hundreds rather than tens of years. To make the switch, we have to solve some economic problems and environmental problems, but they are within the reach of today's technology. We can't just sit back and say that we mustn't burn coal because it pollutes, or because it's too expensive to convert the power plants. We can raise the money and we can control the pollution.

Nuclear power offers one of the most promising ways to get out from under our petroleum dependency, in spite of the economic problem and public controversy associated with it. There is concern about reactor safety, radiation exposure, waste management, and terrorism. Some of these fears are valid, but so is the need to build reactors. We should get to work in both areas, but with a new partnership between government and industry.

Finally, we need to increase the supply of trained professionals in the energy fields. We look to the universities and colleges for the solution to this problem but government and industry can help by publicizing their needs. We need specialists in fossil energy, solar energy, geothermal energy, and nuclear energy reactors. And we need people whose interests and education span more than one discipline. We've got to avoid the kind of polarization we've seen in recent years that pits the environmentalists and the energists against one another, and the economists against both.

For the long term, we must start now to look for the substitutes that will keep us going after the gas and oil run out. There are enormous uncertainties, and it's going to take continuing study and experimentation to remove these uncertainties so we can decide where to spend our time and money.

For example, we need to work the oil shale, particularly in situ approaches to find out whether the oil can be extracted economically and what the environmental considerations are. We need to drill more geothermal wells to find out whether in fact we have enough resources to provide the estimated 20,000 megawatts of



electric power we need by 1985. There's little point in solving the technological problems if the resources aren't there. We need to put a lot of effort into experimenting and evaluating the opportunities from solar energy. But here again, there are a host of social, and financial as well as technical problems to be identified and solved.

The short and the long of it is that we have perhaps two to three years to adjust the international political and economic situation to avoid the strangulation of several of our allies. We have from five to ten years to find several major new sources of oil and gas, and fifteen to twenty-five years to develop alternative energy sources before the oil and gas are gone. These are the milestones we must pass, and on schedule.

It isn't going to happen by accident, or by executive fiat, or by legislation. It will happen only if everyone works together instead of at cross-purposes; scientists, energists, environmentalists, politicians, economists, businessmen, and educators being concerned and working together for the common good.

During the next four days of sessions and discussions many of you will have your minds on the general subject of energy, and within the discipline of electrochemistry which permits us to solve many of the problems that limit not only the availability of energy, but also the flexibility and efficiencies in its use. I hope these remarks will turn out to be of some value in your deliberations. My time is up as of this minute, I thank you for yours.

## SECTION NEWS

### Columbus Section

The monthly noontime meeting of the Columbus Section was held on October 30, 1975, at the Columbus Laboratories of Battelle. Dr. Craig R. Hassler of the Bioengineering and Health Sciences Section of Battelle/Columbus presented a discussion on "Enhanced Bone Healing via Electrical Stimuli."

Dr. Hassler described the observed effects on bone growth of Pt brush electrodes implanted in the skull of a rabbit. At average current densities of 5-15  $\mu\text{A}/\text{cm}^2$ , enhanced bone growth was observed in the vicinity of the cathode. No differences were observed between pulsating and direct currents if the average current densities were of comparable magnitude. Uniformly detrimental effects were noted in the vicinity of the anode, however, and some relationship can be observed between the current and the current density, and the quantity of bone destroyed near the anode.

Larry B. Anderson  
Secretary-Treasurer

### Detroit Section

The Detroit Section held its first monthly meeting of the 1975-1976 season on October 23, 1975, at the Stouffers Northland Restaurant, Southfield, Michigan. The topic of the technical session was "The Future of Electrochemical Energy Conversion—The Next 30 Years." The speaker was Dr. James McBreen from the G. M. Research Laboratories, Electrochemistry Department, Warren, Michigan.

In his presentation, Dr. McBreen discussed the future of electrochemical energy conversion in the light of future primary sources of energy. Energy in the future will be used either as electricity or as fluid fuels. Possible energy sources for electricity generation in the future are fossil fuels, nuclear power, geothermal energy, tidal power, and direct and indirect solar energy. Electrochemistry and electrochemical energy conversion could play an important role in both the distribution and storage of electrical energy. Possible directions for future work were outlined.

Members of the Society interested in attending monthly meetings of the Detroit Section should contact V. Markovac, Ford Motor Company, P.O. Box 2053, Dearborn, Mich. 48121; telephone (313) 323-1504

V. Markovac  
Second Vice-Chairman

### Metropolitan New York Section

On October 15, 1975, Mr. William Hiefner, Executive Secretary of the National Electrical Manufacturers Association, presented to the Metropolitan New York Section two talks of topical interest: "The Relationship of Spent Dry Batteries to the Heavy Metal Content of Solid Wastes" and "The Energy Crisis: The Challenge . . . The Solution."

In his first talk, Mr. Hiefner outlined the heavy metal battery constituents which were monitored via battery manufacturers metal usage patterns from analysis of landfill and from heavy metal drainage off landfill sites. Of the metals, cadmium, lead, zinc, and mercury used in dry batteries in 1970, cadmium (0.22% of total U.S. usage) and lead (less than 0.01% of total U.S. usage) appear to show dry battery manufacturers low in the user list of these two metals. Zinc and mercury (at 1.6% and 12%, respectively, of total U.S. usage) are more significantly related to dry battery manufacture. All four metals were determined in two landfills and it was found that the highest zinc concentration was 4.5 ppm while the other metals were found to be at levels typically well below 1 ppm. In water resulting from drainage through landfill sites, it was shown from a study of similar heavy metal transport (Fe and Ba) that metals resulting from dry batteries would not be transported significant distances from the landfill sites. Of the four metals considered, only mercury appeared marginally acceptable for recycling on economic grounds when metal reprocessing companies were approached. It was concluded that the best disposal technique was to recycle batteries for heavy metal recovery; though when technical or economic factors prevent this, the spent batteries could be disposed of along with normal solid wastes.

In his second talk, Mr. Hiefner outlined the crisis facing the U.S. and the world with respect to oil and natural gas. He emphasized that alternative sources should be utilized and pointed out that "we are burning up oil and gas as if we wanted to get rid of them and saving coal as though it were scarce." Oil and gas supply about 78% of our present energy needs and if we wish to continue without energy-related hardships, we must turn to an electricity-based economy for the long-term solution to our problem. In about 1910, the U.S. shifted its energy base from wood to coal; now is the time to shift from oil and natural gas to coal and uranium. Of the areas of energy use outlined, by far the largest energy consumption sector was transportation. Mr. Hiefner described some of the work being carried out on electric vehicles which could have application in fleet operation of delivery, maintenance, and service vehicles in urban environments.

As previously mentioned in a recent News Item, the Metropolitan New York Section is organizing a one-day symposium. The title will be "Electrochemistry of the Three E's—Energy, Environment, and the Economy," and it will be held at the Stevens Institute of Technology, Hoboken, N. J., on March 17, 1976. For further information, please contact J. Broadhead, Bell Laboratories, Murray Hill, N. J. 07974; telephone (201) 582-6159.

John Broadhead  
Councillor

## DIVISION NEWS

### ECS Call for Papers Las Vegas, Nevada, Meeting

In addition to the previously announced Call for Papers for the Dielectrics and Insulation Division, a General Session is being planned for which papers on the following topics are solicited:

1. Conformal coating materials: their characterization and applications.
2. High temperature polymers: their characterization and applications as dielectrics.
3. Plastics for microelectronic device packaging.
4. Inorganic dielectrics.
  - a.) For receipt no later than May 1, 1976, submit a 75-word abstract of the paper to be delivered, using the appropriate form in the Call for Papers.
  - b.) For receipt no later than June 1, 1976, submit two copies of an extended abstract, 500-1000 words.
  - c.) Send all abstracts to The Electrochemical Society, Inc., P.O. Box 2071, Princeton, N.J. 08540. See details in the Call for Papers.

Suggestions and inquiries concerning the Dielectrics and Insulation General Session should be directed to J. A. Amick or R. Epifano, RCA Solid State Division, Somerville, N.J. 08876.

Section News .....	9C
Division News .....	9C
New Members .....	10C
People .....	10C
New Books .....	10C
Call for Recent News Papers— Washington, D.C., Meeting .....	11C
News Items .....	11C
Obituary .....	11C
Positions Wanted .....	12C
Call for Papers—Las Vegas, Nevada, Meeting .....	13C-16C

## NEW MEMBERS

It is a pleasure to announce the following new members of The Electrochemical Society as recommended by the Admissions Committee and approved by the Board of Directors in December 1975.

### Active Members

Arnoldussen, T. C., Warren, Mi.  
 Baker, T. E., Northboro, Ma.  
 Benoitel, R. W., Fall City, Wa.  
 Bredland, A. M., Middleton, W.  
 Burkett, R. J., Linden, N.J.  
 Burnham, R. D., Palo Alto, Ca.  
 Calderon, J. H., Lorton, Va.  
 Du Rant, P. J., Colorado Springs, Co.  
 Esaki, L., Yorktown Heights, N.Y.  
 Feneau, C. V., Hoboken, Belgium  
 Fino, J., Richardson, Tx.  
 Galvele, J. R., Columbus, Oh.  
 Holt, F. G., Williamsburg, Va.  
 Hoxie, V. L., San Diego, Ca.  
 Hussey, C. L., USAF Academy, Co.  
 Ito, K., Chita-shi, Aichi-ken, Japan  
 Jenkins, M. W., Scottsdale, Az.  
 Klunder, K. W., Washington, D.C.  
 Luther, G. W. III, Union, N. J.  
 Muller, H. R., Furstenfeldbruck, West Germany  
 Prabhu, A. N., Evanston, Il.  
 Reichman, J., Great Neck, N.Y.  
 Robertson, J. M., Eindhoven, The Netherlands  
 Rosnowski, W., Summit, N.J.  
 Sage, A. H. III, Monaca, Pa.  
 Serenyi, R., Pawcatuck, Ct.  
 Simmons, G. W., Bethlehem, Pa.  
 Smith, D. L., Norwalk, Ct.  
 Varshney, R. C., Palo Alto, Ca.  
 Wrobel, J. S., Garland, Tx.

### Student Members

Chang, K.-I., Stanford, Ca.  
 Dzioba, S., Hamilton, Ont., Canada  
 Giani, E., Hamilton, Ont., Canada  
 Moran, P. J., Charlottesville, Va.  
 Nawghare, P. M., Sendai-shi, Japan  
 Niranjani, M. S., Katakira, Sendai, Japan  
 Noufi, R. N., Austin, Tx.  
 Rosenfarb, J., Cincinnati, Oh.  
 Tsai, N.-H., Stanford, Ca.  
 Viswanathan, K., Potsdam, N.Y.  
 Woltman, A. W., Austin, Tx.

### Reinstatement and Transfer

Parker, P. D., Carteret, N.J.

### Reinstatements

Alimonda, A. S., Palo Alto, Ca.  
 Castle, J. E., Horsham, Sussex, England  
 Johansson, B. J. E., Nykoping, Sweden  
 Work, G. W., Pawcatuck, Ct.

### Transfers

Kuo, H. C., Cleveland, Tn.  
 Stankovich, M. T., Ann Arbor, Mi.

### Positions Wanted

Society members of any class may, at no cost and for the purposes of professional employment, place not more than three identical insertions per calendar year, not to exceed 8 lines each. Count 43 characters per line, including box number, which the Society will assign.

## ADVERTISERS' INDEX

Dow Chemical	12C
Honeywell	12C

## PEOPLE

**Dr. Bruce E. Deal**, an Active Member of the Society since 1955 and the 1974 winner of the Electronics Division Award, was among seven U.S. scientists presented with The Certificate of Merit of The Franklin Institute on October 29, 1975, at the 49th annual Medal Day awards ceremonies in the Benjamin Franklin National Memorial in Philadelphia, Pennsylvania. The Certificate, established in 1882, is awarded to persons adjudged worthy thereof for meritorious inventions, discoveries, or improvements in physical processes or devices. Dr. Deal received The Certificate for his work in solid-state technology.

Dr. Deal received his A.B. degree in chemistry from Nebraska Wesleyan University in 1950 and his M.S. and Ph.D. degrees in chemistry from Iowa State University in 1953 and 1955, respectively. During his graduate studies, Dr. Deal worked under an appointment with the Ames Laboratory of the Atomic Energy Commission. In 1955 he joined Kaiser Aluminum and Chemical Corporation's Department of Metallurgical Research in Spokane, Washington.

Since 1959 he has been associated with the semiconductor industry. He started with Rhen Semiconductor (later merged with Raytheon), and worked there until 1963, when he joined Fairchild Semiconductor, a division of Fairchild Camera and Instrument Corporation in Palo Alto, California, where he is now manager of the Integrated Circuits Research and Development division.

Dr. Deal has served as consultant to Stanford University's electrical engineering department, authored or co-authored 32 technical papers, and holds seven patents.



**Charles W. Tobias** has been selected as the first speaker of the "BASF Renowned Scientist" Lecture Series at Wayne State University, Detroit, Michigan. His lecture on "The Future of Electrochemical Engineering" was given December 3, 1975, at Wayne State University and was cosponsored by BASF Wyandotte and the Department of Chemical Engineering and Materials Sciences of Wayne State. In his lecture, Dr. Tobias described some of the key areas of electrochemical technology in which chemical engineers should have an important role in the coming decades and illustrated research problems of current interest.

Over the past 25 years, Dr. Tobias, a member of the chemical engineering faculty at the University of California

at Berkley and Lawrence Berkeley Laboratory and Chairman of the Department from 1966 to 1972, has built an excellent program of teaching and research in electrochemical engineering. President of The Electrochemical Society from 1970 to 1971 and recipient of the Edward Goodrich Acheson Medal and Prize in 1972, Dr. Tobias also serves as a Divisional Editor of **This Journal**. He is on the Advisory Editorial Board of the Journal of Applied Electrochemistry and of the Chemical Engineering Communications. He is also coeditor of the "Advances in Electrochemistry and Electrochemical Engineering" which is currently in its tenth volume. Dr. Tobias has recently been elected as the President-Elect of the International Society of Electrochemistry (ISE).



**Francis L. LaQue** received the Leo B. Moore Medal "for highest achievement, extraordinary contribution and distinguished service in the field of standardization"

from the Standards Engineers Society at their annual fall conference in Syracuse, New York.

Former vice president of The International Nickel Company, Inc., and special assistant to the president of the parent company, The International Nickel Company of Canada, Ltd., Mr. LaQue was recently appointed deputy assistant secretary for product standards, Commerce Department, Washington, D.C.

President of The Electrochemical Society from 1962 to 1963 and recipient of the 1968 Edward Goodrich Acheson Medal and Prize, Mr. LaQue is the author of "Marine Corrosion," recently published by John Wiley & Sons.

## NEW BOOKS

The second volume of "The Primary Battery," edited by N. Corey Cahoon and George W. Heise, has been published by John Wiley & Sons as a volume in The Electrochemical Society Monograph Series. An authoritative review of primary battery technology, this volume covers cells with aluminum anodes and organic electrodes—the most probable new systems for future development. Each of its eleven chapters presents a description of either a battery system or an important field closely related to battery technology and is supported by pertinent data. This book will be of interest to executives, scientists, and technologists in the battery manufacturing and battery-powered appliance manufacturing industries. Members of the Society can order this book at a discount through Society Headquarters.

# CALL FOR RECENT NEWS PAPERS

Washington, D.C., Meeting

May 2-7, 1976

Triplicate copies of a 75-word abstract of Recent News Papers must be received by the Symposium Chairman (as indicated below) not later than April 1, 1976, to be considered for inclusion in the Recent News Papers Session.

## ELECTRONICS DIVISION

Recent News Papers are invited for the sessions sponsored or cosponsored by the Electronics Division for the Spring 1976 Meeting in Washington, D.C. Papers should be brief (15 minutes total including 3 minutes for discussion) and timely. If the presentation requires more than the time normally allotted, please inform the Chairman at the time the abstract is submitted. Topics for Recent News Papers include:

1. The preparation and characterization of thin-film and bulk semiconductors including compound semiconductors, homo- and hetero-epitaxy, and junctions.
2. Semiconductor device fabrication and characterization techniques including LED's, lasers, solar cells, photoconductors, display devices, and other electronic devices.
3. The evaluation and characterization of impurity and structural defects in semiconductor materials and devices.

Triplicate copies of 75-word abstracts should be sent to the Recent News Papers Session Chairman: J. A. Seirmarco, IBM Corp., Dept. 63A, Bldg. 330-122, Route 52, Hopewell Junction, N.Y. 12533, for receipt by April 1, 1976.

## NEWS ITEMS

### Institute on Philosophical Ethics

The Council for Philosophical Studies will present a one month Institute on Philosophical Ethics during the summer of 1976 for science and engineering faculty from colleges and universities throughout the country. The Institute's resident staff will provide intensive exposure, through readings, lectures, seminars, and discussions, to current moral philosophy, especially as applied to problems of science and technology. For further information about dates, location, eligibility, stipends, housing, and application procedures, write immediately to Professor Samuel Gorovitz, The Council for Philosophical Studies, Skinner Hall 1131, The University of Maryland, College Park, Maryland 20742. The Institute is supported by a grant from the National Science Foundation jointly funded by the National Endowment for the Humanities.

### 1976 Electronic Materials Conference

The Eighteenth Annual Conference of the Electronic Materials Committee of The Metallurgical Society of AIME will be held at the University of Utah, Salt Lake City, Utah, June 23-25, 1976. This conference is being coordinated with the Device Research Conference

of the IEEE, which is being held at the same location on June 21-23, 1976. In keeping with the tradition established by previous conferences, the EMC program will provide comprehensive coverage of current research on the entire spectrum of electronic materials, with particular emphasis on those areas that are also of interest to specialists in device research. Special symposia will be organized on "Recent Developments in Photo-voltaic Materials and Devices with Emphasis on Solar Energy Conversion" and "Transport Phenomena and Trapping in Insulators."

Authors should submit 200-300 word abstracts by March 1, 1976; they will be notified of acceptance or rejection in early April. Accepted papers will be considered for publication in the Journal of Electronic Materials. Accordingly, manuscripts must represent original work that is neither published nor intended for publication elsewhere. Conference presentations involving university level research are eligible for the Student Awards Program. Student awards will be based on both scientific content and presentation at the Electronic Materials Conference. For details on the Student Awards Program, see the Journal of Electronic Materials 3, 307 (1974) and 4, 193 (1975).

Abstracts or inquiries should be sent to R. A. Burmeister, Hewlett-Packard Laboratories, 1501 Page Mill Road, Palo Alto, Calif. 94304; telephone (415) 493-1501, ext. 3146.

## OBITUARY

**Dr. Arthur L. Smith**, 60, manager of luminescent material development at RCA, Picture Tube Division, Lancaster, Pennsylvania, died of an apparent heart attack October 29, 1975. A native of New York City, Dr. Smith obtained his B.S. in chemistry from Fordham University and his M.S. and Ph.D. in chemistry from the Polytechnic Institute of Brooklyn. He joined RCA on completion of his doctoral degree.

His major field of work from his Doctoral Thesis through his career at RCA has been luminescent materials. His phosphor developments resulted in commercial products in Flying Spot Scanner Tubes, Projection Television Tubes, and Color Television Receiver Tubes. He has been issued twelve U.S. patents and authored or co-authored fourteen technical papers.

He was an Active Member of The Electrochemical Society serving as Vice-Chairman of the Luminescence Section 1952-1953, Chairman of the Electronics Division 1953-1954, and was a Presidential Candidate in 1955. He was also a member of the American Chemical Society, Sigma Xi, and Phi Lambda Upsilon.

He is survived by his wife Agnes, three children, three step-children, and eight grandchildren.



Research  
ELECTROCHEMIST

Texas Division

DOW CHEMICAL U.S.A.

Dow Chemical U.S.A.—Texas Division has an immediate opening for a graduate electrochemist with a doctorate or equivalent experience. The successful candidate will be given responsibilities in Dow's ongoing, strongly supported program of electrode research. Experience in electrode kinetics is highly desirable and a knowledge of solid-state chemistry would be helpful.

Gulf Coast Location

Excellent relocation and benefit policies

Please send your confidential resume including salary requirements to:

R. L. Hansen, Manager  
Technical Recruiting, B1209  
Dow Chemical U.S.A.  
Texas Division  
Freeport, Texas 77541

An Equal Opportunity Employer M/F

We are seeking a creative individual to carry out sophisticated infrared detector material development programs in the growth and characterization of semiconductor alloy crystals such as mercury-cadmium telluride (HgCdTe).

# Semiconductor Materials Engineer

The ideal candidate should have significant laboratory experience in both the growth of highly pure semiconductor crystals as well as an appropriate advanced degree in Material Science, Solid State Physics, Metallurgy, Physical Chemistry or Electrical Engineering.

It is particularly desirable that you have a working familiarity with the concepts and practical consequences of solid state defect chemistry, phase equilibria and crystal growth kinetics.

In addition to conducting development programs in a modern, well-equipped materials laboratory, you will interact with both customers as well as infrared detector development engineers.

Please direct your resume to Mr. Roy Thistle, Employment Supervisor.

**Honeywell**

RADIATION CENTER

2 Forbes Road

Lexington, Mass. 02173

An Equal Opportunity Employer

## POSITIONS WANTED

Please address replies to the box number shown, c/o The Electrochemical Society, Inc., P. O. Box 2071, Princeton, N. J. 08540.

**Part-time Professor**—Mandatorily retired professor of materials science, vigorous health. Ch.E., Ph.D. metallurgical engineering, Lehigh 1957. Electrochemistry, corrosion, electroplating, materials science, metallurgy. Industrial experience, top-notch teacher, researcher. Desires part-time post. Salary, location open. Reply Box C-164.

**Electrochemist/Battery Engineer**—Ph.D. level. Creative, self-starter with many papers and publications in the battery field. 18 years industrial research and development experience involving various primary, secondary, hybrid, and fuel cell batteries. Specialist in the nickel-cadmium system. Seeking senior R&D position. Reply Box C-165.

**Materials Scientist/Electrochemist**—Ph.D. 1975. Dissertation on effects of aqueous environments on thin anodic oxide films. Two years industrial research experience in high temperature alloys. Seeks challenging R&D position in aqueous or high temperature corrosion. Salary and location open. Publications/presentations. Reply Box C-166.

**Materials Scientist/Device Physicist**—Ph.D. (1975). Experience in CVD, solution growth, diffusion, vacuum technology, photolithography, thin film technology, compound semiconductors, silicon, p-n junctions, Schottky diodes, MIS structures, p-n heterojunctions, and LED's. Presently working on silicon solar cells. Seeks industrial or R&D position. Reply Box C-167.

**Electrochemical/Chemical Engineer**—Ph.D. expected January 1976. Background in applied electrochemistry, transport processes, thermodynamics. Research experience in electrode kinetics, batteries, mass transfer, cell design, and modeling. Seeks position in research, production, process development, or design. Reply Box C-168.

**Materials Scientist**—Ph.D. (1972). Specialist in thin-film technology, preparation, characterization, and fabrication of thin-film devices. Good background in electron optics: TEM, SEM, RHEED, and x-ray analysis. Varied industrial experience in thin-film deposition with emphasis on polycrystalline and transition metal oxides. Seeks R&D position. Publications and patent. Reply Box C-169.

**Electrochemist/Inorganic Chemist**—M.S. seeks a position in production, quality control, or R&D. Two years experience in electroplating industry and two years experience on lead-acid batteries. Research and thesis on Pb(II) ion-selective electrode. Reply Box C-170.

## Certificates, Pins, and Keys

The following items are available to Active Members:

Membership Certificates	\$ 5.00
Gold Membership Pin	\$ 7.50
Gold Membership Key	\$15.00

Those interested should send their order accompanied by check to The Electrochemical Society, Inc., P.O. Box 2071, Princeton, N.J. 08540



# **Call for Papers**

## **150th Meeting, Las Vegas, Nevada, October 17-22, 1976**

Divisions which have scheduled sessions are listed on the overleaf, along with symposium topics.

### **1. Symposium Papers.**

Authors desiring to contribute papers to a symposium listed on the overleaf should check first with the symposium chairman to ascertain appropriateness of the topic.

### **2. General Session Papers.**

Each of the several Society Divisions which will meet in Las Vegas, Nevada, can plan a general session. If your paper does not fit readily into a planned symposium, you should specify "General Session."

### **3. To Submit a Meeting Paper.**

Each author who submits a paper for presentation at a Society Meeting must do three things:

A—Submit one original 75-word abstract of paper to be delivered. Use the form printed on the overleaf or a facsimile. **Deadline for receipt of 75-word abstract is May 1, 1976.**

B—Submit original and one copy of an Extended Abstract of the paper. **Deadline for receipt of Extended Abstract is June 1, 1976.** See (5) below for details.

C—Determine whether the meeting paper is to be submitted to the Society Journal for publication. See (6) below for details.

**Send all material to The Electrochemical Society, Inc., P.O. Box 2071, Princeton, N.J. 08540.**

Unless the 75-word and required Extended Abstracts are received at Society Headquarters by stated deadlines, the papers will not be considered for inclusion in the program.

### **4. Meeting Paper Acceptance.**

Notification of acceptance for meeting presentation, along with scheduled time, will be mailed to authors with general instructions no earlier than two months before the meeting. Those authors who require more prompt notification are requested to submit with their abstracts a self-addressed postal card with full author-title listing on the reverse.

### **5. Extended Abstract Volume Publication.**

All scheduled papers will be published in the EXTENDED ABSTRACTS volume of the meeting. The volume is published by photo-offset directly from typewritten copy submitted by the author. Therefore, special care should be given to the following instructions to insure legibility.

A—Abstracts are to be from 500 to 1000 words in length and should not exceed two pages, single spaced. The abstract should contain to whatever extent practical all significant experimental data to be presented during oral delivery.

B—Abstracts should be typed single spaced on the typing guide forms which are sent to each author after the submission of a short abstract. If it is necessary to use white bond paper, it should be 8½ x 11 inches with 1¼ inch margins on all sides. Submit all copy in black ink. Do not use handwritten corrections.

C—Title of paper should be in capital letters. Author(s) name and affiliation and address should be typed immediately below in capital and lower case

letters. Please include zip code in address. It is not necessary to designate paper as "Extended Abstract" or to quote the divisional symposium involved.

D—If figures, tables, or drawings are used, they should follow the body of the text and should not exceed one page. Submit only the important illustrations and avoid use of halftones. Lettering and symbols should be no smaller than ⅛ inch in size. Figure captions should be typed beneath the figure and be no wider than the figure. Table titles should be typed above, and the same width as, the table.

E—Mail original and one copy of the abstract to: The Electrochemical Society, Inc., P.O. Box 2071, Princeton, N.J. 08540, unfolded.

Abstracts exceeding the stipulated length will be returned to author for condensation and retyping.

### **6. Manuscript Publication in Society Journal.**

All meeting papers upon presentation become the property of The Electrochemical Society, Inc. However, presentation incurs no obligation to publish. If publication in Journal is desired, papers should be submitted as promptly as possible in full manuscript form in order to be considered. If publication elsewhere after presentation is desired, written permission from Society Headquarters is required.

# Las Vegas, Nevada, Meeting Symposia Plans—Fall 1976

## October 17-22, 1976

- a.) For receipt no later than May 1, 1976, submit a 75-word abstract of the paper to be delivered, on the form overleaf.  
 b.) For receipt no later than June 1, 1976, submit two copies of an extended abstract, 500-1000 words.  
 c.) Send all abstracts to The Electrochemical Society, Inc., P.O. Box 2071, Princeton, N.J. 08540. See details on preceding page.

### BATTERY DIVISION

#### Low-Maintenance and Maintenance-Free Lead Acid Batteries

The Battery Division is sponsoring a symposium on low-maintenance and maintenance-free lead acid batteries. The purpose of this symposium is to assess the significant advances and to point out new trends in automotive and nonautomotive applications of this growing field. Both theoretical and practical aspects will be covered. Papers are being solicited under the following topics:

1. Materials and separators.
2. Low and antimony free grid alloys.
3. Reversible and irreversible structural changes of the active mass.
4. Performance under adverse ambient conditions.
5. Methods to minimize water loss (to include oxygen cycle and catalytic converters).
6. Charging requirements (to include fast charging).
7. New potential applications (i.e., load leveling).

Suggestions and inquiries should be directed to the Symposium Chairman: U. S. Sokolov, NL Industries, Central Research Laboratories, P.O. Box 420, Hightstown, N.J. 08520.

#### Porous Electrodes, Theory and Practice

This symposium will review the field of porous electrodes both from a theoretical and practical viewpoint. It will include such types as flooded, flow-through, gas diffusion, and fluidized bed electrodes which are used in energy conversion (e.g., fuel cells, primary and secondary batteries), electrochemical reactors and environmental activities (e.g., waste water treatment, pollution sensors, etc.). Areas of interest involving porous electrodes include:

1. Electrode kinetics and mechanisms.
2. Mass transport phenomena.
3. Electrode structure and properties.
4. Nonuniform reaction rates.
5. Mathematical models of electrode-electrolyte systems.
6. Design theory.

A number of invited papers will be presented and contributed papers are solicited. Suggestions and inquiries should be directed to the Symposium Chairman: E. G. Gagnon, General Motors Corp., Research Laboratories, GM Technical Center, Electrochemistry Dept., Warren, Mich. 48090.

### BATTERY, ELECTRODEPOSITION, AND INDUSTRIAL ELECTROLYTIC DIVISIONS

#### High Current Density Electrode Processes

The Battery, Electrodeposition, and Industrial Electrolytic Divisions have planned a joint symposium on high current density electrode processes.

Papers are solicited for this symposium which is concerned with the theoretical, experimental, and industrial aspects of high current density and high rate electrochemical processes and cells. Topics of interest include:

1. Electrochemical machining.
2. High speed plating.

3. High rate electrosynthesis.
4. High power density battery systems.
5. Molten salt electrochemical cells.
6. Advanced technology in electrolytic processes for energy conservation.

Suggestions and inquiries should be directed to the Symposium Co-Chairmen: N. P. Yao, Argonne National Laboratory, Chemical Engineering Div., 9700 South Cass Ave., Argonne, Ill. 60439; M. A. LaBoda, General Motors Corp., Research Laboratories, GM Technical Center, Warren, Mich. 48090; L. E. Vaaler, Battelle Columbus Laboratories, 505 King Ave., Columbus, Ohio 43201.

6. Techniques and instrumentation for electrochemical studies at high temperatures (50°-350°C) and pressures (50-500 psi).

7. The relationship between scale deposition and the corrosion process.

8. The role of O<sub>2</sub>, CO<sub>2</sub>, CH<sub>4</sub>, H<sub>2</sub>S, and H<sub>2</sub> in brine corrosion processes.

Keynote papers from invited speakers will be presented and contributed papers are solicited. Suggestions and inquiries should be directed to the Symposium Chairman: P. B. Needham, Jr., U. S. Bureau of Mines, College Park Metallurgy Research Center, College Park, Md. 20740.

### CORROSION DIVISION

#### Corrosion in Scrubbing Systems

Stack gas scrubbing is a common method of air pollution control. However, corrosion can often be a problem in these systems because of either contaminants being removed or the quality of the scrubbing water. The purpose of this symposium is to explore the nature of these corrosion problems and document their solution. Papers are solicited on both the engineering and basic data aspects of these questions. An area of particular interest is how scrubber design and operation can influence corrosion performance.

Although scrubbers for fossil-fueled power plants have received a great deal of attention recently, scrubbers are used in many other industries, and papers will be welcome from other sources such as the metallurgical, chemical, and waste disposal industries.

In addition to studies directly involved with scrubbers, papers are solicited for corrosion investigations in chemically similar systems. Work on the evaluation of both metallic and nonmetallic materials is of interest.

Suggestions and inquiries should be directed to the Symposium Chairman: R. F. Steigerwald, Climax Molybdenum Co. of Michigan, P.O. Box 1568, Ann Arbor, Mich. 48106.

#### General Session

The Corrosion Division will schedule a General Session. All aspects of low temperature and high temperature corrosion will be considered. Techniques for the study of corrosion phenomena are of interest. Suggestions and inquiries should be directed to: R. W. Staehle, Dept. of Metallurgical Engineering, Ohio State University, 116 West 19th Ave., Columbus, Ohio 43210.

### CORROSION AND ELECTROTHERMICS AND METALLURGY DIVISIONS

#### Corrosion Encountered in Energy Extraction from Geothermal Brines and Steams

In order to extract an estimated 42,000 megawatt-centuries of power from our geothermal resources, materials must be found to withstand brines at temperatures ranging from 100° to 500°C with dissolved salt contents ranging from 1 to 35 w/o and containing entrapped gases such as O<sub>2</sub>, CH<sub>4</sub>, H<sub>2</sub>, H<sub>2</sub>S, and CO<sub>2</sub>.

Since the number of in situ studies is limited, special attention will be given to all aspects of research on chloride-ion attack at temperatures ranging from 30° to 350°C and pressures ranging from 15 to 500 psi. Papers related to the subject of this symposium, that involve the following topics, are solicited:

1. The chemistry and physics of brines at temperatures up to 350°C.
2. The role of chloride and other halide ions in corrosion processes.
3. Stress corrosion cracking, with emphasis on chloride ion and H<sub>2</sub>S-assisted SCC.
4. Seawater studies applicable to the lower salinity brines.
5. Corrosion experience in operating geothermal power plant field studies in the geothermal environment.

### Properties of High Temperature Alloys

The main emphasis of this symposium will be on the high temperature oxidation behavior of high temperature alloys in multicomponent environments of practical significance, such as oxidation, sulfidation, carburization, hot corrosion, etc.

As an introduction to the main theme of the symposium, three invited papers will discuss the recent advances in the metallurgy and fabrication of high temperature alloys. Several invited papers will also provide an overview of several important aspects such as thermochemical predictions of high temperature alloy behavior in aggressive environments, general kinetic considerations, and the role of stress effects on oxidation.

Contributed papers are solicited which are concerned with the theoretical, experimental, and industrial aspects of reactions of high temperature alloys in multicomponent oxidative environments. Pertinent reactions of interest are oxidation, sulfidation, carburization, nitriding, halogenation, hot corrosion, etc. Papers concerned with the effect of these environments on the mechanical properties of metallic materials are also of interest.

Suggestions and inquiries regarding the symposium should be directed to the Symposium Co-Chairmen: Z. A. Forouli, Exxon Research and Engineering Co., P.O. Box 101, Florham Park, N.J. 07932; or F. S. Pettit, Pratt and Whitney Aircraft Corp., Aircraft Rd., Middletown, Conn. 06457.

This symposium is being cosponsored by the Corrosion-Resistant Metals Committee of The Metallurgical Society of AIME.

### DIELECTRICS AND INSULATION AND ELECTRONICS DIVISIONS

#### Dielectric Isolation and Semiconductors on Insulating Substrates and Silicon on Sapphire

The scope of this symposium will include:

1. Techniques for dielectric isolation of silicon integrated circuits; capabilities, advantages, and disadvantages of the various methods.
2. Materials aspects of realizing dielectric isolation using bulk silicon as the starting material; process schemes, precision mechanical and electrical thinning, selective oxidation, polysilicicn as the dielectric.
3. Materials aspects of realizing dielectric isolation with insulating silicon; substrate crystal growth and surface preparation, deposition of silicon on sapphire.
4. The preparation and properties of semiconductors other than silicon on insulating substrates.
5. The chemical, physical, and electrical characterization of dielectrically isolated semiconductors.
6. Processing of devices in semiconductors on insulating substrates.

Both invited and contributed papers will be presented. Suggestions and inquiries should be directed to the Symposium Co-Chairmen: G. W. Cullen, RCA Laboratories, Princeton, N.J. 08540; or J. R. Szedon, Westinghouse Research Laboratories, Beulah Rd., Churchill Boro, Pittsburgh, Pa. 15235.

## Materials, Devices, and Fabrication Techniques for Image Storage and Display

The purpose of this symposium is three-fold. First, the symposium will focus attention on advances made in display technology in the areas of electroluminescence, liquid crystals, CRT's, plasma displays, and storage devices for display applications. Second, the symposium will contribute to the understanding and characterization of material problems associated with current display technologies. Third, the symposium will provide a forum for presenting new materials and device fabrication techniques for various display devices.

Invited papers will be presented on the current status of the above-mentioned display technologies. Contributed papers are solicited within the general purposes of this symposium. The suggested subjects are:

1. Electroluminescent displays: electroluminescent materials for displays, II-VI electroluminescent devices, EL thin films and phosphors, material preparation and characterization techniques, dielectric materials, insulating and passivating materials for electroluminescent devices.
2. Liquid crystal displays: new liquid crystal materials, devices and device fabrication techniques, physical and electro-optic properties of liquid crystals, organic and electrochemistry of liquid crystals, transitions and new electro-optic effects, and aligning properties of surface layers.
3. CRT, storage CRT, and storage tubes: improvements made on CRT's and storage CRT's, cathodes, phosphor screens, screen fabrication techniques, dielectric materials for storage tubes, and charge storage properties.
4. Plasma displays: dielectric and insulating materials for plasma displays, charge storage and secondary emission properties of dielectric materials, dielectric materials, packaging techniques for both a-c and d-c plasma displays.
5. Phosphors for display applications: CRT phosphors, phosphors for plasma displays, long persistence phosphors, voltage sensitive phosphors, and phosphors for color phosphor characterization, efficiency, and synthesis of phosphors.
6. Electrochemical displays: electrophoretic, electrochemiluminescent, and electrochromic materials and display properties and new electrochemical systems for displays.

Suggestions and inquiries should be directed to the Symposium Co-Chairmen: I. F. Chang, IBM Corp., Thomas J. Watson Research Center, Yorktown Heights, N.Y. 10598; or G. Sprokel (liquid crystals), IBM Research Laboratories, Monterey-Cottle Rds., San Jose, Calif. 95193.

## Materials and Structures for Integrated Optics

Contributed papers for this symposium are solicited covering all aspects of materials and fabrication techniques for integrated optics. Topics pertinent to this symposium should involve the integration or potential integration of active and passive optical devices. These optical devices include: planar optical waveguides; sources like diode lasers with grating structures or with parallel coupled planar waveguides; modulators, detectors, switches, deflectors, second harmonic generators; mode converters, etc.; prisms, resonators, splitters, lenses, polarizers, etc. These devices may involve optical, electro-optic, acousto-optic, magneto-optic interdigital planar waveguides.

Invited papers will present a general overview of the state of the art in the above topics. Suggestions and inquiries should be directed to the Symposium Co-Chairmen: W. Phillips, RCA Laboratories, Princeton, N.J. 08540; or R. J. Quinn-Tann, Bell Laboratories Research Center, 3333 Coyote Hill Rd., Palo Alto, Calif. 94304.

## DIELECTRICS AND INSULATION, ELECTRONICS, AND ELECTROTHERMICS AND METALLURGY DIVISIONS

### The Chemistry and Crystallography of Electronic Materials Formed by Chemical Vapor Deposition (CVD)

The purpose of this symposium is to discuss recent research results in the CVD of electronic materials. Fundamental work which probes the nature of CVD reactions as well as the properties of the deposited films and their interrelation with the substrate are solicited. Application oriented papers which

stress new processes or materials and/or the development of processes which produce certain desired substrate-film properties are also solicited. Several sessions and a number of review papers are planned. Contributed papers in the following areas are particularly appropriate:

1. Fundamental studies of the gas phase related to CVD: chemical kinetics, thermodynamics or hydrodynamics; measurement techniques including light scattering and mass spectrometry; gas reactions including dimerization and condensation.
2. Advances in homo- and heteroepitaxy: process development and applications, properties of the heteroepitaxial interface, lattice mismatch and defects; silicon on sapphire, silicon from SiC<sub>3</sub>H<sub>8</sub>, III-V and II-V structures, lasers and photoemitters, solar conversion devices.
3. Plasma-enhanced CVD.
4. Polycrystalline and amorphous materials: conductive and active device films of silicon, II-IV compounds, solar conversion devices, doped glasses as diffusion sources.
5. New source materials and transporting agents for CVD: organometallics, mixed metal dimers; preparation of oxides, III-V, II-IV, and other compounds.

Suggestions and inquiries should be directed to the Symposium Co-Chairmen: T. O. Sedgwick, IBM Corp., Thomas J. Watson Research Center, P.O. Box 218, Yorktown Heights, N.Y. 10598; G. Wakefield, Texas Instruments Inc., Mail Station 72, P. O. Box 501, Dallas, Texas 75222; or N. Tauber, Xerox Corp., 701 South Aviation Blvd., Al-05, El Segundo, Calif. 90245.

## ELECTRODEPOSITION DIVISION

### Selective Plating

The Electrodeposition Division is planning a symposium on selective plating for this meeting. Selective plating is a very active field these days especially where precious metals such as gold are involved. This symposium will present a broad overview of the science and technologies involved in selective plating of all types. It will also provide a forum for presentation of new work which contributes new knowledge or new technology to the general topic of selective plating. Papers are solicited for the symposium on such topics as: chemical and mechanical masking; fluid flow masking; anode shape effects and techniques; plating cell design theory and techniques; electroless plating; and selectively catalyzed surfaces.

Suggestions and inquiries should be directed to the Symposium Co-Chairmen: D. R. Turner, Bell Laboratories, 600 Mountain Ave., Murray Hill, N.J. 07974; or W. R. Doty, Udville Corp., 21441 Hoover Rd., Warren, Mich. 48089.

### General Session

The Electrodeposition Division will also schedule a General Session if a sufficient number of papers of interest are received. Suggestions and inquiries should be directed to: V. Hospadaruk, Ford Scientific Laboratory, P.O. Box 2053, Dearborn, Mich. 48121.

## ELECTRONICS DIVISION

### Semiconductors

### LED's and Injection Lasers: Process Technology and Degradation Mechanisms

This symposium will be devoted to all aspects of the fabrication and evaluation of visible and infrared light emitting diodes and p-n junction lasers for display and communication applications. Contributed papers are being solicited in the following areas:

1. Crystal growth and p-n junction formation, which may involve liquid phase epitaxy, vapor phase epitaxy, and diffusion studies.
2. Metallization, chip isolation, and bonding.
3. Packaging for displays and/or coupling to optical fibers.
4. Testing and evaluation, with particular emphasis on device reliability and degradation mechanisms.

Suggestions and inquiries should be directed to the Symposium Co-Chairmen: A. J. Springthorpe, Bell-Northern Research Ltd., P.O. Box 3511, Station C, Ottawa, Ont., Canada K1Y 4H7; or N. E. Schumaker, Bell Laboratories, 600 Mountain Ave., Murray Hill, N.J. 07974.

## Lithographic Techniques for Device Processing

A symposium is planned to discuss lithography for integrated circuit processing. Of special interest will be mask and resist materials for new or emerging lithographic techniques and process characterization and control with well-established techniques. Original or substantial review papers are solicited for the following topics:

1. Masks: materials and selection, fabrication, inspection, degradation, cleaning, defects, repairing.
2. Resists: new photon, electron, or x-ray resist materials; chemistry, characterization, and process control; processing techniques (coating, exposure, development, baking, stripping).
3. Printing: contact, proximity, projection, electron scanning or projection, x-ray, automatic alignment.
4. Other: adhesion and undercutting, measurement of microdimensions, diagnostic test and lithographic yield, contamination control.

Suggestions and inquiries should be directed to the Symposium Co-Chairmen: J. L. Bartlett, Texas Instruments Inc., P.O. Box 5012, M/S 72, Dallas, Texas 75222; or M. Hatzakis, IBM Corp., Thomas J. Watson Research Center, P.O. Box 218, Yorktown Heights, N.Y. 10598.

## General Sessions

The Semiconductor General Sessions will consist of papers relating generally to the semiconductor field. Original papers are solicited in the following areas:

1. Preparation and formation techniques for single and polycrystalline semiconductors. Of particular interest will be EFG and gas phase epitaxy. Preparation of semiconductor compatible materials such as single crystal sapphire and spinel are also of interest.
2. Physical and chemical characterization of semiconductors and semiconductor compatible materials particularly as related to electrical performance and changes during processing.
3. Electrical evaluation of semiconductors with regard for the applicability of the evaluation to the parameters of useful devices.
4. Methods and results of modifying the electrical properties of semiconductors and interfaces by preferential doping, oxidation, ion implantation, thermal treatment, or other processing.
5. Techniques for evaluating the suitability of a semiconductor for use in an LSI circuit or other comparably complex application. Specific items of interest are uniformity, defect distribution, reproducibility, photolithographic compatibility, and stability during and after processing.
6. Technology and processes for semiconductor device or circuit fabrication and methods of evaluation.

Suggestions and inquiries should be directed to: W. E. Ham, RCA Laboratories, Princeton, N.J. 08540.

## General Materials and Processes

### General Session

This session covers the general area of materials and processes which is not sufficiently electronic in nature to be included in the semiconductor general session or symposia. Follow-up papers in areas covered in recent symposia of the Electronics Division are encouraged as well as papers in new emerging areas of materials science and technology. Papers are solicited in areas such as magnetic bubbles, integrated optics, energy generation and storage, material preparation, device processing, and other areas of interest.

Suggestions and inquiries should be directed to: M. E. Prist, Bell Laboratories, Room 1C-321, 600 Mountain Ave., Murray Hill, N.J. 07974.

## ELECTROTHERMICS AND METALLURGY DIVISION

### General Session

The Electrothermics and Metallurgy Division's program will include a General Session. All suggestions and inquiries should be directed to: R. Bakish, Bakish Materials Corp., 171 Sherwood Pl., Englewood, N.J. 07631.

# 75-Word Abstract Form

(Deadline for receipt—May 1, 1976)

## LAS VEGAS, NEVADA, MEETING—OCTOBER 17-22, 1976

Submit to: The Electrochemical Society, Inc.  
P.O. Box 2071, Princeton, N.J. 08540

Schedule for ..... of .....  
Symposium ECS Division

Abstract No. ....  
(do not write in this space)

(Title of paper) .....

(Authors) (Underline name of author presenting paper) .....

(Business Affiliation and Address) .....

(ZIP Code)

(Tel. No.)

(Type abstract in this area—double spaced.)

Do you require any audiovisual equipment?

- 35 mm (2 x 2 in.) slide projector
- vugraph
- other (specify)

Is a full length paper on this work to be submitted for Society Journal publication?

- Yes
- No

Papers presented before a Society technical meeting become the property of the Society and may not be published elsewhere without written permission of the Society. Papers presented at Society technical meetings must be authored by a member or sponsored by an active member.

.....  
Insert name of Society member author or sponsor

## THE ELECTROCHEMICAL SOCIETY PATRON MEMBERS

### **Bell Telephone Laboratories, Inc.**

Murray Hill, N.J.

### **Dow Chemical Co.**

Inorganic Chemicals Dept., Midland, Mich.

### **General Electric Co.**

Battery Business Section, Gainesville, Fla.

Chemical Laboratory, Knolls Atomic Power Laboratory,  
Schenectady, N.Y.

Electronic Capacitor & Battery Dept., Irmo, S.C.

Lamp Div., Cleveland, Ohio

Materials & Process Laboratory, Large Steam  
Turbine-Generator Dept., Schenectady, N.Y.

Research and Development Center,  
Physical Chemistry Laboratory & Power Systems Laboratory,  
Signal Processing & Communication Laboratory,  
Schenectady, N.Y.

Semiconductor Products Dept.,  
Syracuse, N.Y.

### **The International Nickel Co., Inc.**

New York, N.Y.

### **Olin Corporation**

Chemicals Div., Research Dept., New Haven, Conn.

### **Philips Research Laboratories**

Eindhoven, Holland

### **Union Carbide Corp.**

Battery Products Div., Corporate Research Dept.,  
New York, N.Y.

### **Westinghouse Electric Corp.**

Electronic Tube Div., Elmira, N.Y.

Lamp Div., Bloomfield, N.J.

Semiconductor Div., Youngwood, Pa.

Research Laboratories, Pittsburgh, Pa.

K. W. Battery Co., Westinghouse Subsidiary,  
Skokie, Ill.

## THE ELECTROCHEMICAL SOCIETY SUSTAINING MEMBERS

**Airco Speer Carbon-Graphite**  
St. Marys, Pa.

**Allied Chemical Corp.**  
Industrial Chemicals Division  
Solvay, N.Y.

**Aluminum Co. of America**  
New Kensington, Pa.

**Aluminum Co. of Canada, Ltd.**  
Montreal, P.Q., Canada

**American Gas & Chemicals, Inc.**  
New York, N.Y.

**American Metal Climax, Inc.**  
New York, N.Y.

**American Smelting and Refining Co.**  
South Plainfield, N.J.

**AMP Incorporated**  
Harrisburg, Pa.

**Analog Devices, Inc.**  
Norwood, Mass.

**Applied Materials, Inc.**  
Santa Clara, Calif.

**BASF Wyandotte Corporation**  
Wyandotte, Mich.

**Beckman Instruments, Inc.**  
Fullerton, Calif.

**Bell-Northern Research**  
Ottawa, Ont., Canada

**Bethlehem Steel Corp.**  
Bethlehem, Pa.

**Boeing Co.**  
Seattle, Wash.

**The Borg-Warner Corp.**  
Roy C. Ingersoll Research Center  
Des Plaines, Ill.

**Brown, Boveri & Co., Ltd.**  
Research Center  
Baden, Switzerland

**Canadian Industries Ltd.**  
Montreal, P.Q., Canada

**Carborundum Co.**  
Niagara Falls, N.Y.

**Cominco Ltd.**  
Trail, B.C., Canada

**Corning Glass Works**  
Corning, N.Y.

**Crawford & Russell Inc.**  
Stamford, Conn.

**Diamond Shamrock Corp.**  
Painesville, Ohio

**Dow Corning Corporation**  
Hemlock, Mich.

**E. I. du Pont de Nemours and Co.**  
Central Research Department  
Wilmington, Del.

**Eastman Kodak Co.**  
Rochester, N. Y.

**Electrode Corporation**  
Chardon, Ohio

**Eltra Corp.**  
Prestolite Div., Toledo, Ohio  
C&D Batteries, Conshohocken, Pa.

**Engelhard Minerals & Chemicals Corp.**  
Murray Hill, N.J.

**ESB Inc.**  
Philadelphia, Pa. (2 memberships)

**Esso Research and Engineering Co.**  
Engineering Technology Div.  
Florham Park, N.J.



## SUSTAINING MEMBERS (CONTINUED)

**Ever Ready Co. (Holdings) Ltd.**  
Whetstone, London, England

**Exmet Corporation**  
Bridgeport, Conn.

**Fairchild Camera & Instrument Corp.**  
Research and Development Laboratory  
Palo Alto, Calif.

**Falconbridge Nickel Mines Ltd.**  
Thornhill, Ont., Canada

**FMC Corp.**  
Inorganic Chemicals Div.  
Buffalo, N.Y.

**Footo Mineral Co.**  
Exton, Pa.

**Ford Motor Co.**  
Dearborn, Mich.

**GAF Corporation**  
Inorganic Chemicals Department  
Glens Falls, N.Y.

**General Motors Corporation**  
Delco Electronics Div., Kokomo, Ind.  
Delco-Remy Div., Anderson, Ind.  
Research Laboratories Div., Warren,  
Mich.

**Globe-Union, Inc.**  
Milwaukee, Wisc.

**GTE Laboratories**  
Waltham, Mass.

**GTE Sylvania Incorporated**  
Chemical & Metallurgical Division  
Towanda, Pa.

**B. F. Goodrich Chemical Co.**  
Cleveland, Ohio

**Gould Inc.**  
Gould Laboratories, Rolling  
Meadows, Ill.  
Gould Laboratories—Energy Research,  
St. Paul, Minn.  
Gould Laboratories—Materials  
Research, Cleveland, Ohio

**Great Lakes Carbon Corp.**  
New York, N.Y.

**Harshaw Chemical Co.**  
Cleveland, Ohio (2 memberships)

**Hill Cross Co., Inc.**  
West New York, N.J.

**Honeywell, Inc.**  
Power Sources Center  
Horsham, Pa.

**Hooker Chemical Corp.**  
Niagara Falls, N.Y. (2 memberships)

**HP Associates**  
Palo Alto, Calif.

**Hughes Research Laboratories**  
Div. of Hughes Aircraft Co.  
Malibu, Calif.

**International Business Machines Corp.**  
New York, N.Y.

**Kaiser Aluminum & Chemical Corp.**  
Pleasanton, Ca.

**Kawecki Berylco Industries, Inc.**  
Boyertown, Pa.

**Kennecott Copper Corp.**  
New York, N.Y.

**Kerr-McGee Corporation**  
Technical Center  
Oklahoma City, Okla.

**Arthur D. Little, Inc.**  
Cambridge, Mass.

**Mallory Battery Company**  
Tarrytown, N.Y. (2 memberships)

**Marathon Battery Co.**  
Cold Spring, N.Y.

**The Marstolin Group**  
Hamilton, Bermuda

**Matsushita Electric Industrial Co., Ltd.**  
Osaka, Japan

**Metallurgical Research Center of Iran**  
Teheran, Iran

**Microwave Associates, Inc.**  
Burlington, Mass.

**Molybdenum Corporation of America**  
New York, N.Y.

**Monsanto Company**  
St. Louis, Mo.

**Motorola Inc.**  
Phoenix, Ariz.

**M&T Chemicals Inc.**  
Detroit, Mich.

**National Steel Corp.**  
Weirton, W. Va.

**NL Industries, Inc.**  
New York, N.Y.

**OKI Electric Industry Co., Ltd.**  
Tokyo, Japan

**Olin Corporation**  
Metals Research Laboratories  
New Haven, Conn.

**Owens-Illinois Glass Co.**  
Toledo, Ohio

**The Parker Company**  
Madison Heights, Mich.

**Perkin-Elmer Corp.**  
Norwalk, Conn.

**Phelps Dodge Refining Corp.**  
Maspeth, N.Y.

**Philips Laboratories, Inc.**  
Briarcliff Manor, N.Y.

**PPG Industries, Inc.**  
Chemical Div.  
Pittsburgh, Pa.

**Princeton Applied Research Corp.**  
Princeton, N.J.

**RCA Corporation**  
Color Picture Tube Division  
Lancaster, Pa.

**Reynolds Metals Co.**  
Reduction Research Div.  
Sheffield, Ala.

**Rockwell International**  
El Segundo, Calif.

**SAFT America, Inc.**  
Valdosta, Ga.

**Sandia Laboratories**  
Albuquerque, N. M.

**Signetics Corp.**  
Sunnyvale, Ca.

**Sobin Chemical Co.**  
Orrington, Maine

**Sprague Electric Co.**  
North Adams, Mass.

**Stackpole Carbon Co.**  
St. Marys, Pa.

**Standard Telecommunication  
Laboratories Ltd.**  
Essex, England

**Stauffer Chemical Co.**  
Dobbs Ferry, N.Y.

**Teletype Corp.**  
Skokie, Ill.

**Texas Instruments Inc.**  
Attleboro, Mass.  
Dallas, Texas

**Tokyo Shibaura Electric Co., Ltd.**  
Toshiba Research and  
Development Center  
Kawasaki, Japan

**TRW Systems and Energy**  
Redondo Beach, Calif.

**Udylite Corp.**  
Detroit, Mich. (4 memberships)

**United States Steel Corp.**  
Research Laboratory  
Monroeville, Pa.

**Varian Associates**  
Palo Alto, Calif.

**Wacker Chemitronic**  
Burghausen, Germany

**Xerox Corporation**  
Rochester, N.Y.

**Yardney Electric Division**  
Pawcatuck, Conn.

**Zenith Radio Corp.**  
Chicago, Ill.